Springer Proceedings in Physics 185

Antonio Segalini *Editor*

Proceedings of the 5th International Conference on Jets, Wakes and Separated Flows (ICJWSF2015)

Springer

Springer Proceedings in Physics

Volume 185

The series Springer Proceedings in Physics, founded in 1984, is devoted to timely reports of state-of-the-art developments in physics and related sciences. Typically based on material presented at conferences, workshops and similar scientific meetings, volumes published in this series will constitute a comprehensive up-to-date source of reference on a field or subfield of relevance in contemporary physics. Proposals must include the following:

- name, place and date of the scientific meeting
- a link to the committees (local organization, international advisors etc.)
- scientific description of the meeting
- list of invited/plenary speakers
- an estimate of the planned proceedings book parameters (number of pages/articles, requested number of bulk copies, submission deadline).

More information about this series at http://www.springer.com/series/361

Antonio Segalini
Editor

Proceedings of the 5th International Conference on Jets, Wakes and Separated Flows (ICJWSF2015)

Springer

Editor
Antonio Segalini
Stockholm
Sweden

ISSN 0930-8989 ISSN 1867-4941 (electronic)
Springer Proceedings in Physics
ISBN 978-3-319-30600-1 ISBN 978-3-319-30602-5 (eBook)
DOI 10.1007/978-3-319-30602-5

Library of Congress Control Number: 2016939567

© Springer International Publishing Switzerland 2016
This work is subject to copyright. All rights are reserved by the Publisher, whether the whole or part of the material is concerned, specifically the rights of translation, reprinting, reuse of illustrations, recitation, broadcasting, reproduction on microfilms or in any other physical way, and transmission or information storage and retrieval, electronic adaptation, computer software, or by similar or dissimilar methodology now known or hereafter developed.
The use of general descriptive names, registered names, trademarks, service marks, etc. in this publication does not imply, even in the absence of a specific statement, that such names are exempt from the relevant protective laws and regulations and therefore free for general use.
The publisher, the authors and the editors are safe to assume that the advice and information in this book are believed to be true and accurate at the date of publication. Neither the publisher nor the authors or the editors give a warranty, express or implied, with respect to the material contained herein or for any errors or omissions that may have been made.

Printed on acid-free paper

This Springer imprint is published by Springer Nature
The registered company is Springer International Publishing AG Switzerland

Preface

The 5th International Conference on Jets, Wakes and Separated Flows (ICJWSF2015) took place at KTH, Royal Institute of Technology, Stockholm, for 4 days in June 2015 and was chaired by Prof. Laszlo Fuchs (KTH) and co-chaired by Prof. Ephraim J. Gutmark (University of Cincinnati) and Prof. Tomomi Uchiyama (Nagoya University). More than 160 researchers from 23 countries gathered at KTH to present their latest contributions in fluid dynamic research. At the conference, 135 oral talks were given with an intensive schedule of 34 parallel sessions. This volume consists of 75 papers that were selected after a strict external peer review process. The papers cover several fundamental and applied aspects of fluid dynamics, such as vehicle aerodynamics, particle flows, and unsteady aerodynamics, to cite a few.

The conference had a strong international character with researchers from Japan, USA, UK, France, Sweden, etc. New experimental results were presented together with numerical simulations that, boosted by the continuous growth of computational resources in universities and industries, appear now as a central aspect of fluid dynamic research. New theoretical developments and/or re-analysis of existing datasets were also presented covering several aspects of the broad area embraced by the framework jets, wakes, and separated flows. Many questions have remained unsolved, but new evidences have been discussed providing answers or clues to solve them. A conference like ICJWSF2015 represented indeed an important opportunity to share ideas and observations and to establish new collaborations between researchers. Therefore, this volume is a thermometer of fluid dynamic research activity around the world.

The book is structured so that the contributions are arranged according to their main topic, i.e., jets, wakes, separated flows, vehicle aerodynamics, wall-bounded and confined flows, noise, turbomachinery flows, multiphase and reacting flows, vortex dynamics, energy-related flows, and a section dedicated to numerical analyses. It has to be said that this classification is quite coarse as many of the papers can be easily placed in several of these categories. This is particularly true for

complex flow scenarios that differ from the canonical cases described by jets, wakes, and boundary layers, for instance.

At this point, I would like to thank all the authors who have contributed to the present proceedings and the referees who have provided valuable comments to improve the quality of the manuscripts. Professor Laszlo Fuchs is greatly acknowledged for his role in the organization of the conference, while Nora Noll (Meetagain Konferens AB), Malin Landin, and Cecilia Ljunglöf (KTH) should have all the credits for the practical organization of the event, together with Dr. Giovanni Lacagnina for the help in the scrutiny of the proceedings. I would also like to thank Thomas Ditzinger from Springer for the help and guidance during the production of the present book.



A photograph of the participants to the ICJWSF2015 in the KTH courtyard

Stockholm, Sweden Antonio Segalini

Contents

Part I Jets

Analysis of Vortical Structures in Intermittent Jets 3
Alexander Nygård, Mireia Altimira, Bernhard Semlitsch, Lisa Prahl Wittberg and Laszlo Fuchs

Flow Structure of a Round Jet with Side-Jet Formation 11
Kenta Kawabe and Akinori Muramatsu

Flow and Heat Transfer Features of an Impinging Annular Jet 19
Victor Terekhov, Svetlana Kalinina and Konstantin Sharov

Investigation of the Flow in Free and Impinging Air Micro- and Macrojets 29
Vadim Lemanov, Victor Terekhov and Konstantin Sharov

Numerical Investigation of a Confined Jet Array Penetrating into a Counterflow 37
Etienne Robert and Martin Thomas

Coherent Structures in a Turbulent Swirling Jet Under Vortex Breakdown. 3D PIV Measurements 43
Sergey V. Alekseenko, Vladimir M. Dulin, M.P. Tokarev and Dmitriy M. Markovich

An Effect of Initial Disturbance on Spatial Development of a Two-Dimensional Jet at a Low Reynolds Number 51
Akinori Muramatsu and Hokuto Tsuchiya

Effect of Buoyancy on the Instability of Light Jets and Plumes 61
Ravilla Vamsi Krishna Chakravarthy, Lutz Lesshafft and Patrick Huerre

Direct Numerical Simulation of Dynamic-Rotational Controlled Jet 69
Koichi Tsujimoto, Toma Onodera, Toshihiko Shakouchi and Toshitake Ando

Enhancement of Turbulent Diffusion in an Axisymmetric Jet by Vortex Generators 77
Mamoru Takahashi, Kensuke Miura, Yasuhiko Sakai, Yasumasa Ito, Koji Iwano and Koji Nagata

Diffusion Control of Jet by Acoustically Driven Secondary Film Flow 85
Norimasa Miyagi and Motoaki Kimura

Numerical Simulation of Flow Structure and Heat Transfer in a Swirling Gas-Droplet Turbulent Flow Through a Pipe Expansion 93
Viktor Terekhov and Maksim Pakhomov

The Influence of an Asymmetric Slot on the Flow Characteristics of Synthetic Jets 101
Yusuke Watabe, Kotaro Sato, Koichi Nishibe and Kazuhiko Yokota

Performance Characteristics of a Fan Using Synthetic Jets 109
Tomoaki Ishizawa, Kotaro Sato, Koichi Nishibe and Kazuhiko Yokota

Part II Wakes

Towards Local Isotropy of Higher Order Statistics in Wakes 119
Shunlin Tang, Robert A. Antonia, Lyazid Djenidi, Luminita Danaila, Yu Zhou and Tongming Zhou

Heat Transfer Enhancement by Grid-Generated Turbulence for a Cylinder in Crossflow 125
Gianfrancesco Melina, Paul John Kenneth Bruce, Geoffrey Frederick Hewitt and John Christos Vassilicos

An Experimental Study on the Relation Between the Wake Inlet Conditions and the Near Wake Topology 133
Renzo Trip and Jens H.M. Fransson

Vortex Structure Extraction from Circular Disk Wake by POD and PIV Processing 139
Makoto Aoki, Takao Mizuno, Hikaru Aono and Hitoshi Ishikawa

Influence of Surface Waves on Kármán Street Behind Vertical Cylinder: Subharmonic Lock-in and Phase Synchronizaton 147
Hans Gunnoo, Nizar Abcha, Isabel Garcia-Hermosa, Anne-Claire Bennis and Alexander Ezersky

Organization of an Axisymmetric Turbulent Wake in Presence of a Central Protrusion 157
Valeria Gentile, Ferdinand F.J. Schrijer, Bas W. Van Oudheusden and Fulvio Scarano

Global Linear Stability Analysis of the Flow Around a Superhydrophobic Circular Cylinder 165
Franco Auteri, Marco Carini, Michel Fournié, Dominique Fratantonio and Flavio Giannetti

Optimal Cancelation of Vortex Street in Flow Past a Circular Cylinder with Controllable Wettability Properties 171
Marios E. Mastrokalos, Christos I. Papadopoulos and Lambros Kaiktsis

Numerical Experiment of Flow Characteristics of a Circular Cylinder with Splitter Plate 181
Yoshifumi Yokoi

Wake Structures of a Particle in Straight and Curved Flows 189
Toshiaki Fukada, Shintaro Takeuchi and Takeo Kajishima

Numerical Flow Simulations of a Flexible Plate Attached to an Obstacle in Crossflow 195
Lukas Schickhofer, Bernhard Semlitsch and Mihai Mihăescu

Effect of Chordwise Flexibility on Flapping Wing Aerodynamics 203
Onur Son and Oksan Cetiner

Part III Separated Flows

Characteristics of Recirculation Regions on Ribs of Varying Length 213
Jacques W. Van der Kindere and Bharathram Ganapathisubramani

Passive Load Control in Backward-Facing Step Flow by Using Chevrons 223
Johan Nilsson, Robert-Zoltán Szász, Per-Erik Austrell and Ephraim J. Gutmark

Active Flow Control Behind a Backward Facing Step Using a Zero-Net-Mass-Flux System 231
Umut Can Coskun, Sertac Cadirci and Hasan Gunes

Control of the Reattachment Length of a Transonic 2D Backward-Facing Step Flow 241
Istvan Bolgar, Sven Scharnowski and Christian J. Kähler

POD Analysis of Jet and Vortex Flows Induced by Oscillating Backward Facing Step 249
Sertac Cadirci, Mustafa Ozsipahi and Hasan Gunes

Characterization of the Massively Separated Wake Behind a Square Cylinder by Means of Direct Numerical Simulation 259
Ricardo Vinuesa, Philipp Schlatter and Dan S. Henningson

Investigations on the Effects of Trip Wires on the Performances of a Rectangular Wing 267
Gabriele Capuano and Giovanni Paolo Romano

Part IV Vehicle Aerodynamics

Comparison of Synthetic and Pulsed Jets Effect for the Flow Around the Ahmed Body 277
Stéphie Edwige, Yoann Eulalie, Philippe Gilotte and Iraj Mortazavi

Large Eddy Simulations of Flow Around Two Generic Vehicles in a Platoon 283
Maryam Mirzaei and Siniša Krajnović

Numerical Study of Aerodynamic Interactions in a Homogeneous Multi-vehicle Formation 289
Maryam Mirzaei and Siniša Krajnović

Numerical Investigation of the Actuated Flow on a Bluff Body 295
Guglielmo Minelli and Siniša Krajnović

Part V Wall-Bounded and Confined Flows

Breakdown of a Low-Speed Streak Caused by Turbulent Fluctuations 305
Huy Quang Ho, Masahito Asai and Shohei Takagi

Advection of a Coherent Structure in a Turbulent Boundary Layer 311
Masaharu Matsubara, Masanari Nagasaki, Akihito Yokoi and Muhammad Azmeer

Wall Similarity in Turbulent Boundary Layers Subjected to Weak Pressure Gradients 317
Shinsuke Mochizuki, Hiroki Suzuki, Hitoshi Tokunaga and Takatsugu Kameda

Interaction Layer Between a Turbulent Boundary Layer and Free-Stream Turbulence 325
R. Jason Hearst, Eda Dogan and Bharathram Ganapathisubramani

Generalization of the Diagnostic Plot to Higher-Order Moments in Turbulent Boundary Layers 333
Ramis Örlü, Antonio Segalini, Joseph Klewicki and P. Henrik Alfredsson

Experimental and Analytical Investigation of Forest Clearings 339
Antonio Segalini

Flow and Heat Transfer of Petal Shaped Double Tube—Effects of Pipe Geometry 347
Toshihiko Shakouchi, Ryosuke Ozawa, Fumi Iwasaki, Koichi Tsujimoto and Toshitake Ando

Loss Reduction of the Flow in the Reducing Elbow Duct by Using Weir Shaped Small Obstacle 355
Toshitake Ando, Toshihiko Shakouchi, Atsushi Hanai and Koichi Tsujimoto

Flow Field Characteristics and Energy Injection in a Tank Stirred by Regular and Fractal Blade Impellers. 363
Konstantinos Steiros, Paul John Kenneth Bruce, Oliver R.H. Buxton and John Christos Vassilicos

Part VI Noise

Numerical Study on the Sound Amplification of a T-Junction with Bias Flow 373
Lin Du, Mikael Karlsson and Mats Åbom

Experiments on Sound Radiation in Flow Past Two Side-by-Side Square Cylinders 383
Ressa Octavianty and Masahito Asai

Turbulent Jet Noise Simulation and Propagation Using a 3rd Order MUSCL/CD Scheme on Unstructured Grid and Ffowcs-Williams Hawkings 389
Mirela Caraeni, Alastair West and Doru Caraeni

Investigation of the Effect of a Realistic Nozzle Geometry on the Jet Development. 399
Mehmet Onur Cetin, Matthias Meinke and Wolfgang Schröder

Linear Stability Analyses and Large Eddy Simulations for Acoustic Wave Generation Mechanism of a Transitional Supersonic Jet 407
Taku Nonomura and Kozo Fujii

Can Jet Noise Be Predicted Using Linear Instability Wavepackets?. . . . 413
Onofrio Semeraro, Lutz Lesshafft and Richard D. Sandberg

Part VII Turbomachinery Flows

A Numerical Model of Fluid Structure Interaction of a Fluttering Valve 421
Umut Can Coskun, Hasan Gunes and Kemal Sarioglu

Capacity Testing and Local Flow Analysis of Geometrically Complex Trims Installed Within a Commercial Control Valve 431
Taimoor Asim, Rakesh Mishra, Matthew Charlton and Antonio Carlos Oliveira

Wall Treatment Effects on the Heat Transfer in a Radial Turbine Turbocharger 439
Shyang Maw Lim, Anders Dahlkild and Mihai Mihăescu

On the Characteristics of the Jet in Film Cooling Applications 449
Hossein Nadali Najafabadi, Arman Farhanieh, Roland Gårdhagen and Matts Karlsson

Similarities and Differences Concerning Flow Characteristics in Centrifugal Compressors of Different Size 457
Elias Sundström, Bernhard Semlitsch and Mihai Mihăescu

Part VIII Multiphase and Reacting Flows

Study of Liquid Breakup Mechanism Through a High-Speed Gas Flow 467
Ryoichi S. Amano and Yi-Hsin Yen

Clustering and Settling of Inertial Particles in Turbulence 475
Sholpan Sumbekova, Alberto Aliseda, Alain Cartellier and Mickael Bourgoin

On Mechanics of Turbulent Gas-Liquid Flows 483
Alexander V. Gorin

Film Behavior of Two-Phase Flow in a Horizontal Pipe with a Sudden Contraction 493
Takahiro Fujimatsu, Mizuki Kito and Kunikazu Kondo

Some Aspects of Design and Modelling of Multi-phase Separation Process in Complex Channels Under Magnetic Fields 501
Maxim Kireitseu

Tire Water Splash Modeling 509
Dragos Moroianu and Alper Cesur

Algorithm for Automatic Quantification of Flashback and Flash Forward Events from High-Speed Chemiluminescence Recordings 519
Robert-Zoltăn Szăsz, Arman Ahmed Subash, Andreas Lantz, Robert Collin, Laszlo Fuchs and Ephraim J. Gutmark

Effect of Grouping of Fuel Droplets on a Flame Formed by an Oscillating Spray Jet 527
David Katoshevski and J.B. Greenberg

Influence of Coaxial Dielectric Barrier Discharge Plasma Actuator on Jet Flame 537
Jun Asakura and Motoaki Kimura

Part IX Vortex Dynamics

Vortex Rings Formed Behind a Free-Flight Butterfly and Their Dynamic Behaviors 547
Masaki Fuchiwaki and Kazuhiro Tanaka

Experimental and Computational Observation of Air Bubble Ring Due to Plughole Vortex 555
Rayhan Ahmed and HeeChang Lim

Penetration by a Negatively Buoyant Vortex Ring 565
Takashi Naitoh, Nobuyuki Okura, Tomomi Tanaka and Fumihito Goto

Part X Energy-Related Flows

Development of Near Wake of a HAWT Depending on Hub Height 573
Ivan Dobrev and Fawaz Massouh

Leading Edge Vortex Development on Pitching and Surging Airfoils: A Study of Vertical Axis Wind Turbines 581
Reeve Dunne, Hsieh-Chen Tsai, Tim Colonius and Beverley J. McKeon

Performance Comparison of a Vertical Axis Wind Turbine Using Commercial and Open Source Computational Fluid Dynamics Based Codes 589
Taimoor Asim, Rakesh Mishra, Sree Nirjhor Kaysthagir and Ghada Aboufares

Measurement and Control of Forces Acting on a Solar Panel 595
Yuta Ikeya, Koji Fukagata, Noriaki Ichijo, Masakazu Hasegawa and Shinsuke Matsuno

Part XI Numerical Analyses

Two- and Three-Dimensional Numerical Analysis for Flow Field Characteristics at Various Low Reynolds Numbers 603
Donghwi Lee, Taku Nonomura, Akira Oyama and Kozo Fujii

Increasing the Critical Reynolds Number by Maximizing Energy Dissipation Problem 613
Takashi Nakazawa

Contributors

Nizar Abcha Morphodynamique Continentale et Côtière, UMR6143, CNRS, Normandie Université, UNICAEN, Caen, France

Mats Åbom The Marcus Wallenberg Laboratory for Sound and Vibration Research, KTH-CCGEx, KTH-FLOW, Stockholm, Sweden

Ghada Aboufares University of Huddersfield, Huddersfield, UK

Rayhan Ahmed School of Mechanical Engineering, Pusan National University, Busan, South Korea

Sergey V. Alekseenko Kutateladze Institute of Thermophysics, Siberian Branch of RAS, Novosibirsk, Russia; Novosibirsk State University, Novosibirsk, Russia

P. Henrik Alfredsson Linné FLOW Centre, KTH Mechanics, Stockholm, Sweden

Alberto Aliseda Department of Mechanical Engineering, University of Washington, Seattle, WA, USA

Mireia Altimira Division of Fluid Mechanics, Lund University, Lund, Sweden

Ryoichi S. Amano Mechanical Engineering, University of Wisconsin Milwaukee, Milwaukee, WI, USA

Toshitake Ando Division of Mechanical Engineering, Graduate School of Engineering, Mie University, Tsu-shi, Mie, Japan

Robert A. Antonia School of Engineering, University of Newcastle, Newcastle, NSW, Australia

Makoto Aoki Tokyo University of Science, Katsushika-ku, Tokyo, Japan

Hikaru Aono Tokyo University of Science, Katsushika-ku, Tokyo, Japan

Masahito Asai Department of Aerospace Engineering, Tokyo Metropolitan University, Hino, Tokyo, Japan

Jun Asakura Nihon University, Tokyo, Japan

Taimoor Asim University of Huddersfield, Huddersfield, UK

Per-Erik Austrell Division of Structural Mechanics, Lund University, Lund, Sweden

Franco Auteri Dipartimento di Scienze e Tecnologie Aerospaziali, Politecnico di Milano, Milan, Italy

Muhammad Azmeer Shinshu University, 4-17-1 Wakasato, Nagano, Japan

Anne-Claire Bennis Morphodynamique Continentale et Côtière, UMR6143, CNRS, Normandie Université, UNICAEN, Caen, France

Istvan Bolgar Bundeswehr University Munich, Neubiberg, Germany

Mickael Bourgoin Physics Laboratory, CNRS/ENS de Lyon, Lyon, France

Paul John Kenneth Bruce Department of Aeronautics, Imperial College, London, UK

Oliver R.H. Buxton Department of Aeronautics, Imperial College, London, UK

Sertac Cadirci Department of Mechanical Engineering, Istanbul Technical University, Istanbul, Turkey

Gabriele Capuano Department of Mechanical and Aerospace Engineering, University La Sapienza, Rome, Italy

Doru Caraeni CD-adapco, Lebanon, USA

Mirela Caraeni CD-adapco, Lebanon, USA

Marco Carini Institut de Mécanique des Fluides de Toulouse, Toulouse, France

Alain Cartellier LEGI, CNRS/Université Grenoble Alpes, Grenoble cedex 09, France

Alper Cesur Volvo Cars, Gothenburg, Sweden

Mehmet Onur Cetin Institute of Aerodynamics, RWTH Aachen University, Aachen, Germany

Oksan Cetiner Department of Astronautical Engineering, Istanbul Technical University, Maslak, Istanbul, Turkey

Ravilla Vamsi Krishna Chakravarthy LadHyX, Ecole Polytechnique, Palaiseau, France

Matthew Charlton Weir Valves & Controls UK Ltd, Elland, UK

Robert Collin Department of Physics, Lund University, Lund, Sweden

Tim Colonius California Institute of Technology, Pasadena, CA, USA

Umut Can Coskun Department of Mechanical Engineering, Istanbul Technical University, Istanbul, Turkey

Anders Dahlkild Competence Center for Gas Exchange (CCGEx), KTH Royal Institute of Technology, Stockholm, Sweden

Luminita Danaila CORIA CNRS UMR 6614, Université de Rouen, Saint Etienne du Rouvray, France

Lyazid Djenidi School of Engineering, University of Newcastle, Newcastle, NSW, Australia

Ivan Dobrev DynFluid, ENSAM, Paris, France

Eda Dogan Engineering and the Environment, University of Southampton, Southampton, UK

Lin Du The Marcus Wallenberg Laboratory for Sound and Vibration Research, KTH-CCGEx, KTH-FLOW, Stockholm, Sweden

Vladimir M. Dulin Kutateladze Institute of Thermophysics, Siberian Branch of RAS, Novosibirsk, Russia; Novosibirsk State University, Novosibirsk, Russia

Reeve Dunne California Institute of Technology, Pasadena, CA, USA

Stéphie Edwige CNRS, Institut de Mathématiques de Bordeaux, Bordeaux, France

Yoann Eulalie Auto Exterior Division, Plastic Omnium, Lyon, France

Alexander Ezersky Morphodynamique Continentale et Côtière, UMR6143, CNRS, Normandie Université, UNICAEN, Caen, France

Arman Farhanieh Department of Management and Engineering, Linköping University, Linköping, Sweden

Michel Fournié Institut de Mathématiques de Toulouse, Université Paul Sabatier, Toulouse, France

Jens H.M. Fransson Linné Flow Centre, KTH Royal Institute of Technology, Stockholm, Sweden

Dominique Fratantonio Dipartimento di Scienze e Tecnologie Aerospaziali, Politecnico di Milano, Milan, Italy

Masaki Fuchiwaki Kyushu Institute of Technology, Iizuka, Japan

Laszlo Fuchs Department of Mechanics, KTH, Stockholm, Sweden

Kozo Fujii Japan Aerospace Exploration Agency, Institute of Space and Astronautical Science, Sagamihara, Japan

Takahiro Fujimatsu Department of Mechanical Engineering, National Institute of Technology, Suzuka College Shirokocho, Suzuka, Mie, Japan

Toshiaki Fukada Department of Mechanical Engineering, Osaka University, Osaka, Japan

Koji Fukagata Keio University, Kohoku-ku, Yokohama, Japan

Bharathram Ganapathisubramani Engineering and the Environment, University of Southampton, Southampton, UK

Isabel Garcia-Hermosa Morphodynamique Continentale et Côtière, UMR6143, CNRS, Normandie Université, UNICAEN, Caen, France

Roland Gårdhagen Department of Management and Engineering, Linköping University, Linköping, Sweden

Valeria Gentile Delft University of Technology, Delft, The Netherlands

Flavio Giannetti Dipartimento di Ingegneria Industriale, Università degli Studi di Salerno, Fisciano, Italy

Philippe Gilotte Auto Exterior Division, Plastic Omnium, Lyon, France

Alexander V. Gorin Swinburne University of Technology, Sarawak Campus, Sarawak, Kuching, Malaysia

Fumihito Goto Nagoya Institute of Technology, Showa-ku, Nagoya, Japan

J.B. Greenberg Faculty of Aerospace Engineering, Technion-I.I.T, Haifa, Israel

Hasan Gunes Department of Mechanical Engineering, Istanbul Technical University, Istanbul, Turkey

Hans Gunnoo Morphodynamique Continentale et Côtière, UMR6143, CNRS, Normandie Université, UNICAEN, Caen, France

Ephraim J. Gutmark Department of Aerospace Engineering and Engineering Mechanics, University of Cincinnati, Cincinnati, OH, USA

Atsushi Hanai Graduate School of Engineering, Mie University, Tsu-shi, Mie, Japan

Masakazu Hasegawa IHI Corporation, Isogo-ku, Yokohama, Japan

R. Jason Hearst Engineering and the Environment, University of Southampton, Southampton, UK

Dan S. Henningson Linné FLOW Centre, KTH Mechanics, Stockholm, Sweden

Geoffrey Frederick Hewitt Department of Chemical Engineering, Imperial College London, London, UK

Huy Quang Ho Department of Aerospace Engineering, Tokyo Metropolitan University, Hino, Tokyo, Japan

Patrick Huerre LadHyX, Ecole Polytechnique, Palaiseau, France

Noriaki Ichijo IHI Corporation, Isogo-ku, Yokohama, Japan

Yuta Ikeya Keio University, Kohoku-ku, Yokohama, Japan

Hitoshi Ishikawa Tokyo University of Science, Katsushika-ku, Tokyo, Japan

Tomoaki Ishizawa Graduate School of Mechanical Engineering, Kogakuin University, Shinjuku-ku, Tokyo, Japan

Yasumasa Ito Department of Mechanical Science and Engineering, Nagoya University, Nagoya, Japan

Koji Iwano Department of Mechanical Science and Engineering, Nagoya University, Nagoya, Japan

Fumi Iwasaki Graduate School of Engineering, Mie University, Tsu-shi, Mie, Japan

Christian J. Kähler Bundeswehr University Munich, Neubiberg, Germany

Lambros Kaiktsis Department of Naval Architecture and Marine Engineering, National Technical University of Athens, Athens, Greece; Department of Mechanical Engineering, Khalifa University of Science, Technology and Research, Abu Dhabi, United Arab Emirates

Takeo Kajishima Department of Mechanical Engineering, Osaka University, Osaka, Japan

Svetlana Kalinina Kutateladze Institute of Thermophysics of SB of RAS, Novosibirsk, Russia

Takatsugu Kameda Faculty of Engineering, Kinki University, Higashi Hiroshima, Japan

Matts Karlsson Department of Management and Engineering, Linköping University, Linköping, Sweden

Mikael Karlsson The Marcus Wallenberg Laboratory for Sound and Vibration Research, KTH-CCGEx, KTH-FLOW, Stockholm, Sweden

David Katoshevski Department of Environmental Engineering, Ben-Gurion University of the Negev, Beer-sheva, Israel

Kenta Kawabe Graduate School of Science and Technology, Nihon University, Tokyo, Japan

Sree Nirjhor Kaysthagir University of Huddersfield, Huddersfield, UK

Motoaki Kimura College of Science and Technology, Nihon University, Chiyoda-ku, Tokyo, Japan

Maxim Kireitseu Aerospace Faculty, Department of Structural Integrity and Composites, Delft University of Technology, Delft, The Netherlands

Mizuki Kito Department of Mechanical Engineering, National Institute of Technology, Suzuka College Shirokocho, Suzuka, Mie, Japan

Joseph Klewicki Department of Mechanical Engineering, University of New Hampshire, Durham, NH, USA; Department of Mechanical Engineering, University of Melbourne, Parkville, VIC, Australia

Kunikazu Kondo Department of Mechanical Engineering, National Institute of Technology, Suzuka College Shirokocho, Suzuka, Mie, Japan

Sinia Krajnović Division of Fluid Dynamics, Department of Applied Mechanics, Chalmers University of Technology, Gothenburg, Sweden

Andreas Lantz Department of Physics, Lund University, Lund, Sweden

Donghwi Lee Department of Aeronautics and Astronautics, University of Tokyo, Tokyo, Japan

Vadim Lemanov Kutateladze Institute of Thermophysics of SB of RAS, Novosibirsk, Russia

Lutz Lesshafft LadHyX, Ecole polytechnique, Palaiseau, France

HeeChang Lim School of Mechanical Engineering, Pusan National University, Busan, South Korea

Shyang Maw Lim Competence Center for Gas Exchange (CCGEx), KTH Royal Institute of Technology, Stockholm, Sweden

Dmitriy M. Markovich Kutateladze Institute of Thermophysics, Siberian Branch of RAS, Novosibirsk, Russia; Novosibirsk State University, Novosibirsk, Russia

Fawaz Massouh DynFluid, ENSAM, Paris, France

Marios E. Mastrokalos Department of Naval Architecture and Marine Engineering, National Technical University of Athens, Athens, Greece

Masaharu Matsubara Shinshu University, 4-17-1 Wakasato, Nagano, Japan

Shinsuke Matsuno IHI Corporation, Isogo-ku, Yokohama, Japan

Beverley J. McKeon California Institute of Technology, Pasadena, CA, USA

Matthias Meinke Institute of Aerodynamics, RWTH Aachen University, Aachen, Germany; Forschungszentrum Jülich, JARAHigh-Performance Computing, Jülich, Germany

Gianfrancesco Melina Aeronautics, Imperial College London, London, UK

Mihai Mihăescu Competence Center for Gas Exchange (CCGEx), BioMEx, Department of Mechanics, KTH Royal Institute of Technology, Stockholm, Sweden

Guglielmo Minelli Division of Fluid Dynamics, Chalmers University of Technology, Gothenburg, Sweden

Maryam Mirzaei Division of Fluid Dynamics, Department of Applied Mechanics, Chalmers University of Technology, Gothenburg, Sweden

Rakesh Mishra University of Huddersfield, Huddersfield, UK

Kensuke Miura Department of Mechanical Science and Engineering, Nagoya University, Nagoya, Japan

Norimasa Miyagi Junior Collage of Nihon University, Funabashi-City, Chiba, Japan

Takao Mizuno Tokyo University of Science, Katsushika-ku, Tokyo, Japan

Shinsuke Mochizuki Graduate School of Science and Engineering, Yamaguchi University, Ube, Japan

Dragos Moroianu Volvo Cars, Gothenburg, Sweden

Iraj Mortazavi M2N, Conservatoire National des Arts et Métiers, Paris, France

Akinori Muramatsu College of Science and Technology, Nihon University, Funabashi, Chiba, Japan

Hossein Nadali Najafabadi Department of Management and Engineering, Linköping University, Linköping, Sweden

Masanari Nagasaki Shinshu University, 4-17-1 Wakasato, Nagano, Japan

Koji Nagata Department of Mechanical Science and Engineering, Nagoya University, Nagoya, Japan

Takashi Naitoh Nagoya Institute of Technology, Showa-ku, Nagoya, Japan

Takashi Nakazawa Tohoku University, Sendai, Japan

Johan Nilsson Division of Structural Mechanics, Lund University, Lund, Sweden

Koichi Nishibe Department of Mechanical Engineering, Tokyo City University, Setagaya-ku, Tokyo, Japan

Taku Nonomura Japan Aerospace Exploration Agency, Institute of Space and Astronautical Science, Sagamihara, Japan

Alexander Nygård Department of Mechanics, KTH, Stockholm, Sweden

Ressa Octavianty Department of Aerospace Engineering, Tokyo Metropolitan University, Hino, Tokyo, Japan

Nobuyuki Okura Meijo University, Tempaku-ku, Nagoya, Japan

Antonio Carlos Oliveira Weir Valves & Controls UK Ltd, Elland, UK

Toma Onodera Division of Mechanical Engineering, Graduate School of Engineering, Mie University, Mie, Japan

Ramis Örlü Linné FLOW Centre, KTH Mechanics, Stockholm, Sweden

Akira Oyama Institute of Space and Astronautical Science, JAXA, Tokyo, Japan

Ryosuke Ozawa Graduate School of Engineering, Mie University, Tsu-shi, Mie, Japan

Mustafa Ozsipahi Department of Mechanical Engineering, Istanbul Technical University, Istanbul, Turkey

Maksim Pakhomov Laboratories of Thermal and Gas Dynamics, Kutateladze Institute of Thermophysics of SB of RAS, Novosibirsk, Russia

Christos I. Papadopoulos Department of Naval Architecture and Marine Engineering, National Technical University of Athens, Athens, Greece

Etienne Robert Polytechnique Montréal, Montreal, QC, Canada

Giovanni Paolo Romano Department of Mechanical and Aerospace Engineering, University La Sapienza, Rome, Italy

Yasuhiko Sakai Department of Mechanical Science and Engineering, Nagoya University, Nagoya, Japan

Richard D. Sandberg University of Southampton, Southampton, UK

Kemal Sarioglu Arcelik Research and Development Center, Tuzla, Istanbul, Turkey

Kotaro Sato Department of Mechanical Engineering, Kogakuin University, Shinjuku-ku, Tokyo, Japan

Fulvio Scarano Delft University of Technology, Delft, The Netherlands

Sven Scharnowski Bundeswehr University Munich, Neubiberg, Germany

Lukas Schickhofer BioMEx, Department of Mechanics, KTH Royal Institute of Technology, Stockholm, Sweden

Philipp Schlatter Linné FLOW Centre, KTH Mechanics, Stockholm, Sweden

Ferdinand F.J. Schrijer Delft University of Technology, Delft, The Netherlands

Wolfgang Schröder Institute of Aerodynamics, RWTH Aachen University, Aachen, Germany; Forschungszentrum Jülich, JARAHigh-Performance Computing, Jülich, Germany

Antonio Segalini Linné FLOW Centre, KTH Mechanics, Stockholm, Sweden

Onofrio Semeraro LIMSICNRS, Orsay, France

Bernhard Semlitsch Department of Mechanics, Linné FLOW Centre and Competence Center for Gas Exchange (CCGEx), KTH Royal Institute of Technology, Stockholm, Sweden

Toshihiko Shakouchi Division of Mechanical Engineering, Graduate School of Engineering, Mie University, Tsu-shi, Mie, Japan

Konstantin Sharov Kutateladze Institute of Thermophysics of SB of RAS, Novosibirsk, Russia

Onur Son Department of Astronautical Engineering, Istanbul Technical University, Maslak, Istanbul, Turkey

Konstantinos Steiros Department of Aeronautics, Imperial College, London, UK

Arman Ahmed Subash Department of Physics, Lund University, Lund, Sweden

Sholpan Sumbekova LEGI, CNRS/Université Grenoble Alpes, Grenoble cedex 09, France

Elias Sundström Department of Mechanics, Linné FLOW Centre and Competence Center for Gas Exchange (CCGEx), KTH Royal Institute of Technology, Stockholm, Sweden

Hiroki Suzuki Graduate School of Science and Engineering, Yamaguchi University, Ube, Japan

Robert-Zoltán Szász Department of Energy Sciences, Division of Fluid Mechanics, Lund University, Lund, Sweden

Shohei Takagi Department of Aerospace Engineering, Tokyo Metropolitan University, Hino, Tokyo, Japan

Mamoru Takahashi Department of Mechanical Science and Engineering, Nagoya University, Nagoya, Japan

Shintaro Takeuchi Department of Mechanical Engineering, Osaka University, Osaka, Japan

Kazuhiro Tanaka Kyushu Institute of Technology, Iizuka, Japan

Tomomi Tanaka Nagoya Institute of Technology, Showa-ku, Nagoya, Japan

Shunlin Tang Shenzhen Graduate School, Institute for Turbulence-Noise-Vibration Interaction and Control, Shenzhen, People's Republic of China; School of Engineering, University of Newcastle, Newcastle, NSW, Australia

Viktor Terekhov Laboratories of Thermal and Gas Dynamics, Kutateladze Institute of Thermophysics of SB of RAS, Novosibirsk, Russia

Martin Thomas Polytechnique Montréal, Montreal, Québec, Canada

M.P. Tokarev Kutateladze Institute of Thermophysics, Siberian Branch of RAS, Novosibirsk, Russia; Novosibirsk State University, Novosibirsk, Russia

Hitoshi Tokunaga Graduate School of Science and Engineering, Yamaguchi University, Ube, Japan

Renzo Trip Linné Flow Centre, KTH Royal Institute of Technology, Stockholm, Sweden

Hsieh-Chen Tsai California Institute of Technology, Pasadena, CA, USA

Hokuto Tsuchiya Graduate School of Science and Technology, Nihon University, Funabashi, Japan

Koichi Tsujimoto Division of Mechanical Engineering, Graduate School of Engineering, Mie University, Tsu-shi, Mie, Japan

Bas W. Van Oudheusden Delft University of Technology, Delft, The Netherlands

Jacques W. Van der Kindere University of Southampton, Southampton, UK

John Christos Vassilicos Department of Aeronautics, Imperial College, London, UK

Ricardo Vinuesa Linné FLOW Centre, KTH Mechanics, Stockholm, Sweden

Yusuke Watabe Graduate School of Mechanical Engineering, Kogakuin University, Shinjuku-ku, Tokyo, Japan

Alastair West CD-adapco, London, UK

Lisa Prahl Wittberg Department of Mechanics, KTH, Stockholm, Sweden

Yi-Hsin Yen Mechanical Engineering, University of Wisconsin Milwaukee, Milwaukee, WI, USA

Akihito Yokoi Shinshu University, 4-17-1 Wakasato, Nagano, Japan

Yoshifumi Yokoi Department of Mechanical Engineering, National Defense Academy of Japan, Yokosuka, Kanagawa, Japan; Chair of Fluid Dynamics, Techniche Universität Berlin, Berlin, Germany

Kazuhiko Yokota Department of Mechanical Engineering, Aoyama Gakuin University, Chuo-ku, Sagamihara-shi, Kanagawa, Japan

Tongming Zhou School of Civil, Environmental and Mining Engineering, University of Western Australia, Crawley, WA, Australia

Yu Zhou Shenzhen Graduate School, Institute for Turbulence-Noise-Vibration Interaction and Control, Shenzhen, People's Republic of China

Part I
Jets

Analysis of Vortical Structures in Intermittent Jets

Alexander Nygård, Mireia Altimira, Bernhard Semlitsch, Lisa Prahl Wittberg and Laszlo Fuchs

Abstract The manipulation of jets has since long been subject to research, due to the wide range of industrial applications in which they are used. A vast number of numerical and experimental studies concerning the physics of the breakup process of continuous jets have been published. Improvements in mixing and ambient gas entrainment have been reported experimentally when using intermittent injection, although the responsible mechanisms have not yet been completely revealed. This work presents a systematic analysis of the mechanisms of jet breakup and mixing with the surrounding fluid and its relation to vorticity generation and transport. Comparisons are made between the redistribution of vorticity and the engulfment of ambient fluid into the core region for different injection strategies.

1 Introduction

Jets have been used in engineering applications for more than a century. The implemented technology spans a wide range of configurations and operating conditions and can be found in different devices such as carburetors, ink jet printers and engines. Due to this interest, a large number of works have been devoted to the study of the mechanisms that control the mixing of the jet. An example where jet control is highly

A. Nygård (✉) · B. Semlitsch · L.P. Wittberg · L. Fuchs
Department of Mechanics, KTH, Stockholm, Sweden
e-mail: alexander@mech.kth.se

B. Semlitsch
e-mail: bernhard@mech.kth.se

L.P. Wittberg
e-mail: prahl@mech.kth.se

L. Fuchs
e-mail: lf@mech.kth.se

M. Altimira
Division of Fluid Mechanics, Lund University, Lund, Sweden
e-mail: mireia.altimira@energy.lth.se

© Springer International Publishing Switzerland 2016

A. Segalini (ed.), *Proceedings of the 5th International Conference on Jets, Wakes and Separated Flows (ICJWSF2015)*,
Springer Proceedings in Physics 185, DOI 10.1007/978-3-319-30602-5_1

desirable is fuel injection in internal combustion (IC) engines. In this case, the jet is highly confined in space and required to mix with its gaseous surroundings in a short time. During this process, ambient fluid is entrained into the jet and key flow features develop close to the orifice [1], although details of the responsible mechanisms can not be captured experimentally under realistic flow conditions. However, it has been shown numerically that improvements in mixing can be achieved by using intermittent injection. Benefits have also been confirmed by practical tests, where the injection strategy variation shows significant influence in terms of emissions control for IC-engines [2]. However, the link between measured results and changes in the spray formation dynamics is not yet well understood. This emphasizes the need for further investigation by an accurate approach able to resolve the flow structures generated. The present paper studies numerically the flow in the near-nozzle region during time-dependent injection of a confined jet. Analysis is performed of the breakup under different injection conditions, specifically targeting the role of vorticity redistribution in jet breakup.

2 Methods

A jet is intermittently introduced with the injection velocity U_{inj} through a circular inlet of diameter D. The nozzle velocity profile has a top hat shape during injection and the fluid in the domain is initially quiescent. The computational domain consists of an elongated box of dimensions $17D \times 8D \times 8D$ in the streamwise and two perpendicular directions, respectively. Our simulations use a high-order, staggered, finite difference approach based on implicit Large Eddy Simulations. The fluids are modeled as immiscible and incompressible and tracking of the jet fluid is handled by the Volume of Fluid (VOF) method. An additional equation for the volume fraction variable α is solved for, representing the local volume fraction of jet fluid to ambient fluid in each cell. By its implementation, the framework supports the transport of fluids with different properties as a one-fluid approach. Formally, local density and viscosity at the interface (where $0 < \alpha < 1$) are computed by weighting, according to

$$\phi = \alpha\phi_{jet} + (1 - \alpha)\phi_{amb} \tag{1}$$

where ϕ denotes the derived value at the interface, while ϕ_{jet} and ϕ_{amb} denote the corresponding property of the jet and ambient fluid, respectively. However, since the work of this paper approximates single-phase injection, the properties of both fluids are in this case equal. Further details on the numerical framework can be found in [3]. All cases are run with an injection Reynolds number of 9300. The gaseous Weber number describes the relative strength of inertial forces to surface tension and is defined as

$$We_g = \frac{\rho_g U_{inj}^2 D}{\sigma} \tag{2}$$

The density ratio between the jet and ambient fluid is unity, with $We_g = 10^8$, resembling the single-phase condition with low mass diffusivity. The injection durations used are $2.5D/U_{inj}$, $5D/U_{inj}$ and $10D/U_{inj}$ for Cases A, B and C, respectively. In between injections, the velocity at the inlet is zero. The non-injection duration matches the injection duration for each of the cases.

3 Results

As injection is started, the jet fluid deforms into a mushroom shape at the jet front. For similar conditions, it has been found that vorticity generated during injection organizes into a single vortex ring, below a certain injection duration [4]. Past this point, called the *formation number*, vorticity generated from injection will remain external to the ring. When the injection velocity is constant, this limit corresponds to an injection duration of $3.8D/U_{inj}$. Considering the three cases in this study, we see that Case A has an injection duration below this value. Cases B and C on the other hand exceed it, which implies the formation of trailing vortices.

As stated previously, we seek to assess the relative strength of different contributions to vorticity redistribution. To make such a comparison, we start from the vorticity transport equation, which under the current conditions (incompressible fluids of equal density) simplifies to

$$\frac{D\omega_i}{Dt} = \omega_j \frac{\partial u_i}{\partial x_j} + \nu \frac{\partial^2 \omega_i}{\partial x_j \partial x_j}. \tag{3}$$

The transient and convective terms represented by the material derivative on the left hand side are balanced by the vortex stretching and viscous terms on the right hand side. In the following section we investigate the specific mechanisms driving the vorticity transfer in between components. To do so, we look at the radial and axial components of the expanded vortex stretching term of (3), assuming axial symmetry. Below, the expressions (4) and (5) describe the change of the axial and radial components of the vortex stretching term, respectively. The different terms are numbered 1-6 for later reference.

$$\left[\underbrace{\omega_r \left(\frac{\partial u_z}{\partial r} \right)}_{1} + \underbrace{\omega_\theta \left(\frac{\partial u_z}{r \partial \theta} \right)}_{2} + \underbrace{\omega_z \left(\frac{\partial u_z}{\partial z} \right)}_{3} \right] \mathbf{e}_z \tag{4}$$

$$\left[\underbrace{\omega_r\left(\frac{\partial u_r}{\partial r}\right)}_{4}+\underbrace{\omega_\theta\left(\frac{\partial u_r}{r\partial\theta}\right)}_{5}+\underbrace{\omega_z\left(\frac{\partial u_r}{\partial z}\right)}_{6}+\underbrace{\frac{\omega_\theta u_\theta}{r}}_{7}\right]\mathbf{e}_r \tag{5}$$

Figure 1 shows a comparison for Case C, between the individual terms included in (5) and (4) as a function of the axial distance from the inlet. A visualization of the vorticity development is shown to the left, where isosurfaces of the jet fluid distribution and each vorticity component magnitude are rendered. A number of vortical structures have been marked by roman numbers for reference. The plots to the right compare the relative size of the terms in the radial direction (the last term is small and is disregarded in the plot for clarity).

In the top plots, the first injection has nearly completed and several distinct structures can be observed. A strong leading vortex ring (I) has been formed at the front and vorticity is partially collecting into coherent flow structures in the trailing region. The induced rotational motion accelerates the jet fluid in the center of the vortex ring. Due to continuity, the jet column is narrowed at the acceleration zone. At the location where the recirculated flow from the leading vortex ring meets the trailing jet column, a restriction is generated which causes a deceleration and diverts the trailing flow outwards. Subsequently, owing to the acceleration and deceleration phase pairs, additional vortex rings (II-V) are generated along the trailing jet. The strongest peaks of the vortex stretching terms all coincide with the location of the vortex rings. The plots to the right show that the leading ring transfers vorticity into the other directions. However, at this time the transfer rate is significantly larger in the trailing region, especially $1.5D$ behind the ring where the first trailing ring (II) is strongly deformed. As it destabilizes and deforms, the flow tilting and stretching caused by the strong velocity gradient behind (I), leads to the growth of radial and axial vorticity. The cross-section integral of terms i, is denoted Ni, and evaluated as a function of z/D. The relative orientation of (I) and (II) raises N_1 and N_2 more than N_4 and N_5, at the time depicted. The net effect is a larger gain of vorticity into the axial component at this location. The presence of small axial and radial structures originating from (II), can be seen at $z/D \approx 3$. These play an important role in the interaction that follows shortly after.

In the center row plots, the injection has been cut off. Ring (I) now displays a wavy pattern and the trailing structures have changed shape and orientation. Long streaks originating from the radial and axial parts of (II) have formed as a result of the strong contraction region behind (I). Structure (III) remains in a ring-like shape and have convected the trailing ends of streaks (II) outward, while at the same time engulfed ring (IV). The deforming action from the streaks (II) onto (I) increases the transfer rate at the leading region, which can be seen in both N_2 and N_5. The rise in N_3 comes from the extensional flow created by (I), which in return amplifies the streaks (II) as they approach the center of (I).

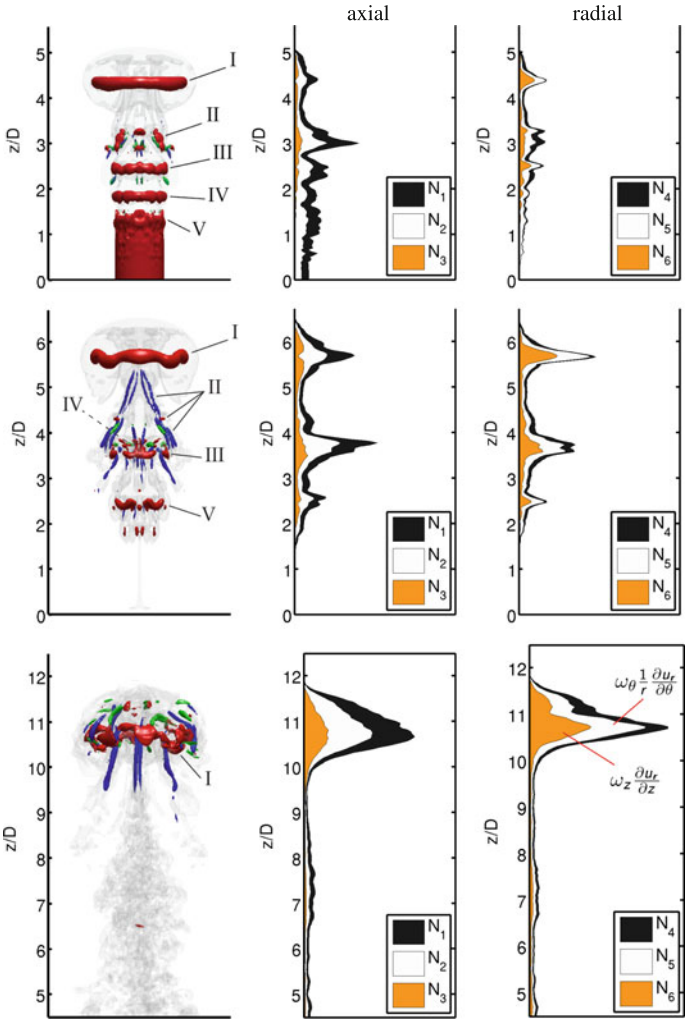


Fig. 1 Vorticity development for Case C. To the *left* is a visualization showing isosurfaces of the volume fraction variable at level $\alpha = 0.5$ (*gray*), as well as each vorticity component magnitude: radial (*green*), azimuthal (*red*) and axial (*blue*). The plots to the *right* are cumulative, with each contribution N_i representing the integral of the absolute values of the corresponding vortex stretching term in (5) or (4), evaluated in each x-y cross-section over the length of the domain. The times are $10D/U_{inj}$ (*top*), $13D/U_{inj}$ (*center*) and $24D/U_{inj}$ (*bottom*)

In the bottom plots, the mid-section vorticity has diminished and the structures II-V can no longer be individually identified. The destabilization of (I) continues as streaks of comparable strength wrap around it, finally resulting in all larger structures breaking up. A peak in the transfer rate is visible at the axial coordinate of (I), especially for the radial vortex stretching components, due to the pronounced gradient

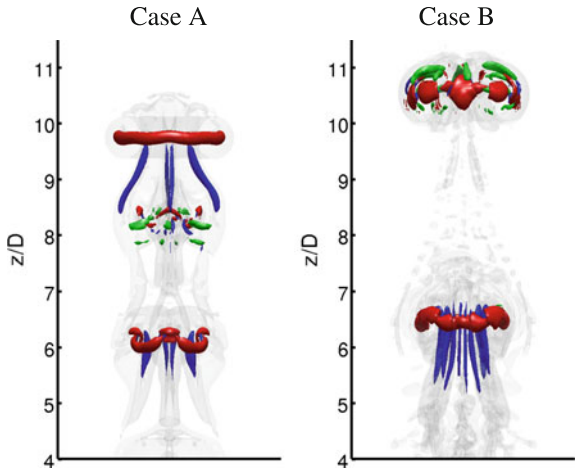


Fig. 2 Snapshot at $t = 24D/U_{inj}$ showing isosurfaces of the jet fluid distribution (*gray*) and each vorticity component magnitude: radial (*green*), azimuthal (*red*) and axial (*blue*)

of the radial velocity caused by the streaks. As expected, once the larger structures have been broken up, the levels of N_1-N_6 are nearly equal.

The vorticity development presented so far has focused on Case C. The development for the other cases is similar, with some exceptions. Figure 2 shows the vorticity component isosurfaces in the front region for Cases A and B, with the same isolevel as was used in Fig. 1. As compared to the transition to chaotic motion observed in Case C at the same time, Case A displays a high degree of symmetry. Each injection gives rise to an individual vortex ring, and until approximately this point in time only minor interaction has taken place in between these rings. The streaks shown behind the leading ring do not originate from secondary structures, but are instead created from the breakup of the second vortex ring located at approximately $8 < z/D < 9$. Similarly to Case C, the second ring is subjected to the strongest perturbation because it is situated in between two stronger structures.

Case B displays similarities to both of the other cases. Injection first creates vortex rings which are well separated. But in contrast to Case A, a small tail of jet fluid and external vorticity lags behind the ring. Case B exceeds the formation number by a fraction compared the Case C. Because of this, the perturbation of the leading ring is weaker in Case B, allowing its leading ring to propagate a longer distance before it breaks up. Once the second pulse is injected, residual motions contribute to ring symmetry break-down closer to the inlet.

Lastly, the vorticity transfer is quantified over a longer time in Fig. 3, by comparing the global (evaluated over the entire computational domain) circulation as defined in (6), in each direction.

$$\Gamma_i = \frac{||\omega_i||}{||\omega||} \tag{6}$$

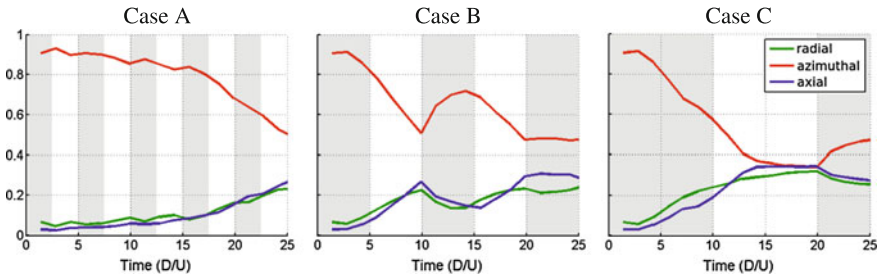


Fig. 3 Comparison of circulation share in the radial, azimuthal and axial directions. The *vertical grey fields* indicate when injection is active

For Case A, the organization into a vortex ring train displays the slowest transfer rate. The global azimuthal circulation share still constitutes the major part when the fourth injection has been completed, at $t = 20D/U$. Global breakup is delayed for a long time partly because the lack of initial external vorticity keeps disturbance growth low. Another contribution is that the vortex rings are relatively strong structures compared to the secondary structures that are generated past the formation number. Once the breakup occurs at the jet front, vorticity is transferred at a higher rate as indicated by the slope change in the leftmost plot in Fig. 3. Case B and C, show a similar azimuthal circulation decay during non-injection. It is interesting to note that nearly equal circulation shares have been obtained $5D/U_{inj}$ after the first injection has ended for Case C. At $t = 20D/U_{inj}$ the same jet volume has been injected for Case B. However, the circulation shares show less vorticity transfer even though two non-injection periods have been completed. This indicates that the generation of trailing structures are advantageous for vorticity redistribution. Once the initial breakup has occurred, the vorticity transfer is increased in all cases. Individual structure interactions are then less important since disturbances are already provided in the domain.

As observed, a longer pulsation duration increases the global vorticity transfer rate. This is partly due to that trailing secondary structures are unstable and lead to faster local mixing. But also since such vortical structures are convected downstream from the trailing region. The contribution to the symmetry breaking of the stronger leading rings depends in turn on the secondary structure strength, thus linking the global breakup rate to the injection duration past the formation number.

Acknowledgments The generous support of this work by the Swedish Research Council (Vetenskapsrådet) through the Linné FLOW Centre is gratefully acknowledged. The simulations were performed on resources provided by the Swedish National Infrastructure for Computing (SNIC) at the National Supercomputer Centre (NSC).

References

1. H. Bing, M. Musculus, J. Oefelein, The influence of large-scale structures on entrainment in a decelerating transient turbulent jet revealed by large eddy simulation. Phys. Fluids **24**, 045106 (2012)
2. M. Badami, F. Mallamo, F. Millo, E.E. Rossi, Experimental investigation on the effect of multiple injection strategies on emissions, noise and brake specific fuel consumption of an automotive direct injection common-rail diesel engine. Int. J. Engine Res. **4**, 299–314 (2003)
3. D. Lörstad, L. Fuchs, High-order surface tension VOF-model for 3D bubble flows with high density ratio. J. Comput. Phys. **200**, 153–176 (2004)
4. M. Gharib, E. Rambod, K. Shariff, A universal time scale for vortex ring formation. J. Fluid Mech. **360**, 121–140 (1998)

Flow Structure of a Round Jet with Side-Jet Formation

Kenta Kawabe and Akinori Muramatsu

Abstract When a low density fluid, such as hot air and helium gas, is discharged from a round nozzle, side jets are generated in the initial region of the jet. These radial ejections of the jet fluid are called *side jets*. The side-jet formation is estimated by the issuing conditions of the jet flow. The issuing conditions are mainly density ratio between the jet fluid and the ambient fluid, velocity profile and issuing speed at the nozzle outlet. However, a process of side-jet formation has not been revealed even now. In present work, we focused on the flow visualization of a gaseous jet flow with side jets, specifically, the vicinity of a jet nozzle issuing helium gas vertically into ambient air. The helium gas jet with the side-jet is visualized by a planar laser Mie scattering (PLMS) and recorded by a high-speed video camera, in order to investigate the process of side-jet formation.

1 Introduction

A complex phenomenon is generated in the near field of a jet if the mass density of the issuing gas is sufficiently lower than that of the ambient gas. This phenomenon is some radial ejections from the main jet stream, which are referred to as *side jets*. The side jets are formed by self-excited oscillations of the jet column [1, 2]. However, until now, it has not been possible to examine the structure of the side jets in great detail. We developed a three-dimensional imaging method using a planar laser Mie scattering (PLMS) and an oscillating mirror to observe a three-dimensional structure of the initial region of the jet with the side-jet formation, as shown in Fig. 1. [3]. The optical system swept a laser sheet at high speed by oscillating a mirror attached to a galvano-scanner. A large number of

K. Kawabe
Graduate School of Science and Technology, Nihon University, Tokyo, Japan

A. Muramatsu (✉)
College of Science and Technology, Nihon University, 7-24-1 Narashinodai, Funabashi, Chiba 274-8501, Japan
e-mail: amura@aero.cst.nihon-u.ac.jp

© Springer International Publishing Switzerland 2016

A. Segalini (ed.), *Proceedings of the 5th International Conference on Jets, Wakes and Separated Flows (ICJWSF2015)*,
Springer Proceedings in Physics 185, DOI 10.1007/978-3-319-30602-5_2

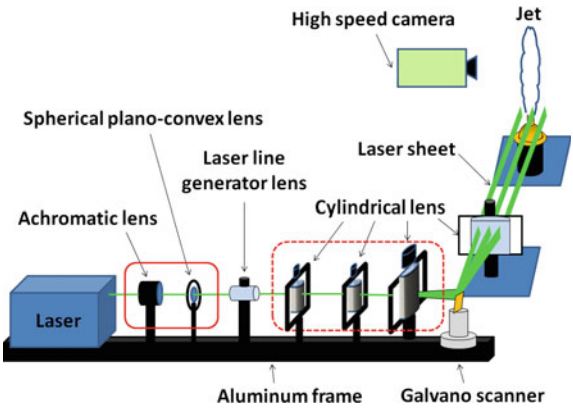


Fig. 1 Experimental apparatus for 3D imaging

cross-sectional images were captured almost simultaneously using a high-speed video camera. The 3D image of the flow field was constructed by image processing with an open software *ImageJ*. The constructed image was interpolated using bicubic interpolation. A helium gas jet with side-jet formation was visualized by three-dimensional imaging, as shown in Fig. 2. A non-dimensional coordinate system is illustrated in Fig. 2. The x and r are respectively streamwise and radial coordinates, and the origin is on the centerline at the nozzle exit. The D_0 is a nozzle diameter. From the 3D visualization, several side jets are generated simultaneously, and a vortex ring is distorted by the side-jet formation at the same time, as painted

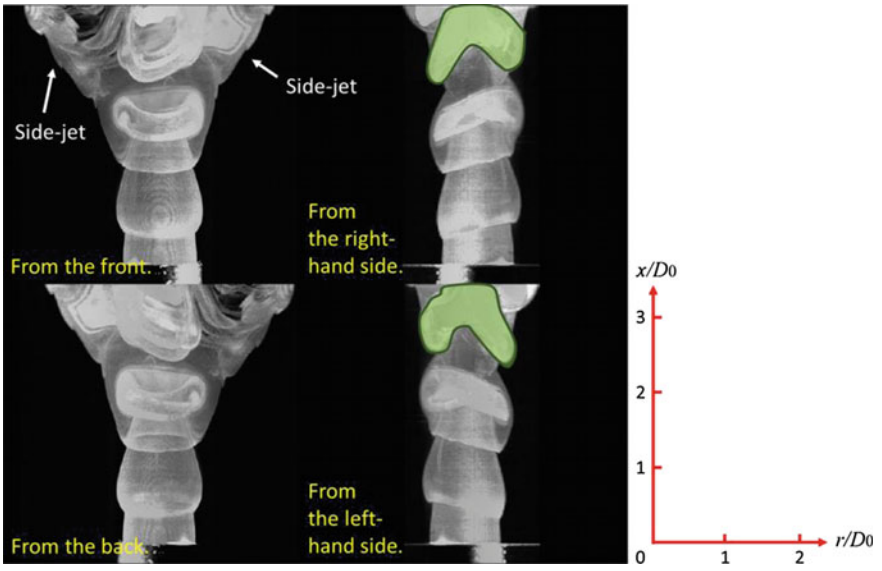


Fig. 2 3D images like the X-ray for a He gas jet at $Re = 800$

with light green in Fig. 2. A process of side-jet formation has not understood even now. In the present work, streamwise cross-sectional images of a helium gas jet are visualized at a few radial points, such as on the jet center line and in the shear layer, by a PLMS and the visualized images are recorded using a high-speed video camera, in order to investigate the process of side-jet formation.

2 Experimental Apparatus and Method

2.1 Target Flow

The visualized flow is a jet column with side jets in the vicinity of a nozzle issuing a low-density gas jet (a helium gas jet). To produce the side-jet formation, helium gas was issued vertically from a round nozzle into ambient air. A round nozzle for this experiment is shown in Fig. 3. A diameter at the nozzle exit D_0 is 16 mm and an area contraction ratio of the nozzle is 17. Slits attached to the nozzle are used as guidelines for positioning of a laser sheet. The jet Reynolds number is 800 and is defined by $Re = U_{c0} \cdot D_0 / \nu_0$. Here, U_{c0} and ν_0 are centerline velocity at the nozzle exit and kinematic viscosity of the jet fluid. The density ratio between the jet fluid (helium gas) and the ambient fluid (air) is 0.14. The jet Reynolds number of 800 is lower limit for the side-jet formation at the used round nozzle. An effect of compressibility is disregarded because the issuing velocity is 5.8 m/s.

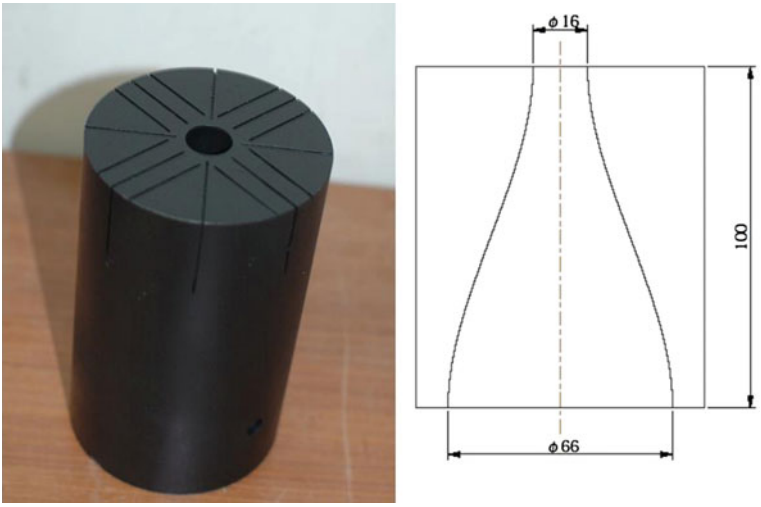


Fig. 3 A round nozzle

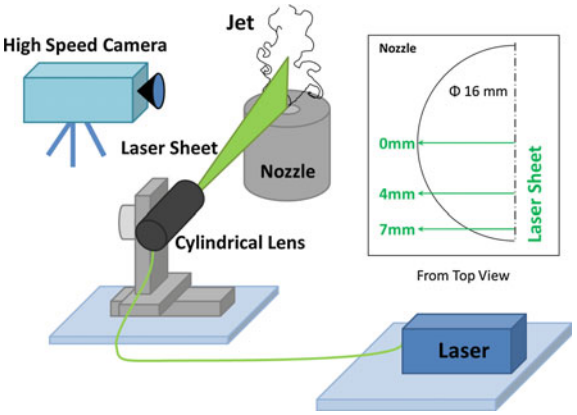


Fig. 4 Experimental apparatus for imaging the streamwise cross-sections in a He gas jet

2.2 Experimental Apparatus and Visualization Method

The experimental apparatus is shown in Fig. 4. The helium gas jet with the side-jet is visualized by PLMS. The gas jet is seeded with very small particles of smoke that functioned as the Mie scattering particles. The smoke is generated using a smoke generator (Dantec Dynamics, Safex Fog Generator 2010). A continuous-wave (CW) Nd:YAG laser (Japan Laser Corp., DPSS Green Laser, 5 W) is transformed to a light sheet through a cylindrical lens system. The laser sheet, which is less than 1 mm in thickness, is perpendicular to a high-speed video camera (Photron Corp., FASTCAM SA-X2). Cross-sectional images of a helium gas jet are visualized by a PLMS and the time series of the visualized images are recorded using the high-speed video camera. In order to observe the phenomenon of side-jet formation at various locations, the streamwise cross-sections of the jet flow is visualized at the radial positions of 0, 4 and 7 mm, where the central axis of the nozzle is defined as 0 mm as shown in Fig. 4.

3 Experimental Results

The visualized cross-sectional images of the helium gas jet at positions of 0 and 7 mm are shown in Figs. 5 and 6. Each of time-intervals between images in Figs. 5 and 6 is 2 ms.

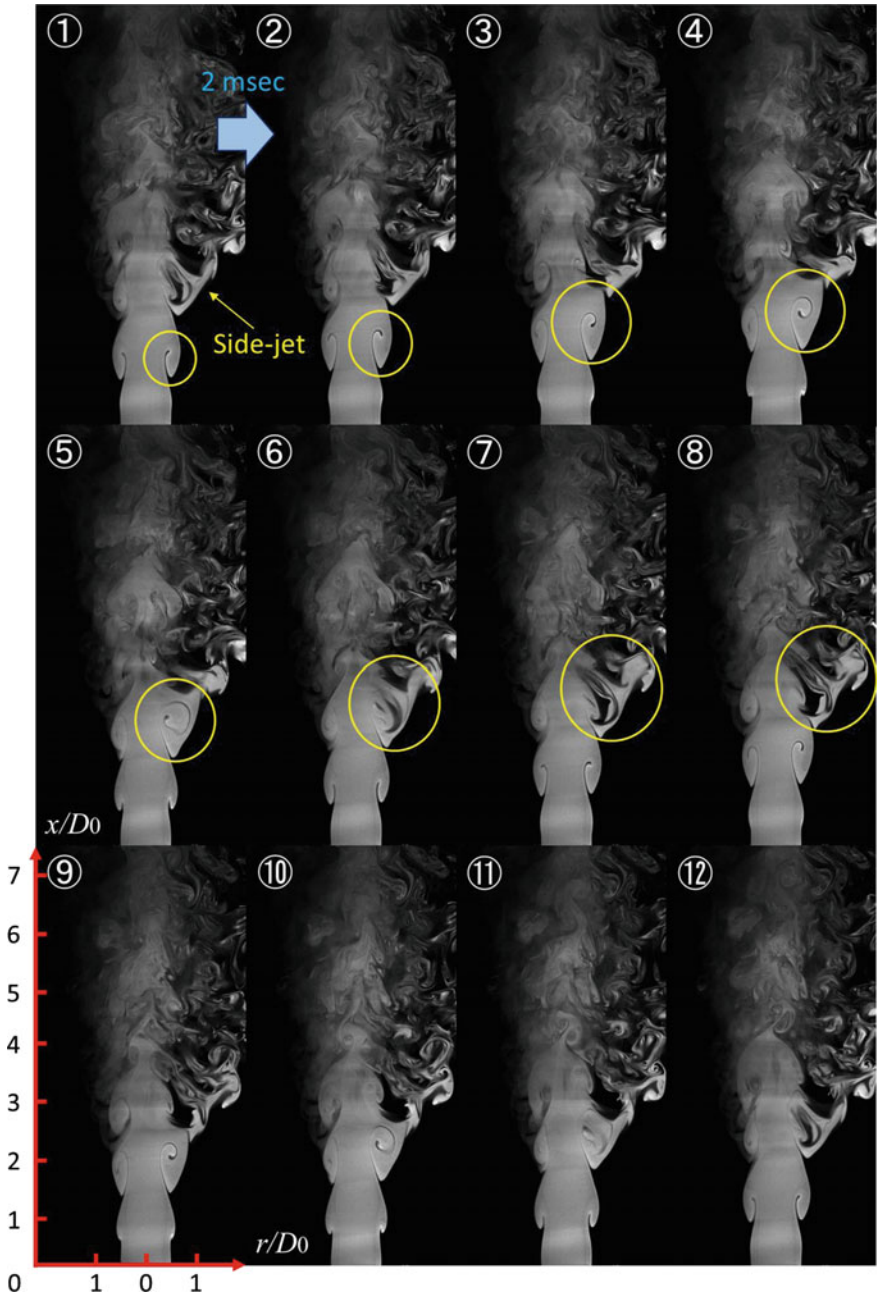


Fig. 5 Streamwise cross-sectional images on the jet centerline (at 0 mm) for He gas jet

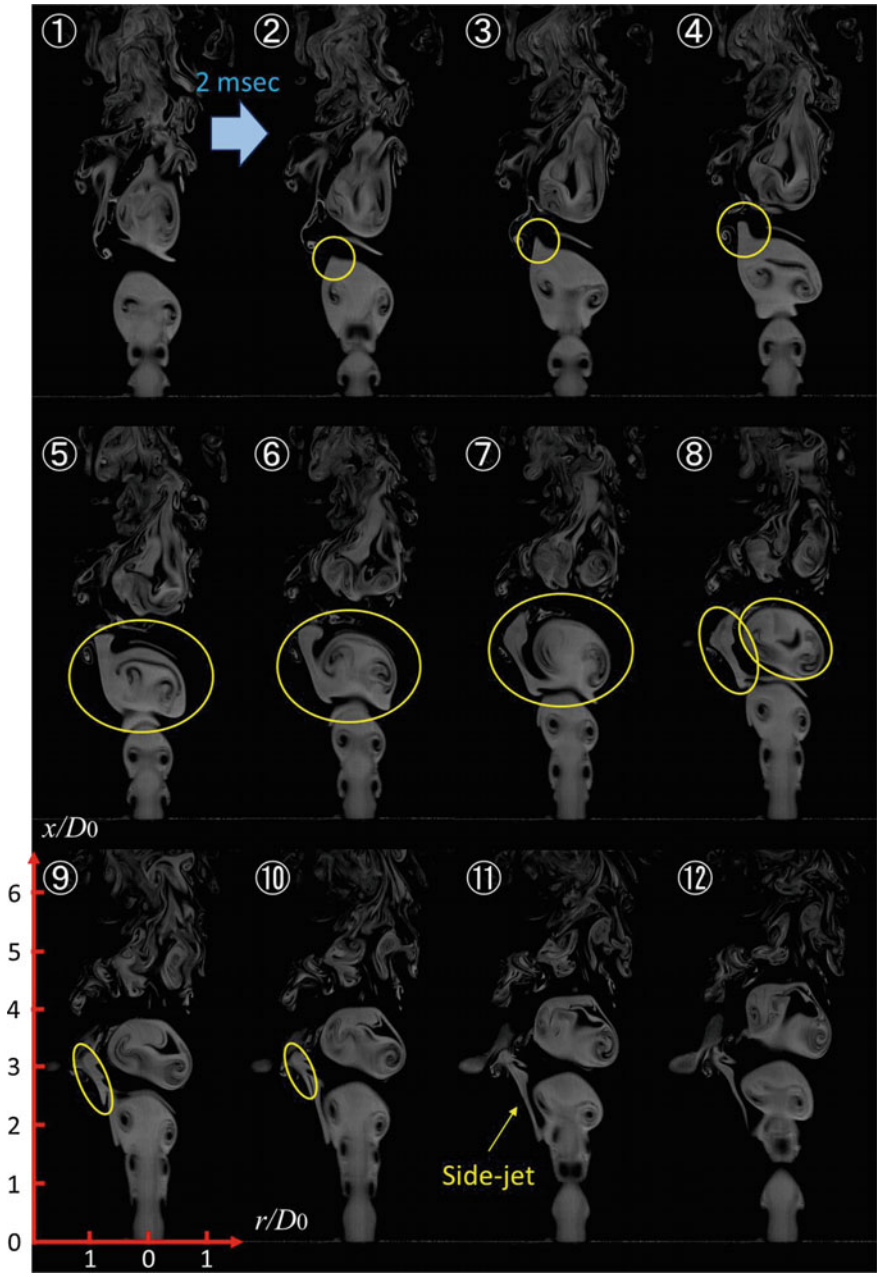


Fig. 6 Streamwise cross-sectional images in the jet shear layer (at 7 mm) for He gas jet

3.1 At 0 mm (on the Jet Center Line)

The jet fluid ejected between the vortex rings radially upward is a side jet, as shown by a yellow arrow in Fig. 5. The vortex ring marked with a yellow circle in the images of No. 1 and 2 in Fig. 5 moves upward. In the image of No. 3, the vortex ring marked with a yellow circle is close to the side jet generated from the preceded vortex ring. In the image of No. 4, the upper right of vortex ring expands toward the side jet. In the images from No. 5 to 8, the part of the expanded vortex ring gradually separates from mainstream of the jet by rotating the vortex ring. This separation looks like a radial ejection from the mainstream flow. The radial ejection, namely a side jet, moves downward on the vortex ring when the vortex ring moves upward, so that the starting point of the side-jet formation is maintained at approximately constant height. In the image of No. 8, the next vortex ring is close to the separated flow like the image of No. 3. After the image of No. 8, a similar process is repeated. Although a side jet seems to eject from a certain height of the jet stream continuously, the side jet is generated intermittently, because the side-jet formation is related to the movement of each vortex. The side jet is seen a continuous phenomenon with the naked eye, because a convection speed of the vortex rings is higher than a moving speed of a side jet. Moreover, in the helium gas jet with this condition, the side jet is generated before merging of the two vortex rings. Consequently, it is thought that the pairing process of vortex rings is not related to the side-jet formation [4]. Visualized images at the 4 mm are similar to the images at 0 mm.

3.2 At 7 mm (in the Jet Shear Layer)

On the other hand, in Fig. 6, the side jet is formed in left-hand side, as shown in a yellow arrow. In the image of No. 2 in Fig. 6, the left side of a vortex ring indicated by a yellow circle is preceded from an opposite side of the vortex ring. This fact shows that the vortex ring is tilting. The portion indicated by this yellow circle is going to become a side jet. The jet fluid ejects from the vortex ring in the direction of upper left in the image of No. 2–4, and the flow is separated simultaneously with rotation of the vortex ring from the upper left of the vortex ring in the image of No. 5–7. In the image of No. 8, the separated flow and the vortex ring are divided. In the image of No. 9 and 10, the separated flow in the image of No. 8 drifts, and it connects with the next vortex ring. Although the ejection from the braid region is not recognized from the Figs. 5 and 6, it is found that the ejected flow not only consists of a separation from the vortex ring, but also of the fluid of the braid region, because the flow in the braid region changes the flow direction by rotation of the vortex ring, when a side jet is formed by rotation of the vortex ring, by watching the original image.

4 Conclusions

The results of flow visualization at the initial region of a helium gas jet are summarized as follows:

(1) A flow is separated simultaneously with rotation of a vortex ring from the upper side of a vortex ring. An ejection from the braid region is also generated because the flow direction changes in the braid region by rotation of the vortex ring. A side jet is formed from these two processes.
(2) A side jet is generated intermittently.
(3) A side of a vortex ring with a side jet is preceded from a side of the vortex ring without a side jet. The vortex ring is tilting when the side jet is formed.
(4) The side-jet formation does not depend on a pairing process of vortex rings.

References

1. P.A. Monkewitz, K.D. Sohn, Absolute instability in hot jets. AIAA J. **26**, 911–916 (1988)
2. P.A. Monkewitz, D.W. Bechert, B. Barsikow, B. Lehmann, Self-excited oscillation and mixing in a heated round jet. J. Fluid Mech. **213**, 619–639 (1990)
3. K. Kawabe, H. Harada, A. Muramatsu, Three-dimensional imaging of a helium gas jet flow using planar laser Mie scattering, in *Proceedings of 16th International Symposium on Flow Visualization, USB-Memory* (2014)
4. A. Muramatsu, Y. Kaneda, Asymmetric structures in a round jet with low density, in *Proceedings of the international symposium, turbulence, heat and mass transfer 7, CD-R*(2012)

Flow and Heat Transfer Features of an Impinging Annular Jet

Victor Terekhov, Svetlana Kalinina and Konstantin Sharov

Abstract This paper presents the results of the comprehensive experimental study of flow and heat transfer of the annular impinging jets. The flow fields were studied using the PIV. To measure heat transfer, the miniature gradient sensors of the heat flux were used under the thermal boundary conditions $T_w = \text{const}$. The experimental conditions were as follows: basic round nozzle had diameter $d_0 = 17.8$ mm; ring nozzles have the same outer diameter and different inner diameters $d_2 = 12.7$ and 9.1 mm. Air was the working medium. The distance between the nozzle and wall ($S/d_0 = 2$, 4 and 6) and air flow rate (Reynolds number for the round nozzle was varied within $Re = U_0 d_0/\nu_0 = 1.2 \times 10^4$–$3.3 \times 10^4$) were varied in experiments. Data obtained for the annular and round jets were compared at the same mass air flow rates. It is shown that replacement of the round nozzle by the annular nozzle leads to an increase in intensity of velocity fluctuations in the axial zone of the jet and heat transfer enhancement in the frontal zone of the obstacle. At that, the value of intensification effect depends on the parameters, characterizing the system.

1 Introduction

The impinging jets, single or in the form of systems flowing out of the nozzles of different shapes and sizes, etc., are widely used in the modern cooling systems, so the problem of their effectiveness use remains relevant.

V. Terekhov (✉) · S. Kalinina · K. Sharov
Kutateladze Institute of Thermophysics of SB of RAS, Acad. Lavrent'ev Avenue, 1, 630090 Novosibirsk, Russia
e-mail: terekhov@itp.nsc.ru

S. Kalinina
e-mail: kalinina@itp.nsc.ru

K. Sharov
e-mail: sharov@itp.nsc.ru

© Springer International Publishing Switzerland 2016

A. Segalini (ed.), *Proceedings of the 5th International Conference on Jets, Wakes and Separated Flows (ICJWSF2015)*,
Springer Proceedings in Physics 185, DOI 10.1007/978-3-319-30602-5_3

According to experiments [1], at the same coolant flow, the annular impinging jets can be significantly more efficient than the round ones. This result was obtained as early as in 1980, but still it has no complete explanation.

The analysis of available publications shows that the structure of the flow field of the annular impinging jets is complex. Depending on the specific conditions, such properties as non-uniqueness and hysteresis of the flow field structure between the nozzle and obstacle can be observed [2, 3], as well as the bundle of pressure and heat transfer intensity and others.

In the present work, which is the development of research [4], the results of experimental studies of the flow and heat transfer of the annular impinging jets at variation of the aspect ratio of the inner and outer nozzles, Reynolds number, and distance between the annular nozzle and obstacle are presented.

2 Experimental Setup and Measurement Methods

The total scheme of experimental setup is shown in Fig. 1. It includes the system of air flow supply and measurement, nozzle of the studied geometry, obstacle and measurement equipment.

Firstly, the flow structure and heat transfer in the round jet was investigated. The diameter of the round nozzle was $d_0 = 17.8$ mm. Velocity distribution at its outlet was almost uniform and turbulent intensity was 3.5−4 %.

To form the annular cross-section, cylindrical rods with the flat end of different diameters d_2 were put inside this nozzle. In aerodynamic experiments the ratio d_2/d_0

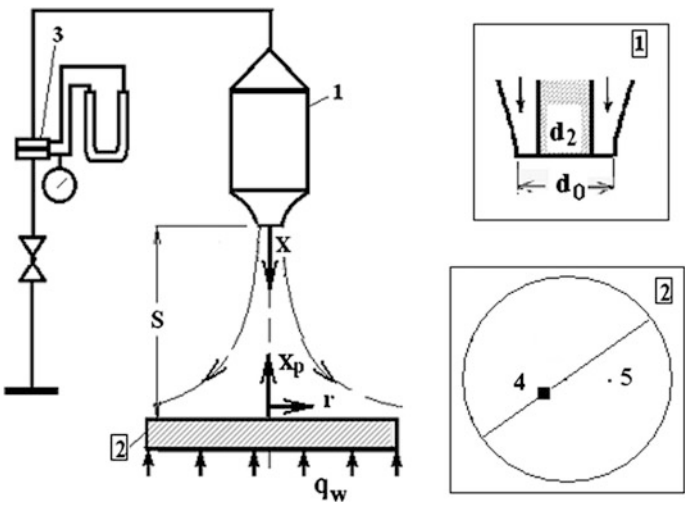


Fig. 1 Experimental setup: *1*—nozzle; *2*—obstacle; *3*—air line; *4*—heat flux sensor; *5*—thermocouples

was 0.71; in thermal—$d_2/d_0 = 0.51$ or 0.71. The distance between the nozzle and obstacle ($S/d_0 = 2$, 4 and 6) and the flow rate were varied. For the given flow regime the characteristic Reynolds number was calculated as $Re = U_0 d_0/\nu_0$, where U_0 is the average flow velocity for the air supply through a round nozzle with diameter d_0. The range of Re numbers in experiments was $Re = 1.2 \times 10^4 - 3.3 \times 10^4$.

In aerodynamic studies we used the measurement PIV—complex [4, 5]. The measuring plane of the PIV—stroboscope of 36 × 45 mm was always located near the obstacle surface and covers the entire area of flow deceleration. The results of PIV experiments are presented in the form of axial or radial (r—the distance from the jets axis) distributions of the averaged and pulsation velocities in the measuring plane. The radial distributions are presented for three cross-sections located at distances $x_p = 0.53d_0$; $1d_0$; $1.68d_0$ from the obstacle.

For thermal measurements, the obstacle (diameter D = 190 mm, thickness H = 50 mm) was made of copper and it was heated by means the electric heater located beneath to the temperature T_w of ~ 60–70°C. The high thermal conductivity of copper met boundary conditions T_w = const. The measurements of wall temperature T_w by the chromel-copel thermocouples at different sites of the obstacles confirmed the validity of such a condition. The air temperature at the nozzle exit T_0 was close to the room temperature and it was measured by a thermometer. To measure the heat fluxes through the wall we used tiny heat flux sensors, glued on the obstacle surface (with the plane size of 2 × 2 mm, 0.2 mm thickness). The small sizes of sensors as well as their low inertia [6] made it possible to measure the local heat flux (q_w) as well as their pulsations. The heat transfer coefficient was determined by the formula $\alpha = (q_w - \Delta q_w)/(T_w - T_0)$, there

Δ qw—the experimentally determined correction due to convection and radiation. For measurements of heat transfer coefficient radial distributions the nozzle was mounted on the traversing mechanism and by it was moved along the obstacle surface. When calculating the Nusselt number $Nu = \alpha d_0/\lambda_0$, the coefficient of thermal conductivity λ_0 was determined by the temperature T_0.

3 Flow Structure. Averaged and Turbulent Characteristics

The instantaneous velocity fields in a round (a) and annular (b) impact jets are compared in Fig. 2. The distance from the nozzle to the wall was 2 d_0, Reynolds number was $Re = 1.2 \times 10^4$. It is seen that in the mixing layer of the round jet the flow is disturbed, the large-scale vortices generate and entrained by the flow there. The vortices generate near the nozzle outlet. Downstream the mixing layer thickness and vortex sizes increase, becoming comparable with the jet diameter.

The flow pattern in the annular jet is considerably different, which is clearly demonstrated in Fig. 2b. Directly behind the outlet section of the annular nozzle, the separated torus-shaped vortex is formed behind the cylindrical insert. The size of the vortex zone along the flow is approximately equal to the insert diameter.

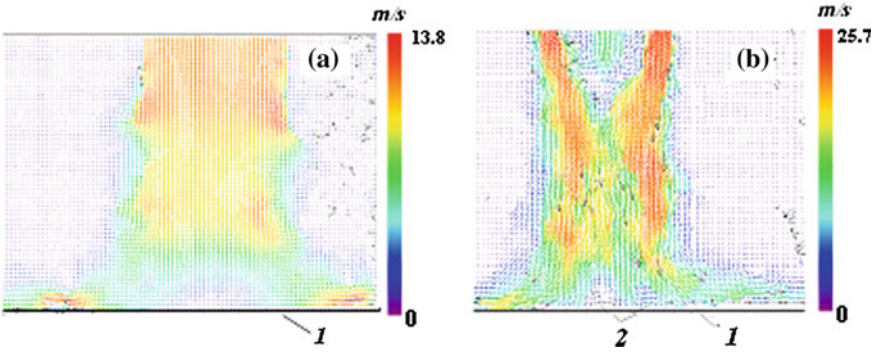


Fig. 2 Instantaneous velocity fields for the round (**a**) and annular (**b**) jets. $S/d_0 = 2$, $Re = 1.2 \times 10^4$. *1*—obstacle; *2*—non-stationary annular zone of deceleration

Further, the annular flow closes in the axial zone. The whole velocity field of the annular jet is essentially unsteady, at that, intense flow vibrations are observed both in the outside mixing layer and near the axis. As a result, the structure of the velocity field of the annular impinging jet near the front point differs from that in a similar zone of a round jet.

Distributions of the longitudinal velocity component and its rms pulsations along the axis of the annular and round jets are compared in Fig. 3. It is seen that these distributions are fundamentally different. In the annular jet directly behind the central insert, the forming torus-shaped vortex leads causes an intense reverse flow, whose length is about half of a caliber $x/d_0 \sim 0.5$. At the distance from the nozzle of about $x/d_0 = 0.7$, the axial velocity of the annular jet becomes equal to the similar velocity of the round jet, and then along the distance to the stagnation point exceeds this value. In addition, the velocity pulsations at the annular jet axis are significantly higher than velocity pulsations in the round jet; they vary non-monotonically along the region length and increase directly near the obstacles. This follows clearly from data comparison in Fig. 3b.

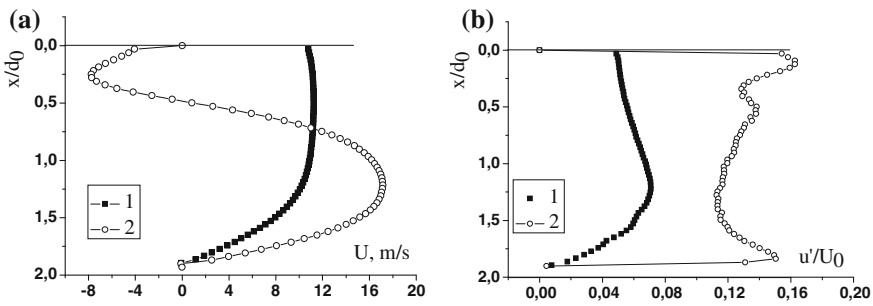


Fig. 3 Distributions of longitudinal velocity component (**a**) and its pulsations (**b**) at the axis of the round and annular jets. $S/d_0 = 2$, $Re = 1.2 \times 10^4$: *1*—round jet; *2*—annular jet

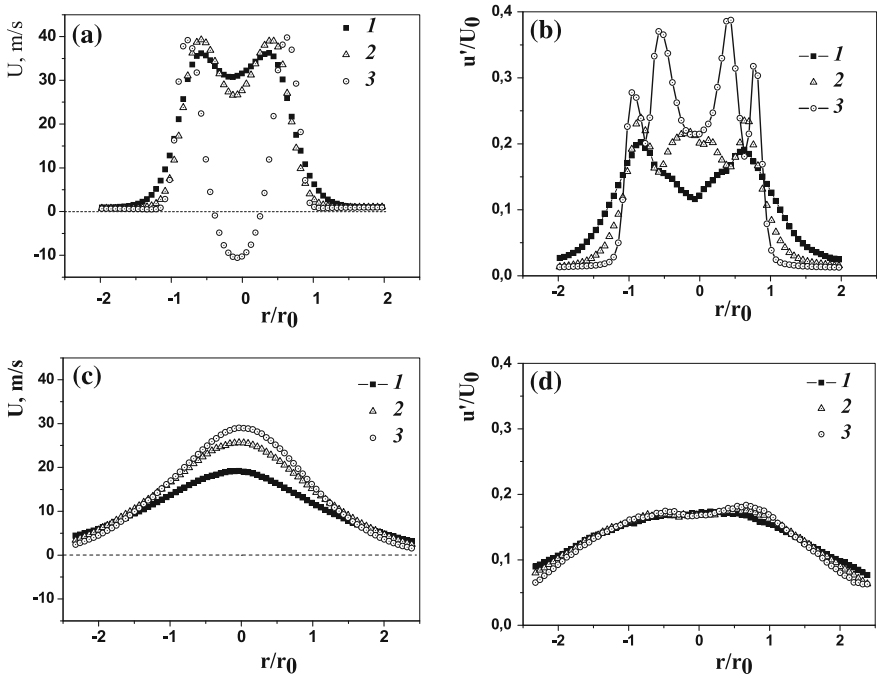


Fig. 4 Radial distributions of longitudinal velocities (**a**, **c**) and their rms pulsations их (**b**, **d**) in the annular jet. Re = 2.4 × 10^4: (**a**, **b**), (**c**, **d**)—S/d_0 = 2, 6; *1–3*—x_p/d_0 = 0.53, 1, 1.68

Radial distributions of longitudinal velocity and it pulsations for the annular jet with $S/d_0 = 2$ and 6 are shown in Fig. 4.

When the distance between the nozzle and obstacle is small ($S/d_0 = 2$), cross-section $x_p/d_0 = 1.68$ crosses the region of the vortex flow behind the inner nozzle insert, as evidenced by the negative values of longitudinal velocity in the axial zone. Downstream this cross-section, the annular jet closes, and the negative values of longitudinal velocity disappear. Distributions of longitudinal velocity in this region have the configuration, typical to the annular jet, with two velocity maxima and two mixing layers. Development of the mixing layers leads to a decrease in the velocity maxima and simultaneously an increase in the flow velocity at the jet axis.

Radial distributions of rms pulsations of longitudinal velocity at $S/d_0 = 2$ are shown in Fig. 4b. It can be seen that even at distance $x = 0.35\ d_0$ from the nozzle (cross-section $x_p/d_0 = 1.68$), pulsation intensity in the annular jet is very high ($u'/U_0 \approx 0.4$). Significant changes in the value of pulsations are observed along the jet radius with two obvious maxima at $r/r_0 \approx 0.5$ and 0.9, corresponding to the boundary of a jet with the near-end vortex and outer layer of jet mixing.

The level of pulsations in the inner mixing layer is higher than in the external one. With an increasing distance from the nozzle, distribution of pulsations

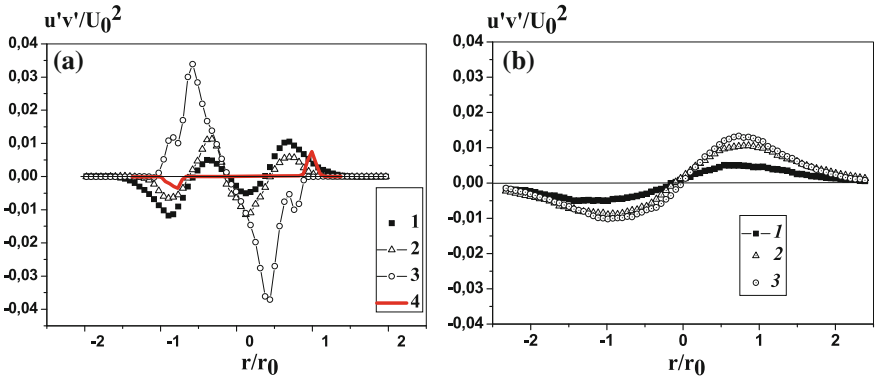


Fig. 5 Radial distribution of Reynolds stresses in the impinging annular jet. Re = 2.4 × 10^4: **a**, **b**—S/d_0 = 2, 6; *1–3*—x_P/d_0 = 0.53, 1, 1.68. *4*—round jet, x_P/d_0 = 1.61

becomes uniform, and despite a decrease in their level, it remains relatively high, about 12 %.

With an increase in the distance from the nozzle to the obstacle to $S/d_0 = 6$ (Fig. 4c, d), the structure of radial distributions of longitudinal velocity component and its rms pulsations near the obstacle changes.

In all considered sections, velocity pulsations are distributed monotonous, without any bends, and they do not change qualitatively from section to section.

Radial distributions of Reynolds stresses near an obstacle for the impinging annular jet at different distances between the nozzle and the obstacle are shown in Figs. 5a, b. In Fig. 5a they are compared with data for the round jet. It is seen that in comparison with the round jet, the shear stresses (caused by turbulence) in the annular jet are substantially higher, not only near the axis, but also in the outer mixing layer. The main reason for this behavior of turbulent stresses can be development of large-scale instability of the jet. This interpretation of results is based on visual observations, showing that the flow of the annular jet is essentially unsteady and it is accompanied by spatial pulsations of the jet as a whole. In turn, the reason for large-scale pulsations can be the development of instability and pulsations in the axial region of the jet.

4 Heat Transfer Between the Annular Jet and the Obstacle

Results of thermal measurement are given in Figs. 6 and 7. In Fig. 6a, c, there are the radial distributions of heat transfer coefficient at variation of the annular gap height and the distance from the nozzle to the obstacle. The lowest values of heat transfer coefficient were obtained, when the round jet flowed on an obstacle. The

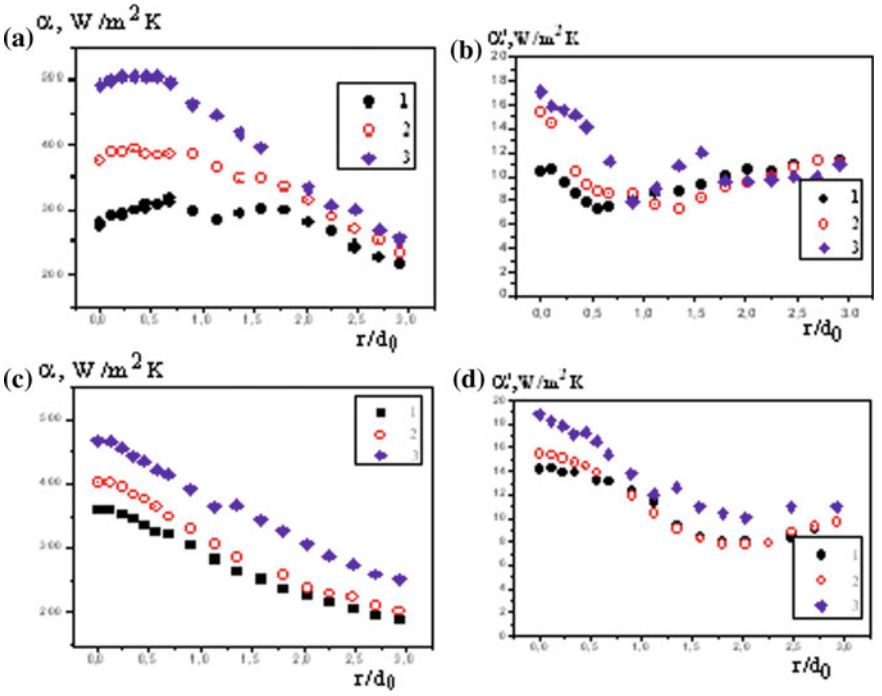


Fig. 6 Radial distributions of heat transfer coefficients (**a**, **c**) and their rms pulsations (**b**, **d**) for the round and annular jets. Re = 3.1 × 10^4: (**a**, **b**), (**c**, **d**)—S/d_0 = 2, 6; *1–3*—d_2/d_0 = 0; 0.51; 0.71

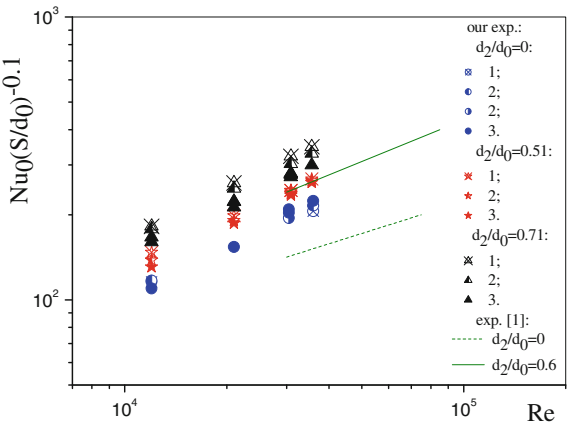


Fig. 7 Dependence of heat transfer at the stagnation point of the annular jet on parameters Re, d_2/d_0 and S/d_0. 1 - S/d_0 = 2; 2 - S/d_0 = 4; 3 - S/d_0 = 6

heat transfer coefficients for the circular nozzles are higher, especially at $S/d_0 = 2$. Moreover, data bundle depending on the ratio of the annular nozzle diameters is observed. The effect of heat transfer enhancement is maximal at the stagnation point, and it decreases with a distance.

It is interesting that the region of intense heat transfer around the stagnation point of the annular jet is large, it extends to radial distances $r = (2 \div 3)d_0$ even at a small distance between the nozzle and the obstacle $S/d_0 = 2$. This result correlates with the results of the PIV investigation of the flow field, with instability of the inner mixing layer, and development of large-scale radial oscillations of the jet along the obstacle surface. With increasing distance from the nozzle to the wall ($S/d_0 = 6$), the effect of these processes becomes weaker, radial distributions of heat transfer coefficients of the annular and round jets converge.

Replacement of the round nozzle by the annular one increases heat transfer pulsations. This follows from (Fig. 6b, d), where radial distribution of pulsations of the heat transfer coefficients of the round and annular jets are compared. Especially strong difference between pulsations of the annular and round jets is characteristic to the stagnation point at a short distance from the nozzle to the obstacle $S/d_0 = 2$. With increasing distance, intensity of pulsations at the stagnation point of the round jet increases, and data bundle decreases.

From the point of practical applications, the great interest is caused by heat transfer in the frontal region, where it is usually maximal. Experimental data for the stagnation point of the annular and round jets are shown in Fig. 7 in the form of dependence of complex $Nu_0(S/d_0)^{-0.1}$ on Reynolds number. They are compared with similar data of [1]. Factor $(S/d_0)^{-0.1}$ is used to account for the effect of the distance between the nozzle and the obstacle on Nu_0 number.

According to [7], this factor can be recommended for the low-turbulent round jet, when the obstacle is in the initial region, and actually it takes into account a change in the degree of turbulence in the jet core that happens with a change in the distance from the nozzle to the obstacle.

According to Fig. 7, data of the current study for the round jet lie higher than the similar data of [1]. The reason for this could be the higher degree of turbulence of the jet. At the considered Reynolds numbers, replacement of the round jet by the annular one increases heat transfer at the stagnation point, and the maximum increase is observed at a small distance between the nozzle and the wall $S = 2d_0$, when pulsations in the jet core are maximal. The use of factor $(S/d_0)^{-0.1}$ graded the bundle of results depending on parameter S/d_0 for the round jet; at the same time for the considered annular jets its use was not effective. This is explained by the fact that not only the magnitude of flow pulsations, but also the whole mechanism of flow development in the central part of the annular and round jets differ substantially.

We should also note that results, obtained in our experiments, agree qualitatively with the results of [1] and in general, they show the prospects of annular jets application for effective heat removal.

5 Conclusions

1. The flow in the annular jet in the considered range of conditions is substantially non-stationary, it is characterized by the development of turbulence in the axial region and pulsations of the jet as a whole in the radial direction.
2. For the similar coolant mass flow rate, the annular impinging jet is more effective than the round one, it leads to heat transfer enhancement.

Acknowledgments The study was supported by the RSF, grant No. 14-19-00402.

References

1. A.I. Mazur, L.E. Yushina, Heat transfer in the impinging annular jet. Promyshlennaya teplotekhnika **2**(2), 35–38 (1980)
2. H. Maki, A. Yabe, Heat transfer by the annular impinging jet. Exp. Heat Transfer **2**, 1–12 (1989)
3. Z. Travnicek, V. Tesar, Hysteresis in annular impinging jets. Exp. Thermal Fluid Sci. **44**, 565–570 (2013)
4. S.V. Kalinina, V.I. Terekhov, K.A. Sharov, Flow structure features of annular impinging jets near to the barrier. Fluid Dyn. **50**(5), 76–84 (2015)
5. V.I. Terekhov, Starodumova D. Yu, K.A. Sharov, PIV measurement of mean and pulsating velocities in a gas-droplet jet with low concentration of dispersed phase. Thermophys. Aeromech. **15**(3), 401–408 (2008)
6. S.Z. Sapozhnikov, V. Yu. Mityakov, A.V. Mityakov, *Gradient heat-flow probes* (Politechnic Univercity, St.-Petersburg, 2003)
7. E.P. Dyban, A.I. Mazur, *Convective heat transfer at jet flow around the bodies* (Naukova Dumka, Kiev, 1982)

Investigation of the Flow in Free and Impinging Air Micro- and Macrojets

Vadim Lemanov, Victor Terekhov and Konstantin Sharov

Abstract The aim of this work is an experimental study of the flow in subsonic free and impinging macro- and microjets of air. Complex measurements have been performed using the PIV method (Particle Image Velocimetry), hot-wire anemometry and flow visualization. In the experiments, we used the axisymmetric and flat micronozzles with the characteristic size of 250−600 μm. The measurement performed for the jets of the larger size of 1−8 mm are presented for comparison and generalization of experimental data. Air, whose thermodynamic parameters are close to the atmospheric conditions, was used as the working gas. Flow visualization allowed us to construct the spatial pattern of formation and decay of the laminar part of the jet and transition to turbulence. It was shown that the range of a free jet can equals 100−200 nozzle sizes. The Reynolds number of transition to turbulence in mini- and microjets takes high values (1000−2600), and this is two-three tens times higher than the Reynolds number of stability loss. In the impinging jet, an obstacle can change the coordinate of transition to turbulence, for instance, due to the feedback effect.

1 Introduction

Modern development of MEMS—technology (MicroElectroMechanical Systems) has stimulated interest in the study of microjets both in scientific and applied aspects [1, 2]. The liquid microjets are widely used for the tasks of Applied Chemistry and Biotechnology. Gas microjets are applied to control the boundary

V. Lemanov · V. Terekhov · K. Sharov (✉)
Kutateladze Institute of Thermophysics of SB of RAS,
Acad. Lavrent'ev Avenue 1, 630090 Novosibirsk, Russia
e-mail: sharov@itp.nsc.ru

V. Lemanov
e-mail: lemanov@itp.nsc.ru

V. Terekhov
e-mail: terekhov@itp.nsc.ru

© Springer International Publishing Switzerland 2016

A. Segalini (ed.), *Proceedings of the 5th International Conference on Jets, Wakes and Separated Flows (ICJWSF2015)*,
Springer Proceedings in Physics 185, DOI 10.1007/978-3-319-30602-5_4

layer and thrust vector, they are used in cooling microelectronic devices, control systems, and others. Due to the low scale parameter in the subsonic microflows, the maximal Reynolds number is limited by the values of 1000−3000. In connection with the low Re numbers the interest in the problem of transition to turbulence is clear. The first experimental results on the study of laminar-turbulent transition in subsonic microjets [3–6], supersonic microjets [7] and impinging microjets [8] have been published. In 2009, when studying the flat air jets (nozzle height of 50−200 microns), the authors of [3] concluded that distribution of microjets differ significantly from their development. For example, in the zone of laminar-turbulent transition of the microjets, neither sinusoidal no varicose instability mode was registered, and this contradicts the known concepts for the jet flows [9]. There is also no mechanism for vortex formation and pairing in the zone of instability. The aim of this work is an experimental study of the flow in subsonic free and impinging macro- and micro- air jets. First, we are interested in what are the Re numbers corresponding to transition to turbulence in such flows. Moreover, for the tasks of the most efficient mixing, it is necessary to know the location of the point of transition to turbulence. The presence of an obstacle, in case of an impinging jet can also change the coordinate of the laminar-turbulent transition.

2 Experimental Methods

The studies were carried out by means of the following methods: PIV (particle image velocimetry), hot-wire anemometry and visualization. The scheme of experiment is shown in Fig. 1. The instantaneous velocity fields were measured with help of 2D PIV "POLIS" (development of the Institute of Thermophysics SB RAS), which included: digital camera, solid-state pulsed laser, pulse synchronizer and computer. Resolution of the matrix of the digital camera was 1024 × 1360 pixels, laser pulse duration was 5 ns, radiant energy was 50 MJ, wavelength of laser radiation was 532 nm, laser sheet thickness was 0.2 mm, and minimal time between the frames was 20 μs. In experiments with PIV: measurement area was 3 × 4 mm and minimal calculation domain was 32 × 32 pixels. The field velocity measurements and flow visualization were performed using the generator of water spray (the typical size of particles was 1−2 μm). The flow pattern during visualization was registered by the digital camera Pentax (matrix of 10 Mpix). The hot-wire anemometer of constant temperature DISA55 M with miniature probe DISA55P11 was also used.

The system of air preparation for jet flow formation is shown in Fig. 1. Air from high-pressure line 1 was fed to fore-chamber 5 through reducer 2, valve 3, and flow meter 4; then, via line 6 it was sent to channel 8. In experiments with the impinging jet, we used organic glass plate 9 of 300 × 300 mm. The pressure at the working channel inlet was registered by micromanometer 7. The submerged jets were formed by means of round and flat channels 8. The round channels were made of metal with diameter d = 500 μm−8 mm and length l/d = 100. The flat jets were

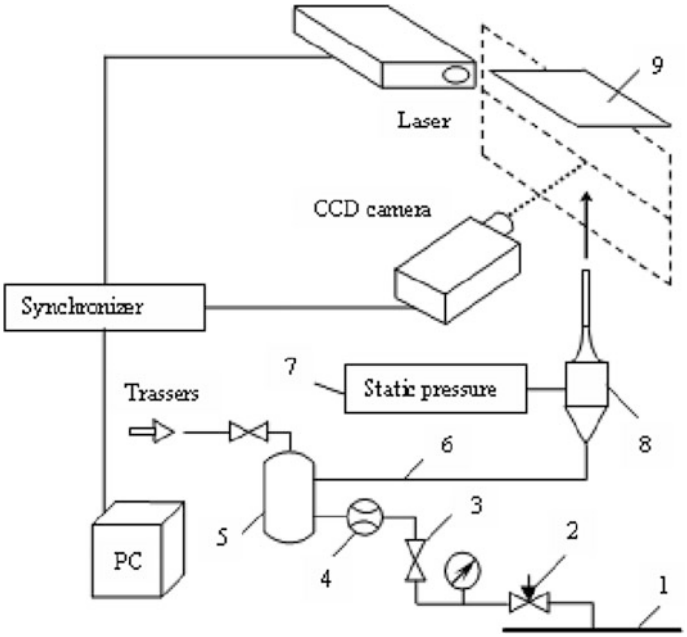


Fig. 1 Scheme of experiment. *1*—high-pressure line; *2*—reducer; *3*—valve; *4*—flow meter; *5*—fore-chamber; *6*—air line; *7*—micromanometer; *8*—channel; *9*—organic glass plate

formed by the flat channels and nozzles made of plastic with height b = 500 μm −1 mm. The air jet flowed to the submerged air space (the organic glass flow chamber of 150 × 150 × 400 mm) with a hole of 95-mm in the bottom part and 120-mm in the top part. The range of Re numbers for the flat jet was $Re = U_0 b/\nu = 80-2800$, for the round jet it was $Re = U_0 d/\nu = 100-5000$ (U_0 is superficial velocity of the jet in the outlet cross-section of the channel).

3 Experimental Results

3.1 Free Jet

As it is known, the flow in the jet depends significantly on the initial conditions. In this regard, great attention was paid to the control of initial conditions; these data are presented in Fig. 2. As it can be seen from the figure, at Re < 2500 distribution of the average velocity (U/U_m) along the jet radius is in a good agreement with Poiseuille formula (U, U_m is the velocity at the radius r and the jet axis, x is the coordinate along the jet axis). For Re > 2500, the velocity profile becomes more filled and it tends to the developed turbulent one. A change in the degree of

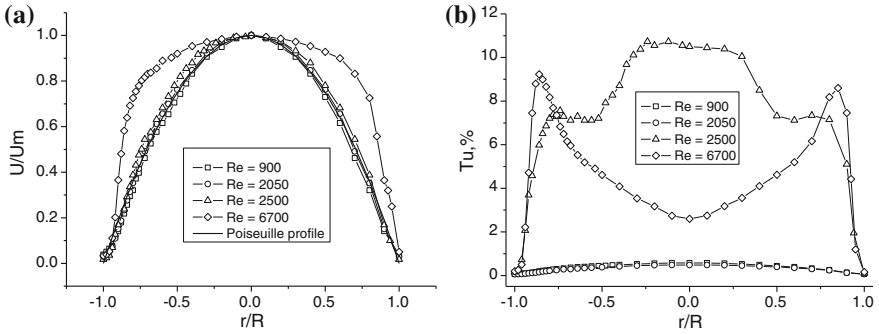


Fig. 2 Distribution of average velocity (**a**) and degree of turbulence (**b**) in the initial cross-section of the jet (tube d = 5 mm, x/d = 0, 1)

turbulence (Tu = $u/U_m \cdot 100$ %, u is the RMS of velocity pulsations) along the jet radius correlates with the behavior of average velocity.

When Re < 2500, the maximum (Tu < 0.5 %) is at the jet axis, within Re ~ 2500 three peaks are observed, and at Re > 2500, the profile of velocity fluctuations corresponds to the turbulent one with the extremum in the wall region. The distribution of the Tu is determined in experiments at Re = 2500 authors suppose due to the laminar-turbulent transition in the tube. It is known, that at the linear stage of the transition the Poiseulle profile deformation is insignificant, but at the same time, turbulent pulsations grow exponentially [10].

Flow visualization made it possible to determine the spatial pattern of the flow: formation and decay of the laminar jet and transition to turbulence. It is known that the free subsonic jets have sufficiently low Reynolds numbers of several hundred, and, this applies not only to the microjets, but also to macrojets. Flow visualization of the subsonic jet from a flat channel with height b = 500 μm is shown in Fig. 3. As it can be seen from the figure, at Re = 410, the flow in the jet is laminar, at Re = 2240, there the transition to turbulence is observed. It follows from experiments that jet length to the transition point L (jet range) can be (20−100) b, i.e., the lengths of the laminar and transitional regions of the jet are sufficiently large.

An example of downstream distribution of average velocity is presented in Fig. 4 for the axisymmetric laminar microjet. Theoretical dependence obtained by Schlichting is also shown there. As it can be seen, the experimental data agree with the theory in the nearby field (x/d < 25). The discrepancy between the experiment and calculation at x/d > 25, can be explained by the fact that the theory does not account for the finite size of the source and initial velocity profile of the jet.

To perform the effectively mixing in the jets, it is important to know the location of the point of transition to turbulence (L). Generalization of experimental data on jet range L for the round jets is presented in [5]. Data for the flat nozzles within b = 22−600 μm are shown in Fig. 5. Here the dotted line shows correlation presented in [3]. As it can be seen from the graph, data of different authors on the jet range of subsonic flat microjets agree. For different experimental conditions, the

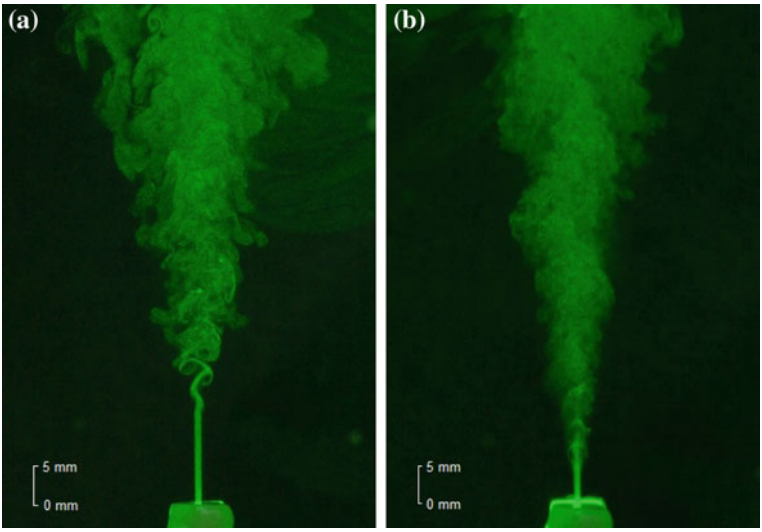


Fig. 3 Visualization of the flow of a flat air microjet (nozzle b = 500 μm, **a**—Re = 410, **b**—Re = 2240)

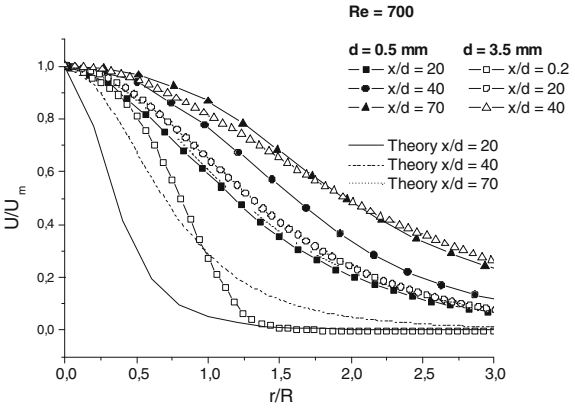


Fig. 4 Distribution of average velocity in different cross-sections of the jet: points—experiments (tube l/d = 100, Re = 700), line-theory

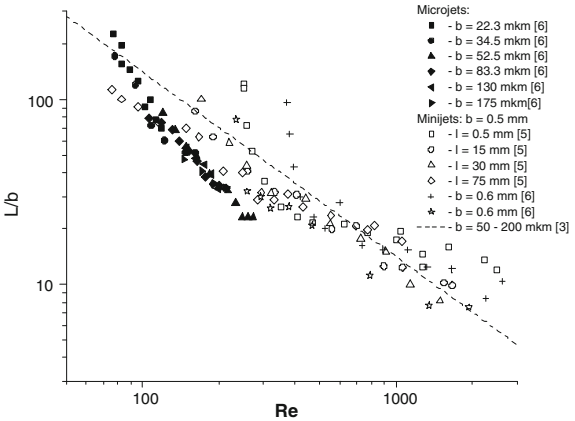


Fig. 5 Coordinate of transition point in the submerged flat jets, 1-length of the slot channel

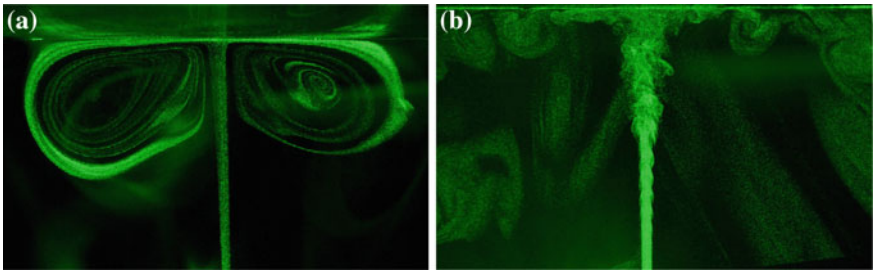


Fig. 6 Visualization of the flow of impinging axisymmetric jet (air, d = 500 μm, h/d = 20, **a**—Re = 80, **b**—Re = 2500)

linear dependence of the relative jet range on Re number in logarithmic coordinates can be observed. The same trend was noted by the authors of [3], but for a narrower range of nozzle heights (50−200 μm).

3.2 Impinging Jet

Jet interaction with the surface complicates the flow pattern. The pattern of flow visualization of an impinging jet from a tube with the diameter of 500 μm is shown in Fig. 6 (h is the distance between the nozzle and the wall). In the laminar flow, a toroidal vortex is formed in the jet. With an increase in the Reynolds number, two regions of laminar-turbulent transition are formed: in a free part of the jet and in a thin wall boundary layer. The experiments showed that the presence of obstacles in the case of an impinging jet could change the coordinate of transition to turbulence, for example, due to the feedback effect [11].

4 Discussion

In our experiments, both for the flat and round jets, we mainly observed the sinusoidal instability mode, and only under the certain conditions we got the decay mechanism of transition as in [3]. Moreover, these data suggest that the transverse dimension of a jet (micro or macro) does not play a significant role for the coordinates of transition. The most important parameters for this problem are: geometry of the jet (round or flat), Reynolds number and initial velocity profile. The question about the influence of initial conditions on development of the jet flows is sufficiently studied for the turbulent regime and it is studied insufficiently for the laminar-turbulent transition. The large range of submerged jets obtained in experiments is apparently explained by the initial parabolic velocity profile and low initial level of turbulence. The theory confirms that the jets with parabolic initial

velocity profile have the higher Reynolds numbers than those with the impact ("top-hat") velocity distribution, but the Re number of transition does not exceed 10 −30 [9].

5 Conclusions

It was shown that the range of free jets could reach 20−200 nozzle calibers. The Reynolds number of transition to turbulence in the mini- and microjets takes large values (1000−2600), and this is three orders of magnitude higher than the Reynolds number of stability loss (10−30). In the case of the impinging jet, an obstacle can change the coordinate of transition to turbulence, for example, due to the feedback effect.

Acknowledgments The work was partially supported by the RFBR (grant No. 14-08-00768), and Russian Scientific Foundation (grant No. 14-19-00402).

References

1. C.M. Ho, Y.C. Tai, Micro-electro-mechanical-systems (MEMS) and fluid flows. Annu. Rev. Fluid Mech. **30**, 579–612 (1998)
2. T.M. Squires, S.R. Quake, Microfluidics: fluid physics at the nanoliter scale. Rev. Mod. Phys. **77**, 977–1026 (2005)
3. C. Gau, C.H. Shen, Z.B. Wang, Peculiar phenomenon of micro-free-jet. Phys. Fluids **21**, 092001 (2009)
4. Y.A. Litvinenko, G.R. Grek, V.V. Kozlov, G.V. Kozlov, Subsonic round and plane macrojets and microjets in a transverse acoustic filed. Dokl. Phys. **56**, 26–31 (2011)
5. V.V. Lemanov, V.I. Terekhov, K.A. Sharov, A.A. Shumeiko, An experimental study of submerged jets at low Reynolds numbers. Tech. Phys. Lett. **39**, 421–423 (2013)
6. V.M. Aniskin, V.V. Lemanov, N.A. Maslov, K.A. Mukhin, V.I. Terekhov, K.A. Sharov, Experimental study of subsonic flow plane mini- and microjets of air. Tech. Phys. Lett. **41**, 26–31 (2015)
7. V.M. Fomin, V.M. Aniskin, A.A. Maslov, S.G. Mironov, I.S. Tsyryul'nikov, Gas-dynamic flow structure and development of perturbations in microjets. Dokl. Phys. **55**, 419–422 (2010)
8. C.J. Chan, H.T. Chen, C. Gau, Flow and heat transfer of a micro jet impinging on a heated chip. Part 1. Micro free and impinging jet flow. Nanosci. Microsci. Therm. **17**, 50–68 (2013)
9. C.M. Ho, P. Huerre, Perturbed free shear layers. Annu. Rev. Fluid Mech. **16**, 365–424 (1984)
10. A.V. Boiko, G.R. Grek, A.V. Dovgal, V.V. Kozlov, *The origin of turbulence in near-wall flows* (Springer-Verlag, Berlin, 2002)
11. C.M. Ho, N.S. Nosseir, Dynamics of an impinging jet. Part. 1 The feedback phenomenon. J Fluid Mech **105**, 119–142 (1981)

Numerical Investigation of a Confined Jet Array Penetrating into a Counterflow

Etienne Robert and Martin Thomas

Abstract A closely spaced jet array penetrating into a counterflow is investigated numerically to identify the location of the stagnation points and the conditions in their vicinity. Of special interest is the spatial homogeneity of the concentration field immediately upstream of the stagnation points for the species being supplied through the jet array. This configuration is used to produce the boundary conditions required in a research burner in order to create unstretched one-dimensional diffusion flames. The aim of the work presented here is to identify the parameter space conducive to the creation of such flames. The ratio of jet velocity to that of the bulk flow is the main control parameter and is investigated in cold-flow simulations. The results are compared with a limited set of experimental measurements available for this configuration.

1 Introduction

The interaction of jets with quiescent fluid, coflows, crossflows and counterflows are canonical configurations in fluid mechanics and have therefore received a lot of attention from the research community, for an exhaustive review see the work of Reynolds et al. [5]. Jets in counterflows have been the subject of comparatively fewer investigations than the other configurations, perhaps because they present additional difficulties both in terms of experimental realization and theoretical modelling [1]. Counter-flowing jets are however relevant in a wide range of applications and provide advantageous mixing capabilities. The work presented here investigates numerically a slightly different configuration, shown schematically in Fig. 1a: a closely spaced and confined jet array introduced into a penetrating counterflow.

E. Robert (✉) · M. Thomas
Polytechnique Montréal, 6079, Station Centre-Ville, Montreal,
Québec H3C 3A7, Canada
e-mail: etienne.robert@polymtl.ca

© Springer International Publishing Switzerland 2016

A. Segalini (ed.), *Proceedings of the 5th International Conference on Jets, Wakes and Separated Flows (ICJWSF2015)*,
Springer Proceedings in Physics 185, DOI 10.1007/978-3-319-30602-5_5

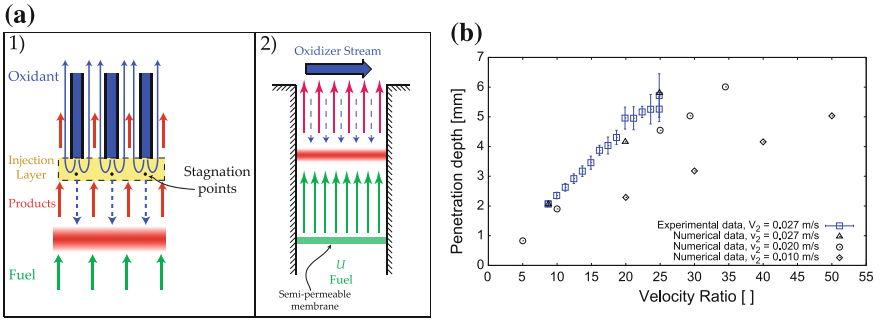


Fig. 1 **a**(*1*) Schematic representation of a jet array introduced into a counterflow. (*2*) Idealized unstrained diffusion flame configuration. The jet array is used to produce experimentally the boundary conditions at the top of the channel. **b** Comparison between experimental and numerical results for the jet penetration depths as a function of the velocity ratio

This jet array is used in a research burner to create nearly unstrained diffusion flames [7]. This experimental realization aims to approach an idealized theoretical construct, shown in Fig. 1a(1), where one reactant is advected to a planar reaction sheet while the other counter-diffuses against the combustion products. This configuration is desirable for the development of theoretical models because all transport processes are 1D and combustion-mediated phenomena can be investigated uncoupled from hydrodynamic perturbations. The counter-flowing jet array overcomes a longstanding obstacle preventing the experimental realization such flames: ensuring the spatially homogeneous supply of the counter-diffusing reactant and removal of the combustion products on the same side of the reaction sheet. The jet array geometry and the velocities used should be chosen to ensure that the region of intense mixing, referred to in the following as the *injection layer*, does not extend far upstream in the burning chamber.

The desirable mixing characteristics of jets arise from the instability of their shear layers, that quickly lead to the formation of turbulence as the velocity of the jets is increased. These instabilities are observed even for very low Reynolds numbers for jets evolving in quiescent fluid, with threshold values obtained experimentally or from modelling ranging from 10 to a few hundreds [2]. Jets inserted in a counterflow are even more unstable because their shear layers contains locally absolutely unstable regions [8]. Single jets in counterflows have been investigated both theoretically and experimentally, usually assuming that the jet cross-sectional area is small compared to that of the counterflow. More specifically, the confinement of individual jets can be characterized through the ratio $Z = (V_j^2 A_j)/(V_\infty^2 A_\infty)$, with V_j the jet velocity, V_∞ the unperturbed velocity of the counterflow, A_j the cross-sectional area of the jet and A_∞ that of the counterflow. Morgan et al. [4] demonstrated that for jets not significantly confined by their surroundings, with $Z < 0.25$, the penetration depth x_p is linearly proportional to the velocity ratio $\alpha = V_j/V_\infty$. Here x_p is defined as the distance between the stagnation point and the jet inlet. This simple relationship has been validated experimentally [1, 10], provided that the momentum flux

ratio Z remains small. The velocity measurements carried out by Bernero et al. [1] have confirmed that for very low $\alpha \approx 1.3 - 1.4$, an intermittent stable case can be observed. However as α is increased, turbulence quickly develops and the jet tip begins to wander asymmetrically, resulting in important fluctuations in the far field and intense mixing [10].

For jets in quiescent flows, coflows and crossflows, investigations addressing confined arrays are scarce, with no in-depth treatment of the counter-flowing jet array configuration found in the literature. Jet arrays (without counterflow) impinging on solid surfaces have been studied in the context of electronic components cooling. The effect of jet spacing [3] was investigated but the issue of penetration depth was not addressed. Instabilities with characteristic length greater than the jet spacing have been observed as a results of the interaction between several jets in closely spaced co-flowing arrays with high α [9]. The investigations described above are of limited use here as they were carried out assuming that diffusion is negligible and that the jet confinement is small. Both of these assumptions do not hold in the configuration of interest here as the jet spacing in the array is on the order of a few jets diameters. The work presented here aims to investigate the effect of the velocity ratio on the suitability of a counter-flowing jet array to provide the required boundary conditions for the burner illustrated in Fig. 1a. The main quantities of interest are the location of the stagnation points and the species concentration field in its vicinity.

2 Experimental and Numerical Configuration

The burner configuration on which this investigation is based has been characterized in details elsewhere [7], demonstrating that it can create a very good approximation of the idealized configuration of Fig. 1a. The region of highest interest is the injection layer located immediately next to the tip of the needles supplying the counter-diffusing reactant to the burning chamber. The jet array is comprised of 31 by 31 stainless steel tubes, 1.0 mm O.D. and 0.8 mm I.D., on a 2.5 mm Cartesian grid. In the combustion experiments, the counter-diffusing reactant is pure oxygen while the bulk flow is CO_2-diluted methane. In order for the flame to be considered 1D and unstrained, the reaction zone must be located in a region where the velocity, temperature and species concentration are constant in the transverse direction relative to the jets axis and vary only with the distance from the needle array [7]. For the combustion experiments, the jet velocity is on the order of 0.1 to 0.4 m/s and the bulk velocity is between 0.01 and 0.03 m/s (based on volumetric flow at standard conditions, actual values at the flame sheet are approximately 4 times higher). This corresponds to Reynolds numbers on the order of 100 in the tubes and much less in the combustion chamber itself. The resulting velocity ratio α is typically in the range of 5 to 10, with the corresponding momentum ratio between 2 and 10, well exceeding the low confinement threshold of $Z < 0.25$.

The numerical calculations are performed using a commercial finite-volume based solver (ANSYS Fluent) on an unstructured three dimensional grid, which consists of 515000 nodes on a 7.5 mm x 7.5 mm x 25 mm physical domain. This volume therefore contains 3 * 3 = 9 jets with a diameter of 0.8 mm, allowing for the investigation of the interactions between jets. To investigate the effect of diffusion, the numerical simulations were carried out assuming that the jets are pure oxygen while the counterflow is pure CO_2. The flow is modelled using the Reynolds Averaged Navier-Stokes (RANS) equations, with the turbulence closure problem addressed through the use of Reynolds stress models (RSM). For the injection tube inlets, a parabolic velocity profile is used and the sidewalls of the domain are modelled as symmetry. The boundary conditions are set to reflect that very low turbulence levels are expected at the advected inlet and at the exit of the injection tubes, as stabilization chambers are used in the experiment. Energy, pressure, species mass fraction and momentum equation are solved using second order spatial approximations, turbulent quantities are calculated using first order approximations.

3 Results and Discussion

The range of α covered here extends from 5 to 50 and isothermal conditions are assumed. Consequently, the results discussed in the following should not be interpreted as providing a precise position for the boundary of the 1D-region or for the stagnation point. They are rather intended to reveal qualitatively the sensitivity of these positions to changes of the velocity ratio α. A limited experimental dataset has been obtained using high speed Particle Image Velocimetry (PIV) on the jet array described in the previous section [6]. These results reveal that the penetration depth increases approximately linearly with the jet to counterflow velocity ratio. The corresponding trend shown in Fig. 1b was gathered with a constant counterflow velocity of 0.027 m/s. These results were however very time consuming to acquire and cannot provide the most critical information for the application at the origin of this study: the concentration field in the vicinity of the stagnation point. Moreover, with a laser sheet thickness on the order of the jet diameter, the PIV velocity fields acquired have limited accuracy because of significant motion of the tracer particles into and out of the measurement plane. The effect of α on the penetration depth was investigated numerically by changing simultaneously the jet and counterflow velocities. Numerical and experimental results gathered in the same conditions show very good agreement, as shown in Fig. 1b. Linear relationships similar to those observed in the experiment are visible between the velocity ratio and the penetration depth. The numerical results however reveal an interesting feature as the jets are highly confined and the momentum ration Z is high: the slope of the linear relationship linking the penetration depth to the velocity ratio is a function of the velocity of the counterflow, with the penetration depth increasing faster with α when the counterflow velocity is higher.

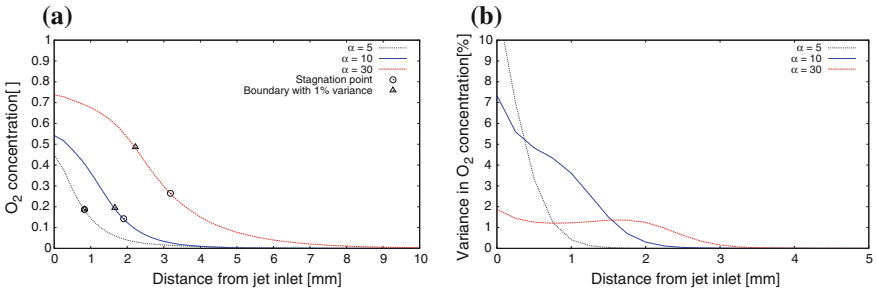


Fig. 2 **a** Average concentration for the counter-diffusing species in planes perpendicular to the jet axis, starting from the jet inlet. **b** Transverse variance in the counter-diffusing species concentration field as a function of distance from the jet array

As the jets expand in the counterflow, oxygen mass fraction declines very quickly, both along the centerline and on average for planes perpendicular to the jet axis. This is shown in Fig. 2a for 3 different velocity ratios. With increasing distance from the jet inlet, turbulence and diffusion mix the oxygen from the jets with the CO_2 from the counterflow and the concentration field becomes progressively more uniform. Eventually this field becomes 1D, providing the conditions sought for the idealized burner configuration. To characterize this smoothening of the counter-diffusing species distribution, the variance of the O_2 mass fraction on a plane perpendicular to the bulk flow is shown in Fig. 2b. By selecting a threshold value for this variance, it is possible to identify a location different from the jets stagnation point that constitutes the burner counter-diffusing boundary, from the point of view of the flame.

In the following, a threshold variance of 1 % has been used, with the corresponding boundary shown in Fig. 2a along with the stagnation points. The flames created in the burner must therefore be located upstream of these points to evolved without perturbing influence from the injection layer. Analysis of the results presented in Fig. 2a reveals that variations in the counter-diffusing species is the limiting factor for low α and the stagnation point is limiting for high α. The transition between the two cases occurs for α between 5 and 10. The evolution of the variance shown in Fig. 2b reveal that intense mixing is occurring in the jets well before the stagnation point when α is high. As a result, the concentration of the counter-diffusing specie observed at the stagnation point is higher when α is high. This is beneficial as it allows for the creation of flames with a broader range of mixture strengths. For the velocity ratios encountered in the combustion experiments, the numerically calculated values for the stagnation point and the 1 % variance threshold are both below 2 mm. The flames investigated experimentally in those conditions were always located at least 5 mm from the tip of the jet array. Consequently the assumptions made regarding the location of the virtual origin of the counter-diffusing specie is indeed a conservative estimate ensuring that the observed flames are always safely created in the 1D region of the burner.

4 Conclusion

A jet array penetrating into a counterflow has been investigated numerically. The investigation focuses on two parameters: The position of the stagnation point and the variance of the counter-diffusing species on a plane perpendicular to the jets axis. The numerical values for the distance between the tip of the injection array and the stagnation point compares very well with the penetration depths obtained experimentally. The same linear relationship between the velocity ratio and the penetration depth is also found in both datasets. The slope of relationship is however a function of the degree of confinement of the jet array, modified through the counterflow velocity. The use of the transverse variance of the counter-diffusing species to evaluate the boundary of the 1D region of the flow reveals that for low velocity ratios, diffusion is the limiting factor to providing uniform boundary conditions to the burning chamber while velocity (inertia) dominates for $\alpha > 5$. The numerical results presented here confirm that the assumptions made in the combustion experiments do result in the flames being created in the 1D region of the burning chamber.

References

1. S. Bernero, H.E. Fiedler, Experimental Investigations of a jet in counterflow, in *Advances in Turbulence VII*, vol. 46, Fluid Mechanics and Its Applications, ed. by U. Frisch (Springer, Netherlands, Dordrecht, 1998), pp. 35–38
2. I. Danaila, J. Dusek, F. Anselmet, Coherent structures in a round, spatially evolving, unforced, homogeneous jet at low Reynolds numbers. Phys. Fluids **9**(11), 3323 (1997)
3. A.M. Huber, R. Viskanta, Effect of jet-jet spacing on convective heat transfer to confined, impinging arrays of axisymmetric air jets. Int. J. Heat Mass Transf. **37**(18), 2859–2869 (1994)
4. W.D. Morgan, B.J. Brinkworth, G.V. Evans, Upstream penetration of an enclosed counterflowing jet. Ind. Eng. Chem. Fundam. **15**(2), 125–127 (1976)
5. W.C. Reynolds, D.E. Parekh, P.J.D. Juvet, M.J.D. Lee, Bifurcating and blooming jets. Annu. Rev. Fluid Mech. **35**(1), 295–315 (2003)
6. E. Robert, On the use of a jet array to create unstrained counter-diffusion flames, in *ICJWSF 2010* (2010)
7. E. Robert, P.A. Monkewitz, Experimental realization and characterization of unstretched planar one-dimensional diffusion flames. Combust. Flame **160**(3), 546–556 (2013)
8. P.J. Strykowski, R.K. Wilcoxon, Mixing enhancement due to global oscillations in jets with annular counterflow. AIAA J. **31**(3), 564–570 (1993)
9. E. Villermaux, E.J. Hopfinger, Periodically arranged co-flowing jets. J. Fluid Mech. **263**, 63 (1994)
10. M. Yoda, H. Fiedler, The round jet in a uniform counterflow: flow visualization and mean concentration measurements. Exp. Fluids **21**(6) (1996)

Coherent Structures in a Turbulent Swirling Jet Under Vortex Breakdown. 3D PIV Measurements

Sergey V. Alekseenko, Vladimir M. Dulin, M.P. Tokarev and Dmitriy M. Markovich

Abstract The current study reports on spatial structure of a global mode of self-sustaining oscillations in a turbulent swirling jet under vortex breakdown conditions. Ensembles of 2D and 3D velocity fields were measured by stereoscopic and tomographic PIV systems, respectively, and were analysed via proper orthogonal decomposition. For the 2D PIV, the spatial resolution was sufficient to resolve most of the turbulent kinetic energy of the turbulent flow. The resolution in the case of tomographic PIV was lower, but the 3D instantaneous velocity fields unambiguously revealing that the global mode corresponds to a spiralling structure, counter-winded to the direction of the jet swirl.

1 Introduction

Swirling jet flows often take place in industrial devices: in burners, mixers, cooling systems, separators etc. [1]. From a practical point of view, the imposed swirl essentially enhances turbulent transfer and mixing in the near field of jets (entrainment rate, turbulent fluxes and fluctuations level can be increased by few times [1–3], see Fig. 1, for example). In combustors, flow swirling promotes flame stabilisation with a compact combustion zone and provides good ignition characteristics [1, 4–6]. This is considered to be caused mainly by formation of the central recirculation zone (RZ), which supplies heat and active chemical species from the hot products to the fresh mixture at the flame root. However, flow structure and dynamics of swirling jets is still not completely understood. Besides, swirling jets serve as model flows for such concentrated vortex phenomena as tornados [7, 8], which are difficult to reproduce in laboratory [9–13].

S.V. Alekseenko · V.M. Dulin (✉) · M.P. Tokarev · D.M. Markovich
Kutateladze Institute of Thermophysics, Siberian Branch of RAS,
Novosibirsk 630090, Russia
e-mail: vmd@itp.nse.ru

S.V. Alekseenko · V.M. Dulin · M.P. Tokarev · D.M. Markovich
Novosibirsk State University, Novosibirsk 630090, Russia

© Springer International Publishing Switzerland 2016

A. Segalini (ed.), *Proceedings of the 5th International Conference on Jets, Wakes and Separated Flows (ICJWSF2015)*,
Springer Proceedings in Physics 185, DOI 10.1007/978-3-319-30602-5_6

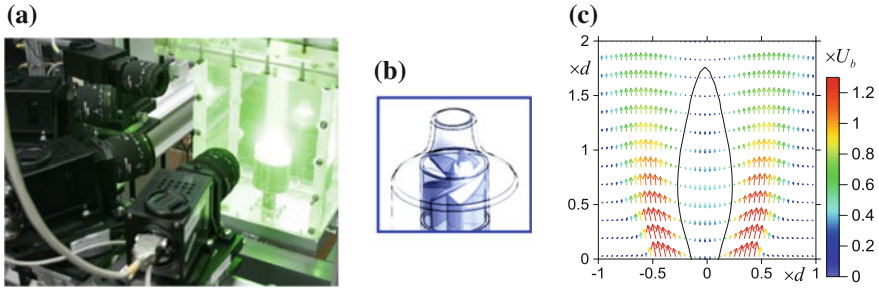


Fig. 1 **a** Photograph of 3D PIV setup. **b** Swirler assembly inside the nozzle block. **c** Mean velocity field for the central plane of the flow (2D measurements, Re = 8900)

It is recognized that vortex rings prevail in mixing layers of non-swirling and weakly swirling jets, whereas strong helical waves become dominant (e.g., [14, 15]) in the shear layer of a jet with a sufficiently high swirl rate (but before the vortex breakdown, VB). A further increase in the swirl rate leads to a breakdown of the swirling jets' vortex core [1, 16, 17], which has been observed in different states: spiral (rarely double helices), bubble, and conical, where the latter two can be either symmetric or asymmetric ([7, 18], among others).

Asymmetric breakdowns are characterised by a quasi-periodic precession of the swirling jet vortex core. It is remarkable that flow structure of strongly swirling jets with bubble-type VB and precession of the vortex core manifests some common features, even for rather different nozzle geometries. Previous studies [19, 20] reported that precession of the vortex core in a strongly swirling jet is the result of global helical instability mode with azimuthal wavenumber|m| = 1 (for a fixed time instant, the disturbance phase function is defined as $[kx + m\theta]$, where x and θ are the axial and angular coordinates, respectively) growth in an absolutely unstable jet flow after appearance of RZ. According to [20], a pair of spiral vortices was present in the mixing layers (one vortex in each mixing layer) of the strongly swirling jet after development of the bubble-type VB.

Based on phase-averaging in a turbulent strongly swirling jet, Cala et al. [21] determined three-dimensional vortex structures in the flow as a pair of secondary helical vortices induced by the precessing vortex core (PVC). One secondary vortex was located inside the vortex core, while the other one was induced in the outer mixing layer. Legrand et al. [22] used correlation coefficients between the proper orthogonal decomposition (POD, [23]) modes and PIV snapshots to reconstruct a phase portrait of quasi-periodic PVC and coherent vortices in the outer and inner mixing layer in a turbulent swirling jet. In [24], the first two modes of POD of PIV data were used in a low-order reconstruction of the CS, associated with PVC in a strongly swirling jet. The shape of CS corresponded well to the profile of a global mode from instability analysis of the mean velocity profiles.

POD was also used in [25] to study impact of PVC on swirling flame dynamics in a model gas turbine combustor by means of high-speed PIV and OH* planar

laser-induced fluorescence. Three vortex structures were identified: central vortex and a pair of counter-rotating helical vortices in shear layers. According to the conditional sampling analysis, it was concluded that the helical vortex structure in the inner shear layer (called PVC) promoted mixing of the combustion products with the fresh mixture. Triple-vortex structure was also detected in a model swirl combustor by [26]. The authors compared POD data to the results of the dynamics mode decomposition [27], which extracts spatial modes associated with specific frequencies. The authors concluded that with the presence of a global mode the vortex core and the entire flow were precessing at the same frequency. Thus the PVC was more energetic and therefore could be extracted by POD.

The aim of the present paper is to retrieve information about 3D global mode, dominating in a turbulent high-swirl jet with bubble-type vortex breakdown. For this purpose POD was applied to the set of 3D instantaneous velocity fields, measured by tomographic PIV [28]. The results of direct 3D measurements are compared to the reconstruction of the phase portrait from 2D PIV data.

2 Experimental Setup

The experiments were performed in a hydrodynamic loop, consisted of a pump, flow meter, temperature stabilising device, and test section. The measurements were performed in a transparent rectangular test Sect. (40 cm high, 20 cm wide, and 20 cm long) made of Plexiglas in order to provide PIV measurements. The jet flows were organized by a contraction nozzle with a vane swirler mounted inside. The nozzle was located at the bottom of the test section (see Fig. 1a). According to the definition given in [1] the geometrically defined swirl rate was 1.0.

$$S = \frac{2}{3}\left(\frac{1-(d_1/d_2)^3}{1-(d_1/d_2)^2}\right)\tan(\varphi), \tag{1}$$

where, $d_1 = 7$ mm is the diameter of the centerbody supporting the blades, $d_2 = 27$ mm is the diameter of the swirler tube, and φ is the inclination angle of blades relatively to the axis.

Figure 2a shows the distributions of the mean velocity components at the nozzle exit (cross-section $z = 0$) for the studied flows. The profiles normalised by the mean flow rate velocity U_0. For the case of $S = 0.41$, the jet centreline velocity has a peak at the nozzle exit, as in [18], and then decreases downstream. For the low swirl case, the mean axial velocity remains positive for the entire measured area. For the cases $S = 0.7$ and 1.0, a bubble-type central recirculation zone was detected in the mean velocity field. Figure 3 plots the mean velocity fields and values of turbulent kinetic energy (TKE) for the cases of $S = 0$, 0.41, and 1.0. These flow cases are referred to as non-swirling, low-swirl and high-swirl jets, respectively. The latter flow case is

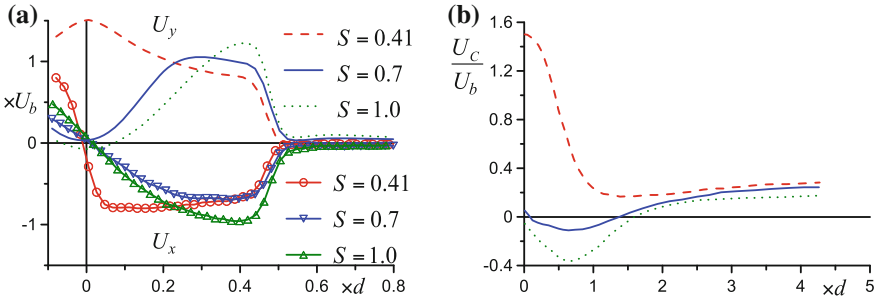


Fig. 2 Profiles of the mean velocity **a** at the nozzle exit and **b** along the centreline (2D measurements, Re = 8900)

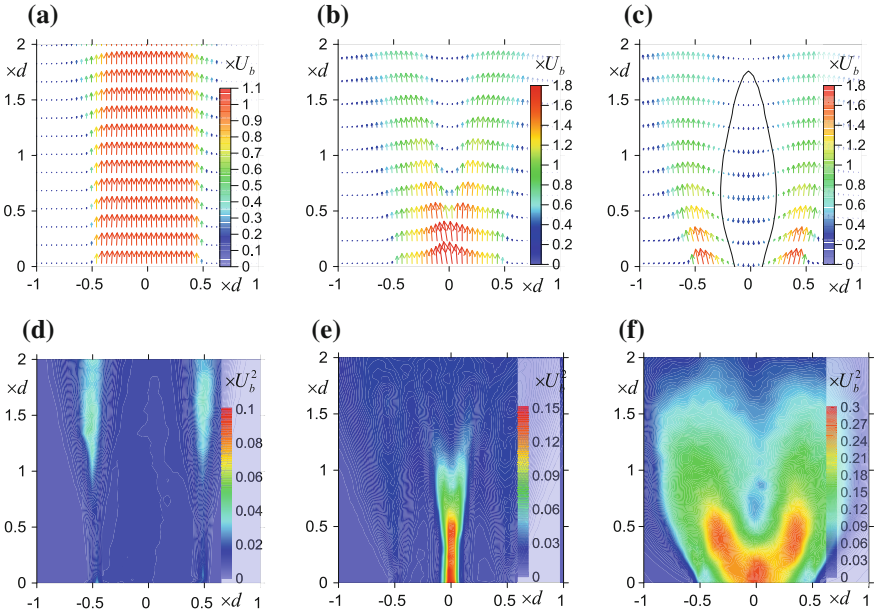


Fig. 3 Spatial distributions of (*top row*) mean velocity and (*bottom row*) TKE (Re = 8900) for: **a**, **d** non-swirling jet ($S = 0$); **b**, **e** low-swirl jet ($S = 0.41$); **c**, **f** high-swirl jet ($S = 1.0$)

associated with a pronounced bubble-type vortex breakdown and intensive flow precession.

In the present work the POD analysis was applies for 2D and 3D velocity snapshots, obtained for the case $S = 1.0$ by using stereoscopic and tomographic PIV systems, respectively. The details on the experiments and data processing can be found in [29, 30]. The Reynolds number (defined as $\mathrm{Re} = U_b d/\nu$, where U_b is the bulk flow velocity; ν is the water kinematic viscosity) during the 2D and 3D experiments was 8900 and 30000, respectively. For the former case, the spatial

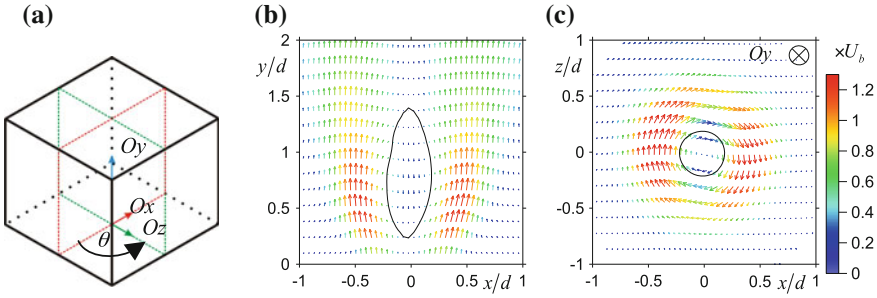


Fig. 4 **a** Coordinate system and measurement volume and planes used for POD of 3D velocity data (Re = 30000). Cross-sections **b** $z = 0$ and **c** $y = 0.7\ d$ of the time-averaged 3D velocity field

resolution of PIV (1.3 mm) was sufficient to resolve most of the turbulent kinetic energy of the flow (with Re = 8900 and integral scale of ~2 mm, see [29]). The resolution in the latter case was lower, but the instantaneous 3D velocity fields were measured. The velocity ensembles were of 1000 and 100 snapshots for 2D and 3D data sets, respectively. Besides, during the POD analysis of the tomographic PIV data, 200 snapshots of 2D slices (*xOy* and *zOy*) were extracted as Fig. 4a shows.

3 Results and Conclusions

The time-averaged velocity field, measured by 2D PIV for the jet (Re = 8900), is shown in Fig. 1c (the colour-scale corresponds to the modulus of the three-component vector). The solid lines bounds the CRZ. For the 3D velocity measurements, the averaged velocity data in shown in Fig. 4. Two perpendicular cross-planes are shown. The 3D PIV captures satisfactory transverse size of the RZ. The longitudinal size of the RZ is affected by a spatial smoothing due to ghost particles. The most pronounced effect is in the vicinity of the nozzle, where there is a strongest velocity gradient.

The radial and axial components of the TKE (2D data) are shown in Fig. 5a, d. To reveal the contribution of the global mode (flow precession) to the TKE, a POD routine is applied to the PIV data. The POD of an ensemble of N instantaneous velocity fields $\mathbf{u}^i$ (2D or 3D) provides:

$$\mathbf{u}^i(\mathbf{x}) = \sum_{n=0}^{N} a_n^i \varphi_n(\mathbf{x}), \text{ where } \langle \varphi_i(\mathbf{x}) \varphi_j(\mathbf{x}) \rangle_\Omega = \delta_{ij}. \tag{2}$$

Spatial functions φ_n are the orthnormal basis functions, δ_{ij} is the Kronecker delta, and $\langle \rangle_\Omega$ denotes the spatial averaging over the domain considered. a_n^i are the "temporal" correlation coefficients. The POD approach is based on determining

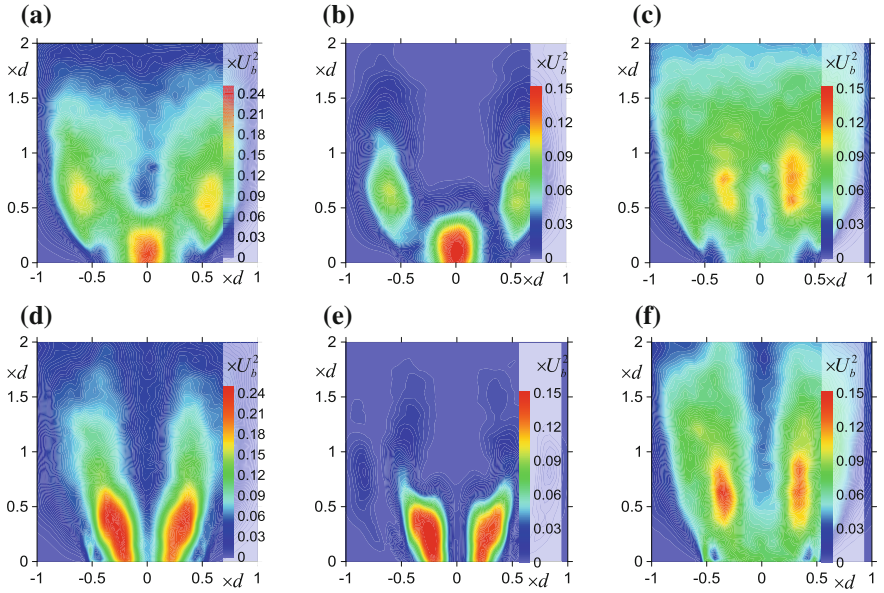


Fig. 5 Spatial distributions of (*top row*) radial and (*bottom row*) axial components of TKE (Re = 8900) for: **a**, **d** entire ensemble of velocity fields (all POD modes); **b**, **e** two the most energetic POD modes; **c**, **f** residual POD modes

"optimal" basis functions φ_n that are the most correlated to the velocity fields (snapshots). Namely, the sums of the correlation coefficients $\sum\left(a_n^i\right)^2 = \lambda_n$ are subsequently maximized for $n = 0$, $n = 1$ and so on. Since POD modes arranged according to λ_n, which corresponds to the amount of TKE in each POD mode, a reduced-order model for each instantaneous velocity snapshot can be obtained on the basis of few the most energetic POD modes:

$$\mathbf{u}^i(\mathbf{x}) = a_0^i\varphi_0(\mathbf{x}) + a_1^i\varphi_1(\mathbf{x}) + a_2^i\varphi_2(\mathbf{x}) + \ldots, \tag{3}$$

where $\boldsymbol{\varphi}_0$ is the mean velocity field. For the ensemble of 2D PIV data, the first two POD modes are almost equally contain about 17 % of spatial-averaged TKE (contribution from the third one is about 2 %). Figure 5b, e, shows the contribution to TKE from the first two most energetic POD modes. After removal of the most coherent part, the spatial distributions of the mean-square velocity fluctuations of the radial and axial components appear to have a similar structure and magnitude.

Figure 6 shows the comparison of coherent structures reconstruction from POD of 3D data and its 2D slices. The analysed domain corresponds to $2d$ in the transverse and longitudinal directions. One can see that for 2D slices (Fig. 6b, c) the reconstruction gives ambiguous direction for the spiralling sense of the structures. The reconstructions in Fig. 6b, c, are produced by correct and incorrect hypothesis

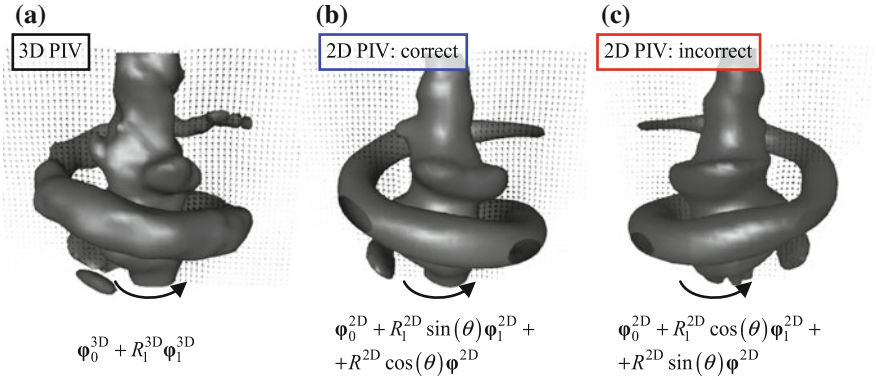


Fig. 6 Low-order reconstruction of coherent mode in a high-swirl jet (Re = 30000) from **a** 3D POD and **b**, **c** 2D POD

for the direction correspondence between the azimuthal angle θ and the phase angle. The 3D data unambiguously reveals that the global mode corresponds to spiralling structures, winded in the opposite direction to jet swirl.

Acknowledgments This work is funded by a grant from the Russian Science Foundation (project No. 14-29-00203 in NSU, supervised by Professor Kemal Hanjalic).

References

1. A.K. Gupta, D.G. Lilley, N. Syred, *Swirl Flows* (Abacus Press, Kent, England, 1984)
2. S.H. Park, H.D. Shin, Measurements of entrainment characteristics of swirling jets. Int. J. Heat Mass Transfer **36**, 4009–4020 (1993)
3. R. Örlü, P.H. Alfredsson, An experimental study of the near-field mixing characteristics of a swirling jet. Flow Turbul. Combust. **80**, 323–350 (2008)
4. N. Syred, N.A. Chigier, J.M. Beér, Flame stabilization in recirculation zones of jets with swirl. Proc. Combust. Inst. **13**, 617–624 (1971)
5. R. Weber, J. Dugué, Combustion accelerated swirling flows in high confinements. Prog. Energy Combust. Sci. **18**, 349–367 (1992)
6. Y. Huang, V. Yang, Dynamics and stability of lean-premixed swirl-stabilized combustion. Prog. Energy Combust. Sci. **35**, 293–364 (2009)
7. S.V. Alekseenko, P.A. Kuibin, V.L. Okulov, in *Theory of concentrated vortices: an Introduction* (Springer, 2007)
8. V. Shtern, F. Hussain, Collapse, symmetry, breaking, and hysteresis in swirling lows. Annu. Rev. Fluid Mech. **31**, 537–566 (1999)
9. A. Yu. Snegirev, J.A. Marsden, J. Francis, G.M. Makhviladze, Numerical studies and experimental observations of whirling flames. Int. J. Heat Mass Transf. **47**, 2523–2539 (2004)
10. K., Kuwana, K. Sekimoto, K. Saito, F.A. Williams, Scaling fire whirls. Fire Saf. J. **43**, 252–257 (2004)
11. A.Y. Varaksin, M.E. Romash, V.N. Kopeitsev, M.A. Gorbachev, Physical simulation of air tornados: some dimensionless parameters. High Temp. **49**, 310–313 (2011)

12. D.S. Nolan, Threedimensional instabilities in tornado-like vortices with secondary circulations. J. Fluid Mech. **711**, 61–100 (2012)
13. A.Y. Varaksin, M.V. Protasov, M.E. Romash, V.N. Kopeitsev, Generation of free concentrated fire vortices under laboratory conditions. High Temp. **53**, 595–598
14. F. Gallaire, J.-M. Chomaz, Mode selection in swirling jet experiments: a linear stability analysis. J. Fluid Mech. **494**, 223–253 (2003)
15. T. Loiseleux, J.-M. Chomaz, Breaking of rotational symmetry in a swirling jet experiment. Phys. Fluids **15**, 511–523 (2003)
16. S. Leibovich, The structure of vortex breakdown. Annu. Rev. Fluid Mech. **10**, 221 (1978)
17. O. Lucca-Negro, T. O'Doherty, Vortex breakdown: a review. Prog. Energy Combust. Sci. **27**, 431–522 (2001)
18. P. Billant, J.-M. Chomaz, P. Huerre, Experimental study of vortex breakdown in swirling jets. J. Fluid Mech. **376**, 183–219 (1998)
19. M.R. Ruith, P. Chen, E. Meiburg, T. Maxworthy, Three-dimensional vortex breakdown in swirling jets and wakes: direct numerical simulation. J. Fluid Mech. **486**, 331–378 (2003)
20. H. Liang, T. Maxworthy, An experimental investigation of swirling jets. J. Fluid Mech. **525**, 115–159 (2005)
21. C.E. Cala, E.C. Fernandes, M.V. Heitor, S.I. Shtork, Coherent structures in unsteady swirling jet flow. Exp. Fluids **40**, 267–276 (2006)
22. M. Legrand, J. Nogueira, A. Lecuona, S. Nauri, P.A. Rodríguez, Atmospheric low swirl burner flow characterization with Stereo-PIV. Exp. Fluids **48**, 901–913 (2010)
23. P. Holmes, J.L. Lumley, G. Berkooz, in *Turbulence, coherent structures, dynamical systems and symmetry* (Cambridge University Press, 1996)
24. K. Oberleithner, M. Sieber, C.N. Nayeri, C.O. Paschereit, C. Petz, H.-C. Hege, B.R. Noack, I. Wygnanski, Three-dimensional coherent structures in a swirling jet undergoing vortex breakdown: stability analysis and empirical mode construction. J. Fluid Mech. **679**, 383–414 (2011)
25. M. Stöhr, I. Boxx, C.D. Carter, W. Meier, Experimental study of vortex-flame interaction in a gas turbine model combustor. Combust. Flame **159**, 2636–2649 (2012)
26. D.M. Markovich, S.S. Abdurakipov, L.M. Chikishev, V.M. Dulin, K. Hanjalic, Comparative analysis of low- and high-swirl confined flames and jets by proper orthogonal and dynamic mode decompositions. Phys. Fluids **26**, 065109 (2014)
27. P.J. Schmid, Dynamic mode decomposition of numerical and experimental data. J. Fluid Mech. **656**, 5–28 (2010)
28. G.E. Elsinga, F. Scarano, B. Wieneke, B.W. van Oudheusden, Tomographic particle image velocimetry. Exp. Fluids **41**, 933–947 (2006)
29. S.V. Alekseenko, V.M. Dulin, YuS Kozorezov, D.M. Markovich, Effect of axisymmetric forcing on structure of a swirling turbulent jet. Int. J. Heat Fluid Flow **29**, 1699–1715 (2008)
30. M.V. Alekseenko, A.V. Bilsky, V.M. Dulin, L.A. Kozinkin, D.M. Markovich, M.P. Tokarev, Diagnostics of jet flows by using tomographic particle image velocimetry. Optoelectr. Instrum. Data Process. **50**, 457–465 (2014)

An Effect of Initial Disturbance on Spatial Development of a Two-Dimensional Jet at a Low Reynolds Number

Akinori Muramatsu and Hokuto Tsuchiya

Abstract When the jet Reynolds number is slightly higher than the Reynolds number which a whole two-dimensional jet maintains laminar, a flapping motion causes in the jet. Before the jet generates laminar-turbulent transition, it moves asymmetrically. A numerical simulation of the two-dimensional jet was carried out to research effect of an initial disturbance on a flapping motion. When white noise is uniformly added at the slit, the disturbance does not grow. If white noise is asymmetrically added at the slit, the disturbance rapidly grows and introduces the flapping motion. The asymmetrical disturbances are selected from natural disturbances in the actually two-dimensional jets at low Reynolds number, so that the flapping motion is formed in the two-dimensional jets.

1 Introduction

Experiments for a two-dimensional jet at low Reynolds numbers was carried out [1, 2]. In the experiment by Sato and Sakao [1], velocity fluctuations in the jet were measured using a hot-wire anemometer. In the experiment by Muramatsu and Namaita [2], a jet was discharged from a rectangular nozzle using a syringe pump in order to keep volume flow rate constant. The velocity profile and maximum turbulent intensity at the outlet are respectively a plane Poiseuille flow and less than 1.0 %. The whole jet was visualized using a planar laser Mie scattering. The visualized jets are shown in Fig. 1. Garg [3] indicated that the jet becomes laminar when the Reynolds number is less than 22 using linear stability theory. However, a jet is laminar when the Reynolds number is less than 60 in the above experiment. When the Reynolds number exceeds 60, the jet is slightly flapping. As shown in

A. Muramatsu (✉)
College of Science and Technology, Nihon University,
7-24-1 Narashinodai, Funabashi, Chiba 274-8501, Japan
e-mail: amura@aero.cst.nihon-u.ac.jp

H. Tsuchiya
Graduate School of Science and Technology, Nihon University, Funabashi, Japan

© Springer International Publishing Switzerland 2016

A. Segalini (ed.), *Proceedings of the 5th International Conference on Jets, Wakes and Separated Flows (ICJWSF2015)*,
Springer Proceedings in Physics 185, DOI 10.1007/978-3-319-30602-5_7



Fig. 1 Visualized air jets. $Re = 50$ (*left*), $Re = 80$ (*center*), and $Re = 200$ (*right*)

Fig. 1(right), when the Reynolds number exceeds 150, the irregular fluctuations are generated in the jet after the jet is flapping. It is thought that the flapping motion in a jet has an important role in the spatial development process of a two-dimensional jet. In this study, a numerical simulation of the two-dimensional jet was carried out to research effect of an initial disturbance on a flapping motion.

2 Numerical Method

Governing equations for a two-dimensional and incompressible flow are continuity equation and Navier-Stokes equation, and are expressed by non-dimensional forms. A jet Reynolds number Re is defined by a velocity on the jet center line at the slit exit U_{c0} and a height of the slit exit h. The Re was set at 300. The advection and viscous terms were discretised by energy-conservative finite difference with fourth-order accuracy [4], and the pressure term was discretised by standard central finite difference with second-order accuracy. An up-wind difference was not used to not introduce a numerical viscosity. The discretised equations were solved using SMAC scheme. Time integration was achieved using third-order Runge-Kutta scheme and the time interval was 0.02. Turbulence model was not adopted.

A jet is discharged into still fluid from a slit. The slit with height of $h = 1$ is located at the center of a wall. The center of a slit exit is an origin of the x−y coordinates, and non-dimensional x and y-axes are respectively taken in the streamwise direction and in the perpendicular direction to the streamwise. Dimensions of the computational domain was $x = 40$ and $y = \pm 10.5$, and the domain was respectively divided by 800 and 440 at same interval. As an inflow condition, a top-hat type velocity profile [5] at the slit exit was given by (1).

$$\frac{U(y)}{U_{c0}} = \frac{1}{2}\left\{1 - \tanh\left[\frac{1}{4}\frac{R}{\theta}\left(\frac{y}{R} - \frac{R}{y}\right)\right]\right\} + \text{disturbance} \tag{1}$$

Here, U is mean velocity, and subscripts c and 0 are the centerline and slit exit, respectively. The θ is a momentum thickness. R/θ was set at 20 to make the velocity gradient low and R was set at 0.4 h. The initial disturbance in (1) was given by a white noise and the maximum amplitude was 0.5 % of U_{c0}. Four kinds of disturbances were given in order to take into consideration the influence of spatial distribution of the disturbance, as shown in Fig. 2. Figure 2a is a case of no

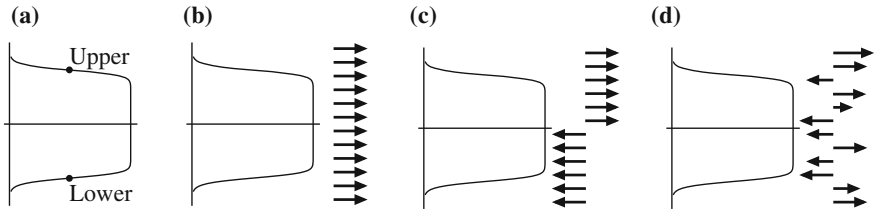


Fig. 2 Initial disturbance of four types **a** Without excitation **b** Symmetric **c** Asymmetric **d** Random

disturbance. Figure 2b, c, d show the cases which temporally random disturbance is given uniformly, asymmetrically, and randomly at the slit exit, respectively.

An outflow condition adopted the modified Sommerfeld radiation condition [6]. A reverse flow is stopped forcibly as $u = 0$ when a reversed flow is generated. Here, u is the streamwise velocity. The advection velocity was 0.7. Side boundary conditions adopted traction-free condition to introduce effect of an entrainment.

3 Numerical Results and Discussions

3.1 *Visualized Jets at* Re *of 300*

Visualized calculation results are shown in Fig. 3. They are non-dimensional speed at the non-dimensional time $t = 1{,}000$. If an initial disturbance is not impressed (Fig. 2a) and is impressed symmetrically (Fig. 2b), the jets go straightly from a slit. When the disturbance is impressed with the asymmetric mode (Fig. 2c) and with the random mode (Fig. 2d), the jets produce a flapping motion from approximately $x = 20$. The flapping motion by the asymmetric mode is large compared with the random mode. Thus, because behavior of whole jet differs by the difference in the given disturbance, the initial disturbance is strongly concerned with the spatial development process of the jet.

3.2 *Streamwise Variation of Time-Averaged Values of Jets*

Streamwise distributions of mean values of the jet are shown in Fig. 4 in order to compare the difference in the spatial development of the jet by the difference in the given disturbance mode. U_c is a jet-centerline velocity and b is the half width at half maximum. The mean values are averaged data from $t = 2{,}000$ to 5,000. The vertical axes are respectively normalized by centerline velocity at a slit exit U_{c0} and the slit width $h = 1$. Theoretical solutions of a laminar jet [7] and a turbulent jet are respectively indicated with red and blue lines in Fig. 4. In all disturbance modes,

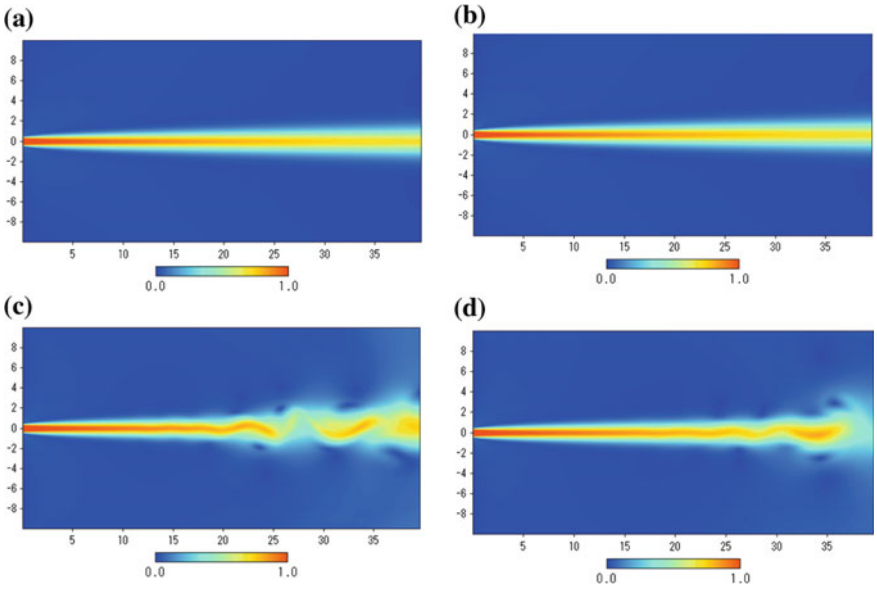


Fig. 3 Contours of velocity magnitude by various disturbances **a** Without excitation **b** Symmetric mode excitation **c** Asymmetric mode excitation **d** Random mode excitation

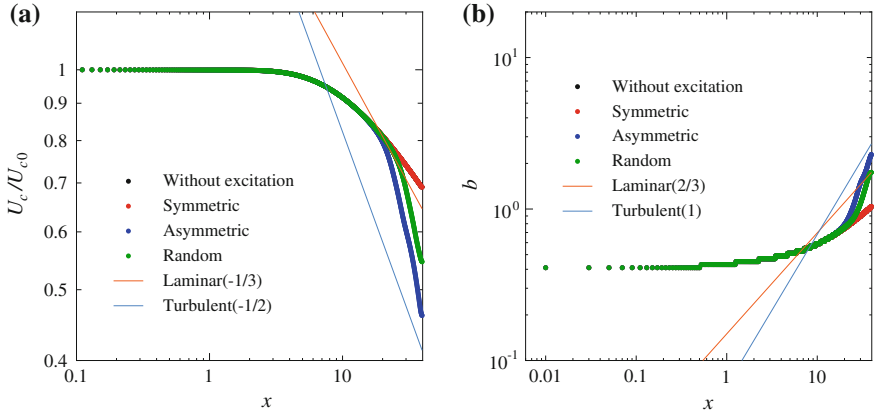


Fig. 4 Streamwise distributions of central velocity U_c and half-breadth b **a** Central velocity U_c **b** Half-breadth b

the U_c maintains an initial value until approximately $x = 2$. The region is a potential core in the jet. The U_c decreases after the potential core and follows the theoretical solution of a laminar jet at about $x = 20$. In the cases of the un-impressing and symmetrical modes, the U_c approximately decreases according to the solution of a laminar jet. On the other hand, in the cases of the asymmetric and random modes, the U_c gradually approaches to the solution of a turbulent jet and decays further in

the downstream. Momentum of mainstream of the jet decreases by the turbulent mixing between the jet and the ambient fluid, so that the jet is almost stagnated and the velocity of the jet rapidly decays. The stagnation of the jet was also observed in the experiment for the jet at the low Reynolds numbers [2]. The b also varies to similar change of U_c and becomes larger than the solution of a turbulent jet in the downstream. Consequently, it is thought that the jets with the un-impressing or symmetrical modes maintain a laminar flow in the computational domain and the jets with the asymmetric or random modes produce the laminar-turbulent transition.

3.3 Time Variations of Velocity at Two Points of Jet Shear Layer

Time variations of the streamwise velocity u at the two points, at which are the upper and lower sides on the half breadth of a jet as shown in Fig. 2a, between $t = 1{,}000$ and 2,000 are shown in Fig. 5. Black and red lines respectively indicate the velocity at the upper and lower points. The time variations of the velocity by exciting the symmetrical mode do not be amplified spatially as shown in Fig. 5a, and the jet goes without the flapping motion, as shown in Fig. 3b. This result is similar to the un-impressing case. In the case of exciting the random mode as shown in Fig. 5b, the asymmetrically fluctuations are chosen from velocity fluctuations given at random at the exit, and are spatially amplified. The asymmetric fluctuations near the slit exit have low frequencies as shown at $x = 5$ and 10 in Fig. 5b. At the downstream of the jet as shown at $x = 20$ and 30 in Fig. 5b, the frequency of fluctuations becomes high. It is suggested that there is a mechanism which received the asymmetric fluctuations selectly, because growth of the asymmetric fluctuations stood high compared with growth in other modes.

3.4 Spatial Development Process of Velocity Fluctuations

Power spectra of the streamwise velocity u obtained in the shear layer are shown in Fig. 6. Figure 6 displays the power spectra of two cases: the symmetric mode excitation and random mode excitation. Except the no-disturbance case, the velocity fluctuations at $x = 0.5$ show the flat spectra with broadband velocity fluctuations by the added white noise. At $x = 1$ in the cases of symmetric and random mode excitations, the power-spectra have the loose peak at $St = 0.2$–0.3. The St is the non-dimension frequency formed by U_{c0} and h. This value of the non-dimensional frequency approximately equals an experimental value by Sato [8]. The experimental non-dimensional frequency was obtained in the two-dimensional jet with the Reynolds number of 2,000–10,000, and is amplified frequency by a symmetrical mode of the jet. It is thought that the value of St of

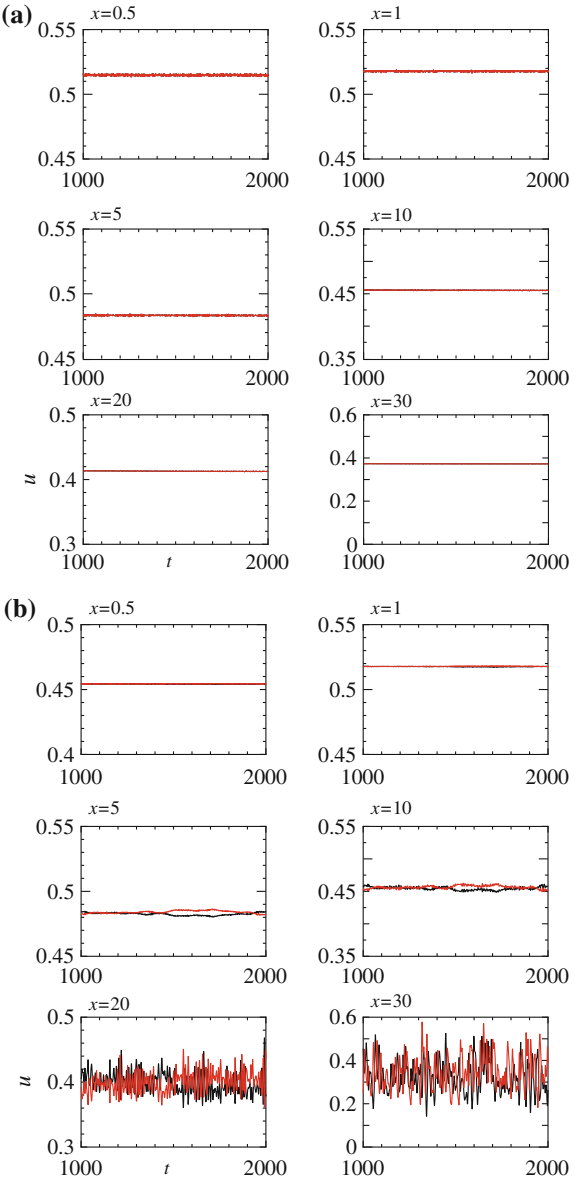


Fig. 5 Time series of streamwise velocity u at symmetrically two points in the shear layer **a** Symmetric mode excitation **b** Random mode excitation

0.2–0.3 is concerned with the symmetrical mode of the jet, although the value of the Reynolds number is slightly different from the experimental results by Sato. The frequencies of the symmetrical mode are not amplified in the above cases.

In the random and asymmetric mode excitation, the power spectra have a line spectrum about $St = 0.005$ and its harmonics. This value of St approximately equals the experimental values by Sato and Sakao [1]. It is extremely amplified toward the

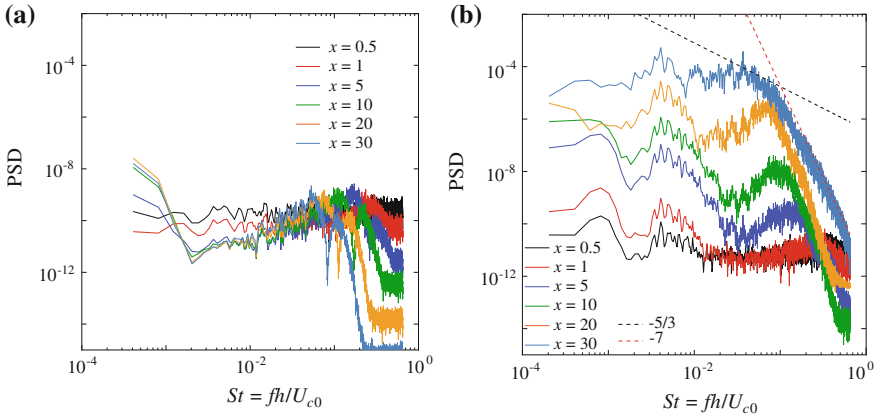


Fig. 6 Power-spectra of streamwise velocity fluctuation in the shear layer **a** Symmetric mode excitation **b** Random mode excitation

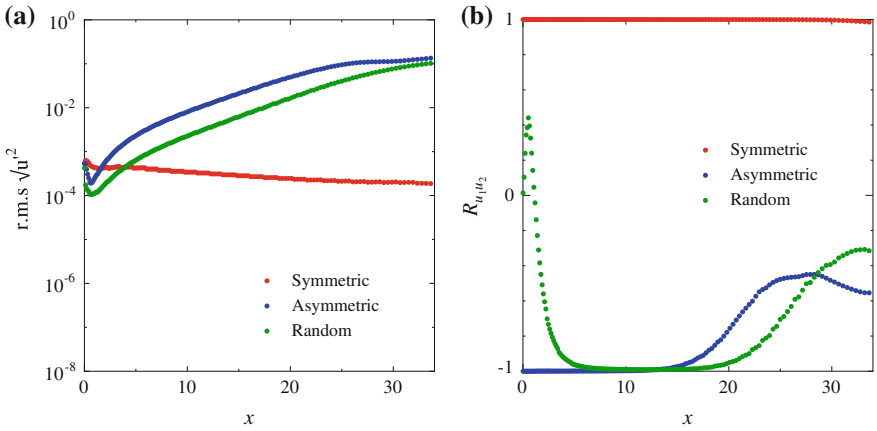


Fig. 7 Streamwise variations of r. m. s. value and cross-correlation coefficient in the shear layer **a** R. m. s. values of velocity fluctuation **b** Cross-correlation coefficients

downstream. The velocity fluctuations with high frequencies are also amplified toward the downstream, and the whole energy of the fluctuations becomes large. The slopes of the powers of −5/3 and −7 are illustrated in Fig. 6b. It is thought that the jet flow becomes turbulent at $x = 30$. The low frequencies measured by Sato and Sakao [1] are concerned with the asymmetric mode in the jet. Consequently, it is thought that this fluctuation with the low frequency produce the flapping motion in the jet because the fluctuation is distinguished in the power-spectra.

The streamwise distributions of the r. m. s. value of velocity fluctuations at the shear layer are shown in Fig. 7a. The case of un-impressing disturbance is not displayed, because the velocity fluctuations do not arise. In the symmetrical mode

excitation, the velocity fluctuations decrease toward the downstream. In the asymmetric and random mode excitations, the velocity fluctuations are amplified, although the fluctuations decrease at the back of the slit exit. Since the velocity fluctuations are exponentially amplified between $x = 1$ and 5, the range is a domain of a linear amplification.

The streamwise distributions of cross-correlation coefficient of the streamwise velocity fluctuations at the two points in the shear layer are shown in Fig. 7b. In the symmetrical mode excitation, since the cross-correlation coefficient becomes about 1 in the whole range, it is shown that the jet does not move asymmetrically. In the asymmetric mode, since the velocity fluctuations include asymmetric components from the slit exit, the cross-correlation coefficient becomes -1 near the slit exit. After $x = 15$, although the cross-correlation coefficient approaches toward 0 gradually, it has a still negative value. The asymmetric fluctuations remain in the jet, although the velocity fluctuation becomes disorder. In the random mode, because the cross-correlation coefficient increases from 0 to a positive value at the back of the slit exit, the symmetrical fluctuation is mainly produced at the neighborhood of the exit. However, because the cross-correlation coefficient decreases rapidly and approaches -1 after the above range, it is shown that the asymmetric fluctuations are mainly formed. The r. m. s. value of the velocity fluctuations in the range where the cross-correlation coefficient changes rapidly grows.

Consequently, a two-dimensional jet at low Reynolds number chooses symmetrical fluctuations at the neighborhood of the exit. However, the symmetrical fluctuations are not developed spatially. After the above domain, the jet selects asymmetric fluctuations, and they are spatially amplified. The frequency is very lower and is approximately 1/100 of a frequency of symmetrical fluctuations.

4 Conclusions

The results of numerical simulations of a two-dimensional jet at low Reynolds number are summarized as follows. If the asymmetric fluctuations are contained in the initial disturbance of the jet, the velocity fluctuations are asymmetrically amplified in the jet. On the other hand, the disturbance is not amplified when only symmetrical fluctuations are included. A frequency of the asymmetric fluctuation in the jet is very lower than that of symmetrical fluctuation. The asymmetrical fluctuations are selectively amplified at the initial region of the jet, so that a flapping motion appears in the jet. When asymmetrical fluctuations are amplified, the fluctuations with higher frequency are generated and the jet causes laminar-turbulent transition.

References

1. H. Sato, F. Sakao, An experimental investigation of the instability of a two-dimensional jet at low Reynolds numbers. J. Fluid Mech. **20**, 337–352 (1964)
2. A. Muramatsu, S. Namaita, The development process of a two-dimensional jet at low Reynolds numbers. J. Vis. Soc. Jpn. **30**(Suppl. 2), 61–62 (2010). (in Japanese)
3. V.K. Garg, Spatial stability of the non-parallel Bickley jet. J. Fluid Mech. **102**, 127–140 (1981)
4. Y. Morinishi, On space-time fully conservative higher order finite difference schemes on non-uniform staggered meshes, CFD2001 (2001), pp. 138–144. (in Japanese)
5. S. Takeuchi, Y. Miyake, T. Kajishima, Secondary instability of round jets by the global instability analysis. Trans. JSME (B) **68**, **665**, 30–37(2002). (in Japanese)
6. T. Yoshida, N. Kato, H. Inoue, Boundary conditions for direct numerical simulation of two-dimensional jet. Prepr. JSME **107–1**, 5–6 (2010). (in Japanese)
7. W.G. Bickley, The plane jet. Phil. Mag. **7**, 727–731 (1937)
8. H. Sato, The stability and transition of a two-dimensional jet. J. Fluid Mech. **7**, 53–80 (1960)

Effect of Buoyancy on the Instability of Light Jets and Plumes

Ravilla Vamsi Krishna Chakravarthy, Lutz Lesshafft and Patrick Huerre

Abstract The linear global stability of light jets and plumes is analyzed to examine the role of buoyancy on the dynamics of the flow by varying the Froude number under low Mach number approximation. In this study, buoyancy is generated due to the heating of fluid injected at the inlet (thermal plume). The results also closely describe the dynamics of an isothermal light jet at the corresponding density ratio, ρ_∞/ρ_j, where ρ_j and ρ_∞ are the jet and ambient density respectively. The analysis is limited to a thermal plume which has a density ratio $\rho_\infty/\rho_j = 7$ corresponding to the value for pure helium injected into air. At large Froude number (or small Richardson number), the dynamics of the flow are shown to be determined by the baroclinic torque resulting in the Kelvin Helmholtz instability as in the case of hot jets. However, as the Froude number is lowered, the dominant growth rate and Strouhal number increase monotonically and the dynamics become strongly buoyancy dependent. The variation of Strouhal number with Richardson number (or Froude number) resulting from the global instability is found to match closely with the experimental and DNS investigations on helium jets injected into air.

1 Introduction

Many investigations have previously addressed, from the stability point of view [2, 5, 8, 9], the local and global dynamics of jets, and confirmed the existence of self-sustained oscillations due to baroclinic torque. However, the same cannot be said about their buoyant counterparts, plumes and light jets. This study aims to extend the

R.V.K. Chakravarthy (✉) · L. Lesshafft · P. Huerre
LadHyX, Ecole Polytechnique, Palaiseau, France
e-mail: ravilla@ladhyx.polytechnique.fr

L. Lesshafft
e-mail: lutz.lesshafft@ladhyx.polytechnique.fr

P. Huerre
e-mail: huerre@ladhyx.polytechnique.fr

© Springer International Publishing Switzerland 2016

A. Segalini (ed.), *Proceedings of the 5th International Conference on Jets, Wakes and Separated Flows (ICJWSF2015)*,
Springer Proceedings in Physics 185, DOI 10.1007/978-3-319-30602-5_8

global stability analysis to strongly buoyant light jets, plumes and explore the variation of the dynamics with Froude number.

Firstly, due to the addition of buoyancy, the base flow of a plume differs from that of a jet. The fundamental difference is that a jet emerges from a nozzle with a given amount of streamwise momentum which diffuses as the fluid convects downstream whereas, in the presence of buoyancy, plumes continue to generate vertical momentum at any given streamwise station.

With regard to unsteady dynamics, the presence of buoyancy generates a torque which could destabilize the flow, in addition to the baroclinic torque and vortex stretching/tilting which result in the classical K-H instability. One of the earliest experiments on strongly buoyant light jets were made by Subbarao and Cantwell [13]. It was observed that helium jets injected into air, in a certain range of parameters, exhibit self-excited axisymmetric puffing. Similar observations were made by Cetegen and Kasper [3] for pure helium and helium—air mixtures over a larger range of parameters and a power law describing the variation of Strouhal number with Richardson number was obtained. More recent studies [2, 6, 10–12] performed a DNS of light jets and their results corroborate the experimental findings. These numerical experiments have demonstrated that at high Richardson numbers, self-sustained oscillations cease to exist in the absence of gravity. Similar observations were also made by Jiang and Luo [6] for the case of a thermal plume. It must be noted that, in all these studies the density variation is strong and therefore non-Boussinesq in nature. However, under the Boussinesq approximation there is no baroclinic torque and the spatiotemporal dynamics are shown to be dominated by the helical mode $m = 1$ rather than the axisymmetric mode $m = 0$ [1].

The current investigation, however, is focused towards understanding the axisymmetric puffing of strongly heated thermal plumes from a global instability point of view. Note that in order to account for the strong inhomogeneity in density, the analysis is performed under the low Mach number approximation. The paper is organised as follows: the governing equations, computation of the base flow and its linear stability are discussed in Sect. 2. Section 3 documents the variation of stability characteristics of the flow with Froude number and a discussion of the role of buoyancy in the dynamics is presented. The findings are summarized and juxtaposed against previous works in Sect. 4.

2 Formulation

A calorically perfect fluid with Prandtl number Pr, is injected into a quiescent ambient of the same fluid with a prescribed velocity and density profile at the station $z = 0$ through a nozzle of radius R at temperature T_j and density ρ_j on the axis. Adopting the radius of the nozzle R as length scale, ambient temperature $T_\infty (< T_j)$ as temperature scale, ambient density $\rho_\infty (> \rho_j)$ as the density scale and centreline velocity at

$z = 0$, u_j, as velocity scale, the non-dimensional governing equations, under the low Mach number approximation, are obtained as:

$$\frac{\partial \rho}{\partial t} + \nabla \cdot (\rho \mathbf{u}) = 0, \tag{1}$$

$$\rho \frac{D\mathbf{u}}{Dt} = -\nabla p + \frac{1}{ReS}\left[\nabla^2 \mathbf{u} + \frac{1}{3}\nabla(\nabla \cdot \mathbf{u})\right] + \frac{1}{Fr^2}(1-\rho)\mathbf{e_z}, \tag{2}$$

$$\rho \frac{DT}{Dt} = \frac{1}{PrReS}\nabla^2 T, \tag{3}$$

$$\rho(1 + T(S-1)) = 1, \tag{4}$$

where T is the reduced temperature, $Re = \rho_j u_j R/\mu$, $Fr = u_j/\sqrt{gR}$, and $S = \rho_\infty/\rho_j$. Instead of the Froude number Fr, one could also define a Richardson number $Ri = (S-1)/Fr^2 = (\rho_\infty/\rho_j - 1)gR/u_j^2$. As we wish to extend this study in the future to various values of S, the Richardson number Ri is preferred over Fr as it was demonstrated to be a better parameter to analyze the variation of Strouhal number [3]. Throughout this analysis, the Prandtl number Pr is set to 0.7.

The base flow is assumed to be axisymmetric and computed by the Newton-Raphson method using the finite element method in FreeFEM++ [4] on a domain which is 80 radii along the axial/streamwise direction and 30 radii along the radial/transverse direction. The non-dimensional axial velocity and temperature at the inlet ($z = 0$) are assumed to be of the form $u_z(r, z = 0) = T(r, z = 0) = 0.5 + 0.5 \tanh\left[0.25(R/\theta)(1/r - r)\right]$ where a moderately thin value $R/\theta = 10$ has been chosen throughout the analysis and the radial velocity is set to zero at the station $z = 0$. Apart from these Dirichlet type boundary conditions for velocity and temperature at the inlet, stress-free boundary conditions are imposed on velocity and pressure at radial and streamwise farfield boundaries. The reduced temperature T is set to zero in farfield radial direction while in the streamwise farfield, a homogeneous Neumann boundary condition is imposed. On the axis, $r = 0$, a Neumann boundary condition is imposed on axial velocity, temperature and density while a Dirichlet boundary condition is imposed on radial velocity [7].

On this base flow, an axisymmetric perturbation of the form $q(r, z)e^{-i\omega t}$ is superposed where $q = \left[\rho', u_r', u_z', p'\right]^T$ is a column vector denoting the perturbation of flow variables. The governing equations (1–4) are linearized to obtain a generalized eigenvalue problem of the form $LNS(q) = \omega M(q)$ with $\omega = \omega_r + i\omega_i$ being the eigenvalue. The matrices LNS and M, denoting the discretized linearized Navier-Stokes operator and the mass matrix respectively, are constructed in FreeFEM++ and the eigenvalues are obtained through Arnoldi method.

3 Results and Discussion

3.1 Base Flow

In this paper, the analysis is limited to the case of $Re = 200, 500$, $S = 7$ while Ri is varied from 0.0006 to 600. The base flow solution was found to be well converged with a residue less than 10^{-9} and is also independent of the grid resolution and domain size. Figure 1 demonstrates the variation of axial velocity in the $r - z$ plane for $Ri = 0.0006$ and 600 at $Re = 200$. Note that smaller Ri indicates small or negligible effect of buoyancy in comparison to inertia while large Ri indicates dominance of buoyancy over inertia. It can be seen that in the case of $Ri = 0.0006$, the inlet momentum is radially dissipated as it is convected downstream similar to jets, while for $Ri = 600$ it is continually accelerated under the effect of buoyancy which is a characteristic feature of plumes.

3.2 Global Stability

For the above two base flows, the global stability is analyzed in a linear framework. Figure 2 shows the spectrum in the complex ω-plane where the black markers indicate the spectrum for $Re = 200$, $S = 7$ in the presence of buoyancy, while the red markers indicate the spectrum in the absence of buoyancy. It is seen that the Strouhal number St ($St = \omega_r/2\pi$) and growth rate ω_i increase as Ri increases. Here, the effect of buoyancy on the flow dynamics is captured by computing the spectrum with and without buoyancy. For the case without buoyancy, the stability matrices *LNS* and *M*

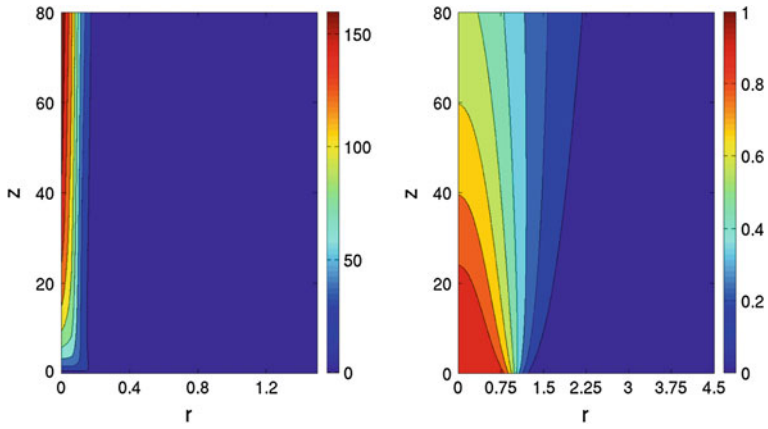


Fig. 1 Spatial distribution of base flow axial velocity in the $r - z$ plane at $Ri = 600$ (*left*) and $Ri = 0.0006$ (*right*) for $S = 7$ and $Re = 200$

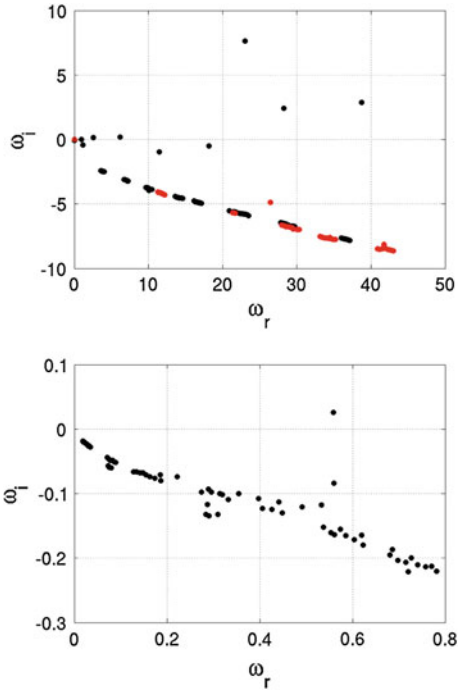


Fig. 2 Eigenvalue spectrum in the complex ω-plane for $Ri = 600$ (*left*) and $Ri = 0.0006$ (*right*) at $S = 7$ and $Re = 200$. The *red markers* denoted the case where buoyancy is switched off in the perturbation equations while *black markers* are obtained by solving the exact perturbation equations

are obtained by artificially setting the Ri to a very low value in the linearized equations, while the base flow corresponds to the exact solution at the higher Ri. The effect of buoyancy is negligible at low Ri (the spectra almost coincide and cannot be distinguished visually), while at high Ri the flow is stabilized in the absence of buoyancy. It is interesting to note the distinct character of buoyancy: as Ri is increased, the base flow which is unstable even in the absence of buoyancy becomes stable to shear while a new instability is triggered by buoyancy on this new base flow.

The variation of St with Ri is shown in Fig. 3 for $Re = 200$ (solid line) and 500 (circular markers) on a log-log scale. It can be seen that Re only weakly influences St. At low values of Ri, St is seen to be invariant with Ri, indicating a negligible influence of Ri. However, for values of $Ri > 1$, St is strongly dependent on Ri and follows the relation $St \propto Ri^{0.42}$ which closely matches the experimental result $St \propto Ri^{0.38}$ obtained for light helium jets by Cetegen and Kasper [3] in the range $1 \leq Ri \leq 100$ (Ri_1 in [3] is equivalent to the current definition of Ri). For $100 \leq Ri \leq 500$, a different power law was proposed by these authors and also the spectrum was seen to exhibit multiple peaks (Fig. 8c, d in [3]). The current investigation, however indicates that the most unstable global mode follows the same power law for all $Ri > 1$. This discrepancy between the two investigations could be due to the multiple unstable modes observed at large Ri. In Fig. 2, it can be seen that apart from the most unstable global mode, which follows the $St \propto Ri^{0.42}$ power law, there are multiple unstable modes with smaller $\omega_i(>0)$ which may interact non-linearly resulting in a different

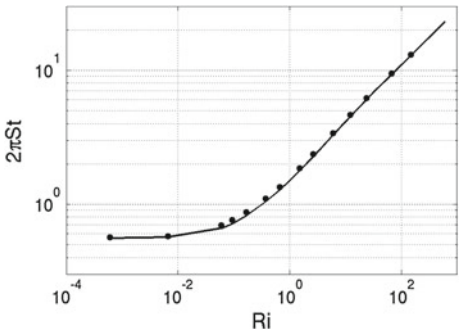


Fig. 3 Variation of Strouhal number with Richardson number in a log-log plot at $Re = 200$ (*solid line*) and $Re = 500$ (*circular markers*). At large Ri, St scales as $Ri^{0.42}$

St. This could be a plausible explanation for the multiple peaks observed in their experiments and a different power law for $Ri > 100$. Another interesting feature of the variation in St is the rather smooth transition from shear-dominated to buoyancy-dominated behaviour similar to the local stability characteristics of the Boussinesq plume [1].

Global stability of the $m = 1$ helical mode was also performed and for all the parameters investigated in this study, the flow was found to be stable. This is in contrast to the Boussinesq limit, where only the $m = 1$ mode is absolutely unstable and the $m = 0$ mode is at most convectively unstable [1]. A plausible explanation for this could be the absence of baroclinic torque in the Boussinesq limit.

4 Conclusions

The global stability of a thermal plume has been investigated in a linear framework under the low Mach number approximation. Variation of the global frequency, ω_r or St, and growth rate, ω_i, with Ri have been documented for $S = 7$ at $Re = 200, 500$. In the range of parameters investigated, only $m = 0$ modes were found become globally unstable. At low Ri, the behaviour of a jet was recovered and the dynamics were independent of buoyancy. However, at large Ri, the instability is strongly effected by buoyancy. It is important to note that the transition from baroclinic and shear dominated behaviour to buoyancy dominated behaviour is smooth which can be seen from the variation of St with Ri. The variation of St with Ri compares well with the experimental data corresponding to isothermal helium jets injected into air [3, 13]. Also, St was observed to be only weakly dependent on Re, which is again consistent with the experimental studies on helium jets.

An important *caveat* of the current investigation is that it is non-Boussinesq in nature and the dynamics are very different from the Boussinesq limit. The local stability analysis on a Boussinesq plume indicates that only a helical $m = 1$ mode is absolutely unstable and therefore might possibly become globally unstable [1].

However, in the current study $m = 0$ is seen to be globally unstable indicating a strong dependence on the value of S. Further analysis is required to establish if there is transition from $m = 0$ to $m = 1$ in a global scenario as we vary the density ratio S.

Acknowledgments This work is being supported by the Agence Nationale de la Recherche (ANR) under the Cool Jazz project, grant number ANR-12-BS09-0024.

References

1. R.V.K. Chakravarthy, L. Lesshafft, P. Huerre, Local linear stability of laminar axisymmetric plumes. J. Fluid Mech. **780**, 344–369 (2015)
2. G.J. Chandler, Sensitivity analysis of low-density jets and flames. Ph.D. thesis, University of Cambridge (2010)
3. B.M. Cetegen, K.D. Kasper, Experiments on the oscillatory behavior of buoyant plumes of helium and helium-air mixtures. Phys. Fluids **8**(11), 2974–2984 (1996)
4. X. Garnaud, L. Lesshafft, P.J. Schmid, P. Huerre, Modal and transient dynamics of jet flows. Phys. Fluids **25**(4), 044103 (2013)
5. P. Huerre, M. Rossi, Hydrodynamic instabilities in open shear flows, in *Hydrodynamics and Nonlinear Instabilities*, ed. by C. Godreche, P. Manneville (Cambridge University Press, New York, 1998), pp. 81–294
6. X. Jiang, K.H. Luo, Direct numerical simulation of the puffing phenomenon of an axisymmetric thermal plume. Theoret. Comput. Fluid Dyn. **14**, 55–74 (2000)
7. M.R. Khorrami, M.R. Malik, R.L. Ash, Application of spectral collocation techniques to the stability of swirling flows. J. Comput. Phys. **81**, 206–229 (1989)
8. L. Lesshafft, P. Huerre, Linear impulse response in hot round jets. Phys. Fluids **19**, 024102 (2007)
9. L. Lesshafft, P. Huerre, P. Sagaut, M. Terracol, Linear impulse response in hot round jets. J. Fluid Mech. **554**, 393–409 (2007)
10. J.W. Nichols, P.J. Schmid, J.J. Riley, Self-sustained oscillations in variable-density round jets. J. Fluid Mech. **582**, 341–376 (2007)
11. Q.A. Quadri, Global stability and control of swirling jets and flames. Ph.D. thesis, University of Cambridge (2013)
12. R.P. Satti, A.K. Agrawal, Computational analysis of gravitational effects in low-density gas jets. AIAA **44**(7), 1505–1515 (2006)
13. E.R. Subbarao, B.J. Cantwell, Investigation of a co-flowing buoyant jet:experiments on the effect of Reynolds number and Richardson number. J. Fluid Mech. **245**, 69–90 (1992)

Direct Numerical Simulation of Dynamic-Rotational Controlled Jet

Koichi Tsujimoto, Toma Onodera, Toshihiko Shakouchi and Toshitake Ando

Abstract In order to develop a new mixing procedure, we conduct DNS (direct numerical simulation) of dynamic controlled free jets. As the dynamic control, it is assumed that the inflow velocity of jet is alternately rotated around streamwise direction. To realize the high accurate computation, the discretization in space is performed with hybrid scheme in which sine or cosine series and 6th order compact scheme are used. From view of instantaneous vortex structures, it is found that the flow pattern considerably changes according to the rotating frequency, i.e., according to the increasing frequency, helical and entangled mode appear in turn. From the ensemble averaged flow properties such as jet width and entrainment, it is confirmed that the jet widely spreads perpendicular to the rotating axis and that the mixing of upstream jet is markedly enhanced due to the dynamic control. Further in order to quantify the mixing efficiency of the dynamic control, as another mixing measure, a statistical entropy is examined. Compared to the uncontrolled jet, it is confirmed that the mixing efficiency is markedly improved, suggesting that the dynamic control can be expected to be useful for the improvement of mixing performance.

1 Introduction

In order to enhance mixing or diffusion in industrial applications, jet mixing control has been examined. The control methods used for jet mixing are categorized into either passive or active methods. Irrespective of the method, understanding the mixing state is indispensable for realizing an effective jet control. The results of linear stability analyses reveal that there are two types of dominant modes characterizing the large-scale flow structures near field of a jet, namely, varicose and helical modes, and diffusion or mixing is effectively controlled through these modes. Further, it is well known that a complex jet is made of a combination of these modes [1]. For

K. Tsujimoto (✉) · T. Onodera · T. Shakouchi · T. Ando
Division of Mechanical Engineering, Graduate School of Engineering,
Mie University, Mie, Japan
e-mail: tujimoto@mach.mie-u.ac.jp

© Springer International Publishing Switzerland 2016

A. Segalini (ed.), *Proceedings of the 5th International Conference on Jets, Wakes and Separated Flows (ICJWSF2015)*,
Springer Proceedings in Physics 185, DOI 10.1007/978-3-319-30602-5_9

example, a flapping mode comprises a pair of helical modes with the same frequency and the same amplitude. Further, it is experimentally confirmed that when the axial mode is added to them, a bifurcating jet or a blooming jet is formed [1]. Such an active control was also investigated using DNS (direct numerical simulation) [2–4], and induced the generation of strong diffusion.

In our previous work [5], from a different view of control method, we focus on the dynamic control in which an inflow direction oscillates perpendicular to the streamwise direction, the so-called "oscillating mode" and demonstrate that the flow pattern considerably changes according to the oscillating frequency, i.e., according to the increasing frequency, wave like mode, bifurcation mode and flapping mode appear in turn, and that the mixing efficiency is improved in order of the wave, the flapping and bifurcating mode. However, since the inflow oscillates on a plane parallel to the streamwise direction, an inhomogeneous mixing state occurs in space under the dynamic control. Therefore in the present simulation, to establish homogeneous mixing state in space, we propose a new dynamic control with rotating mode with which the inflow rotates around the streamwise axis instead the oscillating mode.

In order to investigate the performance of the proposed method, the DNSs of axisymmetric jet under the dynamic control are conducted and the vortical structures are visualized; further the mixing efficiency based on the mixing measure are quantified; the usefulness of dynamic control for jet mixing is demonstrated.

2 Numerical Method

2.1 Governing Equations and Their Discretization

Under the assumption of incompressible and isothermal flow, the continuity, the Navier-Stokes and the energy equations are as follows:

$$\frac{\partial u_i}{\partial x_i} = 0 \tag{1}$$

$$\frac{\partial u_i}{\partial t} + h_i = -\frac{1}{\rho}\frac{\partial p}{\partial x_i} + \frac{1}{Re}\frac{\partial^2 u_i}{\partial x_j \partial x_j} \tag{2}$$

$$(h_i = \varepsilon_{ijk}\omega_j u_k, \omega_j : \text{vorticity})$$

$$\frac{\partial T}{\partial t} + u_i\frac{\partial T}{\partial x_i} = \frac{1}{RePr}\frac{\partial^2 T}{\partial x_i \partial x_i} \tag{3}$$

where the variables u_i, ρ and T stand for the velocity components, density and temperature, respectively. The nonlinear terms of (2) are expressed in the rotational form to conserve the total energy; therefore, p represents the total pressure. As the characteristic length and velocity, the nozzle diameter D and the streamwise velocity V_0 were chosen for nondimensionalization, respectively. The Reynolds number and the

Prandtl number are defined as $Re = V_0 D/\nu$ (ν: kinematic viscosity) and $Pr = \nu/\alpha$ (α: thermal diffusivity), respectively. A Cartesian coordinate system is employed in which y is the streamwise direction and x and z are the lateral directions. Spatial discretization is performed using a hybrid scheme that adopts a sixth-order compact scheme [6] in the streamwise direction and sine or cosine series in the lateral directions. In order to remove the numerical instability due to the nonlinear terms, the 2/3-rule is applied to the lateral directions, and implicit filtering is carried out for the streamwise direction using the sixth-order compact scheme. A third-order Adams-Bashforth method is used for time advancement.

2.2 Calculation Conditions

Figure 1 is schematic drawing of the flow field. The inlet velocity distribution is assumed to be top-hat type, which is given as following:

$$V_b(r) = \frac{V_0}{2} - \frac{V_0}{2} \tanh\left[\frac{1}{4}\frac{R}{\theta_0}\left(\frac{r}{R} - \frac{R}{r}\right)\right] \tag{4}$$

where, V_0 is a center velocity. θ_0 which denotes the initial momentum thickness is set as $\theta_0/R = 0.05$. $R(= D/2)$ is radius of an inlet jet. The inlet velocity profile is determined by referring to the literature [3]. In the present simulations, computational conditions such as the size of computational domain, the Reynolds number, the Prandtl number are $(H_x, H_y, H_z) = (20D, 30D, 20D)$, $Re = 1500$ and $Pr = 0.71$, respectively. The grid number is $(N_x, N_y, N_z) = (128, 150, 128)$. The inflow temperature, T_0 is assumed to be higher than the ambient temperature, T_a, i.e., $T_0 > T_a$. The mean properties are averaged over the time. The mean quantity is denoted with bar (—) and fluctuating components, by prime ($'$). The mean quantities are ensemble-averaged over a non-dimensional time interval $\Delta t V_0/D = 400$ after the flow becomes a fully-developed state.

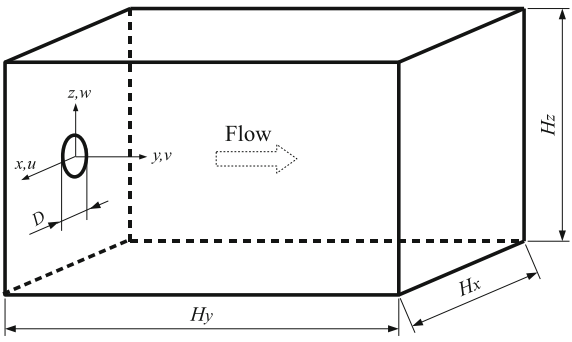


Fig. 1 Coordinate system and computational domain

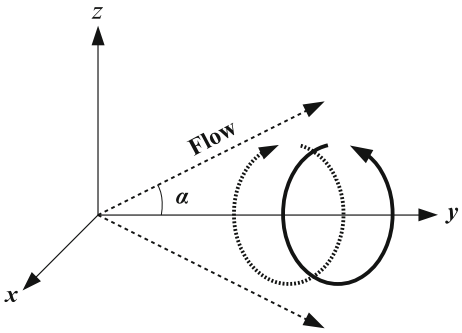


Fig. 2 Calculation conditions of dynamic controlled jets

In the present calculation, as shown Fig. 2, the inflow alternately rotates around y direction. Further so that the flow rate of inflow in the computational volume is constant at all times, the inflow velocity component are determined as follows:

$$\begin{aligned} u(x,0,z) &= -V_b(r)\sin\alpha\sin\beta + u'_{rad} \\ v(x,0,z) &= \quad V_b(r)\cos\alpha + v'_{rad} \\ w(x,0,z) &= -V_b(r)\sin\alpha\cos\beta + w'_{rad} \end{aligned} \tag{5}$$

$$r = \sqrt{x^2 + (z\cos\alpha)^2}, \quad \beta = 2\pi ft \tag{6}$$

where r is the distance from the jet center line. α is the inclination angle shown in Fig. 2. f is the rotating frequency. The Strouhal number is defined as $St = fD/V_0$. In the above equations, a random perturbation, $(u_{rad}, v_{rad}, w_{rad})$ with 1 % of the strength of V_0 are superposed on the inflow mean velocity.

3 Results and Discussions

3.1 Vortical Structures

In order to investigate the effect of rotating frequency, the iso-surface of the second invariance of velocity gradient tensor is visualized from a perpendicular view to rotating axis in Fig. 3. Although the inclination angle at inflow position is small, i.e., $\alpha = 5°$, the controlled jets expand downstream larger than the inclination angle. Also according to the increasing rotating frequency, the flow pattern largely changes: At $St = 0.002$, because of a low-speed rotation, the effect of the vector control does not appear, i.e., the vortex structures evolves in the direction of the nozzle axis at any time. At $St = 0.005 - 0.02$, the structures distribute in a helical manner and

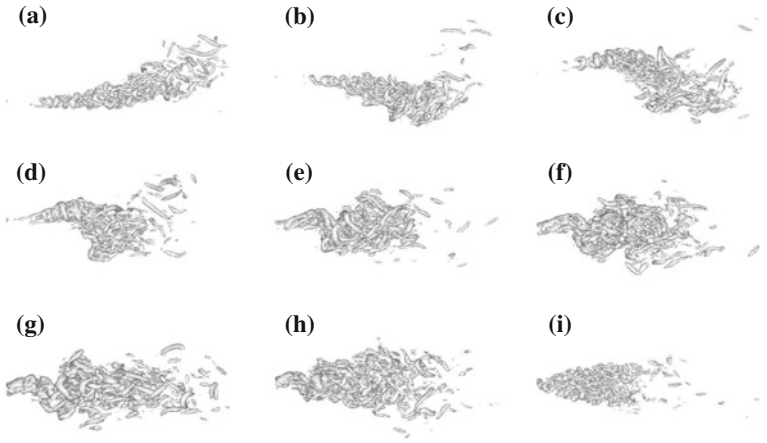


Fig. 3 Instantaneous vortex structures of alternating control. **a** $St = 0.002$, **b** $St = 0.005$, **c** $St = 0.010$, **d** $St = 0.020$, **e** $St = 0.040$, **f** $St = 0.060$, **g** $St = 0.080$, **h** $St = 0.100$, **i** $St = 0.400$

expand radial direction depending on the rotating frequency. At $St = 0.04 - 0.08$, immediately after the injection, the helical structure near the inlet appear and then vortical structures downstream are entangled. From $St > 0.1$, depending on the frequency, it gradually collapse to the feature of uncontrolled jet. Above mentioned results demonstrates that the helical mode is predominant in the low St number, the entangled mode in the medium St number, and the uncontrolled features in the high St number. Namely, by varying the rotating frequency, the dynamic control method is capable of controlling easier the flow state.

3.2 Mixing Characteristics

As a mixing rate, an entrainment has been evaluated so far. Here we adopt the entrainment rate, E being defined as:

$$E = \frac{dQ}{dy} = \frac{d}{dy} \int \int \bar{v} dx dz \tag{7}$$

The streamwsie distribution of the entrainment rate normalized with he volumetric flow rate of inflow, Q_0 is shown in Fig. 4. For the uncontrolled case, the entrainment rate of downstream jet is nearly the same with the experimental results [7, 8]. On the other hand, for the controlled cases the higher entrainment rate than the uncontrolled case is attained upstream region, while the entrainment rate of downstream jet gradually decrease.

In order to quantify the mixing state, Everson et al. [9] investigated the statistical entropy based on the passive scalar concentration, and they demonstrated the

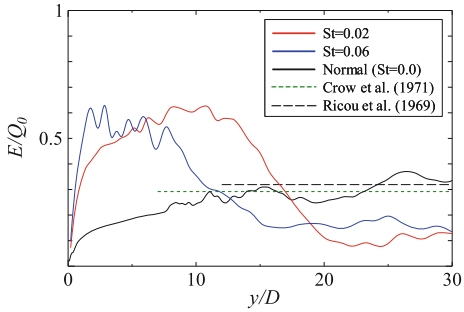


Fig. 4 Streamwise distribution of entrainment rate

characteristics of this measure by examining the experimental data. As well as we validate this mixing measure based on the DNS data of active controlled jet [10]. In the paper [10], compared with simple measures, i.e., jet width, centerline velocity, and turbulent kinetic energy, it is found that the statistical entropy is a good measure for representing the mixing state in different controlled jets. In the following, we provide a simple explanation of this measure.

Boltzmann proposed the statistical entropy, which is defined as the logarithm of combination, W.

$$S = k \ln W \tag{8}$$

where k is the Boltzmann constant. W is the combination of the number of molecules in the ith coarse-grained cell, N_i, namely, $W = \frac{N!}{N_1!N_2!\cdots N_M!} = \frac{N!}{\prod N_i!}$. Since incompressible flow is assumed in the present study, the temperature can be related to the concentration of the passive scalar, i.e., $\phi = (T - T_a)/(T_0 - T_a)$. Considering the small volume surrounding a grid point i, $\Delta V(= \Delta_x \Delta_y \Delta_z)$, the number of molecules is denoted by $N_i = \phi_i \Delta V$; therefore,

$$S = k\Delta V \left[\Phi \ln \Phi - \sum_{i=1}^{M} \phi_i \ln \phi_i \right] \tag{9}$$

where $\Phi = \sum \phi_i$.

In order to investigate the streamwise variation of the statistical entropy, S is summed over the plane perpendicular to the streamwise direction, and $\bar{S}$ is defined as S normalized with the inflow quantity, S_0. M represents the number of grids on the $x - z$ plane. As shown in Fig. 5, the statistical entropy increases downstream. The dynamic control improve the mixing performance compared to the uncontrolled jet, in particular, the helical mode at $St = 0.02$ is most enhanced among the all cases. For the uncontrolled jet, the statistical entropy promptly increases around $y/D = 10$ at which the potential core begins to break down. For the helical mode ($St = 0.005 - 0.02$), the distribution is similar to the uncontrolled case ($St = 0$) until $y/D = 6$. Further downstream the statistical entropy increases, depending on the St number. The reason of these features is that the pitch of a spiral distribution of a vor-

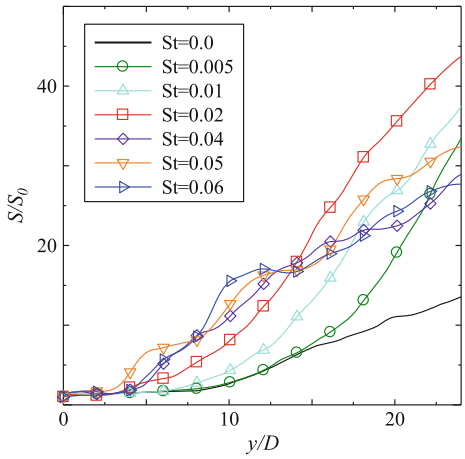


Fig. 5 Mean the statistical entropy distribution

tex structure becomes shorter with increasing the St number and therefore the mixing occurs from a more upstream side. For the entangled mode ($St = 0.04 - 0.06$), the value increases rapidly around $y/D = 5$, and the mixing becomes similar according to that the instantaneous vortical structures and the mean streamwise velocity distribution of the each entangled mode are nearly same independent of St number.

4 Conclusions

In order to improve the mixing performance of free jet, as the useful method, the dynamic control is proposed. As the control parameter, the rotating frequency varies, and the flow and scalar field are investigated. Conclusions are as follows:

1. From the instantaneous view of flow field, according to the increasing of rotating frequency, helical and entangled mode appear in turn. It suggests that the changing rotating frequency is capable of controlling easier the flow state.
2. From the mixing measures using the statistical entropy and the entrainment rate, it is found that the mixing performance is improved compared to the uncontrolled jet.

References

1. W.C. Reynolds, D.E. Parekh, P.J.D. Juvet, M.J.D. Lee, Bifurcating and blooming jets. Annu. Rev. Fluid Mech. 295–315 (2003)
2. A. Hilgers, B.J. Boersma, Optimization of turbulent jet mixing. Fluid Dyn. Res. **29**, 345–368 (2001)
3. C.B. Silva, O. Metais, Vortex control of bifurcating jets: a numerical study. Phys. Fluids **14**, 3798–3819 (2002)

4. K. Tsujimoto, T. Shakouchi, S. Sasazaki, T. Ando, Direct numerical simulation of jet mixing control using combined jets. JSME Int. J. Ser. B **49**(4), 966–973 (2006)
5. K. Tsujimoto, K. Ao, T. Shakouchi, T. Ando, Numerical investigation on flow structures and mixing performances of vector-controlled free jet using DNS. J. Fluid Sci. Technol. **6–4**, 401–411 (2011)
6. S.K. Lele, Compact finite difference schemes with spectral-like resolution. J. Comput. Phys. **103**, 16–42 (1992)
7. S.C. Crow, F.H. Champagne, Orderly structure in jet turbulence. J. Fluid Mech. **48**, 547–591 (1971)
8. F.P. Ricou, D.B. Spalding, Measurements of entrainment by axisymmetrical turbulent jets. J. Fluid Mech. **11**, 21–32 (1961)
9. R. Everson, D. Manin, L. Sirovich, Quantification of mixing and mixing rate from experimental observations. AIAA J. **36**, 121–127 (1998)
10. K. Tsujimoto, S. Kariya, T. Shakouchi, T. Ando, Evaluation of jet mixing rate based on DNS data of excitation jets. Int. J. Flow Control **1**(3), 213–225 (2009)

Enhancement of Turbulent Diffusion in an Axisymmetric Jet by Vortex Generators

Mamoru Takahashi, Kensuke Miura, Yasuhiko Sakai, Yasumasa Ito, Koji Iwano and Koji Nagata

Abstract Effects of vortex generators (VGs) on fluid entrainment and thermal diffusion on an axisymmetric jet are experimentally investigated. A weakly-heated air is introduced from the circular skimmer to the test section. The skimmer diameter is 30 mm and the Reynolds number based on the diameter and the initial jet velocity is set to 20,000. The VGs have a shape of a half delta-wing and they are installed circumferentially on the edge of the skimmer. Eleven VGs configurations are tested by changing the number of the VGs and their intervals. Instantaneous velocity and temperature are simultaneously measured using a hot wire anemometer and a cold wire thermometer, respectively. The results show that the VGs increase fluid entrainment in the upstream region but become ineffective in the downstream region. The VGs also promote thermal diffusion and the effectiveness increases with the number of the VGs. The present study suggests that it is possible to control jet diffusion by arranging the numbers and locations of the VGs.

1 Introduction

Axisymmetric turbulent jets involving scalar mixing and diffusion are widely seen in various industrial applications such as air conditioning units and fuel injection in engines. It is, therefore, important to control the flow and scalar fields for improving their performance.

Some techniques for controlling turbulent jets have been suggested in the previous studies. Suzuki et al. [1] have proposed miniature electromagnetic flap actuators and investigated their influences on an axisymmetric jet. Rogers and Parekh [2] investigated the availability of longitudinal vortices generated by half-delta wings to a jet, particularly with a focus on their angles of attack and shapes, as enhancers of mass entrainment.

M. Takahashi (✉) · K. Miura · Y. Sakai · Y. Ito · K. Iwano · K. Nagata
Department of Mechanical Science and Engineering, Nagoya University, Nagoya, Japan
e-mail: takahashi.mamoru@b.mbox.nagoya-u.ac.jp

© Springer International Publishing Switzerland 2016

A. Segalini (ed.), *Proceedings of the 5th International Conference on Jets, Wakes and Separated Flows (ICJWSF2015)*,
Springer Proceedings in Physics 185, DOI 10.1007/978-3-319-30602-5_10

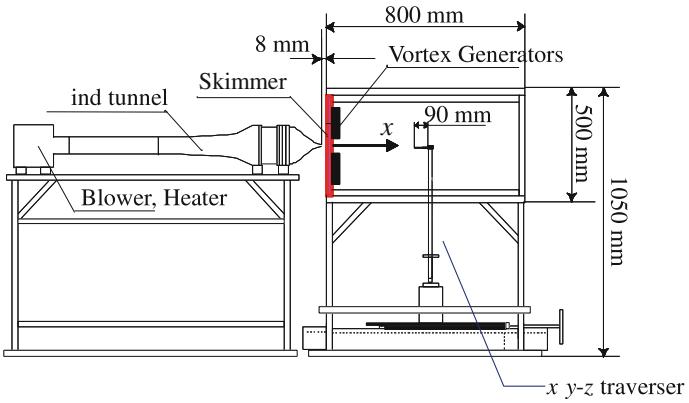


Fig. 1 Schematic of the experimental apparatus

Our group has also carried out experimental studies on an axisymmetric jet controlled by 6 vortex generators (VGs) that are installed with an equal interval around the jet exit [3]. The results show that the VGs enhance turbulent diffusion near the jet exit but the effects gradually vanish as it goes in the downstream direction and turbulent diffusion becomes even smaller in comparison with the case without the VGs. This indicates that the location and number of the VGs are important factors.

Therefore, in this study, the effects of installation locations of the VGs on velocity field and thermal diffusion are experimentally investigated.

2 Experimental Apparatus

2.1 Wind Tunnel

Figure 1 shows a schematic of the experimental apparatus. A circular skimmer, whose diameter d is 30 mm, is installed downstream of a wind tunnel and an axisymmetric jet forms downstream of the skimmer. A heater is installed at the air intake of the blower to provide a slightly heated air. The heater is controlled by a Proportional-Integral-Derivative (PID) controller to maintain a constant temperature and the jet temperature is monitored at the exit of the wind tunnel.

2.2 Vortex Generators (VGs)

In the present study, half delta-wings are used as the VGs to generate longitudinal vortices into the initial shear layer of the jet. Figure 2 shows the schematic of the VG. The sharpest corner is heading in the upstream direction with an angle of attack

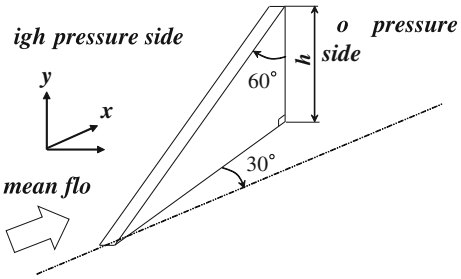


Fig. 2 Schematic of the vortex generator

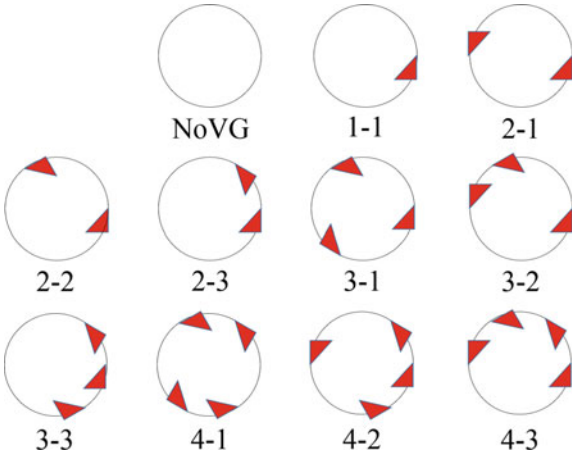


Fig. 3 VGs configurations

of 30°. The projection height of the VGs h is 3.75 mm, and therefore, $h/d = 0.125$. Note that the blockage ratio of each VG is 0.86 %, which is negligibly small.

Figure 3 shows the tested VG configurations. Eleven patterns are tested by changing the numbers of the VGs and their intervals.

2.3 Measuring System

Figure 4 shows the schematic of the probes for velocity and temperature measurements. Instantaneous streamwise velocity of the jet is measured by means of a constant temperature anemometer. A tungsten fine wire, whose diameter and length are 5.0 μm and 1.0 mm, respectively, is used as an I-type hot-wire probe. Instantaneous temperature of the jet is measured by means of a constant current thermometer. A tungsten fine wire, whose diameter and length are 3.0 μm and 2.0 mm, respectively, is used as a cold-wire probe. The whole measuring system is lab-made.

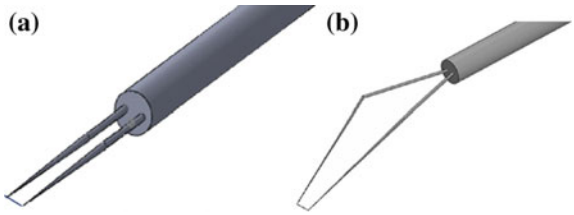


Fig. 4 **a** Hot-wire probe for velocity measurements, **b** cold-wire probe for temperature measurements

2.4 Experimental Condition

The initial velocity of the jet U_0 is set to about 9.6 m/s. The Reynolds number Re based on d, U_0, and kinematic viscosity ν is 20,000. The initial temperature of the jet θ_0 is set 7.5 K higher than that of ambient fluid θ_a. The measurements are performed at $x/d = 2.0$ and 6.0. The sampling frequency and sampling time were 20 kHz and about 13 s, respectively.

3 Results

3.1 Mean Velocity

Figures 5 and 6 show the cross-sectional distributions of the mean velocity U normalized by U_0 for the NoVG, 3-1, 3-2, and 3-3 cases. At $x/d = 2.0$, large velocity defects appear at the back of the VGs and the jet diffuses more to the sides of the VGs. The effects particularly appear when the VGs are closely-spaced as in the 3-3 case. At $x/d = 6.0$, when the VGs are widely-spaced as in the 3-1 case, the jet diffuses to the area where the VGs are not installed. On the other hand, when the VGs are closely-spaced as in the 3-3 case, the jet diffuses not only to the area where the VGs are not installed but also to the area where the VGs are installed.

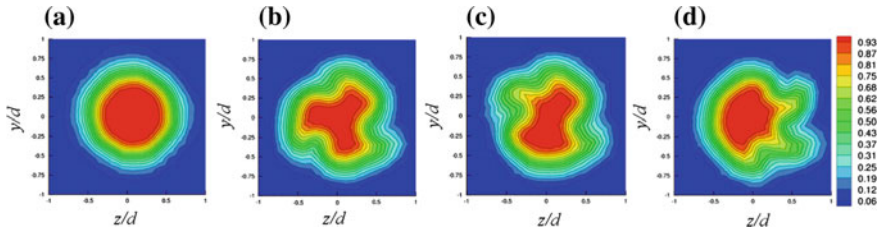


Fig. 5 Cross-sectional distributions of the mean velocity at $x/d = 2.0$. **a** NoVG, **b** 3-1, **c** 3-2, **d** 3-3

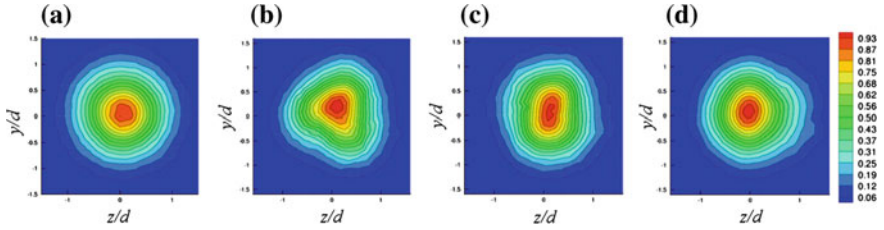


Fig. 6 Cross-sectional distributions of the mean velocity at $x/d = 6.0$. **a** NoVG, **b** 3-1, **c** 3-2, **d** 3-3

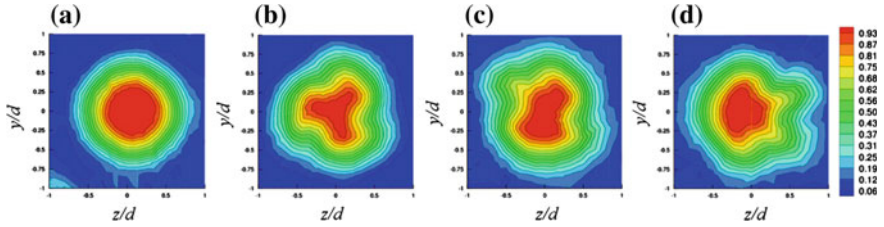


Fig. 7 Cross-sectional distributions of the mean temperature at $x/d = 2.0$. **a** NoVG, **b** 3-1, **c** 3-2, **d** 3-3

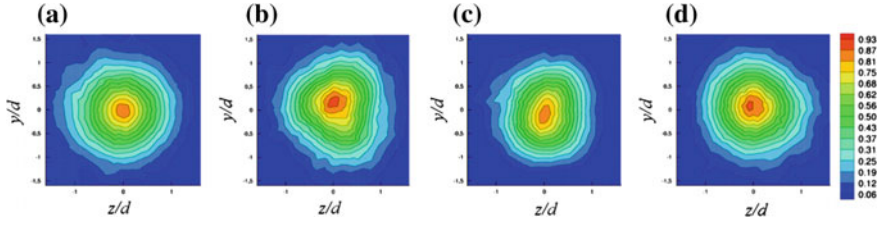


Fig. 8 Cross-sectional distributions of the mean temperature at $x/d = 6.0$. **a** NoVG, **b** 3-1, **c** 3-2, **d** 3-3

3.2 Mean Temperature

Figures 7 and 8 show the same distributions as Figs. 5 and 6 but for mean temperature $\theta - \theta_a$ normalized by $\theta_0 - \theta_a$. It is found that the mean temperature distributions are similar to the mean velocity distributions.

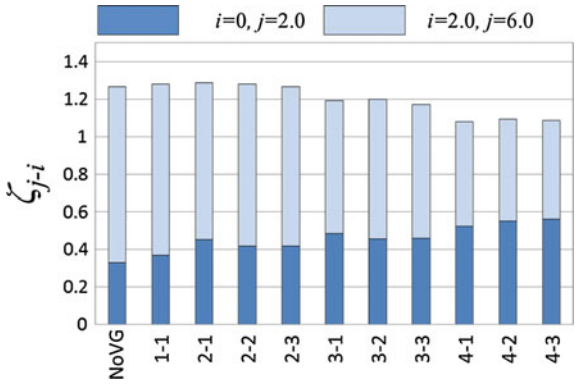


Fig. 9 Fluid entrainment rate ζ_{j-i}

3.3 Fluid Entrainment Rate ζ_{j-i}

The fluid entrainment rate by the jet ζ_{j-i} are shown in Fig. 9. Here ζ_{j-i} is defined by

$$\zeta_{j-i} = \frac{Q_j - Q_i}{Q_0}, \tag{1}$$

here Q_i (Q_j) is the flow rate at $x/d = i(j)$. The VGs increase ζ_{2-0} and the effect becomes large with increasing the number of the VGs. Among the cases of the same number of the VGs as in 2-1 VS 2-2 and 2-3, and 3-1 VS 3-1 and 3-3 cases, the VGs work more effectively when they are widely-spaced. However, ζ_{6-2} decreases with the number of VGs.

3.4 Thermal Diffusion Rate η_{j-i}

Thermal diffusion rate η_{j-i} was calculated by the following equation;

$$\begin{aligned} \eta_{j-i} &= \eta_j - \eta_i, \\ \eta_i &= \frac{\iint_{S_1} (\theta - \theta_a) dS_i}{\iint_{S_{1\cup 2}} (\theta - \theta_a) dS_i}, \end{aligned} \tag{2}$$

here S_1 is the area where $\sqrt{(y/d)^2 + (z/d)^2} \geq 0.5$ and S_2 is the area where $\sqrt{(y/d)^2 + (z/d)^2} \leq 0.5$ at the streamwise location. The result is shown in Fig. 10. η_{j-i} increases with the number of the VGs and the diffusion rate is particularly large in 3-2 and 4-2 cases, in which closely- and widely-spaced VGs are combined. By comparing the 2-1, 2-2, and 2-3 cases, it is found that the closely-spaced VGs work more effectively in the upstream region while widely-spaced VGs work effectively in the downstream region.

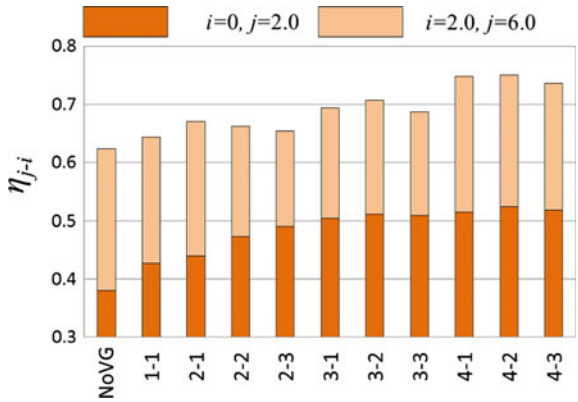


Fig. 10 Thermal diffusion rate η_{j-i}

4 Conclusion

The effects of the VGs configuration are investigated in a weakly-heated axisymmetric jet. The results show that the VGs increase fluid entrainment in the upstream region. However, it becomes ineffective in the downstream region. On the other hand, the VGs promote thermal diffusion and the effect increases with the number of VGs on the entire measured region The present study indicates that the VGs can control jet diffusion by arranging their numbers and locations.

Acknowledgments This study was partially supported by JSPS KAKENHI (Nos. 25289030 and 25289031).

References

1. H. Suzuki, Y. Suzuki, N. Kasagi, Active control of an axisymmentric jet with distributed electromagnetic flap actuators. Exp. Fluids. **36**, 498–509 (2004)
2. C.B. Rogers, D. Parekh, Jet mixing enhancement and noise reduction by streamwise vortices. AIAA J. **32**, 464–472 (1994)
3. K. Miura, K. Nagata, Y. Sakai, O. Terashima, Y. Ito, Control of momentum and heat transfer in a heated axisymmetric jet by means of vortex generators, in *Proceedings of IHTC15. 9647* (2014)

Diffusion Control of Jet by Acoustically Driven Secondary Film Flow

Norimasa Miyagi and Motoaki Kimura

Abstract Active control of the diffusion of a circular jet was attempted by application of a secondary film flow around the jet. Sinusoidal acoustic excitation of the film flow was carried out for VR values 0.5, where VR is the ratio of the film flow velocity to the main jet velocity. For VR = 0.5, the diffusion of the jet was suppressed compared to that of a single jet but it was somewhat enhanced by the acoustic excitation. We conclude that secondary film flow can control diffusion and that acoustic excitation can enhance the diffusion of jet flows. In this paper, it was re-configuration to confirm the condition of the diffusion suppression of the jet. It has analyzed the jet structure by visualization experiment.

1 Introduction

Jet is one of the flows that have been investigated in detail for a long time. The control of the jet has been wide and important research field because of the wide industrial application range such as stability of burner flame, air curtain, heating, cooling or drying device, and promotion of mixing. Many methods of control of jet were used for various studies [1–3]. In these cases, it is intended mainly to promote the gas mixing. Recently, it has been achieved revision of the energy use with a focus on electricity. The airflow control and power reduction in a variety of industries, they are also be mentioned to the investigation. The diffusion suppressing of the jet was expected to efficiency.

In our study [4–6], an active control on the diffusion of a circular jet is tried by applying the secondary film flow around the jet. The secondary film flow is thin

N. Miyagi (✉)
Junior Collage of Nihon University, Narashinadai 7-24-1,
Funabashi-City, Chiba, Japan
e-mail: miyagi.norimasa@nihon-u.ac.jp

M. Kimura
College of Science and Technology, Nihon University,
Kanda Surugadai 1-8-14, Chiyoda-ku, Tokyo, Japan

© Springer International Publishing Switzerland 2016

A. Segalini (ed.), *Proceedings of the 5th International Conference on Jets, Wakes and Separated Flows (ICJWSF2015)*,
Springer Proceedings in Physics 185, DOI 10.1007/978-3-319-30602-5_11

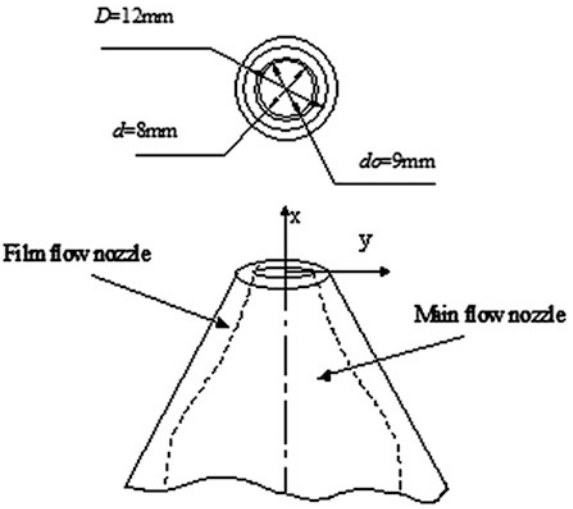


Fig. 1 Nozzle configuration [4–6]

annular flow to wrap circumference of the circular jet. Figure 1 shows the nozzle exit in this study. There are two factors in the experiment performed here. One is the velocity ratio VR, film jet velocity to the main jet velocity. The other is the acoustic excitation frequency. In the case of VR = 0.5, which the secondary velocity is half of main velocity, the most effective suppressed the diffusion of the jet. Because the secondary flow is effectively acts on the mitigation of the shear layer of the mainstream and the surrounding air. In this report, it was organized our research results that have been done so far, it was summarized the factors for diffusion suppression of the jet.

2 Experimental Apparatus

The nozzle used in this study (Fig. 1) was an axisymmetric coaxial jet with the main flow nozzle diameter d = 8 mm, rim thickness 0.5 mm and the slit gap α = 1.5 mm for the film flow. The mainstream velocity V_0 was adjusted to set the Reynolds number Re = 3,000 (V_0 = 5.81 m/s) which was based on main flow nozzle diameter. The origin of the co-ordinate system is fixed to the center of the main stream jet. It was defined that the axial direction to be x-direction, and the radial direction to be y-direction.

Figure 2 shows the experimental apparatus. The air was supplied with an air compressor using two systems for the main flow and the secondary film flow. The volume flow rate of the main stream and film flow were adjusted by the micro flow controller. Both flows were mixed with oil mist in the particle generator as seeding for both LDV and flow visualization. The film flow was pulsated using a loud-speaker driven by the sine-wave of a frequency equivalent to each Strouhal number.

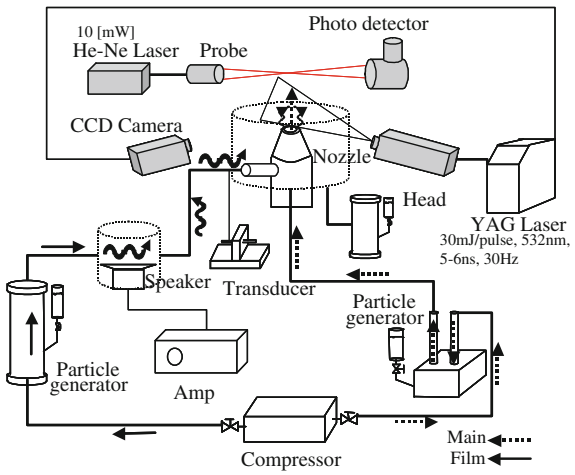


Fig. 2 Experimental apparatus [4]

The acoustic pressure amplitude was adjusted by audio amplifier, to root mean square value of $Ps = 5$ Pa which was measured at the entrance to the nozzle. The Strouhal number St based on the exciting frequency f, main nozzle diameter d and the main jet velocity V_0 was set at 0, 0.3, 0.6 and 0.9. Strouhal number St is defined as following.

$$St = fV_0/d \tag{1}$$

The exciting frequency was based on the preferred frequency. The preferred frequency was 220 Hz which was measured the initial instability for the jet without secondary flow.

3 Result and Discussions

3.1 Effect of Secondary Film Flow

In this paragraph, it was described the effect of secondary film flow by the visualization and velocity distribution result. Figure 3 shows the visualized image for the case of $VR = 0.5$, in which the seed particles were mixed with the film flow only. In the case of $St = 0$, vortices were generated in free shear layer between the main stream and the secondary film flow at $x/d = 4 \sim 6$. With the acoustic excitation to the film flow, the vortex generating point has shifted upstream in all cases. The interval of generated vortices becomes short as frequency increasing.

Figure 4 shows the axial flow direction change of the flux ratio and turbulent energy. The volume flow rate Q was calculated by the area dividing the mean velocity distribution as following the (2) in each cross section.

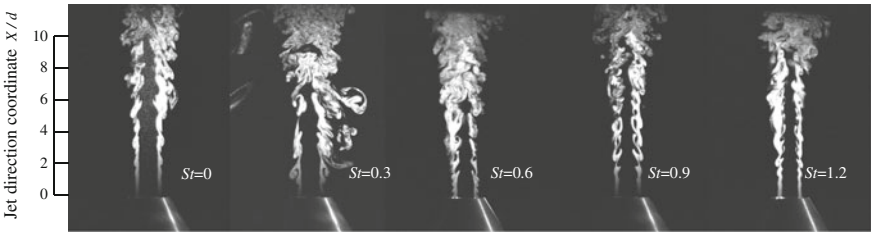


Fig. 3 Visualization of film flow only (VR = 0.5) [4]

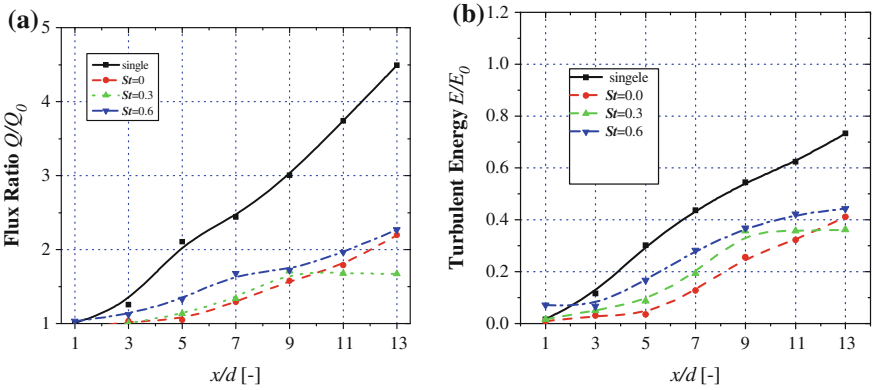


Fig. 4 Axial direction changes of **a** Flux ratio, **b** Turbulent energy [4]

$$Q/Q_0 = \int 2\pi r V dr / A_0 V_0 \tag{2}$$

Turbulent energy determined by the area dividing the turbulence intensity distribution as following the (3) in each cross section.

$$E/E_0 = \int 1/2 u'_{RMS}{}^2 dA / \left(1/2 A_0 V_0^2\right) \tag{3}$$

Volume flow rate was normalized by the value on nozzle exit, and turbulent energy was normalized by the kinetic energy due to ejected velocity. In the case of $VR = 0.5$, because the shear stress with film flow and ambient air was small in this condition, the increase of flux ratio was smaller than that of the single jet in all conditions. In Fig. 4b, the entrainment of the perimeter fluid was restrained at all Strouhal number cases, and according, turbulence energy was restrained in initial region. Because the shear layer was generated the inside and the outside of the film flow. The shear layer generates a small vortex ring respectively. Since the generated outside vortex ring relatively small, the surrounding fluid entrainment is also reduced. In addition, these small vortices applied the small velocity fluctuation, it thought the turbulence energy is also reduced.

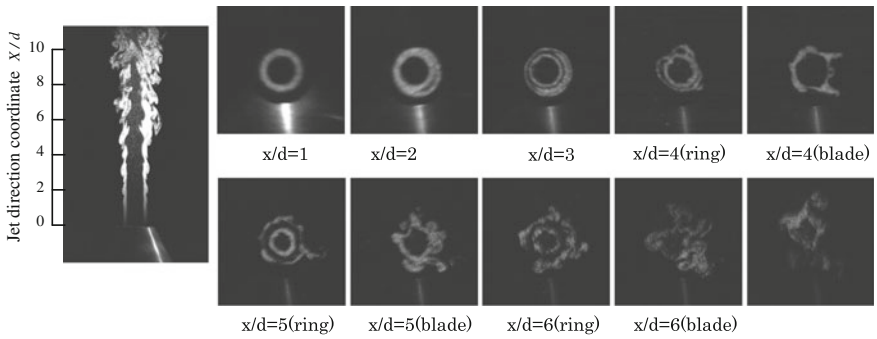


Fig. 5 Crosswise visualization of film flow at VR = 0.5, $St = 0.0$ [5]

4 Three Dimensional Vortex Structure

Figures 5 and 6 show the visualization images in crosswise sections. They show the visualization film flow only. Figures 5 shows the images without excitation. It is known that the circular jets have three-dimensional vortex structure with two elements, as a result of visualization [7], and DNS [8]. One is a vortex ring which is generated in free stream layer. Another is longitudinal vortex generated with destabilization of a shear layer in a blade region (between vortex rings). In Fig. 5, the disturbance is observed in film flow layer after $x/d = 2$, the vortex ring and blade region was confirmed at $x/d = 3 - 4$. However, the diffusion of jet is not observed after $x/d = 6$ as the main flow side has been comparatively stable without much growth of these vortex ring and longitudinal vortices. It's because velocity difference between surrounding air and film flow is small, shear stress is small, and main stream side of film layer is stable.

Figure 6 shows with excitation. The initial disturbance which was caused by velocity fluctuation of the nozzle exit, it generated the initial vortex ring and vortex filament. This vortex filament becomes longitudinal vortices by stretched at the blade region. The longitudinal vortex deform the vortex ring, and it has disrupted the vortex structure of the jet. In order to suppress the diffusion of the jet, to preserve a vortex structure, it is necessary to optimize the interference between the longitudinal vortices and vortex ring.

5 Interaction of Inner Vortices and Advection Velocity

This control method was also applied to different gas. In this case, in the case of 0.5 in the momentum ratio which was considered the difference in density between the main stream gas and the ambient air, the jet was most suppressed. Figure 7 shows the visualized image for carbon dioxide jet with the secondary film flow at air. This image was visualized with the seed particles in the film stream only. There was no

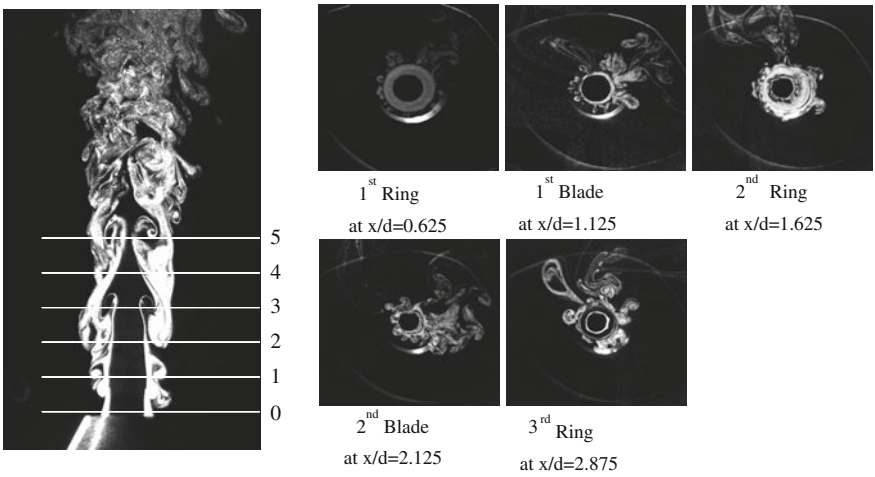


Fig. 6 Crosswise visualization of film flow at VR = 0.5, St = 0.3, T/T_0 = 0

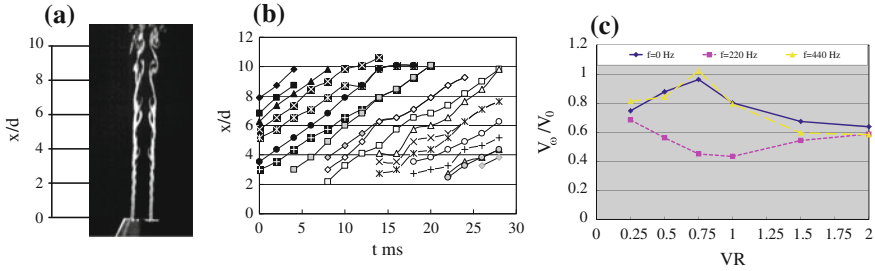


Fig. 7 The suppressed CO2 jet (VR = 0.75, St = 0.0). **a** The visualization image. **b** The position of vortices. **c** The convection velocity [6]

acoustic excitation for velocity ratio VR = 0.75 conditions. This condition controlled to restrain the jet diffusion for carbon dioxide jet. In this experiment, visualization images were captured by high speed camera at 6000 frame per second. Figure 7b shows the position of vortex ring, which was extracted from the time series visualization images. And Fig. 7c shows the advection velocity by the time series images. The advection velocity was defined by the inclined the plot lines at the Fig. 7b. In Fig. 7b, it shows that the vortices has interval distance to the flow direction. But, it was observed that some of the vortex has caught up in front vortex. It is considered that the interference of inside vortices is required to suppress to keep the vortex structure of the jet. In Fig. 7c, it shows that the advection velocity becomes fast in the case of restrained jet structure. Because, the generating of the outside vortex was suppressed, it considered that interference of outside and inside vortices has suppressed in secondary film flow.

6 Summary

For the jet diffusion control using the secondary film flow, it has gotten some suggestions for the jet diffusion suppression.

1. If the velocity ratio or momentum ratio between the mainstream and the secondary flow is 0.5, the diffusion of the jet is suppressed most.
2. When the momentum ratio is 0.5, for shear stress is small by the action of the secondary flow, the vortex structure of the jet is also small.
3. To keep the vortex structure of the jet, it is necessary to suppress the interference between the vortices of the jet.

References

1. K.B.M.Q. Zaman, A.K.M.F. Hussain, Vortex pairing in a circular jet under controlled excitation. Part 1. General jet response. J. Fluid Mech. **101**, 449–491 (1980)
2. H. Suzuki, N. Kasagi, Y. Suzuki, Active control of an axisymmetric jet with distributed electromagnetic flap actuators. Exp. Fluids **36**, 498–509 (2004)
3. W.C. Reynolds, M.J.D. Lee, Bifurcating jet and blooming jet. Annu. Rev. Fluid Mech. **35**, 295–315 (2003)
4. N. Miyagi, M. Kimura, H. Shouji, H. Fujita, K. Hodoya, Study of active jet control by acoustically driven secondary film flow-influence of velocity ratio and acoustic strouhal number. JSME Int J., Ser. B **49**, 974–979 (2006)
5. N. Miyagi, H. Fujita, M. Kimura, H. Shouji, Jet diffusion control by acoustically driven secondary film flow visualization of controlled jet structure, in *International Heat Transfer Conference* (2006b). doi:10.1615/IHTC13.p16.200
6. N. Miyagi, M. Kimura, Study of buoyant jet control by acoustically driven secondary film flow, in *Proceedings of KSME-JSME 8th TFEC, USB* (2012)
7. K. Toyoda, R. Hiramoto, Effect of streamwise vortices on characteristics of jets. JSME Int. J. Ser. B Fluids Therm. Eng. **49**(4), 884–889 (2006)
8. J.E. Martin, E. Meiburg, Numerical investigation of three-dimensionally evolving jets subject to axisymmetric and azimuthal perturbations. J. Fluid Mech. **230**, 271–318 (1991)

Numerical Simulation of Flow Structure and Heat Transfer in a Swirling Gas-Droplet Turbulent Flow Through a Pipe Expansion

Viktor Terekhov and Maksim Pakhomov

Abstract The effect of droplets evaporation on the flow structure, turbulence modulation and heat transfer enhancement in a swirling two-phase flow in a pipe with sudden expansion is numerically investigated. The numerical model is based on the Eulerian approach. The gas phase is treated as a continuum while the droplets are considered as the dispersed phase. The set of steady-state 3D RANS equations is used for the computations of the gas phase. In the study the second moment closure (SMC) is used for the gas phase. Two-way coupling is used along with the particulate feedback onto the mean distribution of the gas phase. Intensification of the heat transfer by increasing the swirl parameter (the maximum increase in heat transfer is up to 50 %) is shown. The position of the maximum heat transfer shifts upstream. The predicted results are in good agreement with the measurement data for the confined two-phase swirling flow with solid particles.

1 Introduction

Swirling droplet-laden turbulent flows in a pipe with sudden expansion are widely encountered in spray dryers, and propulsion and industrial combustors, where they are used to improve flame stabilization and minimize pollutant production. This is a typical case of turbulent recirculating and separating two-phase flow with strongly anisotropic behaviors, and the physics of such flows is extremely complex. The swirling flows are characterized by high local gradients of the mean and fluctuating velocities and other parameters, and they are accompanied by complex flow phenomena due to the centrifugal forces and Coriolis effect [5, 7, 8]. Understanding the flow behavior by means of more accurate numerical modelling of such flows is impor-

V. Terekhov (✉) · M. Pakhomov
Laboratories of Thermal and Gas Dynamics, Kutateladze Institute of Thermophysics of SB of RAS, Acad. Lavrent'ev Avenue, 1, 630090 Novosibirsk, Russia
e-mail: terekhov@itp.nsc.ru

M. Pakhomov
e-mail: pakhomov@ngs.ru

© Springer International Publishing Switzerland 2016

A. Segalini (ed.), *Proceedings of the 5th International Conference on Jets, Wakes and Separated Flows (ICJWSF2015)*,
Springer Proceedings in Physics 185, DOI 10.1007/978-3-319-30602-5_12

tant for design optimization. The recirculation flow affects significantly the intensity of momentum and heat transfer, and the dispersion of particles or droplets, and it determines the structure of the turbulent two-phase flow [6, 10, 12]. The interaction between the small particles and turbulent vortices of the gas phase is a complex and insufficiently studied phenomenon [3]. The effect of droplets evaporation on the flow structure, turbulence modulation and heat transfer enhancement in the swirling two-phase flow downstream of the pipe with sudden expansion is numerically investigated. Turbulence modulation leads to the changes in the turbulence intensity in two-phase flows compared with those in single-phase flows. The mechanism controlling this turbulence modification is of great importance in accurate describing the heat and mass transfer processes in droplet-laden swirling flows. Detachment strongly affects the momentum, heat and mass transfer processes. Knowledge of the hydrodynamics of turbulent mist swirling flows in a pipe with sudden expansion holds significant implications for the successful design, the determination of the optimum operating conditions and pollutant emission of numerous industrial applications. Recent advances in fluid and particle dynamics modeling algorithms and high-performance computing technology make numerical methods a viable alternative for studying droplet-laden swirling flows in a pipe with sudden expansion.

The aim of the present paper is the numerical study effect of droplets evaporation on the flow structure, turbulence modulation and heat transfer enhancement in the swirling two-phase flow downstream of the pipe sudden expansion is numerically investigated.

2 Mathematical Model

In the present paper, the dilute gas-droplet turbulent swirling flow downstream in a pipe with sudden expansion is numerically examined. The numerical model is based on the Eulerian approach. The gas phase is treated as a continuum while the droplets are considered as the dispersed phase. For the gas phase, the set of steady-state 3D RANS equations is used. In the study the second moment closure (SMC) by [9] is used for the gas phase. Two-way coupling is used along with the particulate feedback onto the mean distribution of the gas phase according to the model of [2]. The equations of kinetic stress, temperature fluctuations and turbulent heat flux in the dispersed phase according to [15] are utilized. All the computations carried out for the gas-droplet flow are under atmospheric pressure. The basic grid comprises $256 \times 80 \times 80$ control volumes. Simulations with refined and also coarser grids are performed in the framework of the grid independency study. The computational grid, non-uniform in both axial and radial directions, is applied with a high resolution in the near-wall and entrance regions.

The volume concentration of the dispersed phase is assumed to be lower than $\Phi_1 < 10^{-4}$ and sufficiently fine ($d_1 = 10 - 100\,\mu\text{m}$); therefore the effects of inter-particle collisions are neglected when treating the hydrodynamic and heat and mass transfer processes in the two-phase flow, where d_1 is the initial droplet diameter.

Break-up or droplet deformation processes are not taken into account. The droplet temperature along the droplet radius remains constant because the Biot number is $\mathrm{Bi} = \alpha_L d_1/\lambda_L \ll 1$. The pipe surface is always dry, so there is no liquid film of deposited droplets formed on the wall. This assumption for the heated surface is valid (see, for example, [10]). Furthermore, this condition is valid if the temperature difference between the wall and the droplet is greater than $T_W - T_L > 40\ K$. Break-up or droplet deformation processes are not taken into account. A simple estimation of the Weber number shows that this effect can be eliminated. Break-up occurs when $\mathrm{We} \geq \mathrm{We}_{cr} = 7$, but for any droplet size in the flow, $\mathrm{We} \ll 1$. Therefore, neither break-up nor droplet deformation can occur in the flow.

The mean transport equations for both gas and dispersed phases and the SMC model are solved using a control volumes method on a staggered grid. The QUICK scheme is used to approximate the convective terms, and the second-order accurate central difference scheme is adopted for the diffusion terms. The velocity correction is used to satisfy continuity through the SIMPLEC algorithm, which couples velocity and pressure. All computations are carried out for the gas-droplet flow under the atmospheric pressure. The first cell is located at a distance $y_+ = yU_*/\nu = 0.3 - 0.5$ from the wall, where U_* is the friction velocity obtained for the flow in the inlet pipe. At least 10 control volumes have been generated to be able to resolve the mean velocity field and turbulence quantities in the viscosity-affected near-wall region ($y_+ < 10$). The basic grid comprises $256 \times 80 \times 80$ control volumes. A more refined grid is applied in the recirculation region and in the zones of flow detachment and reattachment. Simulations with refined and also coarser grids are performed in the framework of the grid independency test. The computational grid, non-uniform in both axial and radial directions, is applied with a high resolution in the near-wall and entrance regions. Grid convergence is verified for three grid sizes: $128 \times 60 \times 60$ and $400 \times 100 \times 100$ control volumes.

3 Numerical Results and Its Discussion

In the present paper, the dilute gas-droplet turbulent swirling flow downstream a pipe with sudden expansion is numerically examined. The vertical downward flow is chosen for modeling (see Fig. 1). The primary jet of the air and water droplet mixture (*1*) is fed to the central channel ($2R_1$). The secondary swirling one-phase gas flow (*2*) is supplied through the ring channel ($R_3 - R_2$). The geometry of the computation domain is as follows: $2R_1 = 20, 2R_2 = 26, 2R_3 = 40$ and $2R_4 = 100$ mm, and step height $H = 30$ mm. The length of the computation domain is $X = 1$ m. The mean-mass axial velocity of the primary air jet is $U_{m1} = 15$ m/s and its mass flow rate is $G_1 = 22.6$ g/s. The mass air flow rate in the secondary ring jet is $G_2 = 18$ g/s. The swirl number is

$$S = \frac{\int_0^{R_3} \rho U W r^2 dr}{R_3 \int_0^{R_3} \rho U^2 r dr} = 0 - 1. \tag{1}$$

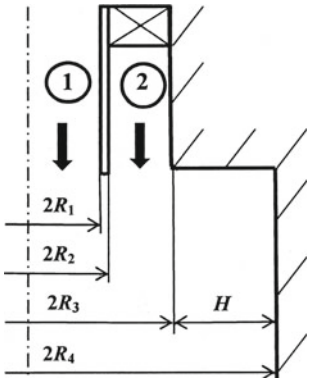


Fig. 1 The scheme of the computational domain. *1* is the gas-droplet flow, *2* is the swirling single-phase gas flow

The Reynolds number of the gas phase is $\mathrm{Re} = U_{m1} 2R_1/\nu = 2 \times 10^4$, and the initial mean axial velocity of the droplets is $U_{L1} = 12$ m/s. The initial diameter of the water droplets is $d_1 = 10 - 100\,\mu$m, and their mass fraction is $M_{L1} = 0 - 0.1$. The particle relaxation time is $\tau = \rho_L d^2/(18\,\rho\nu\mathrm{W}) = 0.3 - 30$ ms. The wall temperature is constant along the length of the computation domain and equal to $T_W = 373$ K. The air and droplet temperature at the inlet is $T_1 = T_{L1} = 293$ K. A dispersed phase with a small Stokes number $\mathrm{Stk} = \tau/\tau_f \ll 1$ is found to be in velocity equilibrium with the gas phase, where τ_f is the turbulent time macroscale. The particles are very responsive to gas-phase fluctuations and will move unaffected through the eddy. Particles with large Stokes numbers $\mathrm{Stk} \gg 1$ are found to no longer be in equilibrium with the fluid phase. They are unresponsive to gas-phase fluctuations and will move unaffected through gas eddies. According to [1], it can be assumed that $\tau_f = X/U_{m1} = 67$ ms, then $\mathrm{Stk} = \rho_L d^2 Re/(18\,\mathrm{W}) = 0.004 - 0.45$, and this proves that the particles are easily involved in the turbulent gas motion. For the direct separated flows behind a sudden tube and flat channel expansion, the following relationship is presented in [3] for $\tau_f = 5H/U_{m1}$. Then, for the conditions of our experiments $\tau_f = 10$ ms and $\mathrm{Stk} = 0.03 - 2.5$.

The streamlines of the gas phase in the separated and swirling gas-droplet flow are presented in Fig. 2. Predictions for the separated flow without swirling ($S = 0$) are carried out for the same geometry and the same parameters as for the swirling gas-droplet flow. In the swirl flows two recirculation zones are formed. One is located near the tube wall and is associated with the phenomenon of flow separation and reattachment. The other one is at the axis region, and it relates to reversing flow in the swirling flows. A large recirculation zone, formed by flow rotation and located at the pipe axis and in the separation zone, can be observed, and this agrees with the measurement data of [13] and the numerical results of [1, 14] for the two-phase swirling flows. In the two-phase flow without swirling behind the pipe's sudden expansion [10], there is a secondary corner vortex (see Fig. 2a), which is not observed in the swirling flow. In the near-wall zone of the pipe, the zone of recirculation with the subsequent reattachment of the two-phase flow is formed due to separation (see Fig. 2b).

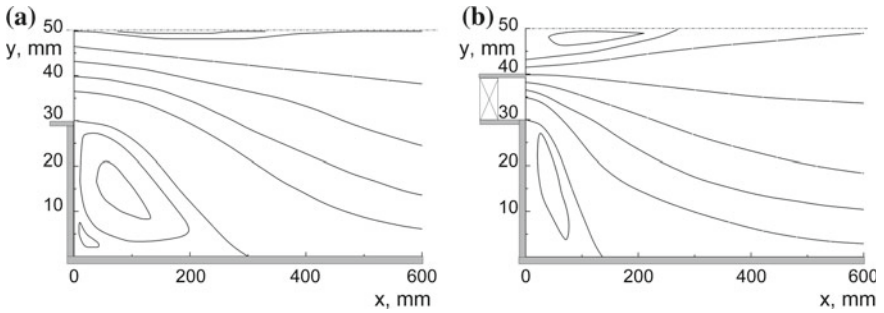


Fig. 2 Streamlines in the separated (**a**) and swirling (**b**) gas-droplet flow in the pipe sudden expansion. Re $= U_{m1}2R_1/\nu = 2 \times 10^4$, $d1 = 30\,\mu$m, Stk $= 0.3$, $M_{L1} = 0.05$, $S = 0.5$

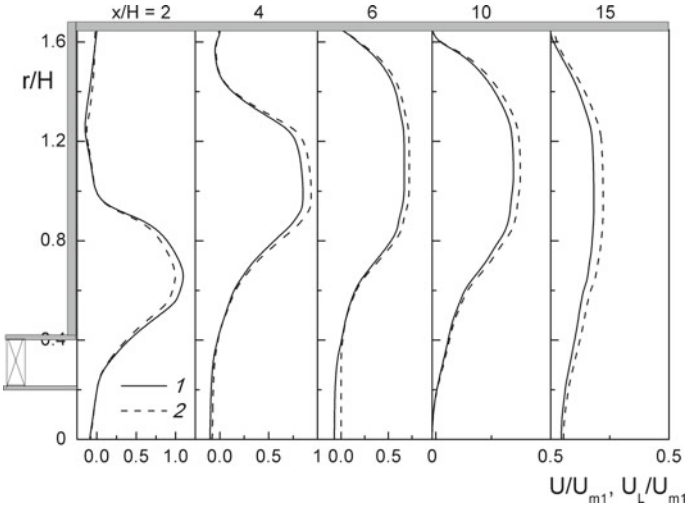


Fig. 3 The radial profiles of mean gas (*1*) and dispersed (*2*) phases in the gas-droplets swirling confined flow

The radial profiles of the mean gas (*1*) and dispersed (*2*) phases in the gas-droplets swirling confined flow are shown in Fig. 3. The presence of regions with negative values of mean axial gas velocity in the near-wall zone is observed. There is a negative magnitude of mean axial droplet velocity in the axis area and the droplets interact with the gas-phase turbulence. The mean velocity of the particles is slightly higher than that of the gas due to their inertia. The gas velocity profiles have an obvious maximum and its position is shifted toward the wall.

The distributions of heat transfer along the pipe length in the separated ($S = 0$) and swirling gas-droplet flow in the pipe with sudden expansion are shown in Fig. 4. The Nusselt number is determined by the formula $\mathrm{Nu} = -(\partial T/\partial y)_W 2R_4/(T_W - T_1)$. An increase in the swirling numbers leads to enhancement of the heat transfer (the maximal heat transfer increase is up to 50 % at $S = 1$). The position of the heat transfer

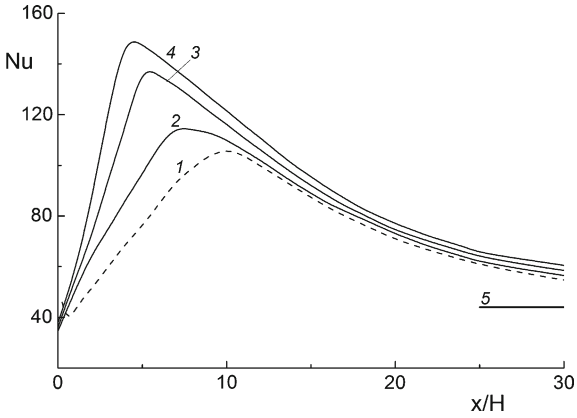


Fig. 4 Heat transfer in the separated at $S = 0$ (*dashed lines*) and swirling (*solid curves*) gas-droplet flow. *1*—S = 0, *2*—0.25, *3*—0.5, *4*—1, *5*—the value of Nusselt number calculated by the single-phase flow under conditions of fully developed pipe flow far from the reattachment point

maximum roughly coincides with the point of flow reattachment. It shifts upstream significantly in swirling flow. The effect of swirling flow on heat transfer is observed until $x/H = 15$, after which the heat transfer value decreases and at $x/H = 30$ it almost coincides with the value for the separated two-phase flow.

4 Comparison with Experimental an Numerical Results of Another Papers

The radial profiles of the diameter of kerosene droplets are shown in Fig. 5. The results of the LES simulations of [11] and experiments of [4] are used for comparative analysis. The swirling two-phase flow of an air and kerosene droplet mixture was studied in a horizontal flow downstream of the channel sudden expansion. The height of the square channel was 130 mm, its length 245 mm, and the step height was $H = 50$ mm. The diameter of the nozzle for the kerosene supply was $2R_1 = 5$ mm and diameter of the peripheral hole for the air supply was $2R_3 = 30$ mm.

The dispersion of particles over the cross-section of a flat channel is typical for these experiments and predictions. The larger particles accumulate in the near-wall zone of the channel due to the action of centrifugal forces, whereas the smaller particles are observed in the central recirculation zone of the chamber. The droplets in the axial separation zone cannot leave it because the level of turbulence in the shear layer is higher than that of the disperse phase, and the recirculation region is a barrier for them. Therefore, the droplets in the central recirculation zone are heated better and they evaporate, which leads to a decrease in their size. It is obvious that there is qualitative agreement with the measurement data presented in [11].

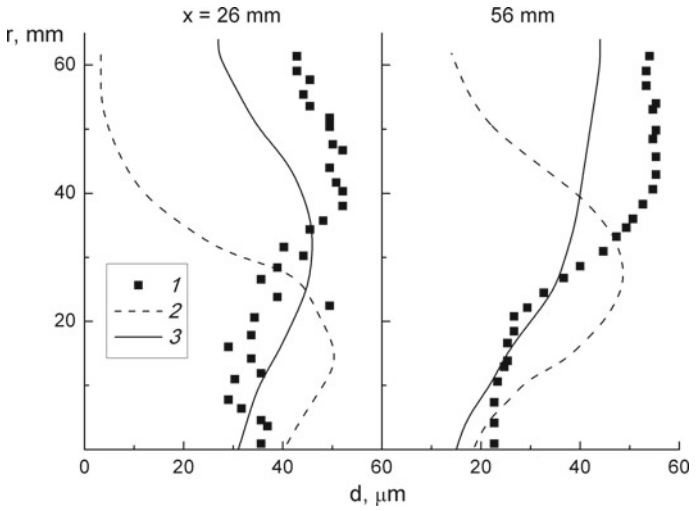


Fig. 5 Radial profiles of kerosene droplets in the swirling gas-droplet flow downstream of the pie sudden expansion. *1*—the measurements by [4], *2*—the LES results of [11], *3*—author's simulations. $d_1 = 55\,\mu$m, Stk = 0.6, $M_{L1} = 0.034$, $S = 0.7$

5 Conclusions

An Eulerian two-fluid model for a two-phase flow laden with small droplets is presented in this paper. The turbulence model is based on second-moment closure, developed by [9] for single-phase turbulent pipe flow, taking into account the presence of evaporating droplets. The turbulence model presented is coupled with the Eulerian two-fluid model. Two-way coupling is achieved between the dispersed and carrier phases in the mean and fluctuating transport.

Two recirculation zones are formed in the swirling flow. The first one is at the tube axis, and it is formed by flow rotation. The second one is near the channel wall. The reason for its formation is flow separation and its subsequent attachment. In the two-phase flow behind the sudden tube expansion without swirling ($S = 0$), there is a secondary corner vortex, which is not observed in the swirling flow. The large particles accumulate in the near-wall of the channel wall due to the action of centrifugal forces. The smaller particles are in the central recirculation zone of the chamber. The droplets in the axial separation zone cannot leave it because the level of turbulence in the ambient space is higher than in the disperse phase. The heat transfer enhancement at an increase in the swirl parameter is shown (the maximal increase in heat transfer is up to 50 % at $S = 1$). The position of the maximum heat transfer, which almost coincides with the point of flow attachment, moves significantly upstream.

Acknowledgments This work was partially supported by the Russian National Foundation (Grant number 14-19-00402).

References

1. S.V. Apte, K. Mahesh, P. Moin, J.C. Oefelein, Large-eddy simulation of swirling particle-laden flows in a coaxial-jet combustor. Int. J. Multiph. Flow **29**, 1311–1331 (1999)
2. N. Beishuizen, B. Naud, D. Roekaerts, Evaluation of a modified Reynolds stress model for turbulent dispersed two-phase flows including two-way coupling. Flow, Turbul. Combust. **79**, 321–341 (2007)
3. J.R. Fessler, J.K. Eaton, Turbulence modification by particles in a backward-facing step flow. J. Fluid Mech. **314**, 97–117 (1999)
4. N. Garcia-Rosa, Phenomenes dallumage dun foyer de turbomachine en conditions de haute altitude. Ph.D. thesis, Universite de Toulouse, Institut Superieur de l'Aeronautique et de l'Espace. Toulouse, France, July 2008
5. A. Gupta, G. Lilley, N. Syred, *Swirl Flows* (Abacus Press, Tunbridge Wells, 1984)
6. K. Hishida, T. Nagayasu, M. Maeda, Augmentation of convective heat transfer by an effective utilization of droplet inertia. Int. J. Heat Mass Transfer **38**, 1773–1785 (1995)
7. S. Jakirlic, K. Hanjalic, C. Tropea, Modeling rotating and swirling turbulent flows: a perpetual challenge. AIAA J. **40**, 1984–1996 (2002)
8. S.S. Kutateladze, E.P. Volchkov, V.I. Terekhov, *Aerodynamics and Heat and Mass Transfer in Confined Vortex Flows* (Publishing House of IT SB of AS of USSR, Novosibirsk, 1987). (in Russian)
9. R. Manceau, K. Hanjalic, Elliptic blending model: a new near-wall Reynolds-stress turbulence closure. Phys. Fluids **14**, 744–754 (2002)
10. M.A. Pakhomov, V.I. Terekhov, Second moment closure modelling of flow, turbulence and heat transfer in droplet-laden mist flow in a vertical pipe with sudden expansion. Int. J. Heat Mass Transfer **66**, 210–222 (2013)
11. M. Sanjose, J.M. Senoner, F. Jaegle, B. Cuenot, S. Moreau, T. Poinsot, Fuel injection model for Euler-Euler and Euler-Lagrange large-eddy simulations of an evaporating spray inside an aeronautical combustor. Int. J. Multiph. Flow **37**, 514–529 (2011)
12. I. Senaha, Y. Miyafuji, S. Kato, M. Higa, M. Yaga, Enhancement of heat transfer in the downstream region of a backward-facing step using a small amount of mist (1st report; Study of heat transfer enhancement), (2nd report; Characteristics of heat transfer and flow behavior with mist). Trans. JSME Pt. B **79**, 1816–1838 (2013)
13. M. Sommerfeld, H.-H. Qiu, Detailed measurements in a swirling particulate two-phase flow by a phase-Doppler anemometer. Int. J. Heat Fluid Flow **12**, 20–28 (1991)
14. M. Sommerfeld, H.H. Qiu, Characterization of particle-laden, confined swirling flow by phase-doppler anemometer and numerical calculation. Int. J. Multiph. Flow **19**, 1093–1127 (1993)
15. L.I. Zaichik, A statistical model of particle transport and heat transfer in turbulent shear flows. Phys. Fluids **11**, 1521–1534 (1999)

The Influence of an Asymmetric Slot on the Flow Characteristics of Synthetic Jets

Yusuke Watabe, Kotaro Sato, Koichi Nishibe and Kazuhiko Yokota

Abstract The purpose of this paper is to elucidate the influence of an asymmetric slot on the flow characteristics of synthetic jets. In this study, the relation between flow characteristics of two-dimensional synthetic jets and beak-shaped asymmetric slots is investigated experimentally and numerically. Results clarify that the vortex pair with different x-direction locations induced by the asymmetric slot produces a large-scale circulation region on the opposite side of the beak in the case of long beaks. It is also demonstrated that flow fields for synthetic jets depend on asymmetric slot beak length; in contrast, continuous jets are independent of asymmetric slot beak length.

Nomenclature

b_0	Slot width [m]
L_0	Stroke length [–]
C	Non-dimensional beak length [–]

Y. Watabe
Graduate School of Mechanical Engineering, Kogakuin University,
Nishi-Shinjuku 1-24-2, Shinjuku-ku, Tokyo 163-8677, Japan
e-mail: am14071@ns.kogakuin.ac.jp

K. Sato (✉)
Department of Mechanical Engineering, Kogakuin University,
Nishi-Shinjuku 1-24-2, Shinjuku-ku, Tokyo 163-8677, Japan
e-mail: at12164@ns.kogakuin.ac.jp

K. Nishibe
Department of Mechanical Engineering, Tokyo City University,
Tamazutsumi 1-28-1, Setagaya-ku, Tokyo, Japan
e-mail: knishibe@tcu.ac.jp

K. Yokota
Department of Mechanical Engineering, Aoyama Gakuin University,
Fuchinobe 5-10-1, Chuo-ku, Sagamihara-shi, Kanagawa, Japan
e-mail: yokota@me.aoyama.ac.jp

© Springer International Publishing Switzerland 2016

A. Segalini (ed.), *Proceedings of the 5th International Conference on Jets, Wakes and Separated Flows (ICJWSF2015)*,
Springer Proceedings in Physics 185, DOI 10.1007/978-3-319-30602-5_13

Re Reynolds number [–]
U_0 Downstream-directed average exit nozzle jet velocity [m/s]
$|\boldsymbol{u}|$ Absolute value of the velocity $= [u^2 + v^2]^{1/2}$
$|\boldsymbol{u}_{\max}|$ Maximum value of velocity

1 Introduction

Two-dimensional plane synthetic jets are generated by the interaction of trains of discrete vertical structures formed by the periodic ejection and suction of fluid at the nozzle exit (slot). Fluid-imparted momentum is discharged from the slot during the expulsion phase of the cycle, and a vortex pair is formed by roll-up of the velocity shear layer. Fluid around the slot is then entrained into the slot in the same manner as in a potential flow sink during the suction phase of the cycle. Thus, the net mass flow rate across the nozzle exit is zero. However, fundamental flow characteristics, such as the jet velocity distribution, fluid force, and the Coanda effect, similar to those of a continuous jet, are induced downstream of the nozzle exit by virtue of the jet entrainment. Thus, it is expected that synthetic jet technologies will be applied in various fields as alternatives to continuous jets. Typical actuators for synthetic jets, such as piezoelectric actuators, speaker actuators, diaphragm actuators, and plasma actuators, have no rotating parts and are suitable for downsizing and weight reduction for applications with micro air vehicle thrusters, flow separation controllers, and so on. Thus far, several experimental and numerical studies have focused on synthetic jets, and onset conditions and formation mechanisms for synthetic jets were examined in fundamental investigations. The formation criterion was found to depend on the non-dimensional stroke length $L_0 = l_0/b_0$, where l_0 is the length of the fluid body ejected during the expulsion phase and b_0 is the slot width [1]. Moreover, the mechanism of synthetic jet formation, jet structure, and unsteady characteristics have been investigated [2]. The development of flow-control actuators using synthetic jets instead of continuous jets has also been investigated [1, 3]. Synthetic jet actuators have also been installed on the suction surface of an airfoil in order to avoid stall [3].

However, the above-described results were unable to reveal the effects of an asymmetric flow field on the behavior of synthetic jets. There have been few reports on the influence of a large-scale asymmetric boundary on the motion of synthetic jets, e.g., along a circular cylinder with a focus on the Coanda effect [4].

The objective of the present paper is to clarify the effects of local asymmetric geometry on the flow field of synthetic jets, which is fundamental to developing a flow controller without variable geometry. Specifically, we experimentally and numerically examine the fundamental flow characteristics of two-dimensional plane synthetic jets generated by a beak-shaped asymmetric slot. In the present paper, we evaluate primarily the influences of beak length on the behavior of synthetic jets

through experimental flow visualization using the smoke wire method and numerical simulations. Furthermore, the results obtained were compared with those for continuous jets.

2 Experimental and Numerical Setup

In the experiment, air was used as the working fluid. As shown in Fig. 1a, the rectangular cylinder of the nozzle is supported at each end by an acrylic plate, and a two-dimensional jet is induced downstream of the two-dimensional slot. The synthetic jet is generated by a loudspeaker driven by a signal generator that sends signals through a power amplifier, whereas the continuous jet is generated by a centrifugal blower. The synthetic and continuous jet velocities at the outlet of the slot are controlled by the signal generator and the inverter, respectively. The slot width b_0 can be varied by changing the spacer thickness (slot width $b_0 = 5$ mm and aspect ratio $W/b_0 = 20$, where W is the slot height). The geometries of symmetric and asymmetric slots are shown in Fig. 1b. The smoke wire method is employed for flow visualization and the observed flow fields are recorded using a digital camera. A halogen lamp is used for lighting and a hot-wire anemometer is used for measuring the velocity distribution. SC/Tetra (Software Cradle Co., Ltd.) was employed as computational fluid dynamics (CFD) software. The k–ε turbulence model was applied and the flow field solved for a two-dimensional incompressible viscous fluid. The boundary planes of the simulation model were set $200b_0$ away from the origin for each upper, lower, and downstream direction. As shown in Fig. 1c, a sine wave is applied to fluid velocity at the slot, the walls near the slot are set with the non-slip condition, inlet velocity is set as $0.01U_0$ for the upper and lower boundary surfaces, and the constant static pressure condition is applied on the downstream boundary plane. The standard symmetric slot and beak-shaped asymmetric slot are shown in Fig. 1b, where c is the beak length and C is the non-dimensional beak

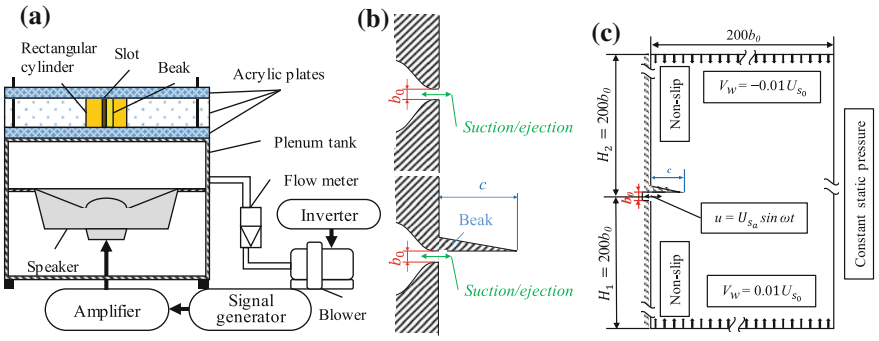


Fig. 1 Experimental apparatus and numerical model. **a** Schematic of experimental equipment. **b** Geometry of symmetric and asymmetric slots. **c** Boundary conditions for numerical simulations

length (= c/b_0). The simulations were conducted by applying the k–ε turbulence model with approximately 100,000 grid points. The flow conditions correspond to a two-dimensional incompressible viscous flow. In this paper, the experimental and the numerical results for Reynolds number $Re = 990$ and the non-dimensional stroke $L_0 = 30$ are presented.

3 Results and Discussions

Flow patterns of continuous jets generated by symmetric and asymmetric slot are shown in Fig. 2. In each figure, the slot center is located at the origin of the coordinate system. Figure 2a, b are the results obtained using a beak-shaped slot with $C = 0$ (symmetric slot) and $C = 5$ (asymmetric slot), respectively. In Fig. 2b, the shape of the beak attached to the upper side of the nozzle exit is indicated in red. Figure 2a(i), b(i) show the experimental results of flow visualization by means of the smoke wire method. Figure 2a(ii), b(ii) show the time-averaged velocity vectors calculated through computational fluid dynamics. In this condition, the behavior of continuous jets can be treated as steady motion. The above figures indicate that the experimental and numerical results are in good qualitative agreement. It can be seen that both of the continuous jets generated by the symmetric and the asymmetric slots proceed straight along the x-axis. From these results, it is clear that the geometry of a slot does not affect the structure (velocity profiles and direction) of continuous jets.

Typical synthetic jet flow patterns for various slot beak lengths are shown in Fig. 3. Photographs taken with an exposure time of 1/10 s are presented in Fig. 3a and the time-averaged velocity vectors acquired by means of numerical simulation are shown in Fig. 3b. Panels (i), (ii), (iii), and (iv) are results for $C = 0$, $C = 3$, $C = 4$, and $C = 5$, respectively. Comparing between (a) and (b), the experimental and numerical results are in good qualitative agreement. As shown in Fig. 3, with respect to synthetic jets, the direction in which the jet proceeds depends on the slot

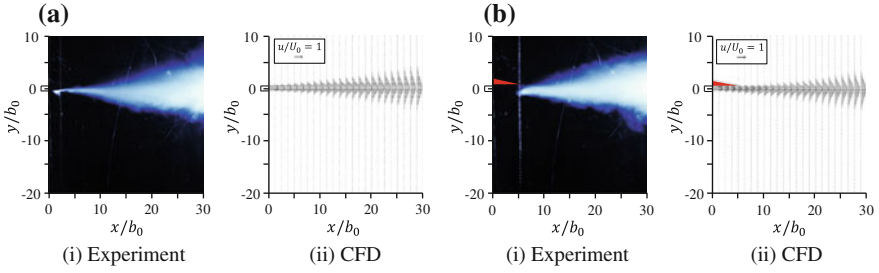


Fig. 2 Flow visualization by the smoke wire method and calculated mean velocity vectors for continuous jets ($Re = 990$, $U_0 = 3.0$ m/s). Exposure time is 1/10 s. **a** Symmetric slot. **b** Asymmetric slot

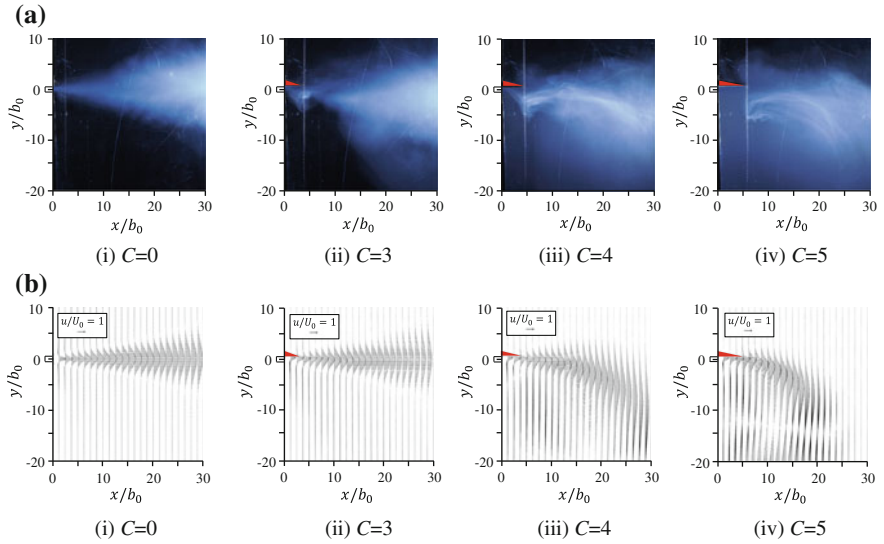


Fig. 3 Influence of slot beak length on flow patterns. **a** Experimental results of flow visualisation. The smoke wire method was employed for visualisation. Exposure time was 1/10 s. **b** Time-averaged velocity vectors from numerical calculations

geometry, i.e., beak length. When vortex pairs are generated through the standard symmetric slot in (i) and the asymmetric slot with short beak length $C = 3$ in (ii), the vortex pair proceeds almost straight along the x-axis with translational motion and a typical jet structure is produced in a manner similar to continuous jets. On the other hand, synthetic jets from the beak-shaped asymmetric slot form a re-circulation region in the clockwise direction in the case of (iii) $C = 4$ and (iv) $C = 5$. In these conditions, it can be considered that the symmetric vortex pair is not formed and that this is caused by the asymmetric geometry of slot, i.e., the lower clockwise vortex is formed at the corner of the slot, whereas the upper counterclockwise vortex is induced near the tip of the beak. Consequently, the vortex pair with different x-direction locations (the upper forward counterclockwise vortex and the lower rear clockwise vortex) produced downward jet flow by the induced velocity of each vortex. Furthermore, another clockwise vortex at the tip of the beak must be produced in the suction phase of the cycle. When the cycle is repeated, the synthetic jet from the beak-shaped asymmetric slot forms a re-circulation region in the clockwise direction. Newly induced clockwise vortices are combined into the large re-circulation region. The deflection of jet flow direction is specific to synthetic jets and is caused by vortex-pair motion. In other words, the location of the vortex pair formation (the roll-up point of the velocity shear layer) should be asymmetric in the x-direction as a result of the existence of the beak. An asymmetric flow field with a large-scale recirculation region is formed by a local break in symmetry. In Fig. 3, it is presumed that the transition exists between $C = 3$ and $C = 4$ under this condition.

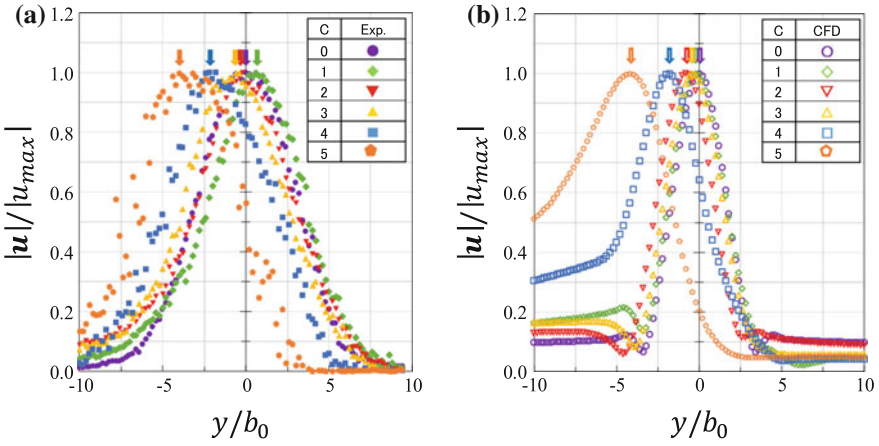


Fig. 4 Time-averaged velocity distribution for various beak lengths at $x/b_0 = 15$. **a** Experiment. **b** CFD

Figure 4 shows the distribution of the non-dimensional time-averaged absolute velocity $|\boldsymbol{u}|/|\boldsymbol{u}_{max}|$ based on the maximum velocity at $x/b_0 = 15$. Panel (a) shows experimental results measured by a hot-wire anemometer and panel (b) shows numerical results. The parameter varied is the beak length C. The arrows in this figure designate the y-direction position of the maximum velocity $|\boldsymbol{u}_{max}|$ for a given beak length C. The position of the maximum velocity $|\boldsymbol{u}_{max}|$ at $x/b_0 = 15$ depends on C.

Assuming that $|\boldsymbol{u}|$ is the maximum value at the jet centers, non-dimensional beak length C versus the y-direction position of the jet center is shown in Fig. 5. The results were designated as filled and open symbols for experimental and numerical

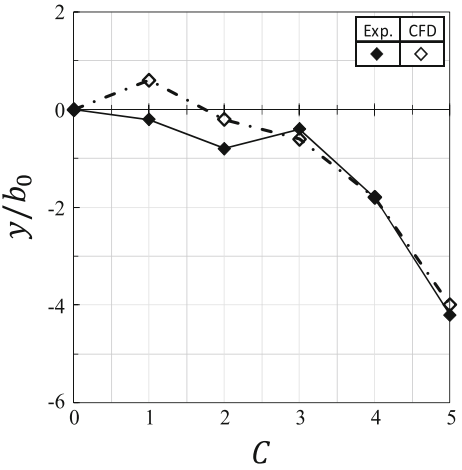


Fig. 5 Beak length versus jet center position

results, respectively. A slight difference between the experimental and numerical results for $C = 1$ and $C = 2$ is observed. However, experimental and numerical results for $C = 0$, 3, 4, and 5 indicate good quantitative agreement. According to the results in Figs. 4 and 5, the jet center position was affected by the beak length C. When C is large, the jet center trajectory moves to the opposite side of the beak and its curvature depends on C.

4 Conclusion

This study evaluated the main effects of beak length in asymmetric slots on the behavior of synthetic jets through experimental flow visualization using the smoke wire method, velocity measurements, and numerical simulations. The results obtained were compared with those for continuous jets.

Acknowledgments The authors would like to thank Mr. Junichiro Kikkawa of Software Cradle Co., Ltd. for his help with the numerical simulations. The present study was carried out with the support of MEXT (Functional Microstructured Surfaces Research Center of Kogakuin University) and Grants-in-Aid for Scientific Research 15K05807.

References

1. R. Holman, Y. Utturkar, Formation criterion for synthetic jets. AIAA J. **43**(10), 2110–2111 (2005)
2. T. Koso, T. Kinoshita, Jet flow formation using an annular synthetic jet actuator, in *JSME Annual Meeting* (2006), pp. 211–212
3. R. Duvigneau, A. Hay, M. Visonneau, Optimal location of a synthetic jet on an airfoil for stall control. J. Fluid Eng. **129**, 825–833 (2007)
4. C. Nakagawa, K. Nishibe, S. Okayasu, K. Sato, K. Yokota, Experimental study of synthetic jet on a circular cylinder. JSME **46**, 531–532 (2009) (in Japanese)

Performance Characteristics of a Fan Using Synthetic Jets

Tomoaki Ishizawa, Kotaro Sato, Koichi Nishibe and Kazuhiko Yokota

Abstract Studies of synthetic jets generated by compact actuators have been conducted for various applications such as drag reduction, boundary layer separation control, and multi-flow mixing. In this paper, a jet fan that utilizes synthetic jets is proposed. The flow patterns inside the jet fan are revealed, and performance curves are drawn. Static pressure distributions in the fan duct are also analyzed to discuss the process of static pressure recovery.

Nomenclature

b_0	Slot width = 10×10^{-3} [m]
C_{pc}	Pressure coefficient for the continuous jet = $(p - p_{in})/0.5\rho U_{c0}^2$ [–]
C_{ps}	Pressure coefficient for the synthetic jet = $(p - p_{in})/0.5\rho U_{sm0}^2$ [–]
D_d	Downstream duct length = 340×10^{-3} [m]
D_u	Upstream duct length = 210×10^{-3} [m]
h	Channel exit height [m]
H	Inlet/outlet channel height of the fan duct = 30×10^{-3} [m]
l_0	Stroke length [m]

T. Ishizawa (✉)
Graduate School of Mechanical Engineering, Kogakuin University,
Nishi-Shinjuku 1-24-2, Shinjuku-ku, Tokyo 163-8677, Japan
e-mail: am14006@ns.kogakuin.ac.jp

K. Sato
Department of Mechanical Engineering, Kogakuin University,
Nishi-Shinjuku 1-24-2, Shinjuku-ku, Tokyo 163-8677, Japan
e-mail: at12164@ns.kogakuin.ac.jp

K. Nishibe
Department of Mechanical Engineering, Tokyo City University,
Tamazutsumi 1-28-1, Setagaya-ku, Tokyo, Japan
e-mail: knishibe@tcu.ac.jp

K. Yokota
Department of Mechanical Engineering, Aoyama Gakuin University,
Fuchinobe 5-10-1, Chuo-ku, Sagamihara-shi, Kanagawa, Japan
e-mail: yokota@me.aoyama.ac.jp

© Springer International Publishing Switzerland 2016

A. Segalini (ed.), *Proceedings of the 5th International Conference on Jets, Wakes and Separated Flows (ICJWSF2015)*,
Springer Proceedings in Physics 185, DOI 10.1007/978-3-319-30602-5_14

L_0 Non-dimensional stroke length [–]
Δp Pressure difference between the inlet and outlet [Pa]
Q_t Total flow rate at the fan outlet [m^3/s]
Re Reynolds number = $U_0 b_0/\nu$ = 5300 [–]
U_{c0} Representative velocity of the continuous jet [m/s] (see [3])
U_{s0} Representative velocity of the synthetic jet [m/s] (see [3])
U_{sm0} $= \sqrt{\frac{1}{T}\int_0^{\frac{T}{2}} u_0^2(t)dt}$ [m/s] (see [5])
W Width of the duct = 30 × 10^{-3} [m]
η_c Efficiency of the continuous jet = $\Delta p Q_t/0.5\rho U_{c0}^2\, b_0 W U_{c0}$ [–]
η_s Efficiency of the synthetic jet = $\Delta p Q_t/0.5\rho U_{sm0}^2\, b_0 W U_{s0}$ [–]
θ_j Blowing angle = 30 [°]
Φ_s Flow rate coefficient for the synthetic jet = $Q_t/b_0 W U_{s0}$ [–]
Φ_c Flow rate coefficient for the continuous jet = $Q_t/b_0 W U_{c0}$ [–]
Ψ_s Discharge pressure coefficient for the synthetic jet = $\Delta p/0.5\rho U_{sm0}^2$ [–]
Ψ_c Discharge pressure coefficient for the continuous jet = $\Delta p/0.5\rho U_{c0}^2$ [–]

1 Introduction

Recently, synthetic jets have received attention as a substitute for continuous jets, and many studies on the flow characteristics of synthetic jets have been conducted to devise means to apply them to active flow control [1]. It has been reported that the flow field of a synthetic jet is governed by two non-dimensional parameters [1], i.e., the Reynolds number and the non-dimensional stroke length $L_0 = l_0/b_0$, where l_0 is the length of the fluid body ejected during the expulsion phase and b_0 is the slot width. An advantage of synthetic jets is that the jet flow can be generated using previously developed actuators that are abundantly available, such as diaphragms, piezoelectric elements [2], speakers [3], and plasma [4]. A magnetic synthetic jet actuator, which can supply energy in a noncontact mode, will be developed in the near future. Because most actuators can function without using rotational parts, synthetic jet technology also facilitates the downsizing, simplifying, and refining of fluid machines, thereby improving their preciseness. However, only few studies have been conducted on fluid machines based on the synthetic jet principle [1–3], and jet pump/fan designs using synthetic jets [5] have not been sufficiently investigated. If pumps or fans that use synthetic jets for energy transformation are developed, they can be used in applications such as air flow production in hermetically sealed aseptic containers, circulation of high-level radiation-contaminated water, and transportation of high-purity chemical liquids.

This study represents fundamental research on jet pump/fan development using a synthetic jet. As the first step, a prototype model of a synthetic jet fan is proposed, and the fan performance characteristics are discussed. In particular, this work is an

attempt to experimentally clarify the effect of the jet oscillation characteristics (e.g., the non-dimensional stroke L_0) on the fan performance, the pressure rise mechanism inside the fan duct, and fan efficiency. The experimental data obtained for the synthetic jet is compared with those for the continuous jet.

2 Experimental Setup

Figure 1 depicts the coordinate system and schematic diagram of the proposed synthetic jet fan. This prototype is the first step to utilizing synthetic jets as a fan; however, in the future, this type of fan, which is based on the principle of simple vibration, is expected to be used in various fields mentioned above. The slot width is represented as b_0. The inlet/outlet channel height of the fan duct is H, and the width of the duct is W. The results presented in this paper are obtained for a blowing angle θ_j of 30°. In the blowing process performed using this model, the synthetic jet should flow downstream because of the slot structure. On the other hand, inhalation flow into the slot without momentum, which is similar to a potential-flow sink, is induced in the suction process. Consequently, the flow in the duct is unidirectional, with the time-averaged velocity directed downstream. A schematic representation of the experimental setup used to evaluate the fan performance of a synthetic jet fan model is shown in Fig. 2. The synthetic air jet is generated by a loudspeaker (Diecook DD-15L) driven by a signal generator (MCPLG1100D), which transmits signals through a power amplifier (Classic Pro V3000). The speaker is replaced with a blower (Showa Denki Co., Ltd., U75-2-313) to generate the continuous jet. A sirocco fan (Mitsubishi, BF-16S3) is used to supply the main flow. The slot length is the same as the duct width, $W = 30$ mm, the slot width $b_0 = 10$ mm, representative velocity U_0, and stroke length l_0 can be adjusted by using a power amplifier. The channel height H, which is a geometric parameter, is set depending on some experimental conditions. The channel exit height is h. The velocities of both jets are measured by a hot-wire anemometer (Kanomax, IHW100) using a traverser (Chuo Precision Industrial, ALS-230-C2P). However, the measurement of flow velocity with a hot-wire anemometer is vulnerable to large errors in the regions

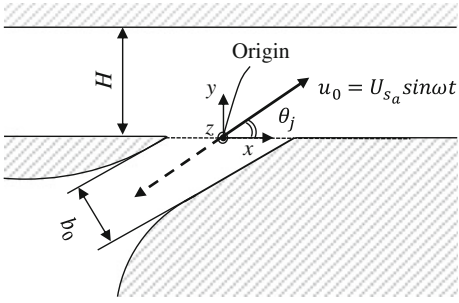


Fig. 1 Coordinate system and geometry of slot

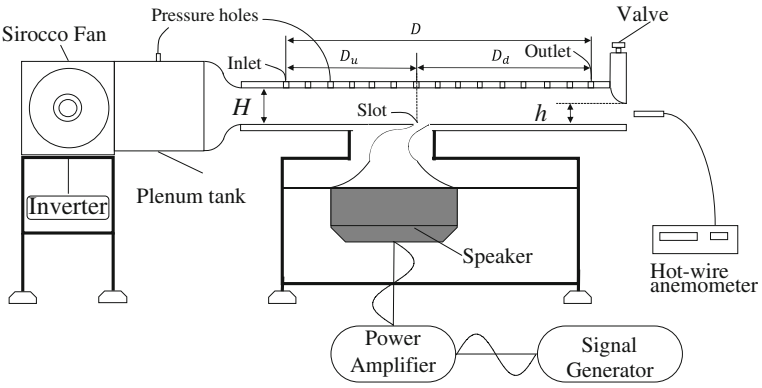


Fig. 2 Schematic diagram of experimental apparatus for synthetic jet

prone to local backflow, such as the complicated flow field near the slot. The static pressure difference between the inlet and outlet of a fan is used to evaluate the fan performance and is measured by a digital manometer (Okano Works, Ltd., DMP301N), and the pressure fluctuations in-side the duct is measured by a pressure transducer.

3 Results and Discussion

Typical fan performance curves for synthetic jets were obtained experimentally for $H/b_0 = 3$ (where the aspect ratio of the duct is $H/W = 1$) and $Re = 5300$, and the results are shown in Fig. 3. The inlet and outlet of the fan are defined as D_u and D_d,

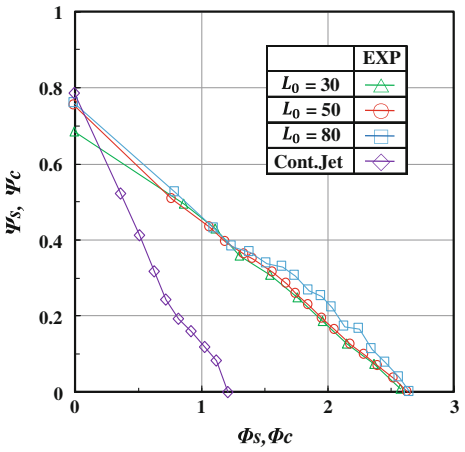


Fig. 3 Typical static pressure–flow-rate performance curves. ($H/b_0 = 3$, $H/W = 1$, $Re = b_0 U_0/\nu = 5300$) (EXP Experiment)

respectively. The non-dimensional stroke L_0 is varied to obtain different curves. The performance curve for the continuous jet in the case of identical representative velocities is also shown in the same figure for reference. The vertical axis represents the discharge pressure coefficient $\Psi_s = \Delta p/0.5\rho U_{sm0}^2$ ($\Psi_c = \Delta p/0.5\rho U_{c0}^2$ for the continuous jets) based on the kinetic pressure (cf. [2]), where Δp ($= p_{out} - p_{in}$) is the pressure difference between the inlet and outlet. The horizontal axis represents the flow rate coefficient $\Phi_s = Q_t/b_0 W U_{s0}$ for the synthetic jet and $\Phi_c = Q_t/b_0 W U_{c0}$ for the continuous jets, where Q_t is the blow flow rate from the outlet of the fan. U_{s0} and U_{c0} are representative velocities of the synthetic and continuous jets (cf. [3]), respectively. In all the cases, including the continuous jet, the performance curves are approximately drawn as straight lines and have negative slopes. These results indicate that the continuous jet of the jet fan/pump can be replaced by the synthetic jet. It can also be seen that the performance curves of the synthetic jets do not depend on the non-dimensional stroke L_0 under the present range of conditions. A comparison of the results for the synthetic and continuous jets indicates that the maximum flow rate coefficients for the synthetic jets are roughly twice those for the continuous jet under the present experimental conditions.

Figure 4 presents the static pressure distributions on the upper surface of the duct for various L_0 values for the synthetic jets and the continuous jet in the case of $\Phi = \Phi_{max}/2$, where Φ_{max} represents the maximum flow rate coefficient. The vertical axis represents the pressure coefficient, defined as $C_{ps} = (p - p_{in})/0.5\rho U_{sm0}^2$ for synthetic jets and $C_{pc} = (p - p_{in})/0.5\rho U_{c0}^2$ for the continuous jet. For both the synthetic jets and the continuous jet, it is obvious that the static pressure under any condition drastically increases owing to the momentum of the jet near the slot and reaches the maximum value through pressure recovery at $x/b_0 \approx 20$, except at the singular stagnation point on the duct surface near the slot. Consequently, it is found that the fundamental characteristics of the fan using a synthetic jet are similar to those of the fan using a continuous jet.

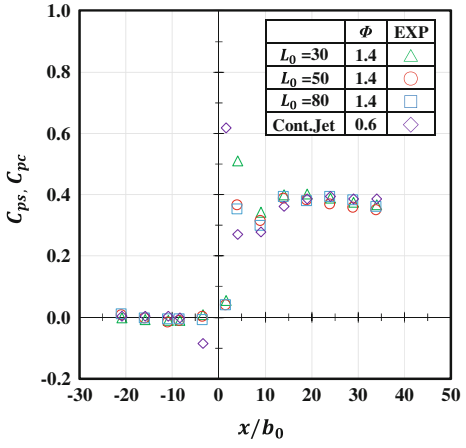


Fig. 4 Static pressure distribution on the upper surface of the duct. ($H/b_0 = 3$, $H/W = 1$, $Re = b_0\, U_0/\nu = 5300$, $\Phi = \Phi_{max}/2$) (*EXP* Experiment)

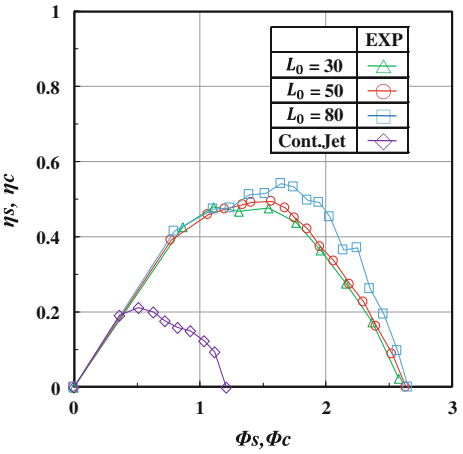


Fig. 5 Typical synthetic jets fan efficiency–flow-rate. ($H/b_0 = 3$, $H/W = 1$, $Re = b_0 U_0/v = 5300$) (*EXP* Experiment)

The fan efficiency curves under the same conditions as those considered in previous figures are shown in Fig. 5. The maximum values of the fan efficiency for every non-dimensional stroke of the synthetic jets should be roughly located at $\Phi_{max}/2$ and should reach around $\eta_s = 0.5$. The maximum fan efficiency values for the synthetic jets are greater than twice that for the continuous jet. It seems that the fan efficiency curves for the synthetic jets are almost independent of L_0.

4 Conclusion

In this study, a prototype model of a synthetic jet fan was developed. The fan performance characteristics, pressure distributions on the duct surface, and fan efficiency curves for various non-dimensional stroke values were analyzed.

Acknowledgments The authors would like to thank Mr. Youhei Nomura of the Tokyo City University and Mr. Junichiro Kikkawa of Software Cradle Co., Ltd., for their help with the numerical simulations. The present study was conducted with the support of MEXT (Functional Microstructured Surfaces Research Center of Kogakuin University) and a Grant-in-Aid for Scientific Research (No. 15K05807 and 25889057).

References

1. R. Holman, Y. Utturkar, Formation criterion for synthetic jets. AIAA J. **43**(10), 2110–2111 (2005)
2. T. Koso, M. Morita, Effect of stroke and Reynolds number on the characteristics of circular synthetic jets. J. Fluid Sci. Technol. **9**(2), 1–15 (2014)
3. K. Nishibe, Y. Fujita, K. Sato, K. Yokota, T. Koso, Experimental and numerical study on the flow characteristics of synthetic jets. J. Fluid Sci. Technol. **6**(4), 425–436 (2011)

4. K. Fujii, A. Oyama, I. Funaki, K. Rinoie, T. Nonomura, Research on plasma actuator flow control that pays attention to localization flow, in *FY2010 Annual Research Report*
5. T. Koso, R. Nakashima, Piezoelectric fan using a synthetic jet principle. JSME No. 088-1 (2008) (in Japanese)

Part II
Wakes

Towards Local Isotropy of Higher Order Statistics in Wakes

Shunlin Tang, Robert A. Antonia, Lyazid Djenidi, Luminita Danaila, Yu Zhou and Tongming Zhou

Abstract In this paper, we test the local isotropy of higher order statistics in the intermediate wake region. We focus on normalized odd moments of the transverse velocity derivatives, $M_{2n+1}(\partial u/\partial z) = \overline{(\partial u/\partial z)^{2n+1}}/\overline{(\partial u/\partial z)^2}^{(2n+1)/2}$ on the wake centreline, which should be zero if local isotropy is satisfied (n is a positive integer). It is found that the relation $M_{2n+1}(\partial u/\partial z) \sim R_\lambda^{-1}$ is supported reasonably well by hot-wire data up to the seventh-order ($n = 3$), although it is also dependent on the initial conditions. In particular, the present data show that the higher the order (e.g. fifth- or seventh-order), the higher R_λ must be for local isotropy to be satisfied (i.e. $M_{2n+1}(\partial u/\partial z) = 0$).

1 Introduction

The analytical framework introduced by Kolmogorov [1, 2], widely known as $K41$, for describing the properties of small-scale turbulence has had a tremendous impact on turbulence research. Local isotropy (LI), which postulates that small-scale turbulence at sufficiently high Reynolds numbers is statistically independent of the

S. Tang (✉) · Y. Zhou
Shenzhen Graduate School, Institute for Turbulence-Noise-Vibration Interaction and Control, Harbin Institute of Technology, Shenzhen 518055, People's Republic of China
e-mail: shunlin.tang88@gmail.com

S. Tang · R.A. Antonia · L. Djenidi
School of Engineering, University of Newcastle, Newcastle, NSW 2308, Australia
e-mail: Lyazid.Djenidi@newcastle.edu.au

L. Danaila
CORIA CNRS UMR 6614, Université de Rouen, 77801 Saint Etienne du Rouvray, France

T. Zhou
School of Civil, Environmental and Mining Engineering, University of Western Australia, Crawley, WA 6009, Australia

© Springer International Publishing Switzerland 2016

A. Segalini (ed.), *Proceedings of the 5th International Conference on Jets, Wakes and Separated Flows (ICJWSF2015)*, Springer Proceedings in Physics 185, DOI 10.1007/978-3-319-30602-5_15

large scales, and is homogeneous, isotropic, and time independent, is one of the key assumptions of $K41$ theory. Even though the influence of the inhomogeneous and anisotropic large scales, which is flow dependent, on the small-scale statistical quantities may linger at finite Reynolds number (FRN), it is expected to decrease rapidly with increasing Reynolds number. An understanding of the rate at which small scales tend towards isotropy is of major importance in turbulence research.

Since the velocity derivatives are small-scale quantities, symmetry requirements of LI demand that $M_{2n+1}(\partial u/\partial z)$ be zero (also the $M_{2n+1}(\partial u/\partial y)$). At finite Reynolds number, they should at least decrease as the Reynolds number increases for a given initial condition. The evolution of $M_{2n+1}(\partial u/\partial y)$ with the Taylor microscale Reynolds number R_λ ($= u'\lambda/\nu$, where λ is the longitudinal Taylor microscale $u'/(\partial u/\partial x)'$ and ν is the kinematic viscosity of the fluid, a prime denotes a rms value), primarily in nearly homogeneous shear flows, has received a significant amount of attention both experimentally [3–5] and via direct numerical simulations [6–8]. This flow is characterised by a constant shear rate $S = dU/dy$, where $U(y)$ is the mean velocity in the streamwise direction x, and y is the direction of the shear. A simple estimate of $M_{2n+1}(\partial u/\partial y)$ can be made by (i) using Kolmogorov's first hypothesis which states that small-scale properties depend solely on the mean turbulent energy dissipation rate $\overline{\epsilon}$ and ν and (ii) assuming that $M_{2n+1}(\partial u/\partial y)$ depends on some power p of the shear [9], viz.

$$M_{2n+1}(\partial u/\partial y) = S^p f(\epsilon, \nu) \sim R_\lambda^{-p}, \tag{1}$$

where it is further assumed that $S \sim u'/L$ and L is a large scale (e.g. the integral scale). If $p = 1$, namely a linear dependence of $M_{2n+1}(\partial u/\partial y)$ on the shear, (1) yields [10]

$$M_{2n+1}(\partial u/\partial y) \sim R_\lambda^{-1}. \tag{2}$$

However, (2) and (1) are not fully supported by the existing experimental and numerical data. For example, Schumacher [9] collected all the existing data for M_3 and showed that the power p differs from one set of data to another while (2) seems to only be satisfied at large Reynolds numbers. For M_5, on the one hand, Shen and Warhaft [5] showed that there is no dependence on R_λ over the range $100 < R_\lambda < 1000$. However, two sets of data from Ferchichi and Tavoularis [4] showed that M_5 decreases with increasing R_λ over the range $140 < R_\lambda < 660$. Note that Warhaft and Shen [11] commented on this difference and showed that the results of Ferchichi and Tavoularis [4] actually support the conclusions of Shen and Warhaft [5] arguing that the difference lies in the interpretation of the data. Schumacher [9] also collected all the existing data for M_5 and showed that it does not diminish perceptibly even when R_λ is as high as 1000. For M_7, Shen and Warhaft [5] showed that it increases with R_λ with $p = -0.63$ instead of decreasing.

These results, especially for M_5 and M_7, have been interpreted as implying that the small-scale anisotropy persists to very high Reynolds numbers in the homogeneous shear flows. The aim of this study is to understand how $M_{2n+1}(\partial u/\partial z)$ evolves on the

wake centerline with increasing R_λ and, its dependence on the initial conditions. We recall here that $M_{2n+1}(\partial u/\partial y)$ should be zero on the axis due to the flow symmetry.

Several studies were devoted to characterising different aspects of wakes, e.g. [12–15]. In particular, Thiesset et al. [12] appraised the LI through both classical kinematic tests and phenomenological approaches, which explicitly account for the large-scale strain, in the intermediate wake of five types of obstacles (a circular cylinder, a square cylinder, a screen cylinder, a normal plate and a screen strip). They showed that, in the presence of an organised motion, the isotropy is not an adequate assumption for the large scales but may be satisfied over a range of scales which depend on the total strain rate that characterises the flow. In this paper, we extend the study of Thiesset et al. [12], which focused on the second- and third-order statistics, in several significant ways. First, we test LI on the wake axis behind different types of bluff bodies through higher-order moments ($M_{2n+1}(\partial u/\partial z)$ up to the seventh order) which may capture the departures from LI more and more effectively as the order or the moment increases [5]. Second, we look at the effect on LI of (i) the initial conditions for a given value of n and (ii) the Reynolds number.

2 Experimental Details

A detailed description of the vorticity probe is given in [12, 14, 15]. Only a brief description is given below. Experiments were carried out in a non-return blower-type wind tunnel with a square crosssection (350 × 350 mm) of 2.4 m in length. The inclination of the bottom wall of the working section was adjusted in order to maintain a zero streamwise pressure gradient. Several wake generators were used: a solid circular cylinder (CC), a solid square cylinder (SqC), a circular cylinder constructed from a screen (0.5 mm wire diameter with a mesh size of 1.6 mm) of 54 % solidity (ScC), a solid plate placed normal to the flow (P), and screen strip (SS) constructed of the same material as the screen cylinder. In each case (Fig. 1), the characteristic

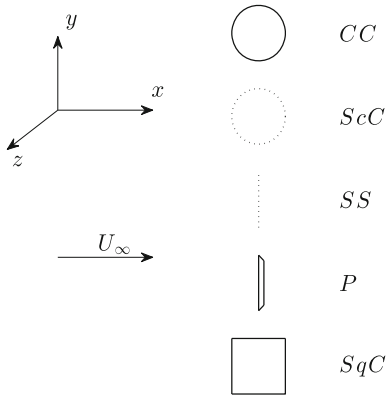


Fig. 1 Cross-section of the four different wake generators. From *top* to *bottom*: a *solid circular* cylinder (CC), a *circular* cylinder constructed from a screen (0.5 mm wire diameter with a mesh size of 1.6 mm) of 54 % solidity (ScC), a *solid plate* placed normal to the flow (P), screen strip (SS), and a *solid square* cylinder (SqC)

dimension (height or diameter) d is the same (25.4 mm). The generators were all installed at a distance of 20 cm downstream of the entrance to the working section and spanned the full width of the working section. The measurement location was at $x/d = 70$. Different velocity fluctuations (u, v, w) were measured with a vorticity probe on the wake centreline.

All the Wollaston (Pt-10 % Rh) hot wires (diameter $d_w = 2.5\,\mu$m) were etched to an active length of 0.5 mm. The length to diameter ratio of the wires was typically 200. The hot wires were operated with in-house constant temperature circuits at an overheat ratio of 1.5. Output signals from the anemometers were passed through buck-and-gain circuits and low-pass filtered at a cut-off frequency f_c; f_c was chosen after examining the spectrum of $\partial u/\partial x$ and identifying the onset of electronic noise. The values of f_c were generally close to the Kolmogorov frequency $f_K = U/2\pi\eta$. The filtered signals were then sampled at a frequency of $f_s \simeq 2f_c$ into a PC using a 12 bit A/D converter. The sampling period T_s is in the range 45–100 s for each wake, which is large enough for the eighth-order velocity structure function to converge. This was verified by examining the closure of $\delta\alpha$ (α stands for either u, v, or w, v and w), weighted by $|\delta\alpha|^m$ (m is a positive integer), for different values of r.

3 Results

Figures 2, 3 and 4 show $M_{2n+1}(\partial u/\partial z)$ $(n = 1, 2, 3)$ versus R_λ in different wakes. In these figures, the solid lines are inferred from the relation $M_{2n+1}(\partial u/\partial z) = CR_\lambda^{-1}$ where the constant C differs from wake to wake. A number of comments can be made. First, the rate at which $M_{2n+1}(\partial u/\partial z)$ on the wake centreline tends towards zero is reasonably well supported by the present data in different wakes. We recall

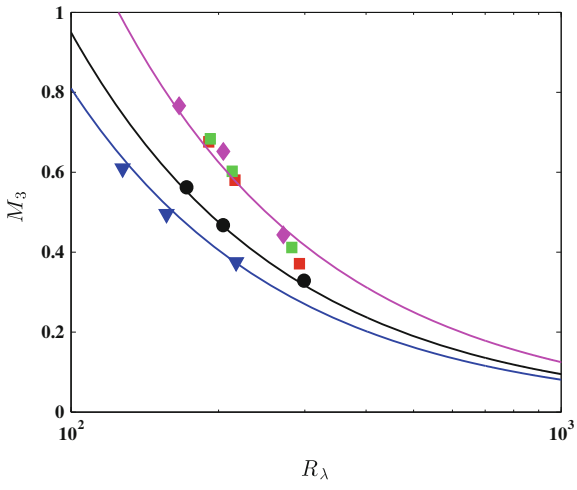


Fig. 2 Dependence of M_3 on R_λ on the wake centreline. ●, CC; ◆, P; ■, SqC; ▼, SS; ■, ScC. *Solid lines* correspond to the relation $M_3 = CR_\lambda^{-1}$ with different C

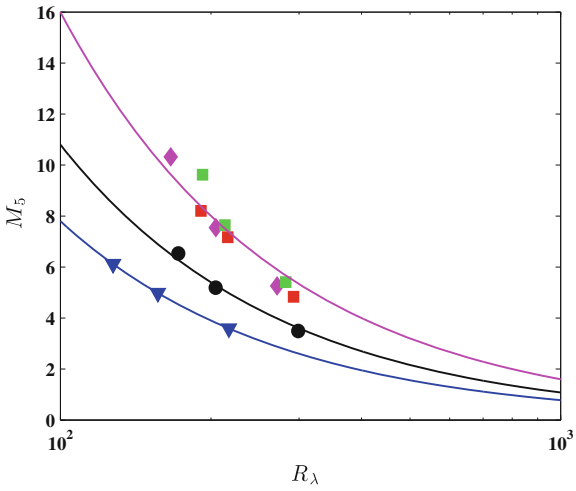


Fig. 3 Dependence of M_5 on R_λ on the wake centreline. ●, CC; ◆, P; ■, SqC; ▼, SS; ■, ScC. *Solid lines* correspond to the relation $M_5 = CR_\lambda^{-1}$ with different C

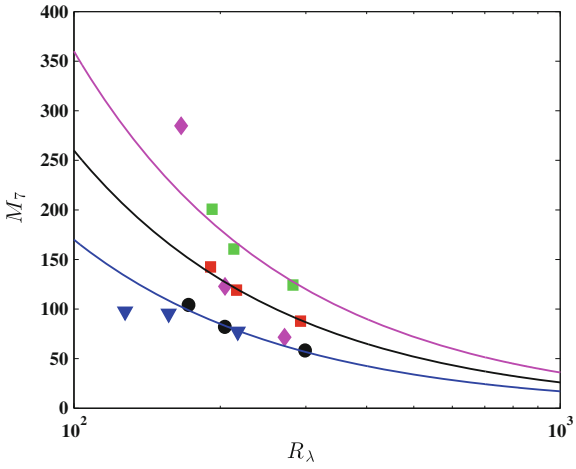


Fig. 4 Dependence of M_7 on R_λ on the wake centreline. ●, CC; ◆, P; ■, SqC; ▼, SS; ■, ScC. *Solid lines* correspond to the relation $M_7 = CR_\lambda^{-1}$ with different C

here that $M_{2n+1}(\partial u/\partial y)$ should be zero on the axis due to the flow symmetry. Second, applying several tests of LI to second- and third-order moments of velocity increments, Thesset et al. [12] showed that LI is a good assumption on the wake centreline with no clear dependence on the initial conditions or on the Reynolds number. However, the present results suggest that both the initial conditions and the Reynolds number have a significant influence on the rate at which $M_{2n+1}(\partial u/\partial z)$ approaches zero. The approach is slow for ScC, SqC, and P but rapid for SS for all tests considered. Third, for $M_{2n+1}(\partial u/\partial z)$ to be zero, R_λ should be sufficiently large, and higher orders (e.g. M_5 or M_7) demand much higher R_λ for the odd-order moments to be zero.

4 Conclusions

Overall, Figs. 2, 3 and 4 strongly supports the idea that LI can be approached as R_λ continues to increase on the wake centreline. The approach is also dependent on the initial conditions for a given value of n. In particular, the present data show that the larger n is, the higher R_λ should be for LI to be satisfied (i.e. $M = 0$).

This has major implications in the context of testing predictions ensuing from $K41$. $K41$ can only be verified in turbulent flows at sufficiently high Reynolds number, when LI should be satisfied. The departure from LI shown in Figs. 2, 3 and 4 (which differs from wake to wake) can certainly have an effect on the statistics of the small-scale turbulent motion. Thus, the expected universality of small-scale turbulent motion, as predicted by $K41$, is unlikely to be obtained at finite (small to moderate) Reynolds numbers. Instead, the variation of small-scale turbulent statistics with R_λ may differ from flow to flow, and, for a given flow, is likely to depend on the initial conditions since the departure from LI differs.

References

1. A.N. Kolmogorov, Local structure of turbulence in an incompressible fluid for very large Reynolds numbers. Dokl. Akad. Nauk SSSR **30**, 299–303 (1941)
2. A.N. Kolmogorov, Dissipation of energy in the locally isotropic turbulence. Dokl. Akad. Nauk SSSR **32**, 19–21 (1941)
3. S. Garg, Z. Warhaft, On small scale statistics in a simple shear flow. Phys. Fluids **10**, 662–673 (1998)
4. M. Ferchichi, S. Tavoularis, Reynolds number effects on the fine structure of uniformly sheared turbulence. Phys. Fluids **12**, 2942–2953 (2000)
5. X. Shen, Z. Warhaft, The anisotropy of the small scale structure in high Reynolds number ($R_\lambda \sim 1000$) turbulent shear flow. Phys. Fluids **12**, 2976–2989 (2000)
6. A. Pumir, Turbulence in homogeneous shear flows. Phys. Fluids **8**, 3112–3127 (1996)
7. J. Schumacher, B. Eckhardt, On statistically stationary homogeneous shear turbulence. Europhys. Lett. **52**, 627–632 (2000)
8. J. Schumacher, Derivative moments in stationary homogeneous shear turbulence. J. Fluid Mech. **441**, 109–118 (2001)
9. J. Schumacher, K.R. Sreenivasan, P.K. Yeung, Derivative moments in turbulent shear flows. Phys. Fluids **15**, 84–90 (2003)
10. J.L. Lumley, Similarity and the turbulent energy spectrum. Phys. Fluids **10**, 855–858 (1967)
11. Z. Warhaft, X. Shen, Some comments on the small scale structure of turbulence at high Reynolds number. Phys. Fluids **13**, 1532–1533 (2001)
12. F. Thiesset, L. Danaila, R.A. Antonia, Dynamical effect of the total strain induced by the coherent motion on local isotropy in a wake. J. Fluid Mech. **720**, 393–423 (2013)
13. R.A. Antonia, J. Mi, Approach towards self-preservation of turbulent cylinder and screen wakes. Exp. Thermal Fluid Sci. **17**, 277–284 (1998)
14. R.A. Antonia, T. Zhou, G.P. Romano, Small-scale turbulence characteristics of two-dimensional bluff body wakes. J. Fluid Mech. **459**, 67–92 (2002)
15. F. Thiesset, R.A. Antonia, L. Danaila, Scale-by-scale turbulent energy budget in the intermediate wake of two-dimensional generators. Phys. Fluids **25**, 115105 (2013)

Heat Transfer Enhancement by Grid-Generated Turbulence for a Cylinder in Crossflow

Gianfrancesco Melina, Paul John Kenneth Bruce, Geoffrey Frederick Hewitt and John Christos Vassilicos

Abstract The heat transfer coefficient is experimentally measured around a cylinder heated by ohmic effect. The heating technique approximates a uniform heat flux on the cylinder's wall. The model is placed downstream of different perturbing grids in a wind tunnel. The Reynolds number based on the cylinder's diameter varies between 10820 and 48830. At large distances from the grids, the heat transfer is significantly enhanced by using a fractal and a single square grid designed to increase turbulence intensity with a low blockage ratio. Significant differences exist between the heat transfer profiles measured in the production and in the decay region in positions where turbulence intensity is the same.

1 Introduction

Heat transfer enhancement for a cylinder in crossflow is a relevant topic for different industrial contexts. Several industrial devices use cylindrical elements in crossflow to exchange heat between two fluids, as for example shell-and-tube heat exchangers or water-air radiators [2]

The heat transfer around a cylinder in crossflow is affected by the characteristics of the incoming turbulent flow [7]. In particular the heat transfer is augmented by increasing turbulence intensity, Tu, the enhancement is greater at higher Reynolds numbers based on the cylinder's diameter, Re, whereas it is reduced if the integral length scale of turbulence, L_u, is large [6].

Hurst and Vassilicos [3] show that low-blockage fractal square grids produce an extended turbulence production region, where Tu increases, followed by a slow-decay region where Tu is considerably higher than for regular grids. The position x_{peak}, where Tu on the centerline is maximum, scales with the wake-interaction length

G. Melina (✉) · P.J.K. Bruce · J.C. Vassilicos
Aeronautics, Imperial College London, London SW7 2AZ, UK
e-mail: g.melina13@imperial.ac.uk

G.F. Hewitt
Department of Chemical Engineering, Imperial College London, London SW7 2AZ, UK

© Springer International Publishing Switzerland 2016

A. Segalini (ed.), *Proceedings of the 5th International Conference on Jets, Wakes and Separated Flows (ICJWSF2015)*,
Springer Proceedings in Physics 185, DOI 10.1007/978-3-319-30602-5_16

scale, $x^* = L_0^2/t_0$ [5]. The peak value of Tu is higher for higher ratios t_0/L_0 [1], where L_0 is the distance between the largest bars of the grids and t_0 is their thickness.

In this work the possibility of using single- and multi-scale square grids with a low blockage ratio to efficiently enhance heat transfer is explored. The local heat transfer coefficient around the median circumference of a cylinder in crossflow is experimentally measured in a wind tunnel for $10820 < Re < 48830$, at several distances from three perturbing grids: a regular square-mesh grid (RG60), a fractal square grid (FSG17) and a single square grid (SSG). Single hot-wire measurements are performed without the cylinder to characterize the turbulent flow downstream of the three turbulence generators. The circumferentially averaged heat transfer coefficient is quantified for each grid along the streamwise direction. The role of the geometrical parameters t_0 and L_0 on heat transfer enhancement is discussed. For both FSG17 and SSG, which create an extended turbulence production region, angular heat transfer profiles are compared in two positions, one in the production and one in the decay region, where Tu is approximately the same.

2 Experimental Technique and Data Reduction

Velocity and heat transfer measurements are performed in an open-loop wind tunnel with a square cross test section $T^2 = 457^2\,\text{mm}^2$.

Scaled diagrams of the three perturbing grids, placed at the inlet of the test section ($x = 0$), are illustrated in Fig. 1. RG60 is a regular bi-planar grid with a blockage ratio $\sigma = 32\,\%$, $L_0 = 60\,\text{mm}$ and $t_0 = 10\,\text{mm}$. FSG17 is a fractal square grid with four iterations, $\sigma = 25\,\%$, $L_0 = 237.8\,\text{mm}$ and $t_0 = 19.2\,\text{mm}$, further details of this grid can be found in [3]. Finally SSG, for which $\sigma = 20\,\%$, is just composed by a single thick square with supporting struts where $L_0 = 229\,\text{mm}$ and $t_0 = 43\,\text{mm}$. Velocity measurements downstream of the grids are performed on the centerline via single hot-wire anemometry along the streamwise direction, x, at two inlet velocities, $U_\infty = 5, 17\,\text{m/s}$. The turbulent flow downstream of the grids is characterized in terms of mean streamwise velocity, U, turbulence intensity, $Tu = u'/U$, where u' is the rms

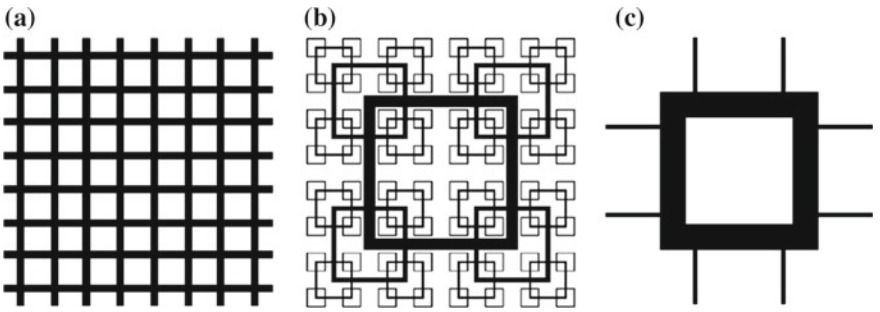


Fig. 1 The perturbing grids used in this work: **a** RG60; **b** FSG17; **c** SSG

value of the fluctuating velocity component, u, and integral length scale, L_u, obtained from the integral time scale, Θ_u, by applying Taylor's hypothesis, $L_u = U\Theta_u$.

Once the flow has been characterized, a Nylon circular cylinder is vertically placed in the working section of the wind tunnel. The diameter of the cylinder is $D = 35$ mm, its blockage is $\sigma_c = 7.7\,\%$ and its aspect ratio is $AR = 13$. The model is placed at several downstream distances from each grid and local heat transfer measurements are performed around its median circumference for $U_\infty = 5, 11, 17$ m/s.

An Inconel foil (25 μm thick), wrapped around the central part of the cylinder, is heated by ohmic effect by providing a large direct current, delivered by a laboratory power supply. Since the surface heater is very thin and the Reynolds numbers sufficiently high, this heating technique allows to approximate uniform heat flux conditions on the cylinder's wall [8]. Thermal insulating material fills the middle section of the model to minimize heat conduction. Eight fine-diameter K-type thermocouples are installed beneath the heated foil to measure the local wall temperature, T_w. The cylinder is rotated using a stepper motor to measure the angular distribution of T_w at 5° intervals. The local heat transfer coefficient is computed with $h = q_{conv}/(T_w - T_\infty)$, where q_{conv} is the convective heat flux obtained subtracting the radiative heat flux from the input heat generation rate, T_∞ is the free-stream temperature measured with a K-type thermocouple at the inlet of the test section. The local Nusselt number is calculated as $Nu = hD/\lambda_f$, where λ_f is the thermal conductivity of air evaluated at the film temperature, $T_f = (T_w + T_\infty)/2$. The Reynolds number is computed as $Re = UD/\nu_f$, with U being the local mean velocity on the centerline at the cylinder's location when the cylinder is not in place, ν_f is the kinematic viscosity of air evaluated at T_f.

3 Heat Transfer Enhancement

The evolution of Tu along the centerline with $U_\infty = 17$ m/s is shown in Fig. 2, the filled symbols indicate the positions where the cylinder is placed for the heat transfer measurements. For RG60 Tu reaches a peak value of about 18 % close to the grid but rapidly drops moving further downstream. On the contrary FSG17 and SSG exhibit

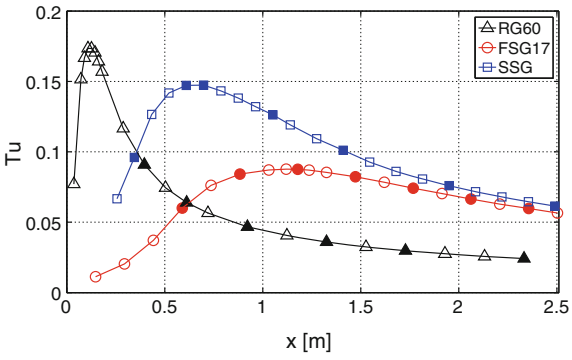


Fig. 2 Turbulence intensity downstream of the grids, $U_\infty = 17$ m/s

protracted turbulence production regions, where Tu increases with x, followed by turbulence decay regions where Tu is significantly higher with respect to RG60. The distance from the grid where Tu is maximum (and therefore the extent of the production region) can be expressed as $x_{peak} = \phi x^*$. For the present measurements the value of ϕ is 0.3 for RG60, 0.4 for FSG17 and 0.5 for SSG. The maximum value of Tu is about 8.8 % for FSG17 whereas it reaches about 14.7 % for SSG despite its lower blockage ratio. This is a result of the bigger ratio t_0/L_0 for SSG which is more than double with respect to FSG17. The integral length scale ratio, L_u/D, is plotted along the centerline in Fig. 3 for $U_\infty = 17$ m/s. For FSG17 and SSG the values of L_u/D are always higher if compared to RG60 since the latter is characterized by a smaller L_0. As originally reported in [3], L_u remains approximately constant in the turbulence decay region of FSG17. This feature can be very useful if one wants to study the effect of Tu on heat transfer for fixed values of L_u.

The enhancement of the circumferentially averaged Nusselt number, Nu_g, with respect to its value under laminar free-stream conditions, Nu_{lam}, is presented in Fig. 4 for $U_\infty = 17$ m/s. The quantity Nu_{lam} is computed with the empirical correlation provided in [11], $Nu_{lam} = 0.23Re^{0.6}$, which was verified by performing heat transfer measurements without perturbing grids at $U_\infty = 5, 10, 15, 20$ m/s. For FSG17 and SSG an optimal position is found where heat transfer enhancement is maximum and

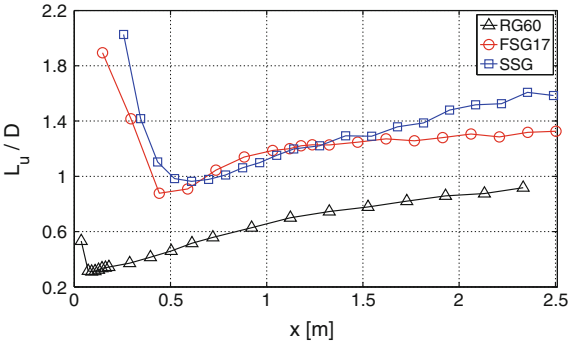


Fig. 3 Integral length scale ratio downstream of the grids, $U_\infty = 17$ m/s

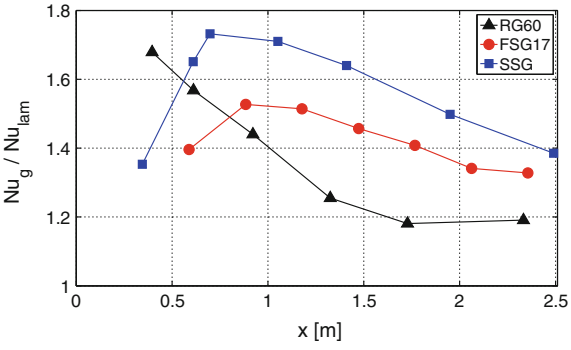


Fig. 4 Enhancement of the circumferentially averaged Nusselt number, $U_\infty = 17$ m/s

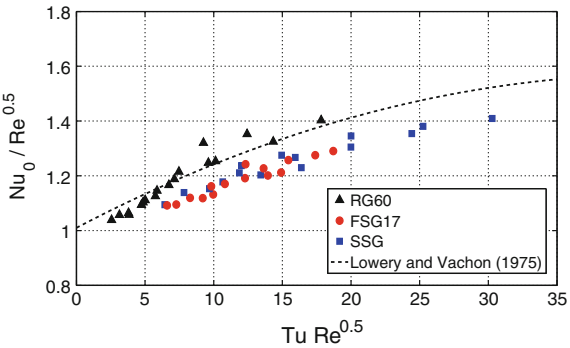


Fig. 5 Frossling number at the front stagnation point in the decay regions

this occurs in the proximity of x_{peak}. For FSG17 the maximum enhancement is 53 % whereas it reaches 73 % for SSG, thanks to its bigger ratio t_0/L_0. In the turbulence decay regions the performance of FSG17 and SSG is always clearly greater if compared to RG60 as a result of the higher turbulence intensity. For example at $x = 1.5$ m the estimate of heat transfer enhancement is 61 % for SSG, 45 % for FSG17 and 22 % for RG60. Such a better performance is achieved using two grids with a lower σ and therefore lower pressure drop. It is important to notice that proceeding further downstream the capability of FSG17 in augmenting heat transfer approaches the performance of SSG, therefore showing that for FSG17 the decay of Nu_g/Nu_{lam} along x is appreciably lower than SSG. This occurs even though for FSG17 the Reynolds number based on the thickness of the largest bars of the grid, $Re_{t_0} = U_\infty t_0/\nu$, is smaller by a factor of 2.2.

The Frossling number at the front stagnation point (subscript '0'), $Nu_0/Re^{0.5}$, is plotted against the turbulence parameter $TuRe^{0.5}$ in Fig. 5 for all the measurements performed in the decay regions, together with the correlation suggested by [4]. For the same $TuRe^{0.5}$, the values of $Nu_0/Re^{0.5}$ are always higher for RG60 as a consequence of the smaller L_u/D [10].

4 Heat Transfer in the Production and in the Decay Region

The angular distributions of $Nu/Re^{0.5}$ in the production and in the decay region are compared, for both FSG17 and SSG, considering two downstream positions where Tu is approximately the same (Fig. 6).

As Re increases, in the decay region $Nu/Re^{0.5}$ conventionally increases on the forward part of the cylinder (where a laminar boundary layer exists), indicating that turbulence becomes more effective in augmenting heat transfer for larger Re. On the contrary in the production region: (i) the values of $Nu/Re^{0.5}$ on the front part of the cylinder are generally lower despite the higher Re; (ii) the growth of $Nu/Re^{0.5}$ with Re is attenuated. In particular for SSG the profiles relative to different Re are almost

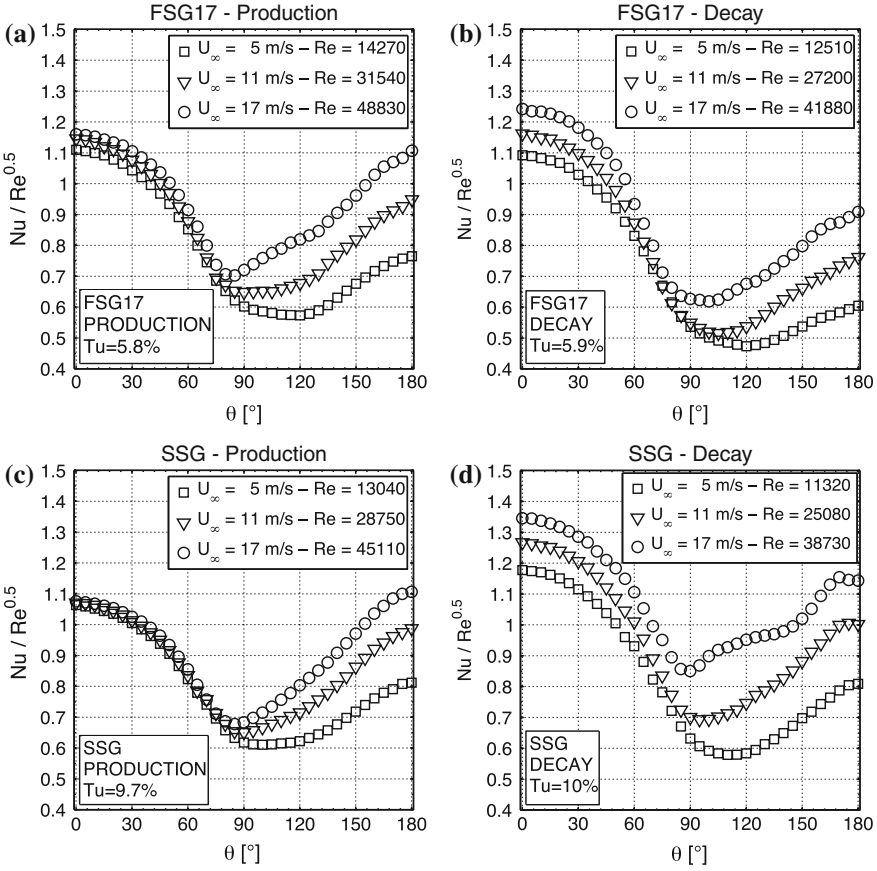


Fig. 6 Angular distribution of the Frossling number in the production and in the decay region of turbulence for FSG17 and SSG, θ is the angular position measured from the front stagnation point

collapsed as one would expect for laminar free-stream conditions. These results are likely to be related to the intermittency of the velocity fluctuations in the production region. An intermittent behaviour of the turbulent flow can contribute to mitigate the effects of *Tu* and therefore reduce the mass and the heat transfer on the forward part of the cylinder [9].

On the other hand, on the backward part of the cylinder (where the flow is separated) the recovery of *Nu* with respect to Nu_0 is significantly enhanced in the production region. For example, for FSG17 at $U_\infty = 17$ m/s, the value of Nu_{180}/Nu_0 (the subscript '180' indicates the rear stagnation point) in the production region is about 30 % higher with respect to the value measured in the decay region. This can be just partially explained by the larger *Re* in the production region. In fact one should consider that Nu_{180}/Nu_0 for $Re = 31540$ in the production region is also larger (about 14 %) if compared to the same quantity in the decay region for $Re = 41880$.

The heat transfer distribution on the backward part of the cylinder is dominated by vortex shedding effects, which are more prominent as Re increases and are largely responsible for an increase in the heat transfer coefficient [8]. The production region is the zone of the flow where the wakes created by the largest bars of the grid are growing and have not yet met, condition which occurs in the proximity of $x = x_{peak}$ on the centerline [5]. It is possible that when the cylinder is placed at $x < x_{peak}$, the interaction between its wake and the wakes originating from the grid promotes a more intense vortex shedding downstream of it. The large scale vortical structures in the production region, where the flow undergoes a laminar-to-turbulent transition, might influence the vortex formation mechanism past the cylinder and therefore contribute to enhance the heat transfer recovery on its backward section.

5 Conclusions

The angular distribution of the heat transfer coefficient is experimentally measured around the circumference of a heated cylinder, placed in a wind tunnel at several distances from three types of grids with different geometries and blockage ratios.

For the same inlet velocity, at large distances from the grid, the heat transfer is always substantially higher when a fractal square grid and a single square grid are used in place of a regular grid with higher blockage ratio. The fractal and the single square grids can be used to efficiently augment heat transfer since they are able to create protracted regions of high turbulence intensity, while maintaining a lower blockage ratio and therefore a lower pressure drop. The fractal grid exhibits a slower decay of its performance along the streamwise direction with the heat transfer enhancement becoming, at large distances, comparable to the case of the single square grid, despite having a lower Re_{t_0} by a factor of 2.2. This feature can be explained by the presence of the smaller fractal iterations in FSG17. The geometrical design of these two types of grids can be optimized according to the specific needs: the ratio t_0/L_0 indicatively sets the value of the maximum heat transfer enhancement whereas the wake-interaction length scale x^* sets the position where this peak occurs.

Clear differences exist between the heat transfer profiles measured in the production and in the decay region of turbulence, in positions where turbulence intensity is almost the same. In particular: (i) the heat transfer coefficient on the front part of the cylinder is higher in the decay region; (ii) the recovery of the heat transfer coefficient on the rear part of the cylinder, with respect to its value at the forward stagnation point, is higher in the production region. These differences are likely to be related both to the intermittent behaviour of the incoming flow and to an enhancement of the vortex formation mechanism past the cylinder in the turbulence production region. Additional research is however required to satisfactorily explain these features.

References

1. R. Gomes-Fernandes, B. Ganapathisubramani, J.C. Vassilicos, Particle image velocimetry study of fractal-generated turbulence. J. Fluid Mech. **711**, 306–336 (2012)
2. G.F. Hewitt, *Heat Exchanger Design Handbook* (Begell House, New York, 2008)
3. D. Hurst, J.C. Vassilicos, Scalings and decay of fractal-generated turbulence. Phys. Fluids **19**, 035103 (2007)
4. G.W. Lowery, R.I. Vachon, The effect of turbulence on heat transfer from heated cylinders. Int. J. Heat Mass Transf. **18**, 1229–1242 (1975)
5. N. Mazellier, J.C. Vassilicos, Turbulence without Richardson-Kolmogorov cascade. Phys. Fluids **22**, 075101 (2010)
6. C. Sak, R. Liu, D.S. Ting, G.W. Rankin, The role of turbulence length scale and turbulence intensity on forced convection from a heated horizontal circular cylinder. Exp. Therm. Fluid Sci. **31**, 279–289 (2007)
7. S. Sanitjai, R.J. Goldstein, Effect of free-stream turbulence on local mass transfer from a circular cylinder. Int. J. Heat Mass Transf. **44**, 2863–2875 (2001)
8. S. Sanitjai, R.J. Goldstein, Heat Transfer from a circular cylinder to mixtures of water and ethylene glycol. Int. J. Heat Mass Transf. **47**, 4785–4794 (2004)
9. N.T. Van Dresar, R.E. Mayle, A quasi-steady approach of wake effects on leading edge transfer rates. J. Turbomach. **111**, 483–490 (1989)
10. G.J. Van Fossen, R.J. Simoneau, C.Y. Ching, Influence of turbulence parameters, Reynolds number, and body shape on stagnation-region heat transfer. J. Heat Transf. **117**, 597–603 (1995)
11. A.A. Zukauskas, Heat transfer from tubes in cross-flow. Adv. Heat Transf. **8**, 93–160 (1972)

An Experimental Study on the Relation Between the Wake Inlet Conditions and the Near Wake Topology

Renzo Trip and Jens H.M. Fransson

Abstract A study on the relation between the wake inlet conditions and the wake characteristics of a bluff body by means of Particle Image Velocimetry is presented. The wake inlet condition, being a laminar boundary layer at the trailing edge of the body, are varied by means of wall-suction. Measurements are carried out at $Re_h = 6.7 \times 10^3$ based on the body thickness h. The induced radius of curvature of the streamlines is shown to be a promising parameter in explaining the increase in base drag and decrease in vortex shedding frequency associated with a thinner boundary layer.

1 Introduction

Vortex shedding is the result of an absolute instability, which is manifested with vortices being shed at a fixed frequency from alternating sides of a bluff body. This phenomena causes an increase in the base drag [1]. Methods to reduce the base drag are either based on manipulation of the vortex interaction or on modification of the boundary layers separating from the trailing edges of the body [2, 3]. Previous studies indicate that an increase of the boundary layer thickness leads to a decrease of the base drag and a reduction of the vortex shedding frequency [4–6]. It has been suggested that the change in curvature of streamlines may be the cause of this altered base drag [7]. In other to gain more fundamental knowledge of the flow around bluff bodies it is therefore of paramount importance to study the boundary layer separating from the trailing edge in combination with the formation recirculation region where the interaction between shear layers takes place [8].

A novel experimental setup that enables the variation of the inlet boundary condition prior to separation of a bluff body has recently been reported [6]. The novelty lies in the way in which the inlet conditions are being modified. The body, that will be

R. Trip · J.H.M. Fransson (✉)
Linné Flow Centre, KTH – Royal Institute of Technology,
SE-10044 Stockholm, Sweden
e-mail: jensf@kth.se; jensf@mech.kth.se

© Springer International Publishing Switzerland 2016

A. Segalini (ed.), *Proceedings of the 5th International Conference on Jets, Wakes and Separated Flows (ICJWSF2015)*,
Springer Proceedings in Physics 185, DOI 10.1007/978-3-319-30602-5_17

described more extensive in Sect. 2, has a perforated top and bottom surface, which allows for boundary layer modifications by means of suction and/or blowing. In the first study [6] an elaborate description of laminar and turbulent boundary layers subject to suction is given. Based on hot-wire anemometry and differential pressure measurements the wake inlet conditions were related to the wake characteristics.

In the present study, the measurements described in [6] are complemented with Particle Image Velocimetry (PIV) measurements to include the near wake topology as well as the region prior to separation. A first result in the study of the wake characteristics including the curvature of streamlines will be shown.

2 Experimental Setup

The measurements have been carried out in the closed circuit Boundary Layer (BL) wind tunnel located in the Odqvist Laboratory at the Royal Institute of Technology (KTH). The background turbulence intensities are 0.04 % and 0.06 % in the streamwise and cross-flow directions, respectively, at a free-stream velocity of 25 m/s. The BL-tunnel has a 4 m long interchangeable test section with a cross-sectional area of 0.5 m in width and 0.75 m in height.

Within the test section a 2 m long rectangular body is mounted horizontally, see Fig. 1. The body spans the entire test section width and is $h = 4.0$ cm thick, which corresponds to a blockage equal to 5.3 %. A smooth, elliptically shaped, leading edge with a length of 30 cm is added to prevent leading edge separation. The trailing edge is blunt, hence, the point of separation is fixed at the trailing edge corner.

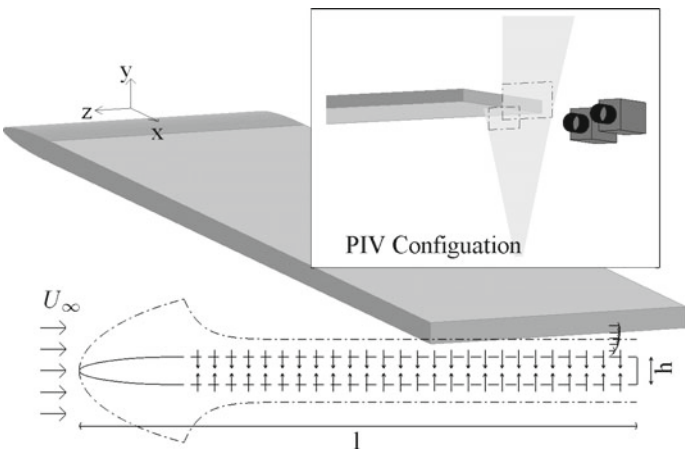


Fig. 1 A schematic *top-* and *side view* of the body studied. *Dash-dotted line* (-.-) indicates the boundary layer edge over the impermeable leading edge and permeable forebody with *arrows* symbolizing wall-suction. The *inset* shows the PIV configuration with *dashed lines* indicating the field of views

The titanium top and bottom surfaces of the body are perforated to allow for suction and blowing. A porosity of 0.5 % is realised by 60 μm laser drilled holes which are uniformly distributed across the total surface. A measure of the wall-normal velocity is obtained by relating the pressure drop over the perforate plate to the velocity of air through the perforations, on the basis of a relation given by [9].

The Particle Image Velocimetry (PIV) measurements were carried out with a Dantec Dynamics PIV system, composed of a Litron DualPower 50–200 laser (50 mJ, 200 Hz) and, in the present configuration, two SpeedSense M120 cameras (12 bits) which have a sensor resolution of 1920×1200 pixels. The cameras, mounted in a planar configuration as shown in Fig. 1, were equipped with 50 mm objectives to obtain field of views of $FOV = 140 \times 88$ mm^2. A number of 1825 images were recorded at a repetition rate of 100 Hz, which is sufficient to resolve the vortex shedding frequency. The pulse separation time of $\Delta t = 700$ μs was based on an average particle displacement of 25 % within the initial interrogation area. This initial interrogation area of 128×128-px is reduced in a multi-pass PIV algorithm to a final interrogation resolution of 16×16-px, corresponding to a resolution of 1.2 mm. Due to the thin boundary layer in case of suction and strong reflection at the titanium surface the boundary layer could not be fully resolved, but information on the streamline curvature prior to separation could be calculated.

Two single hot-wire probes, operated in combination with a Dantec Dynamics StreamLine 90N10 system, are used. One to measure the velocity profiles and another one to obtain the vortex shedding frequency, which is mounted downstream of the trailing edge on the border of the wake. The reference free-stream velocity U_∞ was measured with a Prandtl tube mounted through the ceiling of the test section. The differential pressure was recorded using a Furness FCO510 (0–200/2000 Pa, 0.25 % *FSD*) pressure transducer. The same pressure transducer was used to measure the pressure across the perforated surfaces and the base pressure at the center of the base. The static pressure of the Prandtl tube was used as reference in both cases.

3 Results

All measurements are carried out at a free-stream velocity of $U_\infty = 2.5$ m/s, which corresponds to Reynolds numbers of $Re_h = 6.7 \times 10^3$ and $Re_L = 3.8 \times 10^5$ based on the base height h and the length of the body L, respectively. Hence, the boundary layer is laminar at the point of separation.

For a laminar boundary layer subject to wall suction, the streamwise velocity distribution U/U_∞ will asymptote to an exponential form:

$$\frac{U(y)}{U_\infty} = 1 - \exp\left(\frac{yV_0}{\nu}\right), \tag{1}$$

with $V_0 (< 0)$ being the wall-normal velocity and ν the kinematic viscosity. The displacement thickness δ_1 and momentum thickness δ_2 for the ASBL are given by:

$$\delta_1 = -\frac{\nu}{V_0}, \quad \delta_2 = -\frac{1}{2}\frac{\nu}{V_0}, \tag{2}$$

and hence, independent of the free-stream velocity.

For a flat surface of limited extent, like the body in the present study, the ASBL is only obtained in case a sufficiently large wall-normal velocity relative to the free-stream velocity is applied. Here we define the suction coefficient Γ:

$$\Gamma = -\frac{V_0}{U_\infty} \times 1000\,, \tag{3}$$

as a measure of the amount of suction applied. In Fig. 2a boundary layer profiles at a distance of $1h$ upstream of the trailing edge for several suction coefficients are shown, where a larger suction coefficient corresponds to a lighter shade of gray, black being the neutral suction case. An increase in suction coefficient leads to a thinner boundary layer with a larger velocity gradient at the wall. From Fig. 2b, in which the normalized displacement thickness δ_1 and δ_2 are presented as function of the suction coefficient, it can be concluded that the ASBL in this case is reached for $\Gamma \approx 6$. For more information on laminar and turbulent boundary layers subject to suction the interested reader is referred to [6].

In Fig. 3a the time averaged formation region for the neutral suction case is visualized by means of streamlines and constant streamwise velocity contours. The formation region is characterized here by two parameters. 1: The confluence point x_C, which is here defined as the saddle point where both the wall-normal as well as the streamwise velocity component are equal to zero. 2: The induced curvature of the streamlines. A streamline at a distance y_s from the body surface at the trailing edge

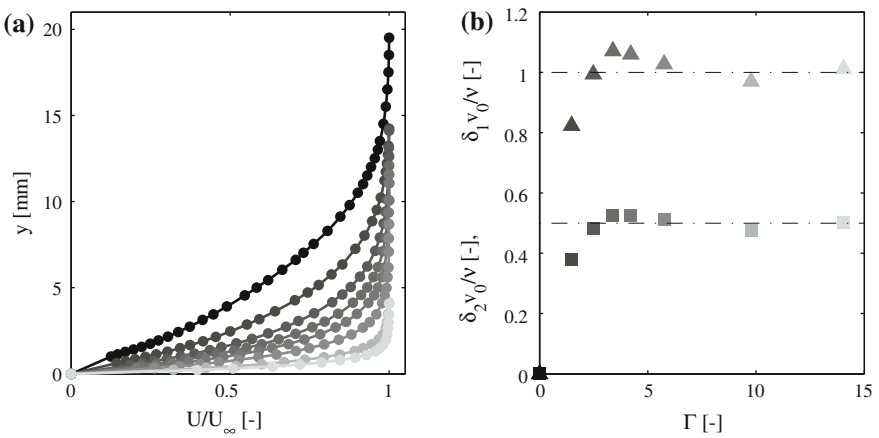


Fig. 2 **a** Boundary layer profiles for increasing suction coefficient Γ at a distance $1h$ upstream of the trailing edge. **b** Normalized displacement and momentum thickness as function of the suction coefficient Γ. The expected values for an ASBL are marked with a *dash-dotted line*

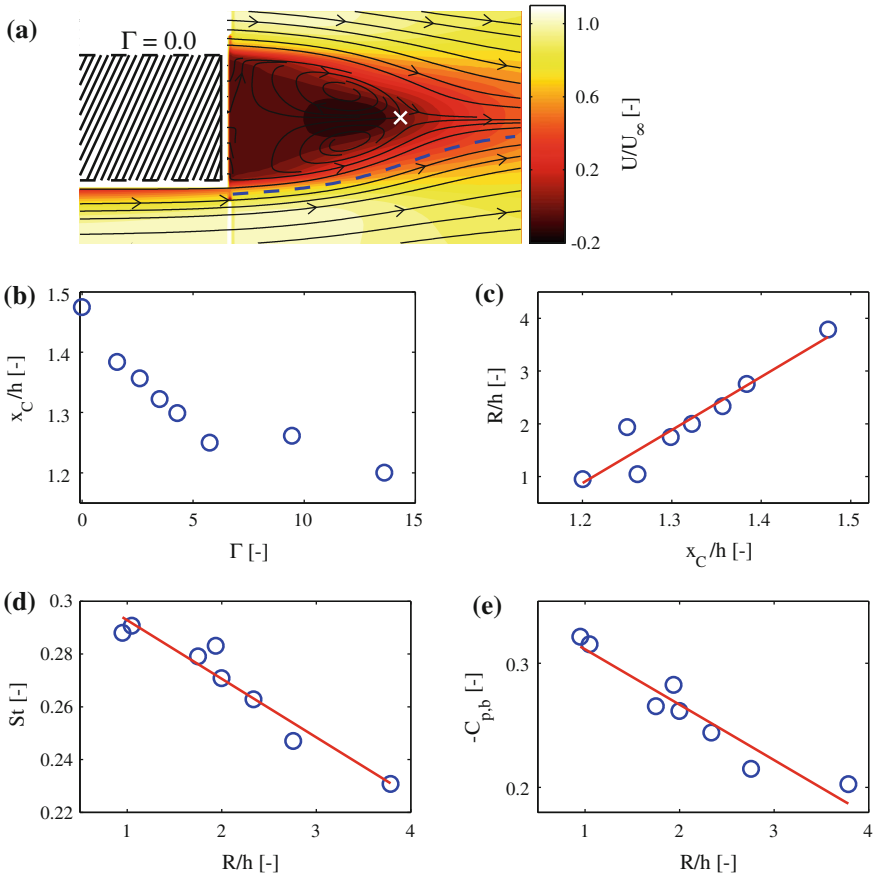


Fig. 3 **a** The time averaged streamwise velocity component U, with the selected streamline to extract the radius of curvature R marked in *blue* and the confluence point marked with a *white* '×', **b** the position of the confluence point x_C as function of the suction coefficient Γ, **c** the maximum radius of curvature R/h along the selected streamline as function of x_C, **d** + **e** the Strouhal number St and base pressure $-C_{p,b}$ as function of R/h, respectively

is selected, where $y_s = \eta\delta_{99}$ is a position relative to the boundary layer thickness δ_{99}. Here $\eta = 0.5$ was chosen. The radius of curvature along this streamline is subsequently found by applying the standard mathematical equation:

$$R = \left| \frac{\left[1 + y'(x)^2\right]^{3/2}}{y''(x)} \right| . \tag{4}$$

The characteristic curvature of the streamline was then decided to be the maximum radius of curvature found along the streamline.

From Fig. 3b it can be derived that an increase in suction leads to a shorter formation region. For $\Gamma > 6$, where the ASBL is reached, the recirculation seems to approach a minimum. This can be explained by the fact that the boundary layer thickness becomes negligible compared to the body thickness to play a significant role in the wake formation. At the same time, in the case of the ASBL the boundary layer shape is constant.

In Fig. 3c the two parameters of the formation region are compared. It is concluded that the a shorter recirculation region corresponds to a proportional change in the radius of curvature of the streamline. This is an indication that an appropriate method to determine a characteristic radius of curvature was chosen.

From Fig. 3d, e it can be observed that both the Strouhal number based on the shedding frequency $St = fh/U_\infty$, and the base pressure coefficient correlate fairly well with radius of curvature, at least for the Re_h studied here. However, we should keep in mind that we have compared the time averaged base pressure coefficient and the time averaged formation region, a flow condition the fluid does never actually experience. Future research will therefore include the phase averaged data of the formation region, as well as a range of Reynolds numbers.

4 Conclusion

A first analysis of velocity field data obtained in the area prior to separation and in the formation region of a bluff body has been shown to be a promising database to investigate the relation between the wake characteristics and wake inlet conditions.

References

1. M.M. Zdravkovich, Flow around circular cylinders, in *Fundamentals*, vol. 1 (1997)
2. V. Durgesh, J.W. Naughton, S.A. Whitmore, Experimental investigation of base-drag reduction via boundary-layer modification. AIAA J. 1–10 (2013)
3. H. Choi, W.-P. Jeon, J. Kim, Control of flow over a bluff body. Annu. Rev. Fluid Mech. **40**, 113–139 (2008)
4. A. Rowe, A.L.A. Fry, F. Motallebi, Influence of boundary-layer thickness on base pressure and vortex shedding frequency. AIAA J. **39**(4), 754–756 (2001)
5. A. Mariotti, G. Buresti, Experimental investigation on the influence of boundary layer thickness on the base pressure and near-wake flow features of an axisymmetric blunt-based body. Exp. Fluids **54**(11), 1–16 (2013)
6. R. Trip, J.H.M. Fransson, Boundary layer modification by means of wall suction and the effect on the wake behind a rectangular forebody. Phys. Fluids **26**(12), 125105 (2014)
7. G. Buresti, *Elements of Fluid Dynamics*, vol. 3 (Imperial College Press, 2012)
8. Z.J. Taylor, E. Palombi, R. Gurka, G.A. Kopp, Features of the turbulent flow around symmetric elongated bluff bodies. J. Fluids Struct. **27**(2), 250–265 (2011)
9. S. Goldstein, *Modern Developments in Fluid Dynamics*, vol. 1 (1938)

Vortex Structure Extraction from Circular Disk Wake by POD and PIV Processing

Makoto Aoki, Takao Mizuno, Hikaru Aono and Hitoshi Ishikawa

Abstract Vortex structures generated from a bluff body in flow causes noise, vibration, and energy loss. Investigation of such vortex structure is useful for solving various engineering problems. The purpose of this study is to extract vortex structures in the wake behind a circular disk, as a typical asymmetric body, by particle image velocimetry (PIV) processing. In order to extract the vortex structure behind the disk, a Proper Orthogonal Decomposition (POD) was applied to correlation matrix of velocity fluctuation. POD can extract optimally dominant structure in energy contribution, without subjectively point of view. POD results showed that the first dominant structure was the reverse flow region behind circular disk. This reverse flow region developed to two times of disk diameter in downstream direction. In Snapshot-POD analysis, eigenfunctions indicated alternate vortex shedding and connecting structures. These structures were similar to staggered vortices observed in the wake behind the sphere.

1 Introduction

Vortex structures behind a bluff body show several phenomena. First, these causes noise and vibration. For example, there are vibrations caused by vortex from high-speed trains and aerodynamic noise waked by vortex from the car side mirror. The other problem caused by vortices is lowering efficiency of fluid machine due to

M. Aoki · T. Mizuno · H. Aono · H. Ishikawa (✉)
Tokyo University of Science, 6-3-1 Niijuku, Katsushika-ku, Tokyo, Japan
e-mail: ishi@rs.tus.ac.jp

M. Aoki
e-mail: 4514602@ed.tus.ac.jp

T. Mizuno
e-mail: 4515650@ed.tus.ac.jp

H. Aono
e-mail: aono@rs.tus.ac.jp

© Springer International Publishing Switzerland 2016

A. Segalini (ed.), *Proceedings of the 5th International Conference on Jets, Wakes and Separated Flows (ICJWSF2015)*,
Springer Proceedings in Physics 185, DOI 10.1007/978-3-319-30602-5_18

energy loss associated with vortex. On the other hand, there are several interests from the view point of fluid dynamics. A couple of studies were conducted to investigate the flow behind a bluff body in flow. By using blunt cylinder, Taniguchi et al. reported the wake structure behind the axial symmetry body. A blunt longitudinal cylinder is a specific cylinder which axial length was equal to a diameter of bottom. The results showed that there were periodical vortices behind the blunt cylinder. The vortex shed from the cylinder had bidirectional hair-pin structures [1]. Makita et al. studied a flow behind a sphere. They reported that vortices behind the sphere showed a large-scale structure (low mode) that consisted of many fine small-scale (high mode) structures. The low mode structure had the integer numbers of high mode structure. The authors defined these structures as staggered vortices [2]. In addition, Sakai et al. analyzed around circular cylinders based on POD (Proper Orthogonal Decomposition) and DMD (Dynamic Mode Decomposition) [3].

As described above, although there are many studies about vortices behind bluff body, vortex structures behind the disk are not adequately investigated. This study focused on vortex structure behind a circular disk as a typical axisymmetric body. Combination of Particle Image Velocimetry (PIV) and POD and Snapshot-POD techniques were adopted to investigate the vortex structures behind the circular disk and identify dominant vortex structure in the wake.

2 Experimental Method

2.1 Wind Tunnel and Flow Conditions

Figure 1 showed the schematic diagram of experimental setup and coordinate system. The *x*-axis is the direction of the main flow, the *y*-axis was the radial and transverse direction, and the *z*-axis was perpendicular direction both to *x*- and *y*-axis.

Experiments were conducted in a closed-circuit wind tunnel, with a test section length of 900 mm, a width of 200 mm and a height of 400 mm. A circular disk

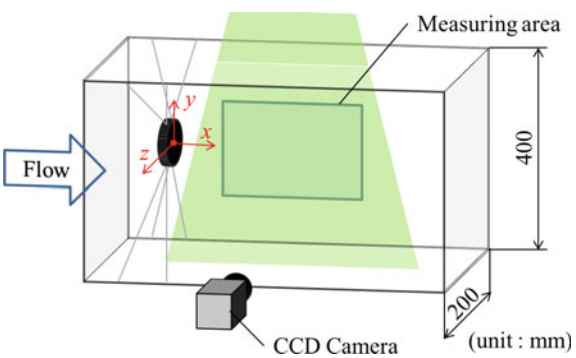


Fig. 1 PIV experimental setup

made of acryl was mounted by thin wires. Measurements were conducted at a mainstream velocity U_∞ of 2 m/s.

The diameter of the circular disk D was 20, 40, and 50 mm respectively. The corresponding Reynolds numbers, based on diameter D of the circular disk were 2.6×10^3, 5.2×10^3, and 6.7×10^3. The mainstream turbulent intensity was about 2.6 %. PIV measurement was carried out in a region of 174 × 128 mm of xy and yz plane behind the disk. 5,000 pairs of images were captured to measure the mean velocity of each measurement region behind the disk.

The flow was seeded with 5 μm dioctyl sebacate (DOS) particles. A double pulse Nd:YAG laser with laser sheet was used to illuminate the measuring region. A 1392 × 1024 pixel CCD camera was utilized to acquire particles images. Each pair of PIV image was analyzed by using the cross-correlation algorithm in an interrogation window of 32 × 32 pixels sub-images with an overlap of 50 % during the interrogation process.

2.2 POD (Proper Orthogonal Decomposition)

POD is a method to evaluate an orthogonal basis that can indicate a multidimensional data most efficiently. In this study, an orthogonal basis was called "Mode". In fluid analysis, it might extract dominant structure in energy contribution of flow. It can reconstruct flow structures based on lower dimension depending on energy ratio [4, 5].

In this study, POD and Snapshot-POD was applied 100 time series of u fluctuation. S(t) was a matrix constructed by 100 time series, then evaluated a correlation function (R) shown in (1).

$$R = \frac{1}{N} S(t) S^T(t) \tag{1}$$

And eigenvalues λ_k and an eigenfunction φ_k were completed by the (2).

$$R\varphi_k = \lambda_k \varphi_k \tag{2}$$

Eigenvalues meant energy contribution and λ_{total} meant original data's energy total.

$$\lambda_{total} = \sum_{k=1}^{K} \lambda_k \tag{3}$$

Therefore flow distribution could be reconstructed by corresponding energy contribution. In analysis by Snapshot-POD, distribution of eigenfunctions are correspond to flow structure. Please see the references about the details of Snapshot-POD [6, 7].

3 Results and Discussion

3.1 Flow Structure

Figure 2 showed instantaneous vorticities and streamwise velocity behind the circular disk of each *Re* number. The contour showed the value of each data. As shown in Figures, reverse flow region was generated behind the disk around $x/D = 2.0$. Also, the wake showed meandering motion from $x/D = 3.0$. This flow meandered resembled the vortices structure of the sphere.

3.2 POD Results

In this section, Mode *N* indicated that the orthogonal bases were superimposed from first orthogonal bases to *N*th orthogonal bases in the order of the energy contribution ratio.

In Figs. 3 and 4, Mode 1 and Mode 2 of each *Re* number were shown respectively. Also Eigenvalues of each *Re* number were presented in Fig. 5a. According to the results of Mode 1 and Mode 2, these two modes were similar to each other. The eigenvalue ratio of Mode 1 is about 80 %, while the eigenvalue ratio associated higher Mode over than Mode 2, steeply decreased. Due to the eigenvalue ratio of

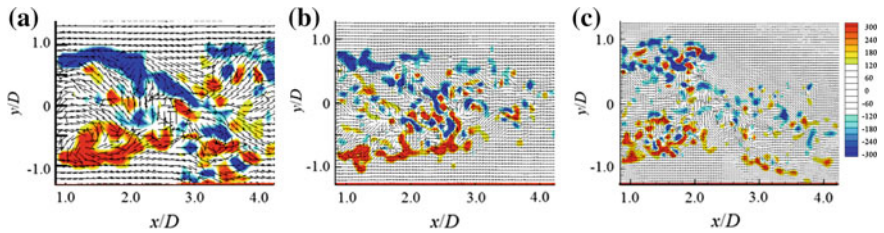


Fig. 2 Instantaneous value vorticities and streamwise velocity. **a** $Re = 2.6 \times 10^3$. **b** $Re = 5.2 \times 10^3$. **c** $Re = 6.7 \times 10^3$

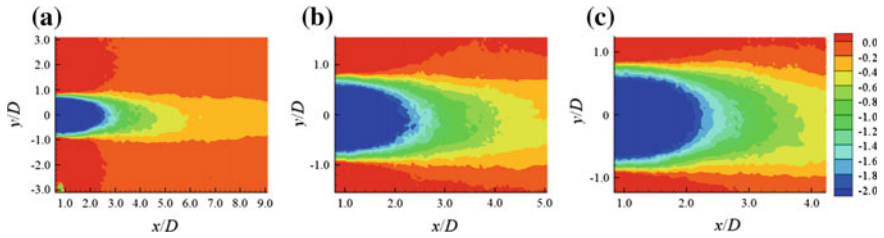


Fig. 3 POD reconstruction of each *Re* numbers (Mode 1). **a** $Re = 2.6 \times 10^3$. **b** $Re = 5.2 \times 10^3$. **c** $Re = 6.7 \times 10^3$

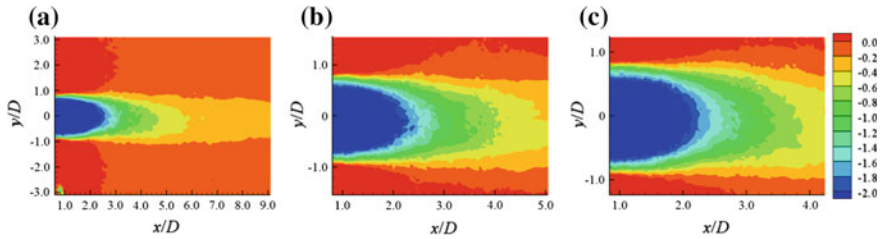


Fig. 4 POD reconstruction of each *Re* numbers (Mode 2). **a** $Re = 2.6 \times 10^3$. **b** $Re = 5.2 \times 10^3$. **c** $Re = 6.7 \times 10^3$

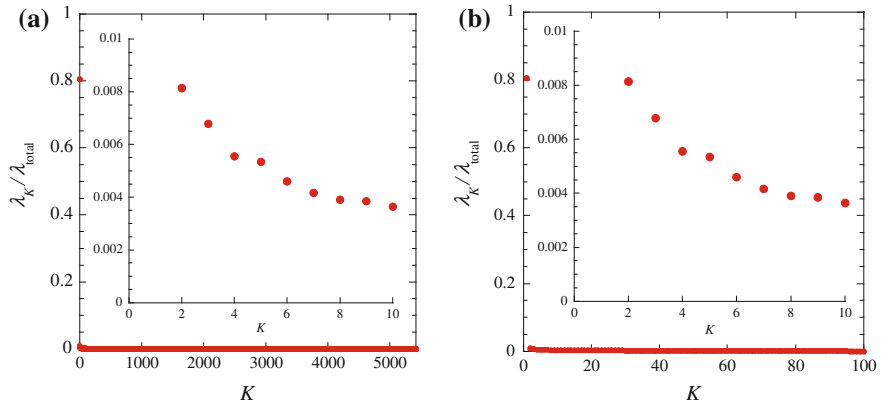


Fig. 5 Eigenvalues of $Re = 2.6 \times 10^3$. **a** POD. **b** Snapshot-POD

Mode 1 was extremely high, other Mode over Mode 2 were hide behind the Mode 1. Some fine scale structure like noise was probably due to the scarcity of data to estimate POD matrix. The eigenvalues of other *Re* numbers were similar to those of Fig. 5a.

3.3 Snapshot-POD

Snapshot-POD Mode represented dominant structure by each eigenfunctions. In Fig. 6, Snapshot-POD eigenfuntion distribution of $Re = 2.6 \times 10^3$ calculated from the fluctuating velocity data derived from PIV data were presented. In the case of POD shown in Fig. 3, these Modes were shown respectively. First, Mode 1 represented streamswise and reverse flow region. Next, Mode 2 showed reverse flow toward to suction side of the disk. Mode 3 showed a periodical structure, so this indicated periodic vortices. Mode 4 suggested that an emphasized region connecting adjacent vortex regions in Mode 3. These connecting structures are similar

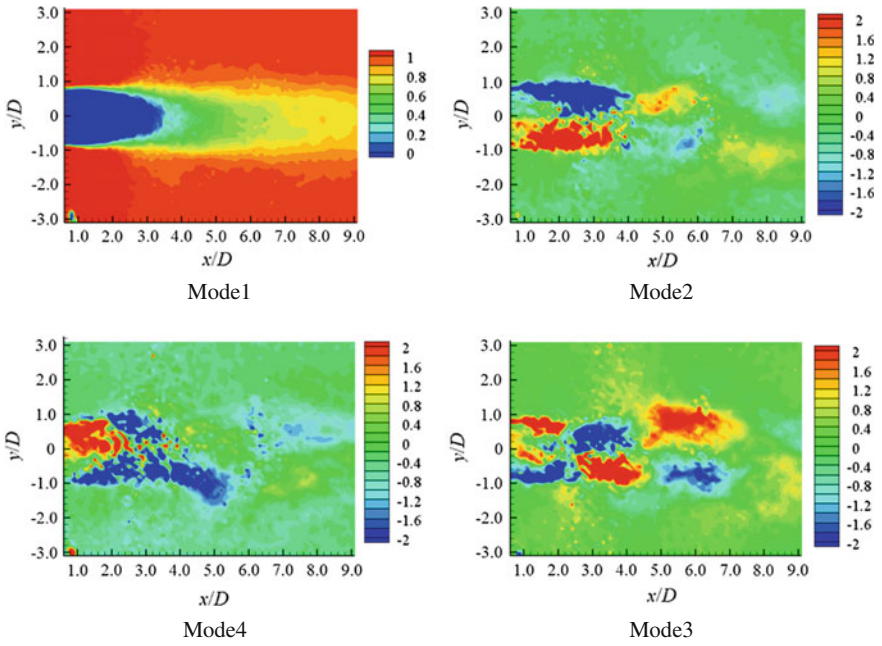


Fig. 6 Snapshot POD Eigen function distributions of $Re = 2.6 \times 10^3$

to staggered vortices observed in the wake behind the sphere [2]. Accordingly, this periodical structure and this similarity indicate that vortices behind the circular disk are so called staggered vortices. Then The snapshot-POD eigenfuntions of $Re = 5.2 \times 10^3$ and 6.7×10^3 were similar to these figures. Lastly, Eigenvalues of the case $Re = 2.6 \times 10^3$ was shown in Fig. 5b. Especially, the eigenvalue ratio of Mode 1 to 10 was shown. Two results showed same tendency in eigenvalue distribution. According to the comparison, two POD methods extracted staggered vortices [2].

4 Conclusions

Vortex structures behind of the circular disk were experimentally investigated. POD and snapshot-POD were applied to the wake structure measured by PIV. It was found that the reverse flow region behind the disk corresponding to POD Mode 1 was further developed to downstream region. The Mode 1 energy contribution occupied 80 %. Mode 2, POD results indicate periodic vortex shedding and alternate mode vortex structure. Snapshot-POD Mode 1 results were resembled to POD Mode 1. Mode 2, the periodical and connecting structures were found, so these results indicated staggered vortices similar to those of the sphere.

References

1. S. Taniguchi, M. Matsumura, Y. Morihira, K. Miyakoshi, Study on the wake structure of an axisymmetric body. Trans. Jpn. Soc. Mech. Eng. B **55**, 62–66 (1989)
2. H. Makita, H. Soga, N. Sekishita, K. Hasegawa, Multi-hotwire measurement of helical and staggered vortices in the wake of a sphere, in *Fluids Engineering Conference of the Japan Society of Mechanical Engineers* (2006), p. 1104
3. M. Sakai, Y. Sunada, K. Rinoie, Flow measurements around circular cylinders based on POD and DMD. J. Jpn. Soc. Aeronaut. Space Sci. **62**, 47–54 (2014)
4. P. Holmes, J.L. Lumley, G. Berkooz, *Turbulence, Coherent Structures, Dynamical System and Symmetry* (Cambridge University Press, 1996)
5. H. Ishikawa, M. Kiya, O. Mochizuki, H. Maekawa, POD and wavelet analysis of coherent structures in a turbulent mixing layer. Trans. Jpn. Soc. Mech. Eng. B **63**, 2001–2008 (1997)
6. L. Sirovich, Turbulence and the dynamics of coherent structures, Part I: Coherent structures. Q. Appl. Math. **45**(3), 561–571 (1987)
7. K. Taira, Proper orthogonal decomposition in fluid flow analysis: 1. Introduction. Jpn. Soc. Fluid Mech. Nagare **30**, 115–123 (2011) (in Japanese)

Influence of Surface Waves on Kármán Street Behind Vertical Cylinder: Subharmonic Lock-in and Phase Synchronizaton

Hans Gunnoo, Nizar Abcha, Isabel Garcia-Hermosa, Anne-Claire Bennis and Alexander Ezersky

Abstract It is demonstrated experimentally that the influence of harmonic surface waves on the turbulent Kármán vortex street leads to lock-in of the shedding frequency and phase synchronization. These effects occur if the frequency of the surface wave is approximately two times higher than the frequency of vortex shedding. A region of frequency lock-in is found on the plane "amplitude—frequency" of the surface waves.

1 Introduction

Effects of external harmonic forcing on the Kármán Street behind an obstacle have been studied for a long time [1, 2]. Lock-in of the shedding frequency and structures in the vortex wake have been investigated in detail under the influence of the longitudinal oscillations of the cylinder in flow [1–6], or the flow rate oscillations [7]. The process of vortex shedding and synchronization have also been investigated under transversal oscillations of the cylinder [8]. This paper examines the influence of surface waves on frequency shedding lock-in and phase synchronization in turbulent Kármán Street. The problem of interaction of surface waves and vortex flows in the vicinity of vertical obstacles is important for different applications, especially for contemporary plans to build wind farms in the coastal zone. The hydrodynamic fields arising from the interaction of tidal currents and surface waves with wind farm masts (vertical cylinders) are not yet well understood. This problem is studied in the present paper in laboratory and numerical experiments.

H. Gunnoo (✉) · N. Abcha · I. Garcia-Hermosa · A.-C. Bennis · A. Ezersky
Morphodynamique Continentale et Côtière, UMR6143,
CNRS, Normandie Université, UNICAEN, 14000 Caen, France
e-mail: hans.gunnoo@unicaen.fr

© Springer International Publishing Switzerland 2016

A. Segalini (ed.), *Proceedings of the 5th International Conference on Jets, Wakes and Separated Flows (ICJWSF2015)*,
Springer Proceedings in Physics 185, DOI 10.1007/978-3-319-30602-5_19

This paper is organised as follows: In Sect. 1, we will deal with experimental set-up, in Sect. 2, we will present our experimental results, and we will show our numerical results in Sect. 4. Conclusions and perspectives of our studies will given in Sect. 5.

2 Experimental Set-up

Experiments were conducted in hydrodynamic channel of laboratory "Morphologie continentale et côtière" (M2C). The channel is 17 m long, 0.5 m wide; it is equipped with wave maker that is computer controlled (Fig. 1). Using the wave maker it is possible to excite waves in the channel with different spectra and amplitudes. The channel is also equipped with a pump and a system for water circulation that allows a steady flow (of velocity U) to be created. To reduce the intensity of turbulent fluctuations caused by pump, two honeycombs with thickness of about 20 cm are used. The honeycombs are placed in the channel, as shown in Fig. 1. Waves are excited at the end of the channel by the wave maker and they propagate upstream. The experiment is implemented with traveling wave because the honeycombs led to a significant decrease in the amplitude of the reflected waves. In the experiments two round cylinders with a diameters d of $d_1 = 4$ cm and $d_2 = 10$ cm are used as models of masts, the depths of flow H are correspondently $H_1 = 0.25$ m and $H_2 = 0.4$ m. Froude number $Fr_{1,2} = U_{1,2}/(gH_{1,2})^{1/2}$ and Reynolds number $Re_{1,2} = U_{1,2}d_{1,2}/\nu$ (U is for flow velocity, d is cylinder diameter, v is kinematic viscosity) at which the measurements were respectively: $Fr_1 = 0.1$, $Fr_2 = 0.045$; $Re_1 = 6.4 \times 10^3$, $Re_2 = 10^4$. Cylinders are placed strictly vertically on the channel axis.

To summarise the experimental set-up,

	d_1	d_2
H (m)	0.25	0.40
Re	6.4×10^3	10^4
Fr	0.1	0.045

To measure the velocity components of the hydrodynamic fields, acoustic Doppler velocimeter (ADV) is used. It is placed at a distance of 3 d downstream of the cylinder's edge and measures the three components of velocity: V_x, V_y, V_z, as shown in Fig. 1. These velocity components are caused by different modes: by vortices formed behind the cylinder (hydrodynamic mode) and by the surface wave. Surface waves excited by the wave maker propagate along the channel.

The waves are two-dimensional (they contain only V_y and V_z components) and they remain consistently 2D while propagating along the channel. The sampling rate of the ADV used is 200 Hz and the latter was placed 5 cm off from the

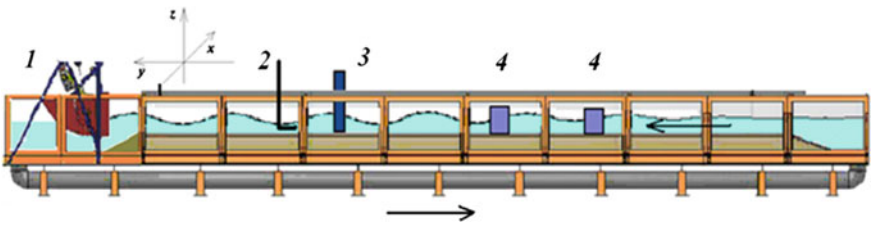


Fig. 1 Experimental sketch: (*1*) refers to the wave maker, (*2*) refers to the ADV, (*3*) refers to the location of the cylinder streamlined by the flow, (*4*) is for the honeycombs; *arrows* indicate the direction of the current

cylinder's central axis and 10 cm under the free surface during our experiments. It should be noted that the acquisition time was 200 s for each measurements carried out.

The vortices formed behind the cylinder have only the vertical component of the vorticity, they contribute only to components V_x, V_y. Obviously, for such high Reynolds numbers that are achieved in the experiments, turbulent vortices occur in the cylinder wake. The turbulent vortices contain all 3 components of the velocity namely: V_x, V_y and V_z but that the impact of the component V_z negligible compared to that of components V_x, V_y.

3 Experimental Results

Two sets of measurements were performed, with the two cylinder diameters. In both cases, the turbulent Kármán vortex street is observed, and the dimensionless vortex shedding frequency (Strouhal number, *Sh*) is about 0.2. Note that *Sh* is defined as: $f_{sh}d_{1,2}/V_{1,2}$, where f_{sh} is the frequency of shedding.

The experiments aim to determine the surface wave amplitudes and frequencies which have maximal influence on the cylinder's vortex shedding. In the experiments we investigate at what frequencies and amplitudes of surface waves, their effect on the vortex street is maximal. The largest impact is observed when the surface wave frequency is twice the vortex shedding frequency (in steady flow). It is revealed that surface waves with an amplitude of only a few mm; maximum value of the slope (ka, k being the wave number and a being the amplitude of the waves) of the free surface is 10^{-3} in this case can suppress the turbulent vortex street and generate temporally periodic vortex shedding behind a cylinder. Examples of spectra demonstrating frequency lock-in for a cylinder diameter of $d_2 = 10$ cm (Reynolds number $Re_2 = 10^4$) are shown in Fig. 2a, b. In (a), a surface wave with an amplitude of 10^{-3} m and a frequency of 0.44 Hz while in (b), the same frequency was used but a wave amplitude of 10^{-2} m was used.

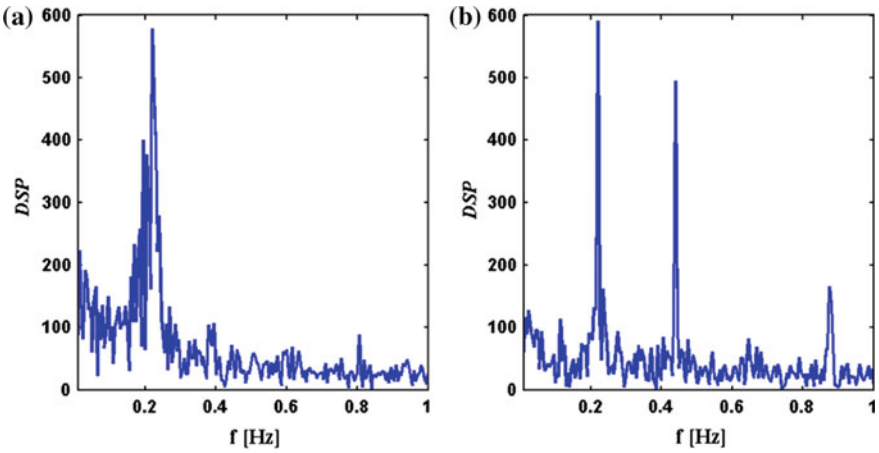


Fig. 2 Examples of spectra of *Vx* fluctuations in the cases of **a** absence of sub-harmonic frequency lock-in **b** sub-harmonic frequency lock-in

The spectrum shown in Fig. 2a corresponds to the vortex shedding in the absence of surface waves, and the spectrum shown in Fig. 2b arises under the influence of a wave with frequency $f = 0.44$ Hz. Note that we calculate spectra of velocity fluctuations for component V_x, where the hydrodynamic mode predominates. As one can see, the spectrum of velocity fluctuations in the absence of a surface wave is a superposition of oscillations with frequencies in the frequency interval $f_{sh} \sim 0.20$–0.24 Hz. The excitation of the surface waves leads to the appearance of a sharp spectral peak at a frequency of 0.22 Hz (half the surface wave frequency). We call this regime "synchronization"; meaning that there is synchronization between the vortex shedding and the displacement of surface caused by the surface waves.

In the diagram (Fig. 3) there are several regions with qualitatively different dynamics. It should be noted that a similar diagram was obtained for a Reynolds number Re = 6400. In the areas marked by triangles, the impact of surface waves does not lead to any significant changes in the spectrum of velocity fluctuations. In these areas, there is no sub harmonic frequency lock-in. Such regimes are typical for small amplitude of surface wave. With an increase in the amplitude of the surface waves in the spectrum of oscillation, the spectral peak appears at half the frequency of surface wave (areas marked by squares and circles). The peak width and peak value around the pedestal depends on the amplitude of the surface waves. The squares mark regimes with a broad peak and a large pedestal. We call this regime as a partial frequency lock-in. For larger amplitudes, the width of the peak and value of the pedestal are reduced (area marked by circles). In this area there is a complete frequency lock-in: the width of the spectral peak at the level of 5 dB is less than 3 %. In the area marked by diamonds, sub harmonic frequency lock-in does not occur. In these areas, hydrodynamic modes with half the frequency of

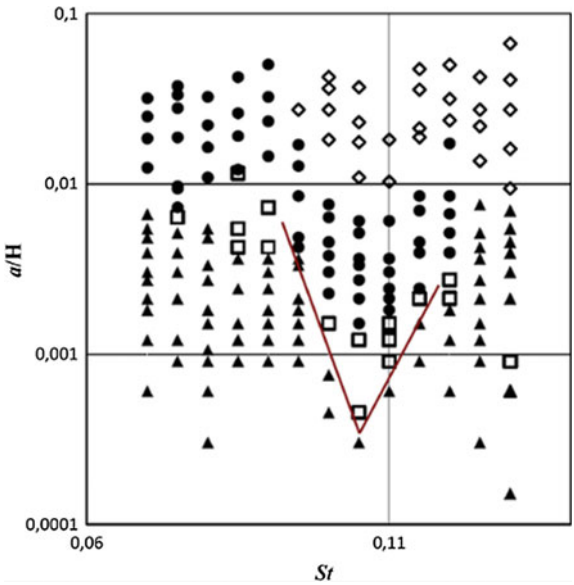


Fig. 3 Partition of the plane (Strouhal number-amplitude) into regions with qualitatively different dynamics at a Reynolds number of Re = 10^4 and with a water height of 0.40 m: *triangles* correspond to the absence of sub-harmonic frequency lock-in, *squares* indicate partial sub harmonic frequency lock-in, *circles* show sub harmonic frequency lock-in, *diamonds* mean lock-in at frequency f_e *inclined straight lines* indicate a region where frequency lock-in is observed for minimum amplitude of surface waves

the surface wave are not generated. The spectrum of the velocity component V_y of the vortex street contains the same regular components as that of the surface waves; the spectrum contains the same frequency as the applied surface waves, not half of the frequency of the surface waves as we obtained in regimes of complete frequency lock-in. It was determined from flow visualization that this spectral component arises from the symmetric vortex shedding: chess-like vortex street (vortices are shed on alternating sides of the cylinder) is suppressed in the wake and vortex street with a symmetric arrangement of vortices is generated by surface waves of large amplitude.

4 Numerical Simulations

Numerical simulations were carried out to study the impact of surface waves in the vortex shedding using OpenFoam [9]. To start, we studied the flow around a cylinder under the action of a uniform current without waves. The flow is turbulent (Re = 6400) and therefore we used DNS (Direct Numerical Simulation) and URANS (Unsteady Reynolds Averaged Navier-Stokes) approaches in our

numerical simulations. The first one consists of solving the Navier-Stokes equations without any assumptions for turbulence (DNS). This technique has the principal advantage of being precise but unfortunately requires a much longer simulation time and will not be useable at the scale of an offshore wind farm as in Courseulles s/mer. In order to overcome this problem, a second approach (URANS) is carried out the flow is averaged and the turbulence is parameterized. The k-ω SST RANS model is used and tested against DNS to evaluate the loss of information due to the averaging procedure.

Numerical simulations used a computational domain that has a length of 500 cm in the X direction, 50 cm in the Y direction and 25 cm in the Z direction. The cylinder had a diameter of 4 cm and the latter is totally submerged under water. Figure 1 shows the non-uniform mesh that was refined near the cylinder and divided into 20 blocks. The mesh counted 2812500 computing cells and had a horizontal and vertical resolution of about 1 cm and 0.33 cm, respectively (Fig. 4). The time step was set to 0.01 s.

Figure 5 shows the domain geometry. Boundary conditions (BC) for the velocity are: (i) No-slip BC at the 'Lower floor', 'Down', 'Up' and 'Cylinder' faces; (ii) An incoming x-velocity of 16 cm/s at the 'Inlet' face; and, (iii) Open BC at the 'Outlet' and 'Upper floor' faces.

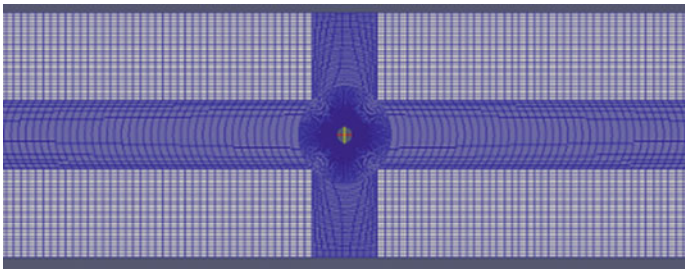
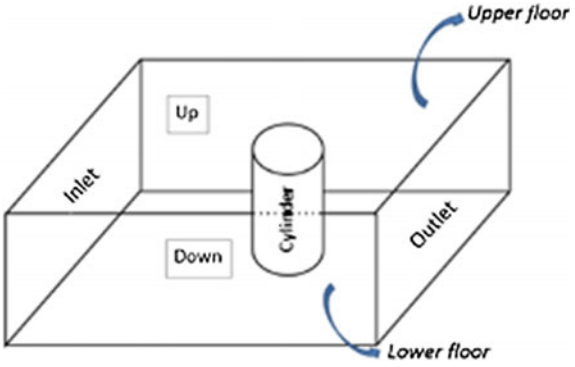


Fig. 4 Mesh

Fig. 5 Domain geometry



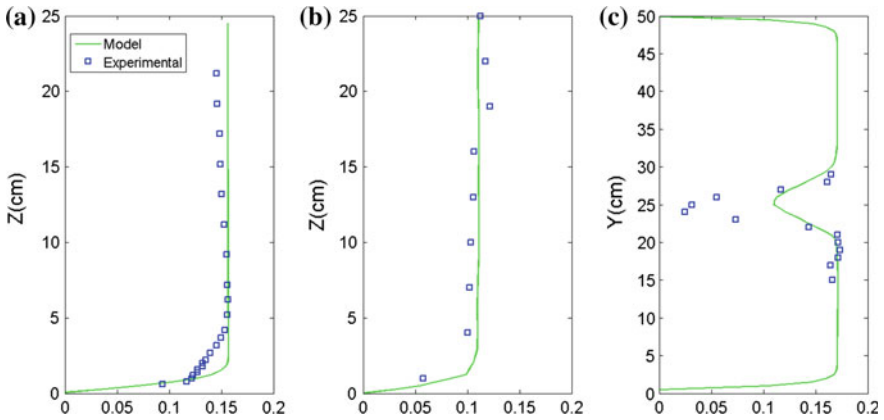


Fig. 6 DNS: **a** Vertical profile at distance of y = 10 d upstream the cylinder; **b** Vertical profile at a distance of y = 2 d downstream the cylinder; and, **c** Horizontal profile at a distance of y = 2 d downstream the cylinder

First, we compared the DNS mean velocity profiles with the experimental ones (see Fig. 6). The mean velocity values are obtained by averaging over a 200 s interval. The numerical vertical profiles are closed to the data (Fig. 6a, b). The numerical horizontal velocity profile shows differences with the data, particularly with an underestimation of the velocity reduction behind the cylinder (Fig. 6c). Maybe due to the mesh which could be more refined near the cylinder to improve the results although we used a spatial resolution of few millimetres.

Second, we also compared the shedding frequency. The characteristics of the Karman street can be obtained by using the Strouhal number. In our case (cylinder with circular section), the Strouhal number stays around 0.2 for a wide range of the Reynolds number; especially for the Reynolds number used in our case. While considering the above points and the physical configuration of our problem, we have; $St = 0.2$, $D = 0.04$ m and $u = 0.16$ m/s; we then obtain $f = 0.80$ Hz. This result as we can see is in excellent accordance with the value of the shedding frequency obtained numerically ($f = 0.79$ Hz) (Fig. 7).

On the whole, comparisons between the numerical and experimental results showed a good agreement, that validates our modelling system.

Third, we tested URANS against DNS to quantify the loss of information due to the averaging procedure. Figure 8 shows the vorticity magnitude behind the cylinder for the two cases. As expected, the Von Karman streets computed by URANS are smoother with a weaker vorticity field than the DNS ones (Fig. 8). Vertical profiles of the vorticity (not displayed here) show a better description of the turbulence near the cylinder when DNS is used which is also in agreement with the literature. As URANS computed an average flow and used a parameterization to represent turbulence, the simulated flow had less vortex than the DNS one [10].

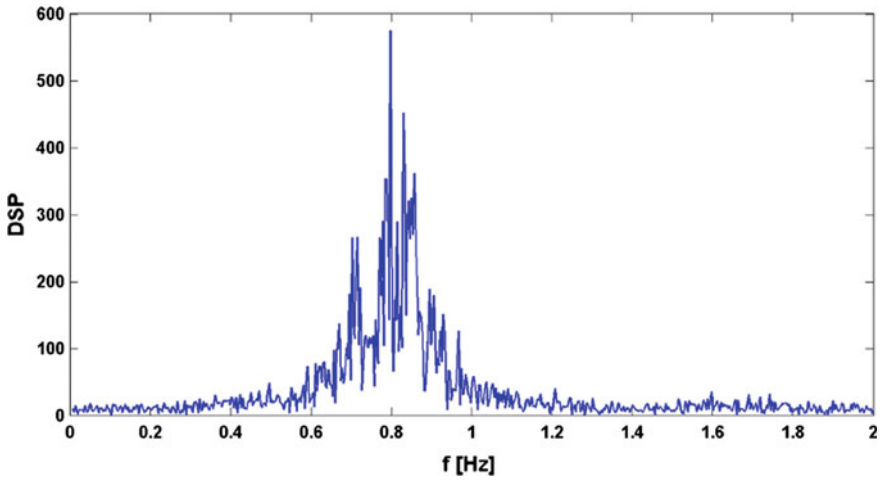


Fig. 7 DNS: shedding frequency

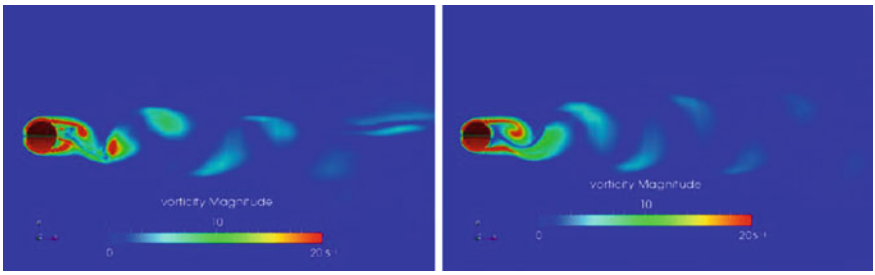


Fig. 8 Vorticity magnitude behind the cylinder for URANS (*left* panel) and DNS (*right* panel). The grey cells represent the cylinder while the Z-vorticity is drawn in color

5 Conclusion and Perspectives

In this paper we investigated the influences of surface waves on the oscillations arising behind a cylinder placed in a water flow. Oscillations in the wake behind a cylinder in cross-flow arise as a result of hydrodynamic instability leading to an increase in the amplitude of small perturbations. The development of instability in the flow leads to the formation of vortices and Kármán vortex street. External perturbations introduced in the hydrodynamic flow can control the characteristics of vortex street in the vicinity of the streamlined cylinder. For the first time we have demonstrated experimentally that surface wave may lead to sub harmonic shedding frequency lock-in. It should be emphasized that the effect of the frequency lock-in is most prevalent when the frequency of the surface wave is twice the frequency of the fundamental cylinder shedding frequency.

Numerical investigations were conducted to validate our modelling system in order to simulate the subharmonic lock-in in the future. As a first step, we carried out DNS simulations with an incoming velocity and without waves. Comparisons between numerical and experimental results showed a good agreement for the vertical profile of the velocity but also for the shedding frequency. In contrast, the velocity reduction behind the cylinder is underestimated by the model due to the size of the mesh near the cylinder. As we aim to simulate wave-current interactions at the scale of an offshore wind farm, we compared DNS and URANS because we will plan to use URANS for that. As expected, URANS simulated less vortex that DNS due to the averaging procedure and the parametrization of the turbulent structures.

As a continuation of this work, we plan to conduct experiments on the effects of irregular waves having Pierson-Moskowitz spectrum on the vortex shedding behind the cylinder. These problems are important for modelling of the processes occurring in the vicinity of masts of wind farms.

References

1. H. Akilli, D. Rockwell, Vortex formation from a cylinder in shallow water. Phys. Fluids **14**, 2957–2967 (2002)
2. D. Chen, G.H. Jirka, Experimental study of plane turbulent wakes in a shallow water layer. Fluid Dyn. Res. **16**, 11–41 (1995)
3. O.M. Griffin, S.E. Ramberg, Vortex shedding from a cylinder vibrating in line with an incident uniform flow. J. Fluid Mech. **75**, 257–271 (1976)
4. J. Carberry, J. Sheridan, D. Rockwell, Forces and wake modes of an oscillating cylinder. J. Fluid Struct. **15**, 523–532 (2001)
5. H.M. Blacburn, R.D. Henderson, A study of two-dimensional flow past an oscillating cylinder. J. Fluid Mech. **385**, 255–286 (1999)
6. C. Williamson, A. Roshko, Vortex formation in the wake of an oscillating cylinder. J. Fluid Structures **2**, 355–381 (1988)
7. E. Konstantinidis, S. Balabani, M. Yianneskis, K. Stansby, Bimodal vortex shedding in a perturbed cylinder wake. Phys. Fluids **25**, 085109, [3] (2013)
8. The lock-in on of vortex shedding due to the crossstream vibration of circular cylinders in uniform and shear flows. J. Fluid Mech. **74**, 641–665 (1976)
9. OpenFOAM The open source CFD toolbox—User Guide version 2.3.1
10. P. Sagaut, S. Deck, M. Terracol, Multiscale and multiresolution approaches in turbulence. Imperial Coll. Press 1–450 (2013)

Organization of an Axisymmetric Turbulent Wake in Presence of a Central Protrusion

Valeria Gentile, Ferdinand F.J. Schrijer, Bas W. Van Oudheusden and Fulvio Scarano

Abstract The wake past an ogive-cylinder was investigated using Stereoscopic Particle Image Velocimetry (PIV) at a Reynolds number $Re_D = 6.7 \times 10^4$, based on the object diameter. The intensity of the vertical fluctuations was found to reduce from 0.18 U_∞, attained in absence of a rear-protrusion, down to 0.1 U_∞ for a main-body to after-body diameter ratio $d/D = 0.4$. The trace of the backflow centroid motion over a time-interval of 2,000 D/U_∞ reflected the occurrence of a random motion of the reverse flow region for $d/D = 0.2$, where no pattern associated with a consistent precession could be identified, whereas a preferred azimuthal direction could be detected for $d/D = 0.4$. Proper Orthogonal Decomposition of the velocity fluctuations indicated the occurrence of large-scale velocity fluctuations for all configurations examined, the energy contribution of modes $k = 1$ and $k = 2$ attaining 20 % and 11 % for $d/D = 0.2$ and $d/D = 0.4$ respectively. Both modes were found to feature a dipole organization for $d/D \leq 0.2$, whereby their linear combination could be linked to a displacement of the wake occurring in all azimuthal directions. For $d/D = 0.4$ such an arrangement appeared to be preserved only by the first mode, thus reflecting wake displacement along a preferred azimuthal direction.

1 Introduction

The wake flow past a bluff body of revolution is typically characterized by a low-frequency unsteadiness related to the shedding of vortices within the shear layer at a non-dimensional frequency $St_D \approx 0.2$ [1, 2] and to the precession of the shedding angle at a non-dimensional frequency of $St_D \approx 10^{-3}$ [5, 7]. Although such low-frequency unsteadiness are common to different bluff geometries, base modifications can significantly alter the spatial organization of the separated flow and influence its fluctuating behavior. Wolf et al. [11] showed that for an ogive-cylinder

V. Gentile (✉) · F.F.J. Schrijer · B.W. Van Oudheusden · F. Scarano
Delft University of Technology, Kluyverweg 2, 2629HT Delft, The Netherlands
e-mail: V.Gentile@tudelft.nl

© Springer International Publishing Switzerland 2016

A. Segalini (ed.), *Proceedings of the 5th International Conference on Jets, Wakes and Separated Flows (ICJWSF2015)*,
Springer Proceedings in Physics 185, DOI 10.1007/978-3-319-30602-5_20

the turbulence intensity reduces by approximately 25 % when adding a rear cylindrical protrusion (i.e. after-body). The studies of Dépres et al. [1] revealed that the elongation of the after-body with respect to the base diameter *L/D* greatly influences the occurrence of a solid reattachment of the shear layer, therefore affecting the overall organization and unsteady behavior of the wake. Gentile et al. [3] recently discussed how the after-body diameter affects the radial velocity fluctuations as well as the non-dimensional recirculation bubble dimensions and overall flow topology. However the effect on the azimuthal flow dynamics was not investigated.

In the current study the azimuthal organization of the separated flow in presence of a rear central protrusion is investigated using Stereoscopic Particle Image Velocimetry (PIV) in a plane perpendicular to the free stream flow. The statistical and instantaneous flow properties are characterized for different values of the main body to after-body diameter ratio *d/D* and the large-scale velocity fluctuations dominating the near-wake dynamics are identified by means of snapshot Proper Orthogonal Decomposition [9].

2 Experimental Apparatus and Technique

The experiments were conducted in the open-exit low-speed wind tunnel of Delft University of Technology. The model is an ogive-cylinder (Fig. 1) equipped with a cylindrical after-body whose length equals 2 main body diameters such to ensure a solid reattachment of the shear layer [1]. The after-body diameter was varied in the range $d/D = d^* = \{0.2, 0.4\}$.

The measurements were performed at a free stream velocity $U_\infty = 20$ m/s. The boundary layer over the model was tripped by means of a carborundum roughness strip. Its thickness 5 mm upstream of separation was measured to be $\delta_{95} = 4.8$ mm. The PIV measurement planes were oriented perpendicular to the free stream flow and located at $x/D = x^* = \{0.375, 0.75\}$, which stations correspond to approximately 0.31 and 0.63 of the reattachment location for $d^* = 0.2$ and to 0.38 and 0.75 for $d^* = 0.4$, based on an average reattachment distance equal to 1.2 *D* for $d^* = 0.2$ and to 1.0 *D* for $d^* = 0.4$ [3].

The flow was seeded by means of a SAFEX smoke generator at a concentration of approximately 5 particles/mm^3. Illumination was provided by a Quantronix Darwin Duo Nd-YLF laser. Three Photron Fast-CAM SA1.1 CMOS cameras

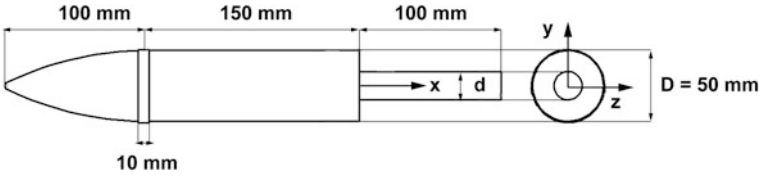


Fig. 1 Model schematic side and end view with coordinate system

Table 1 Main experimental parameters

Laser pulse separation	dt [μs]	25
Laser sheet thickness	t [mm]	3
Field-of-view size	FOV [mm^2]	80 × 80
Optical magnification factor	M [−]	0.17
Acquisition frequency	f [kHz]	0.1
Data ensemble size	N [−]	5,000
Vector pitch	p [mm]	0.9

(1024 × 1024 pixels 5400 fps, 20 μm pixel pitch) were used to record the light scattered by the particles in a field of view (FOV) of approximately 80 × 80 mm (i.e. 1.6 D × 1.6 D) centered on the model base. The maximum angle between the lines of sight of the cameras was 35°, yielding a relative error between the out-of-plane and the in-plane component of the velocity equal to 3 [6]. Illumination and recording systems were synchronized by means of a LaVision High Speed Controller hosted by a PC using Davis 8.1 software.

Light reflections from the model surface affecting the recorded images were attenuated through intensity normalization and sliding minimum subtraction. An iterative multi-grid cross-correlation analysis based on window deformation [8] was used for the vector calculation. Spurious vectors were detected using the universal median filter [10]. The main experimental parameters are listed in Table 1.

3 Flow Field Statistics

The mean velocity fields (normalized with respect to U_∞) for the present study are compared in Fig. 2 with the one obtained for a truncated-base with $d^* = 0$ (see [4] for details on the experiments).

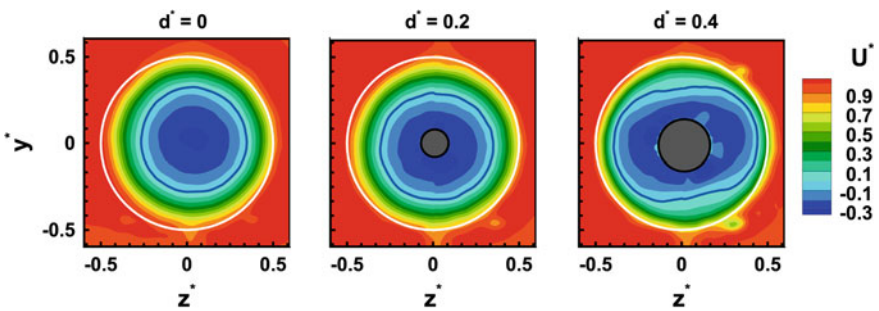


Fig. 2 Time-averaged velocity field at $x^* = 0.75$. Color contours represent the out-of-plane component of the velocity. *Contour line* represents the backflow region. Main body base trace in *solid white*. After-body in *gray*

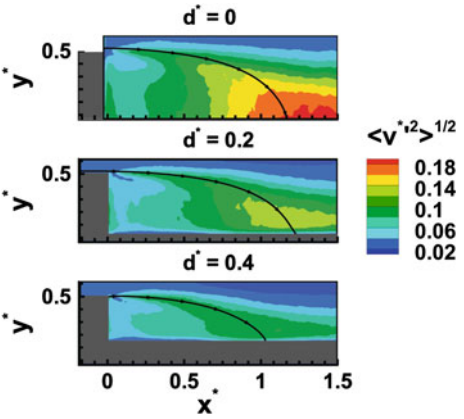


Fig. 3 Velocity fluctuations at $z^* = 0$. Color contours represent vertical component of the RMS (root mean square) of the fluctuating velocity. Reattachment streamline in *black*. Model in *gray*

The addition of a rear protrusion does not appear to alter the mean wake topology or the magnitude of the backflow. The streamwise distributions of the vertical fluctuations presented in Fig. 3 on the other hand (see [3] for details on the experiments) indicate a reduction of the peak value $< v'^2 >^{1/2}_{\max}$ from 0.18 U_∞ for $d^* = 0$ to 0.12 U_∞ and 0.10 U_∞, for $d^* = 0.2$ and $d^* = 0.4$ respectively, which reflects a pronounced sensitivity of the separated flow with respect to the after-body diameter and thus endorses the hypothesis promoted in former investigations [11] that the after-body tends to stabilize the unsteadiness of the separated flow.

4 Recirculation Region Unsteadiness

The time variability of the recirculating flow is examined based on the evolution of the backflow centroid position $\left(z_c^*, y_c^*\right)$.

The latter is estimated from the instantaneous velocity field after applying a sliding-average over a time-interval of 40 D/U_∞ (i.e. 10 raw snapshots) in order to attenuate the scatter in the instantaneous data. Figure 4 shows the coordinates thus obtained collected over an observation-time of 2,000 D/U_∞ (i.e. 5 s) and super-imposed onto the mean velocity field.

Unlike the bluff-based geometry case where a coherent precession about the model symmetry axis can be inferred from the trace of the backflow motion [4, 5, 7], in presence of a central protrusion there is no evidence of such a consistent motion. For $d^* = 0.2$ in particular, the backflow centroid position is rather random and close to the origin, whereas for $d^* = 0.4$ the motion of the recirculating flow is found to occur along one preferred radius in proximity of the y^* axis.

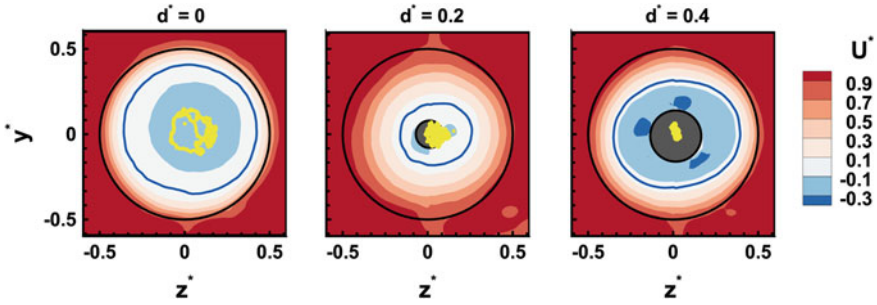


Fig. 4 Trace of backflow motion at $x^* = 0.375$ over an observation-time of 2,000 D/U_∞. Color contours represent the out-of-plane component of the time-averaged velocity. *Contour line* represents the backflow region. Main body base trace in *solid black*. After-body in *gray*

5 Proper Orthogonal Decomposition

The large-scale organization of the flow structures dominating the near-wake dynamics is characterized based on POD analysis.

The POD energy spectra shown in Fig. 5 feature a relatively large contribution of the first couple of modes to the turbulent kinetic energy, thus reflecting the occurrence of large-scale fluctuations. Modes $k = 1$ and $k = 2$ capture up to 20 % and 11 % of the turbulent kinetic energy of the flow for $d^* = 0.2$ and $d^* = 0.4$ respectively, with minor variations in the streamwise direction. In particular, the contribution of the first two modes intensifies while moving away from the base in the streamwise direction for $d^* = 0.2$, whereas the opposite is observed for $d^* = 0$.

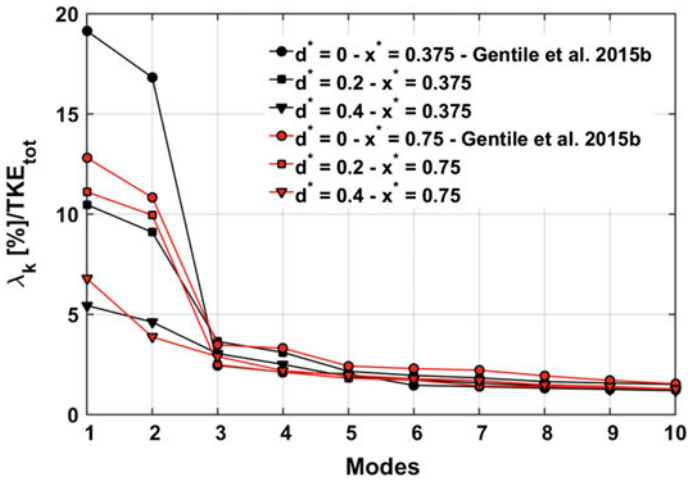


Fig. 5 Turbulent kinetic energy distribution over the first 10 modes

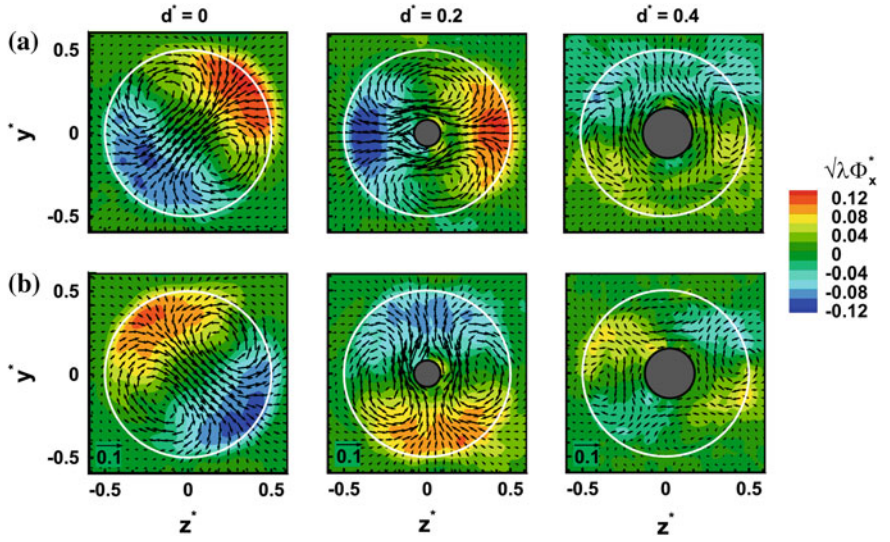


Fig. 6 Eigen-functions of mode $k = 1$ **a** and $k = 2$ **b** at $x^* = 0.75$. Color contours represent out-of plane component of the mode. Vector arrows plotted every 4th grid point represent in-plane components of the mode $\sqrt{\lambda}\Phi_z^*$ and $\sqrt{\lambda}\Phi_y^*$. Main body base trace in *solid white*. After-body in *gray*

This difference in behavior can be mainly attributed to the smaller flow scales associated with the inner backflow dynamics in presence of a central protrusion.

The eigen-functions representing the first two modes are shown in Fig. 6. The color contours outline a *dipolar* organization of both modes $k = 1$ and $k = 2$ characterized by two diametrically opposite regions of excess and defect of streamwise momentum. These modes can be linked to a radial displacement of the wake with arbitrary azimuthal direction.

The spatial coherence of the first two fluctuating modes is found to reduce substantially for $d^* = 0.4$ and the wake movement only seems to be expressed by mode $k = 1$, thus reflecting a preferential azimuthal direction in the wake displacement. This is consistent with the backflow centroid pattern shown in Fig. 4. Similarly mode $k = 2$ features a quadrupole structure which is associated with wake *ovalization* along a preferred azimuthal direction.

6 Conclusions

The turbulent wake of an ogive-cylinder with after-body was investigated by means of Stereoscopic Particle Image Velocimetry (PIV) at a diameter-based Reynolds number $Re_D = 6.7 \cdot 10^4$. The addition of a central protrusion with $d^* = 0.4$ was found to reduce the vertical velocity fluctuations by approximately 44 % compared to the case of a bluff-based configuration. The trace of the backflow centroid motion

over 2,000 D/U_∞ did not indicate any pattern identifiable with a consistent precession about the model symmetry axis for $d^* = 0.2$, whereas it revealed a preferential azimuthal direction of the backflow motion for $d^* = 0.4$.

Snapshot POD analysis indicated the occurrence of large-scale velocity fluctuations for all configurations examined, whereby the contribution of the first two modes $k = 1, 2$ to the turbulent kinetic energy attained 20 % for $d^* = 0.2$ and 11 % for $d^* = 0.4$. Inspection of the associated spatial eigen-functions outlined dipolar organization of both modes for $d^* \leq 0.2$, their linear combination being linked to a wake displacement in all possible azimuthal directions. For $d^* = 0.4$ the same arrangement only featured mode $k = 1$, thus reflecting the occurrence of a radial wake displacement, whereas mode $k = 2$ was found to be arranged as a quadrupole being associated with wake ovalization.

References

1. D. Dépres, P. Reijasse, J.P. Dussauge, Analysis of unsteadiness in afterbody transonic flows. AIAA J. **42**(12), 2541–2550 (2004)
2. H.V. Fuchs, E. Mercker, U. Michel, Large-scale coherent structures in the wake of axisymmetric bodies. J. Fluid Mech. **93**(1), 185–207 (1979)
3. V. Gentile, F.F.J. Schrijer, B.W. Van Oudheusden, F. Scarano, Afterbody effects on axisymmetric base flows, in *Abstracts of the 53rd AIAA Aerospace Sciences Meeting*, Kissimee, 5–9 Jan 2015
4. V. Gentile, F.F.J. Schrijer, B.W. Van Oudheusden, F. Scarano, Time-dependent behaviour of the recirculation region behind an axisymmetric bluff body, in *Abstracts of the 9th Symposium on Turbulence and Shear Flow Phenomena*, Melbourne, 30 June–3 July 2015
5. M. Grandemange, M. Gohlke, O. Cadot, Statistical axisymmetry of the turbulent sphere wake. Exp. Fluids **55**(11), 1–11 (2014)
6. A.K. Prasad, Stereoscopic particle image velocimetry. Exp. Fluids **29**(2), 103–116 (2000)
7. G. Rigas, A.R. Oxlade, A.S. Morgans, J.F. Morrison, Low-dimensional dynamics of a turbulent axi-symmetric wake. J. Fluid Mech. **755**, 185–207 (2014)
8. F. Scarano, M.L. Riethmuller, Advances in iterative multigrid PIV image processing. Exp. Fluids **29**(1), 51–60 (2000)
9. L. Sirovich, Turbulence and the dynamics of coherent structures. Part 1–3. Quarter. Appl. Math. XLV **3**, 561–590 (1987)
10. J. Westerweel, F. Scarano, Universal outlier detection for PIV data. Exp. Fluids **39**(1), 1096–1100 (2005)
11. C.C. Wolf, C.E. Klei, R.M. Buffo, R. Hörnschemeyer, E. Stumpf, Comparison of rocket near-wakes with and without nozzle simulation in subsonic freestream conditions, in *Abstracts of the 42nd AIAA Fluid Dynamics Conference and Exhibit*, New Orleans, 25–28 June 2012

Global Linear Stability Analysis of the Flow Around a Superhydrophobic Circular Cylinder

Franco Auteri, Marco Carini, Michel Fournié, Dominique Fratantonio and Flavio Giannetti

Abstract Over the last few years, superhydrophobic (SH) surfaces have been receiving an increasing attention in many scientific areas by virtue of their ability to enhance flow slip past solid walls and reduce the skin-friction drag. In the present study, a global linear-stability analysis is employed to investigate the influence of the SH-induced slip velocity on the primary instability of the 2D flow past a circular cylinder. The flow regions playing the role of 'wavemaker' are identified by considering the structural sensitivity of the unstable mode, thus highlighting the effect of slip on the global instability of the considered flow. In addition, a sensitivity analysis to slip-induced base-flow modifications is performed, revealing which areas of the cylinder surface provide a stabilising/destabilising effect when treated with a SH coating.

1 Introduction

The non-adhesive property of superhydrophobic (SH) surfaces originates from the presence of a non-wetted contact that holds when a low-viscosity gas is trapped inside the blemishes of the solid surface. From a macroscopical viewpoint, this phenomenon can be mathematically described by substituting the standard no-slip

F. Auteri (✉) · D. Fratantonio
Dipartimento di Scienze e Tecnologie Aerospaziali, Politecnico di Milano,
via La Masa 34, 20156 Milano, Italy
e-mail: franco.auteri@polimi.it

M. Carini
Institut de Mécanique des Fluides de Toulouse, Allée du Professeur Camille Soula,
31400 Toulouse, France

M. Fournié
Institut de Mathématiques de Toulouse, Université Paul Sabatier, 118 route de Narbonne,
31062 Toulouse, France

F. Giannetti
Dipartimento di Ingegneria Industriale, Università degli Studi di Salerno,
Via Giovanni Paolo II 132, 84084 Fisciano, Italy

© Springer International Publishing Switzerland 2016

A. Segalini (ed.), *Proceedings of the 5th International Conference on Jets, Wakes and Separated Flows (ICJWSF2015)*,
Springer Proceedings in Physics 185, DOI 10.1007/978-3-319-30602-5_21

boundary condition in favor of the so called Navier condition [1], which can be expressed in non-dimensional form as:

$$\mathbf{U}\cdot\hat{\boldsymbol{\tau}} = -\ell\left[\left(\nabla\mathbf{U}+\nabla\mathbf{U}^T\right)\cdot\hat{\mathbf{n}}\right]\cdot\hat{\boldsymbol{\tau}}, \quad \text{on} \quad \Gamma_{cyl}, \tag{1}$$

where $\hat{\boldsymbol{\tau}}$ and $\hat{\mathbf{n}}$ are the unit vectors tangent and normal to the cylinder surface Γ_{cyl}, respectively, $\mathbf{U}$ denotes the flow velocity made dimensionless with the incoming uniform flow velocity, and ℓ is the slip length made dimensionless with the diameter D of the cylinder.

Given that, to the best of the authors' knowledge, the highest slip length experimentally achieved with a stable air-liquid interface is ∼400 μm [2], the diameter of the cylinder must be on the order of tens of millimeters if we want SH coatings to have noticeable effects on the flow dynamics. Therefore, the present analysis provides results that are useful for the exploitation of SH surfaces as control devices in microfluidic systems, e.g., for flow mixing control.

Among all the earlier studies on the subject [3–7], Legendre et al. [3] have investigated the influence of a uniform slip length on the two-dimensional wake of a circular cylinder by means of Direct Numerical Simulation (DNS). Legendre et al. [3] traced a stability diagram in the parameter space (ℓ, Re), indicating that a complete suppression of the vortex shedding can be obtained for $\ell \geq 0.25$. Similarly, Mastrokalos et al. [4] carried out DNSs for piecewise-constant slip-length distributions, showing that applying SH coating in the rear and the front stagnation point regions has a destabilising effect or no effect at all on the Bénard-Von Kármán instability.

Starting from past studies, which mainly consist in numerical simulations, the present work aims to shed light on the phenomenology behind the stabilising effect given by SH coatings. In order to do so, we analyse how the base flow, the critical direct and adjoint modes, and the sensitivity of the leading eigenvalue change at increased levels of slip while moving along the neutral curve in the parameter space (ℓ, Re). This investigation is supported by a sensitivity analysis to slip-length modifications and slip-induced base-flow modifications, which gives useful indications on the role played by the slip.

2 Theoretical Framework

The adopted computational domain Ω is a two-dimensional box, whose boundaries are the cylinder surface Γ_{cyl}, the inflow boundary Γ_{in}, the top and bottom boundaries Γ_{lat} and the outflow boundary Γ_{out}. Within Ω, the fluid motion is described by the usual two-dimensional unsteady, incompressible Navier-Stokes (NS) equations supplemented by the following boundary conditions:

$$\begin{aligned} \mathbf{U} &= \hat{\mathbf{x}}, \quad \text{on} \quad \Gamma_{in}, \\ \mathbf{U}\cdot\hat{\mathbf{n}} &= 0, \quad \text{on} \quad \Gamma_{cyl}, \\ \mathbf{U}\cdot\hat{\boldsymbol{\tau}} &= -\ell\left[\left(\nabla\mathbf{U}+\nabla\mathbf{U}^T\right)\cdot\hat{\mathbf{n}}\right]\cdot\hat{\boldsymbol{\tau}}, \quad \text{on} \quad \Gamma_{cyl}, \end{aligned} \tag{2}$$

$$P\hat{\mathbf{n}} - \frac{1}{\mathrm{Re}}\left(\nabla\mathbf{U} + \nabla\mathbf{U}^T\right)\cdot\hat{\mathbf{n}} = \mathbf{0}, \quad \text{on} \quad \Gamma_{out} \text{ and } \Gamma_{lat},$$

where $\mathbf{U}$ and P are the velocity and the pressure of the flow, respectively. The Reynolds number is defined as $\mathrm{Re} = U_\infty D/\nu$, with U_∞ being the free-stream velocity, ν the kinematic viscosity of the fluid, $\hat{\mathbf{x}}$ is the unit vector of the x axis, and D the cylinder diameter.

The linear stability analysis is carried out by decomposing the flow field in a steady part and a small unsteady perturbation $(\hat{\mathbf{u}}(x, y, t), \hat{p}(x, y, t))$, with the *ansatz* $\hat{\mathbf{u}}(x, y, t) = \mathbf{u}(x, y)\exp(\gamma\, t)$ and $\hat{p}(x, y, t) = p(x, y)\exp(\gamma\, t)$ where γ is a complex number (see for instance [8]).

3 Numerical Approach and Code Validation

The numerical approach is based on a finite element method applied on a mesh made of triangular elements, which has been implemented by means of the *GetFem++* library [9]. In the present work, the weak formulation of the linearized NS equations involves the use of the Lagrange-multiplier technique to impose the no-penetration boundary condition, while the slip boundary condition is introduced in the overall weak formulation as commonly done for a Robin condition. The *MUMPS* library [10], the *ARPACK* library [11], and the *LOCA* library [12] are employed to solve the involved algebraic linear systems, the eigenvalue problems, and to track the Hopf bifurcation, respectively. The code has been extensively validated for either no-slip, uniform slip, or piecewise-constant slip boundary conditions. Considering slip-length values up to 0.2 and Reynolds numbers less than 200, we have continued the Hopf bifurcation in the parameter space (ℓ, Re). Figure 1 shows how the

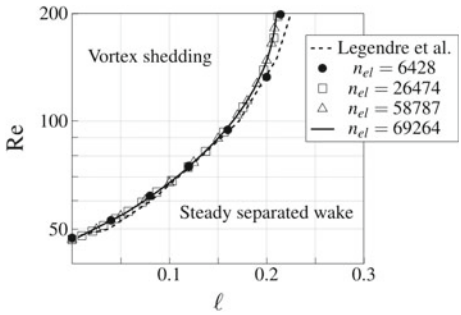


Fig. 1 Hopf-bifurcation neutral curve in the parameter space (ℓ, Re). The *dashed line* represents the extrapolated results of Legendre et al. [3]. The solid *black line* and the marks represent the bifurcation boundary traced with the continuation algorithm in the present work. In the legend, n_{el} denotes the number of triangular elements employed. A logarithmic scale is adopted for the Reynolds axis

neutral curve is almost insensitive to the employed mesh refinement. The obtained results match very well the stability diagram traced by Legendre et al. [3]. The case of piecewise-constant slip-length distribution has also been tested by considering some of the distributions employed by Mastrokalos et al. [4] and by verifying that the results of our global linear stability analysis are consistent with their DNSs.

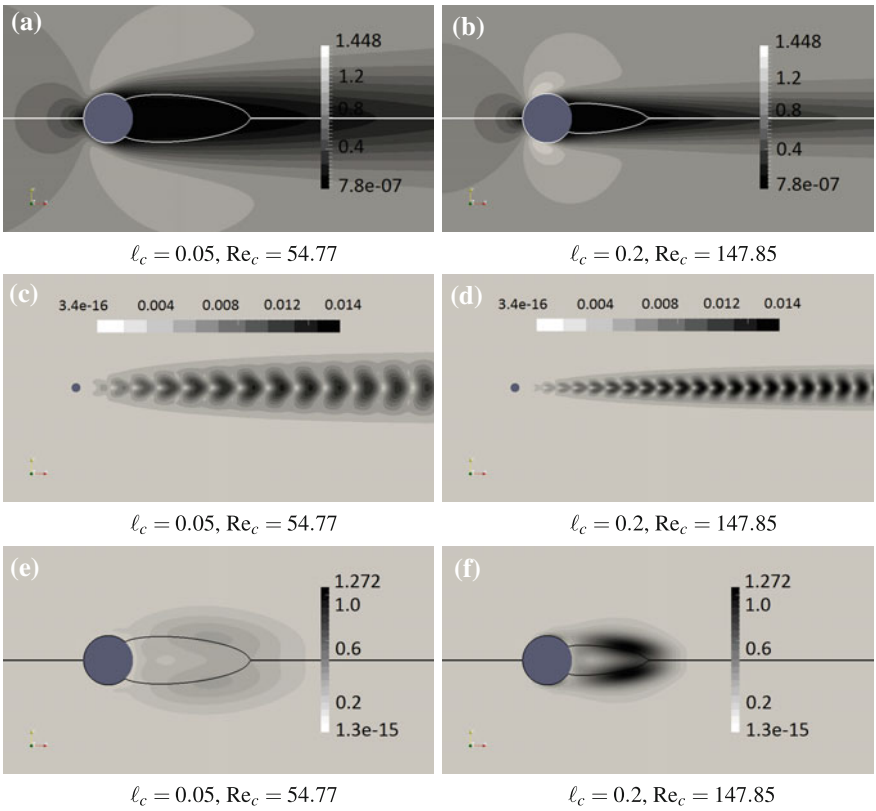


Fig. 2 Variation of the flow properties along the neutral curve: **a**, **b** velocity magnitude of the base flow; **c**, **d** velocity magnitude of the direct mode; **e**, **f** structural sensitivity function

4 Results and Discussion

The influence of the slip on the instability phenomenon is investigated by analysing how the flow properties change along the bifurcation boundary. Figure 2 illustrates the base flow, the direct eigenmode and the structural sensitivity function as defined in Giannetti and Luchini [8] for two points on the neutral curve of Fig. 1, namely at

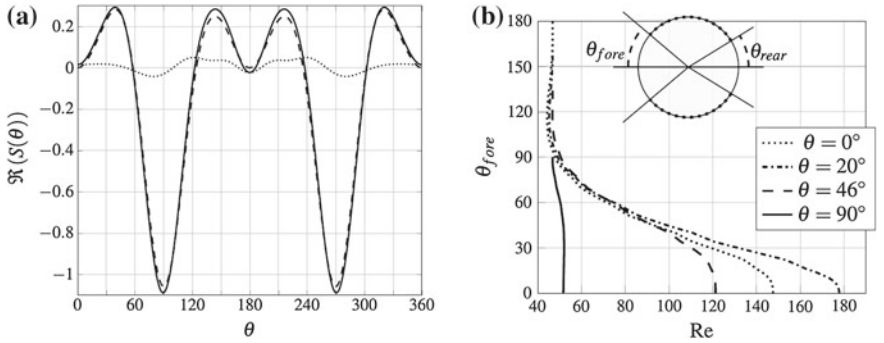


Fig. 3 **a** Sensitivity function to (*dotted line*) slip-length modification S_p and (*dashed line*) slip-induced base-flow modifications S_b as a function of the angular position on the cylinder surface. The solid line represents the overall effect given by the sum of the two functions. **b** Neutral curves in the parameter space (θ_{fore}, Re) for $\theta_{rear} = 0°$, 20°, 46°, 90° and $\ell = 0.2$. The rough areas on the cylinder sketch represent the presence of slip, while the smooth areas are no-slip surfaces

$\ell = 0.05$ and $\ell = 0.2$. As the recirculation bubble of the steady wake gets smaller at increased levels of slip, the direct mode and the structural sensitivity function follow the same trend. Indeed, the instability cores become smaller and more intense, but their position relative to the boundary of the recirculation bubble remains unchanged at increased levels of slip. These observations suggest that the nature of the instability is not modified by the slip. Moreover, we can infer from Fig. 2c, d that the wavenumber of the spatial oscillation of the direct mode increases with the slip, coherently with the increase of the critical Strouhal number.

A slip-length modification results in a double effect on the eigenvalue problem. A localized perturbation of the slip-length $\delta\ell(\theta)$ modifies both the boundary conditions of the eigenvalue problem and the boundary conditions of the base-flow equations [13]. By exploiting the Lagrange identity and the solution of the adjoint eigenvalue problem, we derive two sensitivity functions, i.e., S_p, the sensitivity related to the direct modification of the eigenvalue problem, and S_b, the sensitivity related to the induced base-flow modifications, whose expressions are:

$$S_p(\theta) = \frac{\hat{u}_{\hat{\boldsymbol{\tau}}}^{\dagger *}(\theta)\hat{u}_{\hat{\boldsymbol{\tau}}}(\theta)}{(\hat{\mathbf{u}}^{\dagger}, \hat{\mathbf{u}})_{\Omega}\ell^2(\theta)\mathrm{Re}}, \qquad S_b(\theta) = \frac{U_{b,\hat{\boldsymbol{\tau}}}^{\dagger *}(\theta)U_{b,\hat{\boldsymbol{\tau}}}(\theta)}{(\hat{\mathbf{u}}^{\dagger}, \hat{\mathbf{u}})_{\Omega}\ell^2(\theta)\mathrm{Re}}. \tag{3}$$

In (3), both sensitivity functions are given by the product between the tangential component of two velocity fields, where $\mathbf{U}_b$ is the base flow, $\hat{\mathbf{u}}$ and $\hat{\mathbf{u}}^{\dagger}$ are the critical direct and adjoint modes, respectively, and $\mathbf{U}_b^{\dagger}$ is the adjoint base flow, as defined in Marquet et al. [14]. As illustrated in Fig. 3a, the application of the above sensitivity analysis to the case $\ell = 0$ shows that slip surfaces applied on the flanks of the cylinder surface, namely in the range $\theta = [60, 120]$, provide a stabilising effect, while the front and rear areas provide a destabilization of the base flow. These observations are

in good agreement with the numerical simulations carried out by Mastrokalos et al. [4]. The same conclusions can be inferred from the neutral curves in the parameter space (θ_{fore}, Re) computed at different values of θ_{rear}, where θ_{fore} and θ_{rear} define the no-slip areas in the front and the rear of the cylinder surface, respectively. According to Fig. 3b, the critical Reynolds number can be further increased if the slip surfaces are removed from the rear-stagnation-point area.

5 Summary and Conclusions

Our global linear stability analysis explains how the presence of slip delays the onset of instability and increases the critical Reynolds and Strouhal numbers. The structural-sensitivity analysis at the perturbation level [8] suggests that the flow slip does not modify the instability mechanisms. Moreover, the sensitivity analysis with respect to slip-length modifications and slip-induced base-flow modifications reveals that only slip surfaces applied on the flanks of the cylinder can delay the Von Kármán instability. This observation is further supported by the neutral curves in the parameter space (θ_{fore}, Re), which show an increase of the critical Reynolds number for increasing values of θ_{rear} in the neighbourhood of $\theta_{\text{rear}} = 0°$.

References

1. C.L.M.H. Navier, Mémoires de l'Académie Royale des Sciences de l'Institut de France **6**, 389–440 (1823)
2. C. Lee, C.J. Kim, Langmuir **25**(21), 12812–12818 (2009)
3. D. Legendre, E. Lauga, J. Magnaudet, J. Fluid Mech. **633**, 437–447 (2009)
4. E.M. Mastrokalos, C.I. Papadopoulos, L. Kaiktsis, Comput. Fluids **107**, 256–271 (2015)
5. P. Muralidhar, N. Ferrer, R. Daniello, J.P. Rothstein, J. Fluid Mech. **680**, 459–476 (2011)
6. D. Li, S. Li, Y. Xue, Y. Yang, W. Su, Z. Xia, Y. Shi, H. Lin, H. Duan, J. Fluids Struct. **51**, 211–224 (2014)
7. D. You, P. Moin, Phys. Fluids **19**, 081701 (2007)
8. F. Giannetti, P. Luchini, J. Fluid Mech. **581**, 167–197 (2007)
9. Y. Renard, J. Pommier, http://home.gna.org/getfem (2010)
10. P.R. Amestoy, I.S. Duff, J.L' Excellent, J. Koster, *Applied Parallel Computing. New Paradigms for HPC in Industry and Academia* (Springer, 2001), pp. 121–130
11. R.B. Lehoucq, D.C. Sorensen, C. Yang, SIAM **6** (1998)
12. A.G. Salinger, N.M. Bou-Rabee, R.P. Pawlowski, E.D. Wilkes, E.A. Burroughs, R.B. Lehoucq, L.A. Romero, Sandia National Laboratories, Albuquerque, NM, Technical Report No. SAND2002-0396 (2002)
13. J.O. Pralits, L. Brandt, F. Giannetti, J. Fluid Mech. **650**, 513–536 (2010)
14. O. Marquet, D. Sipp, L. Jacquin, J. Fluid Mech. **615**, 221–252 (2008)

Optimal Cancelation of Vortex Street in Flow Past a Circular Cylinder with Controllable Wettability Properties

Marios E. Mastrokalos, Christos I. Papadopoulos and Lambros Kaiktsis

Abstract Above a critical value of the Reynolds number, flows past bluff bodies are characterized by self-sustained oscillations, due to the formation of the Kármán vortex street. This results in the dynamic loading of the body, which, in practical applications, may lead to structural fatigue. In recent work, it was demonstrated that, in flow past a cylinder, implementing surface hydrophobicity results in decreased drag and lift forces, leading to vortex street cancellation at a critical level of control effort. In order to achieve vortex street suppression at lower levels of control effort, utilizing materials with controllable wettability properties appears as a promising possibility. Thus, in the present work, the effectiveness of a proportional feedback control scheme, utilizing the application of time-dependent slip conditions on the cylinder surface, is investigated by means of CFD simulations. Firstly, the feedback control scheme is tested for a problem definition characterized by the application of slip on the entire cylinder surface, for a wide range of the control scheme parameters; it is demonstrated that flow unsteadiness is reduced at substantially lower levels of control effort, in comparison to corresponding passive control schemes. Secondly, in the frame of feedback control, an optimization problem is formulated and solved, aiming at the partial or full suppression of the Kármán vortex street at a minimal control effort, using time-dependent slip conditions on a part of the cylinder surface. The results demonstrate a further reduction in control effort. Overall, in comparison to passive flow control, a reduction in control effort by two orders of magnitude is attained with the present optimized feedback control scheme.

M.E. Mastrokalos (✉) · C.I. Papadopoulos · L. Kaiktsis
Department of Naval Architecture and Marine Engineering,
National Technical University of Athens, 9 Heroon Polytechniou Str.,
Zografos, 15710 Athens, Greece
e-mail: mmastrok@hotmail.com

L. Kaiktsis
Department of Mechanical Engineering, Khalifa University of Science,
Technology and Research, P.O. Box 127788, Abu Dhabi, United Arab Emirates

© Springer International Publishing Switzerland 2016

A. Segalini (ed.), *Proceedings of the 5th International Conference on Jets, Wakes and Separated Flows (ICJWSF2015)*,
Springer Proceedings in Physics 185, DOI 10.1007/978-3-319-30602-5_22

1 Introduction

Above a critical value of the Reynolds number, flows past bluff bodies, as a circular cylinder, are characterized by global instability, whose non-linear state is the Kármán vortex street. The presence of the vortex street results in time-dependent drag and lift forces exerted on the body. This dynamic loading may lead to structural fatigue in engineering applications as cooling towers, oil risers and heat exchangers. Therefore, several methods have been applied in literature studies, aiming at the suppression of the vortex street, utilizing passive, active feed-forward or active feedback control schemes. Passive control studies have utilized placement of a splitter plate [11] or of a smaller cylinder [13] in the wake, and more recently application of hydrophobic/superhydrophobic materials on the cylinder surface [8, 9, 12]. In active feed-forward and active feedback control studies, cylinder rotation [7], application of a Lorentz force [3] and mass transpiration on the cylinder surface [5, 10] have been used.

Hydrophobic materials appear as an attractive choice for flow control, due to the lack of any other intervention in terms of either energy input or geometry modification. Recent studies demonstrated that implementing hydrophobicity on the entire cylinder surface results in decreased drag and lift forces, and even leads to vortex street cancellation at a critical level of control effort [8]. Furthermore, the optimization study of [9] established that an optimal application of slip on a part of the cylinder surface may lead to a decrease in control effort of up to 50 %, in comparison to implementing slip on the entire cylinder surface. Nonetheless, as the manufacturing of hydrophobic and superhydrophobic surfaces is still quite expensive, a further reduction in control effort is desired. In this frame, using materials with controllable wettability properties is a possible choice. These materials modify their wetting properties when an external forcing is applied, in particular, optical, magnetic, mechanical, chemical, thermal or electrical; see [14] for an extensive review. Thus, materials with controllable wetting properties can enable the application of time-dependent slip conditions on a surface, for feedback control studies.

Regarding feedback control of flow past a cylinder, the computational work of [10] demonstrated that a drastic reduction in control effort is feasible, in comparison to a corresponding active feed-forward control strategy [5]. Thus, it appears plausible that, in the context of a feedback control scheme, the application of time-dependent slip conditions may lead to partial or complete suppression of the vortex street at a substantially lower level of control effort, in comparison to the corresponding passive control scheme [8, 9]. The present work thus investigates the potential of reducing control effort in flow past a cylinder, by implementing a proper proportional feedback control scheme, characterized by controllable surface wettability. In a first stage of the present study, a control scheme with time-dependent slip conditions on the entire cylinder surface is tested; the effects of the sensor location, as well as of the proportional gain value, on the stability of the global flow, as well as on the required control effort, are assessed. Next, the feedback control scheme is

optimized by formulating and solving an optimization problem, aiming at the partial or full suppression of the Kármán vortex street at a minimal control effort.

The paper is organized as follows. In Sect. 2, the flow problem setup, including the feedback control scheme is introduced. In Sect. 3, results of numerical simulations of flow past a cylinder subject to feedback control, characterized by time-dependent slip conditions on the entire cylinder surface, are presented and analyzed. In Sect. 4, the formulation of an optimization problem, aiming at optimizing feedback control, is illustrated, and optimization results are presented and discussed. Finally, in Sect. 5, the main findings of the present study are summarized.

2 Problem Definition

We consider a circular cylinder in uniform cross-flow. Flow fields are computed from the numerical solution of the non-dimensional Navier–Stokes equations for two-dimensional incompressible viscous flow:

$$\text{Continuity/momentum equations: } \nabla \cdot \vec{u} = 0, \quad \frac{\partial \vec{u}}{\partial t} + \vec{u} \cdot \nabla \vec{u} = -\nabla p + \frac{1}{Re} \Delta \vec{u} \qquad (1)$$

where $\vec{u} = (U, V)$ is the velocity vector and p the static pressure. Here, physical variables are non–dimensionalized with proper scales based on the cylinder diameter, D, the free stream velocity, U_{inf}, and the fluid density, ρ. Frequencies are non-dimensionalized as Strouhal numbers, $St = \frac{fD}{U_{\text{inf}}}$. The Reynolds number is defined as, $Re = \frac{U_{\text{inf}} D}{\nu}$ where ν is the kinematic viscosity of the fluid.

The numerical solution of the governing equations utilizes the ANSYS CFX CFD code. Here, a second-order finite volume approach, with quadrilateral finite volumes, is adopted. The center of coordinates ($x = 0$, $y = 0$) is taken at the cylinder center. The following conditions are prescribed at the domain boundaries (see Fig. 1a).

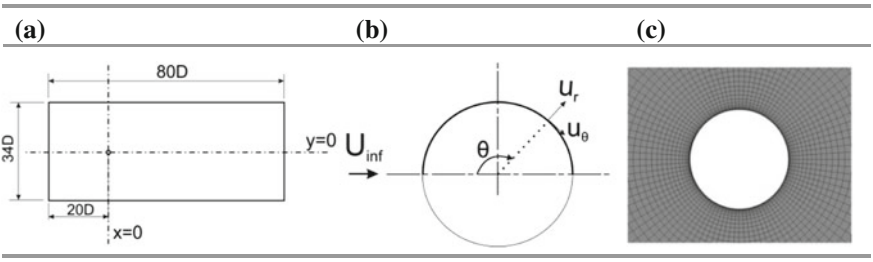


Fig. 1 **a** Flow domain. **b** Definition of local angle, measured from the front stagnation point, and local velocity components on the cylinder surface, u_θ and u_r. **c** Detail of a finite volume mesh close to the cylinder (the number of finite volumes osculating to cylinder surface is close to 100)

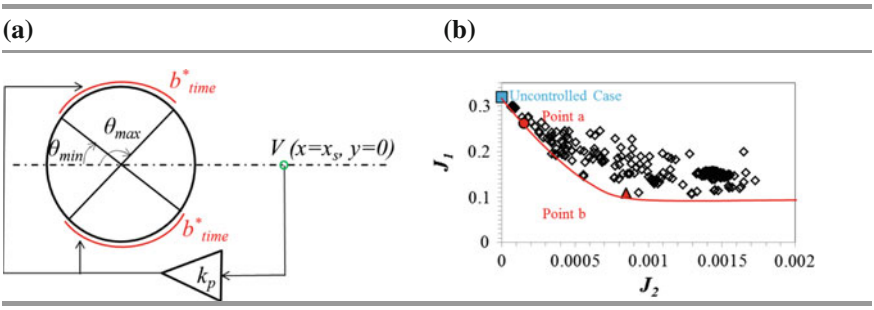


Fig. 2 **a** Proportional feedback control scheme: the location of the feedback sensor, x_s, the extent of the controllable wettability area, delimited by θ_{min} and θ_{max}, as well as the proportional gain, k_p, are depicted. **b** $Re = 90$: objective function J_1 vs. objective function J_2 for solutions of the optimization problem with feedback flow control

Inflow and lateral boundaries: $U = U_{inf} = 1$, $V = 0$.

Outflow boundary*:* $p = 0$, Neumann velocity boundary condition.

Cylinder surface: $u_\theta = \tau^* b^* Re = b^* \frac{\partial u_\theta}{\partial r}$, $u_r = 0$ (Navier model [15]),

where u_θ and u_r are the instantaneous non-dimensional velocity components in the circumferential and radial direction, respectively (see Fig. 1b), τ^* is the instantaneous non-dimensional wall shear stress and b^* is the non-dimensional (time-dependent) slip length.

In the present feedback control scheme, sketched in Fig. 2a, an instantaneous transverse velocity at a point along the domain centerline, $V(x_s,t)$, is used as the sensor signal; a proper value of slip length, $b^*(t)$, is used as the actuator signal, calculated based on a proportional feedback control law within the frame of the Navier model, as follows:

$$b^*(t) = \frac{1}{Re \cdot \tau^*} k_p |V(x_s, t)| \tag{2}$$

where k_p is the proportional feedback gain value.

The present study is performed for two values of Reynolds number, $Re = 60$ and $Re = 90$, for which the flow is unsteady and two-dimensional [1]. The computational domain extends *20D* upstream from cylinder center and *60D* downstream, while the lateral boundaries lie *17D* from $y = 0$, the domain centerline (see Fig. 1a). The adequacy of this domain size has been demonstrated in previous studies of uncontrolled and controlled flow past a cylinder [5]. A particularly fine mesh is prescribed near the region of control action (cylinder surface), as shown in Fig. 1c. Resolution tests have shown that a total number of finite volumes close to 54,000, accompanied by a number of finite volumes osculating to the cylinder surface of about 100, is sufficient to achieve grid-independent solutions. Depending on the physical parameters and spatial resolution, a non-dimensional time step ranging

from 0.005 to 0.05 has been tested. All simulations reported subsequently were performed for a time step of 0.01.

3 Feedback Flow Control: Effect of Control Parameters

The feedback control approach of [10] demonstrated the strong sensitivity of the flow stability state to the parameters of feedback control. To investigate these effects in detail for the case of controlled surface wettability, a parametric study is performed, varying the parameters of feedback control, namely the sensor location, x_s, and the proportional gain value, k_p. Here, the entire cylinder surface is considered hydrophobic, while the value of Reynolds number is $Re = 60$.

First, the proportional gain is fixed at the representative value of 0.5, and the feedback sensor location is varied. Figure 3 presents computed values of representative flow quantities, as a function of the streamwise coordinate of the control sensor, x_s, in particular lift coefficient amplitude, $C_{L,ampl}$ (Fig. 3a), time-averaged drag coefficient, $<C_D>$ (Fig. 3b), and maximum value of the (time-dependent) slip length, b^*_{max} (Fig. 3c). Figure 3a demonstrates the decreasing trend of lift coefficient amplitude, as the sensor is moved farther downstream. When the feedback sensor is placed at $x_s = 7$, the lift coefficient amplitude reaches its minimum value, corresponding to very low levels of flow unsteadiness; however, complete suppression of flow unsteadiness is not achieved. For a sensor location $x_s > 7$, flow unsteadiness is enhanced. Further, the time-averaged drag coefficient, presented in Fig. 3b, is a decreasing function of the sensor location for $x_s < 5$, exhibiting a localized increase for slightly higher values of x_s. Finally, Fig. 3c indicates that the maximum value of

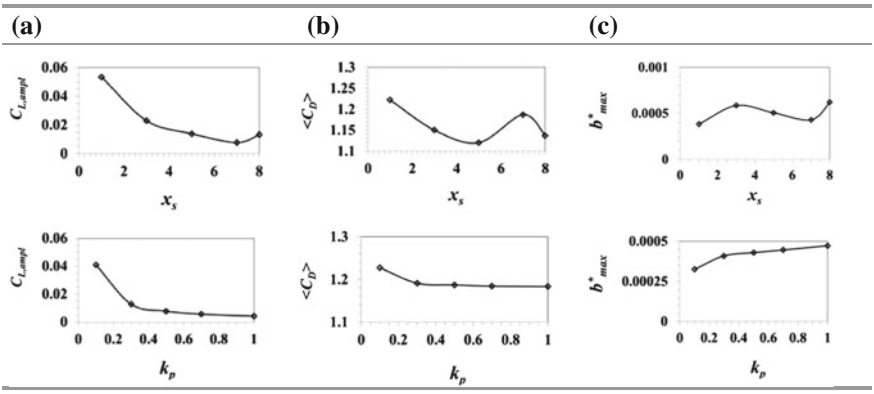


Fig. 3 $Re = 60$: flow quantities versus (i) streamwise sensor location, x_s, at a proportional gain value of $k_p = 0.5$ (upper row), and (ii) proportional gain value, k_p, at a streamwise sensor location of $x_s = 7$ (lower row): **a** lift coefficient amplitude, $C_{L,ampl}$, **b** time-averaged drag coefficient, $<C_D>$, and **c** maximum value of non-dimensional slip length, b^*_{max}. The entire cylinder surface is hydrophobic

the (time-dependent) slip length attains a local minimum for $x_s = 7$, corresponding to a minimum in control effort.

In a second step, utilizing the above results, we fix the feedback sensor location at $x_s = 7$, and vary the proportional gain, k_p; computed values of representative flow quantities are presented in Fig. 3. Figure 3a, b demonstrate that the lift signal amplitude, $C_{L,ampl}$, as well as the time-averaged drag coefficient, $<C_D>$, are both decreasing functions of the proportional gain. On the other hand, the maximum value of the (time-dependent) slip length, b^*_{max}, representative of the control effort, is an increasing function of the proportional gain (Fig. 3c). It is worth noting that, for $k_p > 0.3$, further increase of k_p results in an imperceptible modification of flow statistical quantities.

The present parametric study thus demonstrates that moving the feedback sensor location downstream and increasing the proportional gain value contribute to a substantial reduction of flow unsteadiness. It should be noted that a complete cancelation of flow unsteadiness has not been attained; nonetheless, a comparison with the results of passive flow control reported in [9] (critical value $b^* = 0.09$) suggests a reduction in control effort with feedback control by a factor of 180.

4 Feedback Flow Control: Formulation and Solution of Optimization Problem

In the previous section, a feedback control scheme, utilizing time-dependent slip conditions on the entire cylinder surface, was parametrically investigated. Due to the high cost of surfaces characterized by controllable hydrophobicity, it is essential to reduce the extent of the corresponding regime. In the present section, the feedback control parameters are subject to an optimization procedure, aiming at the partial or complete suppression of the Kármán vortex street at a minimal control effort. To this end, a two-objective minimization problem is formulated. The first objective function is associated with the flow's global stability, while the second one quantifies the time-dependent control effort. Optimization results are reported for $Re = 90$.

Four design variables are utilized in the present implementation: the streamwise location of the transverse velocity sensor, x_s, the proportional gain, k_p, and the angles θ_{min} and θ_{max}, defining the extent of the area in which the time-dependent slip condition is implemented. A broad domain of definition is considered for each of the four design variables: $1 < x_s < 10$, $0 < k_p < 0.5$, $0^o < \theta_{min} < 70^o$, $110^o < \theta_{max} < 180^o$. The selection of θ_{min} and θ_{max} values was guided by the recent study on passive flow control [9], and the selection of k_p and x_s boundaries by the results of the parametric study reported in Sect. 3.

The first objective function, J_1, is related to the flow global stability. Here, a total of M points along the domain centerline ($y = 0$) is considered, and the numerical signal of the transverse velocity (V-component) at large times is analyzed, for each

point. For a total of N data points in time (N being a very large number, corresponding to several flow periods), the objective function J_1 is defined as the average of the standard deviation values, S_j, of the V-velocity signals, in the population of M points:

$$S_j = \sqrt{\frac{1}{N-1}\sum_{i=1}^{N}\left(V_{t_i,x_j}\right)^2},\ J_1 = \frac{1}{M}\sum_{j=1}^{M} S_j \tag{3}$$

where V_{t_i,x_j} is the transverse velocity at point x_j calculated at time instant t_i, and S_j the standard deviation at point x_j. In the present study, $M = 100$, corresponding to equidistant points in the wake region $1 < x_j < 21$.

The control effort increases with the slip length (determined from the product of the transverse velocity signal and the proportional feedback gain, k_p) and the half-arc of the slip region. Thus, a corresponding objective function, J_2, is defined using the standard deviation of the transverse velocity, at the sensor point, x_s, as follows:

$$S_{V_{x_s}} = \sqrt{\frac{1}{N-1}\sum_{i=1}^{N}\left(V_{t_i,x_s}\right)^2},\ J_2 = S_{V_{x_s}} k_p \frac{(\theta_{max} - \theta_{min})}{2} \tag{4}$$

with V_{t_i,x_s} being the transverse velocity at the same point calculated at time instant t_i.

The optimization problem is stated as follows: find the optimum combinations of the problem design variables (x_s, k_p, θ_{min}, θ_{max}), which simultaneously minimize objective functions J_1, J_2. The final set of optimal solutions for the two-objective minimization problem of the present study is obtained by evolving, by means of a genetic algorithm, an initial, randomly generated, population (generation). The evolution produces subsequent generations, utilizing the operations of parent selection, cross–over, mutation and elitism [6]. In the present work, each individual corresponds to different values of the four design variables, and is rated based on the resulting values of the problem objective functions. Here, the evaluator, finally giving the values of objective functions, is the CFD code ANSYS CFX, which is coupled to an optimization tool; the latter utilizes the ParadisEO genetic algorithms library [2], and adopts the Non–dominated Sorting Genetic Algorithm NSGA-II for ranking solutions within a generation [4]. The process terminates when the optimal set of solutions is hardly improved from one generation to the next. The final set of optimal solutions forms the problem's Pareto front; with respect to these solutions, there exist no others improving all of the problem objective functions. In the present implementation, each generation consisted of 20 individuals. The optimization problem was run for 20 generations, and convergence to the final Pareto front was verified. An individual CFD run has required approximately 6.5 h of turnaround time on 24 cores of a parallel cluster.

Figure 2b presents the computed values of objective functions for $Re = 90$, accompanied by a sketch of the Pareto front. Two representative solutions, namely

Table 1 $Re = 90$: values of design variables and objective functions, for the uncontrolled case, for solutions depicted by Points a and b in Fig. 2b, as well as for solutions corresponding to a passive control scheme utilizing steady slip conditions on a part [9] and on the entire cylinder surface [8]; the values of $½b^*\varphi$, quantifying the control effort, are also reported (φ in radians)

Case	k_p	x_s	θ_{min}	θ_{max}	J_1	J_2	b^*	$\varphi = \theta_{max} - \theta_{min}$	$1/2b^*\varphi$
Uncontrolled	–	–	–	–	0.319	0.00000	0.00000	0°	0.0000
Point a	0.043	8.2	56°	119°	0.261	0.00015	0.00018	63°	0.0001
Point b	0.263	8.6	20°	153°	0.112	0.00085	0.00060	133°	0.0007
Point 1 [9]	–	–	41°	129°	0.261	–	0.04100	88°	0.0310
Point 2 [9]	–	–	34°	146°	0.112	–	0.19600	122°	0.1560
$b^* = 0.15$ [8]	–	–	0°	180°	0.112	–	0.15000	180°	0.2350

For feedback control, the reported values of b^* are the maximum in time

Point a and Point b, lying on the Pareto front, as well as the case of uncontrolled flow, are depicted in Fig. 2b; the corresponding values of design variables and objective functions are reported in Table 1. Table 1 also includes passive control optimal solutions of a partial slip setup (Point 1 and Point 2) [9]; a solution corresponding to steady slip conditions on the entire cylinder surface [8] is also reported. Table 1 indicates that, for the optimal solutions considered at Re=90, the decrease of flow unsteadiness is mainly a result of the increase of the proportional gain value, k_p, and of the hydrophobic area, and secondarily of the shift of the sensor location, x_s, farther downstream. For these representative optimal solutions, Fig. 4 presents the computed signals of lift coefficient and slip length. It is demonstrated that, for the solution depicted by Point b in Fig. 2b, the amplitude of the lift signal attains a minimal value, whereas the slip length is increased. Finally,

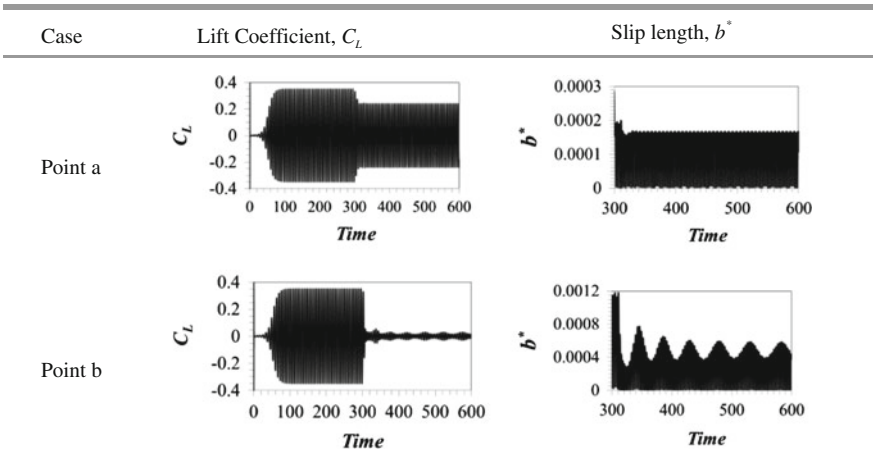


Fig. 4 $Re = 90$: lift coefficient and slip length signals for solutions depicted in Fig. 2b by Point a and Point b. Active feedback control is implemented at $t = 300$

Table 1 highlights that the control effort, also quantified by the product $½b^*(\theta_{max} - \theta_{min})$, introduced in [9], is reduced by more than two orders of magnitude, in comparison to the optimal solutions of the passive control scheme, i.e. flow unsteadiness is reduced substantially with very low levels of control effort.

5 Conclusion

The present computational study has addressed the problem of optimal suppression of the Kármán vortex street in flow past a cylinder, at low Reynolds numbers, by means of an active feedback control scheme. Here, time-dependent slip conditions have been applied on the entire or on a part of the cylinder surface, as enabled by materials with controllable wettability properties. The time-dependent slip conditions are obtained by a proportional control law based on the signal of a velocity sensor, properly placed in the near wake. First, the application of controllable hydrophobicity on the entire cylinder surface has demonstrated that, by proper selection of the sensor location, as well as of the proportional gain value, the vortex street is substantially suppressed, thus leading to low levels of flow unsteadiness. Guided by these simulations, an optimization problem was formulated, aiming at suppressing the vortex street at a minimum control effort. To this end, a multi-objective optimization tool was developed, by coupling a CFD code with an optimization code based on genetic algorithms. In this problem the design variables determine the feedback control parameters, as well as the extent of the hydrophobic area. The solution to the problem has demonstrated that vortex street can be substantially suppressed by using a control effort two orders of magnitude lower than that required in corresponding passive control schemes.

References

1. D. Barkley, R.D. Henderson, Three-dimensional Floquet stability analysis in the wake of a circular cylinder. J. Fluid Mech. **322**, 215–241 (1996)
2. S. Cahon, N. Melab, E.G. Talbi, ParadisEO: a framework for the reusable design of parallel and distributed metaheuristics. J. Heuristics **10**, 357–380 (2004)
3. Z. Chen, N. Aubry, Active control of cylinder wake. Commun. Nonlinear Sci. Numer. Simul. **10**, 205–216 (2003)
4. K. Deb, A. Pratap, S. Agarwal et al., A fast and elitist multiobjective genetic algorithm: NSGA-II. IEEE Trans. Evol. Comput. **6**, 182–197 (2002)
5. Y. Delaunay, L. Kaiktsis, Control of circular cylinder wakes using base mass transpiration. Phys. Fluids **13**, 3285–3302 (2001)
6. C.M. Fonseca, P.J. Fleming, An overview of evolutionary algorithms in multiobjective optimization. Evol. Comput. **3**, 1–16 (1995)
7. E. Lauga, T.R. Bewley, Modern control of linear global instability in a cylinder wake model. Int. J. Heat Fluid Flow **23**, 671–677 (2002)

8. D. Legendre, E. Lauga, J. Magnaudet, Influence of slip on the dynamics of two-dimensional wakes. J. Fluid Mech. **633**, 437–447 (2009)
9. M.E. Mastrokalos, C.I. Papadopoulos, L. Kaiktsis, Optimal stabilization of a flow past a partially hydrophobic circular cylinder. Comput. Fluids **107**, 256–271 (2015)
10. D.S. Park, D.M. Ladd, E.W. Hendricks, Feedback control of von Kármán vortex shedding behind a circular cylinder at low Reynolds numbers. Phys. Fluids **6**, 2390–2405 (1994)
11. A. Roshko, On the wake and drag of bluff bodies. J. Aerosp. Sci. **22**, 124–132 (1995)
12. I.W. Seo, C.G. Song, Numerical simulation of laminar flow past a circular cylinder with slip conditions. Int. J. Numer. Meth. Fluids **68**(12), 1538–1560 (2012)
13. P.J. Strykowski, K.R. Sreenivasan, On the formation and suppression of vortex 'shedding' at low Reynolds numbers. J. Fluid Mech. **218**, 71–107 (1990)
14. N. Verplanck, Y. Coffinier, V. Thomy et al., Wettability switching techniques on superhydrophobic surfaces. Nanoscale Res. Lett. **12**, 577 (2007)
15. W.M. Zhang, G. Meng, X. Wei, A review on slip models for gas microflows. Microfluid. Nanofluid. **13**(6), 845–882 (2012)

Numerical Experiment of Flow Characteristics of a Circular Cylinder with Splitter Plate

Yoshifumi Yokoi

Abstract In this study, some investigation about the flow and the fluid force around a circular cylinder with splitter plate in comparatively low Reynolds number ($Re = 500$) were simulated by the numerical calculation. In order to check the effect of the splitter plate, the numerical calculation to which the length of the splitter plate was varied was performed, and change of the characteristic of fluid force based on the splitter plate length was obtained. Based on the obtained result, some numerical simulations in the state where oscillation was given in the direction of the flow supposing unsteady flow were carried out. As a result, even if it was the case of a circular cylinder with splitter plate, it was shown that the lock-in phenomenon arises. The characteristics of fluid force and typical flow patterns were obtained. It was found that an existence of re-circulation flow supplied to the separating shear layer is important in formation of the vortex shedding flow.

1 Introduction

In order to reduce cylinder fluid resistance and generating noise, it is well known that a splitter plate which deters generating of a Karman vortex on a circular cylinder will be installed. Therefore, many related papers treating the splitter plate of many researchers are seen. However, many of those papers are studied at the high Reynolds number region [1, 8]. This is because people needed the large scale vehicle and the fast speed vehicle as a background of an era. So, the research which reduces fluid resistance, and the research which decreases generating noise were necessary. On the other hand, in recent years, reduction of the scale and energy

Y. Yokoi (✉)
Department of Mechanical Engineering, National Defense Academy of Japan,
1-10-20 Hashirimizu, Yokosuka, Kanagawa 239-8686, Japan
e-mail: yokoi@nda.ac.jp; uniuniuni52@yahoo.co.jp

Y. Yokoi
Chair of Fluid Dynamics, Techniche Universität Berlin, Müler-Breslau-Str. 8,
10623 Berlin, Germany

© Springer International Publishing Switzerland 2016

A. Segalini (ed.), *Proceedings of the 5th International Conference on Jets, Wakes and Separated Flows (ICJWSF2015)*,
Springer Proceedings in Physics 185, DOI 10.1007/978-3-319-30602-5_23

saving attract attention, and employment in the region where velocity is low is seen. For example, in the pilotless airplane for reconnaissance, the Reynolds number becomes low in about three or four digits. Depending for the effect of the splitter plate on the Reynolds number is known. However, there are few researches about the case of low Reynolds number region [2, 5]. So, accumulation of much more research is expected. In a nature, the matter in which small animals reduce resistance using own movement skillfully is observed. In order to investigate this matter, the study which was made to carry out rotation oscillation of the splitter plate, or gave elasticity to the splitter plate is reported [6]. Moreover, the study which took the galloping phenomenon into consideration on the circular cylinder with a splitter plate is also reported [7]. Generally, the flow velocity changeful and it is not constant (unsteady). However, most researches are carried out supposing the uniform and steady flow. There are few studies which performed supposing the unsteady flow. The phenomenon which is not seen by the steady flow may often occur by the unsteady flow. In a design, it is very important to estimate the fluid force of the structure set in the flow. So, accumulation of the knowledge of the unsteady flow in low Reynolds number case is important. In this study, the flow around the circular cylinder with splitter plate in unsteady flow condition was investigated by use of numerical simulation at the Reynolds number $Re = 500$.

2 Numerical Calculations

2.1 Calculation Apparatus and Method

The numerical experiment apparatus was consisted of simulation software and a notebook type computer (NEC; LaVie LC958/T) as calculation hardware which are on the market. The software which named 'UzuCrise 2D ver.1.1.3 rev.H (College Master Hands Inc., 2006)' is used. This software used the vortex method which is based on the Lagrangian analysis. Since the vortex method is the grid-less method, it is suitable for the unsteady problem of such moving boundary. The vortex method is a direct viscid-inviscid interaction scheme, and the emanation of velocity shear layers due to boundary layer separation is represented by introduction of discrete vortices with viscous core step by step of time. In the present study, the flow was assumed incompressible and two-dimensional flow field. The configuration of the circular cylinder with splitter plate was represented by vortex panels which used the boundary element method. The separating shear layers were represented the discreet vortices, which were introduced at the separation points. The details of calculation technique of vortex method and accuracy of calculation are shown in Kamemoto [3, 4].

2.2 Calculation Parameters and Procedure

The main parameters of numerical experiment in this study were a splitter length ratio *SL/d*, an oscillation amplitude ratio 2*a/d*, an oscillation frequency ratio f/f_K and the Reynolds number *Re*. The splitter length ratio *SL/d* is six kinds, and those values are 0.5, 1.0, 2.0, 3.0, 4.0 and 5.0, respectively. Here, the number of vortex panels changed with length of the splitter plate, and the number of used vortex panels was from 60 panels to 204 panels (numbers of vortex panel: 60, 76, 108, 140, 172 and 204). The oscillation amplitude ratio 2*a/d* is two kinds, and those values are 0.25 and 0.5, respectively. The oscillation frequency ratio f/f_K is six kinds, and those values are 0.5, 1.0, 1.5, 2.0, 2.5 and 3.0, respectively. The Reynolds number is 500 in one kind. The Reynolds number is based on main flow velocity U (= 0.04 m/s), cylinder diameter d (= 16 mm) and kinematic viscosity of water ($\nu = 1.2553 \times 10^{-6}$ m^2/s). Here the natural Karman vortex shedding frequency was $f_K = 0.6489$ Hz.

The calculation procedure is the following, at first step, comparison of the previous result and the present calculation result was performed in steady flow around a circular cylinder with splitter plate. In next step, the characteristics of the fluid force when varying the length of the splitter plate was investigated. Based on those results, at the third step, the numerical investigation of flow around a circular cylinder with splitter plate which is oscillating in the direction of the flow was performed. Every calculation continued to until non-dimensional time $T = 200$.

3 Results and Discussions

3.1 Stationary Cylinder Case

In order to verify the calculation software to be used, the experimental result and calculation result of a stationary circular cylinder were compared. The drag oscillation lurking in periodic oscillation and lift oscillation of the lift produced by formation of a Karman vortex street is expressed. The following results were obtained after non-dimensional time $T = 150$. The average value of drag coefficient was $C_{DAVE} = 1.08$ and the root mean square value of amplitude of drag coefficient was $A_{CD} = 0.15$. The average value of lift coefficient was $C_{LAVE} = 0.00$ and the root mean square value of amplitude of lift coefficient was $A_{CL} = 0.73$. The average Strouhal number for which it determined from the lift oscillating period T was $St_{AVE} = 0.26$. (Here, $St = fd/U = d/\Delta tU = 1/T$). When the Reynolds number is $Re = 500$, it is known that the experimental value of Strouhal number *St* is about 0.2. Although it seems that this calculation result is highly calculated as compared with an experimental result, it seems that this calculation has obtained the comparatively good calculation result since a two dimensional calculation result becomes higher than an experimental result about 30 to 40 %. When the Karman

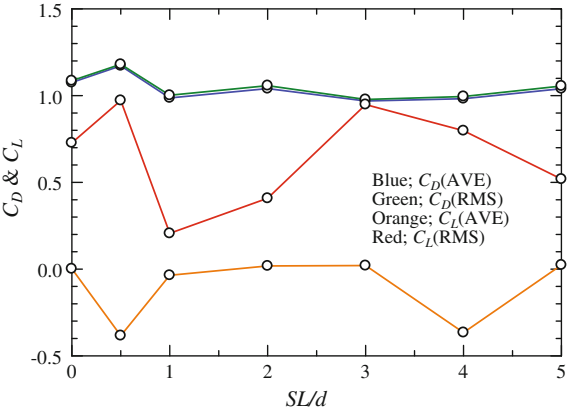


Fig. 1 The variation of drag coefficient C_D and lift coefficient C_L by splitter length ratio *SL/d*. Legends in figure; the *blue*, the *green*, the *orange* and the *red lines* show C_D(AVE), C_D(RMS), C_L(AVE) and C_L(RMS), respectively

vortex shedding frequency f_K was calculated from the average value of Strouhal number, the Karman vortex shedding frequency was $f_K = 0.6489$ Hz.

The length of splitter plate was varied and numerical computation was performed. As a result of the numerical experiments, the characteristics of fluid force act on the circular cylinder with splitter plate when varying the length of splitter plate without cylinder oscillation were obtained, as shown in Fig. 1. When it takes notice of the change of drag coefficient, it was found that the *SL/d* range from 1 to 4, values of drag coefficient were less than the value of drag coefficient of natural cylinder's case. On the other hand, when change of the lift coefficient is seen, it was found that the RMS values of the lift coefficient are decreasing by control of the Karman vortex shedding, in the cases of $SL/d = 1$, 2 and 5. It was confirmed by installing the splitter plate that lift generating is controlled.

3.2 Oscillating Cylinder Case

In the situation where the lift is controlled with the splitter plate, the numerical experiments at the time of making it oscillate in the direction of the flow were performed. Here, it was referred to as $SL/d = 2$. Some interesting results were obtained by oscillating the circular cylinder with splitter plate. The lock-in phenomenon was obtained even if in this case. Figure 2 shows the time histories of fluid force act on the cylinder and flow pattern at the frequency ratio $f/f_K = 2.0$ and the amplitude ratio $2a/d = 0.25$. It is shown that oscillation of the drag coefficient synchronizes with oscillation of the circular cylinder completely. And it can be seen that the oscillating period of lift coefficient is twice the oscillating period of drag coefficient. Since the lift coefficient is larger when the magnitudes of both amplitudes are compared, it becomes an alternate vortex shedding type. Although it is a simultaneous vortex shedding form both separating points on the surface of circular cylinder, an aspect that the vortex of a mushroom section is alternately discharged

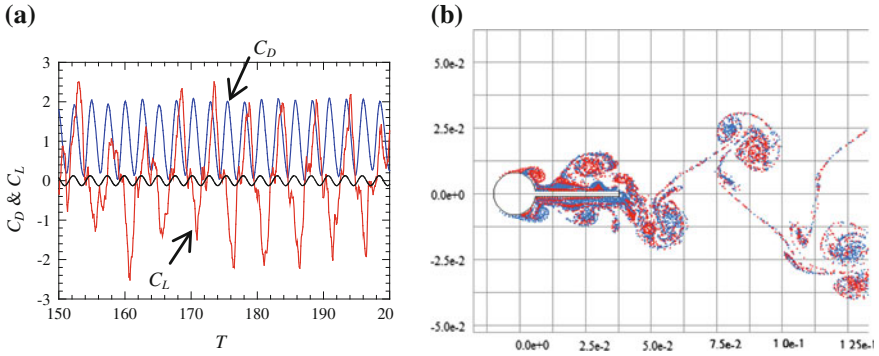


Fig. 2 The flow characteristics in the oscillating frequency ratio $f/f_K = 2.0$. **a** Time histories of drag (blue line) and lift (red line) coefficients and cylinder motion (black line). **b** Instantaneous flow pattern at non-dimensional time $T = 199.68$

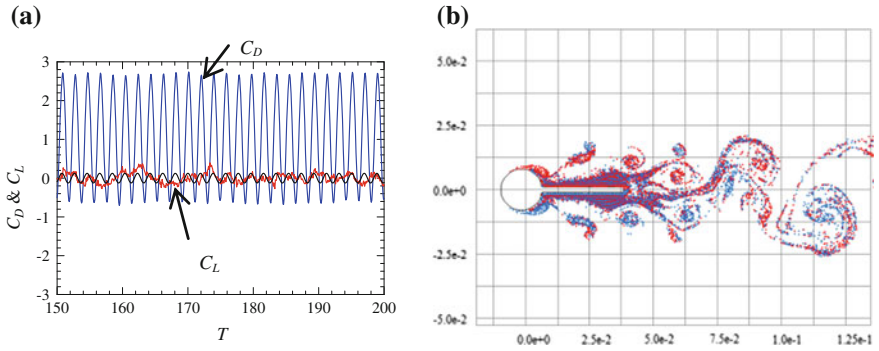


Fig. 3 The flow characteristics in the oscillating frequency ratio $f/f_K = 3.0$. **a** Time histories of drag (blue line) and lift (red line) coefficients and cylinder motion (black line). **b** Instantaneous flow pattern at non-dimensional time $T = 199.68$

at the splitter plate edge is shown. Such a flow pattern is shown by reference 6 and is one of the interesting phenomena. Figure 3 shows the time history of fluid force and the flow pattern at the oscillating frequency ratio $f/f_K = 3.0$ and the amplitude ratio $2a/d = 0.25$. Although the oscillation of drag coefficient synchronizes with oscillation of circular cylinder completely, it is shown that the oscillation of lift coefficient is not certain. Since the drag coefficient is larger when the magnitudes of both amplitudes are compared, it becomes the simultaneous vortex shedding type. In the reference 6, it was described that if the length of the splitter plate increases, the cylinder rotating angle is decreasing. When the circular cylinder with a splitter plate is oscillated in the direction of the flow, it is interesting that an equivalent phenomenon is obtained. Development of the boundary layer and the boundary layer separation are explained by the flow from the main flow side in many cases.

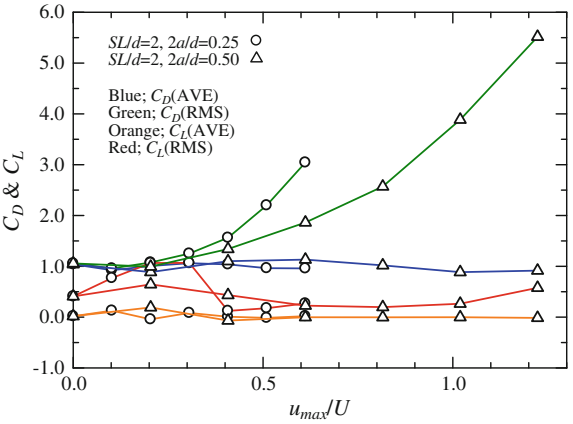


Fig. 4 The variation of drag coefficient C_D and lift coefficient C_L by velocity ratio u_{max}/U. Legends in figure; the *blue*, the *green*, the *orange* and the *red lines* show C_D(AVE), C_D(RMS), C_L(AVE) and C_L(RMS), respectively. Two kinds of the amplitude ratio are distinguished with the symbols of ○ mark ($2a/d = 0.25$) and Δ mark ($2a/d = 0.5$)

However, explanation is impossible only by the flow from the main flow side about the discharge mechanism of a separating shear layer. It is necessary to consider participation of a re-circulating flow. Since the re-circulating flow joins the flow from the mainstream side in case a vortex is alternately formed in formation of the Karman vortex, it is natural consideration to think that the vortex is separated. The reason Karman vortex formation is controlled by preparing the splitter plate is because supply of the re-circulating flow in the separating position is intercepted. If an in-line forced oscillation is given to the circular cylinder, it will become the appearance by which the re-circulating flow is supplied to the separation point, and it becomes the appearance by which two vortexes are simultaneously formed in both sides of cylinder. Accordingly, it means that it was confirmed that existence of a re-circulation flow carries out an important role in vortex discharge.

The variation of the fluid force at the time of oscillation is shown in Fig. 4. The abscissa is a velocity ratio u_{max}/U and it shows the ratio of the maximum movement speed of cylinder and the main flow velocity. Here, the velocity ratio is defined as $u_{max}/U = (2a/d)(f/f_K)\pi\mathrm{St}$. Although the average value of a lift coefficient C_L(AVE) and the average value of a drag coefficient C_D(AVE) were almost changeless, the magnitude of a lift coefficient and the magnitude of a drag coefficient were changing with velocity ratios.

4 Conclusions

Numerical experiments about the vortex flow from a circular cylinder with splitter plate which is oscillating in the direction of the flow were performed by use of vortex method. The following conclusions were obtained.

(1) In the steady flow, it was confirmed that the lift generating is restricted with the splitter plate.

(2) If oscillation is given, even if it is a circular cylinder with splitter plate, the lock-in phenomenon will arise.
(3) In the vortical discharge phenomenon, it was confirmed that a re-circulation flow carries out an important role.

Acknowledgments This study was performed while an author stays in TU-Berlin (Berlin, Germany). Gratitude is expressed to Professor Dr.-Ing. Christian Oliver Paschereit and Dr.-Ing. Christian Navid Nayeri which offered calculation environment. And it is thankful to staff all the persons concerned of the National Defense Academy of Japan which gave the opportunity which can perform research activities in TU-Berlin.

References

1. E.A. Anderson, A.A. Szewczyk, Effects of a splitter plate on the near wake a circular cylinder in 2 and 3-dimensional flow configurations. Exp. Fluids **23**, 161–174 (1997)
2. A. Inasawa, T. Hasaka, M. Asai, Stability of flows behind a circular cylinder with a splitter plate. Trans. Jpn. Soc. Mech. Eng. **74–745**, 1903–1909 (2008)
3. K. Kamemoto, The expandability of the vortex method as a turbulent flow model (the first part: to think a basic of vortex method). Comput. Fluid Dyn. **2–1**, 20–29 (1993)
4. K. Kamemoto, The expandability of the vortex method as a turbulent flow model (the latter part: to think a basic of vortex method). Comput. Fluid Dyn. **2–2**, 28–39 (1994)
5. K. Kwon, H. Choi, Control of laminar vortex shedding behind a circular cylinder using splitter plates. Phys. Fluids **8**, 479–486 (1996)
6. U. Lacis, N. Brosse, F. Ingremeau, A. Mazzino, F. Lundell, H. Kellay, S. Bagheri, Passive appendages generate drift through symmetry breaking. Nat. Commun. **5**, 5310 (2014)
7. A. Orchini, H. Kelly, A. Mazzino, Galloping instability and control of a rigid pendulum in a flowing soap film. J. Fluid Struct. **56**, 124–133 (2015)
8. A. Roshko, Experiments on the flow past a circular cylinder at very high Reynolds number. J. Fluid Mech. **10**, 345–356 (1961)

Wake Structures of a Particle in Straight and Curved Flows

Toshiaki Fukada, Shintaro Takeuchi and Takeo Kajishima

Abstract To investigate the effect of non-axisymmetric shear on the wake structure of a particle, the flows around a single spherical particle in the following two kinds of shear flows are simulated: parallel (streamwise) shear and curved (cross-streamwise) shear flows. The ranges of the particle Reynolds number and the shear Reynolds number are determined by assuming that the particle size is comparable to the Kolmogorov length scale in a turbulent flow. The effect of the parallel shear on the perturbation velocity is small. For the curved shear, the wake region is deflected in space. However, the width of the wake is almost unchanged near the particle. For the fixed and translating particle cases, even if the streamlines of the undisturbed flow relative to the particle translation are similar to each other, the difference of the ambient pressure gradient makes the difference of the velocity distributions.

1 Introduction

Predicting the interaction between particles and a turbulent flow is an important and challenging subject. Although there are many experimental and numerical studies of dilute dispersed multiphase turbulence [4, 8–10], numerical simulation still cannot sufficiently predict the turbulence modulation. Especially when the particle size is comparable to the Kolmogorov length scale, even in a very dilute case such as at a volume fraction of $O(10^{-4})$, the effect of the particle is significant [2, 6].

A point particle approach considering only the translating momentum exchange cannot capture the turbulence modulation [4, 6]. The flow structure itself in the wake and the boundary layer of the particle should be modeled for a large scale multiphase flow simulation. A reliable model of the local flow structure would lead to the correct prediction of a larger scale vortical structure. Moreover, the local structure plays an important role for the energy dissipation [5]. However, the research of the wake structure is limited mainly to the case of uniform flow [11].

T. Fukada (✉) · S. Takeuchi · T. Kajishima
Department of Mechanical Engineering, Osaka University, Osaka, Japan
e-mail: fukada@fluid.mech.eng.osaka-u.ac.jp

© Springer International Publishing Switzerland 2016

A. Segalini (ed.), *Proceedings of the 5th International Conference on Jets, Wakes and Separated Flows (ICJWSF2015)*,
Springer Proceedings in Physics 185, DOI 10.1007/978-3-319-30602-5_24

Lift force and torque of the particle in a non-axisymmetric flow determine the particle motion. The effect of the streamline curvature of the undisturbed flow is significant for the fluid force and the torque [3, 7]. In a simulation of particle-dispersed multiphase flow, we need to know the undisturbed flow around each particle to apply a fluid force model. However, the prediction is difficult because the simulated flow includes disturbances due to the particles [1, 2]. Additionally, even when the undisturbed flow is known, the fluid force is not fully understood so far: for example, the surface stress distribution of the particle is strongly related to the wake structure, however, the relation is not established sufficiently. Therefore, the knowledge of the flow structure around the particle in non-axisymmetric flows is important for predicting both the undisturbed flow and the fluid force.

In this study, we focus on how the wake structure of a single particle is influenced by non-axisymmetric shear flows where the streamlines are either straight or curved. The distribution of the perturbation velocity due to the particle is obtained by the computational simulation and the result is compared to that of the uniform flow case.

2 Problem Statement

Figure 1 shows the schematic images of this study. We consider the following two kinds of shear flows: parallel shear flow ($\mathbf{U} = V\mathbf{e}_x + \gamma y\mathbf{e}_x$) and curved shear flow ($\mathbf{U} = V\mathbf{e}_x - \gamma x\mathbf{e}_y$), where $\mathbf{e}_\alpha$ is the unit vector in α-direction. The spherical particle of diameter d is fixed at the origin of the Cartesian (x, y, z) coordinate system, represented by O in the figure. To investigate the effect of the ambient pressure gradient on the wake structure, a case of a translating particle is also considered, where the flow field is $\mathbf{U} = -\gamma x\mathbf{e}_y$ and the particle is translating toward the origin at the constant velocity $-V\mathbf{e}_x$. In this case, when the particle centre reaches the origin, the streamlines of the undisturbed flow relative to the particle translation are the same as those of the curved shear flow.

The three-dimensional Navier-Stokes equation and the continuity equation of the incompressible fluid are employed as the basic equations of this simulation. The no-slip boundary condition is imposed on the particle surface. We use the body-fitted

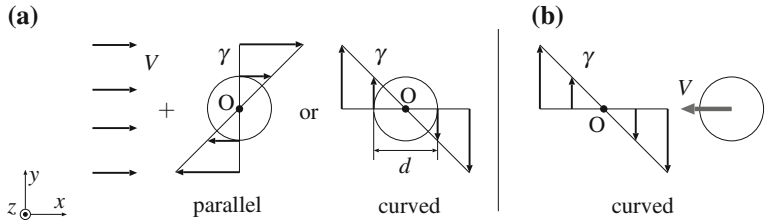


Fig. 1 Schematic images of shear flows. Undisturbed shear and uniform flow components are represented by *arrows*

grid system and the flow field is solved based on a finite difference method. The simulation is performed for the particle Reynolds numbers of $\mathrm{Re}_p = Vd/\nu = 10$ and 40 and the shear Reynolds numbers of $\mathrm{Re}_\gamma = \gamma d^2/\nu = 0, 1, 2$ and 4, where ν is the kinematic viscosity. These values are determined based on the magnitudes of the velocity and the vorticity obtained from our preliminary direct numerical simulation (DNS) of an isotropic homogeneous turbulent flow ($\mathrm{Re}_\lambda = 76$) by assuming that the Kolmogorov length and the particle diameter are comparable. For the fixed particle cases, the flow fields reach steady state under the conditions in this study. For the translating particle case, the initial particle position is set to $x/d = 25$. According to our preliminary test, the extension of the initial position to $x/d = 40$ does not change the results of the velocity and pressure field for the translating particle case.

3 Results and Discussion

3.1 Parallel Shear Flow

The perturbation velocity field due to the particle is represented as $\mathbf{u}' = u_x'\mathbf{e}_x + u_y'\mathbf{e}_y + u_z'\mathbf{e}_z = \mathbf{u} - \mathbf{U}$, where $\mathbf{u}$ is the simulated flow field. Figure 2a shows $-u_x'/V$ and $-u_y'/V$ along the x-axis for the parallel shear flow of $\mathrm{Re}_p = 10$. All the plots of $-u_x'/V$ fall on those of the uniform flow ($\mathrm{Re}_\gamma = 0$) case, suggesting that the x-component of the perturbation velocity is dominant. Figure 2b shows $-u_x'/V$ along the line parallel to y-axis and passing through the point $(2d, 0, 0)$. The distributions of $-u_x'/V$ for different Re_γ cases are similar to each other. The perturbation velocity of $\mathrm{Re}_p = 40$ case is also similar to that of the uniform flow of the same Re_p case.

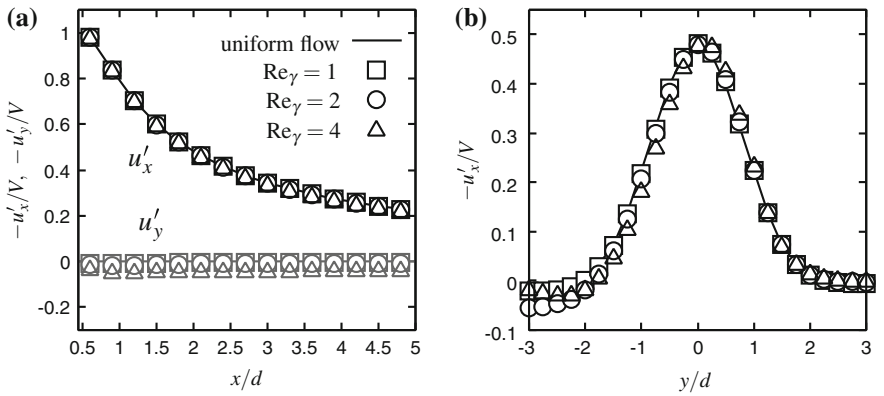


Fig. 2 Distribution of perturbation velocity components for parallel shear flow of $\mathrm{Re}_p = 10$: **a** along x-axis; **b** along the line parallel to y-axis through the point $(2d, 0, 0)$. *Black* and *gray* plots represent $-u_x'/V$ and $-u_y'/V$, respectively

3.2 Curved Shear Flow

In this section, for the translating particle case, only the moment when the particle centre reaches the origin is reported. We pick up some representative points in the wake to investigate the deflection of the wake in the curved shear flow as follows. We consider some concentric circles at the origin in x-y plane. The point of the largest $-u_x'$ on each circle (hereafter referred to as "strongest-u_x'-fluctuation point") is sought as the point that represents the wake structure.

Figure 3 shows the coordinates of the strongest-u_x'-fluctuation points. Note that the vertical axis is normalised as $y/(d\mathrm{Re}_\gamma)$. Assuming that virtual tracers are continuously released from the particle centre and completely follow **U**, the streaklines of the tracers are $y/d = 0.5\ \mathrm{Re}_\gamma (x/d)^2/\mathrm{Re}_p$ for the fixed particle case and $y/d = \mathrm{Re}_\gamma (x/d)^2/\mathrm{Re}_p$ for the translating particle case. These lines are also plotted in Fig. 3. For both fixed and translating particle cases, the points fall near the streaklines of the tracers. Most of the strongest-u_x'-fluctuation points are slightly shifted to $-x$-direction compared to the streaklines because the x-component of the perturbation velocity actually has a negative value.

Figure 4a shows $-u_x'/V$ along the streaklines. The horizontal axis l_s is the length along a streakline. In this graph, the perturbation velocity deviates from that of the uniform flow case compared to the case of the parallel shear flow. The deviation of $-u_x'/V$ becomes larger as Re_γ increases.

The width of the wake is investigated at the referential point P which is located $2d$ downstream of the particle along the streakline. Figure 4b shows $-u_x'/V$ along the line parallel to the y-axis and passing through the point P. The horizontal axis l_y is the distance from the point P in the y-direction. The deviation of $-u_x'/V$ becomes larger as Re_γ increases. However, the entire distribution is similar to that of the uniform flow case. Therefore, the width of the wake region is insensitive to the curved shear though the wake is weakly deflected.

For the fixed particle case, u_y' in the wake region is smaller than that of the translating particle case as shown in Fig. 4a. The reason for this difference is explained

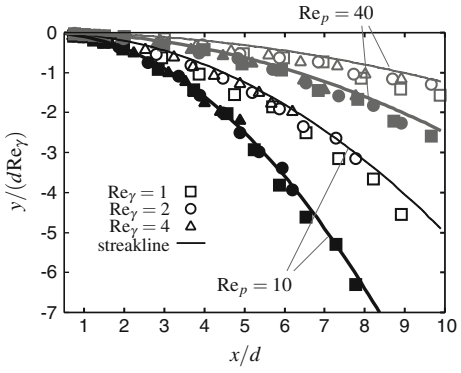


Fig. 3 Strongest-u_x'-fluctuation points and streaklines of virtual tracers. Open and closed symbols represent results of fixed and translating particle cases, respectively. *Black* and *gray* plots represent results of $\mathrm{Re}_p = 10$ and 40, respectively

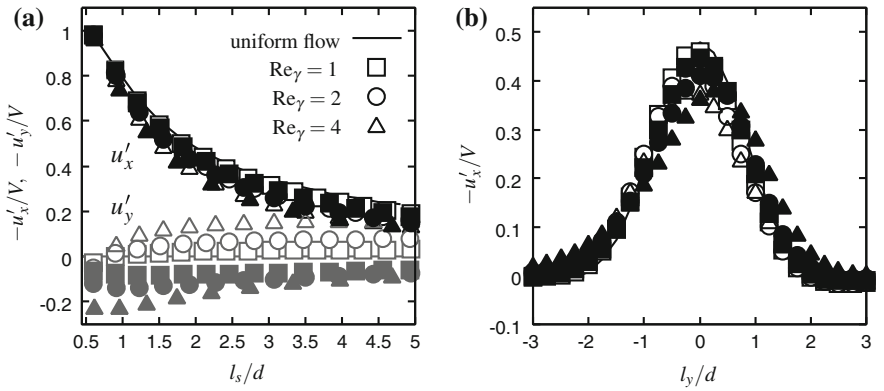


Fig. 4 Distribution of perturbation velocity components for curved shear flow of $\mathrm{Re}_p = 10$: **a** along streaklines; **b** along the line parallel to *y*-axis through the point P. *Black* and *gray* plots represent $-u'_x/V$ and $-u'_y/V$, respectively. Open and closed symbols represent results of fixed and translating particle cases, respectively

as follows. There is an ambient pressure gradient to keep the steady curved flow for the fixed particle case. For the steady inviscid flow, the pressure gradient normal to the velocity is equal to $\rho\kappa q^2$, where ρ is the fluid density, κ is the curvature of the streamline and q is the magnitude of the velocity. In the wake region, the local rotating angle of the velocity along the streamline (i.e. $\kappa\Delta l_s$) becomes larger under the ambient pressure gradient. This pressure gradient makes u'_y smaller. On the other hand, for the translating particle case, there is no ambient pressure gradient to influence the wake.

The shear stress on the particle surface is drastically influenced by the difference of u'_y between the two cases. To evaluate the effect of this difference, the torque coefficient C_T is defined as

$$C_T = -\frac{T_z}{\frac{1}{2}\pi\mu d^3\gamma}, \tag{1}$$

where T_z is the z-component of the torque and μ is the viscosity of the fluid. Note that the value of T_z is always negative in this study. For the Stokes flow, C_T is 1. For the fixed particle case, $C_T = 1.34$ and 2.07 for $\mathrm{Re}_p = 10$ and 40 under $\mathrm{Re}_\gamma = 4$, respectively. On the other hand, for the translating particle case, $C_T = 1.00$ and 1.23 for $\mathrm{Re}_p = 10$ and 40 under $\mathrm{Re}_\gamma = 4$, respectively. The surface shear stress in the downstream side is mainly related to u'_y, and is affected by the ambient pressure gradient in the curved shear flow, which makes C_T larger.

4 Conclusion

To investigate the effect of non-axisymmetric shear on the wake structure, the flows around a spherical particle in a parallel shear flow and a curved shear flow are simulated. For the curved shear flow, fixed particle and translating particle conditions are considered.

The perturbation velocity is unlikely to be influenced by the parallel shear. However, the wake region is deflected by the curved shear. The wake stretches almost along the streakline of the virtual tracers which are completely advected with the undisturbed velocity. Focusing on the area within the distance of $O(d)$ from the particle, the width of the wake is almost unchanged by the parallel and the curved shear. Between the fixed and translating particle cases, the distributions of u_y' are different due to the difference of the ambient pressure gradient. This leads to the difference in the torque of the particle between the two cases.

Acknowledgments One of the authors, T.F., gratefully acknowledges the financial support of the Japan Society for the Promotion of Science (JSPS) KAKENHI Grant No. 15J00439. The authors gratefully acknowledge the financial supports by Mr. Yibin Lin (Hangzhou, China).

References

1. S. Balachandar, A scaling analysis for point-particle approaches to turbulent multiphase flows. Int. J. Multiphase Flow **35**, 801–810 (2009)
2. S. Balachandar, J.K. Eaton, Turbulent dispersed multiphase flow. Ann. Rev. Fluid Mech. **42**, 111–133 (2010)
3. J.J. Bluemink, D. Lohse, A. Prosperetti, L.V. Wijngaarden, A sphere in a uniformly rotating or shearing flow. J. Fluid Mech. **600**, 201–233 (2008)
4. M. Boivin, O. Simonin, K.D. Squires, On the prediction of gas-solid flows with two-way coupling using large eddy simulation. Phys. Fluids. **12**, 2080–2090 (2000)
5. T.M. Burton, J.K. Eaton, Fully resolved simulations of particle-turbulence interaction. J. Fluid Mech. **545**, 67–111 (2005)
6. J.K. Eaton, Two-way coupled turbulence simulations of gas-particle flows using point-particle tracking. Int. J. Multiphase Flow **35**, 792–800 (2009)
7. T. Fukada, S. Takeuchi, T. Kajishima, Effects of curvature and vorticity in rotating flows on hydrodynamic forces acting on a sphere. **58**, 292–300 (2014)
8. W. Hwang, J.K. Eaton, Homogeneous and isotropic turbulence modulation by small heavy ($S_t \sim 50$) particles. J. Fluid Mech. **564**, 361–393 (2006)
9. A.D. Paris, J.K. Eaton, Turbulence Attenuation in a Particle-Laden Channel Flow. Report TSD-137, Department of Mechanical Engineering, Stanford University (2001)
10. K.D. Squires, J.K. Eaton, Particle response and turbulence modification in isotropic turbulence. Phys. Fluids A **2**, 1191–1202 (1990)
11. J.S. Wu, G.M. Faeth, Sphere wakes in still surroundings at intermediate Reynolds numbers. AIAA J. **31**, 1448–1455 (1993)

Numerical Flow Simulations of a Flexible Plate Attached to an Obstacle in Crossflow

Lukas Schickhofer, Bernhard Semlitsch and Mihai Mihăescu

Abstract For biomedical applications with relevance to the human upper respiratory tract, the knowledge of the tissue behavior when exposed to a particular flow field is crucial. Moreover, it is important to quantify how the tissue properties affect the biomechanics of the obstruction. Since in-vivo measurements are often not possible, this is assessed computationally by using simplified geometries. The present study is devoted to the analysis of a fluid-structure interaction scenario relevant to obstructive sleep apnea (OSA) and snoring. The dependence of the solution on the most critical parameters of the system is assessed, with the aim of quantifying their influence on tissue self-excitation and obstruction dynamics.

1 Introduction

One of the challenges involved in biomedical investigations are the material properties of the tissue. Measurements of in-vivo properties are not trivial and sometimes even not possible. Besides, the material characteristics and geometry may vary between subjects. Nonetheless, reasonable if not exact values for these quantities are essential for an accurate numerical prediction of physiological events.

Episodes of total or partial obstruction of the upper airways, like in the case of patients suffering from obstructive sleep apnea (OSA), can have serious consequences on the quality of life of the affected subjects. The soft tissue at the level of the pharyngeal airway can obstruct the respiratory tract under certain circumstances (e.g. muscle tone relaxation during sleep or temporal upper respiratory infections) and thereby limit the amount of oxygen reaching the lungs. The resulting decreased oxygen concentration in the blood leads to weakening or restless sleep. This is the cause for daytime sleepiness and inability to concentrate for patients with OSA. In some severe cases of sleep apnea, where non-surgical treatment plans fail, surgi-

L. Schickhofer (✉) · B. Semlitsch · M. Mihăescu
BioMEx, Department of Mechanics, KTH Royal Institute of Technology,
Osquars Backe 18, 100 44 Stockholm, Sweden
e-mail: schic@mech.kth.se

© Springer International Publishing Switzerland 2016

A. Segalini (ed.), *Proceedings of the 5th International Conference on Jets, Wakes and Separated Flows (ICJWSF2015)*,
Springer Proceedings in Physics 185, DOI 10.1007/978-3-319-30602-5_25

cal procedures are required. Some of these treatments concern reshaping of the soft palate. Nonetheless, determining the way in which the soft palate is reshaped, so that this will lead to the best pertinent cure, is not straightforward. Computational flow simulations based on realistic, patient-specific respiratory tracts can assist to select the optimal intervention [1]. The unawareness of the exact material property values and the precise geometry leads to an uncertainty to predict physiological events, such as apneas (blockage events of the human airway). More accurate statistical assessment of the tissue characteristics could lead to more reliable predictions via numerical tools.

The current investigation is devoted to evaluating the effect of various parameters on flow field and static pressure fluctuation generation downstream of a flexible plate attached to a bluff body (resembling the soft palate attached to the hard palate). The chosen setup mimics the geometrical circumstances leading to the occurrence of snoring. The long term aim of this study is to quantify the significance of the individual parameters related to geometry, flow, and tissue for the probability to cause severe obstructions in the model tract.

2 Methods

For the outlined goal unsteady simulations of the two-dimensional Navier-Stokes equations around a body with an appended element are performed using a finite volume solver. The appended element (mimicking the soft palate) is flexible and can deform according to the loads generated by the flow, with the deformation being calculated using a linear formulation based on the solid stress displacement. A formally third-order spatial discretization scheme has been used for the convective terms and a second-order implicit approach with at least 15 inner iterations has been applied for time integration. The time step has been chosen such that the CFL criterion is fulfilled. The used mesh is equipped with several refinement stages around the obstacle (cf. Fig. 1b) as well as towards the domain boundaries. All the solid surfaces are considered as no-slip walls. A developed laminar flow profile with the mean velocity $\overline{u}$ is imposed at the inlet and the pressure is specified at the outlet.

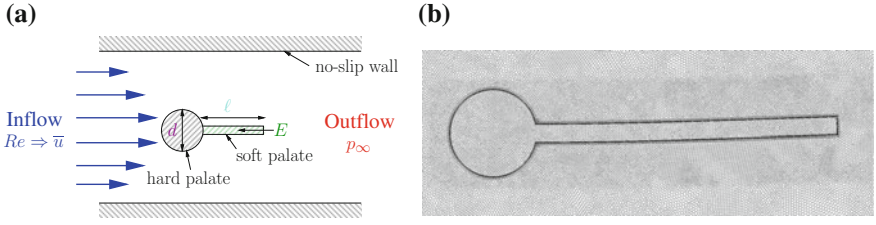


Fig. 1 A sketch of the simulated geometry is illustrated in (**a**) and an example of the numerical grid (in a deformed state) is shown in (**b**)

The geometrical setup is sketched in Fig. 1a and the investigation parameters are indicated. These are the length of the flexible element ℓ, its modulus of elasticity E, and the Reynolds number Re. The Reynolds number is based on the obstacle diameter d, the mean inlet velocity $\overline{u}$, and the kinematic viscosity ν of air at room temperatures. The obstacle diameter d is one-fourth of the channel height and the length of the flexible element ℓ corresponds to 3.5 times the obstacle diameter d.

3 Results

The *von Kármán* vortex street is a classical flow phenomenon occurring downstream of a bluff body in a fluid flow. In a certain range of flow Reynolds numbers, a continuous vortex trail occurs, which can interact with the obstacle. The relation of the shedding frequency of the vortices to the crossflow velocity and the bluff body diameter is known as the Strouhal number St, which is approximately constant 0.2−0.21 over a wide range of Re [2]. The alternating lateral shedding of vortices induces unsteady pressure loads on the body, which can cause vibrations and even acoustic noise generation. If the shedding vortices are induced with the same frequency as the natural frequency of the structure, the resulting excitation can lead to resonance.

This phenomenon is also relevant for the human snoring, which is generated by a strong vibration of the soft palate. In order for it to occur, an airflow through both nose and mouth is required.

The dominant shedding frequencies of a soft palate, which has a high elastic modulus compared to values from literature [3], are tabulated in Table 1 for different Re and lengths. For the investigation of solely the cylinder, a typical von Kármán vortex street is observed for all Re investigated, where St is slightly increased with higher Re. The reported St numbers lie above the values for a cylinder in free stream. However, for high blockage ratios of the obstacle diameter with regards to the channel height, the St values can significantly increase [4].

The attachment of a flexible plate to the cylinder can considerably influence the flow downstream of it. The plate separates the eddies shed from the cylinder and

Table 1 List of the most dominant shedding frequencies observed for $E = 0.1\ MPa$ in terms of the Strouhal number $St = f \cdot d/\overline{u}$

Length	$Re = 100$	$Re = 150$	$Re = 300$	$Re = 500$	$Re = 1000$
Without	0.30	0.31	0.33	0.35	0.35
$1/4\ \ell$	0.32	0.32	0.35	0.18°	⋄
$1/2\ \ell$	–	0.36	0.35	0.34	0.28
$3/4\ \ell$	–	–	0.27	0.27	⋄
$1\ \ell$	–	–	0.24°	0.22°	⋄

The dash—points out the occurrence of a steady flow field and the symbol ⋄ stands for the observation of mostly unorganized broadband fluctuations

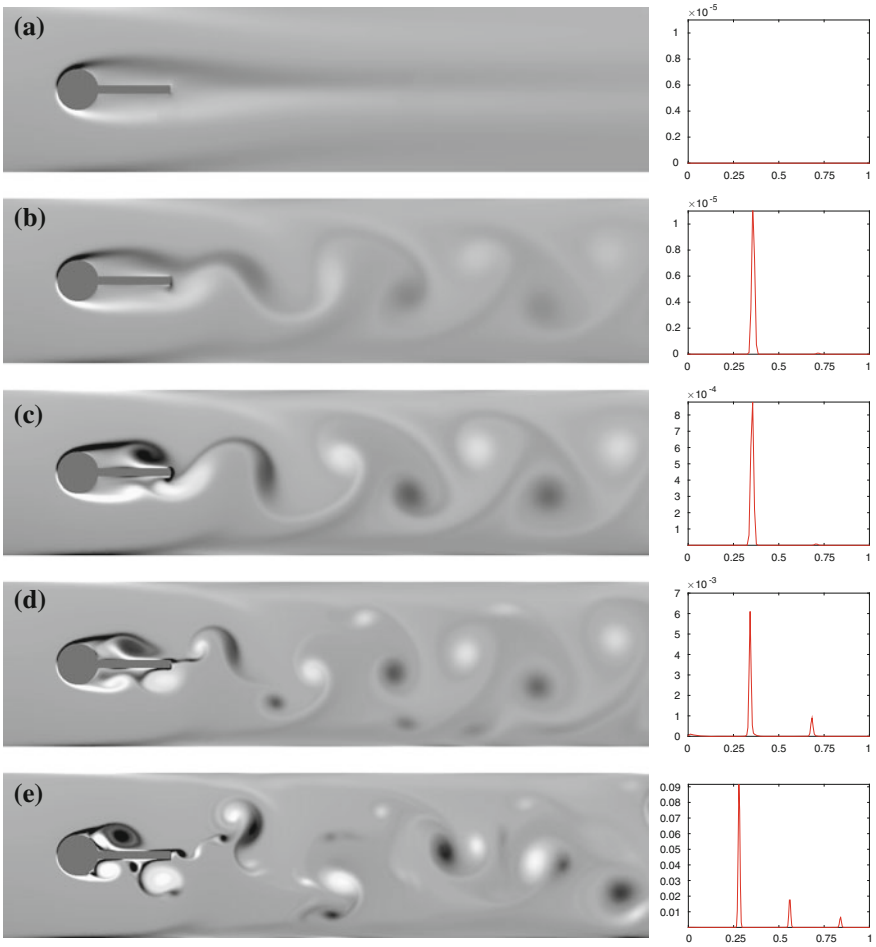


Fig. 2 The effect of *Re* increase on the flow structures in terms of normalized vorticity is illustrated for an element length of $1/2\ \ell$. The power spectral density properties of the pressure time history recorded in a probe located directly below the element tip are illustrated in the right column as a function of *St*. **a** Re = 100 St ≈ 0, **b** Re = 150 St = 0.36, **c** Re = 300 St = 0.35, **d** Re = 500 St = 0.34, **e** Re = 1000 St = 0.28

inhibits thereby their direct interaction. The formation of a vortex trail can be suppressed by using a flexible element of sufficient length and for low enough *Re*. Table 1 reports that a vortex trail at a *Re* of 100 occurs only for the cases without a flexible plate and for the case having the smallest flexible element length (1/4 of the maximum length ℓ). Figure 2a reveals a stable laminar flow field associated with a *Re* of 100 and a soft palate length of $1/2\ \ell$. The possible roll-up of the vorticity sheet is delayed to a location downstream of the flexible element, where the vorticity is not strong enough anymore to cause vortex shedding. A flow at a slightly higher

Reynolds number ($Re = 150$) evolves for the same configuration in a typical von Kármán vortex shedding downstream of the soft palate, as depicted in Fig. 2b. Nonetheless, when the length of the palate is increased from $1/2\ \ell$ to $3/4\ \ell$, a laminar flow field can also be observed for this *Re*. The vorticity induced at the obstacle walls reaches the center of the channel almost at the end of the flexible element, where it interacts with the vorticity shed from the other side. Nonetheless, an apparent vortex street is not initiated until some distance further downstream. By increasing *Re* to 300, a vortex is formed in the generated shear layer much sooner, ahead of the trailing edge of the flexible element. The newly established vortex evolves when propagating downstream, interacts with the vorticity associated with the vortex formed on the other side of the flexible element and a vortex trail is reached faster. Figure 2 illustrates clearly that the further *Re* is increased, the closer to the obstacle these large vortices are initiated. For the higher *Re* investigated, the generation of these large vortices arises that close to the cylinder that strong, counter-rotating, smaller vortical flow structures are created just downstream of the cylinder and are convected downstream. These small intermediate vortices can be clearly identified in Fig. 2d, e and can also be noted in the higher harmonics of the spectral properties monitored in the probe below the element tip. On the first view, Fig. 2e does not seem to show any regular repetitive pattern for the highest simulated *Re* case. Nonetheless, the spectral evaluation of the probe signal reveals a dominant peak at a *St* of 0.28 without any broadband signature. The further analysis of the image series reveals that the initial shedding and the propagation takes place at regular intervals. Small cycle transformations can be recognized only towards the end of the channel. Nevertheless, for smaller and larger flexible element lengths, broadband spectra without any apparent order are observed at this *Re* of 1000.

The shedding of the vortices can be significantly influenced by the confinement. A laminar developed velocity profile is imposed at the inflow boundary. When the flow is diverted around the obstacle, increased flow velocities are induced in the area in between the obstacle and the bounding walls. The alteration of the velocity profile causes higher shear forces at the walls, which leads in turn to higher vorticity generation. Downstream of the obstacle, the amplified velocities close to the obstacle are transferred via the von Kármán vortex shedding towards the center of the channel. As a consequence, the shear stresses at the confining walls are reduced and the generated vorticity at the walls is shed into the flow. Figure 2 shows that the large von Kármán vortices interact with the vorticity from the confining walls, which is engulfed in the bulk flow. At times, this can cause flow separation from the channel walls and even recirculation bubbles are observed for some cases. The occurrence of recirculation bubbles is dependent on both the blockage ratio and the initial lateral spread of the von Kármán vortices, which is governed by the Reynolds number and the length of the plate. A thorough inspection of Fig. 2d reveals that the vortex trail is closer to the bottom wall than to the upper wall. Nonetheless, a flipping to the upper wall is observed after sufficiently long simulation time.

The material properties are of importance for the behavior of a flexible structure in an intermittent flow field. In an idealized oropharyngeal junction there is a large degree of uncertainty associated with the elastic properties of flexible tissue. The

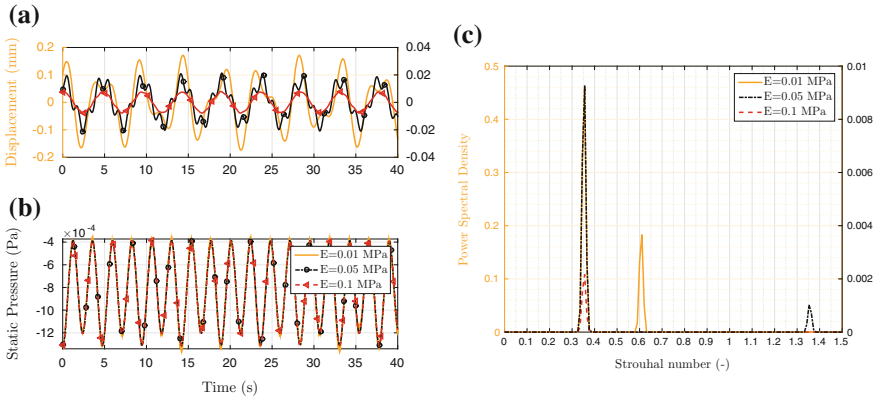


Fig. 3 Characteristics induced by three different Young's moduli of the soft palate with the length $1/2\ \ell$ for a *Re* of 300. Plot **a** shows the displacement monitored at the end of the flexible element. The spectra illustrated in **c** exhibit the frequency content of the signals shown in (**a**). The scale to the *left* of the plots **a** and **c** corresponds to the case $E = 0.01$ *MPa*, and the scale to the right to the cases $E = 0.1$ *MPa* and $E = 0.05$ *MPa*. Plot **b** shows the pressure history recorded in a probe two element lengths downstream of the tip for the three cases on the same scale

displacement of the flexible plate (simulated soft palate) with the length of $1/2\ \ell$ at $Re = 300$ are shown in Fig. 3a for three different Young's moduli. A nearly sinusoidal oscillation (with small perturbations) of the soft palate tip can be observed for the highest Young's modulus simulated. For the flexible elements with the lower Young's moduli additional superimposed oscillations on top of the same ground frequency are notable. This is also expressed more clearly in Fig. 3c, which shows that the spectra of these signals display an additional peak to the von Kármán vortex shedding frequency. This peak is not a higher harmonic of the shedding frequency, but rather a frequency response by the material, which intensifies for lower Young's moduli and might couple to resonance with the flow shedding if the frequencies are matched. The pressure history at a probe downstream of the obstacle is plotted in Fig. 3b revealing the vortex trail, where no significant differences between the cases can be observed. Hence, although the structural fluctuations are amplified several orders of magnitude, the vortex shedding is not influenced for such low displacement amplitudes.

4 Conclusions

An increase of the Reynolds number and length of the elastic element, as well as a lower modulus of elasticity lead to larger fluctuations of the soft palate. For lower Young's moduli, additional introduced oscillations have been observed, which could couple with the flow to a resonance effect. For low Reynolds numbers, a sufficiently long flexible element can suppress the generation of a von Kármán vortex trail. The

wall confinement effect is significant on both flexible element oscillation and flow structures observed. Although this study was limited to a two-dimensional setup, the considered flow features can be assumed to be equally present in a three-dimensional case. This is due to the wake of a circular body in crossflow showing the same dependence of the Strouhal number on the Reynolds number for the investigated range [5]. However, for higher Reynolds numbers turbulence is expected to play a significant role and three-dimensional models need to be taken into account. Boundary effects related to confinement in the spanwise direction might occur in a three-dimensional setup, but are assumed to be negligible in the central plane section, which is examined here. Thus, the validity of the presented results holds for the conditions of the soft palate in the human pharynx.

Acknowledgments This work is supported by the Swedish Research Council (Vetenskapsrådet) through the grant VR 621-2012-4256. This contribution is gratefully acknowledged. The computational resources have been provided by the Swedish National Infrastructure for Computing (SNIC). M.M. acknowledges the support of the Göran Gustafsson foundation.

References

1. G. Mylavarapu, M. Mihăescu, L. Fuchs, G. Papatziamos, E.J. Gutmark, Planning human upper airway surgery using computational fluid dynamics. J. Biomech. **46**(12), 1979–1986 (2013)
2. C. Norberg, An experimental investigation of the flow around a circular cylinder: influence of aspect ratio. J. Fluid Mech. **258**, 287–316 (1994)
3. J.H. Zhu, H.P. Lee, K.M. Lim, S.J. Lee, L.S.L. Teo, D.Y. Wang, Passive movement of human soft palate during respiration: a simulation of 3D fluid/structure interaction. J. Biomech. **45**(11), 1992–2000 (2012)
4. A. Richter, E. Naudascher, Fluctuating forces on a rigid circular cylinder in confined flow. J. Fluid Mech. **78**(3), 561–576 (1976)
5. X. Ma, G.E. Karniadakis, A low-dimensional model for simulating three-dimensional cylinder flow. J. Fluid Mech. **458**(3), 181–190 (2002)

Effect of Chordwise Flexibility on Flapping Wing Aerodynamics

Onur Son and Oksan Cetiner

Abstract In this study, the effect of chordwise flexibility has been investigated experimentally for a plunging foil. A Digital Particle Image Velocimetry (DPIV) system is used to determine instantaneous velocity and vorticity fields around and in the near-wake of the wings in conjunction with simultaneous direct force/moment measurements. The aerodynamic/hydrodynamic performance is studied for rigid and flexible wings undergoing plunge motion at different amplitudes and frequencies in a freestream of Re = 10 000. The thrust coefficient (C_T), the power input coefficient (C_P) and the efficiency (η) values are also obtained and linked with the flexibility, trailing edge motion and flow structures in the near-wake.

1 Introduction

Flexible flapping wings have drawn attention in recent years due to their possible high performance efficiencies compared to rigid ones. Since all natural flyers and swimmers have some degree of flexibility on their wings, it is important to understand the phenomena for a more effective aerial/nautical vehicle design. Although various experimental [1–5] and numerical [6–9] research have been performed on the topic, yet further examination is required to provide further insight into the physics of the flow-structure interaction.

Due to the simplicity of the motion, the earliest theories concerning flapping wing flight are related to purely plunging airfoils. The theory of thrust generation using flapping foils was first proposed by Knoller [10] and Betz [11] and then experimentally confirmed by Katzmayr [12]. The Knoller-Betz theory states that a harmonically plunging wing in a freestream flow results in generation of an effective angle

O. Son (✉) · O. Cetiner
Department of Astronautical Engineering,
Istanbul Technical University, 34469 Maslak, Istanbul, Turkey
e-mail: sono@itu.edu.tr

O. Cetiner
e-mail: cetiner@itu.edu.tr

© Springer International Publishing Switzerland 2016

A. Segalini (ed.), *Proceedings of the 5th International Conference on Jets, Wakes and Separated Flows (ICJWSF2015)*,
Springer Proceedings in Physics 185, DOI 10.1007/978-3-319-30602-5_26

of attack and when the airfoil is oscillated at sufficiently high amplitude and frequency, the downstream velocity distribution becomes jet-like and thus is indicative of a net thrust on the airfoil. A large number of recent studies, both experimental and numerical, have been focusing on the effects of flexibility to mimic the nature with the aim of not only producing energy from flapping but also increasing the efficiency of flapping using the storage and release of elastic energy appropriately. The review paper of Gursul et al. [13] on the control of low Reynolds number flows by means of fluid-structure interactions gives an overall coverage of studies and findings focusing on lift and thrust enhancement of flexible wings. The experimental investigation of Anderson et al. [14] on rigid flapping wings showed that optimum propulsive efficiencies were obtained within an approximate range of Strouhal numbers 0.2-0.4. This range coincides with that presented by Triantafyllou et al. [15] for observed fish and cetaceans swimming at or near their maximum observed speed. Consistent with experimental and computational simulations of rigid airfoils in coupled plunge and pitch motions, for chordwise flexible airfoils, Heathcote and Gursul [1] showed that propulsive efficiency peaks at a Strouhal number of 0.29 which lies in the middle of the range observed in nature. They also concluded that the effect of chordwise flexibility is beneficial for purely plunging airfoils at low Reynolds numbers. Thrust coefficient and propulsive efficiency are found to increase with a degree of flexibility. Higher thrust coefficients are determined with stronger trailing-edge vortices and higher efficiencies are obtained in cases producing weaker leading-edge vortices. Earlier, Prempraneerach et al. [16] also experimentally showed that chordwise flexibility can increase the propulsive efficiency up to 36 % compared to rigid foils undergoing plunging and pitching motion. Timing of shed vortices is also an important issue affecting the performance of the flapping wing. Monnier et al. [17] investigated harmonically pitching airfoils with a flexible tail and focused on circulation, the streamwise and cross-stream spacing of the vortices and the vortex core radius. They found out that flexibility has an effect of switching the wake vortex pattern to reverse von Karman street. Ramaninova et al. [18] suggest that the optimum performance is related to the temporal evolution of the wing shape rather than the resonance of the wing. Phase lag between the leading and trailing edges of the flapping wing up to some level is found to be useful for exploiting the elastic energy. A detailed review on the relation between performance and lower, near, and upper natural frequencies is given in Shyy et al. [19].

The present investigation considers three flat plate wings with different flexibilities, undergoing sinusoidal plunge motion in a freestream of $\mathrm{Re} = 10\,000$, at different frequencies related to fractions of their natural frequencies. The model is either rigid or chordwise flexible and connected to a force/torque sensor which records the variation of performance during a cycle of motion. Instantaneous flow fields around and in the near-wake of flat plates are obtained using a 2D2C DPIV (Digital Particle Image Velocimetry) System which also gives the position of the trailing edges.

2 Experimental Setup

Experiments are performed in the large scale free-surface water channel of Trisonic Laboratories at the Faculty of Aeronautics and Astronautics of Istanbul Technical University. The cross-sectional dimensions of the main test section are 1010 mm × 790 mm. The models are mounted in a vertical cantilevered arrangement in the water channel from their leading edge. The experimental setup is shown in Fig. 1. The rigid model is a thin rectangular plate (t = 0.5 cm) manufactured of transparent plexiglas to allow laser light to illuminate both the suction and pressure sides. The chord length of the models is 10 cm and the span length 20 cm. The flexible wings are produced of polycarbonate (lexan) and acetate and have a metal part of 1 cm on the leading edge that allows chordwise flexibility, however they are rigid in spanwise direction. The experiments are conducted at a Reynolds number of 10,000 which corresponds to a flow speed of U = 0.1 m/s. Force data is collected at 1000 Hz starting after the 3rd period of the motion. The current study on flapping wings considers only plunging of a flat plate. The plunge motion is defined by the sinusoidal function (1) given below, where a is the amplitude and f is the flapping frequency:

$$h(t) = asin(2\pi ft) \tag{1}$$

50 periods of plunge motion data are recorded for each case. Taking into account the natural frequencies of the wing models, a range of 0.222–2.220 Hz is considered for plunging frequencies. Force and moments acting on the plunging flat plate are measured using a six-component ATI NANO-17 IP68 Force/Torque (F/T) sensor. The sensor is attached to the vertical cantilevered mounting beam of the test model, oriented with its cylindrical z-axis normal to the pitch-plunge plane. The plunge motion of the model is accomplished with Kollmorgen/ Danaher Motion AKM54K

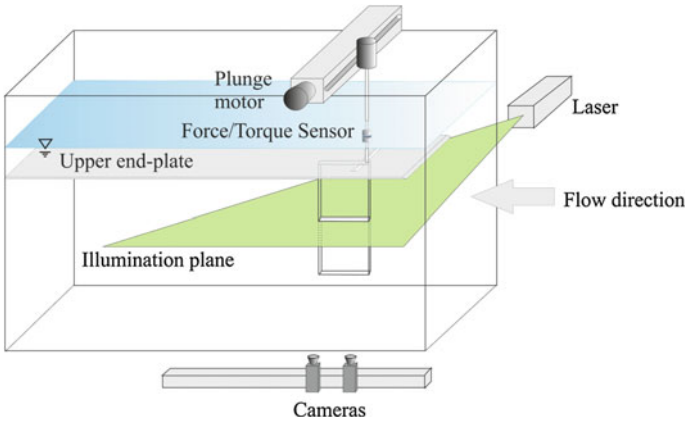


Fig. 1 Experimental setup

servo motor which was connected to a computer via ServoSTAR S700 digital servo amplifier.

3 Results

The frequencies for plunge motion are determined depending on the natural frequency of the materials and limited by the maximum frequency allowed by the motion rig and force/torque sensor. The natural frequency of the rigid, lexan and acetate plates are 7.40 Hz, 2.22 Hz and 0.64 Hz, respectively. The experiments are undertaken for four different amplitudes and five different frequencies of motion; time-averaged power-input and thrust coefficients along with the propulsive efficiency with respect to the motion frequency are shown in Fig. 2. Coefficients are

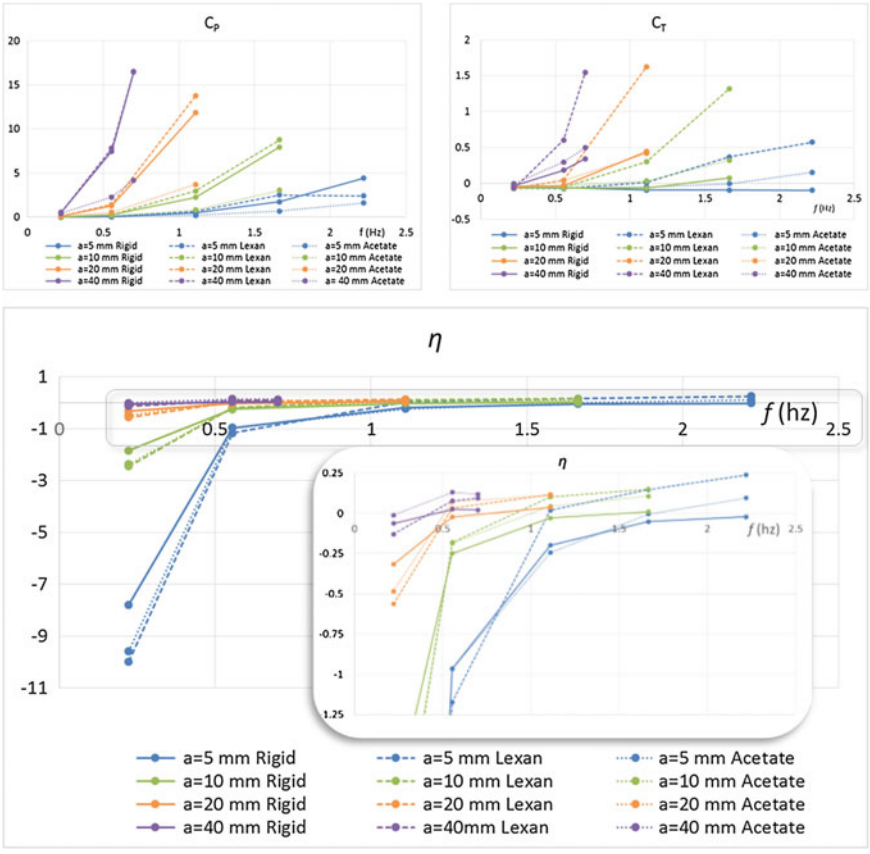


Fig. 2 Time-averaged power-input and thrust coefficients, and the propulsive efficiency

defined according to [1] and given in (2) where the T is time-averaged thrust (or drag) per unit span, F_y is the lift force and v is the instantaneous leading edge velocity.

$$C_T = \frac{T}{\frac{1}{2}\rho U_0^2 c}$$
$$C_P = \frac{\overline{F_y v}}{\frac{1}{2}\rho U_0^3 c}$$
$$\eta = \frac{C_T}{C_P} \tag{2}$$

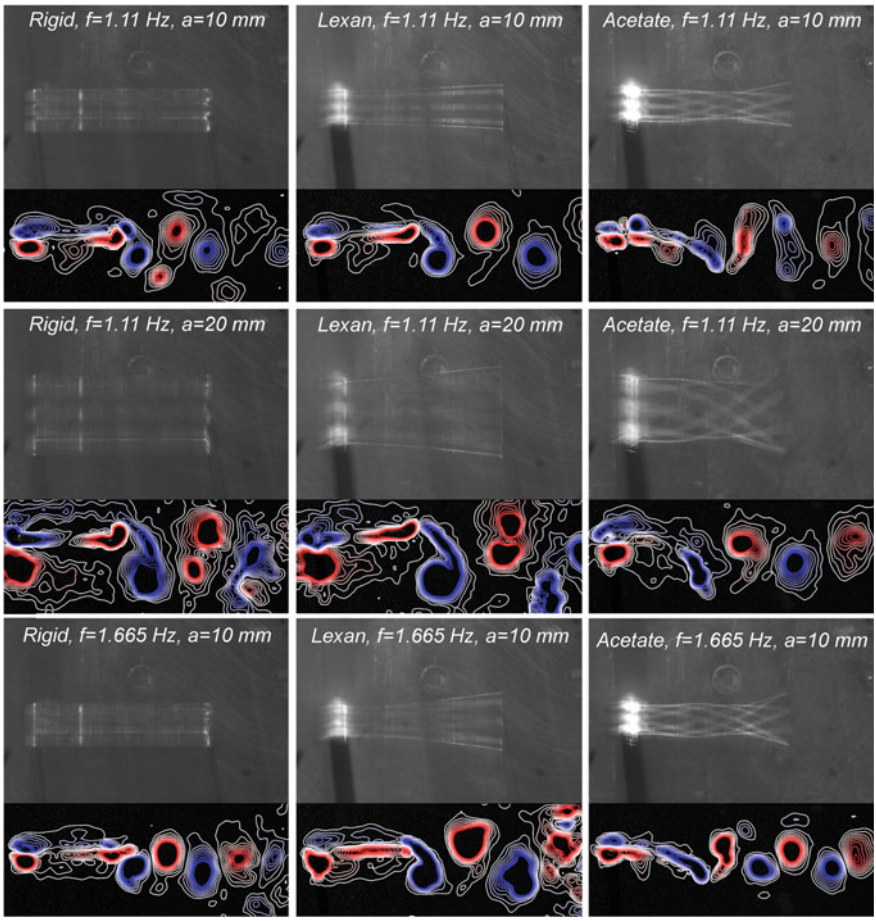


Fig. 3 Instantaneous vorticity plots along with the superposed raw DPIV pictures

As the Reynolds number is fixed, the x-axis can be also regarded as the reduced frequency. We do not prefer to use Strouhal number for the x-axis as different combinations of frequency and amplitude of motion yield the same Strouhal number, however, with different performance results. For each investigated cases, the power-input coefficient increases as the frequency of motion or its amplitude increases. For all investigated frequencies, the acetate plate extracts less power from the fluid. The lexan plate in general extracts the most; however, its power extraction is less than that of the rigid plate when it oscillates around its natural frequency. Figure 2 shows also the thrust production for motions above a certain frequency and/or amplitude. When the plate is flexible, the thrust production is possible for lower frequency and/or amplitude of motion. The lexan plate exhibits the best thrust performance. However, as the acetate plate extracts less power, the efficiency would be a suitable parameter to assess the overall performance. As can also be seen in Fig. 2, especially based on the acetate, the plates seems to show better performance when they plunge near their natural frequency. The efficiency values peak in a Strouhal number range of 0.2–0.3 for the rigid plate, in agreement with the literature.

Figure 3 shows instantaneous vorticity plots when the leading edge (LE) of the plate is about its maximum position, along with the superposed raw DPIV pictures to visualize the bending of the plates. Combined with force measurement results, it is possible to conclude that the vortices should be strong, preferably intact and the vertical distance between the centers of the vortices of opposite sign should be large for a better efficiency. According to the bending shape of the plates, the propulsive efficiency is generally high when the trailing edge (TE) of the plate follows the motion closely, reaching its maximum when LE reaches its. Acetate plates bend more and the delay of TE in following LE is increased, resulting in a decrease of vertical distance between vortices of opposite sign and of vortex strength which in turn degrades the thrust performance. In order to combine the information about the deformation of the plate with the imposed motion and the timing of the vortical structures which is

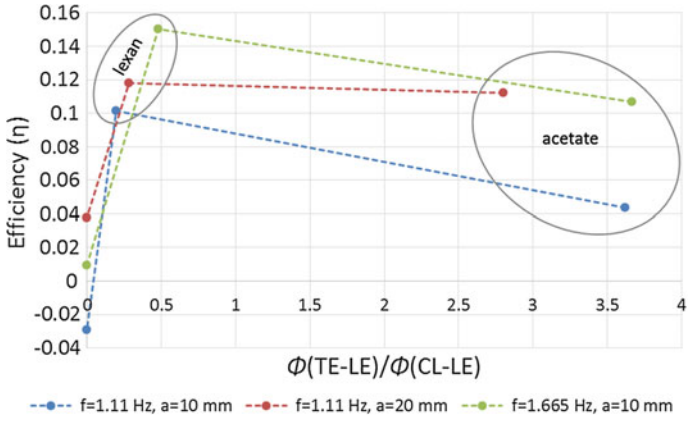


Fig. 4 The propulsive efficiency with respect to the ratio of ϕ (TE-LE)/ϕ (CL-LE)

directly connected to force-time history, the ratio of the phase angle between the TE and the LE to the phase angle between lift coefficient and TE is calculated. Figure 4 shows the propulsive efficiency with respect to this ratio and summarizes the findings. The ratio is zero for the rigid plate as TE and LE moves in parallel. The graph is expected to peak at the ratio of one. The ratios obtained for the lexan plate is between 0 and 0.5 and those obtained for the acetate plate is above 2.5. It is concluded that there is an optimum flexibility for the propulsive efficiency, in agreement with the literature.

4 Conclusion

Chordwise flexibility of a flat plate undergoing sinusoidal plunge motion is investigated using DPIV and direct force measurements. The best thrust performance is obtained when the trailing edge of the plate is closely followed by the lift variation and in general for the lexan plate. On the other hand, the most flexible plate made of acetate extracts less power for all investigated cases. In combination, the plates seem to show better performance in terms of propulsive efficiency when they plunge near their natural frequency. The results show that there is an optimum flexibility for the propulsive efficiency which is close to that of lexan in the current investigation. The existence of the optimum flexibility is shown based on the phase ratio between the lift force vs the imposed motion and LE vs TE, namely the shape of the flexible wing. Further studies will be focused on obtaining a phase ratio around 1–1.5 to lead to the expected higher efficiency.

Acknowledgments The authors acknowledge the funding provided by the Scientific and Technological Research Council of Turkey (TUBITAK) Grant 112M682.

References

1. S. Heathcote, I. Gursul, Flexible flapping airfoil propulsion at low Reynolds numbers. AIAA J. **45**(5), 1066–1079 (2007)
2. L. Zhao, Q. Huang, X. Deng, S.P. Sane, Aerodynamic effects of flexibility in flapping wings. J. R. Soc. Interface **7**(44), 485–497 (2010)
3. H. Hu, A.G. Kumar, G. Abate, R. Albertani, An experimental investigation on the aerodynamic performances of flexible membrane wings in flapping flight. Aerosp. Sci. Technol. **14**(8), 575–586 (2010)
4. N.S. Ha, Q.T. Truong, N.S. Goo, H.C. Park, Relationship between wingbeat frequency and resonant frequency of the wing in insects. Bioinspiration and Biomimetics **8**(4), 046008 (2013)
5. D.B. Quinn, G.V. Lauder, A.J. Smits, Scaling the propulsive performance of heaving flexible panels. J. Fluid Mech. **738**, 250–267 (2014)
6. J.D. Eldredge, J. Toomey, A. Medina, On the roles of chord-wise flexibility in a flapping wing with hovering kinematics. J. Fluid Mech. **659**, 94–115 (2010)
7. D. Qi, G. He, Y. Liu, Lattice Boltzmann simulations of a pitch-up and pitch-down maneuver of a chord-wise flexible wing in a free stream flow. Phys. Fluids **26**(2), 021902 (2014)

8. S. Michelin, S.G.L. Smith, Resonance and propulsion performance of a heaving flexible wing. Phys. Fluids (1994-present), **21**(7), 071902 (2009)
9. D. Qi, R. Gordnier, Effects of deformation on lift and power efficiency in a hovering motion of a chord-wise flexible wing. J. Fluid Struct. **54**, 142–170 (2015)
10. R. Knoller, Die Gesetze des Luftwiderstandes. Flug- und Motortechnik (Wien) **3**, 1–7 (1909)
11. A. Betz, Ein Beitrag zur Erklaerung des Segelfluges. Zeitschrift fuer Flugtechnik und Motorluftschiffahrt **3**, 269–272 (1912)
12. R. Katzmayr, Effect of periodic changes of angle of attack on behaviour of airfoils. NACA 147 (1922)
13. I. Gursul, D.J. Cleaver, Z. Wang, Control of low Reynolds number flows by means of fluid structure interactions. Prog. Aerosp. Sci. **64**, 17–55 (2014)
14. J.M. Anderson, K. Streitlien, D.S. Barrett, M.S. Triantafyllou, Oscillating foils of high propulsive efficiency. J. Fluid Mech. **360**, 41–72 (1998)
15. M.S. Triantafyllou, G.S. Triantafyllou, R. Gopalkrishnan, Wake mechanics for thrust generation in oscillating foils. Phys. Fluids A-Fluid (1989-1993), **3**(12), 2835–2837 (1991)
16. P. Prempraneerach, F.S. Hover, M.S. Triantafyllou, The effect of chordwise flexibility on the thrust and efficiency of a flapping foil. In Proceedings 13th International Symposium on Unmanned Untethered Submersible Technology: special session on bioengineering research related to autonomous underwater vehicles, New Hampshire (2003)
17. B. Monnier, A.M. Naguib, M.M. Koochesfahani, Influence of structural flexibility on the wake vortex pattern of airfoils undergoing harmonic pitch oscillation. Exp. Fluids **56**(4), 1–17 (2015)
18. S. Ramananarivo, R. Godoy-Diana, B. Thiria, Rather than resonance, flapping wing flyers may play on aerodynamics to improve performance. Proc. Natl. Acad. Sci. **108**(15), 5964–5969 (2011)
19. W. Shyy, H. Aono, C.K. Kang, H. Liu, An introduction to flapping wing aerodynamics, vol. 37. Cambridge University Press (2013)

Part III
Separated Flows

Characteristics of Recirculation Regions on Ribs of Varying Length

Jacques W. Van der Kindere and Bharathram Ganapathisubramani

Abstract Ribs represent a class of two-dimensional surface mounted obstacles generating a maximum of three distinct recirculating regions: upstream, on top, and downstream. We investigate the effect of rib length on the shape and strength of phenomena occurring within these three recirculation regions. An experiment was designed accordingly where six ribs of varying length ($0.1 \leq L/H \leq 8$) were submerged in a fully turbulent boundary layer ($\delta/H = 1.37$) with a Reynolds number based on rib height of $Re_H = 20000$. Particle Image Velocimetry (PIV) was carried out along the centre line of the obstacles. Comparable properties show consistency with previous literature (The flow past a surface-mounted obstacle. J Fluids Eng 105:461–463 (1983), [5]). Results of dimensions of recirculation regions in the plane of measurements, as well as results based on proper orthogonal decomposition of flow field velocity as a function of rib length show two different behaviours in the wake of the obstacles which coincide with the presence or absence of a mean reattachment point on the top surface.

1 Introduction

Engineering applications requiring flow mixing exploit the high levels of turbulence produced by blunt obstacles to improve their effectiveness. We are interested in studying one of the families of obstacles which combines two canonical problems. This family regroups surface-mounted rectangular cylinders of infinite span, otherwise known as "two-dimensional ribs". Ribs produce interactions between a forward-facing step and a backward-facing step. Depending on the distance between the upstream and downstream edges, the separated flow of the forward-facing step

J.W. Van der Kindere (✉) · B. Ganapathisubramani
University of Southampton, Southampton, UK
e-mail: jvdk1g09@soton.ac.uk

B. Ganapathisubramani
e-mail: g.bharath@soton.ac.uk

© Springer International Publishing Switzerland 2016

A. Segalini (ed.), *Proceedings of the 5th International Conference on Jets, Wakes and Separated Flows (ICJWSF2015)*,
Springer Proceedings in Physics 185, DOI 10.1007/978-3-319-30602-5_27

may merge to different degrees with that of the backward-facing steps. Consequently up to three regions may interact together: upstream, on top, and downstream of the rib.

Most experimental investigations into the aerodynamics of rib-like geometries have given us insight into their behaviour in various flow conditions. Nevertheless, as described by some authors, instrumentation was a limitation, thus a thorough description of recirculation regions was not possible [2–9, 12]. However the advent of newer experimental instruments as well as numerical simulations opened access to different measurable quantities and analytical methods which improve the description of a separated flow [1, 10, 13].

This current paper endeavours in identifying the unsteady features occurring in flow separation over ribs of different length. The first part of this paper aims to obtain a statistical description of the dimensions of recirculation regions. The second part uses modal decomposition of the flow field properties to illustrate changes in the statistics with varying rib length.

2 Experimental Apparatus and Conditions

The experiment was carried out at the University of Southampton in an open return wind tunnel with a rectangular test section of 0.9 m × 0.6 m × 4.35 m. Speed in the test section (U_e) was set to 10 m/s. The experiment was mounted on a smooth suspended flat plate with a thin leading edge and a trip to control the incoming boundary layer (detailed in Fig. 1).

Six different rib lengths were studied: $L/H = 0.1, 1, 2, 4, 6, 8$ (with height, $H =$ 30 mm). They extended along the entire span of the wind-tunnel, producing a "two-dimensional" obstacle. Three LaVision LX Imager 16MP PIV cameras capture particle image velocimetry (PIV) in conjunction with Sigma 105 mm f2.8 Macro lenses. The field of view covered $-5.4 \leq x/H \leq 14.5$, and $0 \leq y/H \leq 6$ with a vector spacing of ~0.5 mm. $X = 0, Y = 0$ correspond to the bottom of the upstream face of the ribs. 2500 vector fields were obtained per case at a rate of 0.2 Hz. The field of interest was illuminated by two double cavity Nano L 200-15 PIV lasers from Litron lasers

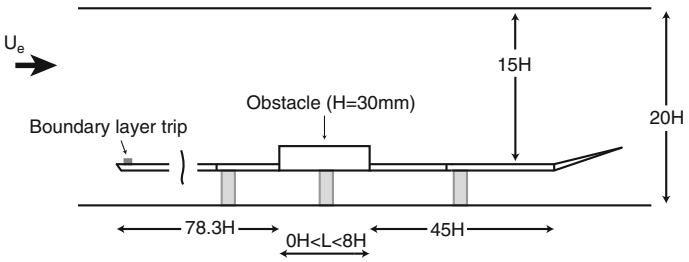


Fig. 1 Illustration of the arrangement in the test section

along the centreline of the test section. As described by [11, 12], the aspect ratio of a step (W/H) exceeding 10 yields "acceptable" two-dimensional flow.

PIV measurements of the flow without obstacle provide the incoming boundary layer properties. With a freestream velocity of $U_e = 10$ m/s, the Reynolds number based on H was $Re_H = 20000$. The boundary layer thickness δ based on 99 % of U_e measured at $\delta/H = 1.3$ and was fully turbulent. The method to obtain boundary layer properties relied on averaging 2000 vector fields without obstacle, then averaging the boundary layer profiles between $X = -5.4\,H$, and $X = 0\,H$. Laser light reflections at the surface caused potentially inaccurate velocity estimations in the first 3 mm above the surface.

3 Dimensions of Recirculation Regions

PIV measurements allow the estimation of length, height and cross-sectional area of the regions of recirculating flow inside which streamwise velocity is negative. The first point of comparison between rib lengths refers to the mean dimensions of all three regions (upstream, on top and in the wake). Figure 2 depicts two trends observed by [5] in recirculation length of the wake region normalized by the height of the obstacle L_R/H as a function of L/H with an incoming turbulent boundary layer thinner than the obstacle. In this case, L_R is the horizontal distance between the corner at which flow separates, and the furthest point downstream where streamwise velocity is negative. Results from the present study are superimposed to display the similarities despite the boundary layer being thicker than the obstacle in the present study. The two trends found by [5] are obtained here as well, and they coincide with the presence or absence of flow reattachment on top of the obstacles. Indeed, short ribs ($L/H < 4$) produce a separated region at the upstream corner which extends

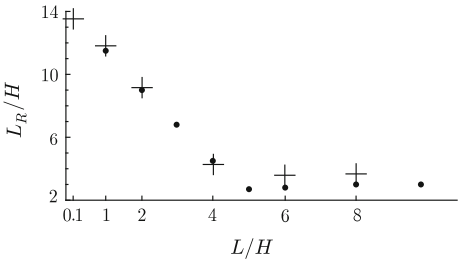


Fig. 2 Two regimes observed in the length of recirculation regions in the wake. Legend: • Bergeles [5], + Experiment

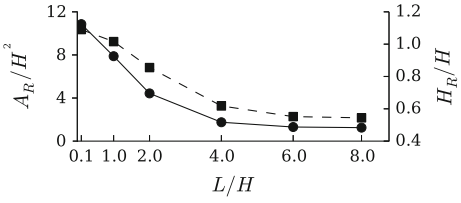


Fig. 3 The evolution of mean recirculation regions dimensions with rib length. Legend: ● A_R/H^2, ■ H_R/H

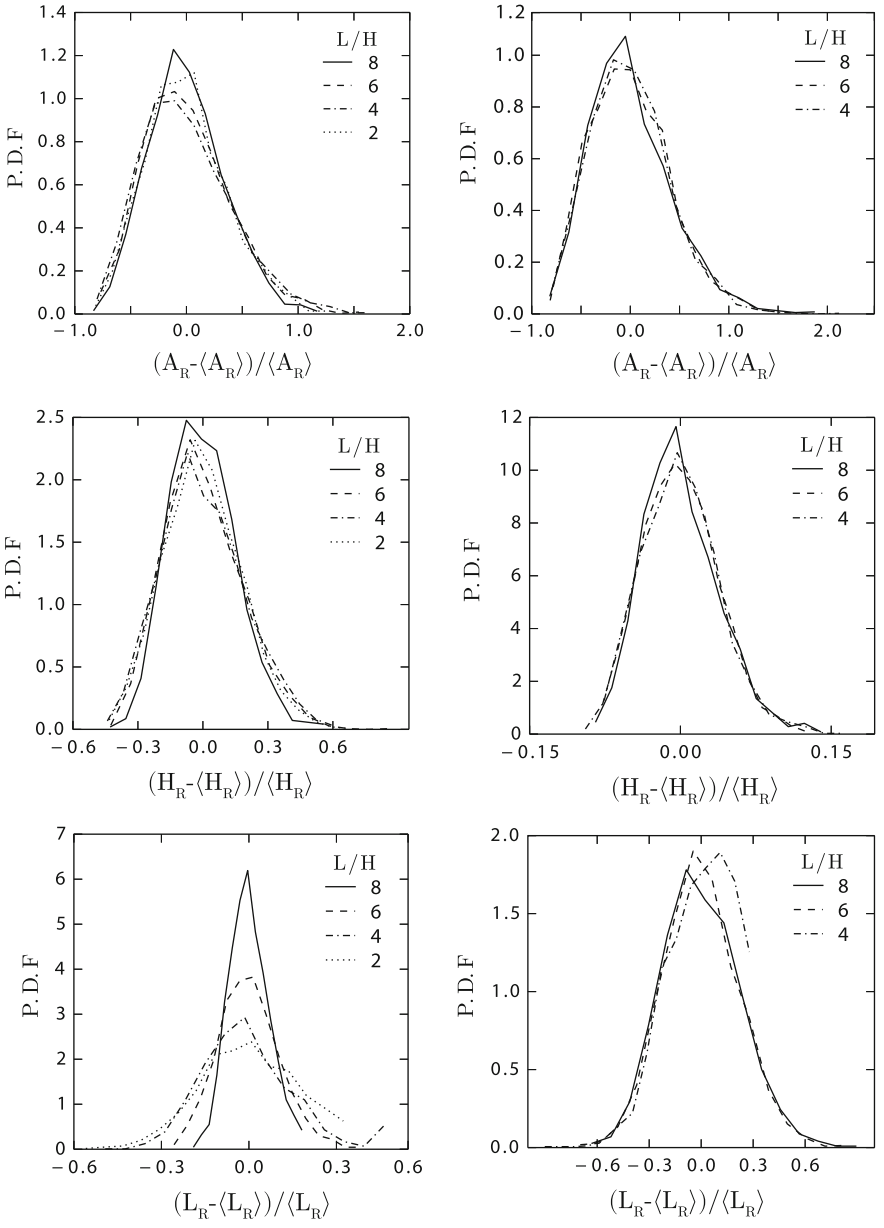


Fig. 4 From *top* to *bottom*, p.d.f. of recirculation regions area, height, length, subtracted and normalized with their respective mean values. *Left* Recirculation region downstream of the obstacle. *Right* Top of the obstacle

downstream of the backward-facing corner. Thus a single large recirculation region covers the entire obstacle. Its length plotted in Fig. 2 varies linearly with rib length as: $L_R/H \approx 14.1-3.47\,L/H$. In the other case, long ribs ($L/H \geq 4$) allow the separated flow from the forward-facing corner to reattach on top before the flow separates again at the backward-facing corner. The length of the recirculation region on the top surface is nearly constant at $2.8\,H$ for long ribs in this experiment where [5] find $3.7\,H$. In addition, the length of the most downstream region plotted in Fig. 2 seems to asymptote to $\approx 3.7\,H$.

In addition to length of recirculation regions, PIV allows the measurement of their mean height, and mean area in the plane of measurement. Figure 3 illustrates that both trends present in recirculation length are also present in height and area. Short ribs produce separated flow regions exhibiting a linear relationship between rib length and area or height of the regions, whereas long ribs produce separated flow regions of nearly constant size. Regarding the top region of long ribs, their area and height appear to be nearly constant, as observed for their length.

Beyond mean quantities, one may use the distribution of quantities to understand the behaviour of the recirculation regions as rib length varies. Figure 4 depicts three pairs of histograms obtained in the wake and on top of each rib. These were obtained by measuring the dimensions of both recirculation regions in each PIV snapshot. After subtracting and dividing by the mean value, all the samples are grouped in 10 bins. The analysis of the histograms of the three normalized geometrical dimensions of the recirculation region indicates various trends:

- In the wake, the height and area of a recirculation region is fluctuating most for case $L/H = 4$, the intermediate length.
- Recirculation length in the wake is less variable as rib length increases.
- Along the top surface, case $L/H = 8$ appears the least variable but the differences are small. A p.d.f. of L_R is invalid for $L/H = 4$ due to recirculation regions often overshooting the trailing edge.

4 Flow Patterns in the Recirculation Regions

In addition to statistical description of the shape of recirculation regions, proper orthogonal decomposition (POD) applied to PIV allows a more visual description of events occurring within recirculation regions [14]. 1500 velocity fluctuation vector fields were used to produce POD modes from the leading edge to $x = 1.25L_R/H$ and from $y = 0.12\,H$ to $y = 3.5\,H$. The base flow over the flat plate is also present, it was computed between $x/H = 0$ and $x/H = 11.8$, which corresponds to the length covered for $L/H = 1$. Varying this region's size does affect the observations made here.

Table 1 Number of modes required to capture a specific amount of kinetic energy

Cases	Number of modes required for 50 %	Number of modes required for 66.6 %	Number of modes required for 90 %
Flatplate	63	218	883
$L/H = 8$	43	145	724
$L/H = 6$	36	124	672
$L/H = 4$	29	101	639
$L/H = 2$	22	86	623
$L/H = 1$	26	95	638
$L/H = 0.1$	28	101	654

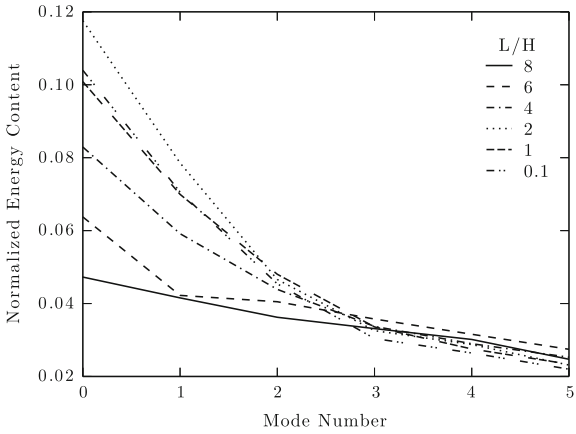


Fig. 5 Distribution of the energy content of the first 6 modes for each case

The distribution of relative energy content between modes can be linked to the contribution of each mode in describing a flow. A flow requiring only few modes to capture a large portion of the total kinetic energy is deemed less complex than a flow requiring more modes. Table 1 reports how many modes are required to capture 50, 66.6 and 90 % of the kinetic energy out of a total of 1500. It is clear that these turbulent recirculation regions produce complex flow patterns from the high number of modes required. However it is also clear that rib lengths closest to $L/H = 2$ produce the least intricate flow. This is also visible in the distribution of energy content in POD modes in Fig. 5. Indeed, it indicates a smooth distribution for all cases, but $L/H = 2$ having the largest relative energy content in the first three modes.

Although the distribution of energy content presented in Fig. 5 is relatively smooth, there is a clear organization in the POD mode shapes themselves. Studying individual mode shapes of streamwise and vertical velocity components reveals adjacent patches of high or low velocity. When vertically aligned, the patches of low and high velocity can be associated with rolling vortices. On the contrary, when aligned horizontally, they indicate flow acceleration or deceleration, a sign of the presence of waves. This can be confirmed by conditionally averaging snapshots with

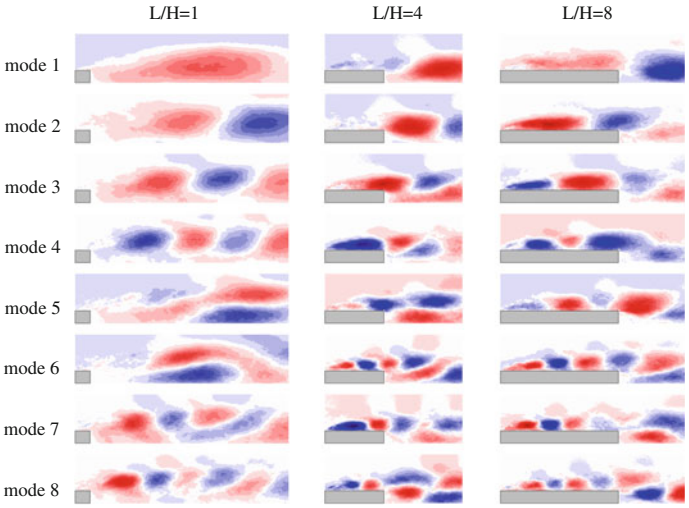


Fig. 6 POD mode shapes extracted from streamwise velocity component indicating the dominance of bubble dimensions in low mode numbers, in contrast with the appearance of small fluctuations in shear layers at high mode numbers

respect to coefficients for these recognizable patterns. Figure 6 represents the patterns found in POD mode shapes for a short, a medium, and a long obstacle illustrating the gradual evolution of the flow over ribs of varying length. It appears the first mode is linked with variations in size of the recirculation region in the wake of each obstacle. Indeed, conditionally averaging samples with low or high energy content compared to the average value yields small or large recirculation region areas in the wake. As mode number increases, the POD modes of short ribs tend to deform the boundary of the recirculation region into a wave pattern. Above mode number 6, recurring patterns of smaller and smaller fluctuations appear along the upper boundary of the mean recirculation region. It is worth noting that very little energy comes from the leading edge of short ribs in these modes, fluctuations there do not appear until mode 13. This would indicate that most fluctuations in dimensions of recirculation regions would originate from a large scale "breathing" of the recirculation region also observed in simple backward-facing steps. Ribs of intermediate length ($L/H = 4$), first produce two modes which affect the size of the wake region. Higher mode numbers show strong fluctuations from the leading edge (mode 3 and above) down to the wake region. Furthermore, at mode 6 and above, fluctuations from the leading edge tend to turn towards the floor once past the trailing edge. This would indicate that for this rib length, fluctuations from the leading edge interact directly with the recirculation region in the wake. Consequently it is possible that the former affect directly the instantaneous dimension of the latter. Lastly, the second, third and fourth mode shapes around a long rib show strong fluctuations from the leading edge travelling above the obstacle but comparatively weaker fluctuations in the

wake region. Higher mode numbers display more homogeneous fluctuation intensity throughout. Because of the decreasing energy distribution of these modes, they indicate that the strongest fluctuations are caused by the forward-facing portion. These travel downstream and decay above $y/H = 1$, but persist below. In fact, mode 8 of the long rib indicates stronger fluctuations in the wake with little intensity above the rib showing some independence of the wake region. These observations could indicate that the fluctuations produced by the leading edge affect to some extent the wake region, however much less than the medium-length rib.

5 Conclusions

The effect of rib length was evaluated on the dimensions and shape of their recirculation regions using PIV measurements. The presence or absence of a reattachment point on top of the obstacles defines two categories of ribs for which two distinct behaviours may be observed. Short ribs seem to produce large and steady recirculation regions were waves are the dominant structures. Long ribs however produce short but more variable recirculation regions where fluctuations in velocity above the top surface dominate in intensity. Future investigations should involve the correlation of properties from all three regions, as well as investigating which dimensions of recirculation regions are linked to mechanical loading to determine the feasibility of controlling this type of flow in industrial applications.

References

1. Y. Addad, D. Laurence, C. Talotte, M. Jacob, Large eddy simulation of a forward-backward facing step for acoustic source identification. Int. J. Heat Fluid Flow **24**, 562–571 (2003)
2. J. Antoniou, G. Bergeles, Development of the reattached flow behind surface-mounted two-dimensional prisms. ASME Trans. J. Fluids Eng. **110**, 127–133 (1988)
3. M. Arie, M. Kiya, H. Tamura, Y. Kanayama, Flow over rectangular cylinders immersed in a turbulent boundary layer: Part 1, correlation between pressure drag and boundary-layer characteristics. Bull. JSME **18**, 1260–1268 (1975)
4. M. Arie, M. Kiya, H. Tamura, M. Kosugi, K. Takaoka, Flow over rectangular cylinders immersed in a turbulent boundary layer: Part 2 flow patterns and pressure distributions. Bull. JSME **18**, 1269–1276 (1975)
5. G. Bergeles, N. Athanassiadis, The flow past a surface-mounted obstacle. J. Fluids Eng. **105**, 461–463 (1983)
6. I. Castro, Relaxing wakes behind surface-mounted obstacles in rough wall boundary layers. J. Fluid Mech. **93**, 631–659 (1979)
7. I. Castro, M. Dianat, Surface flow patterns on rectangular bodies in thick boundary layers. J. Wind Eng. Ind. Aerodyn. **11**, 107–119 (1983)
8. J. Counihan, J. Hunt, P. Jackson, Wakes behind two-dimensional surface obstacles in turbulent boundary layers. J. Fluid Mech. **64**, 529–564 (1974)
9. M. Dianat, I. Castro, Fluctuating surface shear stresses on bluff bodies. J. Wind Eng. Ind. Aerodyn. **17**, 133–146 (1984)

10. R.R. Hwang, Y. Chow, Y. Peng, Numerical study of turbulent flow over two-dimensional surface-mounted ribs in a channel. Int. J. Numer. Methods Fluids **31**, 767–785 (1999)
11. M. Kiya, K. Sasaki, Structure of a turbulent separation bubble. J. Fluid Mech. **137**, 83–113 (1983)
12. D. Moss, S. Baker, Re-circulating flows associated with two-dimensional steps. Aeronaut. Q. **31**, 151–172 (1980)
13. L. Shi, Y. Liu, J. Wan, Tr-piv measurement of separated and reattaching turbulent flow over a surface-mounted square cylinder. J. Mech. Sci. Technol. **24**, 421–428 (2010)
14. L. Sirovich, Turbulence and the dynamics of coherent structures. part i: Coherent structures. Q. Appl. Math. **45**, 561–571 (1987)

Passive Load Control in Backward-Facing Step Flow by Using Chevrons

Johan Nilsson, Robert-Zoltán Szász, Per-Erik Austrell and Ephraim J. Gutmark

Abstract The ability of chevrons at the top edge of a backward-facing step to reduce downstream surface pressure fluctuations is investigated numerically. Three different chevron configurations are compared against a baseline case without chevrons. Low frequency reduction in the surface pressure fluctuations is observed for two of the configurations. The chevrons do not appear to have a significant effect on the flow as the mean reattachment length for all configurations is nearly constant and there is only a small increase in streamwise turbulence for one configuration with the other configurations unchanged.

1 Introduction

Aircraft structures can be subjected to very high sound intensities (as high as over 150 dB) which can lead to acoustic fatigue (also known as sonic fatigue) and severe damages. The source of these high intensities can be for example jet engine exhaust or geometrical features such as control surfaces, flaps and cavities. Due to their severe consequences, it is desired to predict and reduce the acoustic loads already in the design phase. In this paper, a passive method of reducing the pressure load on the surface downstream of a backward-facing step (BFS) is investigated. Chevrons, or ser-

J. Nilsson (✉) · P.-E. Austrell
Division of Structural Mechanics, Lund University, PO Box 118, SE-221 00 Lund, Sweden
e-mail: Johan.Nilsson@construction.lth.se

P.-E. Austrell
e-mail: per_erik.austrell@construction.lth.se

R.-Z. Szász
Division of Fluid Mechanics, Lund University, PO Box 118, SE-221 00 Lund, Sweden
e-mail: Robert-Zoltan.Szasz@energy.lth.se

E.J. Gutmark
Department of Aerospace Engineering and Engineering Mechanics,
University of Cincinnati, PO Box 210070, Cincinnati, OH 45221–0070, USA
e-mail: gutmarej@ucmail.uc.edu

© Springer International Publishing Switzerland 2016

A. Segalini (ed.), *Proceedings of the 5th International Conference on Jets, Wakes and Separated Flows (ICJWSF2015)*,
Springer Proceedings in Physics 185, DOI 10.1007/978-3-319-30602-5_28

rations, are placed at the step edge. The intention is that the chevrons are to increase the mixing and introduce streamwise vorticity that can increase the break-up rate of the long spanwise Kelvin-Helmholz (K-H) vortices.

Chevrons placed in jet nozzles are used to reduce noise from jet exhaust [2, 3, 9, 16]. Circular jets feature shedding of K-H vortices in a similar way as the BFS. As demonstrated in [16], these K-H vortices undergo a pairing process similar to the corresponding process in the BFS as described in [7]. These large-scale structures are responsible for the low frequency noise propagating in the aft direction where the sound pressure level (SPL) is the highest [2]. The increased mixing near the jet nozzle by chevrons suppresses the described large scale structures [2]. This results in a reduction of low frequency noise in the aft directions [2, 3]. The increased mixing generates small scales which increase the high-frequency noise being propagated at right angles to the jet. However, the SPL in these directions is much lower than in the aft directions. Finally, chevron count and penetration have been demonstrated to be important factors for effective noise suppression [3].

Trailing edge serrations (TES) is another related method of reducing trailing edge noise from airfoils [6, 10, 12, 14]. Similarly to jet exhaust chevrons, TES have been shown to reduce low frequency noise but with an increase in high frequency noise [6, 12]. The numerical study in [14] also found that TES made no difference below a certain frequency. In addition, TES has also been shown to greatly attenuate the blunt trailing edge vortex shedding noise on a flat plate [10]. Similarly to the chevron count in jet exhaust, the width of the serrations is an important parameter for the noise suppression effectiveness [10].

2 Method

Numerical simulations are carried out on the geometry given in Fig. 1. The chevrons have a height of $2h_s = h/10$ and, as indicated by the grey lines on the ramp, extend in the streamwise direction over the entire length of the ramp. Cyclic boundary conditions are used in the spanwise direction with a domain width of $6h$. The Mach number is $\mathrm{Ma} = 0.2$, Reynolds number $\mathrm{Re}_h = 2.37 \cdot 10^5$, boundary-layer thickness $\delta = 0.75h$, the ramp inclination angle $\alpha = 6.3°$ and the expansion ratio is 12/11. The boundary-layer thickness δ is essentially the same at the inlet and at the step edge.

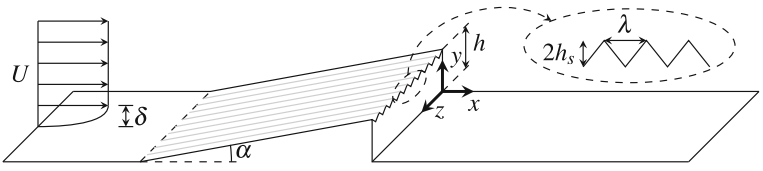


Fig. 1 Case geometry. Figure not to scale

Three configurations with different values of λ were simulated in addition to the baseline case without chevrons: $\lambda/h_s = 12.5$, $\lambda/h_s = 6.25$ and $\lambda/h_s = 3.125$.

The software used is the open-source finite-volume library OpenFOAM [13]. The chosen solver is an incompressible solver based on the PISO algorithm called `pisoFoam`. The LUST (Linear-Upwind Stabilised Transport) scheme is used for the discretisation of the convection of velocity term. It uses a blend of 75 % central differencing with 25 % upwind differencing for stability while maintaining second order behaviour [13]. Second order schemes are used in the spatial discretisation of the other terms. Time integration is performed using a backward second order implicit scheme. To prevent the demands on the near wall resolution to become too high, a wall-function based on Spalding's law of the wall [15] is used. This wall-function should converge to a DNS boundary-layer as the near-wall cells are refined [5]. The mean y^+ values for the base case without any chevrons are $y^+ \approx 11$ near the inlet and increases to $y^+ \approx 16$ near the step edge. All configurations used a mesh with 46 million cells except for the $\lambda/h_s = 3.125$ configuration mesh which had 92 million cells. The reason for this was a need for a higher resolution in the spanwise direction for this configuration. The inflow data used as inlet boundary condition is generated by a separate precursor simulation using the method of Lund et al. [8]. The simulation methodology used in this work has been established on the backward-facing step without chevrons in [11] where good agreement was observed between the predicted and measured pressure fluctuation levels.

3 Results

In this paper, only comparisons between the simulation configurations with chevrons and the baseline configuration without chevrons will be made. The baseline configuration has been validated against measurements in [11] and the reader is referred to that paper for comparisons against measurements.

A visualisation of the turbulent structures with a Q-criterion isosurface plot is displayed in Fig. 2. The Q-value set in Fig. 2 was set low enough to hide most of the turbulence in the turbulent boundary layer. However, it is still very difficult to see the spanwise structures being shed at the step edge. This difficulty was also noted in [4]. In the chevron case displayed in Fig. 2b, one can see that the chevron contour quickly disappears in the turbulent structures downstream of the step. On the downstream bottom surface no chevron related variation could be found in the spanwise direction. Therefore, all of the following results are averaged in the spanwise direction with the exception of the streamwise turbulence profiles in Fig. 5.

The mean reattachment length x_r for all configurations are given in Table 1. No configuration with chevrons differs more than 6 % in x_r from the baseline case.

The streamwise distribution of the r.m.s. pressure p_{rms} on the surface downstream of the step is given in Fig. 3. For all configurations, the most intensive pressure fluctuations appear near the mean reattachment point x_r and the maximum value is essentially in the range of $0.045 < p_{\mathrm{rms}}/(0.5\rho U_\infty^2) < 0.05$. Upstream of $x \approx 7h$, all

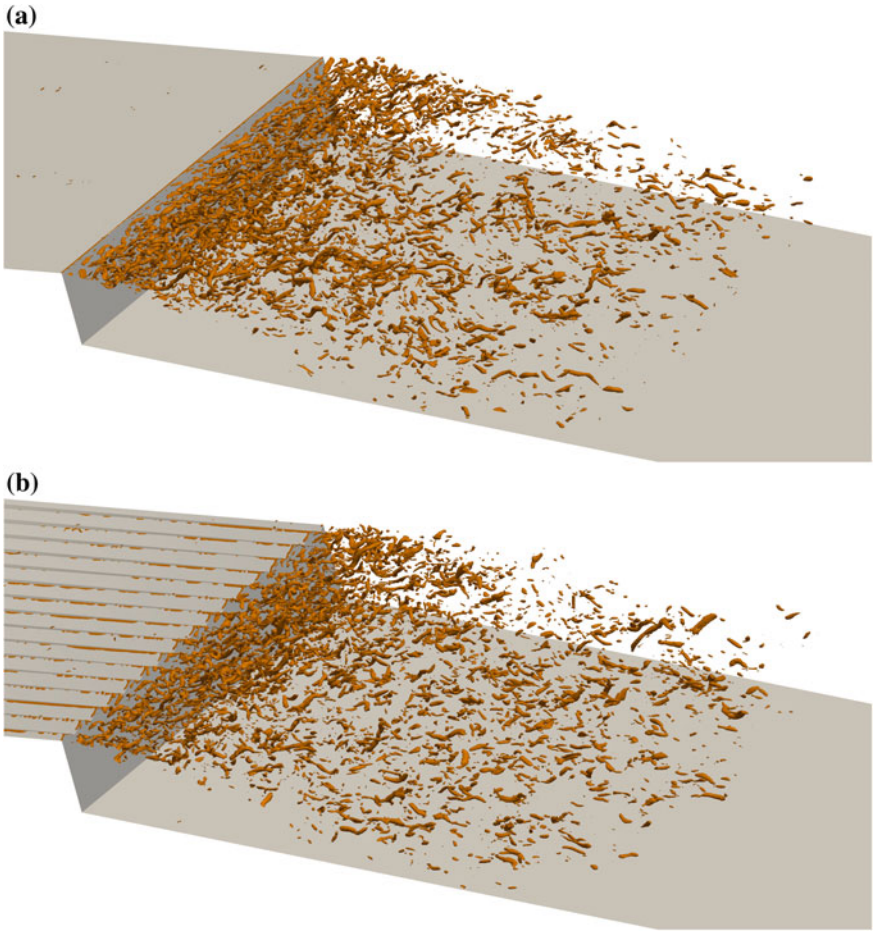


Fig. 2 Q-criterion isosurfaces of **a** the reference configuration without chevrons and **b** the $\lambda/h_s = 6.25$ case

Table 1 Mean reattachment length x_r for the different configurations

λ/h_s	x_r
No chevrons	$7.1h$
12.5	$6.7h$
6.25	$7.1h$
3.125	$7.3h$

configurations except the $\lambda/h_s = 12.5$ configuration are very similar, with the $\lambda/h_s = 12.5$ being higher. In addition, the $\lambda/h_s = 12.5$ has a hump at $x = h$ which is not present in the other configurations. Downstream of $x \approx 7h$ are the $\lambda/h_s = 12.5$ and

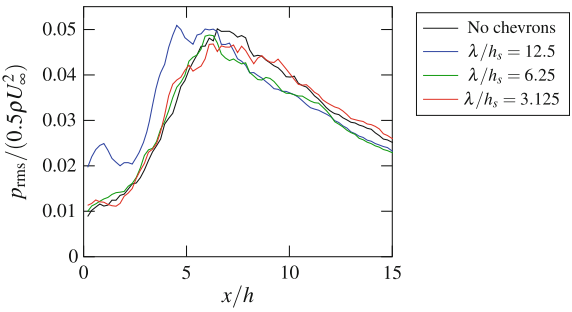


Fig. 3 Streamwise distribution of the r.m.s. pressure downstream of the step. $x = 0$ at the step edge

$\lambda/h_s = 6.25$ configurations curves lower than the baseline case and the $\lambda/h_s = 3.125$ configuration.

Figure 4 shows Power Spectral Densities (PSD) of the surface pressure spectra in three different locations. The PSD's are computed using Welch's method. For $x = 1.2h$, Fig. 4a show that all configurations are dominated by very low frequencies. The total sampling time is too short to draw any certain conclusions in this frequency range. With nearly all energy in the very low frequency range in the region close to the step, this means that there is also some uncertainty in the region closest to the step in Fig. 3. Figure 4b gives the spectra near $x = x_r$. Here the $\lambda/h_s = 12.5$

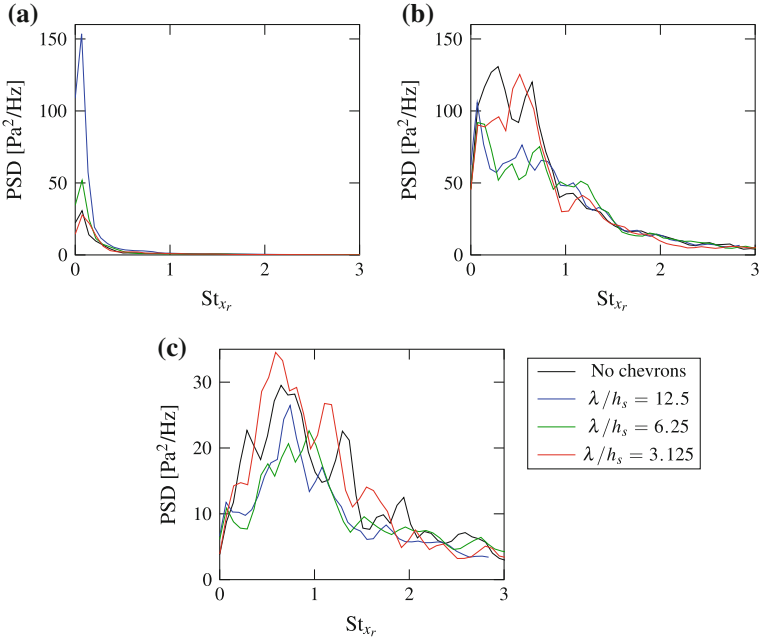


Fig. 4 PSD of the surface pressure at **a** $x = 1.2h$, **b** $x = 6.9h$ and **c** $x = 14.0h$

and $\lambda/h_s = 6.25$ configurations are significantly lower than the other configurations for frequencies $0.2 < St_{x_r} < 0.8$. There is still a reduction in a similar range further downstream as seen in Fig. 4c, but both the relative and absolute reduction levels are lower. The decrease in low frequencies where most of the energy content is, as observed in Fig. 4b, c, is consistent with both jet nozzle chevrons [2, 3] and TES [6, 12]. However, the increase in high frequencies that is usually simultaneously seen is not observed in Fig. 4b, c. Similarly to the jet chevron count dependence [3] and the λ dependence in TES [10], a dependence on λ can be observed in Fig. 4b, c as the $\lambda/h_s = 12.5$ and $\lambda/h_s = 6.25$ configurations produce reductions, while the $\lambda/h_s = 3.125$ configuration does not.

Four streamwise turbulence intensity profiles are shown in Fig. 5. A comparison of Fig. 5a, b reveals that at $x = h$ there is a small but noticeable difference between a profile taken at the spanwise coordinate of a chevron tip and root. At $x = 3h$ and further downstream there is no significant difference and only the root profile is given in Fig. 5c, d. The only significant deviation from the baseline case is the $\lambda/h_s = 12.5$ configuration showing increased levels at $x = h$ and $x = 3h$, but not at $x = 7h$ or further downstream. The $\lambda/h_s = 12.5$ configuration is similar to jet nozzle chevrons where the chevrons increase the $u'_{\mathrm{rms}}/U_\infty$ levels near the nozzle [2] compared to a round nozzle. However, further downstream there was a reduction in $u'_{\mathrm{rms}}/U_\infty$ which does not appear in Fig. 5d nor further downstream (not shown). Also, the difference

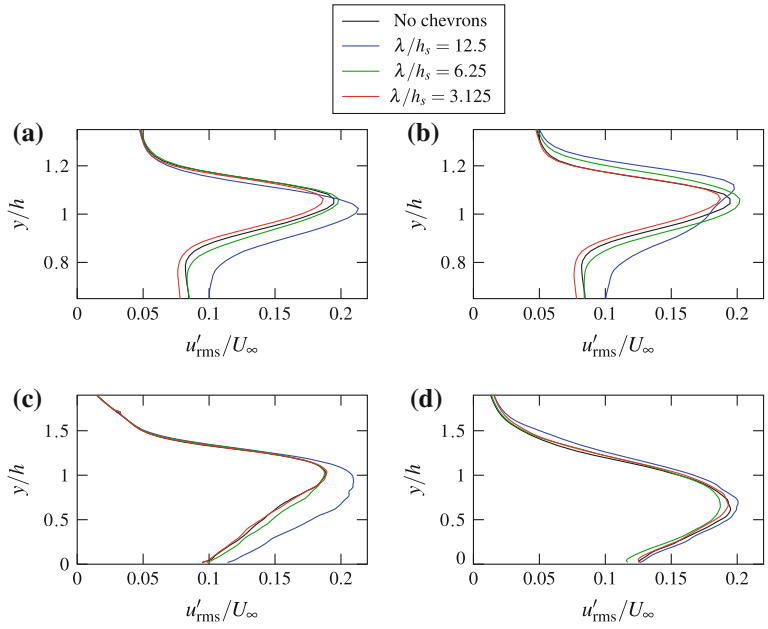


Fig. 5 Streamwise turbulence intensity $u'_{\mathrm{rms}}/U_\infty$ at **a** $x = h$, **b** $x = h$, **c** $x = 3h$ and **d** $x = 7h$. **a**, **c** and **d** is the mean at the root of the chevrons and **b** is the mean at the tip

relative to the base case is much stronger in jet nozzle chevron compared to what is seen in Fig. 5. The reason that there is such a small difference between the different configurations in this paper is attributed to the turbulence found in the turbulent boundary layer which is present and important in the break-up of the K-H vortices in the backward-facing step case [1]. There is no turbulent boundary layer in [2].

4 Conclusions

Chevrons, or serrations, are placed at the top edge of a backward-facing step with the objective to reduce the surface pressure fluctuations downstream of the step. Three chevron configurations and a baseline case are investigated numerically. From the vicinity of the mean reattachment point x_r and further downstream, some reduction in the low frequency content of the pressure fluctuations is found for two of the three configurations. This indicates a dependence on the tip to tip distance λ similar to TES and chevron count for jet nozzle chevrons. Some increase in the pressure fluctuations near the step is observed for the $\lambda/h_s = 12.5$ configuration. However, this region is dominated by frequencies that are too low compared to the sampling time to be accurately resolved. The general impact of the chevrons on the mean flow appears to be small. The mean reattachment length x_r is nearly constant between the different configurations and only one configuration produces any significant difference in the streamwise turbulence levels.

Acknowledgments Joachim Hodara at Georgia Institute of Technology is gratefully acknowledged for sharing his implementation of the Lund inlet BC. This work was supported by the Swedish Governmental Agency for Innovation Systems (VINNOVA) and SAAB AB under the National Aviation Research Programme (NFFP5). The simulations were performed on resources provided by the Swedish National Infrastructure for Computing (SNIC) at Lunarc and HPC2N.

References

1. J.L. Aider, A. Danet, M. Lesieur, Large-eddy simulation applied to study the influence of upstream conditions on the time-dependant and averaged characteristics of a backward-facing step flow. J. Turbul. **8**(N51) (2007). doi:10.1080/14685240701701000
2. M.B. Alkislar, A. Krothapalli, G.W. Butler, The effect of streamwise vortices on the aeroacoustics of a mach 0.9 jet. J. Fluid Mech. **578**, 139–169 (2007). doi:10.1017/S0022112007005022
3. J. Bridges, C.A. Brown, Parametric testing of chevrons on single flow hot jets, in *10th AIAA/CEAS Aeroacoustics Conference* (2004). doi:10.2514/6.2004-2824. AIAA-2004-2824
4. J. Dandois, E. Garnier, P. Sagaut, Numerical simulation of active separation control by a synthetic jet. J. Fluid Mech. **574**, 25–58 (2007). doi:10.1017/S0022112006003995
5. E. de Villiers, The potential of large eddy simulation for the modeling of wall bounded flows. Ph.D. thesis, Imperial College of Science, Technology and Medicine, London (2006)

6. M. Gruber, M. Azarpeyvand, P.F. Joseph, Airfoil trailing edge noise reduction by the introduction of sawtooth and slitted trailing edge geometries, in *Proceedings 20th International Congress on Acoustics, ICA 2010* (2010)
7. M.A.Z. Hasan, The flow over a backward-facing step under controlled perturbation: laminar separation. J. Fluid Mech. **238**, 73–96 (1992). doi:10.1017/S0022112092001642
8. T.S. Lund, X. Wu, K.D. Squires, Generation of turbulent inflow data for spatially-developing boundary layer simulations. J. Comput. Phys. **140**(2), 233–258 (1998). doi:10.1006/jcph.1998.5882
9. M. Mihăescu, C. Harris, E. Gutmark, Flow and acoustics characteristics of chevron nozzles in coaxial jets—LES & acoustic analogy investigation, in *13th AIAA/CEAS Aeroacoustics Conference* (2007). doi:10.2514/6.2007-3609. AIAA-2007-3609
10. D.J. Moreau, L. Brooks, C.J. Doolan, On the noise reduction mechanism of a flat plate serrated trailing edge at low-to-moderate reynolds number, in *18th AIAA/CEAS Aeroacoustics Conference* (2012). doi:10.2514/6.2012-2186. AIAA-2012-2186
11. J. Nilsson, R.Z. Szász, P.E. Austrell, E.J. Gutmark, Load and response prediction using numerical methods in acoustic fatigue. J. Aircraft **53**(2), 406–415 (2016). doi:10.2514/1.C033414
12. S. Oerlemans, M. Fisher, T. Maeder, K. Kögler, Reduction of wind turbine noise using optimized airfoils and trailing-edge serrations. AIAA J. **47**(6), 1470–1481 (2009). doi:10.2514/1.38888
13. OpenFOAM Foundation: OpenFOAM, the open source CFD toolbox user guide, version 2.1.1 (2012)
14. R. Sandberg, L. Jones, Direct numerical simulations of low Reynolds number flow over airfoils with trailing-edge serrations. J. Sound Vib. **330**(16), 3818–3831 (2011). doi:10.1016/j.jsv.2011.02.005
15. D. Spalding, A single formula for the "law of the wall". J. Appl. Mech. **28**(3), 455–458 (1961). doi:10.1115/1.3641728
16. D. Violato, F. Scarano, Three-dimensional evolution of flow structures in transitional circular and chevron jets. Phys. Fluids **23**(12), 124104 (2011). doi:10.1063/1.3665141

Active Flow Control Behind a Backward Facing Step Using a Zero-Net-Mass-Flux System

Umut Can Coskun, Sertac Cadirci and Hasan Gunes

Abstract In this numerical study, the effect of combined suction and blowing with constant mass flux on heat transfer enhancement and flow separation control behind a backward facing step (BFS) in a sufficiently long channel is investigated. The simulations have been carried out by a laminar, incompressible, unsteady open-source flow solver (OpenFoam). Using three different Reynolds numbers for the base-flow (Re = 200, 400 and 600), a parametric investigation of ejections and suctions is performed where the jet configurations are modeled as to produce a zero net mass flux in the channel. The three equally-sized slots for flow control are located on the upper, lower walls of the channel and on the vertical step wall. The magnitudes of jet velocities for suction and blowing are determined with respect to the mean base flow velocity for four different values and jet off-condition. The representative variation of the mean friction coefficient and Nusselt number along the bottom wall downstream the step are reported in an effort to determine the most effective operation condition.

1 Introduction

In the last decades researchers devoted their attention to different flow control strategies since it is necessary in most engineering applications to delay or prevent flow separation and/or improve heat transfer by means of flow mixing. Flow behind

U.C. Coskun · S. Cadirci (✉) · H. Gunes
Department of Mechanical Engineering, Istanbul Technical University,
Gumussuyu, 34437 Istanbul, Turkey
e-mail: cadircis@itu.edu.tr

U.C. Coskun
e-mail: ucoskun@itu.edu.tr

H. Gunes
e-mail: guneshasa@itu.edu.tr

© Springer International Publishing Switzerland 2016

A. Segalini (ed.), *Proceedings of the 5th International Conference on Jets, Wakes and Separated Flows (ICJWSF2015)*,
Springer Proceedings in Physics 185, DOI 10.1007/978-3-319-30602-5_29

a backward facing step is one of the most commonly investigated cases since this configuration represents recirculation zones of different sizes and reattachment lengths for various Reynolds numbers, therefore there are many numerical and experimental studies to control backward-facing step (BFS) flows and enhance heat transfer through mixing. Decreasing or eliminating the size of the recirculation zone and preventing flow separation is one of the main goals of flow control strategies applied to BFS flows.

Flow characteristics behind a backward facing step has long been determined both experimentally and numerically. In a leading experimental study conducted by Armaly et al. [1] numerous BFS flows in a wide range of step-height based Reynolds number between 70 and 8000 were investigated. The aspect ratio which is the ratio of the step height to the total channel height was kept at two and they identified laminar flow for $Re < 1200$, the transitional flow between $1200 < Re < 6600$ and the turbulent flow for $Re > 6600$.

Depending on the inlet Reynolds number based on the inflow velocity and the aspect ratio of the channel, the size of the recirculation zone and reattachment length vary, thus flow control strategies must be selected accordingly. There are many flow control strategies which can be applied to BFS flows which include steady suction and blowing through slots; known as localized wall discharges, actuator-induced jets and vortices, pulsations by mechanical, piezoelectric or electromagnetic flap actuators. Uruba et al. [8] showed that both blowing and suction were able to reduce the length of the separation zone to one third of its value without flow control. Inaoka et al. [5] showed that a certain oscillation frequency of electromagnetic flap actuators could enhance heat transfer in a BFS flow. Nada [7], on the other hand, used another strategy to enhance heat transfer downstream a BFS: dispersing nanoparticles into a BFS flow at low Reynolds numbers increased the averaged Nusselt number distribution along the top and bottom walls using different volume fractions of the nanoparticles.

Kiwan [6] studied the effect of localized wall discharge to control flow separation and heat transfer downstream a BFS and found that wall discharges from slots on the upper wall had a significant influence on the flow and heat transfer characteristics. Cadirci et al. [2, 3] used a jet-and-vortex-actuator (JaVA) which is a zero-net-mass-flux system and applied it to energize the boundary layer flow over a sufficiently long flat plate at low Reynolds numbers. It was found that with increasing oscillation frequency of the actuator, fuller velocity profiles could be obtained and increased friction coefficients and decreased shape factors were provided compared to the base flow without flow control. Coskun et al. [4] numerically investigated laminar flow over a BFS with localized suction and blowing on the channel and step walls and indicated that the location of the slots and mass flow rates of suction or blowing strongly determined the effectiveness of flow separation control and heat transfer enhancement.

2 Problem Description of the BFS Flow

Computational domain and boundary conditions: In this study, we keep the step height $h = 0.01$ m and the total channel height is $H = 0.02$ m. The upstream and downstream channel lengths are 4 h and 30 h respectively. The location of the outflow section has been chosen sufficiently far from the step so that the position of the recirculation zone is not affected. The working fluid is air and it is assumed to be Newtonian and incompressible with constant thermo-physical properties (kinematic viscosity $\nu = 1.5 \times 10^{-5}$ m^2/s, thermal expansion coefficient $\beta = 3.348 \times 10^{-3}$ K^{-1} and Prandtl number is 0.712). The inlet Reynolds numbers based on the double step height (=2 h) are selected 200, 400 and 600 to remain in the stable laminar flow regime and the corresponding mean inlet velocities are then calculated as 0.15, 0.30 and 0.45 m/s respectively. The inlet velocity is defined as a fully developed second order polynomial (1) where U_{max} denotes the centerline velocity which is 3/2 of the mean inlet velocity and y is the vertical cell-centered locations along the inlet of the channel. At the inlet, the fluid has a uniform temperature of $T_\infty = 300$ K.

$$u(y) = -4U_{max}\left[\left(\frac{y}{h}\right)^2 - \left(\frac{y}{h}\right)\right] \tag{1}$$

At the outlet of the channel (yellow line in Fig. 1a) outflow boundary condition is prescribed. The top wall of the channel and the vertical and horizontal edges of the backward-facing step (green lines in Fig. 1a) are treated as adiabatic walls. The bottom wall of the channel (red line in Fig. 1a) has a uniform temperature distribution of $T_H = 350$ K. On all walls, no-slip condition for velocities are imposed. Figure 1b indicates the locations of the three slots on the top, bottom and step walls and the boundary conditions for velocity and temperature in an enlarged scale. If fluid is sucked ($v = -V_J$), zero temperature gradients are imposed.

The slots located on the top, step and bottom walls of the channel are denoted by (A), (B) and (C) respectively. The jet velocities are defined according to the mean velocity at the inlet for three Reynolds numbers. The magnitudes of the jet velocities can be 1 or $2U_m$ which means that the jet velocity is either equal to the inlet mean velocity or two times of the inlet mean velocity. A zero value stands for a closed slot which is treated as wall with local thermal boundary conditions. Positive and negative signs indicate the jet's direction, in other words, a plus sign denotes blowing at constant ambient temperature into the base flow and a minus sign refers to suction from the base flow with zero temperature gradient.

Flow solver settings for OpenFoam:
Before initializing computations, the appropriate mesh was determined with sufficient element number. The mesh convergence tests were performed for Re = 400 ($U_m = 0.3$ m/s) and the jet configuration of (A = 2, B = −2, C = 0) using coarse, medium and fine meshes with 17,199, 34,398 and 68,796 elements respectively. Mesh convergence tests for velocity and temperature fields revealed that a

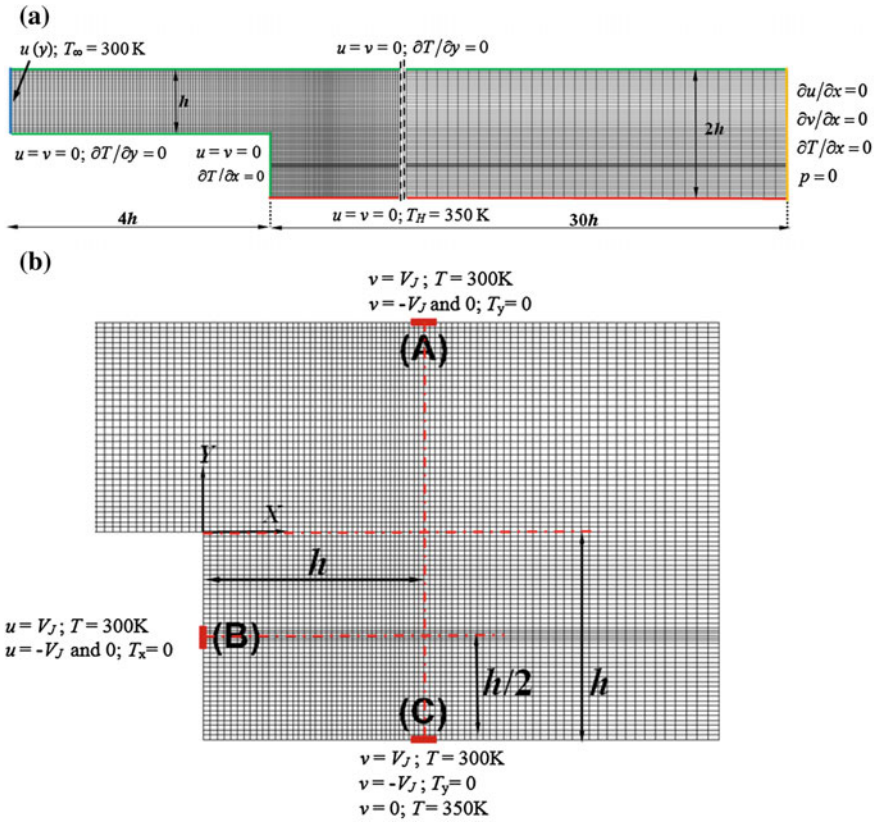


Fig. 1 **a** The computational domain showing the grid distribution with boundary conditions, **b** The computational domain near the backward-facing step with three slot locations. Here $T_x = \partial T/\partial x$ and $T_y = \partial T/\partial y$

structured mesh with 34,398 elements, clustered near the step, was sufficient to obtain reliable numerical results. The selected controlled case (A = 2, B = –2, C = 0) denotes that a jet is blown into the base-flow through the slot (A) and sucked from the base-flow through the slot (B) by a magnitude of $2U_m$ (=0.6 m/s) where slot (C) is treated as a wall.

The selected flow solver was 'Buoyant-Boussinesq-PIMPLE FOAM' which fitted best to the problem. Since the flow was transient and incompressible, PIMPLE (merged PISO-SIMPLE) algorithm was used with preconditioned bi-conjugate gradient method (PBiCG) for momentum and energy equations. The time step was 0.01 s and the total time integration of the flow required was 30 s to reach the steady state condition. Diagonal incomplete LU (DILU) decomposition was used as preconditioner to allow minimum number of iterations in order to reduce computational time.

3 Results

Flow and temperature fields

Figure 2a, b show the velocity fields for the reference flow (A = 0, B = 0, C = 0) and the selected controlled case (A = 2, B = –2, C = 0) respectively. Steady jet ejection from slot (A) on the top wall and steady suction from slot (B) on the step wall assist the flow to resist flow separation by momentum transfer into the boundary layer at the bottom wall. As a result the size of flow separation zone in the original base flow reduces significantly and the reattachment length on the bottom wall which is near $x/h = 10$ in the base flow is pulled back to approximately $x/h = 2$ for the configuration of (A = 2, B = –2, C = 0).

Figure 2c, d show the temperature fields for the reference flow and the selected controlled case respectively. The active flow control is also effective in heat transfer enhancement due to flow direction to the bottom wall by the jets, thus in the controlled case the temperature gradients on the bottom wall become larger compared to the reference case and the Nusselt number increases. Theoretically, the local Nusselt number sufficiently far from the jet-manipulations for instance at the exit of the channel should be the same as the reference flow.

To show the effectiveness of flow control on the flow fields, velocity and temperature profiles for Re = 400 have been extracted downstream of the BFS at locations $x/h = 4$ and 8 in Fig. 3. The velocity profiles reveal that the flow separation zone on the bottom wall vanishes due to suction and ejection while a new flow separation zone is occurring on the top wall of the channel (due to the continuity equation). By appropriate suction and blowing introduced to the BFS flow, the backflow on the bottom wall can be prevented and fuller velocity profiles can be obtained leading to higher velocity gradients (i.e., higher wall shear stresses). Figure 3 also indicates that by flow control, steeper temperature profiles are observed which means that the temperature gradients are much higher compared to the base flow at bottom wall, thus the Nusselt number increases significantly. Figure 4 shows the friction coefficient and Nusselt number distribution along the bottom wall for the investigated cases.

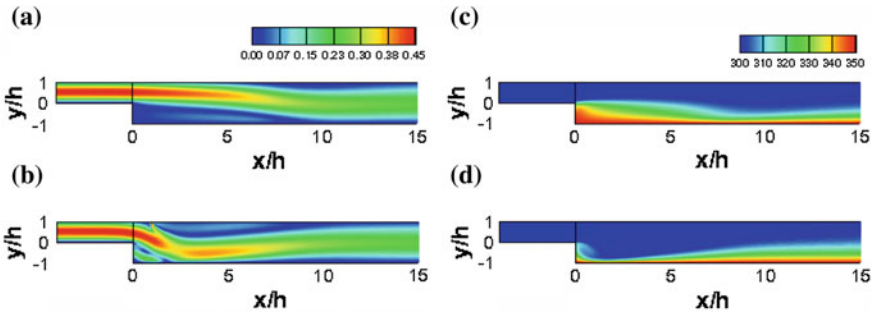


Fig. 2 The velocity (**a**, **b**) and temperature (**c**, **d**) fields for Re = 400: first row reference case (0, 0, 0) and second row case (2, –2, 0); colors denote the contour level in m/s and K

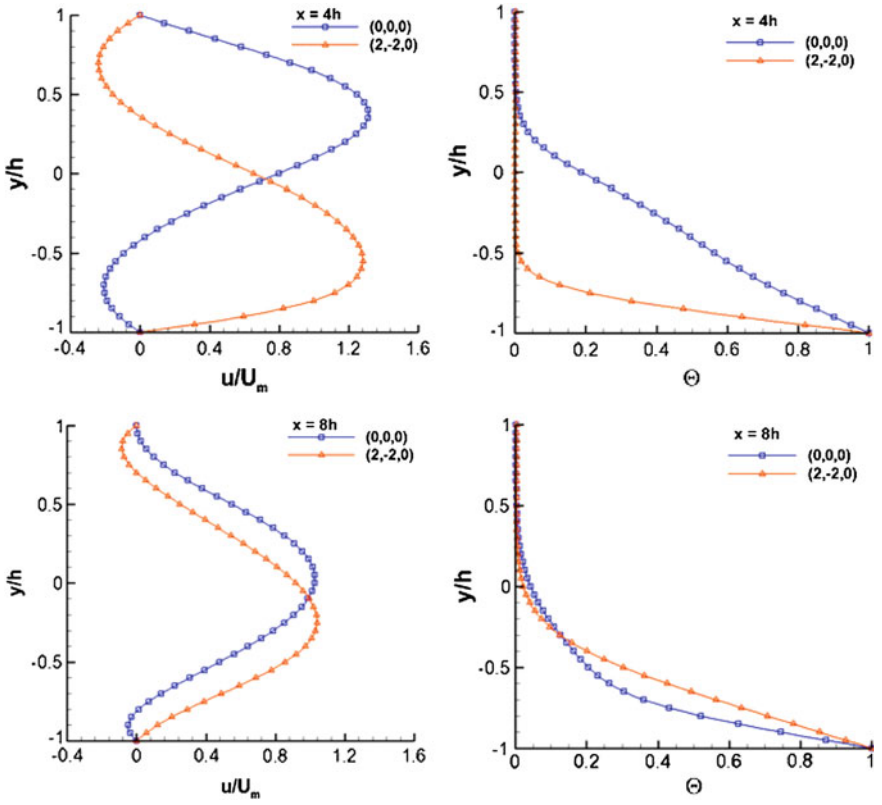


Fig. 3 Comparison of the reference case with the most efficient jet configuration for Re = 400, *left column* streamwise velocity, *right column* temperature

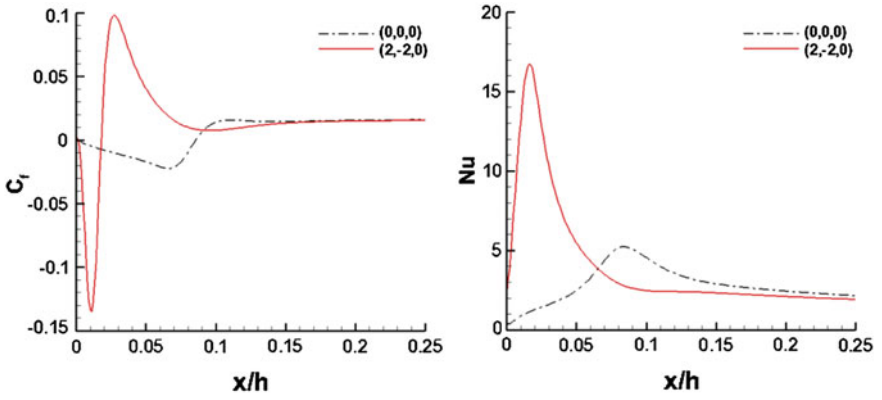


Fig. 4 Comparison of the reference case with the most efficient jet configuration for Re = 400, *left column* friction coefficient, *right column* Nusselt number

Mean friction coefficient and Nusselt number distributions

Figure 5 shows the averaged friction coefficient (C_f) and Nusselt number (Nu) distribution along the bottom wall downstream the step on a mass flow rate space. The averaged C_f and Nu numbers on the bottom wall of the channel for Re = 400 are also given in Table 1. After steady state conditions have been achieved, C_f and Nu for 19 configurations are calculated from wall shear stress and temperature difference respectively and their interpolated values are plotted on a (A−B) jet-space. The axis of the graphics denote the mass flow rate ratios of the upper jet (A) and step jet (B) to the inlet mean velocities respectively.

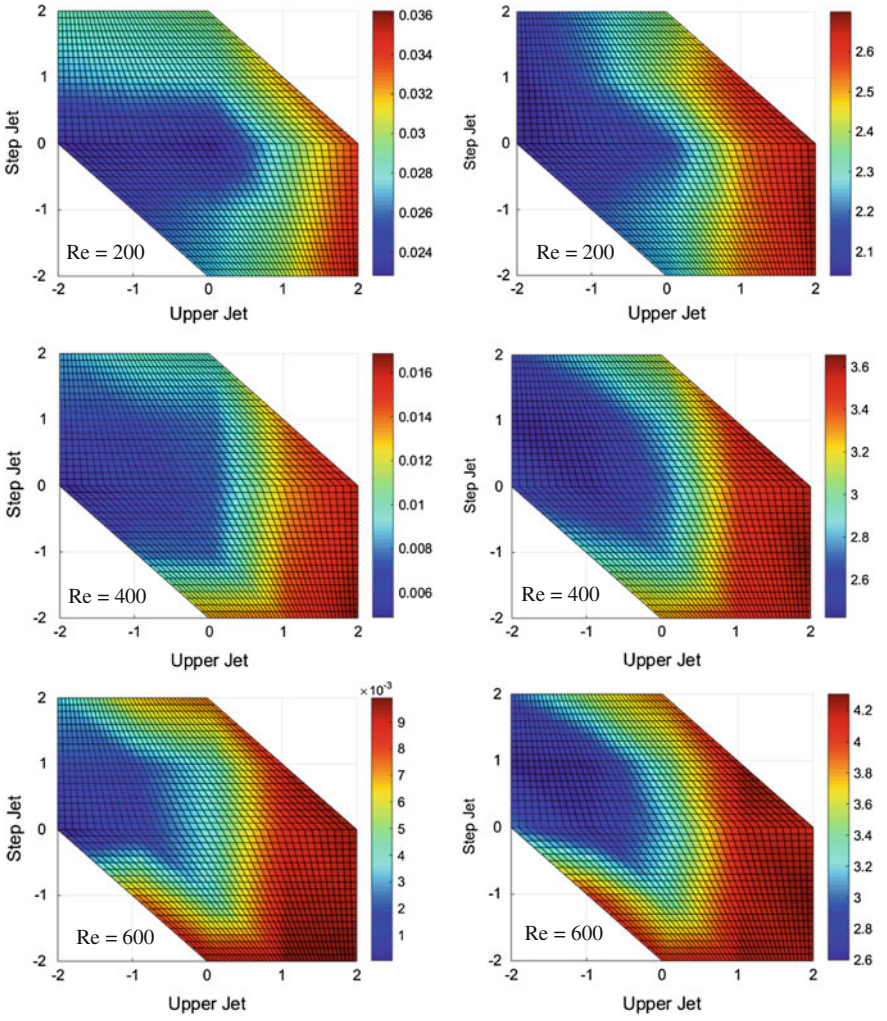


Fig. 5 Averaged friction coefficient and Nusselt number distribution along the bottom wall: *left column* C_f, *right column* Nu, (for Re = 400, see Table 1)

Table 1 Averaged friction coefficient and Nusselt numbers for Re = 400

(A)	(B)	(C)	C_f	*Nu*	(A)	(B)	(C)	C_f	*Nu*
2	–2	0	0.016865	3.596	–1	2	–1	0.009760	2.883
2	0	–2	0.016271	3.577	–2	2	0	0.008368	2.609
2	–1	–1	0.016249	3.654	–1	–1	2	0.007893	2.899
1	–2	1	0.014514	3.491	0	1	–1	0.007853	2.857
1	1	–2	0.014122	3.566	0	–1	1	0.007784	2.811
1	–1	0	0.013978	3.446	0	0	0	0.007419	2.725
0	–2	2	0.013859	3.329	–1	1	0	0.007065	2.477
1	0	–1	0.013398	3.452	–2	1	1	0.007045	2.423
0	2	–2	0.009777	3.129	–1	0	1	0.006270	2.450
					–2	0	2	0.004888	2.597

Since the system is a zero-net-mass flux system, the mass flow rate ratios of the lower jets (C) can be predicted easily. For all Reynolds numbers, the most effective configurations are clustered in the right hand side of the reference case (A = B = C = 0) where blowing at mass flow rate ratios between [+1 and +2] from the slot on the top wall and suction and/or blowing at mass flow rate ratios between [–2 and +1] from the step slot are combined with each other. This indicates that blowing from the top wall and mostly suction from the step wall will yield in higher C_f and *Nu* for all cases. The least effective configurations are on the left hand side of the reference case where suction from the slot on the top wall and blowing from the slot on the step wall is performed.

4 Conclusion

In this numerical study, the velocity and temperature profiles extracted downstream of the BFS are obtained to show that the recirculation zone behind the BFS can be reduced significantly and the heat transfer is enhanced by proper suction and blowing configurations. It is shown that the mean friction coefficients and Nusselt numbers along the bottom wall downstream the step can be increased significantly by blowing from the slot on the top wall and suction from the slot on the step wall. Other configurations are found to be less effective.

References

1. B.F. Armaly, F. Durst, J.C.F. Pereira, B. Schönung, Experimental and theoretical investigation of backward-facing step flow. J. Fluid Mech. **127**, 473–496 (1983)
2. S. Cadirci, H. Gunes, U. Rist, Active flow control applications with a jet and vortex actuator in a laminar cross flow. Int. J. Heat Fluid Flow **39**, 146–159 (2013)

3. S. Cadirci, H. Gunes, U. Rist, Numerical investigation of a jet and vortex actuator in a cross flow boundary layer. Eur. J. Mech. B **44**, 42–59 (2014)
4. U.C. Coskun, S. Cadirci, H. Gunes, Heat Transfer Enhancement behind a Backward Facing Step Using Localized Suction and Blowing, in *Proceedings of CONV-14, International Symposium on Convective Heat and Mass Transfer*. Kuşadası, Turkey, 8–13 June 2014
5. K. Inaoka, K. Nakamura, M. Senda, Heat transfer control of a backward-facing step flow in a duct by means of miniature electromagnetic actuators. Int. J. Heat Fluid Flow **25**, 711–720 (2004)
6. S. Kiwan, Using localized wall discharge to control the fluid flow and heat transfer for the flow over a backward facing step. Int. J. Numer. Methods for Heat Fluid Flow **18**(6), 745–765 (2008)
7. E.A. Nada, Application of nanofluids for heat transfer enhancement of separated flows encountered in a backward facing step. Int. J. Heat Fluid Flow **29**, 242–249 (2008)
8. V. Uruba, P. Jonas, O. Mazur, Control of a channel flow behind a backward facing step by suction blowing. Int. J. Heat Fluid Flow **28**, 665–672 (2007)

Control of the Reattachment Length of a Transonic 2D Backward-Facing Step Flow

Istvan Bolgar, Sven Scharnowski and Christian J. Kähler

Abstract When a turbulent flow reaches a sudden expansion as in the case of a backward-facing step (BFS), a turbulent separated shear layer originates from the trailing edge. The reattachment location of this shear layer varies in time and space, causing high dynamic loads on the reattachment surface. This is an inherent problem on some of today's cryogenic space launchers, where the main engine's nozzle suffers from high buffeting loads during the transonic phase of the ascent, due to a turbulent reattaching shear layer, especially originating from a geometric discontinuity, similar to a BFS. For this reason the aim of the current research focuses on stabilizing and reducing the reattachment length of the separated shear layer on a BFS in transonic flow by the means of passive flow control devices. Several streamwise vortex generators were examined in the Trisonic Wind Tunnel Munich (TWM) with particle image velocimetry (PIV). The investigations were conducted on a 2D model at Mach 0.8 and a Reynolds number of 1.8×10^5 with respect to the step height (h). The results show that streamwise vortex generators have a tremendous effect on reducing the size of the recirculation region, reducing the reattachment location by 75 % or more, when compared to the reattachment location of a BFS wake.

1 Introduction

The separated wake flow behind a BFS has been of scientific interest for several decades [2, 3, 5, 9, 12]. Experiments in the past show that the mean reattachment location varies between $5–8h$ [5]. This large deviation can partly be attributed to the fact that reattachment is sensitive to the adverse pressure gradient present in the wind tunnel, altering the reattachment location by as much as $\pm 1h$ [10]. Looking at the temporal behavior of a turbulent shear layer behind a BFS, not only the reattachment location fluctuates, but the entire region of reverse flow oscillates with

I. Bolgar (✉) · S. Scharnowski · C.J. Kähler
Bundeswehr University Munich, Werner-Heisenberg-Weg 39,
85577 Neubiberg, Germany
e-mail: istvan.bolgar@unibw.de

© Springer International Publishing Switzerland 2016

A. Segalini (ed.), *Proceedings of the 5th International Conference on Jets, Wakes and Separated Flows (ICJWSF2015)*,
Springer Proceedings in Physics 185, DOI 10.1007/978-3-319-30602-5_30

several modes [18, 19]. It has been shown that these fluctuations are caused by well-organized large-scale coherent structures, with a characteristic periodicity into the spanwise direction, that appear in the wake of the BFS [15]. These phenomena cause high dynamic loads on the reattaching surface downstream of the step. This problem also arises on the main engine of the Ariane 5 launch vehicle for instance, and is most severe in the transonic phase of the flight [6]. In a simplified version, the aft body of such a space launcher can be mimicked by a BFS. For this reason, it is the aim of the current investigations to examine the sensitivity of the reattachment location and its temporal dynamics aft of a transonic BFS flow, on the amplitude and spatial periodicity of passive flow control devices. This is important for reducing the moment arm, and with that, the dynamic loads.

It has been shown, that by increasing the streamwise vorticity ahead of the step, the reattachment length can be reduced by as much as 25 % [7]. This can be explained by the enhancement of the turbulent mixing in the shear layer due to coherent vortices, which then increase the momentum near the wall and thus cause an upstream shift of the reattachment location [7]. One approach to introduce streamwise vortices into the flow would be the application of so-called chevrons. This technology is successfully used in gas turbines today, with the aim to reduce noise emissions by destroying coherent shear layer vortices. They also have been investigated on a BFS, however with minimal advantages on the Reynolds shear stress fluctuations, and a negligible effect on the size of the reverse flow region [16]. This implies that a more advanced manipulation of the flow is required to enhance the turbulent mixing aft of a BFS.

Another approach used for flow mixing in gas turbines is the so-called lobed mixer, which is the geometry under investigation within the framework of this work. It has been shown, that the larger the velocity shear between the two parallel flows is, the further upstream they mix out [11]. This is due to the shear present between the two flows, adding normal vorticity (due to Kelvin-Helmholtz instabilities) along with streamwise vorticity from the lobes to the flow, further increasing turbulent mixing within the shear layer. Due to the recirculation behind the BFS, strong shear exists at that location naturally. This amplifies the effect of the streamwise vortices, created by the lobes, in the shear layer mixing, thus providing good conditions for a shorter reattachment location.

A sketch of a BFS with such a convoluted trailing edge, or so-called lobes, is provided in Fig. 1 on the right. Due to the geometrically induced aerodynamic loading along the spanwise direction of the lobes, the streamwise vortices shedding off of such a wavy trailing edge are much larger in both, intensity and scale, than the ones developing naturally in boundary layers and shear layers [20]. In effect, the turbulent mixing within the shear layer is enhanced, as counter-rotating vortices from neighboring lobes diffuse into one another, breaking down the coherent structures and becoming fully three-dimensional, a driving criterion for reattachment [17].

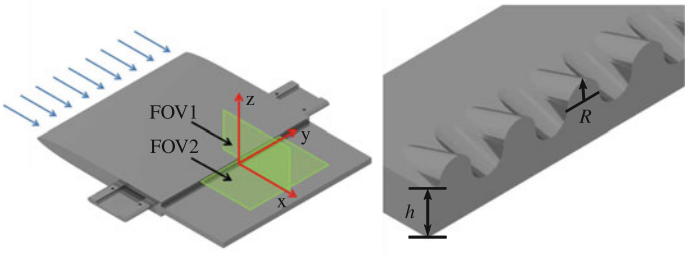


Fig. 1 *Left* Illustration of the quasi-2D model and the 2 FOV under investigation; *Right* illustration of a BFS with so-called lobes on its trailing edge

2 Experimental Set-Up

All experiments were conducted in the Trisonic Wind Tunnel at the Bundeswehr University Munich, which is a blow-down type wind tunnel with an operating total pressure range of 1.2–5 bar, and a Mach number range of 0.15–3. Up to 20 bar (above ambient) of pressurized dry air is stored in two tanks, holding a total volume of 356 m^3. The test section is 300 mm wide and 675 mm high with suction capabilities at both, the horizontal and the vertical walls. More details about the facility are discussed by Bitter et al. [1]. For the experiments discussed here, a total pressure of 1.73 bar, a total temperature of 285 K, and a Mach number of 0.8 were examined, yielding a Reynolds number of 1.8×10^5 based on the step height. A quasi-2D model symmetric about its horizontal plane, spanning across the entire test section was investigated. It has a 150 mm long gently curved nose, in order to ensure subsonic conditions locally (at $M_\infty = 0.8$), which then transitions into a 100 mm long flat plate prior to the step. The step is 7.5 mm high (symmetric on the top and bottom sides of the model), followed by a 125 mm long splitter plate. The overall model's thickness is 25 mm, while the step height to step width ratio is 1:40, providing an unaffected recirculation region from side wall effects [5]. Furthermore, the side wall suction capability of the wind tunnel was taken advantage of, in order to compensate for the increasing displacement thickness of the side wall boundary layers.

Two planar fields of view (FOV) were evaluated; a horizontal one and a vertical one located at 85 % of the step height (refer to Fig. 1 on the left). The PIV set-up consisted of a double pulse PIV laser with 100 mJ per pulse, an sCMOS camera with a 70 mm (FOV1) and a 100 mm (FOV2) objective, and an optical set up to construct the light sheet. The flow was seeded with Di-Ethyl-Hexyl-Sebacat (DEHS) tracer particles with a mean diameter of 1 μm (for details refer to [8]).

The sCMOS camera has a resolution of 2560 × 2160 pixel. The double pulses of the laser were separated by a time difference of 2 μs, corresponding to a 15 pixel particle image shift in the free stream, which allows to avoid bias errors due to curved streamlines [13]. The data processing included iterative image deformation and Gaussian window weighting. The final interrogation-window size was 16 × 16 pixel with an overlap of 50 %, yielding a vector grid spacing of 250 μm (3.3 % of the

step height). Finally, a post-processing step replaced vectors that differed by more than two times the standard deviation from the median of their neighbors for each component, with the median of the neighbors, in order to reject outliers. The mean velocity fields were then calculated by averaging 800 instantaneous vector fields.

3 Results

First, the baseline case was investigated to have a foundation for comparison. The results showed that the mean flow reattached at approximately $6h$ downstream of the step (illustrated in Fig. 2), which is within the range of other experiments [3, 5], as well as simulations on 2D models [18], whereas it is shifted downstream compared to the axisymmetric case [4, 14]. The maximum mean back flow velocity was about 30 % of the freestream velocity. The streamlines in the recirculation region are completely closed, indicating that the mean flow field is two-dimensional. Also, a secondary recirculation region can be observed at the base of the step, rotating in the opposite direction to the primary one.

Making use of the convoluted trailing edge, also referred to as lobes (refer to Fig. 1 on the right), the results from the vertical plane (FOV1) show that the reattachment length of the mean flow field was drastically reduced. The best case of the circular lobes ($R = 0.4h$) showed reattachment at $1.5h$ at most. It has to be noted however, that the lobes create a highly three-dimensional flow environment not only instantaneously, but also when looking at the mean. This means that behind the peak, the reverse flow region extends to about $2.5h$ aft of the step, while at the middle and valley locations the recirculation regions look rather like generic separation regions (refer to Fig. 3). Furthermore, the streamlines are not closed, also indicating the presence of a flow component along the spanwise direction, going either into or out of the images. The maximum back flow velocity is also reduced to about 25 % of the freestream.

As the effect of the amplitude and spatial periodicity of the lobes was not known, lobes with radii of 0.2 and $0.3h$ were also investigated, while all lobe radii had lobe deflection angles of 18°. Similar flow behavior was observed with these scalings

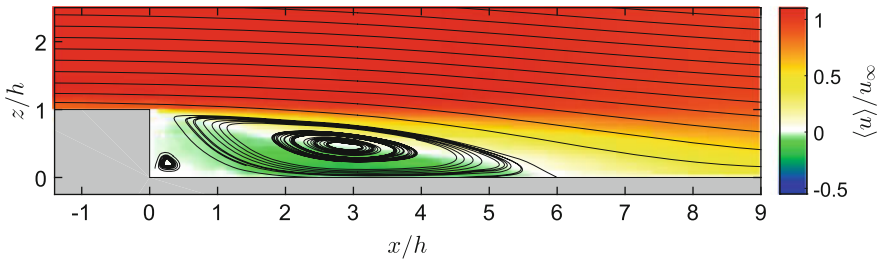


Fig. 2 Mean vertical flow field (FOV1) of the baseline case

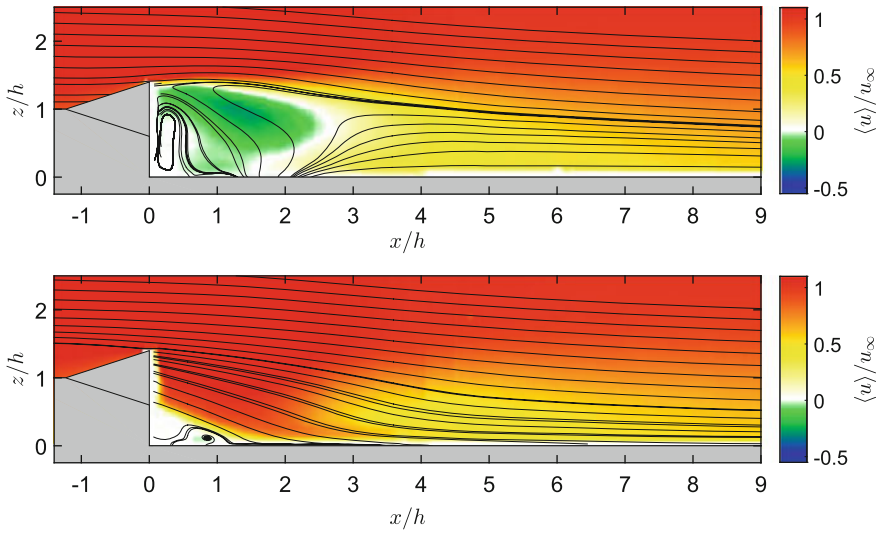


Fig. 3 Mean vertical flow field (FOV1) of the circular lobes with $R = 0.4h$ at lobe peak (*top*) and valley locations (*bottom*)

as for the circular lobes $0.4h$. While the reattachment location went slightly downstream with decreasing lobe size, it is notable that the shape of the recirculation region behind the peaks changed. When looking at the flow field behind the peak of the circular lobe $0.4h$ in detail (Fig. 3 on the top), one can see two distinct maxima in the reverse flow region; an upper and a lower maximum. With decreasing lobe size, the reverse flow region around the upper maximum shrinks while the lower one grows, diffusing the two maxima into one another, making the shape of the reverse flow area resemble that of a common reverse flow region aft of a BFS (refer to Fig. 4). This can be attributed to the fact that with decreasing lobe size not only the scale and intensity of the streamwise vortices decreases, but also the blockage behind the upwards extending lobes decreases, reducing the shear strength that ultimately drives the intensity of the normal vortices. This then leads to an overall longer reattachment, where the reattachment location of the circular lobes $0.2h$ is around $3h$, which is still a 50 % reduction when compared to the baseline case.

Looking at the mean flow in the horizontal plane (FOV2) for the circular lobes $0.2h$ case, the presence of the strong counter-rotating streamwise vortices can be inferred due to the orientation of the velocity vectors (refer to Fig. 5 on the bottom). It can also be seen that from around 3 step heights onward, these vortices diffuse into one another, as the orientation of the velocity vectors becomes axial in that plane. By shaping the trailing edge of the BFS with the lobes, these large-scale flow structures are forced to appear time independently at set locations. In contrast, the mean flow field in the horizontal plane of the baseline case does not contain any structures in the spanwise direction (refer to Fig. 5 on the top).

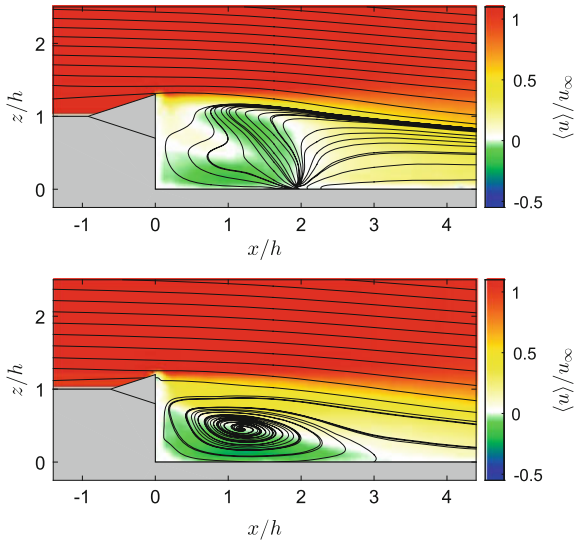


Fig. 4 Mean vertical flow field (FOV1) of the circular lobes with $R = 0.3h$ (*top*) and $R = 0.2h$ (*bottom*) at lobe peak

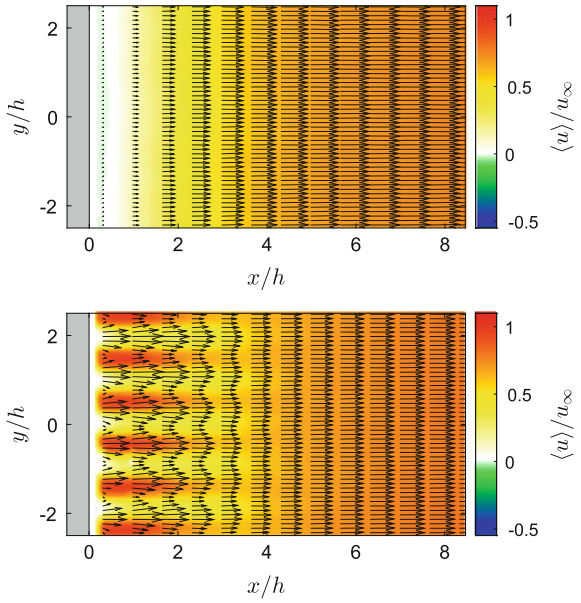


Fig. 5 Mean horizontal flow field (FOV2) for the baseline case (*top*) and the circular lobes with $R = 0.2h$ (*bottom*)

4 Conclusions

From the results it can be concluded that the introduction of large-scale streamwise vortices into the flow drastically reduce the separation length aft of a BFS. A reduction of up to 75 % was achieved with the largest lobes, which decreases the moment

arm of the dynamic loads on the reattaching surface downstream of the step significantly. With decreasing lobe radii the effect on the reattachment length slightly diminished, however a 50 % reduction in the reattachment length was still achieved with a lobe radius of $0.2h$. A remaining question is whether these flow control devices yield benefits throughout a wide range of Mach numbers, such as flown by a space launcher, without creating drawbacks such as a large drag penalty. Regardless, the findings of this work show promising results for such a lobe geometry as a passive means of flow control, where the reduction in the recirculation region is of paramount interest. Such flow control devices could be adopted in many aeronautical applications.

Acknowledgments Financial support from the German Research Foundation (DFG) in the framework of the TRR 40—Technological foundations for the design of thermally and mechanically highly loaded components of future space transportation systems—is gratefully acknowledged by the authors.

References

1. M. Bitter, S. Scharnowski, R. Hain, C.J. Kähler, High-repetition-rate PIV investigations on a generic rocket model in sub- and supersonic flows. Exp. Fluids **50**, 1019–1030 (2011)
2. I. Bolgar, S. Scharnowski, C.J. Kähler, Control of the reattachment length of a transonic 2D backward-facing step flow, in *ICJWSF 2015* (2015)
3. P. Bradshaw, F.Y.F. Wong, The reattachment and relaxation of a turbulent shear layer. J. Fluid Mech. **52**, 113–135 (1972)
4. S. Deck, P. Thorigny, Unsteadiness of an axisymmetric separating-reattaching flow: numerical investigation. Phys. Fluids **19**, 065103 (2007)
5. J.K. Eaton, J.P. Johnston, A review of research on subsonic turbulent flow reattachment. AIAA J. **19**, 1093–1100 (1981)
6. K. Hannemann, H. Lüdeke, J.-F. Pallegoix, A. Ollivier, H. Lambaré, J.E.J. Maseland, E.G.M. Geurts, M. Frey, S. Deck, F.F.J. Schrijer, F. Scarano, R. Schwane, Launch vehicle base buffeting—recent experimental and numerical investigations, in *Proceedings European Symposium Aerothermodynamics Space Vehicles 7* (2011)
7. K. Isomoto, S. Honami, The effect of inlet turbulence intensity on the reattachment process over a backward-facing step. J. Fluids Eng. **111**, 87–92 (1989)
8. C.J. Kähler, B. Sammler, J. Kompenhans, Generation and control of particle size distributions for optical velocity measurement techniques in fluid mechanics. Exp. Fluids **33**, 736–742 (2002)
9. H.-J. Kaltenbach, Turbulent flow over a swept backward-facing step. Eur. J. Mech. B Fluids **23**, 501–518 (2004)
10. D.M. Kuehn, Effects of adverse pressure gradient on the incompressible reattaching flow over a rearward-facing step. AIAA J. **18**, 343–344 (1980)
11. D.C. McCormick, J.C. Bennett Jr., Vortical and turbulent structure of a lobed mixer free shear layer. AIAA J. **32**, 1852–1859 (1994)
12. K.O. O'Malley, A.D. Fitt, T.V. Jones, J.R. Ockendon, P. Wilmott, Models for high-Reynolds-number flow down a step. J. Fluid Mech. **22**, 139–155 (1991)
13. S. Scharnowski, C.J. Kähler, On the effect of curved streamlines on the accuracy of PIV vector fields. Exp. Fluids **54**, 1435 (2013)
14. S. Scharnowski, C.J. Kähler, Investigation of a transonic separating/reattaching shear layer by means of PIV. Theor. Appl. Mech. Lett. **5**, 30–34 (2015)

15. S. Scharnowski, I. Bolgar, C.J. Kähler, Control of the recirculation region of a transonic backward-facing step flow using circular lobes, in *TSFP 9* (2015)
16. F.F.J. Schrijer, A. Sciacchitano, F. Scarano, Experimental investigation of flow control devices for the reduction of transonic buffeting on rocket afterbodies, in *International Symposium on ALTFM*, pp. 1–12 (2010)
17. L.R. Simpson, Turbulent boundary-layer separation. Annu. Rev. Fluid Mech. **21**, 205–232 (1989)
18. V. Statnikov, I. Bolgar, S. Scharnowski, M. Meinke, C.J. Kähler, W. Schröder, Analysis of characteristic wake flow modes on a generic planar transonic space launcher configuration, in *EUCASS 6* (2015)
19. V. Statnikov, T. Sayadi, M. Meinke, P. Schmid, W. Schröder, Analysis of pressure perturbation sources on a generic space launcher after-body in supersonic flow using zonal turbulence modeling and dynamic mode decomposition. Phys. Fluids **27**, 016103 (2015)
20. I.A. Waitz, Y.J. Qiu, T.A. Manning, A.K.S. Fung, J.K. Elliot, J.M. Kerwin, J.K. Krasnodebski, M.N. O'Sullivan, D.E. Tew, E.M. Greitzer, F.E. Marble, C.S. Tan, T.G. Tillman, Enhanced mixing with streamwise vorticity. Prog. Aerosp. Sci. **33**, 323–351 (1997)

POD Analysis of Jet and Vortex Flows Induced by Oscillating Backward Facing Step

Sertac Cadirci, Mustafa Ozsipahi and Hasan Gunes

Abstract An oscillatory, zero-net-mass flux actuator system, Jet and Vortex Actuator (JaVA), is implemented on the step wall of a backward facing step (BFS) in order to control the recirculation zone behind BFS. The actuator plate has a sinusoidal motion determined by the amplitude and the operating frequency. The proposed control method based on suction and blowing with an oscillating backward facing step seems to be effective in reducing the recirculation zone length and preventing flow separation downstream of BFS. Modal investigation of flow fields are performed by means of Proper Orthogonal Decomposition (POD). POD is applied to time-dependant snapshots of velocity fields at several operating frequencies. The POD modes revealed the behavior of the flow past a BFS under the effect of active flow control.

1 Introduction

In the last decades, researchers devote their attention to active flow control which is gaining popularity in many aerodynamics applications. Active flow control can be employed to prevent or delay flow separation and/or enhance heat transfer. Flow control strategies can be in a wide range of applications: steady suction and blowing through slots; actuator induced jets and vortices, pulsations by mechanical, piezoelectric or electromagnetic flap actuators. One of the mechanically-driven actuator which can be used for active flow control is the Jet and Vortex Actuator

S. Cadirci · M. Ozsipahi (✉) · H. Gunes
Department of Mechanical Engineering, Istanbul Technical University, Gumussuyu, 34437 Istanbul, Turkey
e-mail: ozsipahimu@itu.edu.tr

S. Cadirci
e-mail: cadircis@itu.edu.tr

H. Gunes
e-mail: guneshasa@itu.edu.tr

© Springer International Publishing Switzerland 2016

A. Segalini (ed.), *Proceedings of the 5th International Conference on Jets, Wakes and Separated Flows (ICJWSF2015)*,
Springer Proceedings in Physics 185, DOI 10.1007/978-3-319-30602-5_31

(JaVA). There are various numerical and experimental studies concerning the effects of JaVA on laminar boundary layers over flat plates and over BFS. Cadirci et al. investigated the effect of JaVA on the laminar boundary layer over a flat plate for various governing parameters such as actuator plate frequency, amplitude and plate position. It was shown that fuller velocity profiles could be obtained compared to the reference flow without flow control, thus lower displacement thicknesses and higher friction factors could be obtained [1, 2]. The application of JaVA on separated flows over BFS showed that the active flow control reduced the size of the recirculation zone and enhanced heat transfer, thus on the bottom wall of the channel higher friction coefficients and Nusselt numbers could be achieved compared to the reference flow [3, 4].

In this study, POD analysis is applied to numerical simulations of JaVA-induced flows over a BFS. POD is a powerful approach to obtain low-dimensional dynamical models of thermo-fluid applications. The basics of POD and its applications have been reported by Lumley and Berkooz [5, 6]. The "snapshot version" of POD introduced by Sirovich [7] is an efficient implementation for "time-dependent" snapshots to extract coherent flow structures (modes). Gunes and Cadirci used POD as a 'modeling and inverse-design' tool for convection in a grooved channel [8]. Cadirci and Gunes [9] employed snapshot version of POD to the database consisting of time-dependent snapshots of numerically obtained two-dimensional velocity fields. Gunes and Rist [10] used POD as a 'modeling and reconstruction' tool for transitional boundary layer flow with and without flow control.

2 Computational Domain and Boundary Conditions

The JaVA-induced flows emerge out of the wide gap and are injected into the boundary layer, thus an average jet flow speed (V_J) should be defined to obtain jet Reynolds number. Time-averaged integration of the jet velocity over a half period reveals the averaged jet velocity given in (1).

$$V_J = \frac{2}{T}\int_0^{T/2} v_j(t)dt = \frac{4abf}{w_w} \tag{1}$$

The jet Reynolds number (Re_J) in (2) can be calculated using the averaged jet velocity and the wide slot gap. The jet Reynolds number varies with the frequency (f = 1 and 2 Hz) where the amplitude (a = 1 mm) and plate width (b = 25 mm) are kept constant. Depending on the oscillation frequency, the jet Reynolds number is 100 and 200.

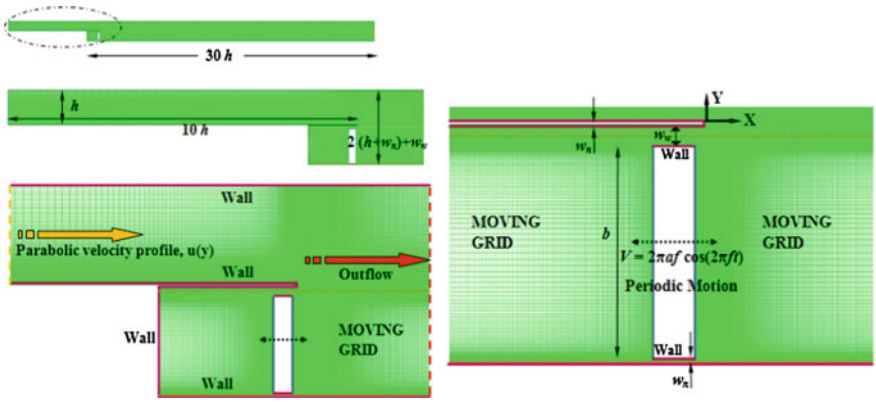


Fig. 1 JaVA model and boundary conditions

$$\mathrm{Re}_J = \frac{V_J w_w}{v} = \frac{4abf}{v} \tag{2}$$

The computational domain and imposed boundary conditions are shown in Fig. 1. The upstream and downstream lengths of the channel are 10 and 30 times larger than the channel inlet height (h = 25 mm). The Reynolds number for the channel inlet flow is defined based on the step height and selected as 400 and 800 to remain in the laminar flow regime. Parabolic velocity profile and outflow boundary conditions are defined at the channel inlet and outlet respectively. The motion of the actuator plate is defined as a sinusoidal function depending on the amplitude and frequency.

3 POD Analysis

POD provides a basis for the modal decomposition of a system of functions, usually data obtained from numerical simulations or experimental measurements. The basis functions retrieved are called proper orthogonal modes. It provides an efficient way of capturing the dominant components of a multidimensional system and representing it to the desired precision by using the relevant set of modes [5–7]. The "snapshot version" of POD introduced by Sirovich [7] is an efficient implementation for "time-dependent" flow fields. In this study snapshot version of POD is employed as the database consists of time dependent snapshots of numerically obtained two-dimensional velocity fields. In the snapshot version, a correlation between the temporal snapshots is done. An average operator is evaluated as a space average over the domain of interest and the variable of interest is assimilated to time. To derive the discrete eigenvalue problem corresponding to the snapshot

POD, it is assumed that the eigenfunctions have a special form in terms of the original data in (3) where M is the total number of snapshots, A_{ki} are the elements of *k*th eigenvectors in the correlation matrix C_{ij}. The elements of the correlation matrix are calculated in (4).

$$\vec{\phi}_{\mathrm{k}}(\mathrm{x},\mathrm{y}) = \sum_{\mathrm{i}=1}^{\mathrm{M}} \mathrm{A}_{\mathrm{ki}} \vec{\mathrm{V}}(x, y, t_{\mathrm{i}}) \tag{3}$$

$$\mathrm{C}_{\mathrm{ij}} = \frac{1}{\mathrm{M}} \iint \vec{\mathrm{V}}(x, y, t_{\mathrm{i}}) \vec{\mathrm{V}}(x, y, t_{\mathrm{j}}) \mathrm{dxdy} \tag{4}$$

The correlation matrix is symmetric and positive-definite therefore its eigenvalues are real positive numbers. The eigenvalues can be sorted in descending order. The sum of all the eigenvalues is the total flow energy and each POD mode is represented by the magnitude of the corresponding eigenvalue [11, 12].

Each space-time realization V(x, y, t) can be expanded into orthogonal basis functions with uncorrelated coefficients as given in (5). The spatial and temporal modes are specified to be orthonormal. The velocity field can be expanded in a series in (5) where N (usually $\mathrm{N} \ll \mathrm{M}$) is the number of most energetic modes. In this formulation a_k is the time varying expansion coefficient and the temporal coefficients for POD are calculated using (6). Together with (5) it is called reconstruction formula.

$$\vec{\mathrm{V}}(x, y, t) = \sum_{\mathrm{k}=1}^{\mathrm{N}} \mathrm{a}_{\mathrm{k}}(\mathrm{t})\, \vec{\phi}_{\mathrm{k}}(\mathrm{x},\mathrm{y}) \tag{5}$$

$$\mathrm{a}_{\mathrm{k}}(\mathrm{t}) = \iint \vec{\mathrm{V}}(x, y, t)\, \vec{\phi}_{\mathrm{k}}(\mathrm{x},\mathrm{y}) \mathrm{dxdy} \quad k = 1, 2, \ldots N \tag{6}$$

It is necessary to pay special attention to flow directions to be homogenous, stationary or periodic. On the other hand, the 'phase-indetermination' is one of the most important limitations of the POD. This indetermination is due to the use of two-point correlations and appears only for directions where a harmonic decomposition is used [13]. Among the advantages of POD, the following points can be underlined: The method is objective and methodic. The POD is a linear method but it does not neglect the nonlinearities of the original vector field and the basis functions are optimal in terms of kinetic energy. Additionally, the efficiency of POD increases with the level of inhomogeneity of the process. Useful studies concerning POD-analysis of numerical simulations concerning thermo-fluid problems are given in the [11–16].

4 Results

In the current study, the POD is applied for the periodic motion of the backward facing step flow for two channel Reynolds numbers. The spatio-temporal coherent structures depend on the jet Reynolds numbers. Figure 2 indicates the first six most energetic POD-modes of the streamwise velocity component for the channel Reynolds number 400 and the jet Reynolds number 100 (f = 1 Hz), thus the cross-flow parameter r equals to 0.25.

The first mode (M = 1) contains the highest energy and it represents the "averaged" flow field, in other words, the first mode of the flow is equivalent to the time-averaged channel flow. Modes such as 3 and 4 reveal very significant shifting phases in the flow direction downstream of the channel. Similarly mode six indicates distorted coherent structures. The POD-expansion coefficients for these modes are shown in Fig. 3a. However, modes such as 2, 5 and 7 do not indicate any significant shifting phases downstream of the channel and the corresponding POD-expansion coefficients are shown in Fig. 3b. The numerical flow data includes 10 periods thus the number of the peaks in the expansion coefficients for the second and fifth modes is 10. These coefficients are used to reconstruct time-dependent flow field from the CFD database. With increasing mode number the reconstruction can be achieved in a desired accuracy. On the other hand, the POD expansion coefficients combined with an interpolation algorithm can be used as an inverse design tool to obtain any flow fields which does not exist in the original database [8].

Increasing the cross-flow parameter r constant to 0.50; a simulation has been performed for channel Reynolds number 400 and jet Reynolds number 200

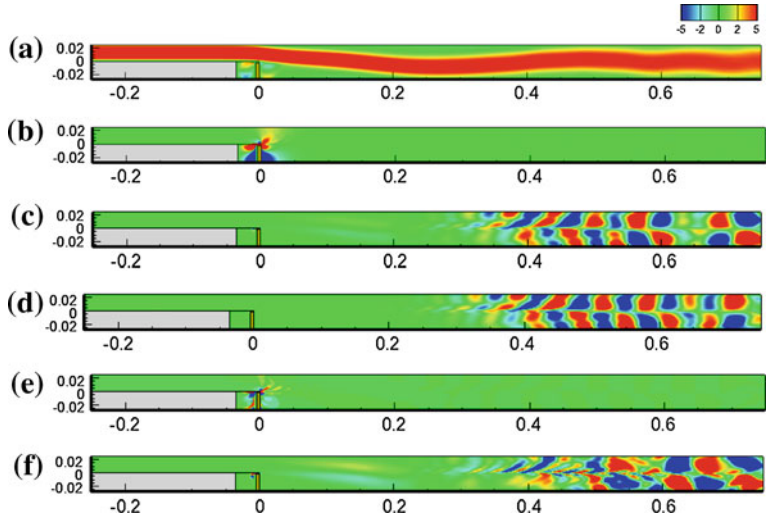


Fig. 2 POD-modes of the streamwise velocity component for Re = 400 and Re_J = 100: **a** M = 1, **b** M = 2, **c** M = 3, **d** M = 4, **e** M = 5 and **f** M = 6

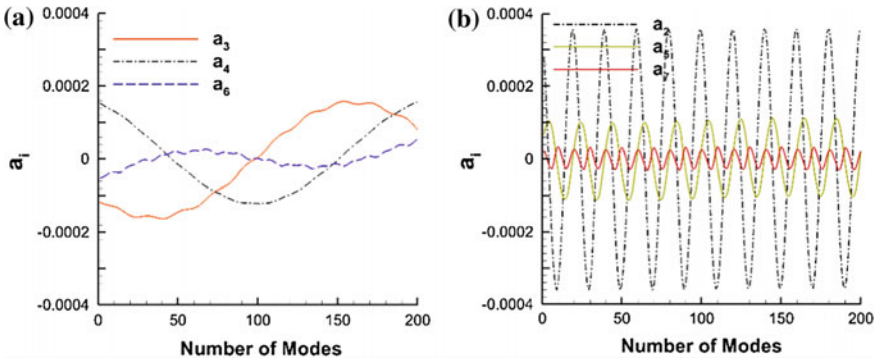


Fig. 3 Variation of expansion coefficients for Re = 400 and Re_J = 100: **a** 3, 4 and 6 modes, **b** 2, 5 and 7 modes

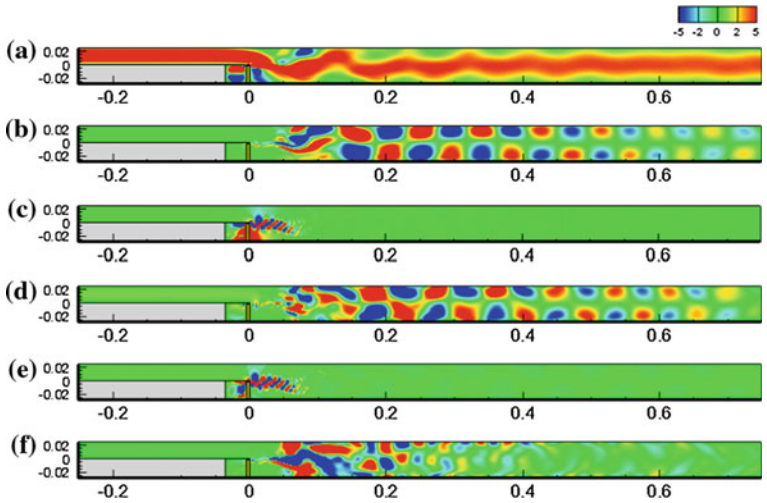


Fig. 4 POD-modes of the streamwise velocity component for Re = 400 and Re_J = 200: **a** M = 1, **b** M = 2, **c** M = 3, **d** M = 4, **e** M = 5 and **f** M = 6

(f = 2 Hz). Figure 4 displays the first six most energetic POD-modes of the streamwise velocity component for the channel Reynolds number 400 and jet Reynolds number 200.

It can be seen that the first mode represents the mean flow field with more noticeable disturbances caused by the actuation frequency compared to the case Re = 400, f = 1 Hz. Modes 2, 4 and 6 reveal traveling waves with phase shifting which are distributed to the whole flow region and weaken near the exit of the channel. Modes 3 and 5 do not contribute to the overall flow structure downstream

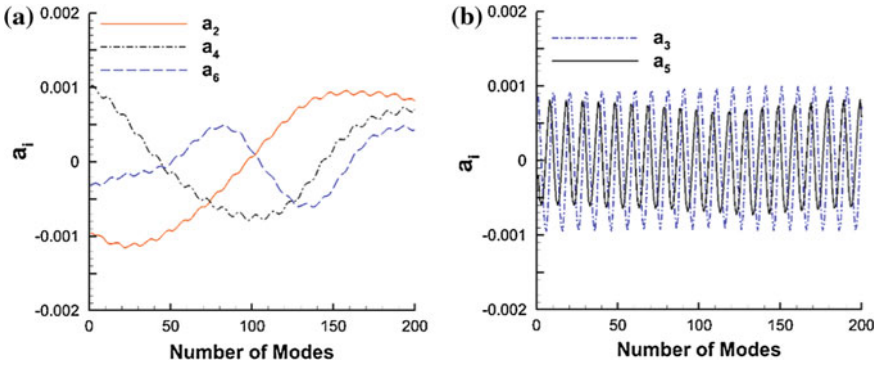


Fig. 5 Variation of expansion coefficients for Re = 400 and Re_J = 200: **a** 2, 4, and 6 modes, **b** 3 and 5 modes

of the channel, however small coherent structures appear near the actuator where the jet flow emanates into the channel flow.

Figure 5 shows the variation of the POD-expansion coefficients with respect to mode's numbers. Similar to the first case, POD modes which do not indicate any traveling waves in the downstream region of the channel; such as the third and fifth modes do not contribute to the overall flow structure downstream of the channel, thus the expansion coefficient variation of those modes has the lowest periodicity compared modes 2, 4 and 6.

Figure 6 shows the cumulative eigenvalues (λ_i) for the investigated cases. The cumulative eigenvalues are obtained by the summation of the "normalized eigenvalues" where the first mode is purposely left out of the list since it contains the

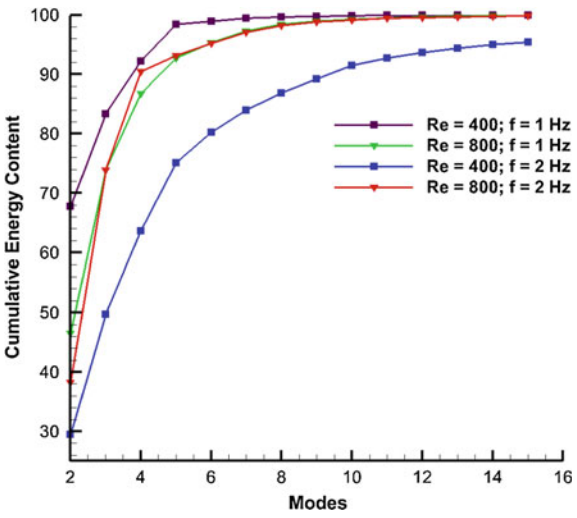


Fig. 6 The "16" largest cumulative eigenvalues (λ_i) and their respective contributions to the total flow energy

highest energy level representing the mean flow. On the other hand, to reconstruct an arbitrary snapshot with a very high accuracy, the first eight modes are required since the respective contribution of the cumulative eigenvalues to the total flow energy is more than 95 % except the case Re = 400 and f = 2 Hz.

5 Conclusion

In this study the POD analysis of JaVA-induced flow regimes over an oscillating BFS is carried out in an effort to employ a modal analysis. The numerical database consists of time-dependant snapshots obtained from CFD simulations of the interaction of JaVA-induced flows with the channel flow. The dataset (Re_J = 100 and 200) are evaluated by POD separately. The spatio-temporal coherent structures are identified as travelling waves that depend on the jet Reynolds number and mode numbers. It is observed that for Re = 800, the cumulative energy content is not affected by the frequency significantly since 95 % of the cumulative energy content can be reached at M = 8. For the case Re = 400 and f = 2 Hz; it is shown that much more modes are needed to reach the cumulative energy level compared to the case Re = 400 and f = 1 Hz. For Re = 400 and f = 2 Hz, it is observed that modes with higher mode numbers contain higher cumulative energy since the reference flow is influenced by JaVA-induced flows more significantly. For both cases it can be concluded that modes with observable coherent structures possess expansion coefficients with higher periodicity while expansion coefficients with much lower periodicities are being noticed for modes with coherent structures just in the vicinity of the actuator.

References

1. S. Cadirci, H. Gunes, U. Rist, Numerical investigation of a jet and vortex actuator in a cross flow boundary layer. Eur. J. Mech.-B **44**, 42–59 (2014)
2. S. Cadirci, H. Gunes, U. Rist, Active flow control applications with a jet and vortex actuator in a laminar cross flow. Int. J. Heat Fluid Flow **39**, 146–159 (2013)
3. U.C. Coskun, S. Cadirci, H. Gunes, Heat transfer enhancement behind a backward facing step using localized suction and blowing, in *Proceedings of CONV-14, International Symposium on Convective Heat and Mass Transfer*, 8–13 June 2014, Kuşadası, Turkey
4. S. Cadirci, H. Gunes, Active flow control with an oscillating backward facing step, in *ESDA2012-82645, Proceedings of the ASME 2012, 11th Biennial Conference on Engineering System Design and Analysis ESDA2012*, 02–04 July 2012, Nantes, France
5. J.L. Lumley, The structure of inhomogeneous turbulence, in *Atmospheric Turbulence and Wave Propagation* ed. by A.M. Yaglom, V.I. Tatarski (Moscow, 1967), pp. 166–178
6. G. Berkooz, P. Holmes, J.L. Lumley, The proper orthogonal decomposition in the analysis of turbulent flows. Ann. Rev. Fluid Mech. **25**, 539–575 (1993)
7. L. Sirovich, Turbulence and the dynamics of coherent structures. Appl. Math. **45**(561) (1987)

8. H. Gunes, S. Cadirci, Modeling and inverse design of convective heat transfer in grooved channel using proper orthogonal decomposition, in *ASME International Mechanical Engineering Congress and Exposition, IMECE2009*, 13–19 Nov 2009, Lake Buena, Florida, USA
9. S. Cadirci, H. Gunes, Proper orthogonal decomposition analysis of JaVA flows for cross flow conditions, *ASME 2011-International Mechanical Engineering Congress and Exposition (IMECE)*, 11–17 Nov 2011, Denver, USA
10. H. Gunes, U. Rist, Proper orthogonal decomposition reconstruction of a transitional boundary layer with and without control. Phys. Fluids **16**, 2763 (2004)
11. H. Gunes, Low-order dynamical models of thermal convection in high-aspect ratio enclosures. Fluid Dyn. Res. **30**, 1–29 (2002)
12. H. Gunes, Low-dimensional modeling of non-isothermal twin-jet flow. Int. Comm. Heat Mass Transf. **29**, 77–86 (2002)
13. Von Karman Institute for Fluid Dynamics (VKI), Lecture Series 2008-1, Evaluative Summary of the POD Approach, vol. 2
14. B. Galletti, C.H. Bruneau, L. Zannetti, A. Iollo, Low-order modelling of laminar flow regimes past a confined square cylinder. J. Fluid Mech. **503**, 161–170 (2004)
15. A. Qamar, S. Sanghi, Steady supersonic flow field predictions using proper orthogonal decomposition technique. Comput. Fluids **38**, 1218–1231 (2009)
16. F. Selimefendigil, Numerical analysis and POD based interpolation of mixed convection heat transfer in a horizontal channel with a cavity heated from below. Eng. Appl. Comput. Fluid Mech. **7**(2), 261–271 (2013)

Characterization of the Massively Separated Wake Behind a Square Cylinder by Means of Direct Numerical Simulation

Ricardo Vinuesa, Philipp Schlatter and Dan S. Henningson

Abstract The massively separated wake behind a wall-mounted square cylinder is investigated by means of direct numerical simulation (DNS). The effect of inflow conditions is assessed by considering two different cases with matching momentum-thickness Reynolds numbers $Re_\theta \simeq 1000$ at the location of the cylinder: one with a fully-turbulent boundary layer as inflow condition, and another one with a laminar boundary layer. The main simulation is performed by using the spectral element code Nek5000. While in the laminar-inflow simulation the horseshoe vortex forming around the cylinder can be observed in the instantaneous flow fields, this is not the case in the turbulent-inflow simulation. Besides, the streaks in the turbulent case become greatly attenuated on both sides of the obstacle. By analyzing the Reynolds shear stress $\overline{uv}$, we show that this is due to the modulation of the horseshoe vortex by the turbulence from the incoming boundary layer.

1 Introduction

The case under consideration in the present study, namely the flow around a wall-mounted square cylinder, is of great interest both from a scientific and a technological perspective. In the particular configuration under analysis here, the cylinder exhibits an aspect ratio of 4 (defined as the cylinder height H divided by the square side d), and the incoming boundary layers have 99 % thickness δ_{99} below d at the location of the obstacle. With this setup, the incoming boundary layer interacts with the upstream side of the obstacle, which produces a recirculation bubble and an adverse pressure gradient (APG). Note that the APG contributes to increase the incoming boundary layer thickness. Besides, a horseshoe vortex forms around the obstacle, and the sharp edges of the cylinder produce what is called geometry-induced separation, resulting in a massively separate wake which sheds at some particular frequency.

R. Vinuesa (✉) · P. Schlatter · D.S. Henningson
Linné FLOW Centre, KTH Mechanics, Osquars Backe 18, Stockholm, Sweden
e-mail: rvinuesa@mech.kth.se

© Springer International Publishing Switzerland 2016

A. Segalini (ed.), *Proceedings of the 5th International Conference on Jets, Wakes and Separated Flows (ICJWSF2015)*,
Springer Proceedings in Physics 185, DOI 10.1007/978-3-319-30602-5_32

Wall-mounted square cylinders have been studied experimentally by Wang et al. [12], in a configuration with $H/d = 5$ and a Reynolds number based on freestream velocity U_∞ and square side of $Re_d = 11,500$. They identified differences in the wake structure dependent on the characteristics of the incoming boundary layer, which will be further analyzed numerically in the present study. Here we use the spectral element code Nek5000, developed by Fischer et al. [3], to perform direct numerical simulations (DNSs) of the flow around the square cylinder at $Re_d = 11,000$. The flow case was studied experimentally by Bourgeois et al. [1], and in this computational campaign two inflow conditions were considered: a fully-turbulent and a laminar boundary layer.

2 Computational Setup

The wall-mounted square cylinder is a moderately complex geometry, in the sense that it is a fully three-dimensional flow and therefore it is not possible to discretize any directions by means of Fourier expansions as it is done in traditional spectral methods, which are extremely efficient when simulating simple geometries. However, given the temporal and spatial disparity of scales characteristic of turbulent flows, it is still important to use high-order methods for the simulations, in order to accurately capture the most relevant flow physics. Therefore, we considered the code Nek5000 [3] to perform the simulations, which is based on the spectral element method (SEM). This method, developed by Patera [6], combines the geometrical flexibility of finite element methods with the accuracy of spectral methods. The main idea of the SEM is to subdivide the computational domain into macro-elements, or spectral elements, which can be located at any position and exhibit C^0 continuity at their boundaries. In Nek5000 those elements are hexahedrons, and their faces may be curved in order to better adapt to the particular geometries under consideration. For instance, we are currently using the same code to simulate the flow around a wing section at a Reynolds number based on freestream velocity and chord length of 400,000 (Vinuesa et al. [8]). Then within the spectral elements the velocity is expressed in terms of tensor-products of Legendre polynomials of order N. Note that in this study we consider the so-called $\mathbb{P}_N - \mathbb{P}_{N-2}$ formulation by Maday and Patera [4], where the pressure field is solved in a space of polynomials of order $N - 2$. Although there are no restrictions on the location of the elements, the position of the grid points within elements is prescribed and follows the Gauss–Lobatto–Legendre (GLL) distribution. In the present simulations we considered $N = 11$, which according to our experience in other simulations of complex turbulent flows [9, 11] yields very accurate results, and continuity across element boundaries of the velocity gradient tensor.

In order to study the effect of the incoming boundary layer on the characteristics of the wake, we considered two cases: one with a fully-turbulent boundary layer as inflow condition, and the other with a laminar one. The numerical experiments are designed such that the two boundary layers have the same Reynolds number based on momentum thickness, $Re_\theta \simeq 1000$, at the obstacle location. Note that in the case of the laminar boundary layer, the inflow conditions can be defined in terms of the Blasius profile. In the case of the turbulent boundary layer, it is important to highlight that the inflow conditions can be computed independently by means of an auxiliary simulation, where the canonical character of the flow can be exploited. To this end, we considered the Fourier–Chebyshev code SIMSON [2] to simulate a canonical zero pressure gradient (ZPG) turbulent boundary layer, and periodically stored flow fields to generate time-dependent Dirichlet conditions for the main simulation, still computed with Nek5000. SIMSON takes advantage of the two homogeneous directions of the boundary layer (spanwise, and streamwise due to the use of a fringe at the outflow), and therefore it is a very computationally efficient way to generate the inflow conditions for the simulation around the cylinder.

Two computational domains are thus considered: one in Nek5000 (around the cylinder), and one in SIMSON (for the turbulent-inflow conditions). A total of 145,744 spectral elements were considered in the cylinder simulation, which results in around 252 million grid points, and in this coordinate system x, y and z denote respectively streamwise, vertical and spanwise directions. In the experiments by Bourgeois et al. [1] the leading edge of the flat plate where the ZPG boundary layer develops is located $16d$ upstream of the cylinder, but only up to $x/d = -8$ was simulated in the Nek5000 domain. The SIMSON simulation starts at $x/d = -28$ with a laminar Blasius profile which is tripped to produce transition to turbulence as in Schlatter and Örlü [7]. This simulation, which requires around 160 million grid points, is designed to produce a boundary layer thickness of $\delta_{99} = 0.72d$ at the location of the obstacle, as reported by Bourgeois et al. [1]. Regarding the interface between the two simulations, the velocity fields at $x/d = -8$ are stored every 0.08 convective time units, and are interpolated to match the SEM mesh. In the cylinder simulation, third-order Lagrangian interpolation is performed at every time step between two stored planes of data in order to obtain the adequate inflow condition. No-slip conditions are applied on the wall and the surface cylinder, periodic boundary conditions are applied in the spanwise direction, and the natural stress-free condition is applied on the top boundary and the outflow. Note that the upper boundary is located $12d$ above the wall, the outflow is $16d$ downstream of the cylinder and the spanwise width of the domain is $16d$. Finally, in the case of the laminar-inflow simulation the Blasius similarity solution that would lead to $Re_\theta = 1000$ at $x/d = 0$, i.e. a profile with $Re_\theta = 975$, was considered as inflow condition. The flow configuration, together with a schematic view of the computational domains, are shown in Fig. 1.

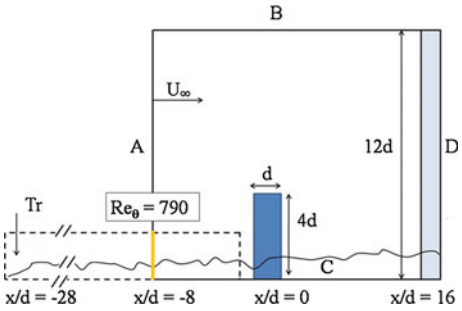


Fig. 1 Setup of the simulations presented in this study, showing the computational domain where the flow around the cylinder is simulated with Nek5000 (*solid*), and the domain where the incoming turbulent boundary layer is computed with SIMSON (*dashed*). The *yellow line* shows the interface between the two simulations, and *light blue* indicates a sponge region of length 2*d* upstream of the outflow

3 Results and Discussion

Instantaneous velocity fields obtained after 100 convective time units from the beginning of the simulation are shown, for both inflow cases, in Fig. 2. In the turbulent-inflow case the Nek5000 simulation is started after discarding initial transients in the SIMSON simulation. This figure shows the most relevant physics in the flow, and how it differs according to the inflow conditions. The incoming boundary layer thickens in both cases due to the effect of the APG forming on the upstream side of the obstacle, but the recirculation bubble is significantly longer in the laminar-inflow case. In this cases it is also interesting to observe how the APG produces transition to turbulence by generating instabilities in the incoming boundary layer. In both simulations the flow behind the obstacle is massively separated, and exhibits a self-sustained oscillation, together with large areas of reversed flow. It is also interesting to note that Fig. 2 shows how both simulations capture with great detail the occurrence of near-wall streaks, characteristic of wall-bounded turbulence. In the laminar-inflow case these streaks appear downstream of the obstacle, although their structure is not as clear as in the turbulent-inflow simulation. This is a manifestation of transitional effects, as well as of the impact of the cylinder on the flow. On the other hand, the streaks observed in the turbulent-inflow simulation are straight and basically undisturbed up to a a streamwise distance of around 4*d* ahead of the obstacle, which highlights the quality of the inflow condition produced with SIMSON. After this point, the streaks are slightly bent and deflected due to the presence of the obstacle. Also note that at a spanwise distance of around 6*d* from the cylinder the streaks are again straight in the turbulent-inflow simulation. Transition to turbulence is observed in the thin shear layers on the sides and the top of the cylinder that bound the separation bubbles on these surfaces. Figure 2 also shows an interesting phenomenon: the horseshoe vortex that forms around the cylinder can be observed even in the instantaneous fields in the laminar-inflow case, but not in the turbulent-inflow

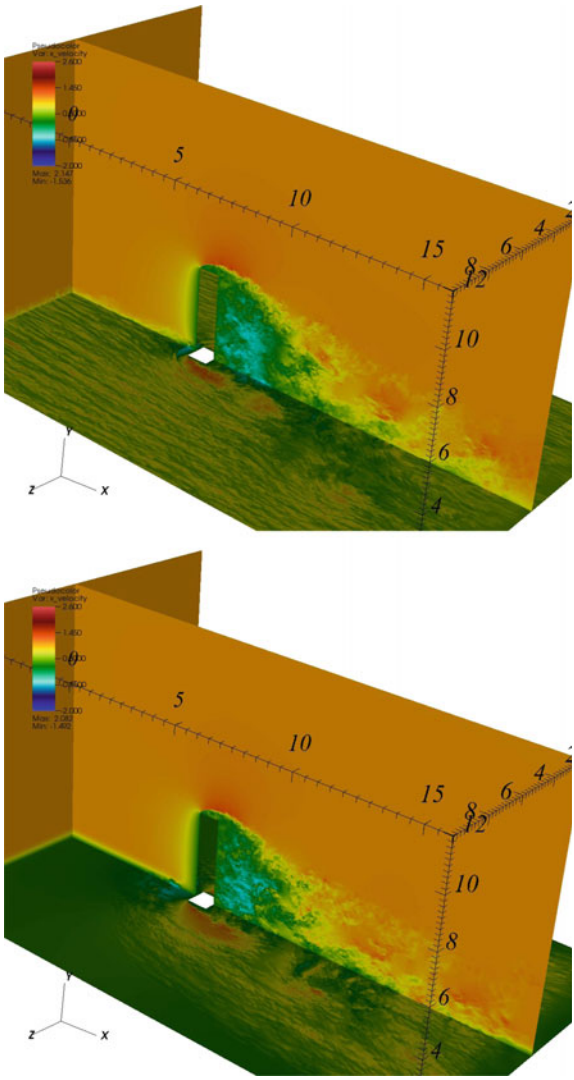


Fig. 2 Streamwise velocity fields at intersection planes $x/d = -8$, $y^+ = 15$ and $z/d = 0$ corresponding to (*top*) turbulent and (*bottom*) laminar-inflow simulations, extracted after 100 convective time units. Note that here '+' denotes scaling with the viscous length $\ell^* = \nu/u_\tau$, where ν is the fluid kinematic viscosity and u_τ is the friction velocity. Velocities range from -2 (*dark blue*) to $+2.6$ (*dark red*) and the cylinder is transparent to allow better visualization

simulation. In a previous study, we showed that when the instantaneous flow fields from the turbulent-inflow simulation are averaged in time, the horseshoe vortex is also visible [10]. Nagib and Corke [5] also observed this experimentally, by performing smoke-wire visualizations and controlling the exposure time of the camera (which emulates the effect averaging in time). In both cases the point of separation on the cylinder is fixed to the sharp upstream edges (two vertical and one horizontal), thereby falling into the category of so-called geometry-induced separation.

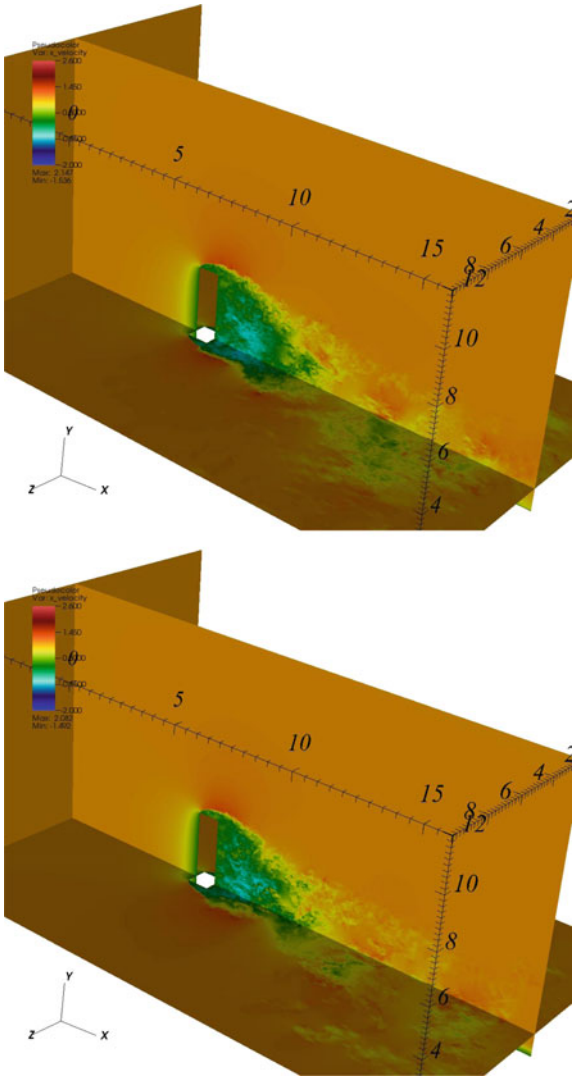


Fig. 3 Streamwise velocity fields at intersection planes $x/d = -8$, $y/d = 1$ and $z/d = 0$ corresponding to (*top*) turbulent and (*bottom*) laminar-inflow simulations, extracted after 100 convective time units. Velocities range from -2 (*dark blue*) to $+2.6$ (*dark red*) and the cylinder is transparent to allow better visualization

Further insight on the complex physics from both wakes can be gained by analyzing the flow farther from the wall. Figure 3 shows the same flow fields from Fig. 2, but this time at $y/d = 1$. This position is beyond the boundary layer thickness at the obstacle in both cases, i.e., $\delta_{99} \simeq 0.71d$ in the turbulent-inflow case, and $\delta_{99} \simeq 0.64d$ in the laminar-inflow one. This difference is also consistent with the setup, since we are matching the Reynolds number based on momentum thickness Re_θ, but for the same Reynolds number the turbulent boundary layer is thicker than the laminar one. At this wall-normal location the two wakes have similar thicknesses up to $x/d \simeq 7$, but beyond this point the wake from the laminar-inflow case becomes wider, and

less coherent than the one from the turbulent-inflow configuration. One of the reasons for this difference comes from the effect of the boundary layers on both sides of the cylinder, which in the turbulent-inflow case add coherence to the wake, and this is not the case in the laminar-inflow simulation. In addition to this, the thinner boundary layer thickness in the laminar-inflow case would lead to more concentration of vorticity close to the wall than in the turbulent-inflow simulation. This incoming vorticity leads to a progressively wider wake when interacting with the obstacle, effect that attenuates farther away from the wall as shown by Vinuesa et al. [10].

4 Conclusions

In the present study we have analyzed the differences between turbulent- and laminar-inflow simulations of the flow around a wall-mounted square cylinder, with the same $Re_\theta \simeq 1000$ at the location of the obstacle. One of the most relevant differences is the fact that the horseshoe vortex that forms around the cylinder can be observed even in the instantaneous fields in the laminar-inflow case, but not in the turbulent-inflow simulation. The geometry induces a favorable pressure gradient which accelerates the boundary layers on both sides of the cylinder, and interestingly in the turbulent-inflow case the streaks become significantly attenuated in this region, which suggests a connection between the incoming turbulence and the horseshoe vortex. In Fig. 4 we show the Reynolds shear stress $\overline{uv}$ at $1.5d$ from the centerplane, i.e. at the location where streaks are observed to become attenuated. In the turbulent-inflow case a

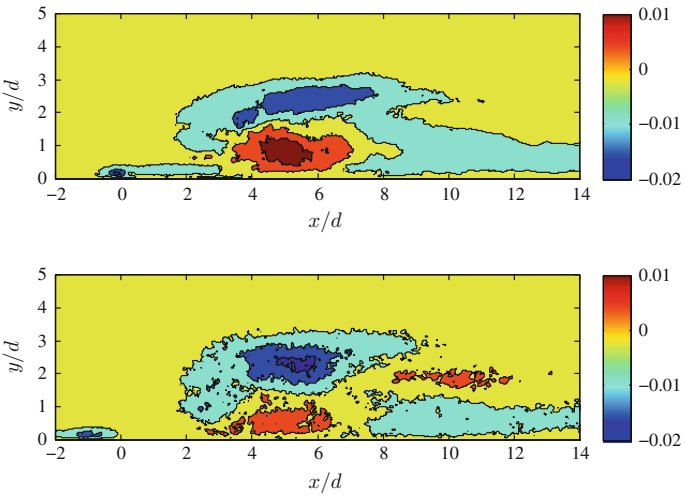


Fig. 4 Time-averaged Reynolds shear stress fields $\overline{uv}$ normalized with U_∞^2 at a distance of $1.5d$ from the centerplane, for the (*top*) turbulent and (*bottom*) laminar-inflow simulations. Fields obtained as the average between the corresponding fields at $z = +1.5d$ and $-1.5d$

large negative value of $\overline{uv}$ is observed, which indicates intense wall-normal turbulent transport. A different pattern is observed in the laminar case, with larger values closer to the separated region before the obstacle. These differences can be associated with the fact that in the turbulent case the near-wall turbulent cycle is clearly distorted by the effect of the horseshoe vortex, yielding a possible explanation of the significant attenuation of the streaks. It can be conjectured that in the turbulent simulation the adverse pressure gradient forces the turbulent structures in the incoming boundary layer, then the streamwise turbulence intensity modulates the horseshoe vortex, feeding its streamwise vorticity. This modulation would lead to the changes in the streak structure, and would also explain why the horseshoe vortex is not observed in the instantaneous visualizations of the turbulent-inflow case.

Acknowledgments The first author acknowledges financial support from the Knut and Alice Wallenberg Foundation. Computer time provided by the Swedish National Infrastructure for Computing (SNIC) is also gratefully acknowledged.

References

1. J.A. Bourgeois, P. Sattari, R.J. Martinuzzi, Coherent vortical and straining structures in the finite wall-mounted square cylinder wake. Int. J. Heat Fluid Flow **35**, 130–140 (2012)
2. M. Chevalier, P. Schlatter, A. Lundbladh, D.S. Henningson, A pseudospectral solver for incompressible boundary layer flows Technical report. TRITA-MEK. Stockholm: KTH (2007)
3. P.F. Fischer, J.W. Lottes, S.G. Kerkemeier, Nek5000: open source spectral element CFD solver (2008), http://nek5000.mcs.anl.gov
4. Y. Maday, A.T. Patera, Spectral element methods for the navier-stokes equations, in *State of the Art Surveys in Computational Mechanics*, ed. by A.K. Noor (ASME, New York, 1989), pp. 71–143
5. H.M. Nagib, T.C. Corke, Wind microclimate around buildings: characteristics and control. J. Wind Eng. Ind. Aerodyn. **16**, 1–15 (1984)
6. A.T. Patera, A spectral element method for fluid dynamics: laminar flow in a channel expansion. J. Comput. Phys. **54**, 468–488 (1984)
7. P. Schlatter, R. Örlü, Turbulent boundary layers at moderate reynolds numbers: inflow length and tripping effects. J. Fluid Mech. **710**, 5–34 (2012)
8. R. Vinuesa, S.M. Hosseini, A. Hanifi, D.S. Henningson, P. Schlatter, Direct numerical simulation of the flow around a wing section using high-order parallel spectral methods, in *International Symposium Turbulence & Shear Flow Phenomena (TSFP-9)*, 30 June–3 July, (Melbourne, Australia, 2015)
9. R. Vinuesa, A. Noorani, A. Lozano-Durán, G.K. El Khoury, P. Schlatter, P.F. Fischer, H.M. Nagib, Aspect ratio effects in turbulent duct flows studied through direct numerical simulation. J. Turbul. **15**, 677–706 (2014)
10. R. Vinuesa, P. Schlatter, J. Malm, C. Mavriplis, D.S. Henningson, Direct numerical simulation of the flow around a wall-mounted square cylinder under various inflow conditions. J. Turbul. **16**, 555–587 (2015)
11. R. Vinuesa, P. Schlatter, H.M. Nagib, On minimum aspect ratio for duct flow facilities and the role of side walls in generating secondary flows. J. Turbul. **16**, 588–606 (2015)
12. H.F. Wang, Y. Zhou, C.K. Chan, K.S. Lam, Effect of initial conditions on interaction between a boundary layer and a wall-mounted finite-length-cylinder wake. Phys. Fluids **18**, 065106 (2006)

Investigations on the Effects of Trip Wires on the Performances of a Rectangular Wing

Gabriele Capuano and Giovanni Paolo Romano

Abstract This work investigates the effects of small cylindrical elements ("trip wires") on the aerodynamic performances of a rectangular wing at Reynolds numbers between 5×10^4 and 2×10^5. The diameter and position of the perturbing cylinders are changed in order to evaluate modifications in drag and lift coefficients in comparison to the unperturbed wing, as also detailed information on the velocity field around the wing itself. Such modified wings can be mounted on small wind turbines and in Micro Air Vehicles.

1 Introduction

Low Reynolds number aerodynamics and related boundary layer separation control have a prominent role in advanced research in last 20 years due to the increasing number of engineering applications, as those related to Micro Air Vehicles (MAV) and low size wind turbines. Among the whole set of possible flow control devices, the attention is here focused onto passive ones, due to the usually simplest manufacturing, continuous working operation and more precise computation of improvements in performances. The starting point for such investigations is the observation that aerodynamic performances are highly dependent on Reynolds number. For Reynolds numbers lower than 10^5, there is a sharp reduction of performances of conventional wings (as for example the efficiency). On the other hand, the use of passive rough elements placed at specific positions on the wing surface allows improving the wing efficiency of one order of magnitude in comparison to a smooth wing [3]. This happens for Reynolds numbers around 10^5, i.e. just in situations encountered in previous mentioned applications.

G. Capuano · G.P. Romano (✉)
Department of Mechanical and Aerospace Engineering,
University La Sapienza, Rome, Italy
e-mail: giampaolo.romano@uniroma1.it

© Springer International Publishing Switzerland 2016

A. Segalini (ed.), *Proceedings of the 5th International Conference on Jets, Wakes and Separated Flows (ICJWSF2015)*,
Springer Proceedings in Physics 185, DOI 10.1007/978-3-319-30602-5_33

The main source of performance degradation at low Reynolds number is the separation bubble on the wing upper surface, which increases drag and reduce lift [5]. The perturbing element allows delaying the separation bubble formation, so far leading to performance improvements. However, this is not obtained for every perturbing element size, shape, location and local velocity. Regarding size and local velocity, previous investigations on flat plates highlight the existence of a critical local Reynolds number, (Re_k, obtained using the surface element height, k, and the undisturbed local velocity outside the boundary layer U_e) equal to 840 [8]. For local Reynolds numbers lower than this value, the perturbation is not altering the main flow behavior, whereas for values over such a threshold, the flow gains enough energy to delay flow separation [7]. For curved surfaces, this critical number moves into the interval from 690 to 830 [1]. Thus for a given perturbing element size, the derived effects are basically related to the value of the local velocity, i.e. linked to the global flow Reynolds number.

Regarding the perturbing element shape, in the past, the use of three-dimensional perturbing elements as in Kerho and Bragg [2] with semi-spheres at the leading edge of a NACA 0012 airfoil, in Lyon and Selig [4] with single or multiple rectangular strips at different positions and in Santhanakrishnan and Jacob [6] with regular bumps over the whole surface, leads to a reduction of the separation bubble and of pressure drag by forcing the transition from laminar to turbulent conditions. On the other hand, the use of a small cylinder along the span, i.e. trip wires, allows Huber and Mueller [1] to attain also a slightly increased efficiency, depending on the wire position. Such a solution, which has the advantage to be easily adaptable to the wing geometry, was reconsidered in much detail by Choi et al. [7] emphasizing the similarities with solutions observed in nature (biomimetics). It is quite hard to determine theoretically the optimal position for the perturbing transition element, being this possible only for very small pressure gradient, i.e. for small angle of attack, a condition not so relevant for practical applications. Therefore, it is fundamental to exploit extended experimental and numerical investigation on specific perturbing elements. In addition, it is important to relate the improvement in wing performances to the detailed features of the separation bubbles and of the entire flow field.

The objective of the present work is to investigate the effects of small cylindrical trip wires on the aerodynamic features of a rectangular wing at Reynolds numbers between 5×10^4 and 2×10^5 (based on the wing chord) which are just below and above the critical value. Specifically, the diameter and position of the perturbing cylinders are modified to evaluate global indicators of performances as drag and lift, together with detailed information on the flow field around the wing, aiming to derive improvements and related explanations. The relevance of the present investigation lies in applications of such wings in wind turbines, especially those of small and intermediate scales, in Unmanned Air Vehicles (UAV) and in Micro Air Vehicles (MAV), working in the same interval of Reynolds numbers.

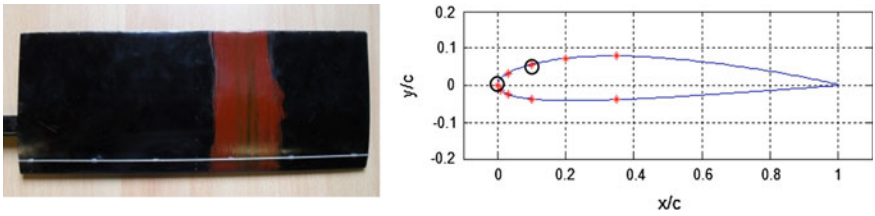


Fig. 1 The wing airfoil with trip wire application (on the *left*) and positions of the trip wires tested (indicated by *asterisks* on the *right*). The *black circles* indicate the positions with best performances

2 Experimental Set-Up

Measurements have been performed with the rectangular wing model (airfoil NACA 2412, aspect ratio ≈ 3) in a subsonic wind-tunnel with circular open section (diameter equal to 1 m). The free stream velocity of the wind tunnel allows to attain Reynolds numbers (*Re*, based on the wing chord, $c = 133$ mm) between 5×10^4 and 2×10^5. The trip wires used are single or multiple cylinders stuck along the span having the same wing aperture as reported in Fig. 1. The diameters of the cylinders range from 0.005 *c* to 0.015 *c*, corresponding from 0.044 to 0.125 in terms of wing thickness, while several positions have been tested, as detailed in Fig. 1. The Reynolds number based on the trip wire height, Re_k, is around 500 for the lowest Reynolds number tests and around 1400 for the largest one.

Two types of measurements have been performed, global lift and drag by using a calibrated force balance and velocity fields over the wing by using Particle Image Velocimetry (PIV). The last employed a Nd-Yag laser (wavelength 532 nm, 200 mJ per pulse) synchronized with a cross-correlation camera, whereas tracer are provided by oil droplets (mean diameter less than 5 μm) from a Laskin nozzle operating at 1.8 atm. The illuminated part of the wing was painted with a water solution containing Rhodamine WT (as can be noticed in Fig. 1), to reduce light reflections on the surface by applying a narrow band filter on the camera objective. PIV images are processed with DaVis 7.2 by LAVISION Gmbh using a multi-pass algorithm with final interrogation window equal to 32×32 pixel, with overlapping 75 %. About 1000 images are averaged for each condition. Typical relative errors for global force coefficients, removing the strut contribution to drag, are between 3 and 8 % at the stall, depending on Reynolds number. The errors in PIV are around 1 % for instantaneous fields, while the statistical error is smaller.

3 Results: Global Force Measurements

Preliminary measurements with the calibrated balance revealed that the configurations with multiple trip wires (placed both on the upper, lower or both wing surfaces) increase drag and reduce lift, so that they will not be considered further.

Table 1 Maximum lift coefficients and angles of stall for the unperturbed and trip wire wings at the tested Reynolds numbers

Re	Unperturbed		Trip Wire	
	α_s(°)	*Cl max*	α_s(°)	*Cl max*
50000	14	0.7870	14	0.7535
70000	14	0.7754	15	0.8893
100000	14	0.8158	16	0.8526
130000	14	0.8206	16	0.8261
150000	14	0.8168	16	0.8303
182000	14	0.8287	16	0.8261
200000	14	0.8290	16	0.8293

Regarding the configurations with single trip wire, the first effect to be considered is that of Reynolds number (from 5×10^4 to 2×10^5). For the case of wire diameter equal to 0.0075 *c*, placed at 10 % of the chord (black circle in Fig. 1), the maximum effect in comparison to the unperturbed wing is obtained for Reynolds numbers $> 10^5$. In these conditions, at stall angles (around 14°–15°), the lift coefficient is larger and the drag is lower than the unperturbed wing (in which no relevant differences are observed when the Reynolds number is changed, as derived from Table 1). On the other hand, as reported in Table 1, the results using the trip wire are strongly dependent on Reynolds number. Specifically, it is observed that there is a remarkable increment of maximum lift (*Cl max*) with trip wire, only in the interval of Reynolds numbers between 6×10^4 and 1.2×10^5, whereas the increment in stall angle (α_s) with trip wire is noticed in the whole range $Re > 5 \times 10^4$.

The attention is then focused on the effect of wire diameter at a fixed position (10 % of the chord on the upper surface), with fixed Reynolds number $Re = 1.5$ 10^5, as displayed in Fig. 2. It is clearly noticed that the highest lift and stall angle are obtained for a diameter of 1 mm (0.0075 *c*), in comparison to the unperturbed wing and to smaller or larger diameters. Regarding drag, it is generally equivalent for the unperturbed wing in comparison to those equipped with trip wires, while around the stall again the wing with the 1 mm wire gives the best performances.

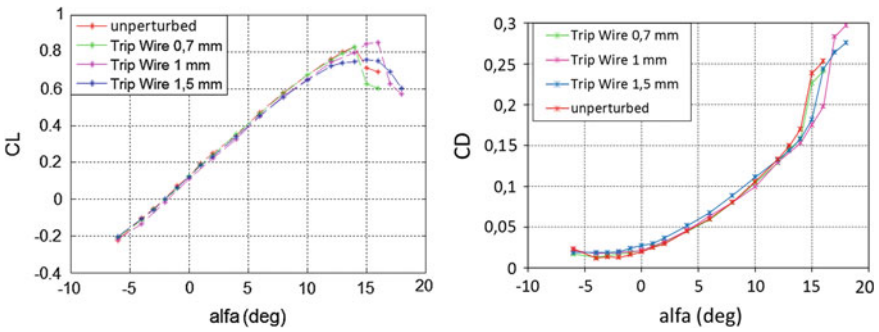


Fig. 2 Lift and drag coefficients versus angle of attack, measured for different size of the trip wire positioned at 10 % of the chord for $Re = 1.5 \times 10^5$

Starting from the previous results, the attention is focused on such a 0.0075 *c* trip wire at Reynolds numbers around 10^5, by looking at the effect of a change in the position of the wire. Among all tested configurations, the other one which gives performance improvement is the one with trip wire positioned just at the leading edge (the second black circle in Fig. 1). In this case (not shown), the stall angle increases less (about 1°) in comparison to the unperturbed wing, but the stall is smoother and more regular, thus also interesting for applications. In addition, far from the stall, the performances are much closer to the undisturbed wing in comparison to the wire positioned on the upper wing surface.

4 Results: Velocity Measurements

To investigate deeply these behaviors, the velocity fields on the wing were measured by PIV. The comparison among the unperturbed wing, the one with trip wire at 10 % of the chord on the upper surface and that with trip wire at the leading edge for an angle of attack equal to 12° and $Re = 1.5 \times 10^5$ (i.e. just before the stall in Fig. 2) is given in Fig. 3. The increment of velocity at the upper surface is noticed

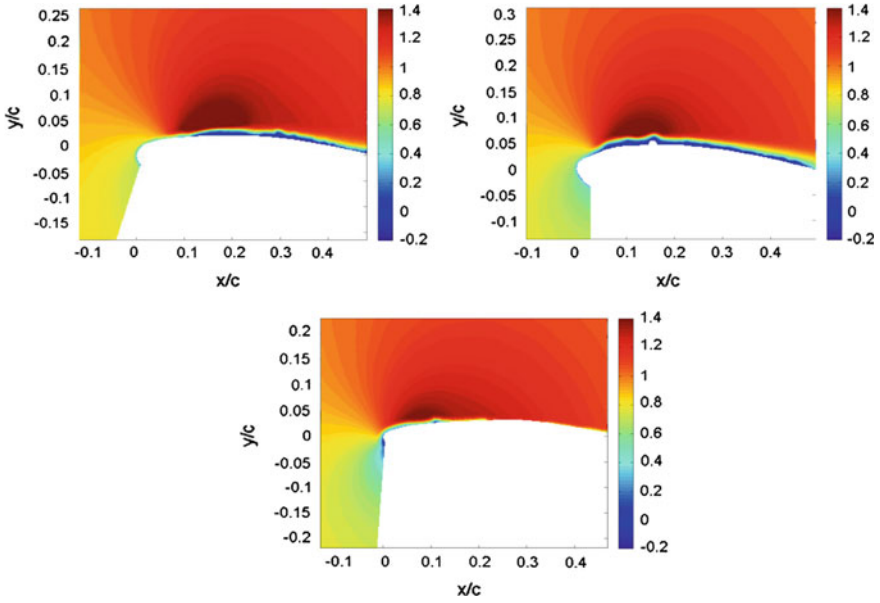


Fig. 3 Comparison of mean streamwise velocity fields for the unperturbed wing (at the *top left*), trip wire at 10 % of the chord (at the *top right*) and wire with trip wire at the leading edge (at the *bottom*). Angle of attack equal to 12°, $Re = 1.5 \times 10^5$

as also the position of the wire element (the bump on the upper surface). Even in these not separated conditions, it is evident that the region with maximum streamwise velocity moves upstream when trip wires are used. Specifically, while for the unperturbed wing the maximum is centered at about 0.17 c, for the wing with wire at 10 % of the chord, this moves to 0.14 c and for the wing with wire at the leading edge to less the 0.1 c. This is a clear indication of a modification in the upper flow as also pointed out by the reduced extension of the incremented velocity region. In all three conditions, the boundary layer is not separated even just downstream the perturbing elements. The situation changes when stall is approached. In Fig. 4, the comparison among the same three configurations of Fig. 3 are presented for an angle of attack equal to 15° and $Re = 1.5 \times 10^5$ (i.e. in the stall region in Fig. 2). While in the first condition, there is a large separation region, with the use of the trip wire the flow is perfectly stuck on the wing. Therefore, for the configurations with perturbing elements a delay of stall with increased maximum lift and decreased drag must be expected, as reported in global force measurements. In the wings equipped with trip wires, the separation is completely avoided with only a boundary layer thickening along the wing surface.

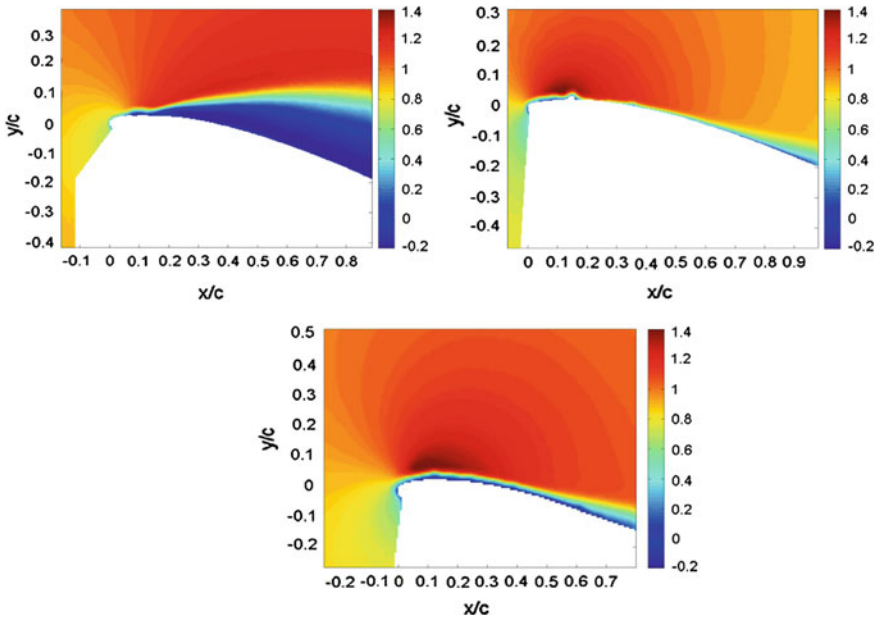


Fig. 4 Comparison of mean streamwise velocity fields for the unperturbed wing (at the *top left*), trip wire at 10 % of the chord (at the *top right*) and wire with trip wire at the leading edge (at the *bottom*). Angle of attack equal to 15°, $Re = 1.5 \times 10^5$

References

1. A.F. Huber, T.J. Mueller, The effect of trip wire roughness on the performance of the Wortmann FX 63-137 airfoil at low Reynolds numbers. Exp. Fluids **5**(4), 263–272 (1987)
2. M.F. Kerho, M.B. Bragg, Airfoil boundary-layer development and transition with large leading-edge roughness. AIAA J. **35**, 1 (1997)
3. P. Lissaman, Low Reynolds number airfoils. Annu. Rev. Fluid Mech. **15**, 223–239 (1983)
4. C. Lyon, M. Selig, A. Broeren, Boundary layer trips on airfoils at low Reynolds numbers. AIAA 97-0511 (1997)
5. R. Radespiel, Numerical and experimental flow analysis of moving airfoil with laminar separation bubbles. AIAA J. **45**, 1346–1356 (2007)
6. A. Santhanakrishnan, J.D. Jacob, Effect of regular surface perturbations on flow over an airfoil, in *35th Fluid Dynamics Conference*, Toronto (2005)
7. K. Son, J. Choi, W.P. Jeon, H. Choi, Mechanism of drag reduction by a surface trip wire on a sphere. J. Fluid Mech. **672**, 411–427 (2011)
8. I. Tani, H. Sato, Boundary layer transition by roughness element. J. Phys. Soc. Jpn. **11**(12), 1284–1291 (1956)

Part IV
Vehicle Aerodynamics

Comparison of Synthetic and Pulsed Jets Effect for the Flow Around the Ahmed Body

Stéphie Edwige, Yoann Eulalie, Philippe Gilotte and Iraj Mortazavi

Abstract In this work, the effect of three different active control strategies namely, pulsed blowing, pulsed suction, and synthetic jets, is studied for a square back Ahmed body. Using a LES numerical simulation, the efficiency of the synthetic actuation on the rear pressure distribution is highlighted.

1 Introduction

This work focus on flow control strategy to reduce aerodynamic forces around a ground vehicle. Several techniques have already been proposed to improve aerodynamics efficiency of ground vehicle. Contrary to passive control techniques based on energy-free devices (such as porous layer), active control are techniques requiring an additional source of energy balanced by their efficiency. Jet inflow is one of the active control solution.

Considering that about 30 % of global aerodynamic loss on a classical vehicle is due to pressure forces, active flow control with jet devices is an interesting approach. Previous studies have already proved that periodic forcing at high frequencies can be a promising strategy for drag reduction and they often recommend blowing pulsed, suction or synthetic jets (e.g. [1, 2]). But differences between these three signals have never been pointed out. Based on numerical simulations of the flow around the Ahmed body, [3] the purpose of this work is to bring a renewed analysis of active control techniques and to identify the signal type influence on global aerodynamical

S. Edwige
CNRS, Institut de Mathématiques de Bordeaux, Bordeaux, France
e-mail: stephie.edwige@gmail.com

Y. Eulalie · P. Gilotte
Auto Exterior Division, Plastic Omnium, Lyon, France

I. Mortazavi (✉)
M2N, Conservatoire National des Arts et Métiers, Paris, France
e-mail: iraj.mortazavi@cnam.fr

© Springer International Publishing Switzerland 2016

A. Segalini (ed.), *Proceedings of the 5th International Conference on Jets, Wakes and Separated Flows (ICJWSF2015)*,
Springer Proceedings in Physics 185, DOI 10.1007/978-3-319-30602-5_34

quantities, rear pressure/drag coefficient behavior and wake strutures. Once the validation of the numerical results achieved, a further control study has been realized in order to compare these three strategies.

2 Numerical Model

To do so, simulations on the square back Ahmed body benchmark has been used [4, 5]. It consists in a simplified car-shaped body, illustrated in Fig. 1 placed in a wind tunnel. The sharp edge at the rear back end leads to separation of the flow that fed the recirculation area. The pressure drop generated is the main responsible of drag force. The flow developped around this benchmark is used to analyse main 3D structures generated in a car's wake for a high Reynolds number of 500 000

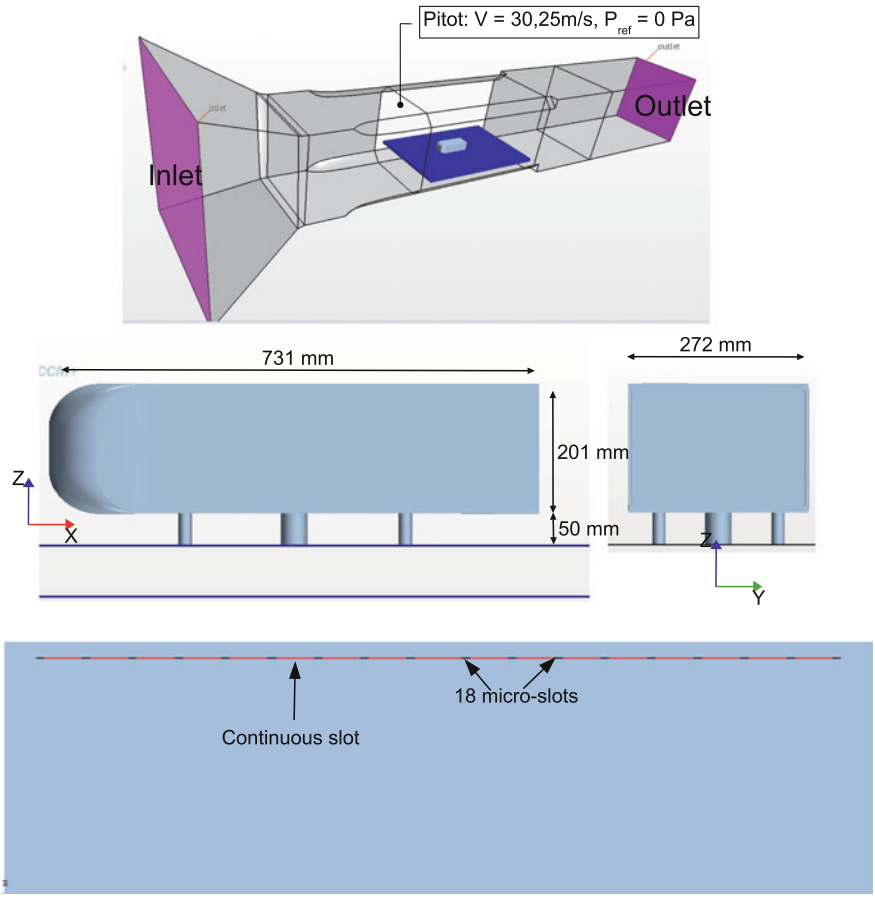


Fig. 1 Wind tunnel (*Top*), Ahmed body geometry (*Center*) and slots geometry (*Bottom*)

(based on the body height). This 3D unsteady flow at a Reynolds number of 500 000 (based on the body height) has been computed using a finite element solver with a Large Eddy Simulation approach [3]. Thus, large turbulent scales are directly solved using filtered Navier-Stokes (4) while smaller scales are estimated thanks to the Smagorinski subgrid scale model.

Mathematically, the filtered incompressible Navier-Stokes equations are written:

$$\frac{\partial \bar{u}_i}{\partial x_i} = 0 \tag{1}$$

$$\frac{\partial \bar{u}_i}{\partial t} + \frac{\partial \bar{u}_i \bar{u}_j}{\partial x_j} = -\frac{1}{\rho}\frac{\partial \bar{P}}{\partial x_i} + 2\nu \frac{\partial \bar{S}_{ij}}{\partial x_j} - \frac{\partial \tau_{ij}}{\partial x_j} \tag{2}$$

With $\bar{S}_{ij}$ the strain rate tensor and τ_{ij} the turbulent stress tensor defined as:

$$\bar{S}_{ij} = \frac{1}{2}\left(\frac{\bar{u}_i}{\partial x_j} + \frac{\bar{u}_j}{\partial x_i}\right) \tag{3}$$

$$\tau_{ij} = \overline{u_i u_j} - \bar{u}_i \bar{u}_j \tag{4}$$

The resolution of these equations requires a closure relation for the turbulent stress tensor. A common method consists in doing an analogous of the molecular model using the Boussinesq hypothesis: the deviatoric part of the turbulent stress tensor is modeled as a function of the strain rate tensor:

$$\tau_{ij} - \frac{1}{3}\tau_{ij}\delta_{ij} = 2\nu_T \bar{S}_{ij} \tag{5}$$

with δ_{ij} the Dirac function. Then a subgrid scale model is required to estimate the turbulent viscosity. In this work, it is computed with the Smagorinsky model:

$$\nu_T = (C_S f \Delta)^2 \sqrt{2\bar{S}_{ij}\bar{S}_{ij}}\,, \tag{6}$$

With Δ the cut-off length size, f the Van Driest damping function for wall boundary condition and C_S a constant.

The discretization has been perfomed considering time and spatial turbulence scales for this Reynolds number. Thus, the domain of 56 m^3 has been meshed with 120 millions of cells mainly located around the body boundary layer and in the wake. This simulation also requires $1.25.10^{-4}$ s time discretization for a 0.3 s averaging time simulation.

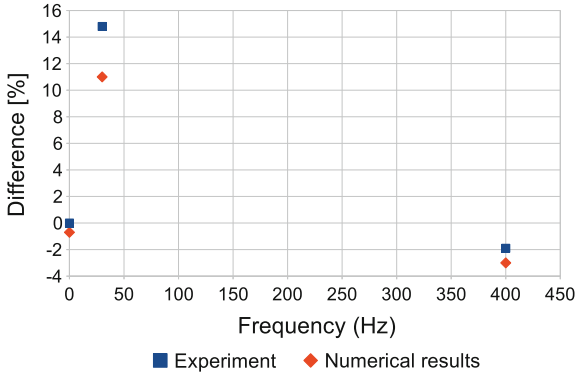


Fig. 2 Measure drag difference with respect to the experimental no-control test case

3 Validation

First, experimental comparison is performed to ensure numerical results reliability as shown in Fig. 2.

A first test case is realized without actuator as a reference case. Drag and pressure coefficients defined in (7) yield less than 1 % error compared to the experiments. The reference C_D value obtained by both experiments and numerics is 0.36. value Moreover, time average pressure field denotes a similar flow topology characterized by a torus shape iso-pressure in the flow wake.

$$Re = \frac{\rho U H}{\mu}\ ,\ C_D = \frac{F_x}{0.5\rho U_\infty^2 S_{ref}}\ ,\ C_P = \frac{P - P_{pitot}}{0.5\rho U_\infty^2}\ ,\ C_\mu = 2\frac{h_{slot}}{H}\frac{V_{jet}^2}{U_\infty^2}\ ,\ St = \frac{fH}{U_\infty}\ , \tag{7}$$

Then, active flow control computation is compared to experiment using blowing pulsed jets with 30 and 400 Hz frequencies. Experimental campaign revealed a strong deterioration of actuators performances for 30 Hz pulsed jet and 4 % drag reduction for 400 Hz pulsed jet. Numerical results lead to the same behaviour. Figure 2 shows that active test case results are also in good agreement with experimental data for that range of forcing frequencies.

Once the computations validated, we can start the numerical comparison of the three control approaches. All test cases for this study are based on the 400 Hz actuation frequency.

4 Comparison of Synthetic, Pulsed and Suction Actuators

It is difficult to determine the best operating point of active devices. Design parameters such as the angle between the jet direction and the rear surface, the jet velocity magnitude, the micro-slots position or the actuation frequency have more or less

influence on the wake topology. The above mentioned computational set-up enables the computation of a design of experiment in order to investigate these parameters influence: to achieve an efficient jet comparison, several types of case studies with various geometrical jet implementations are performed to choose the best configuration. Then, this work focuses on the influence of the jet signal type (suction, blowing, pulsed or synthetic jets). The comparative study is based on the best drag reduction configuration that is to say 18 micro-slots close to the rear top edge. Jet velocity oscillates at 400 Hz frequency with a maximum velocity of 75 m/s as shows Fig. 2.

Finally, these simulations highlight real behaviour differences between these control strategies. Considering time average quantities, synthetic jet gave the best drag reduction with 8.61 % gain followed by the suction jet with 7.9 % gain. The last one is the blowing pulsed jet with a gain of 6.7 %.

Pressure fields observation prove that the blowing phase of blowing pulsed and synthetic jets tend to smooth the shear layer gradient in the near velocity of the jet

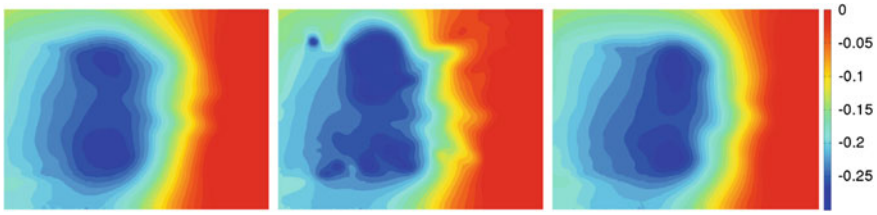


Fig. 3 Time averaged pressure coefficient in the wake in the vertical cut-plane (Oxz) for blowing pulsed jet (*left*) suction pulsed jet (*center*) and synthetic jet (*right*)

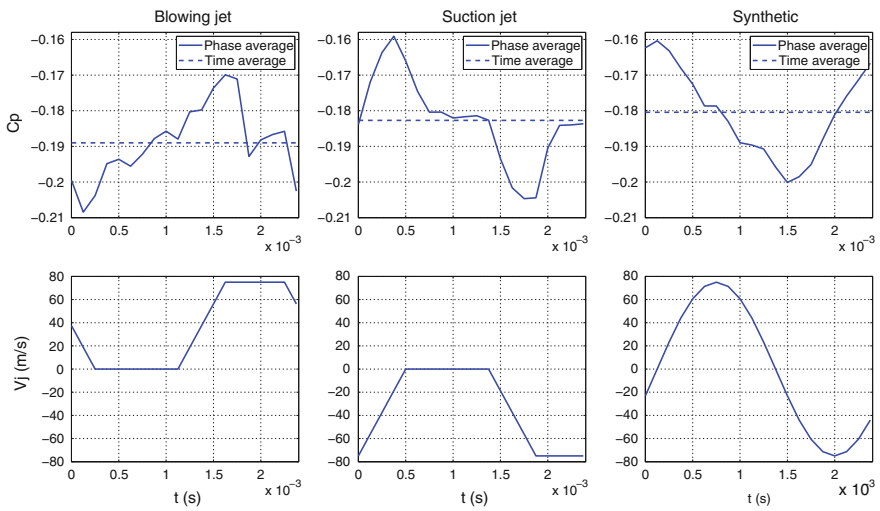


Fig. 4 Phase averaged pressure integrated on the rear and corresponding actuation velocity magnitude for pulsed jet actuator (*left*), suction jet (*center*) and synthetic jet (*right*)

inflow and spread the mixing layer. In the other hand, suction phases increase pressure fluctuations downstream of the actuator generating more turbulence (see Fig. 3). The resulting torus shape observed with time averaged iso-pressure is pushed back downstream. Synthetic jet combines both processes of mixing source and pressure fluctuations. Thus, this actuator enables a more efficient flow control. This is reflected on the rear back pressure distribution in Fig. 4: phase average pressure on the rear back end evolves in the same way as the jet velocity. Hence, synthetic jets have more impact on the recirculation bubble allowing a more efficient flow control.

5 Conclusion

In this work, a Large Eddy Simulation approach was successfully applied to compute the flow around the square back Ahmed body. Indeed, numerical results reach same results than experimental observation. This method allowed the comparison of blowing pulsed, suction and synthetic actuations. The flow response to these actuators was identified and linked to their performances. Finally, these simulations highlighted real behaviour differences between these control strategies in terms of aerodynamical average efficiency, shear layer and recirculation topology. The impact and the superiority of the synthetic jet on the resulting rear pressure distribution was also clearly demonstrated.

The next step is to achieve an automatic process to control the flow in order to avoid control heuristic parametric study.

Acknowledgments This work was funded by AMIES agency as well as LJK Grenoble in collaboration Plastic Omnium. The authors are grateful to ALTAIR for providing the AcuSolve license. Computation time at PLAFRIM at the Institute of Mathematics of Bordeaux is gratefully acknowledged.

References

1. C. Leclerc, Réduction de la traînée d'un véhicule automobile simplifié à l'aide du contrôle actif par jet synthétique. Ph.D. thesis, Institut National Polytechnique de Toulouse, Jan 2008
2. J. Östh, S. Krajnovic, D. Barros, Active flow control for drag reduction of vehicles using large eddy simulation experimental investigation and reduce order modeling, in *Proceedings of the 8th International Symposium On Turbulent and Shear Flow Phenomena (TSFP-8)* (2013)
3. Y. Eulalie, I. Mortazavi, P. Gilotte, Etude aérodynamique et contrôle de la traînée sur un corps de Ahmed culot droit. Ph.D. thesis, University of Bordeaux, Dec 2014
4. S. Krajnović, L. Davidson, Large eddy simulation of the flow around simplified car model. SAE Technical Paper (2004)
5. S.R. Ahmed, G. Ramm, Some salient features of time-averaged ground vehicle wake. SAE technical paper series 840300 (1984)

Large Eddy Simulations of Flow Around Two Generic Vehicles in a Platoon

Maryam Mirzaei and Siniša Krajnović

Abstract A detailed analysis of the effect of inter-vehicle distance on the flow structure of a two-model platoon is presented. Simulations are made for two Ahmed bodies with a slant angle of 25° and for three inter-vehicle distances, $d/L = 0.3, 0.5$ and 1. The Reynolds number based on the body height was 30000. A drag increase was observed for the follower with $d/L = 0.5$, compared to the drag value of a single body in isolation. To explain the underlying reasons for the increase in drag, various instantaneous and time-averaged plots are presented and compared for different distances, and a significant change in flow structure was found in flows between the set-ups with $d/L = 0.5$ and $d/L = 1$.

1 Introduction

Driving in a platoon has generally been considered to offer a reduction in aerodynamic drag for all the vehicles. However, it has been reported in various studies that the aerodynamic advantages of platooning are not always enhanced with decreasing the vehicles' spacing [1, 2]. For some particularly close distances (for example $d/L < 1$ [2] or $d/L < 0.35$ [1], where x and L are vehicle spacing and vehicle length, respectively), the drag force on the trailing body is higher than the leading one. Zabat et al. [1] experimentally studied the effects of vehicles' spacing on the drag coefficients of a platoon with two, three and four vehicles using mini-van geometries. For all the studied cases, the drag coefficient of the trailing body was larger than that of the leading one at close inter-vehicle distances ($d/L < 0.35$ for two vehicles and $d/L < 1$ for three and four vehicles). The recent relevant publication that provided the motivation for the present study was written by Watkins and Vino [2]. These

M. Mirzaei · S. Krajnović (✉)
Division of Fluid Dynamics, Department of Applied Mechanics,
Chalmers University of Technology, Gothenburg, Sweden
e-mail: sinisa@chalmers.se

M. Mirzaei
e-mail: marmir@chalmers.se

© Springer International Publishing Switzerland 2016

A. Segalini (ed.), *Proceedings of the 5th International Conference on Jets, Wakes and Separated Flows (ICJWSF2015)*,
Springer Proceedings in Physics 185, DOI 10.1007/978-3-319-30602-5_35

authors experimentally studied the effect of vehicle distances on the behavior of the lift and drag coefficients of both the leading and trailing vehicles. They used two Ahmed bodies with a 30° back light angle and studied the flow for a spacing region varied from 0.1 to 4.0 L, with L being the vehicle length. Their experimental investigation showed that the drag force of the trailing body significantly increases for spacings of 0.1–1.0, compared to the corresponding drag value of a single body in isolation. For example, for the vehicle spacing of $d/L = 0.5$, the drag coefficient of the trailing body is about 30 % higher than that of a single body. They observed that the presence of a following body significantly increases the base pressure of the leader. The impingement of flow structure shedding from the leader to the follower also highly increases the pressure on the fore-body of the follower. They showed that this phenomenon is more significant at inter-vehicle spacing $d/L = 0.5$, where there is enough space for the leader to produce strong longitudinal vortex structures; this impingement increases the down-wash over the follower and thus results in a higher drag value for the follower. The objective of the present study is to provide an accurate observation of the flow interaction between two Ahmed bodies at close distances. The aim of this paper is to increase our understanding of the flow structures between the bodies and to find out more about the unexpected variations of drag or lift coefficients at close distances. The paper provides a thorough description of the flow by using both instantaneous and time-averaged results from LES solutions for three different vehicle distances.

2 Numerical Details

Two identical Ahmed bodies are chosen as the geometry of the present study. Figure 1a represents a schematic view of the geometry of Ahmed bodies placed in the computational domain. Simulations are made for three inter-vehicle distances, $d/L = 0.3, 0.5$ and 1, where d and L are vehicle spacing and vehicle length, respectively. The Reynolds number based on the model height was $Re_H = 30000$. A schematic side view of the generated grid in the computational domain is presented in

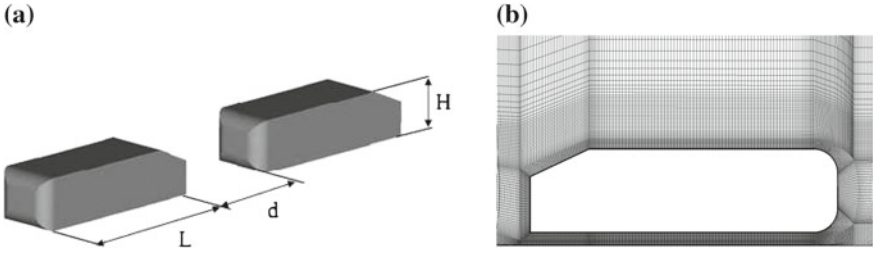


Fig. 1 Schematic views of the geometry and grid resolution. **a** Slanted back bodies. **b** Grid around a body

Fig. 1b. The total number of the computational cells is 8.5×10^6. The averaged wall normal resolution in the model is $n^+ = 0.7$. The resolution in the stream-wise and span-wise directions are $\Delta s^+ < 100$ and $\Delta l^+ < 35$, respectively. Here, $n^+ = nu_\tau/\nu$, $\Delta s^+ = \Delta s u_\tau/\nu$ and $\Delta l^+ = \Delta l u_\tau/\nu$, where u_τ is the wall friction velocity. LES with Standard Smagorinsky model is used in the present study. The incompressible Navier-Stokes equations are solved by employing the AVL FIRE commercial finite volume solver. A collocated grid arrangement is used. Convective fluxes are approximated by a blend of 99 % central differences of second-order accuracy and of 1 % upwind differences. The second-order three-time level scheme is used for time discretization. The SIMPLE algorithm is used to update the pressure and velocity fields.

3 Results and Discussions

Table 1 presents the experimental and numerical results of the averaged normalized drag coefficient (the ratio of drag coefficient to the corresponding value of a single body in isolation, C_d/C_{d0}) for two vehicles as the leader and the follower with three inter-vehicle distances of $d/L = 0.3, 0.5$ and 1. The experimental results are reported by Pagliarella [3] ($\alpha = 25°$ at $Re_H = 6 \times 10^5$) and Watkins and Vino [2] ($\alpha = 30°$ at $Re_H = 7 \times 10^5$). The numerical drag values of the present study are given at $Re = 30000$. The drag value of the follower is higher than the drag of the leader for all three distances. The presence of the follower increases the base pressure of the leader, leading to a decrease in the leader drag value. On the other hand, the low pressure wake region of the leader decreases the pressure of the follower's fore-body, and this results in a decrease in the follower drag value. Considering the normalized drag values of the present study for the leader and the follower, it can be noted that, for $d/L = 0.3$, the values for both the leader and the follower are smaller than one, meaning that platooning decreased the drag values of both bodies, and this reduction is higher for the leader than for the follower. For $d/L = 0.5$, the drag value for both bodies increases, compared to $d/L = 0.3$ (1.5 % for the leader and 8 % for the follower), and the drag value of the follower is higher than that of a single body in isolation. It means that the platooning has a negative effect on the follower's drag value. Increasing the vehicle distance to $d/L = 1$ increases the drag value of the leader and decreases the drag value of the follower (compared to $d/L = 0.5$).

Table 1 Averaged normalized drag values of two Ahmed bodies for three inter-vehicle distances

	$Re = 30000$	*EXP.* [3]	*EXP.* [2]
$d/L = 0.3$, leader	0.69	0.4	0.4
$d/L = 0.3$, follower	0.93	1.35	1.19
$d/L = 0.5$, leader	0.7	0.65	0.78
$d/L = 0.5$, follower	1.007	1.2	1.31
$d/L = 1$, leader	0.915	0.85	0.98
$d/L = 1$, follower	0.92	0.98	1.03

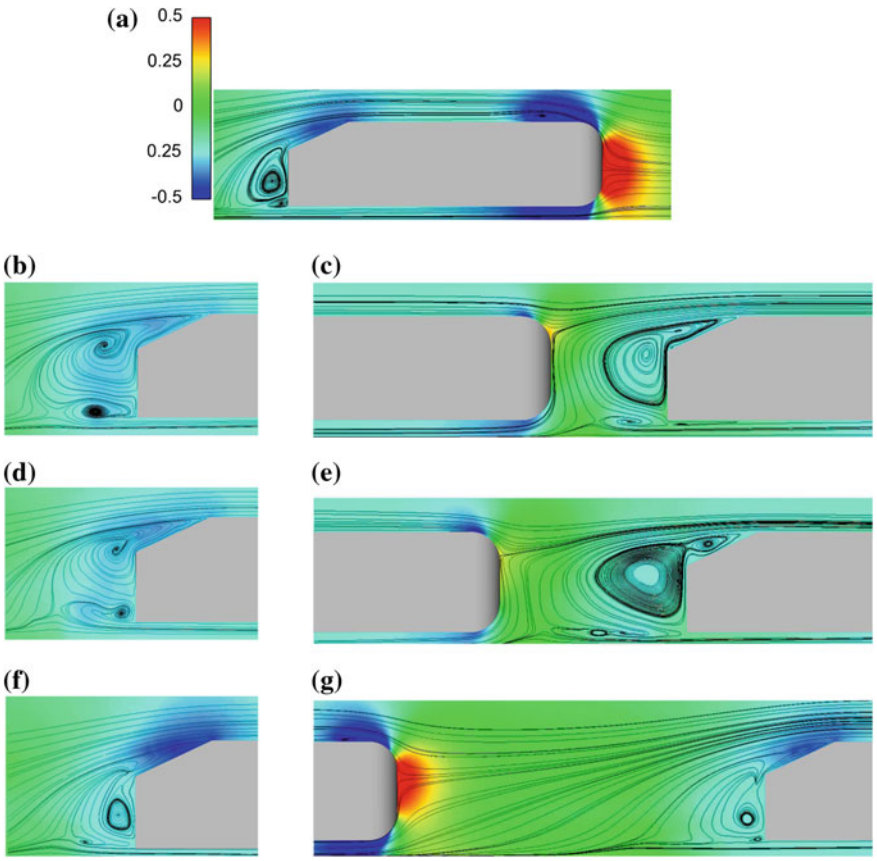


Fig. 2 Averaged pressure contours and streamlines between the leader and the follower (*right side*) and behind the follower (*left side*) for three vehicle distances of $d/L = 0.3, 0.5$ and 1. **a** Single. **b** d/L = 0.3. **c** d/L = 0.3. **d** d/L = 0.5. **e** d/L = 0.5. **f** d/L = 1. **g** d/L = 1

Figure 2 shows the averaged contours of static pressure between the leader and the follower (left side) and behind the follower (right side) for the three vehicle distances of $d/L = 0.3, 0.5$ and 1. The results are also compared with the corresponding pressure contour of a single body. Consistent with the experiments [3], the rear surface pressure of the leader increases with a decrease in the distance, which results in a decrease in the drag value of the leader (Table 1). The high pressure region around the stagnation point of the follower's fore-body moves up for spacings $d/L = 0.3$ and 0.5 (compared to the single body), and no separation occurs on top of the followers. When the distance increases to $d/L = 1$, the stagnation point position and the size of the high pressure region become similar to that of a single body, and a small recirculating region is created on top of the follower. A clearer picture of vortex cores is shown in Fig. 3. As can be seen, the center of the lower vortex for $d/L = 0.3$ is farther from the base surface than that of the upper vortex.

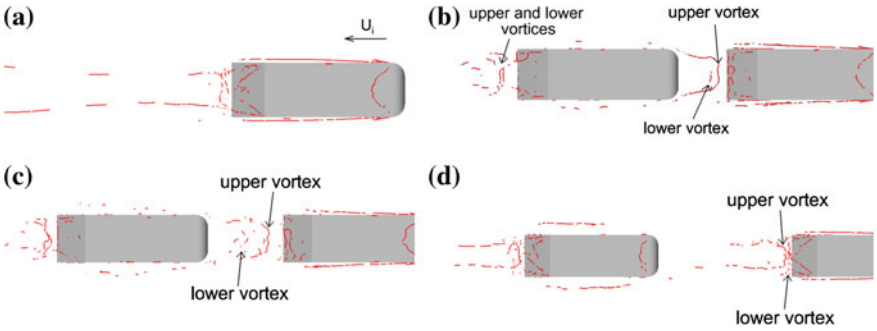


Fig. 3 Vortex cores of the time-averaged flow around two bodies with different distances. **a** Single. **b** d/L = 0.3. **c** d/L = 0.5. **d** d/L = 1

At $d/L = 0.5$, the upper vortex moves slightly away from the leader, while the lower vortex moves rather toward the follower. For both of the cases $d/L = 0.3$ and 0.5, the upper and the lower vortices are farther from the leader than those behind a single body. By increasing the distance to $d/L = 1$, both the upper and lower vortices move toward the base surface and are similar to those behind the single body. Similar to the case of the leader, two counter-rotating vortices are created behind the follower for all the distances. However, the lower vortex is larger than that behind the leader. The instantaneous iso-surfaces of the second invariant of velocity gradient, $Q = 400$, colored by ω_x are shown in Fig. 4. The three-dimensional longitudinal flow structures

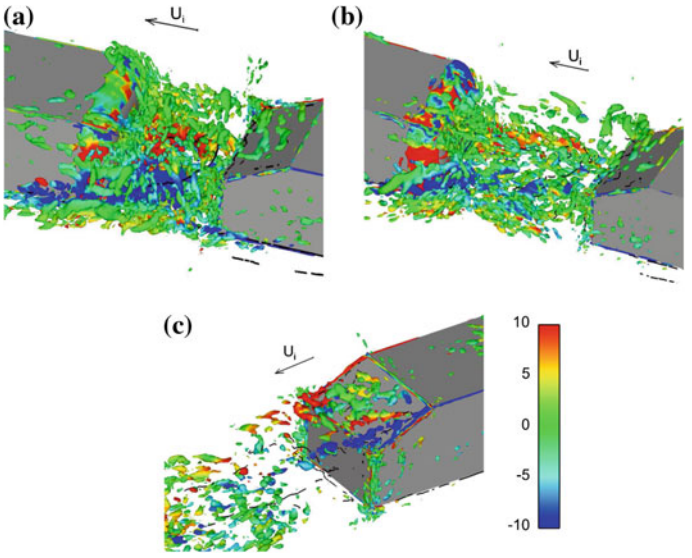


Fig. 4 Iso-surfaces of instantaneous $Q = 400$ colored by ω_x for three inter-vehicle distances. **a** d/L = 0.3. **b** d/L = 0.5. **c** d/L = 0.1

coming from the right and left sides of the leader impinge on the follower. The local high velocity gradient can be observed around the follower's fore-body, indicating the impingement effect of the flow. Two distinct counter-rotating trailing vortices can be observed over the rear surface of the leader with $d/L = 1$. These vortices are responsible for keeping the separated flow from the roof-backlight edge reattached on the surface. Thus, a bubble is created over the rear surfaces of the leader and the follower with $d/L = 1$. No significant trailing vortex is detected over the rear surfaces of leaders with $d/L = 0.3$ and 0.5. Thus, the flow separated on the top edge of the rear surface continues without reattachment to the rear surface.

4 Conclusions

A comprehensive numerical analysis of the effect of inter-vehicle distance on the flow structures between two Ahmed bodies was presented in this paper. The present study predicts a similar trend in the change of the aerodynamic drag as previous experimental observations [2, 3]. The drag of the follower is higher than one for the platoon with $d/L = 0.5$, which means that the platooning has a negative effect on the follower's drag value and increases the drag even higher than the drag of a single body in isolation. The time-averaged and instantaneous two-dimensional contours and three-dimensional iso-surfaces of the flow structures around the bodies were presented. A significant change in the flow structure was observed when the inter-vehicle distance was increased from $d/L = 0.5$ to $d/L = 1$.

Acknowledgments This work was supported financially by the Transport Area of advance at Chalmers. Software licenses were provided by AVL List GMBH. Computations were performed at SNIC (Swedish National Infrastructure for Computing) at the Center for Scientific Computing at Chalmers (C3SE) and the National Supercomputer Center (NSC) at LiU.

References

1. M. Zabat, N. Stabile, S. Farascaroli, F. Browand, The aerodynamic performance of platoons: a final report. California Partners for Advanced Transit and Highways (PATH) (1995)
2. S. Watkin, G. Vino, The effect of vehicle spacing on the aerodynamics of a representative car shape. J. Wind Eng. Ind. Aerodyn. **96**, 1232–1239 (2008)
3. M.R. Pagliarella, On the aerodynamic performance of automotive vehicle platoons featuring pre and post-critical leading forms, Ph.D. thesis, RMIT University (2009)

Numerical Study of Aerodynamic Interactions in a Homogeneous Multi-vehicle Formation

Maryam Mirzaei and Siniša Krajnović

Abstract An accurate and affordable method to study the flow features associated with vehicles in a homogeneous platooning is presented in this paper. It was found that only one pitch of a long-line periodic platoon would provide a sufficiently accurate observation of the flow interaction in the inter-vehicle region of the vehicles offering a significant reduction of the computational effort. The simulations of flow at Reynolds number of 30000 are made for a periodic platoon including slanted-back Ahmed bodies with a slant angle of 25° and for four inter-vehicle distances, $d/L = 0.1, 0.3, 0.5$ and 1.

1 Introduction

The concept of platoon is a long-line configuration of vehicles driving behind each other. The averaged drag values of vehicles in a platoon change by varying the number of vehicles, in which the averaged drag value of the entire platoon decreases until reaching a certain number of vehicles after which the drag asymptotically approaches a constant value. This means intuitively that the flow structures between the bodies nearly stay the same after a specific number of vehicles. The experimental study of Schito and Barghin [1] showed that, for a platoon of six squared back vehicles, the mean drag values of the entire platoon, as well as the vehicles individually, decreases until the fourth one in the line and follows an almost constant value for the rest of the bodies. It was also found that the importance of distance between the vehicles is significant and the averaged drag of platoons with reduced inter-body gaps approaches a lower asymptotic value. On the other hand, it has been reported in some studies that the aerodynamic advantages of platooning are not always enhanced

M. Mirzaei · S. Krajnović (✉)
Division of Fluid Dynamics, Department of Applied Mechanics,
Chalmers University of Technology, Gothenburg, Sweden
e-mail: sinisa@chalmers.se

M. Mirzaei
e-mail: marmir@chalmers.se

© Springer International Publishing Switzerland 2016

A. Segalini (ed.), *Proceedings of the 5th International Conference on Jets, Wakes and Separated Flows (ICJWSF2015)*,
Springer Proceedings in Physics 185, DOI 10.1007/978-3-319-30602-5_36

with decreasing the vehicles' spacing [2, 3]. For some particularly close distances (for example $d/L < 1$ [3] or $d/L < 0.35$ [2], where x and L are vehicle spacing and vehicle length, respectively), the drag force on the trailing body is higher than the leading one. In some cases, the drag force of both of the bodies (leading or trailing) may even exceed the corresponding value for a single vehicle in isolation. The other paper of the authors at the present conference [4], provided a detailed analysis of the effect of inter-body distance on the flow structures of a two-vehicle platoon. A drag increase was observed for the follower with $d/L = 0.5$, compared to the drag value of a single body in isolataion which was corresponded to the significant change of flow structure between the set-ups with $d/L = 0.5$ and $d/L = 1$. Owing to a lack of experimental equipment and computational resources, investigations have been mainly conducted for two or three bodies. Moreover, most of the knowledge of the aerodynamic behavior of platoons comes from steady experimental studies by presenting the global variations of the averaged drag values of vehicles. The aim of this paper is two fold. First, we demonstrate an affordable technique for accurate prediction of the flow in a long-line platoon. Secondly, the flow structures in the inter-vehicle region of such a platoon and their change with the inter-vehicle spacing are investigated. This study will hopefully help us gain a deeper understanding of the near wake flow structures of a long platoon and to find out whether the unexpected variations in drag coefficients would also occur for long formations of vehicle bodies.

2 Geometrical Model and Numerical Methodology

It is assumed that the platoon consists of a long-line of identical vehicles (Fig. 1a). The vehicles are slanted back Ahmed bodies with a slant angle of 25°. To reduce computational costs, only one pitch of the domain is regarded as the computational domain (dashed blue line in Fig. 1a) and periodic boundary condition is used in streamwise direction [5]. To verify the sufficiency of the computational domain in terms of selecting one or more pitches as the domain, computations are also performed for a two-pitch domain [5] (dashed red line in Fig. 1a) with the vehicle

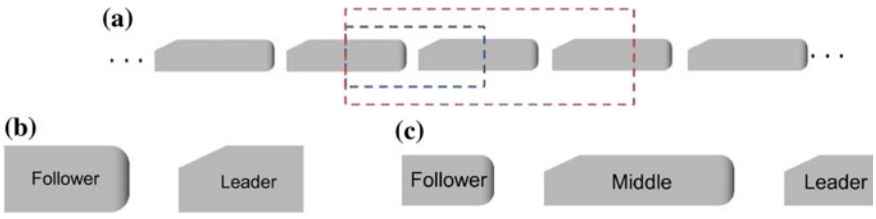


Fig. 1 Schematic views of the computational domains. **a** Long-line platoon. **b** One pitch. **c** Two pitches

distance of $d/L = 0.5$. Simulations are made for four inter-vehicle distances, $d/L = 0.1, 0.3, 0.5$ and 1, where d and L are vehicle spacing and vehicle length, respectively. The Reynolds number based on the model height is $Re_H = 30\,000$. Computational grids are generated by the ICEM-CFD grid generator. The total number of the computational cells in one- and two-pitch domain grids are 4.2×10^6 and 8.5×10^6, respectively. The number of the computational cells for a two-body platoon grid with an identical inter-body distance is 8.5×10^6. Comparison of the computational grid resolutions reveals that employing the periodic geometry would greatly decrease the computational costs. For all the grids employed in the present study, the averaged wall normal resolution in the model is $n^+ = 0.7$. The grid resolutions in the stream-wise and span-wise directions are $\Delta s^+ < 100$ and $\Delta l^+ < 35$, respectively. Here, $n^+ = nu_\tau/\nu$, $\Delta s^+ = \Delta s u_\tau/\nu$ and $\Delta l^+ = \Delta l u_\tau/\nu$, where u_τ is the wall friction velocity. The time step $dt^* = dtU_\infty/H$ for all the simulations is selected to be 1×10^{-3}, leading to the CFL number having a value of less than one in over 99 % of the cells.

LES with the Standard Smagorinsky model is used in the present study. The periodic boundary condition is employed in the streamwise direction. The symmetry boundary condition is used for the lateral sides and the ceiling of the computational domain. The no-slip boundary condition is used on the surface of the body and channel floor. The channel floor is set as a moving ground having the same velocity as the inlet boundary condition. The incompressible Navier-Stokes equations are solved by employing the AVL FIRE commercial finite volume solver. A collocated grid arrangement is used. Convective fluxes are approximated by a blend of 99 % central differences of second-order accuracy and of 1 % upwind differences. The second-order three-time level scheme is used for time discretization. The SIMPLE algorithm is used to update the pressure and velocity fields.

3 Results and Discussions

To ensure the sufficiency of the chosen portion of the periodic computational domain, simulations are made for one and two pitches of the periodic domain. The averaged streamlines on the symmetric plane of the inter-body region of a one-pitch domain (between the leader and follower) and a two-pitch domain (between the leader and middle bodies and the middle and follower bodies) are shown in Fig. 2. The results are displayed for the vehicle distance of $d/L = 0.5$. Regarding the size and form of the separated flow over the slanted surface and the wake region, a reasonably close agreement is observed between the two flow regions, the one between the leader and the middle body and the one between the middle and the follower body. This point confirms the periodicity of the flow structures in the selected domain. Good agreement is also observed between the streamlines predicted by one-pitch and two-pitch domains, implying the sufficiency of selecting one pitch of the periodic geometry as the computational domain.

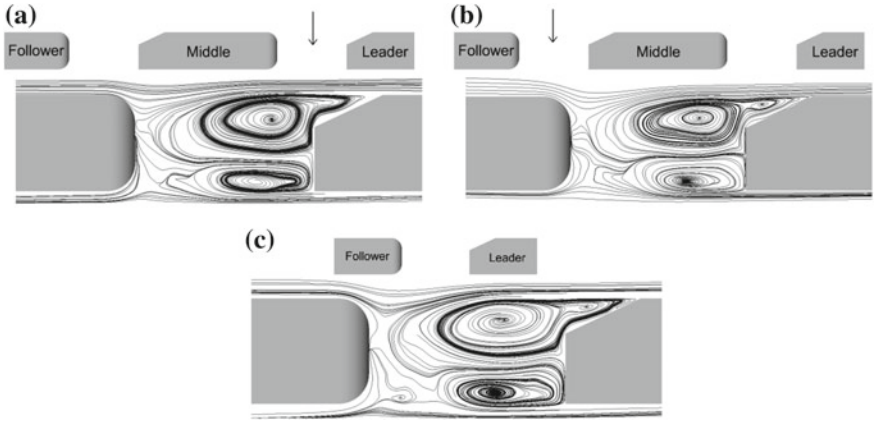


Fig. 2 Averaged streamlines in the region between the bodies of one and two pitches of the domain. **a** First pitch. **b** Second pitch. **c** One pitch

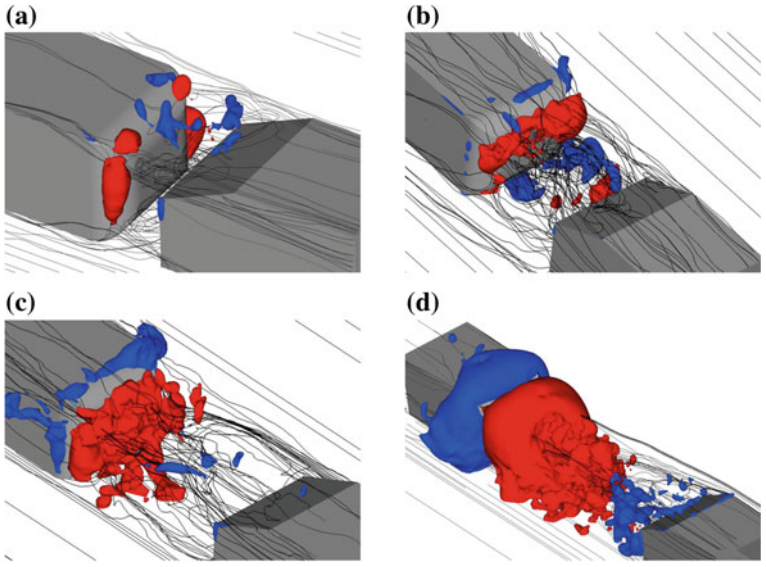


Fig. 3 Instantaneous iso-surfaces of the static pressure (P = 0.025 (Pa)) and streamlines for different inter-body distances $d/L = 0.1, 0.3, 0.5$ and 1. *Blue* iso-surface: P = −0.025 (Pa), *Red* iso-surface: P = 0.025 (Pa). **a** d/L = 0.1. **b** d/L = 0.3. **c** d/L = 0.5. **d** d/L = 1

Figure 3 provide the instantaneous iso-surfaces of static pressure in the region between the leader and the follower portions of a periodic platoon for four vehicle distances of $d/L = 0.1, 0.3, 0.5$ and 1. The instantaneous streamlines surrounding the bodies are also plotted. Consistent with the concept of platooning, the presence of the follower in the low-pressure wake region of the leader increases the pressure over the rear part of the bodies and, on the other side, decreases the pressure over

their frontal part. For $d/L = 0.1$, the frontal part of the follower is located completely in the wake region of the leader and is surrounded by the streamlines coming from the upstream. The separated flow from the upper edge of the leader is pushed up by the follower, and no vortices are produced in the region between the bodies. Increasing the distance to $d/L = 0.3$ and 0.5, the pressure variation over the bodies becomes more noticeable. The rotational wake region of the leader part covers nearly the whole region between the bodies. Larger high-pressure zones can be recognized close to the upper and side rounded edges of the leader, showing that the upstream streamlines would find a longer distance to flow between the bodies and more strongly impinge to the frontal surface of the follower. Depending on the distance of the bodies, the streamlines coming from the upstream body surround the two-dimensional vortices in the wake region of the leader and then start to bias toward the center of the frontal surface of the follower. Figure 4 presents the time-averaged streamlines on the symmetric plane between the bodies, predicted for four different inter-body distances, $d/L = 0.1, 0.3, 0.5$ and 1. As is observed in Fig. 3, placing the follower bodies close to the leaders increases the pressure over the rear surface of the leaders. Therefore, the separated flow from the upper edge of the leader (junction of the roof and rear surfaces) does not reattach over the slanted surface. Except in the case of $d/L = 0.1$, two counter-rotating vortices over each other are formed behind the leader part. The size of the upper vortex is much larger than that of the lower one and, it extends almost to the frontal face of the leader for $d/L = 0.3$ and 0.5. The interesting flow structure is observed for the inter-body gap $d/L = 0.1$ in terms of the location of the vortices formed behind the leader body. The presence of the follower very close to the leader pushes the upper vortex up, over the rear surface, and the lower vortex down, under the leader. The upstream flow from the leader flows parallel over the upper vortex, and no significant impingement is noticed. When the gap between the bodies is increased, the high-pressure stagnation point moves down and is biased toward the center of the leader's frontal face (similar to the one for a single body).

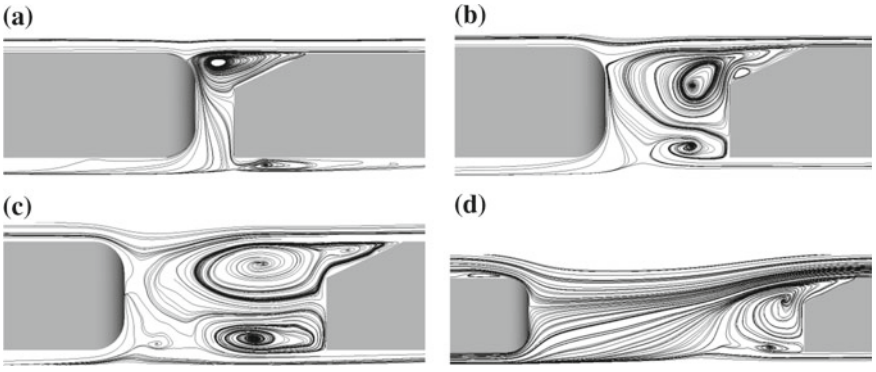


Fig. 4 Averaged streamlines on the symmetric plane of the region between the bodies with inter-body distances $d/L = 0.1, 0.3, 0.5$ and 1. **a** d/L = 0.1. **b** d/L = 0.3. **c** d/L = 0.5. **d** d/L = 1

4 Conclusions

This paper presents a comprehensive numerical investigation of the flow structures in a long-line homogeneous platoon. The simulations were made for the Ahmed body with a slant angle of 25° and at four inter-vehicle distances, $d/L = 0.1, 0.3, 0.5$ and 1. The Reynolds number based on the height of the body was $Re_H = 30000$. The instantaneous and time-averaged three-dimensional flow structures in the region between the bodies were compared for four different inter-body distances. The predicted results showed that the presence of the follower very close to the leader ($d/L = 0.1$) pushes the upper vortex over the rear surface and the lower vortex under the leader, the upstream flow coming from the leader flows over the upper vortex, and no significant impingement is noticed. For $d/L = 0.1$ and 0.3, the high-vorticity flow structures start from the leader and continue until the follower's fore-body, whereas, for $d/L = 0.5$, the flow structures break close to the middle of the bodies' gap and smaller structures shed toward the follower. Owing to the effects of the surrounding vehicles in a long-line platoon, the trailing vortex formed in a periodic geometry is significantly shorter and thinner than the one in a single body or two-body platoon.

Acknowledgments This work was supported by Transport Area of Advance at Chalmers. Software licenses were provided by AVL List GMBH. Computations were performed at SNIC (Swedish National Infrastructure for Computing) at the Center for Scientific Computing at Chalmers (C3SE) and the National Supercomputer Center (NSC) at LiU.

References

1. P. Schito, F. Braghin, Numerical and experimental investigation on vehicles in platoon, SAE paper 2012-01-0175 (2012)
2. M. Zabat, N. Stabile, S. Farascaroli, F. Browand, *The aerodynamic performance of platoons: a final report* (UC Berkeley, California Partners for Advanced Transit and Highways (PATH), 1995)
3. S. Watkin, G. Vino, The effect of vehicle spacing on the aerodynamics of a representative car shape. J. Wind Eng. Ind. Aerodyn. **96**, 1232–1239 (2008)
4. M. Mirzaei, S. Krajnovic, Large-eddy simulations of flow around two-generic vehicles in a platoon, in *International Conference on Jets, Wakes and Separated Flow*. (Stockholm, Sweden, June 2015), pp. 16–18
5. M. Mirzaei, L. Davidson, A. Sohankar, F. Innings, The effect of corrugation on heat transfer and pressure drop in channel flow with different Prandtl numbers. Int. J. Heat Mass Transf. **66**, 164–176 (2013)

Numerical Investigation of the Actuated Flow on a Bluff Body

Guglielmo Minelli and Siniša Krajnović

Abstract Large Eddy Simulations (LES) are conducted to study the Active Flow Control (AFC) of the separation of the boundary layer on a rounded leading edge frontstep. This bluff body imitates the flow around a section of a simplified truck cabin and focuses on the separation arising at the front rounded corner, the so called A-pillar. The LES data show the connection between the actuation and drag reduction. The actuated and unactuated flows are analysed using modal decomposition and frequency analysis. Two different actuation frequencies are tested and a strong influence of the control on both drag reduction and separation mechanism was observed. Relevant results, in terms of drag coefficient and recirculation bubble reduction, are achieved when the flow is actuated. LES shows an increased unsteadiness in the flow, introduced by the actuation. An analysis that investigates the connection between actuation and induced unsteadiness is presented.

1 Introduction

The optimization of the aerodynamic performances of a vehicle, can be achieved manipulating the flow to a more desired state, by an imposed actuation. A recent review of these technique was provided by Gad-el-Hak et al. in [1] and by Zhang et al. in [2]. In the present study one Active Flow Control (AFC) technique, known as Zero Net Mass Flux jet (ZNMF), a synthetic jet, has been used to reduce or prevent the separation of the boundary layer from the surface of a bluff body. Promising results were found in several flow control studies, both experimental [3] and numerical [4]. Many studies that focus on the actuation at the trailing edge of bluff bodies have been carried out, [5, 6]. In contrast to this, the present work focuses on the front part

G. Minelli (✉) · S. Krajnović
Division of Fluid Dynamics, Chalmers University of Technology,
412 96 Gothenburg, Sweden
e-mail: minelli@chalmers.se

S. Krajnović
e-mail: sinisa@chalmers.se

© Springer International Publishing Switzerland 2016

A. Segalini (ed.), *Proceedings of the 5th International Conference on Jets, Wakes and Separated Flows (ICJWSF2015)*,
Springer Proceedings in Physics 185, DOI 10.1007/978-3-319-30602-5_37

of a bluff body. The AFC aims to reduce the aerodynamic drag by reduction of the separated flow region.

A CFD investigation is performed in this study. The necessity of reproducing unsteady flow and analysing the effect of the actuation on the boundary layer leads to use of Large Eddy Simulation (LES) as it can resolve a large part of the unsteady structures of the flow. Thus, LES equations with the standard Smagorinsky subgrid scale (SGS) are employed, and the actuation is set applying a time varying inlet boundary condition at the area of interest.

Understanding the flow separation mechanism acting at the mentioned front part (the so called A-pillar) is likewise challenging. Thus, Proper Orthogonal Decomposition (POD) and Fast Fourier Transform (FFT) analysis are employed to extrapolate the salient features of the flow field. In [7], LES were post-processed using POD in order to analyse the structures in the turbulent flow field behind a square back Ahmed body. However, POD does not give a complete picture of the frequencies characterizing the flow. Hence, in order to have a more complete description, the FFT study is compared to the POD results.

2 Numerical Set-Up

The model is placed in a computational domain shown in Fig. 1a. The reference dimension of the section is, $W = 1.25$ m. The model has a length $L = 8W$, and a height $H = 1.12W$. The domain has a length $S = 19.2W$, and a width $I = 8W$. A uniform and steady velocity, $U_{inf} = 0.64$ m/s, is applied at the inlet. The resulting Reynolds number based on the double width of the section, $2W$, and U_{inf} is $Re = 1 \times 10^5$. A homogeneous Neumann boundary condition is applied at the outlet. The surfaces of the body are treated as no slip walls. Periodic boundary conditions are imposed at the upper and lower walls which define the height H of the section. Symmetry boundary conditions are set at the two side walls, which define the width I of the domain. A time varying velocity, $U_{AFC} = 0.1U_{inf} \sin\left(\frac{t2\pi}{T}\right)$, is set at the actuation area highlighted by red arrows in Fig. 1b. The period T is defined by the chosen frequency, f_a, as $T = 1/f_a$. In the present work all the frequencies

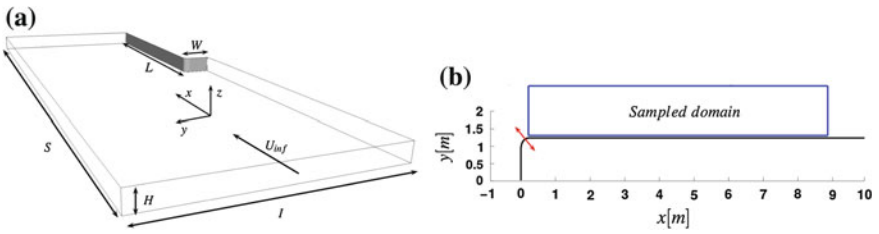


Fig. 1 The computational domain and the sampling plane

are described in terms of Strouhal number (St), computed as, $St = \frac{f_a 2W}{U_{inf}}$. A finite grid plane, placed at $z = H/2$, is used to sample snapshots of the flow field, Fig. 1b. Velocity and pressure fields are sampled during time and post processed using a modal approach. The governing LES equations are the spatially implicitly filtered Navier-Stokes equations, where the spatial filter is determined by the characteristic width $\Delta = (\Delta_1 \Delta_2 \Delta_3)^{\frac{1}{3}}$, where Δ_i is the computational cell size in the three coordinate directions.

$$\frac{\partial \bar{u}_i}{\partial t} + \frac{\partial}{\partial x_j}\left(\bar{u}_i \bar{u}_j\right) = -\frac{1}{\rho}\frac{\partial \bar{p}}{\partial x_i} + \nu \frac{\partial^2 \bar{u}_i}{\partial x_j \partial x_j} - \frac{\partial \tau_{ij}}{\partial x_j} \tag{1}$$

and

$$\frac{\partial \bar{u}_i}{\partial x_i} = 0. \tag{2}$$

Here, $\bar{u}_i$ and $\bar{p}_i$ are the resolved velocity and pressure, respectively, and the bar over the variable denotes the operation of filtering. The influence of the small scale in (1) appears in the SGS stress tensor, $\tau_{ij} = \overline{u_i u_j} - \bar{u}_i \bar{u}_j$. The algebraic eddy viscosity model, described in [8], is employed in this work. The Smagorinsky model represents the anisotropic part of the SGS stress tensor, τ_{ij}.

$$\tau_{ij} - \frac{1}{3}\delta_{ij}\tau_{kk} = -2\nu_{sgs}\bar{S}_{ij} \tag{3}$$

where the SGS viscosity is

$$\nu_{sgs} = (C_s f \Delta)^2 |\bar{S}|; \quad \bar{S} = \sqrt{(2\bar{S}_{ij}\bar{S}_{ij})}; \quad \bar{S}_{ij} = \frac{1}{2}\left(\frac{\partial \bar{u}_i}{\partial x_j} + \frac{\partial \bar{u}_j}{\partial x_i}\right) \tag{4}$$

The Smagorinsky constant, $C_s = 0.1$, previously used in bluff body LES, [9], is used in the present work. f in the expression for the SGS viscosity is the Van Driest damping function.

$$f = 1 - exp\left(\frac{-n^+}{25}\right) \tag{5}$$

where n^+ is the wall normal distance in viscous units. The simulations in this work are made with the commercial finite volume CFD solver, AVL FIRE, [10]. AVL FIRE is based on the cell-centered finite volume approach. The grid topology is constructed using the O-grid technique in order to concentrate most of the computational cells close to the body. The grid average resolution in the wall-normal direction is $n^+ = 0.45$ with a maximum value of $n^+ = 1.7$. The resolution in the spanwise direction is $\Delta l^+ < 30$, and the resolution in the streamwise direction is $\Delta s^+ < 100$. The chosen timestep is $\Delta t^* = \Delta t U_{inf}/2W$ is 1.28×10^{-3}, resulting in a CFL number lower

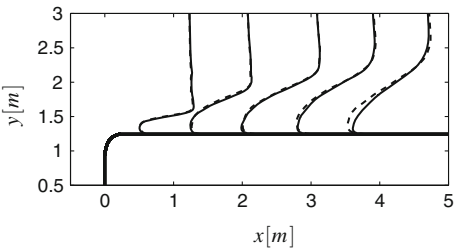


Fig. 2 Averaged streamwise velocity component profiles. (------) coarse grid, (——) fine grid

than 1 in the entire domain. An averaging of $t^* = tU_{inf}/2W = 25$ is done for all the simulations.

2.1 Numerical Accuracy

The numerical accuracy is ensured by performing the unactuated flow field simulation on a coarser grid. The number of computational cells of the coarse grid has been reduced by 30 %. The coarsening procedure affects only the streamwise and spanwise directions and thus the grid has not been coarsened in the wall normal direction. Figure 2 shows the streamwise velocity profiles of both the fine and the coarse grids. The mean value of C_d differs by 1 %, and a good agreement between the measured profiles, Fig. 2, confirms that mesh independence is achieved.

2.2 Proper Orthogonal Decomposition

As it is originally proposed by Lumley in [11], A POD analysis is made of a snapshots sequence $V_1^N = (v_1, ..., v_n)$ of the sampled area shown in Fig. 1b. The POD modes are contained in the singular value decomposition of the matrix V_1^N as,

$$V_1^N = U\Sigma W^T \tag{6}$$

Here the matrix U contains the spatial structures, and the matrix W contains the temporal coefficients. The matrix Σ contains the singular values that rank the energy content of each mode. In the present work the POD study is performed over 1000 snapshots, equispaced by a non dimensional $\Delta t^\star = 1.28 \times 10^{-2}$. Mode 1 represents the mean value of the flow field and it contains the largest amount of energy. Every travelling structures is represented by a couple of modes, containing the same amount of energy but shifted in time. For example the most energetic travelling structures is represented by the sum of mode 2 and 3, visualised as 1_{st} *pair* in Fig. 3. Figure 3b shows the temporal coefficients of mode 2 and 3, which are similar but shifted in

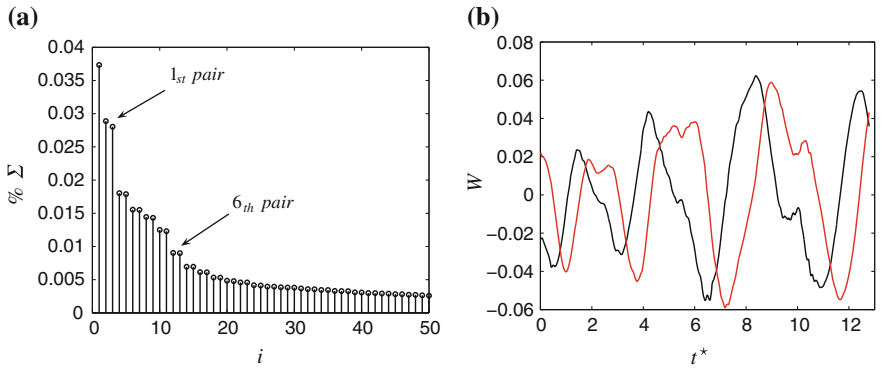


Fig. 3 **a** Energy content of the first 50 most energetic modes. **b** Comparison of the temporal coefficient W_2 (*black*) and W_3 (*red*) for mode 2 and 3 respectively. Unactuated flow

time. This shifting is necessary to reconstruct the temporal changing and movement of the considered flow structures.

3 Results

3.1 Unactuated Flow Field

A description of the unactuated flow field and a comparison between two different actuations, the first at $St = 1.95$ and the second at $St = 3.9$, is presented. For simplicity, the first configuration, actuated at $St = 1.95$, is called St_1 and the second configuration, actuated at $St = 3.9$, is called St_2. Figure 4 (right side) shows a comparison between a snapshot described by streamlines of the streamwise velocity field and the POD most energetic travelling structures of the unactuated flow. The structures described by modes 12 and 13 define the separation process at the rounded corner, Fig. 4 (left side). The reconstruction of the mean features of the flow field shows that small vortices are formed at the rounded corner with a high separation frequency. These structures feed the bigger travelling vortices downstream, which are characterized by a lower Strouhal number.

3.2 Actuated Flow Field

In St_2, the first two couples of modes contain the same amount of energy, Fig. 5a. Both the orbit plot and the spatial distribution of the first couple of modes, Fig. 5b, c respectively, show a double periodicity at two different Strouhal numbers in St_2, and

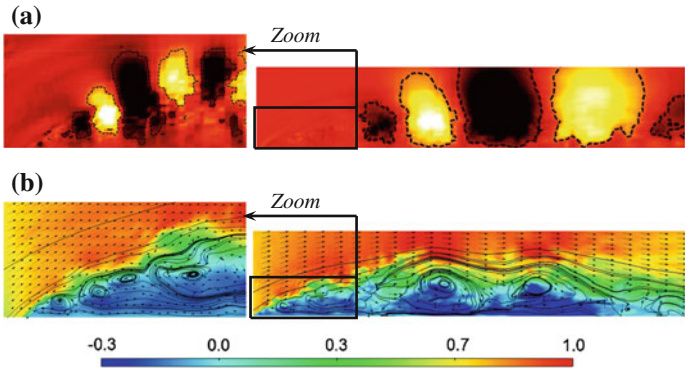


Fig. 4 **a** Spanwise velocity POD modes. Modes 12–13 (*left*) and modes 2–3 (*right*). **b** Streamwise instantaneous velocity flow field described by streamlines. Zoom of the front part (*left*). Unactuated flow

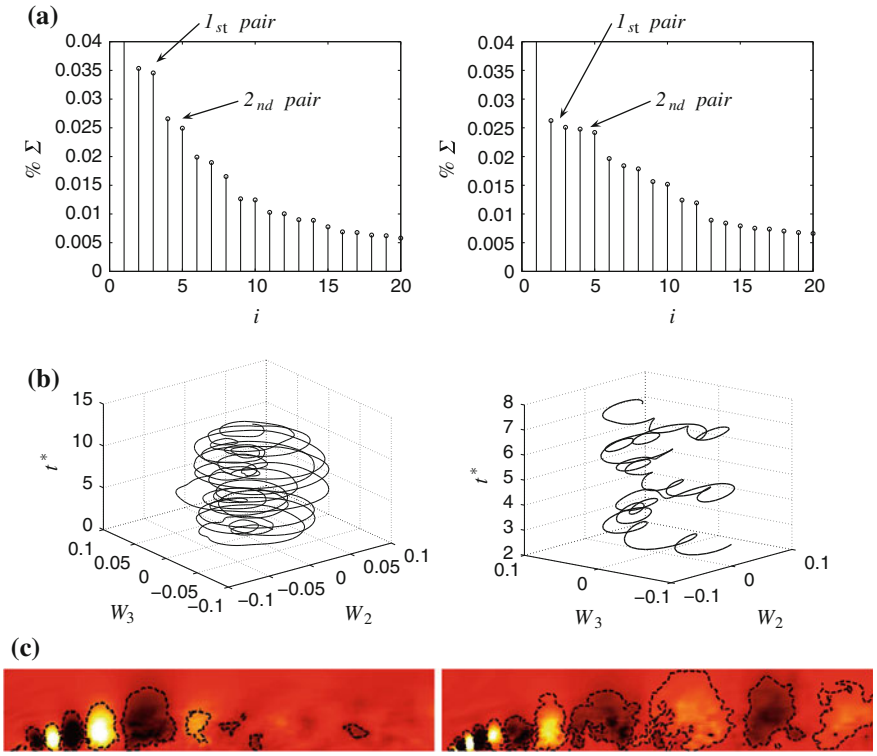


Fig. 5 **a** Energy content of the first 20 most energetic modes. **b** Orbit plot of temporal modes 2 and 3 for spanwise velocity. **c** Travelling structures of the first spanwise velocity pair of modes. Actuated flow at $St = 1.95$ (*left*). Actuated flow at $St = 3.9$ (*right*)

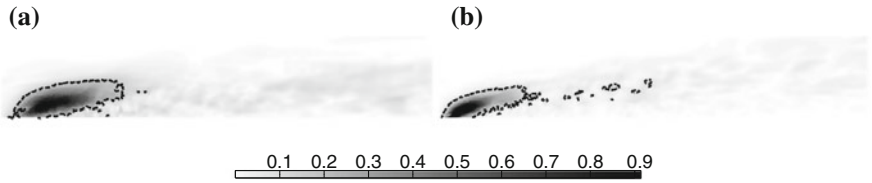


Fig. 6 Spatial distribution of the actuation frequency for spanwise velocity. Actuated flow at 1.95 (*left*). Actuated flow at 1.95 (*right*). The plots are normalized with the maximum value of the FFT signals all over the sampled domain

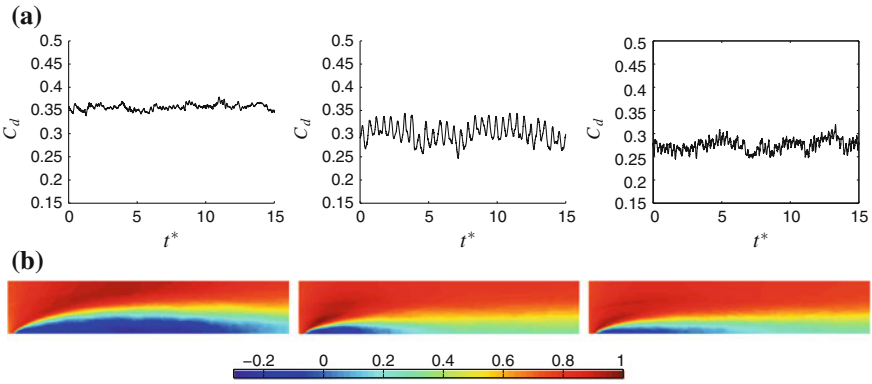


Fig. 7 **a** C_d coefficients time history. **b** Averaged streamwise flow field. From left to right, unactuated flow, actuated flow at $St = 1.95$, actuated flow at $St = 3.9$

Table 1 Coefficient of aerodynamic drag C_d and its root mean square value

Case	C_d	C_d *RMS*
Unactuated	0.36	0.007
$St_1 = 1.95$	0.30	0.020
$St_2 = 3.9$	0.27	0.013

a single periodicity at the forcing frequency in St_1. The first pair of modes in St_2 depicts the presence of two different structures having the same amount of energy. The first are the small structures arising due to the actuation frequency and the second are the larger structures developing further downstream the separation. This fact leads to the conclusion that the actuation in St_2 is not dominant as it is in St_1. Figure 6 shows the area where the forcing Strouhal number acts. St_2 presents a more localized actuated area compared to St_1, affecting less the flow all over the domain. Figure 7a shows the achieved drag reduction and depicts the oscillations introduced by the actuation. The induced oscillations, as well as the C_d mean value, decrease with the increase of the actuation frequency, Table 1. Figure 7b shows a comparison of the averaged streamwise flow velocity and a significant reduction of the recirculation bubble.

4 Conclusion

LES at $Re = 1 \times 10^5$ were conducted to analyse the actuation of the flow field around a bluff body. The bluff body is a frontstep characterized by a rounded leading edge, that represents a simplified section of a truck cabin A-pillar. Both the averaged and the instantaneous flows, are analysed and described. A frequency and modal analyses of the flow using FFT and POD, respectively, were conducted in order to gain a deeper understanding of the main structures depicting the flow cases. The unactuated flow is mostly dominated by low frequencies, characteristics of the large Kelvin Helmotz vortices arising after the separation. At the front leading edge, the flow is clearly described by small, high frequency structures that define the dimension of the recirculation bubble, and feed the large eddies downstream the surface of the body. Induced fluctuations and the area of influence of the actuation decrease increasing actuation frequencies. St_2 shows that, the energy content present in the small structures, arising from the actuation, is comparable with the larger structures downstream the flow field. The two different structures appear together in the first pair of mode.

The actuation of the flow improves significantly the performance in terms of the mean value of the C_d. In particular, a C_d reduction by 25 % was obtained in St_2.

Acknowledgments This work is supported financially by the Swedish Energy Agency. Software licenses were provided by AVL List GMBH. Computations were performed at SNIC (Swedish National Infrastructure for Computing) at the Center for Scientific Computing at Chalmers (C3SE) and the National Supercomputer Center (NSC) at LiU.

References

1. M. Gad-el Hak, A. Pollard, J.P. Bonnet, *Flow Control: Fundamentals and Practices*, vol. 53. (Springer-Verlag, 1998)
2. P. Zhang, J. Wang, L. Feng, Review of zero-net-mass-flux jet and its application in separation flow control. Sci. China Ser. E: Technol. Sci. **51**, 1315–1344 (2008)
3. M. Amitay, A. Glezer, Role of actuation frequency in controlled flow reattachment over a stalled airfoil. AIAA J. **40**, 209–216 (2002)
4. D. You, P. Moin, Active control of flow separation over an airfoil using synthetic jets. J. Fluids Struct. **24**, 1349–1357 (2008)
5. M. Pastoor, L. Henning, B.R. Noack, R. King, G. Tadmor, Feedback shear layer control for bluff body drag reduction. J. Fluid Dyn. **608** (2008)
6. D.J. Parkin, M.C. Thompson, J. Sheridan, Numerical analysis of bluff body wakes under periodic open-loop control. J. Fluid Mech. **739**, 94–123 (2013)
7. J. Östh, B.R. Noack, S. Krajnović, D. Barros, J. Borée, On the need for a nonlinear subscale turbulence term in POD models as exemplified for a high-Reynolds-number flow over an Ahmed body. J. Fluid Mech. **747**, 518–544 (2014)
8. J. Smagorinsky, General circulation experiments with the primitive equations. Mon. Weather Rev. **91**(3), 99–165 (1963)
9. S. Krajnovic, Large eddy simulation of flows around ground vehicles and other bluff bodies. Philos. Trans. Ser. A, Math. Phys. Eng. Sci. **367**, 2917–2930 (2009)
10. AVL, *AVL Fire manual*, v2010, 11th edn. (2010)
11. J.L. Lumley, *Stochastic Tools in Turbulence SE—Applied Mathematics and Mechanics*, vol. 12. (Academic Press, New York, 1970)

Part V
Wall-Bounded and Confined Flows

Breakdown of a Low-Speed Streak Caused by Turbulent Fluctuations

Huy Quang Ho, Masahito Asai and Shohei Takagi

Abstract Streak instability and subsequent breakdown caused by disturbances whose frequency-spectrum was similar to that of wall turbulence were examined experimentally. A low-speed streak was generated by using a small piece of wire-gauze-screen and disturbances were introduced to excite the streak instability through two small holes behind the screen. Two kinds of turbulent signals having different spanwise coherency were considered. Occurrence and growth of sinuous instability mode were compared with those for anti-symmetric forcing with the same frequency-spectrum. The results showed that the occurrence of sinuous instability mode was dependent on the spanwise coherency of the forcing disturbance.

1 Introduction

Instability of low-speed streaks and the resulting breakdown of streaks into quasi-streamwise vortices are considered to be key events for generation and sustenance of wall turbulence structures [1]. In transition to turbulence, especially in bypass boundary-layer transition, these important events were visualized clearly in experiments [2–4], in which streak breakdown was caused by the growth of sinuous instability modes. Numerical simulations of bypass boundary-layer transition under free-stream disturbances consisting of continuous Orr-Sommerefeld modes also showed that sinuous instability modes led to the streak breakdown in zero-pressure-gradient boundary layer [5, 6]. In order to study the mechanism of streak instability and breakdown in our laboratory, a single low-speed streak was generated

H.Q. Ho (✉) · M. Asai · S. Takagi
Department of Aerospace Engineering, Tokyo Metropolitan University,
6-6 Asahigaoka, Hino, Tokyo 191-0065, Japan
e-mail: ho-huyquang@ed.tmu.ac.jp

M. Asai
e-mail: masai@tmu.ac.jp

S. Takagi
e-mail: pantaka@tmu.ac.jp

© Springer International Publishing Switzerland 2016

A. Segalini (ed.), *Proceedings of the 5th International Conference on Jets, Wakes and Separated Flows (ICJWSF2015)*,
Springer Proceedings in Physics 185, DOI 10.1007/978-3-319-30602-5_38

artificially in a laminar boundary layer by using a small piece of screen set normal to the boundary-layer plate and the detailed instability characteristics were obtained [7, 8]. However, when disturbances triggering the streak instability were frequency-rich like in turbulent boundary layer or in a boundary layer subject to residual free-stream disturbances, the breakdown process of low-speed streak might be different from that observed in the well-controlled experiments due to possible interactions among many spectral components. In the present study, aiming at giving further insights on instability and breakdown of low-speed streak(s) in a turbulent environment experimentally, a screen-generated low-speed streak is forced by disturbances with a continuous spectrum similar to that of developed wall turbulence.

2 Experimental Setup

The experiment was conducted in a low-turbulence wind tunnel with an exit cross-section of $400 \times 400\,\text{mm}^2$. This facility is the same as that used in experiments [7, 8]. The free-stream velocity U_∞ was fixed at 4 m/s throughout the experiment. A single low-speed streak was produced in the boundary layer by using a small peace of 40-mesh screen (wire-gauze) set normal to the boundary-layer plate (10 mm thick and 1100 mm long) at a station 500 mm downstream of the leading edge (see Fig. 1). The screen height and width were respectively 3 mm and 5 mm. Here, in the absence of the screen, the displacement thickness δ^* of Blasius boundary layer was about 2.5 mm at $x = x_0$ (=500 mm). The streak flow was forced by external disturbances consisting of the same frequency-spectrum as turbulent fluctuations; they were introduced through two small holes (which were connected to two loudspeakers) immediately downstream of the screen. The turbulent signals used here were those deduced

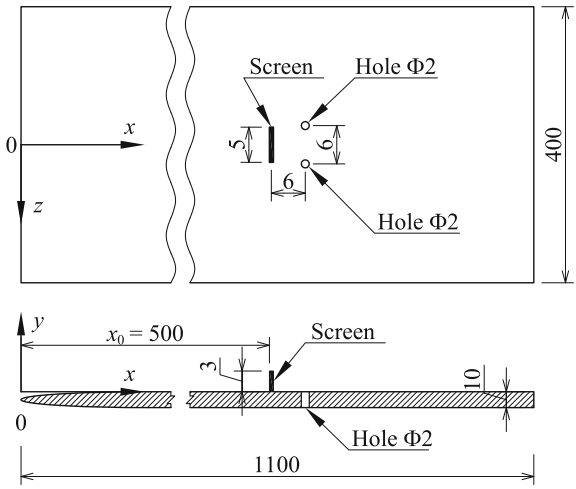


Fig. 1 The schematic of boundary-layer plate (Dimensions is mm)

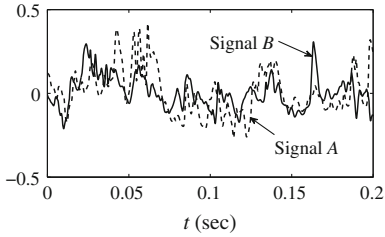


Fig. 2 Input turbulent signals (Case 1); their original data were measured at two z positions of 45 wall-units apart

by two hot-wires in a buffer region of turbulent boundary layer ($y^+ = 23$) generated in the same free-stream condition. Here, two pairs of forcing signals (to the two loudspeakers) were applied: One is a pair of turbulent fluctuations deduced at two z-positions of 45 wall units apart (Case 1), and the other is a pair at two z-positions of 90 wall units apart (Case 2). Note that the most probable value of the spanwise spacing of near-wall low-speed streaks is about 90 in wall units. We also applied anti-symmetric forcing (Case 3) in which two loudspeakers were driven with turbulent signals that were 180° out of phase to compare to the cases 1 and 2. Figure 2 displays typical waveforms of turbulent signals supplied to the two loudspeakers for Case 1. Spectra of streamwise velocity fluctuations excited with these signals were found to be similar to the spectrum of the input signals just downstream of the holes. A constant-temperature hot-wire anemometer was used to measure time-mean and fluctuation velocities in the streamwise direction, U and u. A smoke-wire was also used to visualize the streak breakdown process: Time sequences of top-view pictures were taken by a digital high-speed video camera.

3 Results and Discussions

Figure 3 illustrate $y - z$ distributions of the mean velocity U/U_∞ at $x - x_0 = 120$ mm. A low-speed streak developed downstream of the screen. The low-speed streak maintained laminar completely at least in the observation region up to $x - x_0 = 300$ mm. We examined frequency-selective amplification of disturbances due to the streak instability caused by external disturbances consisting of turbulent spectral components. Figure 4a, b illustrate power spectra of u at $x - x_0 = 20$ mm, 60 mm, 100 mm

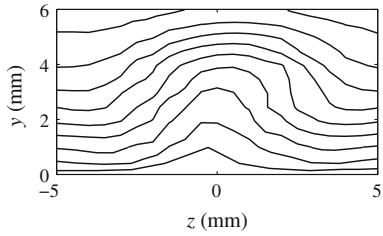


Fig. 3 Contour of U/U_∞ in (y, z) plane at $x - x_0 =$ 120 mm. Contour levels range from 0.1 to 0.9

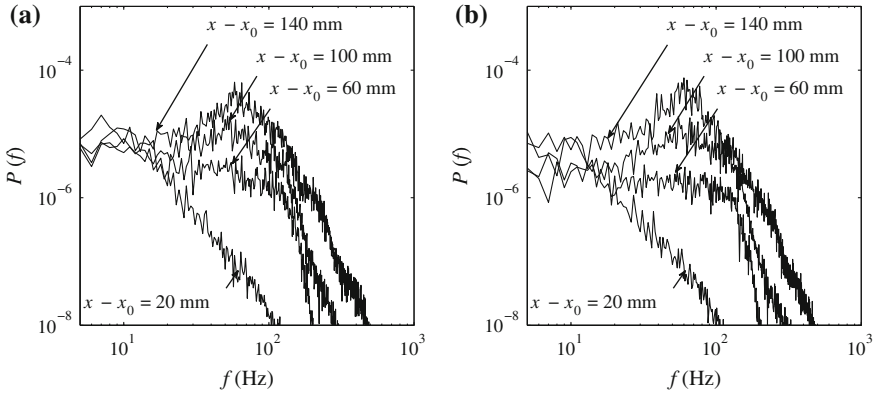


Fig. 4 Power spectra of u-fluctuations at $x - x_0 = 20$, 60, 100 and 140 mm. **a** Case 1; **b** Case 2

and 140 mm for Case 1 and Case 2, respectively; they were measured at the maximum shear ($\partial U/\partial z$) position where the disturbance took a maximum in amplitude at each x station. We can see disturbances are amplified over the frequency range of 40–100 Hz for both the cases. Figure 5a, b display the amplitude distribution of the spectral components over 40–100 Hz (denoted by u'_{40-100}/U_∞) in the $y - z$ plane at $x - x_0 = 140$ mm for both the cases.

The amplification of the growing disturbances was not largely different for both the cases, as seen from the comparison of the spectra. To understand the response of the streak to turbulent fluctuations more quantitatively, we compared the result to the case of an anti-symmetric forcing using the same turbulent signal (Case 3). Figure 6 illustrates the disturbance amplification in terms of power spectra of u for Case 3. The frequency-selective growth of 40–100 Hz components are more distinguished

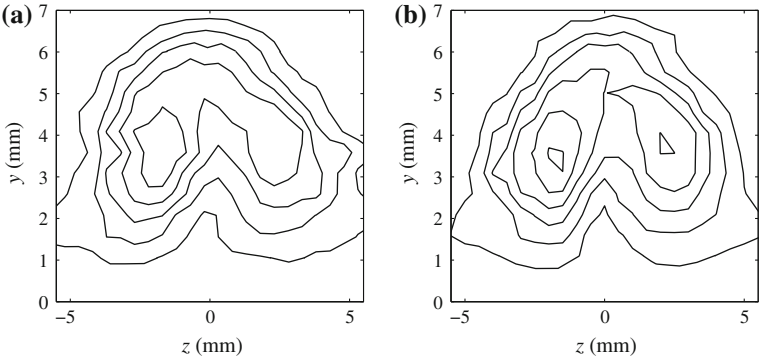


Fig. 5 Contours of rms amplitude of u-fluctuations (u'_{40-100}/U_∞) in the $y - z$ plane at $x - x_0 =$ 140 mm. **a** Case 1, contour levels range from 0.01 to 0.05; **b** Case 2, contour levels range from 0.01 to 0.06

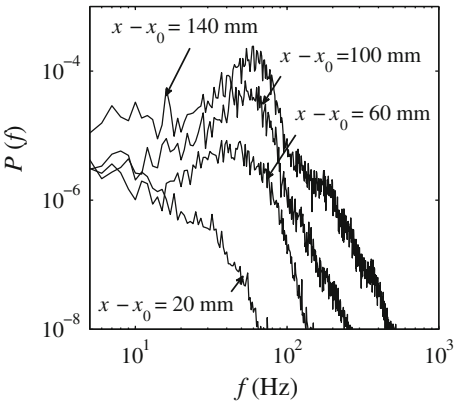


Fig. 6 Power spectra of u-fluctuations at $x - x_0 = 20$ mm, 60, 100 and 140 mm in Case 3

at downstream stations, compared to Cases 1 and 2 (Fig. 4a, b). In order to compare the frequency-selective amplification of disturbances (over 20 to 100 Hz) in Case 1 and Case 2 to that for the case of anti-symmetric excitation (Case 3), we estimated the N-factor defined as $N = \ln[P_2(f)/P_1(f)]^{1/2}$ where P_1 and P_2 are power spectra at $x - x_0 = 60$ mm and 140 mm, respectively. The maximum values of N (denoted by N_{max}), which were obtained around $f \sim 60$ Hz, were about 1.65 and 1.35 for Case 1 and Case 2, respectively, though both the values were smaller than that for the anti-symmetric excitation ($N_{max} \approx 1.95$). This is because the correlation of two turbulent signals was small but slightly positive (~ 0.1) for Case 1, while slightly negative (~ -0.1) for Case 2.

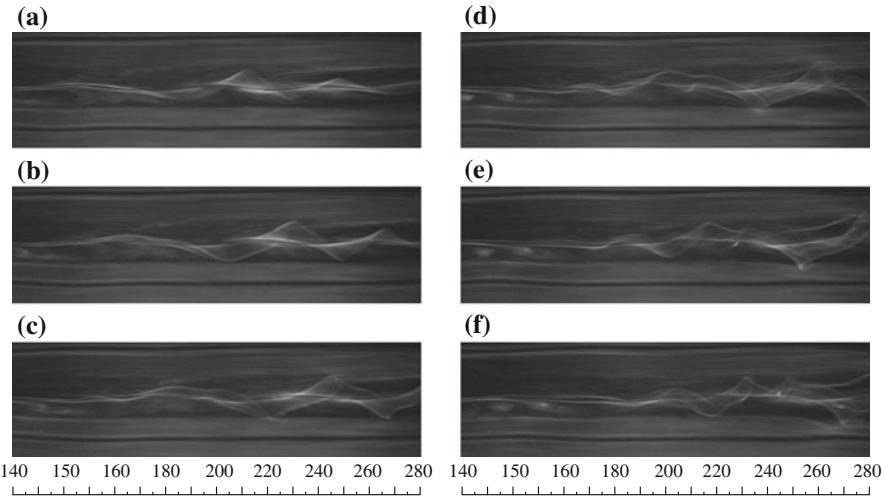


Fig. 7 Smoke-wire visualization of the development of anti-symmetric mode for Case 1. Smoke was released from $(x, y) = (80\,\text{mm}, 2\,\text{mm})$. Time increases from **a** to **f**, the interval between two consecutive pictures was 5 ms

To see development of streak instability in the present initial disturbance condition more clearly, Fig. 7 visualizes a sequence of the sinuous streak instability and subsequent breakdown processes. Smoke was released from a smoke wire stretched at $(x, y) = (80\,\text{mm}, 2\,\text{mm})$, and the top-view pictures were taken using a digital high-speed video camera. Concentrated smoke represents the low-speed streak. We see occurrence of sinuous spanwise motions of the low-speed streak, which corresponds to the frequency-selective disturbance growth observed in the spectra.

4 Conclusion

In the present experimental study, instability of low-speed streak was excited by disturbances with continuous frequency-spectrum similar to that of developed wall turbulence. Two kinds of disturbances which have the same frequency-spectrum but different spanwise coherency were introduced. Similar frequency-selective growth of sinuous instability mode was observed in the downstream stations for both the cases, but the result demonstrated that the magnitude of the instability mode was dependent on the spanwise coherency of the initial disturbance even though the frequency-spectrum was the same.

Acknowledgments This work was, in part, supported by Grant for Scientific Research from Tokyo Metropolitan Government.

References

1. J. Jiménez, A. Pinelli, The minimal flow unit in near-wall turbulence. J. Fluid Mech. **389**, 335–359 (1999)
2. M. Matsubara, P.H. Alfredsson, Disturbance growth in boundary layers subjected to free stream turbulence. J. Fluid Mech. **430**, 149–168 (2001)
3. J. Man, H.C. de Lange, A.A. van Steenhoven, Sinuous breakdown in a flat plate boundary layer exposed to free-stream turbulence. Phys. Fluids **19**, 088101 (2007)
4. M. Asai, Y. Konishi, Y. Oizumi, M. Nishioka, Growth and breakdown of low-speed streaks leading to wall turbulence. J. Fluid Mech. **586**, 371–396 (2007)
5. P. Schlatter, L. Brandt, H.C. de Lange, D.S. Henningson, On streak breakdown in bypass transition, Phys. Fluids **20**, 101505 (2008)
6. M.J.P. Hack, T.A. Zaki, Streak instabilities in boundary layers beneath free-stream turbulence, J. Fluid Mech. **741**, 280–315 (2014)
7. M. Asai, M. Minagawa, M. Nishioka, The instability and breakdown of a near-wall low-speed streak. J. Fluid Mech. **455**, 289–314 (2002)
8. Y. Konishi, M. Asai, Development of subharmonic disturbance in spanwise-periodic low-speed streaks. Fluid Dyn. Res. **42**, 035504 (2010)

Advection of a Coherent Structure in a Turbulent Boundary Layer

Masaharu Matsubara, Masanari Nagasaki, Akihito Yokoi and Muhammad Azmeer

Abstract Recently, a new extraction method, which is available for scrutiny of a coherent structure in turbulent shear flows, has been developed with introducing initial disturbances and applying an ensemble-average technique. The coherent structure extracted in a turbulent boundary layer forms into a streak elongating in the streamwise direction, and drifts downstream. As an initial disturbance, a periodical sinusoidal disturbance generated by a round speaker was introduced into the turbulent boundary layer from the wall in order to excite the linear coherent structure. Utilizing periodicity of the initial disturbance, ensemble averages were applied to the instantaneous wall pressure measured by a MEMS microphone array installed inside the wall. In the ensemble-averaged pressure distribution, high and low regions alternate in the streamwise direction and their phase shifts downstream. The advection velocity evaluated from this phase shift is proportional to the friction velocity. The proportionality constant of 14 expresses the advection velocity in the wall unit, indicating the universality of the wall scale can apply not only to the mean velocity profile but also to the dynamical fluid motions near the wall.

1 Introduction

A new extraction method for a coherent structure in turbulent shear flows with introducing initial disturbances and applying an ensemble-average technique has been recently developed. Surprisingly, the extracted structure has properties of linear

M. Matsubara (✉) · M. Nagasaki · A. Yokoi · M. Azmeer
Shinshu University, 4-17-1 Wakasato, Nagano 380–8553, Japan
e-mail: mmatsu@shinshu-u.ac.jp

M. Nagasaki
e-mail: 13tm130a@shinshu-u.ac.jp

A. Yokoi
e-mail: 14tm132a@shinshu-u.ac.jp

M. Azmeer
e-mail: 15tm128f@shinshu-u.ac.jp

© Springer International Publishing Switzerland 2016

A. Segalini (ed.), *Proceedings of the 5th International Conference on Jets, Wakes and Separated Flows (ICJWSF2015)*,
Springer Proceedings in Physics 185, DOI 10.1007/978-3-319-30602-5_39

dynamics that its structure is independent of the initial disturbance intensity, and that its amplitude is proportional to it [1, 2]. The linear coherent structure extracted from a turbulent boundary layer forms into a streak elongating in the streamwise direction, and it drifts downstream locating inside an area where a mean velocity profile follows the law of the wall. Therefore, it is inferred that dynamics of the structure also follows the wall scale. In this study, the advection velocity of the linear coherent structure is focused for revealing that the law of the wall also dominates fluid dynamics near the wall.

2 Experimental Method

The experiment were carried out in a closed circuit wind tunnel at Shinshu University. The wind tunnel was specially designed for a low turbulence level in the free stream and it consisted a 9 : 1 nozzle, expansion corners, diffusers, an air blower and a test section. The test section was 400 mm wide, 580 mm high and 4 m long, and a 580 mm wide, 10 mm thick, 2190 mm long flat plate shown in Fig. 1 was inserted vertically. A boundary layer developing on one of surfaces of the plate was tripped to turbulence by 2 mm diameter rod placed on the plate surface 140 mm downstream from the leading edge for keeping transition state stable. A periodical initial disturbance was ejected into the boundary layer from a tiny hole of 1.0 mm diameter drilled in the test plate. A small round speaker was attached backside of the hole. The test plate coordinate system is defined as the streamwise x, wall-normal y, and spanwise z directions.

A hot wire measurement for the mean velocity was carried out with a single hot wire sensor of the length of 0.5 mm and diameter of 2.5 μm. A three-axis robot arm positioned the sensor probe in $(y - z)$ plane and a rack-and-pinion mechanism on the test section roof shifted the arm in the streamwise direction. The pressure sensor

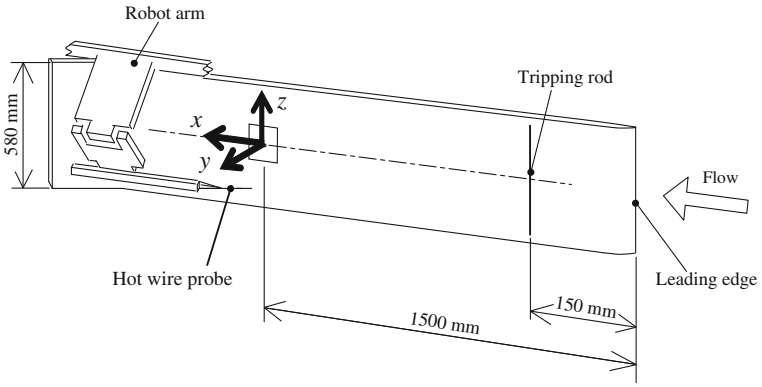


Fig. 1 Test plate and robot arm

array had 64 holes of a 0.5 mm diameter with a 0.6 mm spanwise space. Each hole was connected to a MEMS digital microphone.

When the initial disturbance has periodicity, the physical quantity q can be taken an ensemble average defined as

$$\langle q \rangle(x, y, z, \phi) = \frac{1}{N} \sum_{j=1}^{N} q(x, y, z, \phi + jT), \tag{1}$$

where T is a period of the initial disturbance, N is the number of times of the ensemble average and ϕ is phase. With the time mean $\bar{q}$, a periodic fluctuation component $\tilde{q}$ and a non-periodic component $\hat{q}$ are defined as $\tilde{q} = \langle q \rangle - \bar{q}$ and $\hat{q} = \bar{q} - \langle q \rangle$, so that the instantaneous quantity can be decomposed into the three components as $q = \bar{q} + \tilde{q} + \hat{q}$.

3 Results

To investigate the relationship between phase velocity C and friction velocity u_τ, the free stream velocity was gradually changed for 8 m/s $< U_\infty <$ 16 m/s. The Reynolds number based on the boundary thickness, Re_θ, at 1500 mm from the leading edge ranged from 1543 to 2475, with variation of Re_τ from 641 to 1027. The pressure sensor array mounted into the special plug and it is movable only with changing the plug hole, so that the streamwise positioning is very coarse. Instead of moving the pressure sensor array, the initial disturbance hole was relocated in the streamwise direction in order to measure the phase velocity of wall pressure distributions. The pressure sensor array was located at 1500 mm and distance from initial disturbance hole, Δx, was set at 25, 35 and 45 mm. A periodical sinusoidal signal was applied to the round speaker. Its frequency f and amplitude E were 200 Hz and 0.16 V, respectively. These parameters were decided so that the artificially excited coherent structure has properties of linear dynamics [1].

Figure 2 shows the mean velocity profiles at 1500 mm. The $^+$ notation represents the wall unit with the friction velocity u_τ and the kinematic viscosity ν. The friction velocity u_τ was evaluated with fitting to the universal profile proposed by Chauhan et al. [3]. In spite of the comparatively low Reynolds numbers, the velocity profiles for $y^+ < 200$ collapse well and demonstrate a characteristics of turbulent boundary layer.

The friction velocity was also measured by means of the oil film interferometry method. Figure 3 shows the result of interferometry of the oil film 900 s after it was spread on the test surface. Because a ordinary fluorescent light that has two sharp peaks in its spectra was used, light and dark stripes in different colors appear. The wall shear stress was evaluated from the drift speed of the stripes that color-filtered for extraction of red color of the sharp peak.

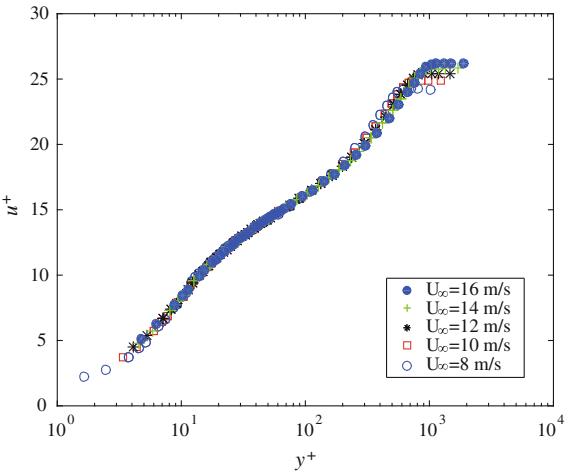


Fig. 2 The mean velocity profiles

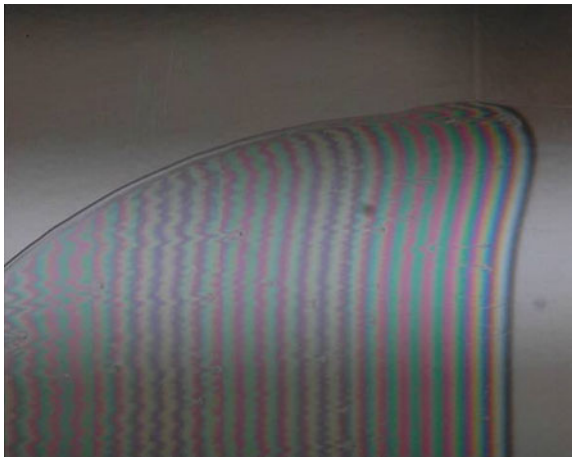


Fig. 3 The interference fringes after 900 s. The air flows from the right of the photograph

Figure 4 shows the wall pressure distributions at $U_\infty = 16$ m/s measured by the pressure sensor array. The pressure distributions are ensemble-averaged on the basis of phase of the initial disturbance, and they are mapped for two cycles on the time-space plane of the phase ϕ and the spanwise position z. It was found that the high and low pressure regions alternatively appear corresponding to the sinusoidal initial disturbance. The concentrate fluctuations are observed at $z = 0$ mm just downstream of the initial disturbance hole, though the pressure fluctuations spread in the spanwise direction within -15 mm $< z < 15$ mm. Comparing the distributions at the different streamwise positions, it is noticed that the distribution of the high and low pressure pattern drifts in a phase ϕ.

Figure 5 shows the advection velocity C calculated with the distance Δx and the phase shift ϕ of the pressure distributions. The linear fitting line for the friction

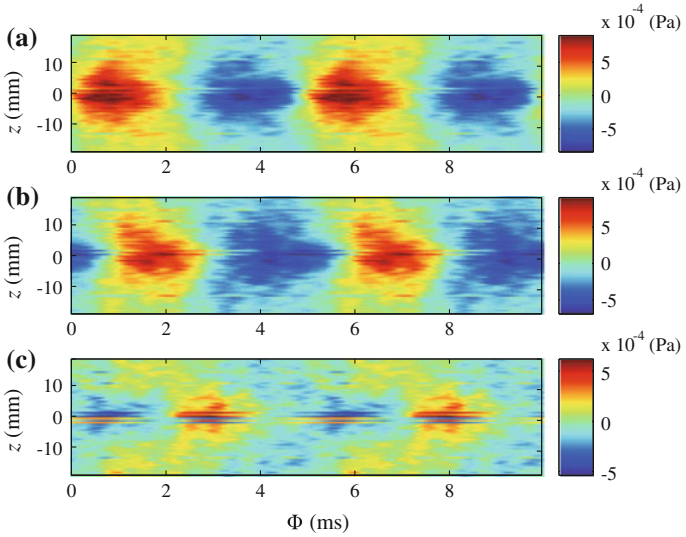


Fig. 4 Wall pressure distributions at $U_\infty = 16$ m/s. **a** $\Delta x = 25$ mmC, **b** $\Delta x = 35$ mm, **c** $\Delta x = 45$ mm

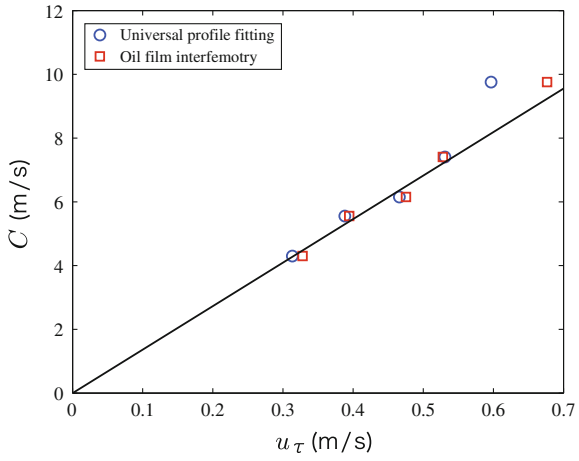


Fig. 5 The relationship between advection velocity of the coherent structure C and the friction velocity u_τ

velocity obtained by the oil film interferometry method indicates that C is in direct proportion to it, though the friction velocity from the universal profile fitting has some deviates from the line. The proportionality constant of the line is $C/u_\tau = C^+ = 13.5$. Though a wall-normal fluctuation distribution of the ensemble-averaged velocity is not shown here, the mean velocity at its peak position is about 14 in wall unit. This velocity corresponds well with the proportionality constant, suggesting that the coherent structure artificially excited by the point-like disturbance from the wall advects at the mean velocity at the position where it exists. This result confirms that

the wall unit is valid not only for turbulent statistics but also for the dynamics of the coherent structure. Because the coherent structure has properties of linear dynamics [1], it is inferred that the advection velocity is independent of intensity of the initial disturbance. If it is also independent of Reynolds number, the advection velocity would have universality for wall-bounded turbulent shear flows.

4 Conclusion

From the pressure distribution at the wall surface, it is found out that the phase velocity C of the linear coherent structure artificially excited by the initial disturbance from the wall is in directly proportional to the friction velocity u_τ. This confirms that the wall unit is valid not only for turbulent statistics but also for the dynamics of the linear coherent structure. The proportionality constant corresponds with the mean velocity at the place where the linear coherent structure exists. If the advection velocity has universality for wall-bounded turbulent shear flows, it can inversely estimate the friction velocity. This method would be exceptional with regard to a new evaluation technique not via wall shear stress measurement.

References

1. M. Matsubara, M. Nagasaki, K. Matsumoto, T. Mishiba, Linear-disturbance structure in a turbulent boundary layer, in *4th International Conference on Jets, Wakes and Separated Flows, ICJWSF2013-1211* (2013)
2. S. Shirosaki, D. Saito, S. Tazoe, S. Aruga, M. Matsubara, Comparison of linear disturbance in a two-dimensional turbulent jet with a linear stability theory, in *4th International Conference on Jets, Wakes and Separated Flows, ICJWSF2013-1217* (2013)
3. K.A. Chauhan, P.A. Monkewitz, H.M. Nagib, Criteria for assessing experiments in zero pressure gradient boundary layers. Fluid Dyn. Res. **41**, (2009)

Wall Similarity in Turbulent Boundary Layers Subjected to Weak Pressure Gradients

Shinsuke Mochizuki, Hiroki Suzuki, Hitoshi Tokunaga and Takatsugu Kameda

Abstract In this study, the effects of adverse and favorable pressure gradients on the law of the wall were investigated experimentally in turbulent boundary layers. The divergence and convergence of the mean streamline in the wall layer are considered to yield suitable velocity scales in the wall layer by integrating the equations of motion at finite Reynolds number.

1 Introduction

The effect of pressure gradients on the law of the wall is one of the main issues in studying wall turbulence, and experimental and theoretical studies can provide methods of predicting and controlling the boundary layer development on wing shaped bodies or in diffusers. Since a landmark study on turbulent boundary layer theory by Ludwieg and Tillman [1], it has been supposed that the law of the wall is independent of the pressure gradient. The logarithmic law can be used to calculate the mean velocity and estimate the local wall shear stress in accelerating and decelerating boundary layer flows. Numerous turbulence models have been proposed to simulate wall turbulence subjected to pressure gradients.

In recent years, the similarity of turbulent statistics under canonical wall turbulence has been discussed to confirm behavior at sufficiently high Reynolds numbers. Asymptotic values of the Kármán constant were proposed by a carefully designed experimental study of flat plate turbulent boundary layers. Experimental evidence has contributed to confirming the validity of turbulence models and the development of a more precise understanding of the law of the wall.

S. Mochizuki (✉) · H. Suzuki · H. Tokunaga
Graduate School of Science and Engineering, Yamaguchi University,
2-16-1 Tokiwadai, Ube 755-8611, Japan
e-mail: shinsuke@yamaguchi-u.ac.jp

T. Kameda
Faculty of Engineering, Kinki University, Umenobe Takaya,
Higashi Hiroshima 739-2116, Japan

© Springer International Publishing Switzerland 2016

A. Segalini (ed.), *Proceedings of the 5th International Conference on Jets, Wakes and Separated Flows (ICJWSF2015)*,
Springer Proceedings in Physics 185, DOI 10.1007/978-3-319-30602-5_40

This paper will discuss an extension of the classical law of the wall to describe wall layers under weak favorable and adverse pressure gradients by considering the effect of the nonparallel behavior of the mean stream lines in the wall layer at finite Reynolds numbers. In this method, pressure gradients are given such that the boundary layer undergoes self-preserving development, and the wall shear stress is obtained using some independent techniques.

2 Experimental Equipment and Conditions

This experiment was conducted in an Eiffel type wind tunnel. The test section was 910 mm in width and 6000 mm in length [6]. U_e is the free stream velocity at each streamwise position. The turbulent boundary layer under a zero pressure gradient (ZPG) flow develops in the upstream region. To induce self-preserving development [7], the free stream velocity was varied as

$$\boldsymbol{U_e} \propto (\boldsymbol{x} - \boldsymbol{x}_0)^{-0.188} \text{ for APG} \quad \text{and} \quad \boldsymbol{U_e} \propto (\boldsymbol{x}_0 - \boldsymbol{x})^{-1.0} \text{ for FPG.} \tag{1}$$

The experimental conditions under zero, favorable, and adverse pressure gradients, which are hereafter referred to as ZPG, FPG, and APG, respectively, are listed in Table 1. The velocity components were measured using a single hot wire probe operated with a constant temperature anemometer. The hot wire sensor was a tungsten filament with a diameter of 2.5 μm and an active length of 0.5 mm. The signal from the anemometer was stored in a personal computer (PC) after it was converted to a digital signal by an analog-to-digital (AD) converter. The recording time was 40 s, and the sampling frequency was 10 kHz.

The local skin friction coefficients obtained from various independent methods such as drag balance (see Fig. 1), Preston tube and the semi-empirical method are compared in Fig. 2. The local skin friction coefficients estimated by the three methods are in good agreement with that obtained using the Kármán–Schoenherr equation for the ZPG case. In the FPG case, the skin friction coefficient estimated using the proposed method was 10 % higher than that obtained using the Kármán–Schoenherr equation. In APG case, the local skin friction coefficient obtained from the three methods are agreed well and its value is 0.00204 at $R_\theta = 10400$.

Table 1 Experimental conditions for the three pressure gradient cases in this study

	$\boldsymbol{R_\theta}(= U_e\,\theta/\nu)$	$\boldsymbol{P^+}\,(= \nu/(\rho\, u_\tau^3)\boldsymbol{dP_e/dx})$	$\beta = (\delta^*/\tau_w)\boldsymbol{dP_e/dx}$
Z.P.G.	2,200	–	–
F.P.G.	2,160	−0.00351	−0.43
A.P.G.	10,200	0.00274	1.32

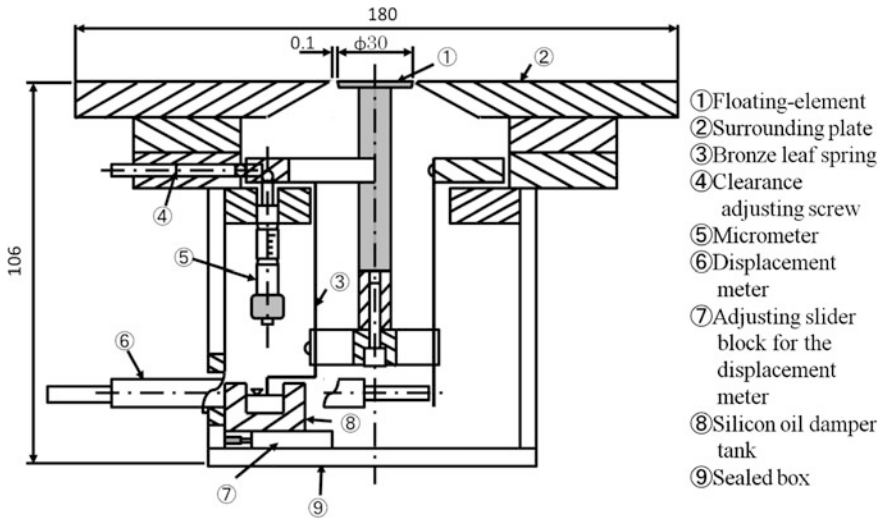


Fig. 1 Drag balance device for local wall shear stress measurement [6]

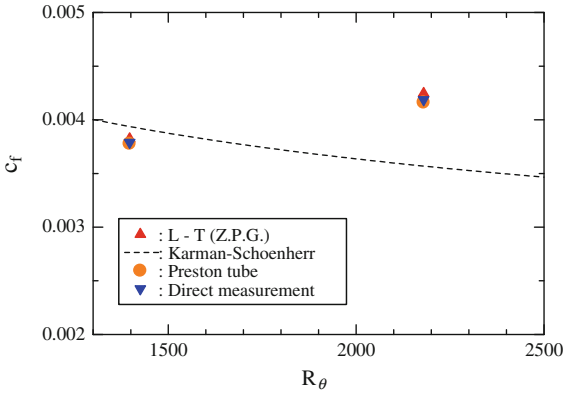


Fig. 2 Local skin friction coefficient as a function of the momentum thickness Reynolds number for FPG case. *L–T* indicates the semi-empirical Ludwig–Tillman formula

3 Velocity Scale at Finite Reynolds Numbers

The traditional velocity scale, which is given by the friction velocity u_τ, is defined as

$$\boldsymbol{u}_\tau = \sqrt{\tau_w/\rho}. \tag{2}$$

At high Reynolds numbers, it is generally known that for ZPG flows, the Reynolds shear stress $-\overline{uv}$ is almost equal to the wall shear stress near the wall and that the streamwise mean velocity gradient $\partial U/\partial y$ scales with the friction velocity u_τ and the

distance y in the vertical direction. It is believed that the streamwise mean velocity profile becomes the well-known logarithmic function called the logarithmic law:

$$U^+ = \frac{1}{\kappa_0}\ln y^+ + C_0, \text{ where } U^+ = \frac{U}{u_\tau} \text{ and } y^+ = \frac{yu_\tau}{\nu}. \tag{3}$$

The standard Kármán constant κ_0 and additive constant C_0 are $\kappa_0 = 0.384$ and $C_0 = 4.17$ at high Reynolds numbers [4].

The pressure gradient alters the profile of the Reynolds shear stress in the wall layer. Therefore, it is thought that the streamwise mean velocity gradient does not scale in the same manner as the ZPG. Nakamura et al. [5] introduced a new velocity scale from the Reynolds shear stress using the Reynolds-averaged Navier–Stokes equations for the turbulent boundary layer under an adverse pressure gradient and proposed a modified logarithmic formula. In this paper, we discuss whether the velocity scale is also applicable to FPG flows. The velocity scale and the modified logarithmic formula are derived briefly as follows. The Reynolds-averaged equations applied to the boundary layer approximation reduce to

$$U\frac{\partial U}{\partial x} + V\frac{\partial U}{\partial y} = -\frac{1}{\rho}\frac{dP_e}{dx} + \frac{1}{\rho}\frac{\partial \tau}{\partial y}, \text{ where } \tau = -\rho\overline{uv} + \mu\frac{\partial U}{\partial y}. \tag{4}$$

As a first approximation, it is assumed that the streamwise mean velocity U can be replaced by (3). Using order analysis, the normal mean velocity V near the wall region may be given as

$$V \cong -\frac{dU_e}{dx}y. \tag{5}$$

Substituting (3) and (5) into (4) and integrating with respect to y from 0 to any height near the wall, the shear stress τ can be given by

$$\tau = \tau_w\left(1 + \left[1 - \left(\frac{1}{\kappa_0}\ln y^+ + C_0 - \frac{2}{\kappa_0}\right)\omega\right]P^+ y^+\right), \tag{6}$$

where the shear stress is approximated as $\tau = -\rho\overline{uv}$ except for that in the viscous sublayer, $\omega(= u_\tau/U_e)$ is the friction parameter, and $P^+\left(=\nu/\rho u_\tau^3\right)(dP_e/dx)$ is the pressure gradient parameter. The relevant velocity scale is defined as

$$u_s = u_\tau\sqrt{\left(1 + \left[1 - \left(\frac{1}{\kappa_0}\ln y^+ + C_0 - \frac{2}{\kappa_0}\right)\omega\right]P^+ y^+\right)}. \tag{7}$$

Furthermore, by applying the Maclaurin expansion with respect to P^+ to (7), the velocity scale can be rewritten as

$$u_s = u_\tau\left(1+\frac{1}{2}\left[1-\left(\frac{1}{\kappa_0}\ln y^+ + C_0 - \frac{2}{\kappa_0}\right)\omega\right]P^+ y^+\right). \quad (8)$$

Equation (8) confirms that u_s approaches u_τ as P^+ approaches zero. By integrating the nondimensional streamwise mean velocity gradient scaled with the new velocity scale and height, the proposed modified logarithmic function is given by

$$U^+ = \frac{1}{\kappa}\ln y^+ + \frac{1}{2\kappa}\left\{(1-C_0\omega)+3\frac{\omega}{\kappa_0}\right\}P^+ y^+ - \frac{1}{2\kappa}\frac{\omega}{\kappa_0}P^+ y^+ \ln y^+ + C_p, \quad (9)$$

where the Kármán constant κ and additive constant C_p are determined experimentally.

4 Results and Discussion

Figure 3 shows the logarithmic mean velocity profile, and Fig. 4 compares the standard and modified logarithmic laws with the experimental data. In the APG and FPG cases, the mean velocity deviates from the standard logarithmic law, whereas the modified logarithmic law agrees well with the experimental data.

Smaller Kármán constants may be connected with larger eddies; this relationship is given by $\ell = \kappa y$. The experimental results suggest that the size of the eddy increases under an APG but decreases under an FPG. Based on the sign of the rate of strain containing $\partial V/\partial y$, it appears that transverse stretching under the APG increased the eddy size and transverse squeezing under the FPG reduced the eddy size.

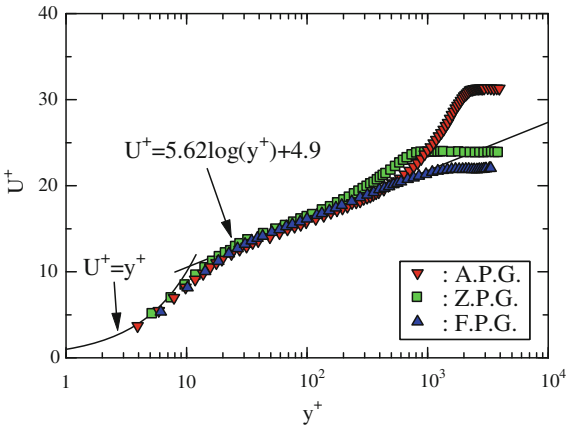


Fig. 3 Logarithmic mean velocity profiles under zero, adverse, and favorable pressure gradients. The *solid lines* represent the standard logarithmic law and linear velocity profile in the sublayer

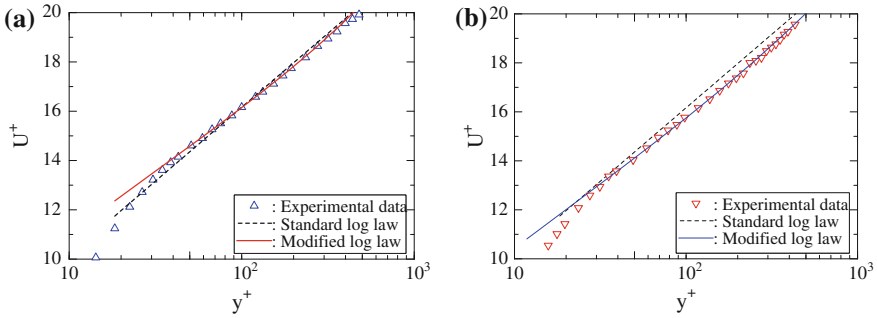


Fig. 4 Comparison of the standard and modified logarithmic laws with the experimental data for adverse and favorable pressure gradients. **a** Adverse pressure gradient. **b** Favorable pressure gradient

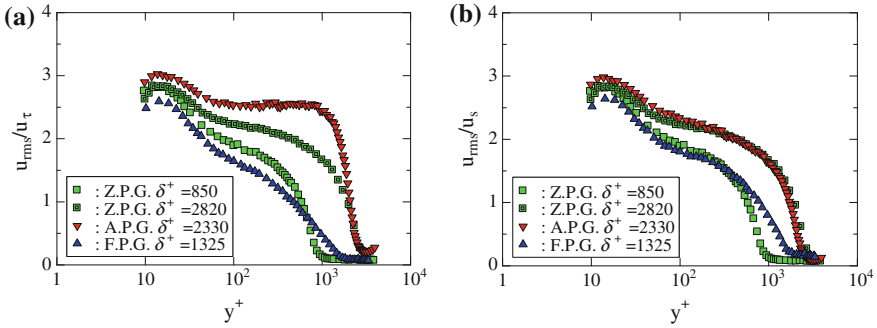


Fig. 5 Streamwise turbulence intensity profiles normalized by different velocity scales. Comparisons are made under zero, adverse, and favorable pressure gradients. The Kármán number $\delta^+ = \delta \boldsymbol{u}_\tau / \upsilon$ denotes the Reynolds number. **a** Normalized by the friction velocity. **b** Normalized by the proposed velocity scale given in (8)

Furthermore, the velocity scale in the wall layer was used to normalize the streamwise turbulence intensity. The streamwise turbulence intensity profiles were normalized by the friction velocity and the new velocity scale, as shown in Fig. 5. For different Reynolds numbers, the streamwise turbulence intensity profiles were found to be in reasonable agreement with the velocity scale.

Next, the nondimensional streamwise turbulence intensity at a height of $y^+ = 100$ was investigated to determine its dependence on the pressure gradient parameter. This height is within the range where the logarithmic law holds: $y^+ \gg 1$. Figures 6 and 7 show the variation in the streamwise turbulence intensity normalized by the friction velocity and the proposed velocity scale at $y^+ = 100$ with the pressure gradient parameter. In addition, the data from Nakamura et al. [5]

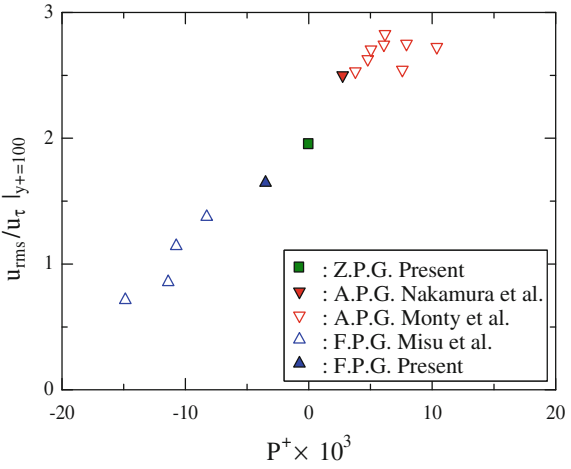


Fig. 6 Dependence of the turbulence intensity normalized by the friction velocity on the pressure gradient parameter in the wall layer

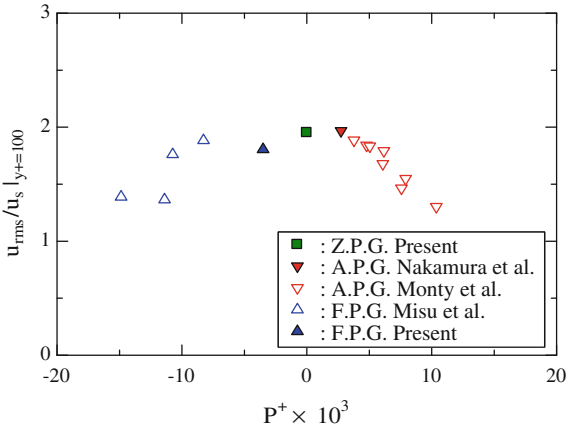


Fig. 7 Dependence of the turbulence intensity normalized by the proposed velocity scale on the pressure gradient parameter in the wall layer

and Monty et al. [3] for APG flows and Misu et al. [2] for FPG flows are plotted in these figures. Figure 6 shows that the value of u_{rms}/u_τ increases linearly with the pressure gradient parameter.

The decrease in the turbulence intensity in the of FPG flow range ($P^+ < 0$) indicates that the relaminarization of the turbulent flow progressed as the absolute value of the pressure gradient parameter increased. Conversely, the value of u_{rms}/u_s in Fig. 7 remained constant in the range of $-0.008 < P^+ \leq 0.006$ because of the Maclaurin expansion with respect to P^+. In this range, it is expected that the mean velocity profiles become similar regardless of the pressure gradient parameter.

5 Conclusions

The nonparallel behavior of mean stream lines was discussed at finite Reynolds numbers to assess the local similarity argument in the wall layer. Under weak adverse and favorable pressure gradients, the mean velocity profile agrees reasonably well with the modified logarithmic law derived by considering the equations of motion. The velocity scale is applicable to the normalization of the turbulence intensity in the pressure gradient range of $-0.008 < P^{+} \leq 0.006$.

References

1. H. Ludwieg, W. Tillmann, Investigations of the wall-shearing stress in turbulent boundary layers, National Advisory Committee for Aeronautics, TM1285 (1950)
2. I. Misu, N. Sada, T. Yatabe, Correlation between velocities and wall shear stress in the bursting under favorable pressure gradients. Trans. Jpn. Soc. Mech. Eng. **65**(632), 1312–1317 (1999)
3. J.P. Monty, Z. Harun, I. Marusic, A parametric study of adverse pressure gradient turbulent boundary layers. Int. J. Heat Fluid Flow **32**, 575–595 (2011)
4. H.M. Nagib, K.A. Chauhan, Variation of von Kármán coefficient in canonical flows. Phys. Fluids **20**(101518) (2008)
5. T. Nakamura, T. Kameda, S. Mochizuki, Effect of an adverse pressure gradient on the local similarity for a turbulent boundary layer. Trans. Jpn. Soc. Mech. Eng. **77**(775), 771–780 (2011)
6. H. Osaka, T. Kameda, S. Mochizuki, Re-examination of the Reynolds-number-effect on the mean flow quantities in a smooth wall turbulent boundary layer. JSME Int. J. Ser. B **41**(1), 123–129 (1998)
7. J.C. Rotta, Turbulent boundary layers in incompressible flow. Prog. Aeronaut. Sci. **2** (1962)

Interaction Layer Between a Turbulent Boundary Layer and Free-Stream Turbulence

R. Jason Hearst, Eda Dogan and Bharathram Ganapathisubramani

Abstract The interaction between a turbulent free-stream and a turbulent boundary layer is investigated through particle image velocimetry measurements. An 'interaction layer' located between $0.12 \leq y/\delta \leq 0.19$, at the end of the log layer, is identified whereby the kinetic energy in this layer describes the flow above it. Conditional averages about the interaction layer indicate that it is home to peaks in the Reynolds stresses and that it is the location of a change in the vortical structure. Furthermore, the conditional information identifies that low kinetic energy deficit states in the interaction layer result in a more full boundary layer profile due to increased movement of the bulk flow towards the wall.

1 Introduction

The 'turbulent/non-turbulent interface' (TNTI) has been the subject of several recent investigations of the interaction between a turbulent boundary layer and an approximately laminar free-stream [1, 2, 9]. However, many engineering flows experience a turbulent free-stream. In such flows, one might expect there to be a 'turbulent/turbulent interface' (TTI) that distinguishes the turbulent boundary layer from the turbulent free-stream and where significant phenomenological interactions between these regions occur. As such, our focus here is to characterize these turbulent/turbulent interactions. This work differs from prior work examining the interaction of two different decaying turbulent free-streams (e.g., [3, 4]) in that the boundary layer is a source of continuous production.

R.J. Hearst (✉) · E. Dogan · B. Ganapathisubramani
Engineering and the Environment, University of Southampton,
Southampton SO17 1BJ, UK
e-mail: r.j.hearst@southampton.ac.uk

© Springer International Publishing Switzerland 2016

A. Segalini (ed.), *Proceedings of the 5th International Conference on Jets, Wakes and Separated Flows (ICJWSF2015)*,
Springer Proceedings in Physics 185, DOI 10.1007/978-3-319-30602-5_41

In the present study, we use an active grid to produce free-stream turbulence and measure the turbulent boundary layer on a flat plate, a setup inspired by Sharp et al. [10]. Using techniques pioneered for determining the TNTI between a canonical turbulent boundary layer and a laminar free-stream, we identify a layer—near the junction between the log and wake layers of the turbulent boundary layer—where significant interactions occur which are highly dependent on the local kinetic energy deficit.

2 Experimental Details

An active grid, inspired by the original design of Makita [8], was used to generate free-stream turbulence. The active grid features an 11×7 array of square wings mounted to rods that are rotated in a random pattern by stepper motors to create a transient blockage. The grid has a mesh length, M, of 81 mm. Changing the grid parameters and the free-stream velocity, U_∞, allows for a variety of turbulence conditions to be produced. In the present study, we focus on one free-stream turbulence case in particular with the wings set to a rotational velocity of $\Omega = 4.0$ Hz with $U_\infty = 8.1$ m/s, resulting in $u'/U_\infty \approx 12.2\,\%$. For these conditions, the relevant free-stream and boundary layer Reynolds numbers were $Re_\lambda = 510$ and $Re_\tau = 4050$, respectively.

Measurements were performed in the wake of the grid in a $0.9\text{ m} \times 0.6\text{ m} \times 4.5\text{ m}$ wind tunnel using planar particle image velocimetry (PIV) and hot-wire anemometry. The boundary layer was formed on a flat plate that begins 300 mm downstream of the grid and extends 4.2 m downstream. A single-wire, with a 1 mm sensing length, was located 3.5 m from the grid. It was operated with a Dantec StreamLine constant temperature anemometer at an overheat ratio of 1.8. The hot-wire was traversed in the wall-normal direction to measure a profile. Separately, PIV images were captured with three LaVision ImagerProLX CCD 16 mega-pixel cameras fitted with Nikon Nikkor 200 mm lenses. The light sheet was illuminated by a Litron Lasers Nano L200 15PIV Nd:YAG laser (523 nm wavelength, 200 mJ/pulse, 15 Hz repetition rate). The cameras were oriented to create a T-shaped field of view (FOV) extending 320 mm ($\sim 2.6\delta$) in the streamwise direction and 268 mm ($\sim 2.2\delta$) in the wall-normal direction after stitching the instantaneous images. The FOV begins 3240 mm downstream of the grid. The FOV was offset by 1.06 mm from the wall. A total of 2000 images were acquired. The boundary layer thickness was $\delta = \delta_{0.99} = 122$ mm. In order to reduce the influence of pixel-locking, a Gaussian kernel filter was applied to the image pre-processing, window deformation was used during processing, and histogram equalization was applied on a vector-by-vector basis in post-processing [5].

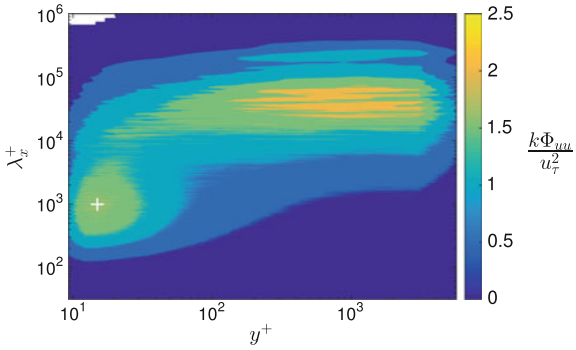


Fig. 1 Contour map of one-dimensional pre-multiplied spectra with wall-normal position. The (+) marks the inner energy peak location identified by [6]

3 Results

3.1 Wall-Normal Spectra

The pre-multiplied energy spectra ($k\Phi_{uu}$) measured by the hot-wire are briefly discussed here prior to investigating the PIV results. Contours of $k\Phi_{uu}$ for various wall-normal positions are shown in Fig. 1. The spectra are plotted against inner variable normalised wavelength, λ_x^+. Hutchins and Marusic [6] found that the near-wall peak in $k\Phi_{uu}$ in a canonical turbulent boundary layer did not significantly vary from $y^+ \approx 15$ and $\lambda^+ \approx 1000$ for $1010 \leq Re_\tau \leq 7300$, which is recovered for the present case despite significant free-stream turbulence. As Hutchins and Marusic [6] increased Re_τ, they found that an outer peak in $k\Phi_{uu}$ emerged, and there was some indication this outer peak may be Reynolds number dependent. The present flow exhibits this outer peak, however, it is imposed by the free-stream turbulence. In essence, the near-wall spectra resemble those in a canonical turbulent boundary layer, while the Re_τ has been artificially increased by the imposition of the free-stream turbulence spectrum on the outer regions of the boundary layer.

3.2 Interaction Layer Detection

The instantaneous distribution of the local 2D turbulent kinetic energy deficit over a 3×3 area, may be estimated from [1, 2]:

$$\tilde{k} = 100 \times \frac{1}{9U_\infty^2} \sum_{m,n=-1}^{1} \left[(\tilde{U}_{m,n} - U_\infty)^2 + \tilde{V}_{m,n}^2 \right], \tag{1}$$

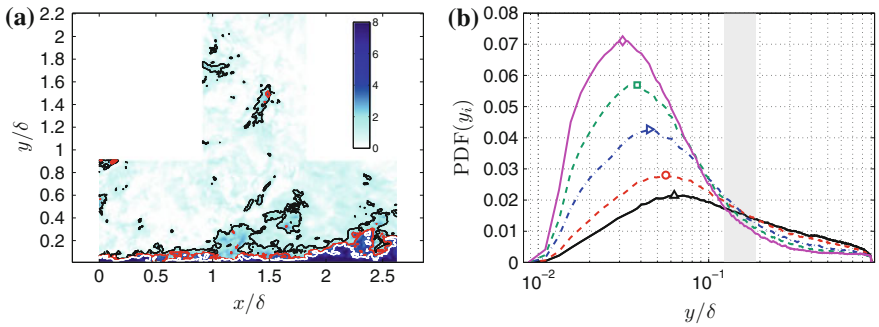


Fig. 2 **a** Representative image of instantaneous $\tilde{k}$ with contours at (*black*) $\frac{3}{2}k_0$, (*red*) $3k_0$, and (*white*) $5k_0$. **b** Probability density functions of the instantaneous wall-normal contour position with symbols marking peaks: (△) $\frac{3}{2}k_0$, (○) $2k_0$, (▷) $3k_0$, (□) $4k_0$, (◇) $5k_0$

where $\tilde{U}_{m,n}$ and $\tilde{V}_{m,n}$ are the local streamwise and wall-normal velocities, respectively. When determining the TNTI, a threshold value, k_{th}, is chosen that is representative of k_0 in the non-turbulent free-stream (typically, k_0 is near zero). At locations where $\tilde{k} > k_{th}$, the flow is turbulent, and conversely $\tilde{k} < k_{th}$ is non-turbulent. The contour drawn between the regions can be averaged over all images to determine the mean position of the TNTI (see [1] for more details). We employ a similar technique at several multiples of k_0, noting $k_0 \gg 0$ in the present free-stream, to determine the various kinetic energy zones in the flow.

In Fig. 2, contours at $k_{th} = \frac{3}{2}k_0$, $2k_0$, $3k_0$, $4k_0$, and $5k_0$, are presented. Figure 2a shows three of these contours on an instantaneous image, while Fig. 2b shows the probability density functions (PDFs) composed over all images of the instantaneous wall-normal contour location, y_i. The symbols mark the PDF peak. The PDFs are non-Gaussian, and as such the mean of y_i is not representative of the most-likely position of the contour. This contrasts with the results for the TNTI where the y_i distribution is Gaussian [1].

Of particular interest in Fig. 2b is that all the PDFs cross within a narrow band of the boundary layer ($0.12 \leq y/\delta \leq 0.19$), which is highlighted in Fig. 2b and subsequent figures. This suggests that there is approximately the same likelihood of $\tilde{k}$ being at any state $\geq \frac{3}{2}k_0$ within this region. In Fig. 3 the boundary layer profile is plotted in wall units with the canonical layers identified [7]. The 'interaction layer,' where the probability is the same that $\tilde{k}$ can take-on a wide range of values, occurs at the end of the log layer, prior to transition to the wake layer.

3.3 Conditional Averages

In order to ascertain the significance of the interaction layer, conditional averages were calculated for given ranges of the mean value of $\tilde{k}$ within the interaction layer;

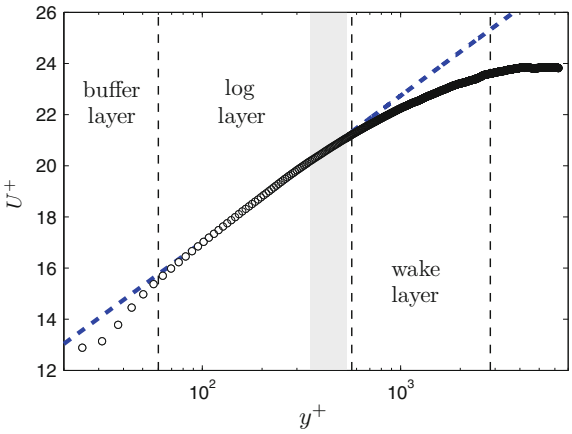


Fig. 3 Wall unit normalized mean velocity profile with log layer fit. *Shaded area* represents the interaction layer

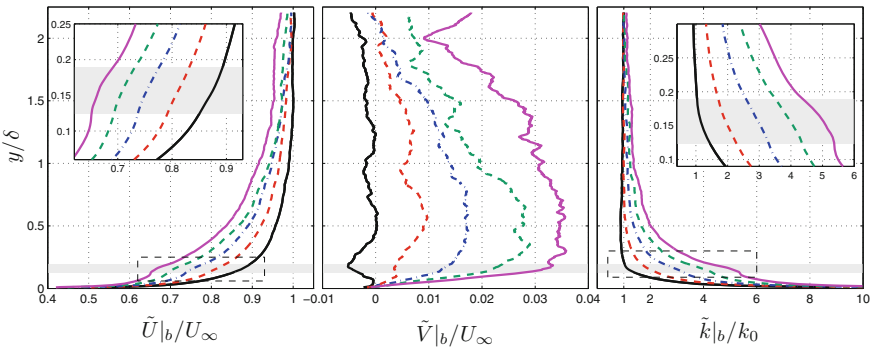


Fig. 4 Conditional averages of the local velocities and kinetic energy deficit. (—) $0.9 \leq \tilde{k}_b/k_0 < 1.5$, (– –) $1.5 \leq \tilde{k}_b/k_0 < 2.5$, (– · –) $2.5 \leq \tilde{k}_b/k_0 < 3.5$, (– –) $3.5 \leq \tilde{k}_b/k_0 < 4.5$, (—) $4.5 \leq \tilde{k}_b/k_0 < 5.5$

this quantity is denoted $\tilde{k}_b$, and a conditional average based on $\tilde{k}_b$ is denoted $\cdot|_b$. The conditional averages of $\tilde{U}$, $\tilde{V}$, and $\tilde{k}$ are presented in Fig. 4. The value of $\tilde{k}_b$ distinctly influences the mean velocity profile to wall normal positions exceeding δ. The boundary layer is the most 'full', i.e., has an extended region of high velocity close to the wall, for the instances with the lowest $\tilde{k}_b$. This is confirmed by the $\tilde{V}|_b$ plot which reveals that the lowest kinetic energy deficit state draws the bulk flow towards the wall, whereas the other states push it away. Interestingly, the energy within the interaction layer appears to approximately set the values of $\tilde{U}$ and $\tilde{V}$ above it.

In Fig. 5 the conditional averages of the Reynolds stresses are shown. In particular, it is identified that the peak of $u'u'$ occurs in the interaction layer and scales with $\tilde{k}_b$. The near-wall peak of $u'v'$ scales with $\tilde{k}_b$, both in magnitude and in depth into the

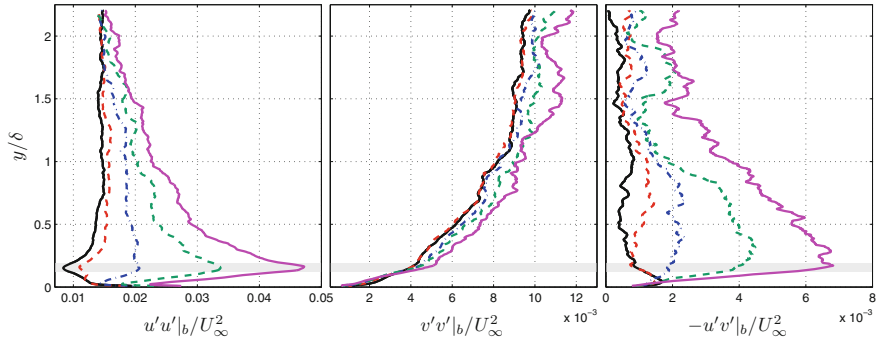


Fig. 5 Conditional averages of the local Reynolds stresses. (—) $0.9 \leq \tilde{k}_b/k_0 < 1.5$, (– –) $1.5 \leq \tilde{k}_b/k_0 < 2.5$, (– · –) $2.5 \leq \tilde{k}_b/k_0 < 3.5$, (– –) $3.5 \leq \tilde{k}_b/k_0 < 4.5$, (—)$4.5 \leq \tilde{k}_b/k_0 < 5.5$

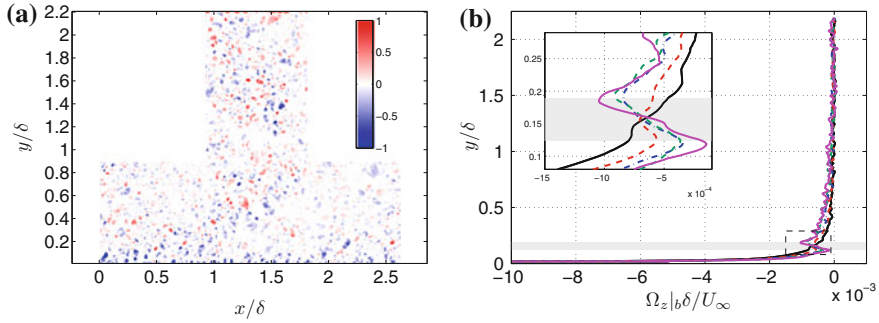


Fig. 6 **a** Representative image of instantaneous signed swirling strength. **b** Conditional averages of the transverse vorticity. (—) $0.9 \leq \tilde{k}_b/k_0 < 1.5$, (– –) $1.5 \leq \tilde{k}_b/k_0 < 2.5$, (– · –) $2.5 \leq \tilde{k}_b/k_0 < 3.5$, (– –) $3.5 \leq \tilde{k}_b/k_0 < 4.5$, (—)$4.5 \leq \tilde{k}_b/k_0 < 5.5$

boundary layer. This is suggestive of locally higher skin-friction velocity, u_τ, for the higher energy deficit states, which is consistent with the decreased boundary layer profile fullness for these same states shown in Fig. 4.

3.4 Vorticity and Swirl

The interaction between the free-stream and the boundary layer can also be accessed through the distribution of the vortices by observations of either the signed swirling strength or the vorticity. In the free-stream turbulence, one expects an equal number of vortices rotating clockwise and counter-clockwise, while in the boundary layer dominated flow one expects a prevalence of clockwise rotating vortices due to reduced velocity near the wall. In Fig. 6a this principle is illustrated in a single

snapshot, showing that indeed the near-wall flow is dominated by clockwise rotating vortices. The profiles of vorticity in Fig. 6b indicate that near the wall the vorticity is negative signed, while as we move towards the free-stream the vorticity is equally distributed between positive and negative values resulting in a near zero mean. In the interaction layer, a local maximum and minimum follow each other in short succession for all cases save the lowest $\tilde{k}_b$. These peaks are separated by 30 vectors, which is highly suggestive that it is in fact in the flow and not an artefact of the resolution. From the wall to the interaction layer, the vorticity evolves monotonically, however, the local minimum near the top of the interaction layer appears to entrain fluid with positive vorticity to the bottom of the interaction layer where it is unable to penetrate further as the wall effects dominate. As such, the interaction layer may represent a barrier to intense vortical structures in the boundary layer.

4 Conclusions

An interaction layer has been identified in a turbulent boundary layer with a turbulent free-stream. This layer exists in the range $0.12 \leq y/\delta \leq 0.19$ for the present flow and was investigated because the PDFs of the instantaneous kinetic energy deficits with different thresholds all took-on approximately the same value here. This region occurs at the end of the log layer and is home to the peaks in the Reynolds stresses as well as rapid changes in the vortical structure of the flow. It was also shown that for lower levels of the energy deficit near the wall, the boundary layer is more full. The low energy deficit state is accompanied by mean motion of the fluid towards the wall, which results in the more full profile.

Subsequent studies should focus on identifying clear criteria to instantaneously differentiate the turbulent boundary layer from the turbulent free-stream, if such a distinction is possible. Here, we have significantly identified a region of the flow that is home to energy dependent interactions and that may act as a barrier to the penetration of intense vortical structures. It was also demonstrated that the energy state within the interaction layer is representative of the flow structure above it, even exceeding $\delta_{0.99}$.

Acknowledgments We gratefully acknowledge the financial support of the European Research Council (ERC Grant agreement No. 277472) and EPSRC (Grant Ref No: EP/I037717/1), as well as the support of Dr. R. Hanson throughout the measurement campaign. RJH acknowledges the financial support of the Natural Sciences and Engineering Research Council of Canada (NSERC).

References

1. K. Chauhan, J. Philip, C.M. de Silva, N. Hutchins, I. Marusic, The turbulent/non-turbulent interface and entrainment in a boundary layer. J. Fluid Mech. **742**, 119–151 (2014)

2. K. Chauhan, J. Philip, I. Marusic, Scaling of the turbulent/non-turbulent interface in boundary layers. J. Fluid Mech. **751**, 298–328 (2014)
3. S. Gerashchenko, Z. Warhaft, Conditional entrainment statistics of inertial particles across shearless turbulent interfaces. Exp. Fluids **54**(1631) (2013)
4. G.H. Good, S. Gerashchenko, Z. Warhaft, Intermittency and inertial particle entrainment at a turbulent interface: the effect of the large-scale eddies. J. Fluid Mech. **694**, 371–398 (2012)
5. R.J. Hearst, B. Ganapathisubramani, Quantification and adjustment of pixel-locking in particle image velocimetry. Exp. Fluids **56**(191) (2015)
6. N. Hutchins, I. Marusic, Evidence of very long meandering features in the logarithmic region of turbulent boundary layers. J. Fluid Mech. **579**, 1–28 (2007)
7. J.C. Klewicki, Reynolds number dependence, scaling, and dynamics of turbulent boundary layers. J. Fluids Eng. **132**(094001) (2010)
8. H. Makita, Realization of a large-scale turbulence field in a small wind tunnel. Fluid Dyn. Res. **8**, 53–64 (1991)
9. J. Philip, C. Meneveau, C.M. de Silva, I. Marusic, Multiscale analysis of fluxes at the turbulent/non-turbulent interface in high Reynolds number boundary layers. Phys. Fluids **26**(015105) (2014)
10. N. Sharp, S. Neuscamman, Z. Warhaft, Effects of large-scale free stream turbulence on a turbulent boundary layer. Phys. Fluids **21**(095105) (2009)

Generalization of the Diagnostic Plot to Higher-Order Moments in Turbulent Boundary Layers

Ramis Örlü, Antonio Segalini, Joseph Klewicki and P. Henrik Alfredsson

Abstract The present work extends the diagnostic plot concept for the streamwise turbulence intensity in wall-bounded turbulent flows [Alfredsson and Örlü, Eur. J. Mech. B/Fluids **42**, 403 (2010)], and generalizes it for higher-order (even and odd) moments, thereby providing a general description of the probability density distribution of streamwise velocity fluctuations. Turbulent boundary layer data up to a friction Reynolds number of 20000 are employed and demonstrate the feasibility of the diagnostic plot to scale data throughout the logarithmic and wake regions.

1 Background and Motivation

The recent emergence of reasonably well-resolved data from high Reynolds number (*Re*) pipe and turbulent boundary layer (TBL) flows has challenged the classical understanding of wall turbulence. In particular, the failure of inner-scaling (henceforth denoted through the superscript '$^+$') for the streamwise velocity root mean square (rms) profile (Fig. 1a) has avalanched a number of experimental campaigns to provide well-resolved high-*Re* data both in pipe and zero pressure gradient (ZPG) TBL flows (see e.g. Klewicki [11], and references therein). While the debate regarding the scaling of the inner peak of the variance profile (at least in TBL flows) has come close to a settlement [11], the emergence of a second peak (cf. Fig. 1a as well as Hultmark et al. [9]; Vincenti et al. [24] among others) continues to stir the minds:

R. Örlü (✉) · A. Segalini · P.H. Alfredsson
Linné FLOW Centre, KTH Mechanics, Stockholm, Sweden
e-mail: ramis@mech.kth.se

J. Klewicki
Department of Mechanical Engineering, University of New Hampshire, Durham, NH 03824, USA

J. Klewicki
Department of Mechanical Engineering, University of Melbourne, Parkville, VIC 3010, Australia

© Springer International Publishing Switzerland 2016

A. Segalini (ed.), *Proceedings of the 5th International Conference on Jets, Wakes and Separated Flows (ICJWSF2015)*,
Springer Proceedings in Physics 185, DOI 10.1007/978-3-319-30602-5_42

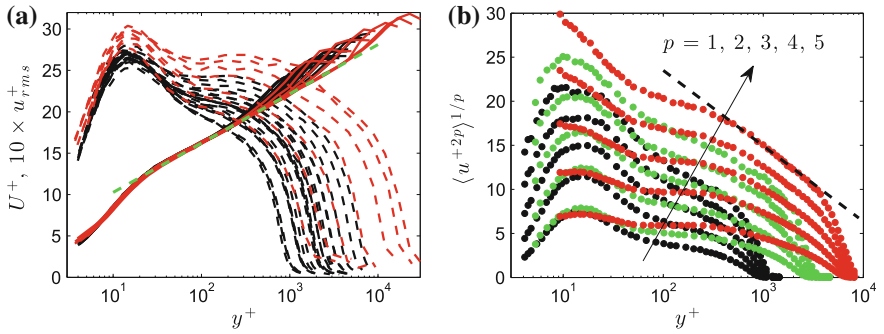


Fig. 1 **a** Inner-scaled streamwise mean (*solid line*) and rms (*dashed line*) profiles for 22 (*black*) and 7 (*red*) ZPG TBL experiments covering a range of $Re_\tau = 800$–6000 [17, 19] and 1400–20000 [24], respectively. The *green dashed line* indicates the logarithmic law with the constants given by [24], i.e. $\kappa = 0.387$ and $B = 4.32$. **b** Generalized logarithmic law for the $2p$-order moments according to Meneveau and Marusic [15] for $Re_\tau = 850$ (*black*), 2400 (*green*) and 5600 (*red*) [17, 19]. The *dashed line* indicates the logarithmic behaviour for the 10th moment (i.e. $p = 5$) for $Re_\tau = 5600$

relating its presence either to structural changes in the flow [16], a predictable feature inherent already in lower *Re* data [3] or possibly to measurement insufficiencies.

The availability of high *Re* data has, on the other hand, compiled compelling empirical evidence for the existence of a logarithmic mean velocity profile [14]. These recent data also support the existence of the logarithmic law for the streamwise variance profile, as predicted by Townsend [23] based on the attached-eddy hypothesis. Recent efforts have probed its validity for the variance, but also higher-order even moments [15, 25] as depicted in Fig. 1b for the 2nd to 10th central moment. As apparent in that figure, a logarithmic behaviour is visible over a significant interior region for all even moments presented. These profiles adhere to $\langle u^{+2p} \rangle^{1/p} = D_p(Re_\tau) - A_p \ln y^+$, where D_p and A_p are flow case, *Re* and moment-dependent parameters, while A_p is expected to asymptote to a universal value at large *Re* [15, 25]. The renewed interest in Townsend's logarithmic law for the streamwise velocity variance is also related to its equivalence to the k^{-1} spectral law (k denoting the streamwise wave number) [21] and Kolmogorov's two-thirds law [7].

An alternative scaling behaviour has emerged from the diagnostic plot [1], where the turbulence intensity is plotted against the outer-scaled mean velocity (U/U_∞) rather than the wall distance. The diagnostic plot has shown promising success to merge ZPG TBL data (but also pipe and channel flows) covering a wide *Re* range throughout the logarithmic and wake layers [4]. This is made apparent in Fig. 2, where the data from Fig. 1a is demonstrated to merge; independent of *Re* and linearly dependent on U/U_∞ for an increasingly wide range of U/U_∞ as *Re* increases. Hence, with a measured or modelled mean velocity profile, the streamwise variance profile of turbulent pipe, channel and boundary layer flows could be described [4]. Furthermore, the success of the diagnostic scaling could also be extended to turbulent boundary layers on rough walls when taking the roughness function into the

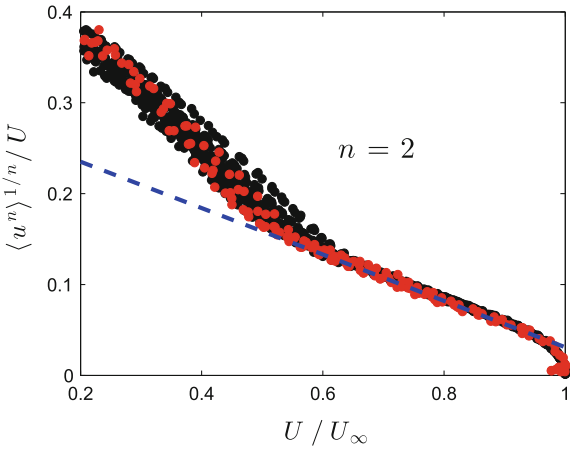


Fig. 2 Extended diagnostic plot for the entire data set shown under Fig. 1a. *Dashed line* corresponds to the linear relation $u_{rms}/U = \alpha - \beta\, U/U_\infty$ with constants given in [4], i.e. $\alpha = 0.286$ and $\beta = 0.255$

scaling [6], and pressure gradient when accounting for the shape factor [8], as well as in wall-free flows such as mixing layers, jets and wakes [5]. Based on these promising outcomes, the present efforts aim at extending the description of the streamwise turbulence intensity to higher-order (both even and odd) central moments.

2 The Generalized Diagnostic Plot

The invariance under the diagnostic scaling promotes consideration of the intrinsic relationships between turbulence quantities rather than functions of the wall distance. Such a perspective has, for example, revealed a clear interrelation between the higher-order moments of streamwise velocity fluctuations, in particular between the skewness (S) and flatness (F) factors in the form $F = f(S)$ [10], which is apparent from Fig. 3a, where F is plotted against S. In particular the outer region exhibits a one-to-one relation, which is also visible within the viscous sublayer, but not in regions close to the zero-crossing of S, i.e. the buffer region. This interrelation between the third and fourth order moments (non-dimensionalized by means of the second order moment), coupled to the success of the diagnostic plot (expressing the interrelation between normalized first and second order moments), suggests self-similarity of the probability density function (PDF) in diagnostic scaling. The implied self-similarity of the PDF is demonstrated in Fig. 3b for the three *Re*-cases shown in Fig. 2; the contour lines of the PDFs, irrespective of *Re*, collapse both near the median and in the tails of the PDF. The found collapse over a substantial U/U_∞-range confirms therefore not only the aforementioned implication, but indicates also that *all* higher-order moments should scale in diagnostic form. A generalized form of higher-order moments in diagnostic scaling can hence be expressed as $|\langle u^n \rangle|^{1/n}/U$ as function of U/U_∞ and is shown in Fig. 4a for odd moments ($n = 3, 9, 17$) and in

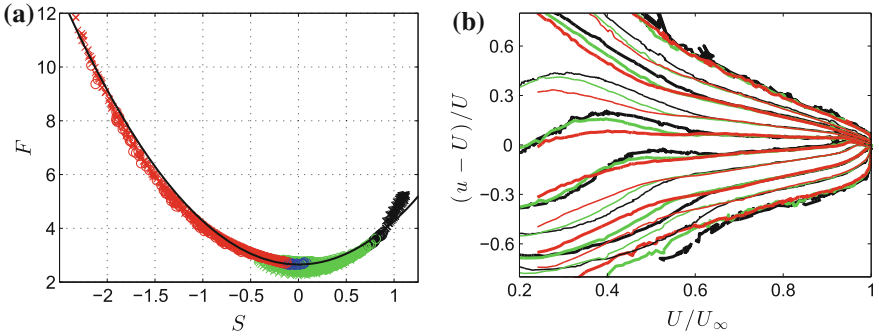


Fig. 3 **a** Interrelation between skewness and flatness factors for the streamwise velocity component. Color code marks the viscous sublayer (*black*, $y^+ < 5$), buffer region (*green*, $5 \leq y^+ < 100$), logarithmic layer (*blue*, $100 \leq y^+ < 0.2Re_\tau$), and outer region (*red*, $0.2 \leq y^+/Re_\tau < 1$) for data shown in Fig. 1b (∘) supplemented through direct numerical simulations (×) [22], in order to cover the viscous sublayer. *Line* represents the parabola given by Jovanovic et al. [10], i.e. $F = 2.65 + 1.62\,S^2$. **b** Probability density distribution map in diagnostic scaling for the same profiles shown in Fig. 1b. Contour levels correspond to **0.01**, 1, **10**, 50, and **90**% of the local peak PDF value of each *Re* case

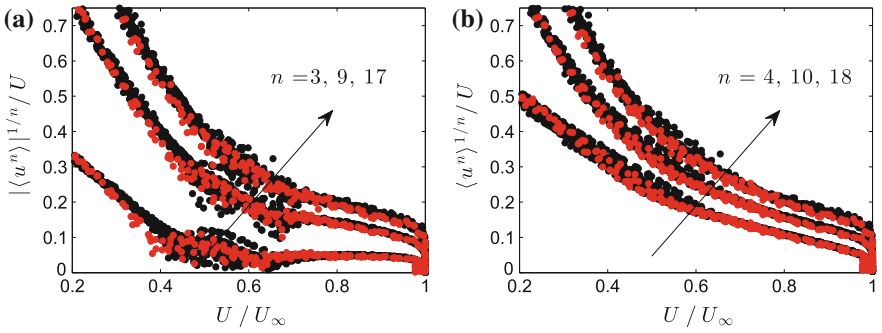


Fig. 4 Generalized diagnostic plot for the entire data set shown under Fig. 1a for **a** odd and **b** even moments

Fig. 4b for even moments ($n = 4, 10, 18$). These are the same 29 data sets as shown in Fig. 1a and, as can be seen, they exhibit Reynolds number invariance throughout the boundary layer except in the region $0.4 \lesssim U/U_\infty \lesssim 0.6$; corresponding to a wall-normal distance covering the buffer layer and lower end of the logarithmic layer.

3 Discussion and Conclusions

The profile invariance exhibited by the data over a wide *Re*-range throughout the boundary layer, with the exception of the buffer layer, generalises the diagnostic scaling to higher-order even and odd moments. However the spread of the data in a region $0.4 \lesssim U/U_\infty \lesssim 0.6$ shows that this region does not exhibit self-similarity in the fluctuations. Interestingly, the upper bound of this region is found to be related to the mid-layer zero-crossing of the skewness factor, i.e. $y^+ \simeq 2.6\sqrt{Re_\tau}$ [24], which also coincides with the onset of the inertial domain [12, 13]. One may hypothesise that this is due to an influence on the fluctuations both from the wall itself and from the outer region and that this mixed influence prohibits self-similarity of the fluctuations. Further away from the wall, the restrictive influence of the wall (no-slip and non-permeability) becomes negligible and the outer region becomes self-similar. In close wall proximity, the viscous sublayer acts more or less as a lubrication layer which is forced by the outer flow, resulting in a near log-normal scaling of the velocity fluctuations [2], thereby the outer flow is forcing a more or less passive layer.

The diagnostic plot was originally proposed as a tool for detecting inadequate measurement points, for instance, in the viscous sublayer (due to measurement problems, cf. [18]), however, it quickly arose to a practically useful scaling for the streamwise turbulence intensity; none-withstanding its lack of a physical basis. The present work documents empirical evidence covering a wide *Re* range that extends the scaling of the turbulence intensity in the diagnostic plot to *all*, both even and odd, central moments (and therefore PDF) of the streamwise velocity component. Although only zero pressure gradient turbulent boundary layer data have been employed, the scalings identified should readily be applicable to turbulent pipe and channel flows.

Disclaimer: Parallel to the present paper, a largely extended and more detailed study based on the present work has been published by Örlü et al. [20].

References

1. P.H. Alfredsson, R. Örlü, The diagnostic plot-a litmus test for wall bounded turbulence data. Eur. J. Mech. B-Fluid **29**, 403–406 (2010)
2. P.H. Alfredsson, R. Örlü, P. Schlatter, The viscous sublayer revisited-exploiting self-similarity to determine the wall position and friction velocity. Exp. Fluids **51**, 271–280 (2011a)
3. P.H. Alfredsson, A. Segalini, R. Örlü, A new scaling for the streamwise turbulence intensity in wall-bounded turbulent flows and what it tells us about the "outer" peak. Phys. Fluids **23**, 041702 (2011b)
4. P.H. Alfredsson, R. Örlü, A. Segalini, A new formulation for the streamwise turbulence intensity distribution in wall-bounded turbulent flows. Eur. J. Mech. B-Fluid **36**, 167–175 (2012)
5. I.P. Castro, Turbulence intensity in wall-bounded and wall-free flows. J. Fluid Mech. **770**, 289–304 (2015)
6. I.P. Castro, A. Segalini, P.H. Alfredsson, Outer-layer turbulence intensities in smooth- and rough-wall boundary layers. J. Fluid Mech. **727**, 119–131 (2013)
7. P.A. Davidson, T.B. Nickels, P.Å. Krogstad, The logarithmic structure function law in wall-layer turbulence. J. Fluid Mech. **550**, 51–60 (2006)

8. A. Drózdz, W. Elsner, S. Drobniak, Scaling of streamwise Reynolds stress for turbulent boundary layers with pressure gradient. Eur. J. Mech. B-Fluid **49**, 137–145 (2015)
9. M. Hultmark, M. Vallikivi, S.C.C. Bailey, A.J. Smits, Turbulent pipe flow at extreme Reynolds numbers. Phys. Rev. Lett. **108**, 094501 (2012)
10. J. Jovanovic, F. Durst, T.G. Johansson, Statistical analysis of the dynamic equations for higher-order moments in turbulent wall bounded flows. Phys. Fluids A **5**, 2886–2900 (1993)
11. J.C. Klewicki, Reynolds number dependence, scaling, and dynamics of turbulent boundary layers. J. Fluid Eng. **132**, 094001 (2010)
12. J.C. Klewicki, P. Fife, T. Wei, On the logarithmic mean profile. J. Fluid Mech. **638**, 73–93 (2009)
13. J.C. Klewicki, C. Morrill-Winter, A. Zhou, Inertical logarithmic layer properties and self-similar mean dynamics, in *Proceedings of 9th International Symposium on Turbulent Shear Flows*, Melbourne, Australia (2015)
14. I. Marusic, J.P. Monty, M. Hultmark, A.J. Smits, On the logarithmic region in wall turbulence. J. Fluid Mech. **716**, R3 (2013)
15. C. Meneveau, I. Marusic, Generalized logarithmic law for high-order moments in turbulent boundary layers. J. Fluid Mech. **719**, R1 (2013)
16. J.F. Morrison, B.J. Mckeon, W. Jiang, A.J. Smits, Scaling of the streamwise velocity component in turbulent pipe flow. J. Fluid Mech. **508**, 99–131 (2004)
17. R. Örlü, Experimental studies in jet flows and zero pressure-gradient turbulent boundary layers. Ph.D. thesis, Royal Institute of Technology, Stockholm, Sweden (2009)
18. R. Örlü, J.H.M. Fransson, P.H. Alfredsson, On near wall measurements of wall bounded flows—the necessity of an accurate determination of the wall position. Prog. Aerosp. Sci. **46**, 353–387 (2013)
19. R. Örlü, P. Schlatter, Comparison of experiments and simulations for zero pressure gradient turbulent boundary layers at moderate Reynolds numbers. Exp. Fluids **54**, 1547 (2013)
20. R. Örlü, A. Segalini, J. Klewicki, P. H. Alfredsson, High-order generalisation of the diagnostic scaling for turbulent boundary layers. J. Turbul. (2016). doi:10.1080/14685248.2016.1169282
21. A.E. Perry, S. Henbest, M.S. Chong, A theoretical and experimental study of wall turbulence. J. Fluid Mech. **165**, 163–199 (1986)
22. P. Schlatter, R. Örlü, Assessment of direct numerical simulation data of turbulent boundary layers. J. Fluid Mech. **659**, 116–126 (2010)
23. A.A. Townsend, *The Structure of turbulent Shear Flow*, 2nd edn. (Cambridge University Press, 1976)
24. P. Vincenti, J.C. Klewicki, C. Morrill-Winter, C.M. White, M. Wosnik, Streamwise velocity statistics in turbulent boundary layers that spatially develop to high Reynolds number. Exp. Fluids **54**, 1629 (2013)
25. A. Zhou, J.C. Klewicki, Properties of the streamwise velocity fluctuations in the inertial layer of turbulent boundary layers and their connection to self-similar mean dynamics. Int. J. Heat Fluid Flow **51**, 372–382 (2015)

Experimental and Analytical Investigation of Forest Clearings

Antonio Segalini

Abstract A numerical model of forest clearings is proposed based on the linearised Euler equations. The forest is replaced by distributed body forces that decrease the flow momentum entrained inside the canopy. The model is compared with available wind-tunnel measurements of clearings areas. It is observed that the model deviates from the measurements over the forest surface, but the performance improve over the clearing surface, probably associated to an incorrect evaluation of the forest intensity. The proposed model suggests that the clearing is associated to an internal boundary layer with intensity function of the clearing length.

1 Introduction

The understanding of the atmospheric boundary layer over forested areas has numerous applications in micrometeorology and wind energy. Intensive research efforts have focussed on the comprehension of the flow field over a homogeneous forest canopy: under this condition, it can be expected that the flow should achieve an equilibrium state within the internal boundary layer (in the sense that streamwise variations can be neglected when compared to the vertical ones) both above and below the canopy top, located at $z/h_c \approx 1$, where z and h_c indicate the local height from the ground and the canopy height, respectively [3, 5, 6]. However, in real forests this state is never achieved because forested areas are not infinitely long and they always have boundaries [1]. In particular, if there is a significant area where trees are absent (generally referred to as a *clearing*), a new roughness-transition scenario takes place.

Townsend model [8, 9] suggests that the flow should quickly recover an equilibrium dictated by the local skin friction away from the roughness elements. However, it has been generally observed that this model is not valid close to the

A. Segalini (✉)
Linné FLOW Centre, KTH Mechanics, SE-100 44 Stockholm, Sweden
e-mail: segalini@mech.kth.se

© Springer International Publishing Switzerland 2016

A. Segalini (ed.), *Proceedings of the 5th International Conference on Jets, Wakes and Separated Flows (ICJWSF2015)*,
Springer Proceedings in Physics 185, DOI 10.1007/978-3-319-30602-5_43

roughness elements (within the so-called *roughness sublayer*) [4], because it is expected that the flow will be affected by the canopy top and by the local pressure field determined by the individual roughness elements. Forest clearings, for instance, represent an example where the flow field becomes perturbed by the simultaneous presence of the various forest boundaries. At the moment, the only analytical model developed to account for the effect of different forest clearings is the one proposed by Belcher et al. [2], although limited to sparse canopies. The model is based on a linearisation of the Navier-Stokes equations to obtain a first-order correction of the basic incoming flow that accounts for the canopy drag. The present work is aimed at the characterisation of forest clearing effects by means of the numerical solution of the linearised Euler equations with a generic inflow. To validate the model, a comparison of it against wind-tunnel results will be reported and discussed.

2 Model Description

Let us consider an incoming boundary layer, $U_0(z)$, approaching the canopy. The density ρ is assumed to be constant through the domain. Here, an orthogonal reference frame xyz is introduced with x and z indicating the streamwise and vertical direction, respectively. The origin of the reference frame is placed at the windward edge of the forest (the velocity components will be indicated by u and w in the x and z directions, respectively). The forest configuration is assumed to be two-dimensional. All quantities in the model are normalised by the free-stream velocity upstream of the forest, U_∞, and the forest height, h_c.

The Reynolds-Averaged Navier-Stokes (RANS) equations are linearised around the undisturbed flow, $U_0(z)$, by assuming that the forest produces a small perturbation of the velocity field $\left(U_0 + u,\, w\right)$ (so that the products of perturbation quantities can be neglected). The boundary-layer approximation is further enforced, implying that streamwise variations happen on a length scale much larger than vertical variations and must be accounted only in the convection terms.

By considering only for the dominant Reynolds-stress term, $\overline{u'w'}$, the equations governing these linearised perturbations can be written as

$$\begin{aligned} U_0\frac{\partial u}{\partial x} + w\frac{\mathrm{d}U_0}{\mathrm{d}z} &= -\frac{1}{\rho}\frac{\partial p}{\partial x} + \frac{\partial \tau^{(\mathrm{per})}}{\partial z} + f_x\,, \\ U_0\frac{\partial w}{\partial x} &= -\frac{1}{\rho}\frac{\partial p}{\partial z}\,, \\ \frac{\partial u}{\partial x} + \frac{\partial w}{\partial z} &= 0\,, \end{aligned} \tag{1}$$

where $\tau^{(\mathrm{per})}$ and f_x indicate the streamwise Reynolds-stress modification and volume force due to the forest presence. A similar set of equation has been solved by

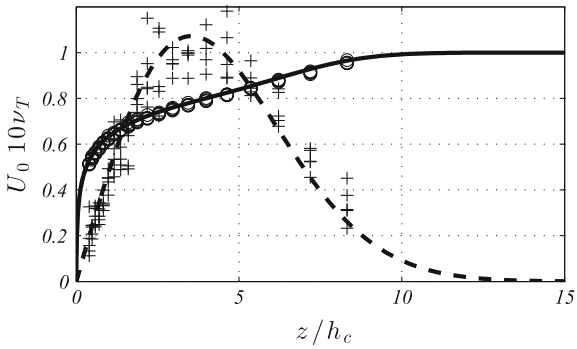


Fig. 1 Profiles of the used streamwise velocity U_0 (*solid line*) and turbulent viscosity $10\nu_T$ (*dashed line*) profiles measured at $10h_c$ upstream of the canopy edge. Experimental results: (*Circles*) U/U_∞, (*pluses*) $10\nu_T$

Belcher et al. [2] with a linear mixing-length hypothesis. In this work, a turbulent viscosity profile has been selected and linearised to yield a relationship between the perturbation stress and the perturbation velocity gradient as

$$\tau^{(\mathrm{per})} = -\overline{u'w'}^{(\mathrm{per})} = \nu_T \frac{\partial u}{\partial z} . \tag{2}$$

The turbulent viscosity, ν_T, in (2) has been determined from the available measurements of mean velocity and shear stress as $\nu_T = -2\overline{u'w'}/(\mathrm{d}U_0/\mathrm{d}z)$, where the factor 2 is due to the closure scheme that assumes a constant mixing length rather than a constant turbulent viscosity. The inlet mean velocity and turbulent viscosity profiles are shown in Fig. 1: as visible, the used profile had to be extended to the wall and towards the free stream to be used in the numerical model. While the former was accomplished through the no-slip condition, the latter was determined by means of Pitot-static measurements available outside the boundary layer, and used to determine the free-stream velocity, together with an assumed wake function.

As usually done in numerical simulations of forestry [7], the trees are replaced by body forces distributed over the forest of the form $f_x = -C_d a_f U^2$, where C_d and a_f indicate the drag coefficient and the leaf-area density, respectively. Consistently with the linearisation, the only force term should be $f_x = -C_d a_f U_0^2$ at the leading order, but this can be done only in the case of weak canopies. As the flow goes through the forest, the constant negative force will decelerate it until the streamwise velocity becomes negative and beyond, representing an unphysical condition. This problem can be circumvented by considering the body force as the small perturbation of the problem, so that $f_x = -C_d a_f \left(U_0 + u\right)^2$ as suggested by Belcher et al. [2]. By means of this approach, the force decreases as the velocity does inside the canopy, so that a negative velocity becomes unlikely within the forest region.

The boundary conditions of the problem (1) are imposed away from the canopy (where u, p, $w \to 0$ as $z \to \infty$) and near the wall at the roughness height (where $u = w = \partial w/\partial z = 0$ as $z = z_0$). The discretisation used in this model is based on

Table 1 List of the different cases analysed in the present work

Case	(*a*)	(*b*)	(*c*)	(*d*)
x_0/h_c	24.5	19.5	14.5	14.5
L/h_c	5	10	15	5

a Fourier decomposition in the streamwise direction (uniform grid spacing) and Chebyshev polynomials in the vertical direction (with an exponential spacing). A fringe region has been introduced at the end of the domain to enforce the decay of the velocity perturbation by means of additional body forces, allowing for the use of FFT algorithms.

3 Experimental Setup

The experiments were performed in the Minimum Turbulence Level (MTL) wind tunnel at KTH in Stockholm, with a setup similar to [6]. The canopy model consists of four plates (each 0.5 m long) where 3500 holes were drilled in a staggered arrangement in each plate. Cylindrical pins with diameter 5 mm were clamped in these holes to replicate the forest. Four clearings configurations were tested with different clearing length, L, and windward edge position, x_0, as reported in Table 1.

Most of the measurements were performed with an in-house manufactured X-wire probe with 1.5 mm long wires of 5 μm in diameter, with a measurement volume of 1 mm^3. The streamwise, u, and vertical, w, velocity time series were measured along the middle plane of the forest model, at different streamwise and wall-normal positions, mostly above the forest model to avoid the accuracy loss of hot-wire measurements inside the canopy due to back-flow events.

4 Results and Discussions

The comparison of the streamwise velocity and shear stress $\overline{u'w'}$ fields at some of the available streamwise locations is shown in Figs. 2 and 3, respectively. The profiles at $x/h_c \approx 15$ differ significantly from the available measurements as the velocity inside the canopy is overestimated by the model. However, the discrepancy is decreased downstream of the clearing, implying that the model underestimates the effect of the canopy but has the correct transitional effect from high-to-low roughness and vice versa. Interestingly, the experimental data indicate that the mean velocity is affected by the clearing, while the shear stress has almost no sensitivity to the lower roughness change, as if the turbulence is just convected above the clearing.

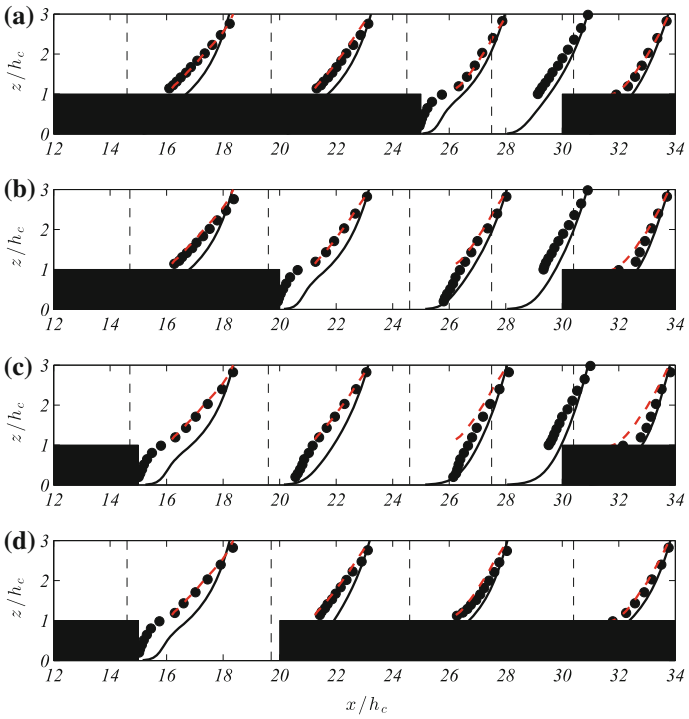


Fig. 2 Profiles of the streamwise velocity U/U_∞ (times 5 and shifted by the corresponding x location) measured at the axial positions indicated by the *vertical dashed black lines* for four clearing conditions. Symbols indicate the experimental measurements, while *solid lines* mark the model predictions. The *red dashed lines* indicate the measurements without clearings

What seems evident is that the clearing perturbation introduces a local acceleration of the flow field that remains confined to the clearing region. Interestingly, Fig. 4 indicates that the clearing perturbation spreads in the wall-normal direction with a nearly-linear growth rate. The intensity of the clearing perturbation scales with the clearing length, although the initial growth rate seems independent of it, as expected as that should be dictated by the turbulent activity near the edge region. However, a scaling law seems possible only in the limit of small clearings since for long clearings the difference between the full forest and clearing case approaches a constant function (given by the difference between the inflow and the flow over the forest).

Additional tests done with large-eddy simulations (with known canopy force) showed better agreement with the proposed model than what shown with the experiments, suggesting that the force intensity of the cylindrical pins (here computed by means of the relationships suggested in [3]) was not properly estimated. Therefore, it appears that the proposed simplified model can be used at a qualitative level to estimate the flow field around clearing areas during the evaluation of the wind resource over complex terrains.

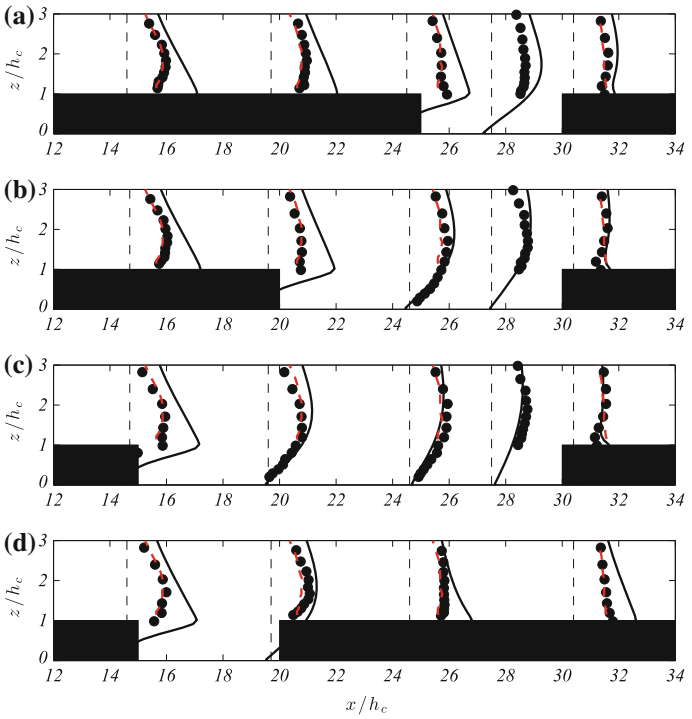


Fig. 3 Profiles of the Reynolds stress $-\overline{u'w'}/U_\infty^2$ for four clearing conditions (times 200 and shifted by the corresponding x location). See the caption of Fig. 2 for the used list of symbols

5 Conclusions

A simplified model to assess the flow over canopies with and without clearings has been discussed. The method is a generalisation of the analysis proposed by Belcher et al. [2], although here the existence of a general analytical solution is not investigated. The model is based on a linearisation of the Euler equations around an incoming turbulent mean velocity profile. The turbulent Reynolds stress has been linearised by assuming a constant mixing-length closure scheme provided by the upstream conditions.

The model predictions have been here compared against wind-tunnel measurements where the forest has been replaced by cylindrical pins [6]. The comparison demonstrated reasonable agreement between the model and the experimental results for both the mean velocity and shear-stress profiles. The greatest discrepancy was observed over the forested region indicating that the forest intensity was not properly characterised through the available experimental results. Nevertheless, the model is able to perform a reasonably good qualitative analysis of the flow over canopies, especially in the transitional region occurring over the clearings.

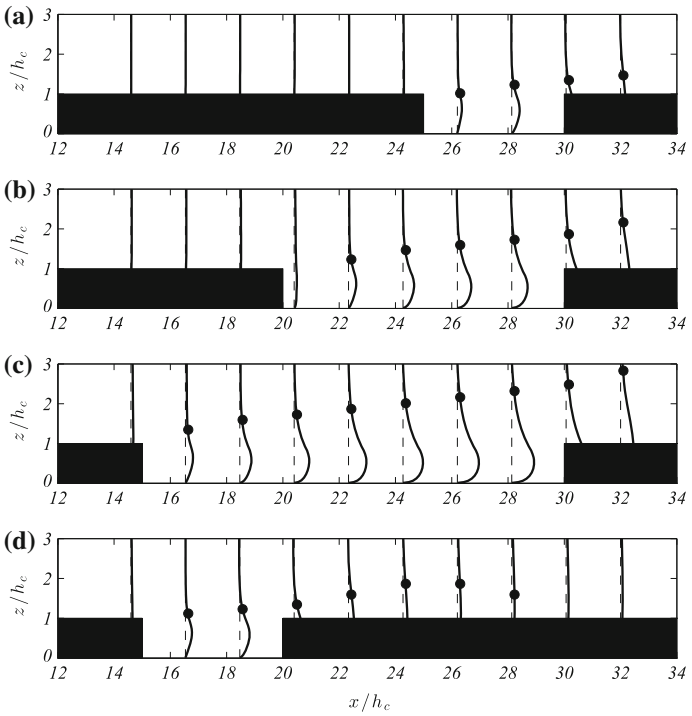


Fig. 4 Model profiles of the streamwise velocity difference between the cases with and without the clearing (times 5 and shifted by the corresponding x location) measured at the axial positions indicated by the *vertical dashed black lines* for four clearing conditions. The *circles* indicate a velocity perturbation of 2 % of U_∞

Acknowledgments This work was supported by the Swedish strategic research programs STandUP for Wind and Vindforsk IV.

References

1. J. Arnqvist, A. Segalini, E. Dellwik, H. Bergström, Wind statistics from a forested landscape. Bound.-Lay. Meteorol. (2015). doi:10.1007/s10546-015-0016-x
2. S.E. Belcher, N. Jerram, J.C.R. Hunt, Adjustment of a turbulent boundary layer to a canopy of roughness elements. J. Fluid Mech. **488**, 369–398 (2003)
3. I.N. Harman, J.J. Finnigan, A simple unified theory for flow in the canopy and roughness sublayer. Bound.-Lay. Meteorol. **123**, 339–363 (2007)
4. J. Jiménez, Turbulent flows over rough walls. Annu. Rev. Fluid Mech. **36**, 173–96 (2004)
5. M.D. Novak, J.S. Warland, A.L. Orchansky, R. Ketler, S. Green, Wind tunnel and field measurements of turbulent flow in forests. Part I: Uniformly thinned stands. Bound.-Lay. Meteorol. **95**, 457–495 (2000)
6. A. Segalini, J.H.M. Fransson, P.H. Alfredsson, Scaling laws in canopy flows: a wind-tunnel analysis. Bound.-Lay. Meteorol. **148**, 269–283 (2013)

7. Silva Lopes, A., Palma, J.M.L.M., Viana Lopes, J.: Improving a two-equation turbulence model for canopy flows using large-eddy simulation. Bound.-Lay. Meteorol. (2013). doi:10.1007/s10546-013-9850-x
8. A.A. Townsend, The response of a turbulent boundary layer to abrupt changes in surface conditions. J. Fluid Mech. **22**, 799–822 (1965)
9. A.A. Townsend, The flow in a turbulent boundary layer after a change in surface roughness. J. Fluid Mech. **26**, 255–266 (1966)

Flow and Heat Transfer of Petal Shaped Double Tube—Effects of Pipe Geometry

Toshihiko Shakouchi, Ryosuke Ozawa, Fumi Iwasaki, Koichi Tsujimoto and Toshitake Ando

Abstract Heat exchangers are widely used to transfer heat from one fluid flow to another. Over time, various types of heat exchangers have been developed to decrease energy consumption and increase efficiency, including compact fin tube and double tube with special inner pipe geometries (ribbed, spiral, and petal shapes) [1, 2]. In this study, we experimentally investigated the heat transfer efficiency of petal-shaped double tubes with a large wetted perimeter or heat transfer area. Moreover, the influence of the number of petals was studied. Our results show that a larger heat transfer area improves heat transfer rate in heat exchangers but the heat transfer efficiency of the five petal-shaped double tube (5P-tube) is much higher than that of the 6P-tube because of a smaller flow resistance of the 5P-tube.

Nomenclature

A, a	cross sectional area
A'_{in}	heat transfer area
d_h	hydraulic diameter (= $4A/p$)
d_e	equivalent diameter
h_i	heat transfer coefficient
k	thermal conductivity
m	mass flow rate
Nu	Nusselt number
P	pressure
Pr	Prandtl number
p	perimeter
Q	heat transfer rate
Re	Reynolds number (= $u_m\, d_h/\nu$ or = $u_m\, d_e/\nu$)
T	temperature
U	over all heat transfer coefficient [= $Q_{in}/(A_{in}\, \Delta T_m)$]

T. Shakouchi (✉) · R. Ozawa · F. Iwasaki · K. Tsujimoto · T. Ando
Graduate School of Engineering, Mie University, Kurimamachiya-cho 1577, Tsu-shi, Mie 514-8507, Japan
e-mail: shako@mach.mie-u.ac.jp

© Springer International Publishing Switzerland 2016

A. Segalini (ed.), *Proceedings of the 5th International Conference on Jets, Wakes and Separated Flows (ICJWSF2015)*,
Springer Proceedings in Physics 185, DOI 10.1007/978-3-319-30602-5_44

u_m mean velocity
V volumetric flow rate
Δp pressure loss
x, r coordinate in axial and radius direction, respectively

Index
all total
c center
in, *out* inner and outer pipe, respectively
I, *II* area I, and II (Fig. 3), respectively

1 Experimental Apparatus and Procedure

Figure 1 shows the schematic diagram of the tested double tube made of copper with a total length of 2.4 m. The origin of the test section is at 230 mm downstream of the inlet of the inner tube. The positive x-coordinate is along the downstream of the inner tube, while the r-coordinate is perpendicular to the x-coordinate. Hot water with a temperature of 60 °C flows through the inner pipe, while cold water with a temperature of 20 °C flows through the outer pipe (counter flow). To calculate the bulk temperature and logarithmic mean temperature difference, measurements were performed at the positions of ④ and ⑦ in the inner and outer pipes using Cu-Co thermo-couples.

The size and configuration of a double tube are closely related to the flow and heat transfer performance, in this study we tested the tube shown in the following as an example.

Figure 2 shows the cross section of the six or five petal-shaped double tubes (6P- or 5P-tubes). A circular double tube (CP-tube) with the same inner cross-sectional area as for the 6P-tube was also tested for comparison.

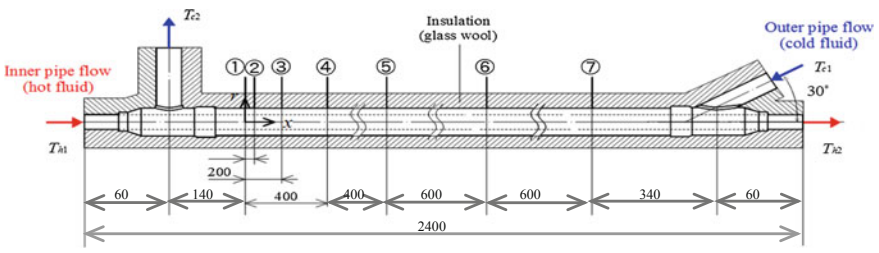


Fig. 1 Schematic diagram of petal shaped double tube

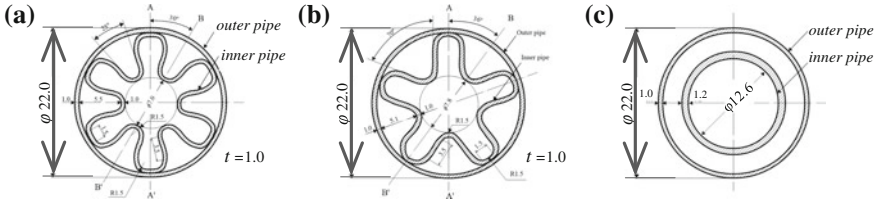


Fig. 2 Cross section of double tube. **a** 6P-tube. **b** 5P-tube. **c** CP-tube

1.1 Shape and Size of Petal Shaped Double Tube

The cross sectional area, perimeter, circle equivalent diameter and hydraulic diameter of the 6 petal shaped inner tube are $A_{in} = 124$ mm^2, $p_{in} = 96.47$ mm, $d_{in,e} = 4(A_{in}/\pi)^{1/2} = 12.5$ mm and $d_{in,h} = 4(A_{in}/p_{in}) = 5.1$ mm, respectively. These values are $A_{out} = 108$ mm^2, $p_{out} = 120$ mm, $d_{out,e} = 11.7$ mm and $d_{out,h} = 3.6$ mm, respectively, for the outer pipe.

Their size of the 5 petal shaped inner tube are $A_{in} = 131$ mm^2, $p_{in} = 71.2$ mm, $d_{in,e} = 4(A_{in}/\pi)^{1/2} = 12.9$ mm and $d_{in,h} = 4(A_{in}/p_{in}) = 7.3$ mm, respectively. These values are $A_{out} = 130$ mm^2, $p_{out} = 121.4$ mm, $d_{out,e} = 12.9$ mm and $d_{out,h} = 4.3$ mm, respectively, for the outer pipe.

The wetted perimeter of the petal-shaped inner tube is considerably large and then the hydraulic diameter ($d_{in,h} = 4A_{in}/p_{in} = 5.1$ mm) becomes too small. Hence, as a conventional double tube the inner tube with the equivalent diameter of $d_{in,e} = 12.5$ mm for the 6P-inner tube was tested for a comparison [see Fig. 2c].

1.2 Pressure Loss, Δp

The pressure distributions along the inner and outer tubes were measured using pressure holes with a diameter of 0.8 mm on the positions of ⑥ and ⑦ and a liquid column manometer (in Fig. 1).

1.3 Heat Transfer, Q

After measuring the flow rate, hot water with a temperature of 60 °C was introduced from the water tank into the petal-shaped inner tube using a pump. Cold water with a temperature of 20 °C was flowing as a counter-current flow in the outer pipe. The outer pipe was covered with an insulator. The Cu-Co thermo couples were located at the centre of the inner and outer tubes at the positions of ①–⑦ in Fig. 1. In order to estimate the bulk temperature, T_b, at the positions of ④ and ⑦, two thermo couples were used at different radius positions (Fig. 3).

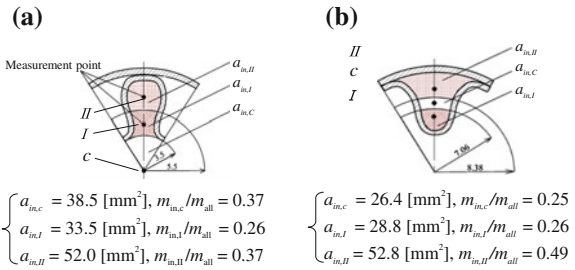


Fig. 3 Position of 6P-tube thermo couples at ④ and ⑦ in Fig. 1. **a** Inner pipe. **b** Outer pipe

The bulk temperature was estimated as follows:

$$T_b = T_c(m_c/m_{all}) + T_I(m_I/m_{all}) + T_{II}(m_{II}/m_{all}) \tag{1}$$

The heat transfer rate Q_{in} between the positions of ④ and ⑦ in Fig. 1 is:

$$Q_{in} = mc_p\Delta T_m \tag{2}$$

where,

c_p : specific heat
ΔT_m : logarithmic mean temperature difference [$=(\Delta T_1 - \Delta T_2)/\ln(\Delta T_1/\Delta T_2)$]
$\Delta T_1 = T_{h1} - T_{c2}$, $\Delta T_2 = T_{h2} - T_{c1}$
T_{h1}, T_{h2} : bulk temperature at the position of ④ and ⑦ of inner pipe
T_{c1}, T_{c2} : bulk temperature at the position of ⑦ and ④ of outer pipe

The overall heat transfer coefficient, U, is obtained as follows:

$$U = Q_{in}/(A'_{in} \times \Delta T_m) \tag{3}$$

where, A'_{in} heat transfer area.

2 Results and Discussion

2.1 Pressure Loss, Δp, Friction Coefficient, λ

Figure 4 shows the pressure loss, Δp, of the inner and outer pipes between the position of ⑥ and ⑦ (defined in Fig. 1) in the fully developed flow region. The results for the tube with an equivalent circular diameter of 12.5 mm are also shown in Fig. 3. The pressure loss Δp [Pa/m] can be expressed by the following equations:

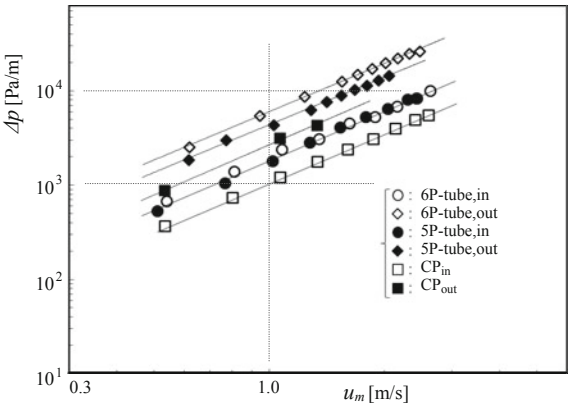


Fig. 4 Pressure loss, Δp

$$\begin{cases} \Delta p = 6010 \times u_m^{1.79} & \text{for} \quad 6\text{P} - \text{tube} \quad (4) \\ \Delta p = 4370 \times u_m^{1.67} & \text{for} \quad 5\text{P} - \text{tube} \quad (5) \\ \Delta p = 2690 \times u_m^{1.53} & \text{for} \quad \text{CP} - \text{tube} \quad (6) \end{cases}$$

As the mean velocity, u_m, increases the pressure loss rises. The pressure drops the of 6P- and 5P-tubes are larger than that in the circular tube (around 2.0 and 1.5 times, respectively). This depends on the wetted perimeters of the inner and outer tubes, which are 2.5 and 3.1 times of that of the circular tube, respectively. In addition, there are some longitudinal vortices that increase the turbulence effect.

Figure 5 shows the friction coefficient, λ, of the 6P- and 5P-tubes calculated from the pressure loss. Where, the Reynolds number is $Re_e = u_m d_e/\nu$. The friction coefficient can be expressed by the following equations.

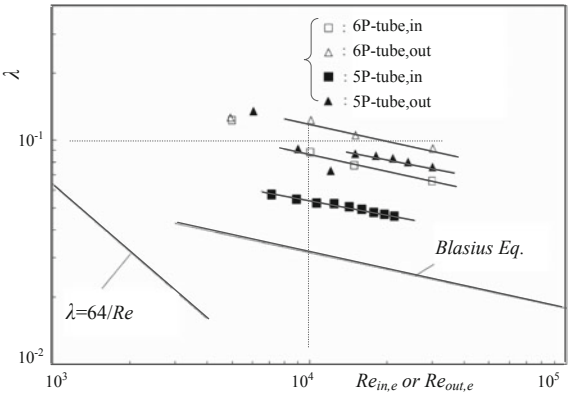


Fig. 5 Friction coefficient, λ

$$\begin{cases} \lambda_{6P,in} = 1.034 \times Re_{in,e}^{-0.268} & \text{for} \quad 6P-\text{tube, in} \quad (7) \\ \lambda_{6P,out} = 1.308 \times Re_{out,e}^{-0.258} & \text{for} \quad 6P-\text{tube, out} \quad (8) \\ \lambda_{5P,in} = 0.326 \times Re_{in,e}^{-0.195} & \text{for} \quad 5P-\text{tube, in} \quad (9) \\ \lambda_{5P,out} = 0.610 \times Re_{in,e}^{-0.201} & \text{for} \quad 5P-\text{tube, out} \quad (10) \end{cases}$$

2.2 Mean Nusselt Number, Nu

The heat transfer characteristics of a counter flow type heat exchanger with 6P- and 5P-tubes were experimentally studied.

Figure 6 shows the mean Nusselt number, Nu, obtained by:

$$Nu = Ud_{in,h}/k_{in} \quad (11)$$

In Fig. 6, the dotted line represents the results obtained for the CP-tube using the Dittus-Boelter equation [3, 4]. The heat transfer coefficient, h_{in}, was obtained using the Wilson plot method [1, 2] and the overall heat transfer coefficient U in (11) [5].

$$Nu = 0.023 \times Re_{in,h}^{0.8} Pr^{0.3} \quad (12)$$

It can express well the experimental results represented by the symbol "□" in Fig. 6. The mean Nusselt number, Nu, for the 6P- and 5P-tubes can be expressed by the following experimental equations:

$$\begin{cases} Nu = 0.10 \times Re_{in,h}^{0.81} & \text{for} \quad 6P-\text{tube} \quad (13) \\ Nu = 0.53 \times Re_{in,h}^{0.69} & \text{for} \quad 5P-\text{tube} \quad (14) \end{cases}$$

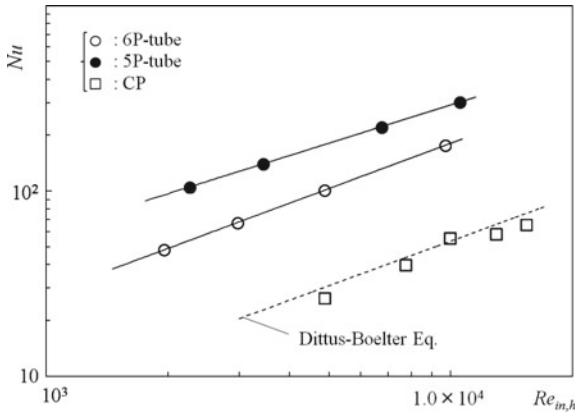


Fig. 6 Mean Nusselt number, Nu

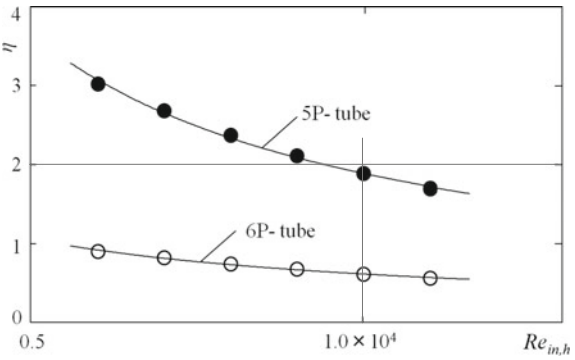


Fig. 7 Heat Transfer efficiency, η

Nu increases as $Re_{in,h}$ increases, Nu distribution of the petal-shaped tubes is much larger than that for the CP-tube in all ranges of $Re_{in,h}$, because of their large wetted perimeters (heat transfer areas). It can express well the experiments.

2.3 Heat Transfer Efficiency, η

Figure 7 shows the heat transfer efficiency, η, defined as:

$$\eta = (Nu/Nu_{CP})/\left[V\Delta p/(V\Delta p)_{CP}\right] \tag{15}$$

where the subscript CP represents a CP-tube. In the range of $Re_{in,h} = (0.6–1.1) \times 10^4$ the heat transfer efficiency, η, of the 6p-tube is about 0.52–0.88 times that of the CP-tube, while is 1.7–3.3 times for the 5P-tube. The 5P-tube has a large heat transfer efficiency because of the large wetted perimeter compared with that of the CP-tube. However, it has a smaller pressure loss compared with that of the 6P-tube.

3 Conclusions

In this study, we examined and experimentally compared the heat transfer and fluid flow performance between the petal-shaped double tubes and other different double-tube type. The main conclusions derived from our work are as follows.

1. The pressure loss, Δp, of the 6P- and 5P-tubes is larger than that of the circular tube. At $u_m = 1.0$ m/s, they are around 2.0 and 1.5 times that of the CP-tube, respectively.

2. The mean Nusselt number, Nu, of the 6P- and 5P-tubes is larger than that of the CP-tube. At $Re_{in,h} = 1.0 \times 10^4$, they are around 3.2 and 5.6 times that of the CP-tube, respectively.
3. In the range of $Re_{in,h} = (0.6–1.1) \times 10^4$, the heat transfer efficiency, η, of the 5P-tube is around 3.3–1.7 times that of the CP-tube.

The 5P-tube has a high heat transfer efficiency because of its larger wetted perimeter compared with that of the CP-tube and a smaller pressure loss compared with that of the 6P-tube.

The high heat transfer performance of the petal-shaped double tubes makes them a very useful tool for compact heat exchangers.

References

1. T. Shakouchi, Y. Oshima, Y. Kawashima, K. Tsujimoto, T. Ando, Compact heat exchanger by petal-shaped special double tube, in *Proceedings of 23rd International Symposium on Transport Phenomena*, CD-ROM (2012), pp. 1–4
2. H. Shokouhmand, M.R. Salimpour, M.A. Akhavan-Behabadi, Experimental investigation of shell and coiled tube heat exchangers using Wilson plots. Int. Commun. Heat Mass Transf. **35** (1), 84–92 (2008)
3. F.W. Dittus, L.M.K. Boelter, Heat transfer in automobile radiators of tubular type. Univ. Calif. Publ. Eng. **2**, 443–461 (1930)
4. V. Gnielinski, New equations for heat and mass transfer in turbulent pipe and channel flow. Int. J. Chem. Eng. **16**(2), 359–368 (1976)
5. J.W. Rose, Heat-transfer coefficient, Wilson plots and accuracy of thermal measurements. Exp. Thermal Fluid Sci. **28**, 77–86 (2004)

Loss Reduction of the Flow in the Reducing Elbow Duct by Using Weir Shaped Small Obstacle

Toshitake Ando, Toshihiko Shakouchi, Atsushi Hanai and Koichi Tsujimoto

Abstract Reducing elbow is 90° bend or elbow pipe/duct which has smaller outlet than inlet. This type of element is frequently used in the industrial facilities. After the corner of this element separated flow from the corner flows away from the inner wall. And then, effective cross-sectional area of downstream pipe/duct near the corner is reduced. Reduction of effective cross-sectional area causes extremely large flow resistance. In this study, loss reduction method with weir-shaped obstacle for reducing elbow duct is newly proposed. To clarify the effects of obstacle on the flow in the reducing elbow, pressure measurement and flow visualization were carried out. As a result, it is made clear that the loss of reducing elbow is reduced by maximum of about 63 % by using obstacle.

1 Introduction

Reducing elbow is 90° bend or elbow pipe/duct which has smaller outlet than inlet [Fig. 1a]. This type of element of pipe system is frequently used in the industrial facilities. The main flow in this element is separated from the inner wall at the corner, and flows away from the inner wall. As a result, effective cross-sectional area of downstream pipe/duct of the corner is reduced and flow resistance becomes extremely large. Generally, elbow corner is rounded or guide vane is mounted near the corner in order to reduce of this type of flow resistance. Hibara et al. [1] reported the rectifying effects of guide vane installed in the bend part and the loss reduction with that. Mochizuki et al. [2] proposed simpler method using half trip or short obstacle on the inner wall of the upstream of corner of normal elbow pipe. In the case of reducing elbow pipe, it is possible to mount taller obstacle to control the flow separation with its small drag, because upstream mean velocity is smaller than the case

T. Ando (✉) · T. Shakouchi · A. Hanai · K. Tsujimoto
Graduate School of Engineering, Mie University,
Kurimamachiya-cho 1577, Tsu-shi, Mie 514-8507, Japan
e-mail: ando@mach.mie-u.ac.jp

© Springer International Publishing Switzerland 2016

A. Segalini (ed.), *Proceedings of the 5th International Conference on Jets, Wakes and Separated Flows (ICJWSF2015)*,
Springer Proceedings in Physics 185, DOI 10.1007/978-3-319-30602-5_45

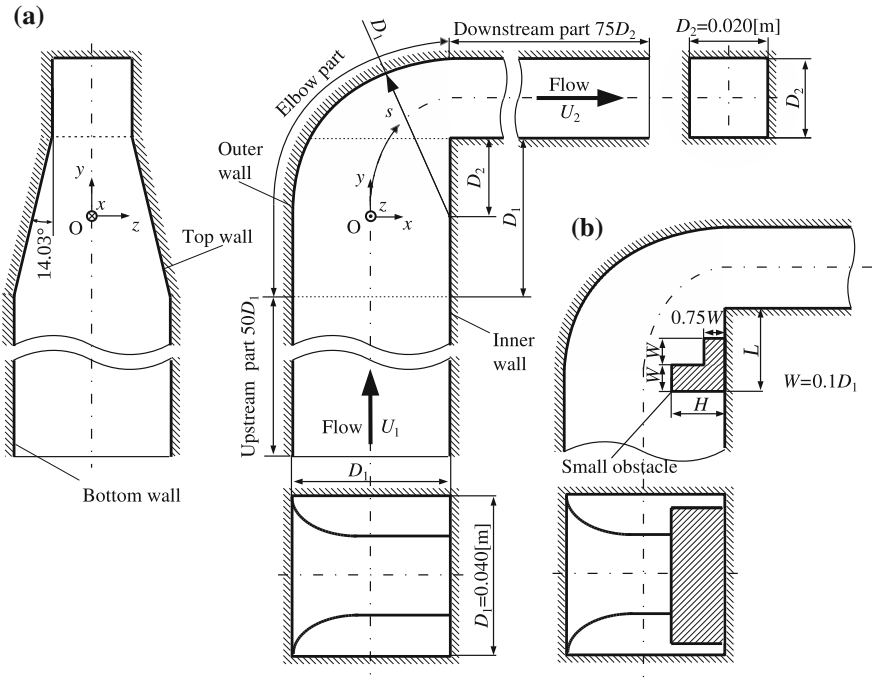


Fig. 1 Test section. **a** Dimensions and coordinate system **b** Small obstacle

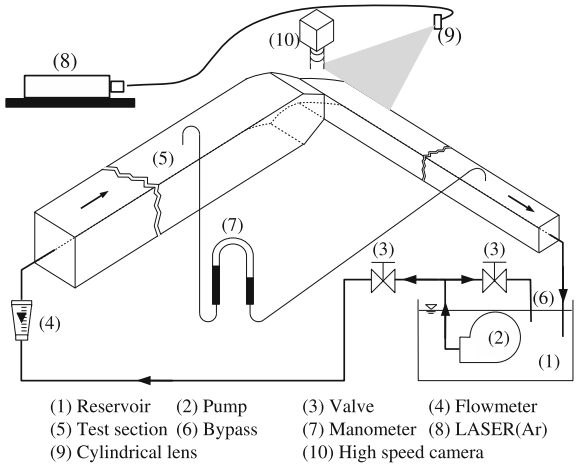
of normal elbow pipe. Ando et al. [3] shown that this type of obstacle is effective for T-junction pipe of counter flow type. In this study, weir-shaped obstacle was examined for reducing elbow duct [Fig. 1a].

2 Experimental Setup and Procedure

2.1 Experimental Setup

The experimental setup is shown in Fig. 2. The working fluid, water, was stored in the reservoir (1) and pressurized by the pump (2), and it was introduced into the test section (5) after passing through the valve (3) and flowmeter (4). The flow rate of water, Q, was controlled by using the valve and flowmeter and bypass (6) to maintain the Reynolds number $\mathrm{Re} = U_1 D_1/\nu$ ($U_1 = Q/D_1^2$, ν: viscosity) of 30,000. The water coming out of the test section was returned into the reservoir. The pressure at the many taps on the center line of top wall was measured as pressure difference from the pressure at $s/D_1 = -12$ (s: see Fig. 1) by using reversed U-shaped manometer (7)

Fig. 2 Experimental setup



and non-dimensionalized to C_p by using U_1 measured at a time. In the cases without obstacle and of maximal reduction of the loss, flow visualization was carried out. The flow patterns were visualized by using tracer of *Diaion HP20* (diameter and density are 0.24 mm and 1.01 kg/m^3, respectively) and LASER light sheet (8), (9), and they were recorded by digital video camera (10).

2.2 Details of Testsection

The test section and its dimensions and coordinate system are shown in Fig. 1. The test section consists of three parts, upstream, elbow and downstream part. Cross section and length of upstream part are square of $D_1 \times D_1 = 0.040 \times 0.040$ m and $50D_1$, respectively. And those of downstream part are $D_2 \times D_2 = 0.5D_1 \times 0.5D_1$ and $75D_2$, respectively. The elbow part consists of seven flat planes and a quarter cylindrical plane of radius of D_1. s axis was set along the center line of center height plane of test section and the origin is placed at $0.5D_1$ upstream of corner on s axis. Quarter ellipse of which major and minor axis are $1.5D_1$ and D_1, respectively, was regarded as center line of elbow part. It is made of transparent resin and many pressure taps connected to pressure holes of diameter 0.6 mm was placed along s center line of upper wall. For flow visualization, elbow part was changed to the one without pressure taps and Laser light sheet was emitted horizontally at center height of the duct.

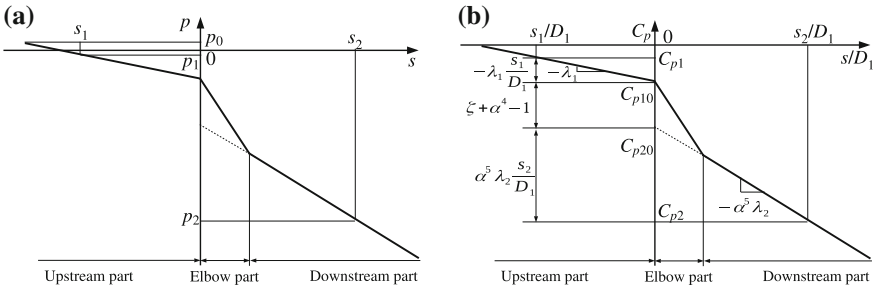


Fig. 3 Outline of pressure distribution and definition of loss coefficient ζ. **a** pressure distribution **b** non-dimensional form of (**a**)

2.3 Definition of Loss Coefficient

The pressure distribution is outlined in the Fig. 3. The regions of $-6.25 \leq s/D_1 \leq -1.50$, and $26.74 \leq s/D_1 \leq 37.49$ are regarded as parts of fully developed region. Following equation shows the energy conservation between two points in the fully developed regions of upstream and downstream part, s_1 and s_2, respectively.

$$\frac{\rho U_1^2}{2} + p_1 = \frac{\rho U_2^2}{2} + p_2 + \lambda_1 \frac{0 - s_1}{D_1} \frac{\rho U_1^2}{2} + \lambda_2 \frac{s_2 - 0}{D_2} \frac{\rho U_2^2}{2} + \zeta \frac{\rho U_1^2}{2} \tag{1}$$

where, λ_1 and λ_2: friction factors, ζ: loss coefficient. After taking reference pressure p_0 from both side, this equation is non-dimensionalized by being divided by $\rho U_1^2/2$.

$$1 + C_{p1} = \alpha^4 + C_{p2} - \lambda_1 \frac{s_1}{D_1} + \lambda_2 \alpha^5 \frac{s_2}{D_1} + \zeta \tag{2}$$

where, $C_p = 2(p - p_0)/\rho U_1^2$, $\alpha = D_1/D_2$. Linear pressure distributions in the fully developed regions can be described by following equations:

$$C_p = -\lambda_1 \frac{s}{D_1} + C_{p10} \qquad \text{(for upstream part)} \tag{3}$$

$$C_p = -\lambda_2 \alpha^5 \frac{s}{D_1} + C_{p20} \qquad \text{(for downstream part)} \tag{4}$$

$(s/D, C_p) = (s_1/D, C_{p1})$ and $(s_2/D, C_{p2})$ are the points on the lines corresponding to (3) and (4), respectively, and are substituted into each equation. Then loss coefficient ζ is eliminated by deducting the pressure drop caused of flow acceleration $\alpha^4 - 1$ from the gap of those linear pressure distributions at $s = 0$, $C_{p10} - C_{p20}$.

$$\zeta = C_{p10} - C_{p20} - \alpha^4 + 1 \tag{5}$$

This loss coefficient includes the loss caused of drag of obstacle in the case with obstacle.

3 Results and Discussion

3.1 Pressure Distribution

The effects of obstacle position L/D_1 on pressure distribution is shown in Fig. 4a. In the cases without obstacle and with obstacle of $H/D_1 = 0.2$, the pressure distribution over $-12 \leq s/D_1 \leq 37.5$ are shown, but in the other cases, the pressure distribution in only regions which is needed to calculate loss factor, ζ, are shown. In the upstream part ($s/D_1 < 0$), the pressure linearly decreased with increasing s/D_1. And then the pressure decreased rapidly because of flow acceleration due to reduction of cross-sectional area of the duct and flow separation. After pressure took local minimum of $C_p = -50$ at $s/D_1 = 1.5$, pressure increased with increasing s/D_1 because of recovery of effective cross sectional area and took local maximum of $C_p = -30$ at $s/D_1 = 3$–5. Finally, pressure linearly decreased with increasing s/D_1 In the cases with obstacle, the pressure in the downstream part took larger value than the case without obstacle, especially in the case of $L/D_1 = 0.25$. In this case, the loss of the elbow part was much smaller than the case without obstacle, and local minimum was larger by 15. It is thought that it is caused by reduction of region of backward flow on the inner wall of inlet of downstream part. The effect of obstacle height H/D_1 is shown in Fig. 4b. The pressure in the downstream part took larger value in the case with obstacle and took maximum at $H/D_1 = 0.20$ like the case of constant L/D_1 [Fig. 4a].

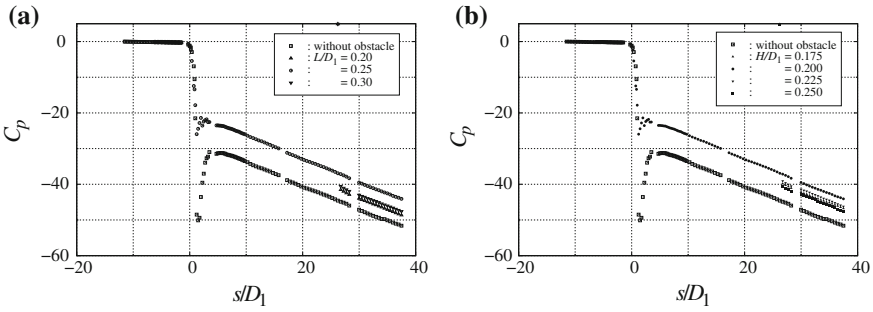


Fig. 4 Pressure distribution. **a** $H/D_1 = 0.2$ **b** $L/D_1 = 0.25$

3.2 Loss of Reducing Elbow

The reduction ratio of loss factor is shown in Fig. 5. In this Figure, the vertical axis shows reduction ratio, $(\zeta_0 - \zeta)/\zeta_0$ (ζ_0: ζ without small obstacle). The upper and lower horizontal axes show the H/D_1 and L/D_1 and correspond to symbols ○ and •, respectively. For $L/D = 0.25$, reduction rate of ζ increased with increasing H/D, at first. After reduction rate took the maximal value of about 0.63 at $H/D = 0.2$, it decreased with increasing H/D. As same way as the case of $L/D_1 = 0.25$, reduction rate took maximal value for $H/D = 0.2$. The loss of reducing elbow ζ was reduced by maximum of about 63 % at $(H/D_1, L/D_1) = (0.2, 0.25)$.

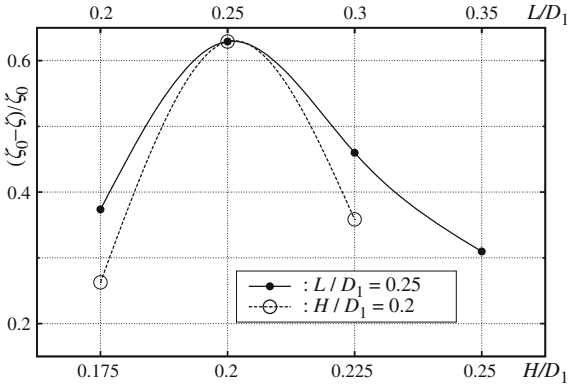


Fig. 5 Reduction rate of ζ

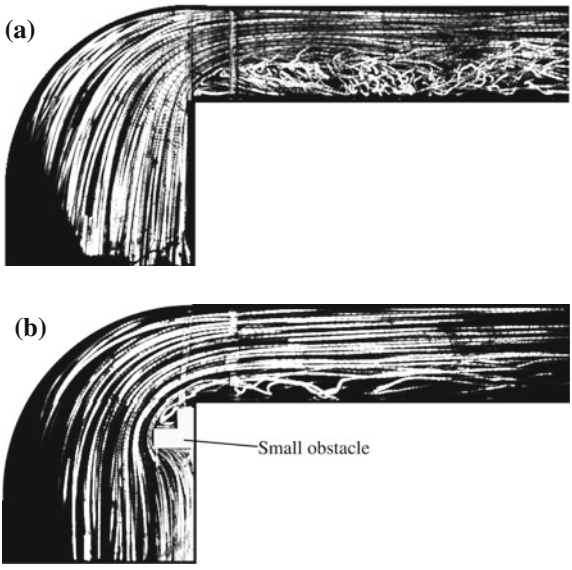


Fig. 6 Visualized flow pattern. **a** without obstacle **b** $(H/D_1, L/D_1 = (0.2, 0.25)$

3.3 Flow Pattern and Velocity Distribution

Visualized flow patterns which were composed of 400 frames image captured by using fast digital camera (2,000 fps), and velocity distributions which were obtained by PIV are shown in Figs. 6 and 7. In these Figures, (a) shows the case without obstacle and (b) shows the case with obstacle of $(H/D_1, L/D_1) = (0.2, 0.25)$. In the case without obstacle, the separated flow from the corner flowed almost $0.5D_2$ away from inner wall. In the other hand, this distance became the half of the case without obstacle in the case with obstacle. Figure 8 shows the distribution of velocity component in the direction of main flow u. In the case without obstacle, the regions of backward flow were observed at $s/D_1 = 1, 1.5$. In the other hand, these regions were suppressed in the case with obstacle. Therefore effective cross-sectional area of downstream part was increased and flow resistance was reduced by mounting small obstacle.

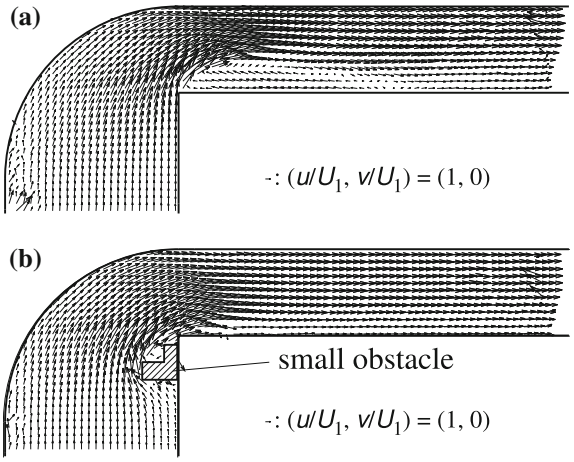


Fig. 7 Velocity distribution. **a** without obstacle **b** $(H/D_1, L/D_1) = (0.2, 0.25)$

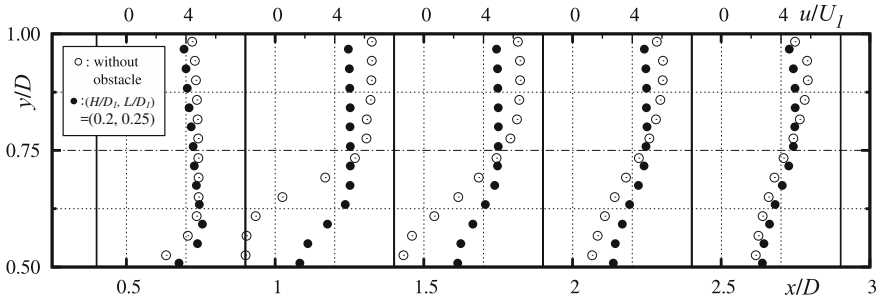


Fig. 8 Distribution of velocity component u

4 Conclusion

We clarified that loss of reducing elbow duct could be reduced by mounting small weir-shaped obstacles on pipe walls upstream of the corner. Major results are summarized as follows:

1. Weir shaped obstacle of height $H/D_1 = 0.2$ at the distance from the corner $L/D_1 = 0.25$ on the inner wall minimize loss, and its reduction rate is about 63 %.
2. With obstacle of condition of above, region of reverse flow on the inner wall of downstream of corner is suppressed, and effective cross-sectional area becomes larger than the case without obstacle.

References

1. H. Hibara, K. Sudou, M. Sumida, Y. Ishibashi, Rectifying effects of guide vanes on the flow downstream from the bend (in Japanese). Turbomachinery **29**(8), 472–481 (2001)
2. S. Mochizuki, M. Yokota, H. Kondo, H. Osaka, Drag Reduction in a 90-degree bend pipe with a half trip (in Japanese). Trans. JSME, Ser. B **69**(679), 595–601 (2003)
3. T. Ando, T. Shakouchi, K. Nishibata, K. Tsujimoto, Drag reduction of t-junction pipe flow by small obstacles. J. Fluid Sci. Technol. **6**(4), 614–624 (2011)

Flow Field Characteristics and Energy Injection in a Tank Stirred by Regular and Fractal Blade Impellers

Konstantinos Steiros, Paul John Kenneth Bruce, Oliver R.H. Buxton and John Christos Vassilicos

Abstract Experiments with regular flat-blades and two fractal modifications have been performed in an unbaffled octagonal stirred tank (tank diameter $T = 0.45$ m), producing a turbulent regime. Shaft torque was monitored to assess differences in input of power of the different impellers. Fractal blade impellers showed a decrease of power number N_p of over 12 % in comparison to normal blades. Phase-locked PIV measurements in the impeller discharge region and spectral analysis of the radial velocity component revealed that the tip vortices produced by the regular blades are more coherent and have higher kinetic energy, being advected by a stronger radial jet compared with their fractal counterparts. This implies that the reduction in torque can be attributed to differences in the vortex formation mechanism. PIV measurements in the bulk of the flow show an increase in turbulence intensity of over 20 % for the fractal blades relative to normal blades. These results suggest that fractal blade turbines are candidates for higher mixing efficiency.

1 Introduction

Stirred tank reactors with top-entering mixers are commonly used by pharmaceutical, chemical and food companies in a variety of industrial applications including homogenizers, emulsifiers, colloidal mills, and generally processes requiring a highly turbulent regime [1].

In order for the highest possible mixing efficiency to be achieved, (i.e. high turbulence with low power input) research has been centred during the last decades on the optimization of impeller blade shape [1–3]. This procedure is often done by trial and error, and as a result an abundance of impeller types have been developed over the years, with different flow fields produced. However, the increase of mixing efficiency is not always substantial [3], showing that there is room for improvement.

K. Steiros (✉) · P.J.K. Bruce · O.R.H. Buxton · J.C. Vassilicos
Department of Aeronautics, Imperial College, London, UK
e-mail: k.steiros13@imperial.ac.uk

© Springer International Publishing Switzerland 2016

A. Segalini (ed.), *Proceedings of the 5th International Conference on Jets, Wakes and Separated Flows (ICJWSF2015)*,
Springer Proceedings in Physics 185, DOI 10.1007/978-3-319-30602-5_46

Specifically, radial turbines (i.e. Rushton, flat blade) cause the formation of stagnant cells in the flow, and highly localized turbulent regions, connected to the blade tip vortices [4], which overall lead to a poor mixing performance [3]. Therefore, a design that would improve this behaviour, would be beneficial.

One possible candidate for blade modification is the fractal design of [5], since recent wind tunnel experiments [5, 6] have shown that, compared to square plates of the same frontal area, fractal plates of this design produce turbulent wakes with higher turbulence intensities, higher local Reynolds numbers and weaker vortex shedding at the cost of higher drag. Therefore, implementation of fractal shape blades seems promising in terms of improving the mixing performance of radial turbines.

In this study, two fractal shaped turbines of different fractal iterations and a regular flat blade turbine are experimentally tested and compared, in order to test the above. Shaft torque and angular velocity were monitored for the different cases, and the non-dimensional power number N_p was determined. Furthermore, planar PIV measurements were performed in the blade discharge region and in the bulk of the flow, in order to quantify the turbulence intensities, and the different flow field characteristics. These measurements allow a quantitative assessment and comparison of the mixing performance of the different mixing impellers.

2 Experimental Details

Experiments have been performed in an octagonal-shaped unbaffled tank made of acrylic, whose schematic can be seen in Fig. 1. The tank's inner diameter T is 0.45 m, with liquid column height $H = T$. The octagonal shape of the tank was chosen as an alternative to the standard cylindrical configurations, so as to minimize the errors caused by optical refraction. An acrylic lid is installed on top of the vessel, at a height equal to the liquid column height H, in order to reduce the effect of the surface vortex that is formed in unbaffled stirred tanks [2]. The working liquid was regular tap water.

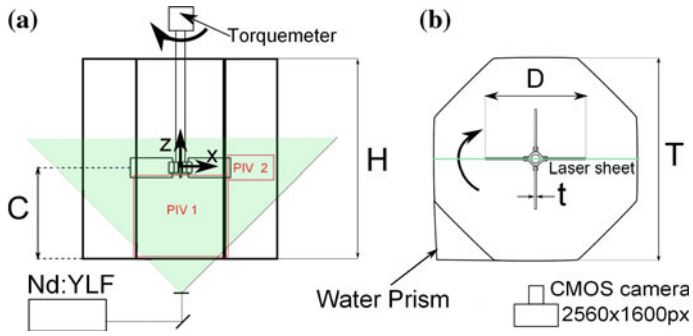


Fig. 1 Schematic of the experimental apparatus and PIV setup. **a** *Front view*. **b** *Top view*. $D = 0.45$ m, $H = T$, $C = T/2$, $D = T/2$, $t = 4$ mm.

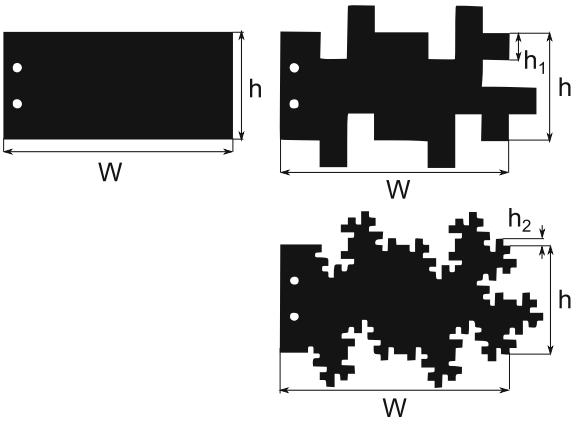


Fig. 2 **a** Regular-rectangular blade, **b** fractal blade with one iteration and **c** fractal blade with two iterations. $h = 4h_1 = 16h_2 = 44.8$ mm, $W = 95$ mm

The impeller used is a common flat blade turbine, classified as radial [2]. It was mounted on a stainless steel shaft with a clearance of $C = T/2$ from the tank bottom. A stainless steel hub was attached at the end of the shaft, enabling the mounting of four acrylic blades. Three sets of blades were used (Fig. 2), namely regular-rectangular and fractal blades of fractal dimension $D_f = 1.5$ with one and two iterations, following Nedić et al. [5]. The thickness and frontal area of the blades were kept the same in all cases, $t = 4$ mm and $A = 4230\,\text{mm}^2$ respectively. The perimeters of the blades were not equal, due to the inherent shape of the fractals, which are comprised of small segments, according to their iteration number. This led to differences in the three impellers' diameter and blades' height: While for the regular case these parameters are easily defined ($D_{Regular} = T/2$, $h_{Regular} = 44.8$ mm), for the fractals case they are position dependent. We therefore choose their average values $D_{Fractal1} = D_{Fractal2} = D_{Regular} = D = T/2$ and $h_{Fractal1} = h_{Fractal2} = h_{Regular} = h = 44.8$ mm to define them.

The turbines were driven by a stepper motor (Motion Control Products), controlled by a function generator (Agilent Technologies). The power consumption $P(= 2\pi NDT)$ was measured with the shaft torque T and rotational speed N by using an in-line torque transducer (Magtrol). The range of rotational speed investigated was from 60 to 300 RPM, corresponding to a Reynolds number range ($Re = ND^2/\nu$) of 50,000 to 250,000.

A 2-D high speed PIV system was employed including a Nd:YLF laser (LDY300-Litron) and a CMOS camera (Phantom v641). Two PIV windows were investigated (Fig. 1), one in the impeller discharge region to document the behaviour of the tip vortices of the different impellers, and a larger one below the shaft, in order to measure the turbulence intensity in the bulk of the flow. Both fields of view were in the plane passing from the axis of rotation. Three rotational speeds were chosen to investigate the scale-up effect, with corresponding Reynolds numbers of 50,000, 150,000 and 250,000.

3 Results and Discussion

3.1 Power Measurements

Plotted in Fig. 3 is the variation of the measured power number, $N_p = P/\rho N^3 D^5$ (N being the impeller rotational frequency, D the impeller's diameter and ρ the water's density) with respect to the Reynolds number, for the three different impellers tested. The results for the rectangular blades follow the same trend with the correlation relation proposed by Furukawa et al. [7] for rectangular blades in unbaffled cylindrical vessels, with a 35 % offset. This difference is attributed to the octagonal shape of the tank, since the corners have a baffling effect, increasing the power number values [2, 8].

Comparing the different cases tested, we observe that there is a consistent reduction in power number between regular and fractal geometries (namely 11–12 % compared to fractal1 blades and 17–20 % compared to fractal2 blades). This result is qualitatively different to the conclusions of the static experiments of [5], where the fractal plates had a systematic increase in drag of up to 6.5 %, compared to square plates. Fractal blades with two iterations produce 3–10 % less power number compared to fractal blades with one iteration, implying that the power number can be modified according to the iteration number of the blades.

3.2 PIV Measurements

In order to investigate the torque difference described in Sect. 3.1, a series of PIV experiments were performed in the discharge region on the blades (Fig. 1). This was done to observe the tip vortices emanating from the impellers. Two sampling frequencies were chosen, one slow to ensure a large sampling time for statistical con-

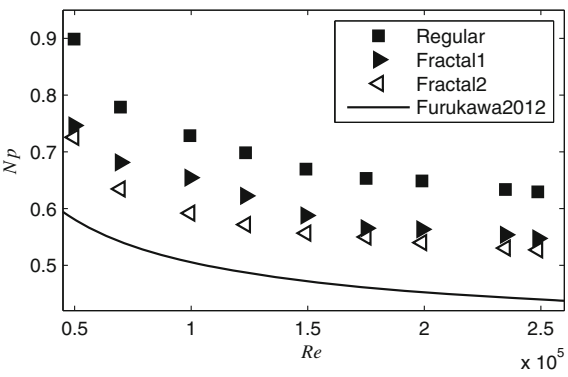


Fig. 3 Variation of the power number, Np, with Reynolds number, for the three tested blades. Also plotted is the correlation relation of Furukawa et al. [7] for regular-rectangular blades

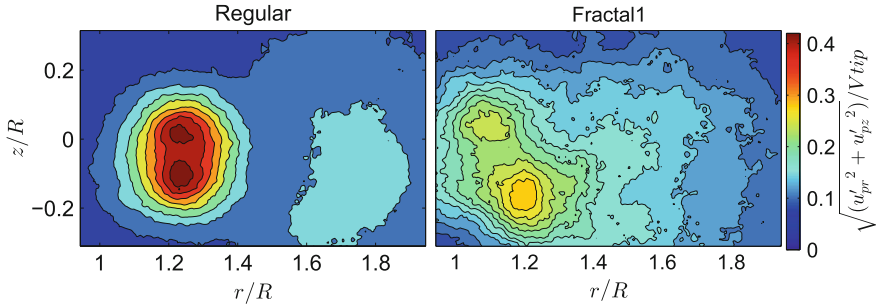


Fig. 4 Contour plots of the phase averaged normalized square root fluctuating kinetic energy at the impeller stream, measured via PIV for Re = 150,000. The phase is about 36° after the blades' passage

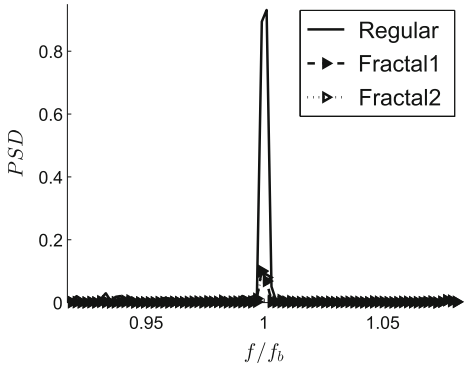


Fig. 5 PSD of the radial velocity fluctuations versus frequency normalized by the blade passing frequency, for the three tested blades at the impeller stream location $(r/R, z/R) = (1.25, -0.01)$ for Re = 150,000

vergence before the buffer of the camera was full, and one high to investigate the spectral characteristics.

From the studies of [4] it is known that in order to avoid the "pseudoturbulence" from the periodic motion of the impeller in its near-field, it is necessary to perform phase (angle) locked measurements. In our case this was done by triggering the high speed PIV system at a frequency that was a multiple of the rotational frequency of the impeller, and then binning the images appropriately in phases. Contours of the angle-locked turbulence intensity at $Re = 150,000$, around 36° after the impeller passage, are shown in Fig. 4 for the regular and the fractal1 turbines. In the regular case, two coherent vortices can be seen, that contain the highest levels of turbulence. However, in the fractal case the vortices are much less coherent, with smaller turbulence levels.

In Fig. 5 can be seen a PSD plot of the radial velocity fluctuations versus frequency normalized by the blade passing frequency, for the three tested blades, at the position $(r/R, z/R) = (1.25, -0.01)$ for $Re = 150,000$. The energy at the blade passing frequency, signifying the radial jet, is an order of magnitude higher for the regular case compared to the fractals, showing that the tip vortices and the radial jet are stronger in the regular case.

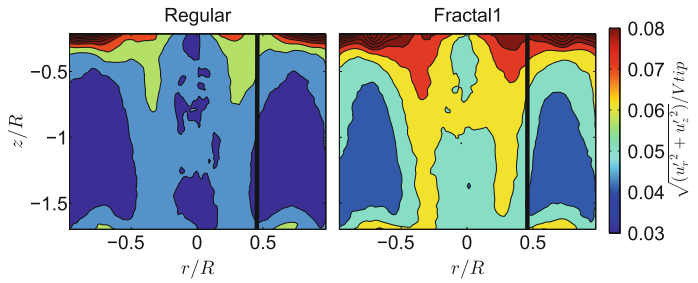
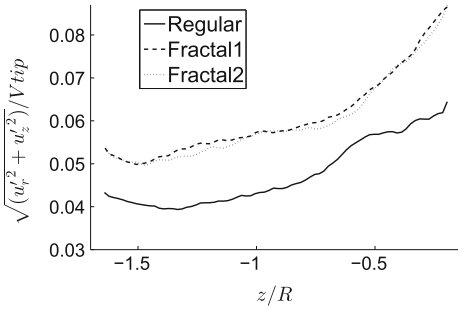


Fig. 6 Contour plots of the turbulence intensity below the impeller, measured via planar PIV for Re = 150,000

Fig. 7 Distribution of the turbulence intensity below the impeller for the three blades, at the location of the *black line* in Fig. 3 ($r = 0.46R$) and Re = 150,000



The above suggest that the difference in power/ torque, described in Sect. 3.1, is related to the differences in the tip-vortex formation mechanism, between the fractal and regular impellers. More specifically, tip vortices have been shown to be related with low pressure regions in the trailing side of the blades of radial turbines [9]. It is possible that the weaker vortices of the fractal blades diminish this effect, therefore contributing to the decrease of the overall shaft torque/ power number.

In order to assess turbulence levels, PIV measurements were performed in the bulk of the tank, below the shaft (Fig. 1). In Fig. 6 contour maps of turbulence intensity are shown for the regular and fractal1 impellers. While the pattern is similar in both cases, the turbulence intensity is over 20 % higher in the fractal case. This can be seen more easily in Fig. 7, where turbulence intensity profiles for the different blades are plotted at the location of the black line in Fig. 6.

The above suggest that while the fractal blade turbines inject less energy in the form of tip vortices compared to the regular blade turbine, the overall turbulence level they generate is higher and more homogeneous throughout the tank. This effect combined with the fact that their weaker tip vortices should generate lower shear [3], makes them suitable candidates for purposes such as bioreactor applications where shear sensitive cells are involved [10], and bacteria sterilization [3] among others.

4 Conclusions

The effect of fractal blade modification in terms of power injection and turbulence produced in stirred tanks, was experimentally investigated, by performing PIV and shaft torque measurements. The blades tested were a common flat blade turbine and two modified fractal turbines, according to the design of [5]. The results show that the fractal blade impellers have a smaller power number, compared with their regular counterpart, a result which is qualitatively different to the conclusions of the static experiments of [5]. PIV experiments in the discharge region of the impeller showed differences in the vortices produced by the different types of impellers, suggesting that there is a connection between the reduction in power and the tip vortex formation and behaviour for the different impellers. PIV in the bulk of the flow showed that the fractal impellers produce higher levels of turbulence than the regular impeller, making them suitable candidates for a number of applications.

Acknowledgments The authors would like to acknowledge the financial support given by European Union FP7 Marie Curie MULTISOLVE project (Grant Agreement No. 317269).

References

1. T. Kumaresan, B. Joshi Jyeshtharaj, Effect of impeller design on the flow pattern and mixing in stirred tanks. Chem. Eng. J. **115**, 173–193 (2006)
2. E.L. Paul, V. Atiemo-Obeng, S.M. Kresta, *Handbook of Industrial Mixing* (John Wiley & Sons, Hoboken, New Jersey, 2004)
3. F. Trivellato, On the efficiency of turbulent mixing in rotating stirrers. Chem. Eng. Process. **50**, 799–809 (2011)
4. H. Wu, G.K. Patterson, Laser-Doppler measurements of turbulent-flow parameters in a stirred mixer. Chem. Eng. Sci. **44**, 2207–2221 (1989)
5. J. Nedić, B. Ganapathisubramani, J.C. Vassilicos, Drag and near wake characteristics of flat plates normal to the flow with fractal edge geometries. Fluid Dyn. Res. **45**, 061406 (2013)
6. J. Nedić, J.C. Vassilicos, B. Ganapathisubramani, Axisymmetric turbulent wakes with new nonequilibrium similarity scalings. Phys. Rev. Lett. **111**, 144503 (2013)
7. H. Furukawa, Y. Kato, T. Kato, et al., Correlation of power consumption for several kinds of mixing impellers. Int. J. Chem. Eng. **2012**(6) (2012)
8. H. Furukawa, Y. Kato, F. Kato, et al., Correlation of power consumption for rectangular mixing vessel. Kagaku Kogaku Ronbun **39**, 94–97 (2013)
9. L.G. Lane, D.G. Rigby, M.G. Evans, Pressure distribution on the surface of rushton turbine blades-experimental measurement and prediction by CFD. J. Chem. Eng. Jpn. **34**, 613–620 (2001)
10. A. Busciglio, G. Caputo, F. Scargiali, Free-Surface shape in unbaffled stirred vessels: experimental study via digital image analysis. Chem. Eng. Sci. **104**, 868–880 (2013)

Part VI
Noise

Numerical Study on the Sound Amplification of a T-Junction with Bias Flow

Lin Du, Mikael Karlsson and Mats Åbom

Abstract This paper reports a numerical study on the aeroacoustic response of a rectangular T-junction with bias flow in the side-branch. The primary motivation of the present work is to study and explain the in recent experiments observed high sound amplification at small bias flows. The study is conducted by performing numerical simulation, which solves the 2D compressible linearized Navier-Stokes equations (LNSEs) in the frequency domain. The time averaged flow is first solved by using RANS along with a k-ε turbulence model. The overall agreement with the experimental acoustic 3-port scattering data is good. It is found that the base flow changes significantly with the presence of a small bias flow. Compared to the case with no bias flow, a strong shear layer is created along the downstream main duct by the mixed grazing-bias flow. For small bias flows (Mach-number < 0.02) this shear layers extends far downstream of the actual junction. This creates a region of vortex-sound interaction much larger than for the no bias flow case, which is the main explanation behind the large amplification.

1 Introduction

T-junctions are common elements in pipe networks. Most of the previous studies [1–5] focus on the acoustic response of a T-junction with closed side-branches. For such a T-junction system with grazing flow in the main duct and closed side-branches, the acoustic power generation depends on the Strouhal number [2, 3], which is determined by the frequency f, width of the side-branch L and grazing flow velocity $U_g = M_g c_0$, as shown in Fig. 1. This is because the acoustic power absorption or production mainly occurs over the opening, where vorticity

L. Du (✉) · M. Karlsson · M. Åbom
The Marcus Wallenberg Laboratory for Sound and Vibration Research, KTH-CCGEx, KTH-FLOW, 100 44 Stockholm, Sweden
e-mail: ldu@kth.se

© Springer International Publishing Switzerland 2016

A. Segalini (ed.), *Proceedings of the 5th International Conference on Jets, Wakes and Separated Flows (ICJWSF2015)*,
Springer Proceedings in Physics 185, DOI 10.1007/978-3-319-30602-5_47

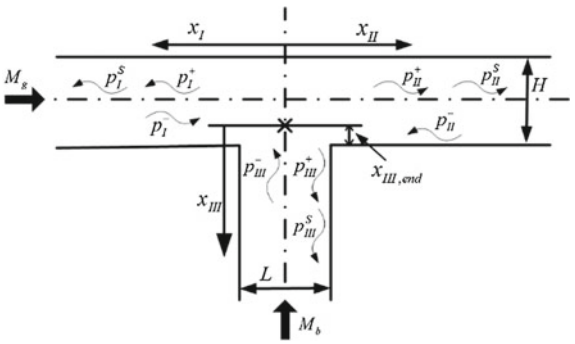


Fig. 1 Definition of coordinate system and acoustic centre (marked with *X*) for the studied T-junction. *p* denotes the pressure amplitude of travelling waves and *M* the Mach-number

levels are high due to the presence of a strong shear layer. However, there are applications where bias flow in the side-branch (flow through the opening) is important. The flow distribution across a T-junction may be changed by the presence of bias flow, thereby impacting the acoustic response.

The acoustic characteristics of a T-junction with grazing-bias flow have been studied experimentally and numerically in recent years [6–10]. The 3-port scattering method is proposed by Karlsson and Åbom [6] to analyze the acoustic properties of a T-junction system. The scattering matrix describes the reflection and transmission of an incident acoustic wave. The experimental results by Karlsson and Åbom [6] were well predicted by simulations [7, 8] at zero bias flow case. Recently Holmberg et al. [9] performed an experimental study on the acoustic response of a T-junction consisting of rectangular ducts with merging grazing-bias flow configuration. An interesting result is that a very high level sound amplification is observed when the bias flow Mach number is small. The primary objective of the present study is to explain this phenomenon of high level sound amplification at small bias flow Mach numbers recently reported by Holmberg et al. [9]. To study this phenomenon, the numerical method developed by Holmberg et al. [10] will be used.

It is known that acoustic energy can be absorbed or produced by flow-acoustic interaction when the acoustic field interacts with hydrodynamic instabilities in the shear layer formed over a side-branch opening by a grazing flow. Using the vortex-sound theory developed by Howe [11], the acoustic power generation *P* from the hydrodynamic (vortex) and sound interaction can be expressed as

$$P = -\rho_0 \int \langle \omega \wedge \boldsymbol{\nu} \cdot \boldsymbol{u} \rangle dV, \tag{1}$$

where *V* is the volume of integration, ρ_0 is the mean fluid density (assumed constant), $\boldsymbol{\nu}$ is the incompressible velocity, $\boldsymbol{u}$ is the acoustic particle velocity and $\langle\rangle$ denotes a time average. In the present work this case will be further examined by introducing a bias flow and first investigating the mean flow using RANs. The mean flow is then used as inputs for calculations of the LNSEs to predict the acoustic response of a T-junction system with grazing-bias flow combination.

2 The Linearized Navier-Stokes Equations

The perturbation quantities are assumed to have harmonic time dependence, and a frequency domain approach is hence adopted. The acoustic perturbation density and velocity ρ', u' (horizontal or x-direction) and v' (vertical or y-direction) can be written as

$$\rho'(\mathrm{x},\mathrm{y},\mathrm{t}) = \mathrm{Re}\left\{\hat{\rho}(\mathrm{x},\mathrm{y})\mathrm{e}^{-j\omega \mathrm{t}}\right\},\ u'(\mathrm{x},\mathrm{y},\mathrm{t}) = \mathrm{Re}\left\{\hat{u}(\mathrm{x},\mathrm{y})\mathrm{e}^{-j\omega \mathrm{t}}\right\},\ v'(\mathrm{x},\mathrm{y},\mathrm{t}) = \mathrm{Re}\left\{\hat{v}(\mathrm{x},\mathrm{y})\mathrm{e}^{-j\omega \mathrm{t}}\right\}, \tag{2}$$

where $\hat{\rho}$, $\hat{u}$ and $\hat{v}$ are complex quantities, ω is the angular frequency, j is the imaginary unit and x, y are Cartesian co-ordinates. Similar to the previous studies [8, 10, 12], we assume that the relation between pressure and density can be regarded as isentropic. In this case the pressure and density perturbations are related as [13]

$$\frac{\partial \hat{\mathrm{p}}}{\partial \mathrm{x_i}} = \mathrm{c}^2 \frac{\partial \hat{\rho}}{\partial \mathrm{x_i}}, \tag{3}$$

where c^2 is the local adiabatic speed of sound. The two-dimensional linearized Navier-Stokes equations [10] can be written in the following forms:

$$\hat{\rho}\text{:}\quad (u_0 v_0)\nabla\hat{\rho} + \left(\frac{\partial u_0}{\partial x} + \frac{\partial v_0}{\partial y} - j\omega\right)\hat{\rho} = -\left(\frac{\partial \rho_0 \hat{u}}{\partial x} + \frac{\partial \rho_0 \hat{v}}{\partial y}\right), \tag{4}$$

$$\hat{u}\text{:}\quad \nabla^T\left[-\begin{pmatrix}\frac{4}{3}\mu_t & 0\\ 0 & \mu_t\end{pmatrix}\nabla\hat{u}\right] + \rho_0(u_0 v_0)\nabla\hat{u} + \rho_0\left(\frac{\partial u_0}{\partial x} - j\omega\right)\hat{u} = \rho_0\hat{F}_x - \left(u_0\frac{\partial u_0}{\partial x} + v_0\frac{\partial u_0}{\partial y}\right)\hat{\rho} - c_0^2\frac{\partial \hat{\rho}}{\partial x} + \frac{\partial}{\partial y}\left(\mu_t\frac{\partial \hat{v}}{\partial x}\right) - \frac{2}{3}\frac{\partial}{\partial x}\left(\mu_t\frac{\partial \hat{v}}{\partial y}\right) - \rho_0\frac{\partial u_0}{\partial y}\hat{v}, \tag{5}$$

$$\hat{v}\text{:}\quad \nabla^T\left[-\begin{pmatrix}\mu_t & 0\\ 0 & \frac{4}{3}\mu_t\end{pmatrix}\nabla\hat{v}\right] + \rho_0(u_0 v_0)\nabla\hat{v} + \rho_0\left(\frac{\partial v_0}{\partial y} - j\omega\right)\hat{v} = \rho_0\hat{F}_y - \left(u_0\frac{\partial v_0}{\partial x} + v_0\frac{\partial v_0}{\partial y}\right)\hat{\rho} - c_0^2\frac{\partial \hat{\rho}}{\partial y} + \frac{\partial}{\partial x}\left(\mu_t\frac{\partial \hat{u}}{\partial y}\right) - \frac{2}{3}\frac{\partial}{\partial y}\left(\mu_t\frac{\partial \hat{u}}{\partial x}\right) - \rho_0\frac{\partial v_0}{\partial x}\hat{u}. \tag{6}$$

here ρ_0, u_0, v_0 and p_0 are the mean flow components. $\nabla = (\partial/\partial x + \partial/\partial y)^T$ and $\mu_t = \mu + \mu_\tau$ is the total viscosity, including the dynamic viscosity μ and eddy viscosity μ_τ.

3 Analysis Method

Assuming linear aeroacoustic models are valid the T-junction can in the plane wave range be described as an acoustic 3-port [6], defined by:

$$\begin{pmatrix} \hat{p}^{I}_{+} \\ \hat{p}^{II}_{+} \\ \hat{p}^{III}_{+} \end{pmatrix} = \begin{bmatrix} S_{11} & S_{12} & S_{13} \\ S_{21} & S_{22} & S_{23} \\ S_{31} & S_{32} & S_{33} \end{bmatrix} \begin{pmatrix} \hat{p}^{I}_{-} \\ \hat{p}^{II}_{-} \\ \hat{p}^{III}_{-} \end{pmatrix} + \begin{pmatrix} \hat{p}^{I}_{+} \\ \hat{p}^{II}_{+} \\ \hat{p}^{III}_{+} \end{pmatrix}^{S} \text{ or } \hat{p}_{+} = S\hat{p}_{-} + \hat{p}^{S}_{+}, \quad (7)$$

where the $+/-$ represent outgoing and incoming waves and $\hat{p}^{S}_{+}$ is the sound that is generated independent on the incoming sound waves. The scattering matrix describes the reflection and transmission of any incident wave in a T-junction. In order to analyze whether acoustic energy is produced or absorbed in the T-junction due to vortex-sound interaction, the acoustic power ratios (=total power scattered/incident power) can be calculated based on the scattering matrix elements as:

$$\frac{\langle P^{I}_{out} \rangle}{\langle P^{I}_{in} \rangle} = \frac{|S_{11}|^2 (1 - M_I)^2}{(1 + M_I)^2} + \frac{|S_{12}|^2 (1 + M_{II})^2 A_{II}}{(1 + M_I)^2 A_I} + \frac{|S_{13}|^2 (1 - M_{III})^2 A_{III}}{(1 + M_I)^2 A_I}, \quad (8)$$

$$\frac{\langle P^{II}_{out} \rangle}{\langle P^{II}_{in} \rangle} = \frac{|S_{22}|^2 (1 + M_{II})^2}{(1 - M_{II})^2} + \frac{|S_{21}|^2 (1 - M_I)^2 A_I}{(1 - M_{II})^2 A_{II}} + \frac{|S_{23}|^2 (1 - M_{III})^2 A_{III}}{(1 - M_{II})^2 A_{II}}, \quad (9)$$

$$\frac{\langle P^{III}_{out} \rangle}{\langle P^{III}_{in} \rangle} = \frac{|S_{33}|^2 (1 - M_{III})^2}{(1 + M_{III})^2} + \frac{|S_{31}|^2 (1 - M_I)^2 A_I}{(1 + M_{III})^2 A_{III}} + \frac{|S_{32}|^2 (1 + M_{II})^2 A_{II}}{(1 + M_{III})^2 A_{III}}, \quad (10)$$

where A_i is the duct cross-sectional area of duct i. A larger than unity power ratio indicates that acoustic power is produced in the T-junction. In the recently reported experiments [9], very high power ratios were observed in specific frequency (or Strouhal) regimes at small bias Mach number flows.

4 Numerical Setup

The mean flow is calculated using the incompressible low Reynolds number (RANs) $k-\varepsilon$ model found in Comsol Multiphysics®. To avoid numerical errors caused by the boundary reflections and to allow for a long downstream region with vortex-sound interaction, "very long" computational domains are chosen for both the RANs and LNSEs calculations. In physical units the length of the computational domain main duct is 5 and 2.5 m for the side-branch. Based on the experiments reported by Holmberg et al. [9], the duct and side-branch height are both 0.025 m.

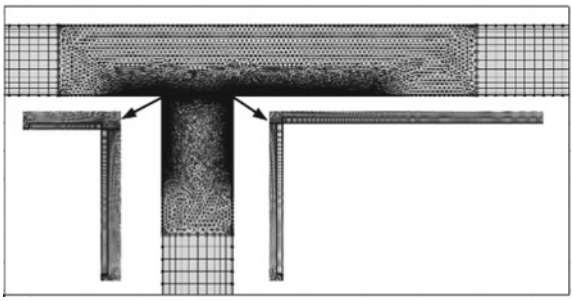


Fig. 2 Mesh used for acoustic calculations unit [m]

The speed of sound is 343 m/s and the medium air (20 °C) at standard pressure (100 kPa). The Mach number of the grazing flow in the main duct is fixed at 0.1.

The close-up mesh for the calculation of the acoustic field is shown in Fig. 2. The frequency range studied is 100−2500 Hz, i.e., there are only plane waves outside the nearfield region in each branch (first cut-on 6800 Hz). For a T-junction system, three linearly independent sound fields are needed to determine the scattering matrix in (7). The sound fields were excited by applying the source term $\hat{F}_x$ and $\hat{F}_y$ in the momentum equations at each branch. At the in- and outflow boundaries of each branch, only plane waves are assumed to be present. Based on the Helmholtz equation, we can apply non-reflecting boundary conditions there

$$\mathbf{n} \cdot \nabla \hat{\rho} = j\mathrm{k}\hat{\rho},\ \mathbf{n} \cdot \nabla \hat{u} = j\mathrm{k}\hat{u},\ \mathbf{n} \cdot \nabla \hat{v} = j\mathrm{k}\hat{v}, \tag{11}$$

where $\hat{v}$ is zero for horizontal boundaries and $\hat{u}$ is zero for vertical boundaries (no slip), $\mathbf{n}$ is a unit vector normal to the in- and outlet boundaries of each branch and k is the wave number at the boundaries. However, the boundary conditions described by (11) break down when vorticity exists. Therefore, an additional variable viscosity is applied in the buffer zones $2\,\mathrm{m} \le x_i \le 2.5\,\mathrm{m}$, $i = I, II\ and\ III$ as

$$\mu_t = \mu + \mu_\tau + \mu_{artifical}(x_i), \tag{12}$$

where $\mu_{artifical}(x_i) = 2(x_i - 2.0)\mu_0$, $\mu_0 = 10^4\mu$ is applied in the simulations. Once the LNSEs are solved, the incoming and outgoing waves can be extracted from the acoustic fields.

5 Results

In this section, we first show the results with zero bias flow given by the present method. The numerical results are compared with measurements [9]. Figure 3 shows the results for a mean flow field at $M_b = 0.00$. There is a clear recirculation in the side-branch and a shear layer can be identified across the opening. The

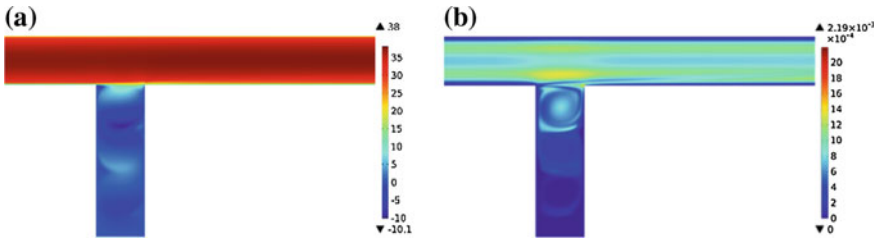


Fig. 3 RANS mean flow data at $M_b = 0.00$; **a** vorticity field [1/s] **b** turbulence viscosity μ_τ Pa s

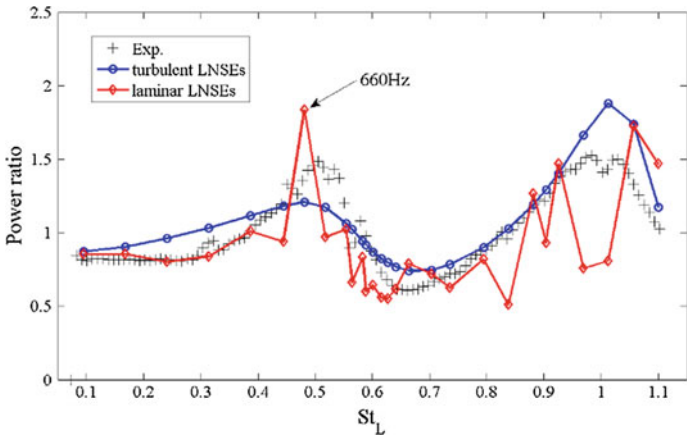


Fig. 4 Power ratios of side-branch excitation versus St_L at zero bias flow

turbulence viscosity is two orders of magnitude larger than the dynamic viscosity. For a T-junction system, the width of the side-branch is commonly thought as the characteristic length for defining a St-number defined as $St_L = fL/u_g$. Figure 4 shows the power ratio for a pure side-branch excitations by referring to (10) at zero bias flow. The "turbulent" LNSEs means the total viscosity consisting of both dynamic viscosity μ and turbulent viscosity μ_τ. The "laminar" LNSEs represents the effect when the turbulent viscosity is ignored. The results show that only a model including eddy viscosity will give a stable result that fits the measured amplification well. The result based on the laminar LNSEs can predict the trend of the power ratio, but the variation of power ratio with St_L is not smooth.

The above method has also been applied to grazing-bias flow combinations with success. Figure 5 shows the flow configuration of $M_g = 0.10$ and $M_b = 0.015$. It can be seen that the mean flow field is completely changed due to the presence of a bias flow. There is no recirculation in the side branch. A recirculation is instead created at the downstream edge, which is similar to the results reported by Lam et al. [14]. The merged grazing and bias flow accelerates because of the existence of recirculation at the downstream edge. The stress level is very high at the boundary of the

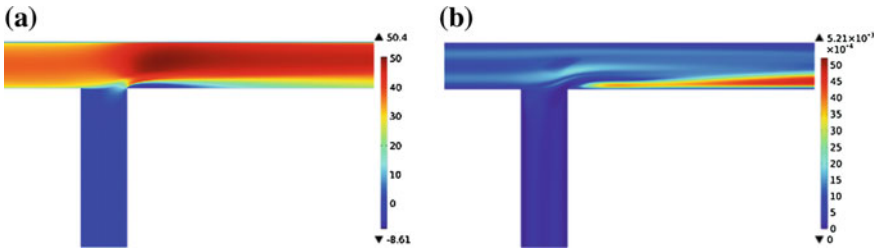


Fig. 5 RANS mean flow data at $M_b = 0.015$; **a** vorticity field 1/s **b** turbulence viscosity μ_τ Pa s

recirculation. Comparing the results in Figs. 3 and 5, the flow field in the downstream branch is non-uniform and a very long boundary layer and recirculation zone, with high turbulent viscosity, is created by the presence of the bias flow.

The magnitudes for the scattering matrix are plotted in Fig. 6. The simulation results are shown in the range of $M_b = 0.01 \sim 0.02$. Comparing the magnitude of the elements S31, S32 and S33, which according to 10 determines the side branch amplification, with the zero bias flow case given by Holmberg et al. [10] it is clear that for small bias flow we get a large increase in amplification. Power ratios of side-branch excitation versus St_L of different grazing-bias flow combinations based on (10) is compared in Fig. 7. The numerical results also show that when the bias flow is increased beyond ~0.02 this strong amplification disappears.

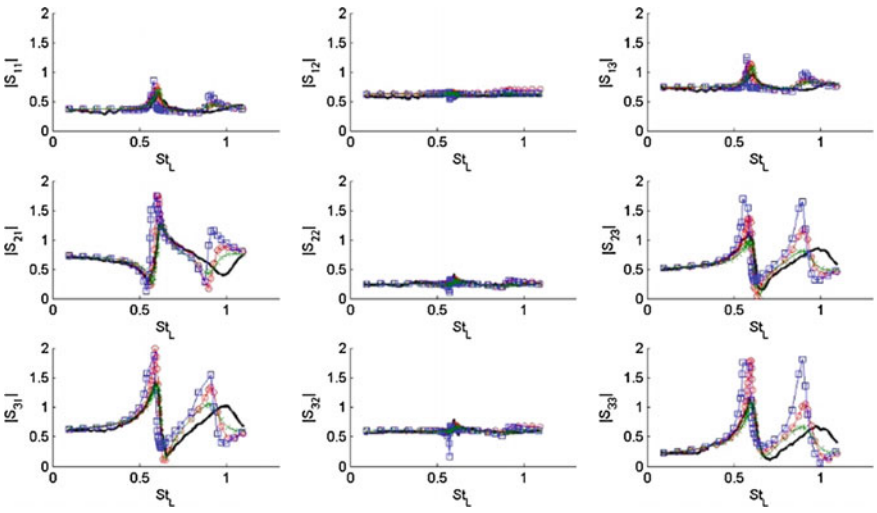


Fig. 6 Magnitude of the scattering matrix elements of a grazing-bias flow combination, Experiments: Black line: $M_b = 0.01$; Simulations: Blue line with squares: $M_b = 0.01$; Red line with circles: $M_b = 0.015$; Green line with crosses: $M_b = 0.02$

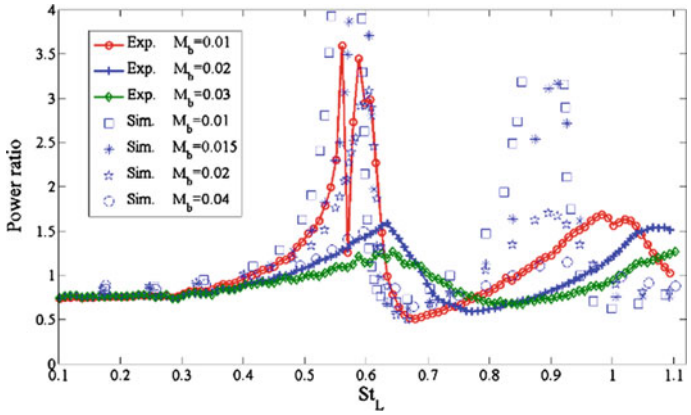


Fig. 7 Power ratios of side-branch excitation versus St_L of different grazing-bias flow combinations based on (10). The grazing flow Mach number is 0.1

6 Conclusion

The acoustic properties of a rectangular T-junction subject to grazing-bias flow combination are studied in the present work by numerical simulations. The mean flow is calculated using an incompressible low Reynolds number $k-\varepsilon$ model. The time averaged part of the flow is used as inputs for the calculations of LNSEs. There is no recirculation in the side branch any more due to the presence of a bias flow. Instead the time-averaged flow is non-uniform far from the downstream edge creating a long recirculation zone, see Fig. 5. Compared to zero bias flow case this moves the amplification of sound from the side-branch to a much larger zone down-stream of the side-branch. This zone only exists for small bias flows < 0.02 and results in an amplification which is up to 4 times larger than for the no bias flow case [9]. Although the LNSE model offers an explanation of the phenomena first reported by Holmberg et al. [9], one can still note deviations in the detailed predictions of, e.g., the power ratios. This is believed to be related primarily to limitations of the $k-\varepsilon$ turbulence model and secondarily to 3D effects not captured by the 2D model used.

References

1. D. Rockwell, E. Naudascher, Review-self-sustaining oscillations of flow past cavities. J. Fluids Eng. **100**, 152–165 (1978)
2. J.C. Bruggeman, A.P.J. Wijnands and J. Gorter, Self-sustained low frequency resonance in low Mach number gas flow through pipelines with side branch cavities, in *AIAA 10th Aero-acoustics conference*, Seattle, Washington, AIAA paper 86-1924, 9–11 July 1986

3. J.C. Bruggeman, A. Hirschberg, M.E.H. van Dongen, A.P.J. Wijnands, J. Gorter, Self-sustained aero-acoustic pulsations in gas transport systems: experimental study of the influence of closed side branches. J. Sound Vib. **150**, 371–393 (1991)
4. S. Ziada, E.T. Bühlmann, Self-exited resonances of two side-branches in close proximity. J. Fluids Struct. **6**(5), 583–601 (1992)
5. S. Ziada, A flow visualization study of flow-acoustic coupling at the mouth of a resonant side-branch. J. Fluids Struct. **8**(4), 391–416 (1994)
6. M. Karlsson, M. Åbom, Aeroacoustics of T-junctions—an experimental investigation. J. Sound Vib. **329**, 1793–1808 (2010)
7. S. Föller, W. Polifke D. Tonon, Aeroacoustic characterization of T-junctions based on large eddy simulation and system identification, in *AIAA aeroacoustics conference*, p. 3985 (2010)
8. J. Gikadi, S. Föller, T. Sattelmayer, Impact of turbulence on the prediction of linear aeroacoustic interactions: acoustic response of a turbulent shear layer. J. Sound Vib. **333**, 6548–6559 (2014)
9. A. Holmberg, M. Karlsson, M. Åbom, Aeroacoustics of rectangular T-junctions subject to combined grazing and bias flows—an experimental investigation. J. Sound Vib. **340**, 152–166 (2015)
10. A. Holmberg, A. Kierkegaard, C. Weng, A frequency domain linearized Navier-Stokes method including acoustic damping by eddy viscosity using RANS. J. Sound Vib. (2015). doi:10.1016/j.jsv.2015.02.030
11. M.S. Howe, *Acoustics of Fluid-Structure Interactions* (Cambridge University Press, Cambridge, 1998)
12. A. Kierkegaard, S. Boij, G. Efraimsson, A frequency domain linearized Navier-Stokes equations approach to acoustic propagation in flow ducts with sharp edges. J. Acoust. Soc. Am. **127**(2), 710–719 (2010)
13. S. Temkin, *Elements of Acoustics* (Acoustical Society of America, Melville, New York, 2001)
14. G.C.Y. Lam, R.C.K. Leung, S.K. Tang, Aeroacoustics of T-junction merging flow. J. Acoust. Soc. Am. **133**(2), 697–708 (2013)

Experiments on Sound Radiation in Flow Past Two Side-by-Side Square Cylinders

Ressa Octavianty and Masahito Asai

Abstract Vortex shedding and sound radiation from two side-by-side square cylinders was examined experimentally at low-Mach-number flow. The center-to-center distance (L/d) between two cylinders was 3.6, 4.5 and 6.0 which are still in the regime of non-biased flow. At $L/d = 3.6$ and 4.5, the wake behind the cylinders showed symmetric vortex shedding which generate the in-phase sound pressure. The vortex shedding exhibited a high spanwise coherency and thus strong sound was radiated compared to that in a single-cylinder case. It was also shown that when a short splitter plate with $c/d = 0.2$ was glued on the rear side of each cylinder, the sound pressure level was reduced significantly.

1 Introduction

The present paper studied sound radiation from side-by-side square cylinders placed in a uniform flow. Many experiments have been conducted on the vortex shedding from cylinders in side-by-side arrangement and classified the flow field into several typical wake patterns as reviewed by Sumner [1]. By contrast to detailed observations of the wake structures, sound radiation from the corresponding cylinder array have been much less investigated in spite of many engineering applications. Inoue et al. [3] numerically studied sound fields radiated in the response to the wake patterns that are classified in the flow field, though the computation was limited to low Reynolds number conditions ($Re = 150$). When the Reynolds number increased, wake vortices could generally lose pure two-dimensionality and its spanwise correlation (or correlation length) would be significant for determination of the sound pressure level. The correlation length is only a few reference transverse length (diameter) of cylinder for

R. Octavianty (✉) · M. Asai
Department of Aerospace Engineering, Tokyo Metropolitan University,
6-6 Asahigaoka, Hino, Tokyo 191-0065, Japan
e-mail: ressa-octavianty@ed.tmu.ac.jp

M. Asai
e-mail: masai@tmu.ac.jp

© Springer International Publishing Switzerland 2016

A. Segalini (ed.), *Proceedings of the 5th International Conference on Jets, Wakes and Separated Flows (ICJWSF2015)*,
Springer Proceedings in Physics 185, DOI 10.1007/978-3-319-30602-5_48

a single circular or square cylinder at large Reynolds numbers; see Fujita [5] for circular cylinder wake at $Re = 2.5 - 3.5 \times 10^5$. So, further investigation is desirable to better understand sound generation in flow past side-by-side cylinders in a Reynolds number range of engineering application. It is also interesting to see effects of small splitter plates (which have been used for drag reduction of a bluff body) on the sound radiation for a cylinder pair. For a single square cylinder, a numerical simulation (at $Re = 150$) by Ali et al. [6] demonstrated that a splitter plate with length of $\leq d$ (d is the side length of the cylinder) can reduce the sound pressure level (SPL) by 3 dB. In the present paper, sound radiation from side-by-side square cylinders were examined experimentally at $Re = 1.0 - 3.3 \times 10^4$, with the center-to-center distances (scaled with the side length) of 3.0, 4.5 and 6.0 which are in the non-biased flow regime for side-by-side square cylinders [2]. Effects of tiny splitter-plate(s) glued on the cylinder's rear side on noise reduction were also examined.

2 Experimental Setup

The experiment was conducted in a low-turbulence, low-noise wind tunnel of the open-return type. The flow entered the contraction after six damping screens and a honeycomb in a settling chamber with a $1800 \times 1800\,\text{mm}^2$ cross section. The area ratio of the contraction to the nozzle exit with a $500 \times 500\,\text{mm}^2$ cross section was 13. A 1.6 m long test section was placed in an anechoic chamber that was 4.5 m long, 3.4 m wide and 3 m high. The A-weighted sound pressure level (SPL) of the background noise was 65.5 dB and the residual turbulence was about 0.1 % at $U_\infty = 50$ m/s. Two square cylinders (made of aluminum) with a side-length d of 10 mm were installed perpendicularly to the oncoming freestream in the test section (see Fig. 1); both the cylinders had a zero angle of incidence. Two large end-walls made of wood and Plexiglas, respectively, were used to maintain the two-dimensionality of the main stream. The distance between the centers of two cylinders was denoted by L. In order to examine effects of splitter plate(s) on the noise generation, a short splitter-plate of 1 mm thickness was glued on the rear surface of each cylinder. The length c was 2 to 5 mm, i.e., $c/d = 0.2$ to 0.5.

Two microphones were set perpendicular to the cylinder axis, in the opposite sides, at the mid-span of the cylinders to measure the radiated sound. A PIV measurement was also conducted and 500 images were captured by a CCD camera with 2048 pixels × 2048 pixels to understand the vortex shedding patterns. In addition, a constant-temperature hot-wire anemometer was used to measure velocity fluctuations in the wake. As for the coordinate system, x, y, and z are the streamwise, transverse and spanwise directions, respectively, with the x-origin placed on cylinder's trailing-edge.

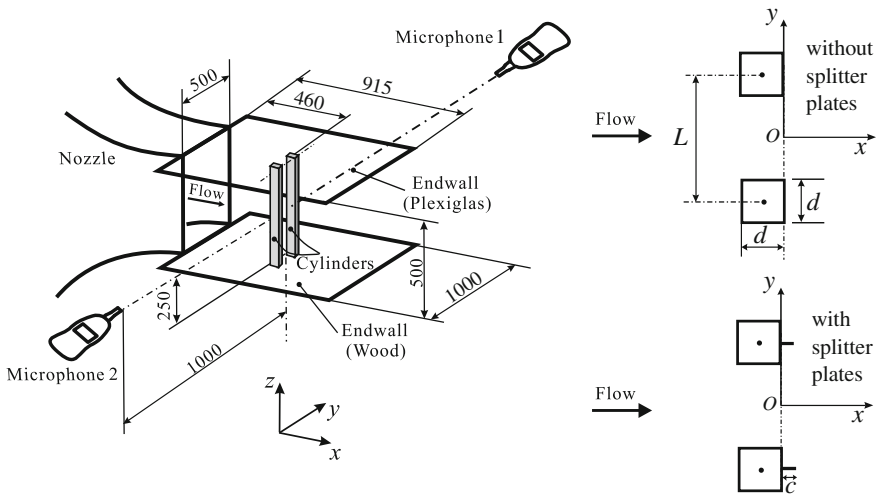


Fig. 1 Schematic of experimental setup

3 Results and Discussions

Figure 2a–c display the spectra of sound pressure for two side-by-side square cylinders with various center-to-center distances ($L/d = 3.6, 4.5$, and 6.0) at $U_\infty = 50$ m/s ($Re = 3.3 \times 10^4$) by comparing to the corresponding spectrum for a single square cylinder. At $L/d = 3.6$, the radiated sound had a very sharp spectrum at $St = 0.133$ and its SPL value was larger than that for the single cylinder case by about 10 dB; the Strouhal number (St) was only slightly higher than that from single square cylinder case ($St = 0.128$). When the cylinder spacing was increased, the spectrum became broader and similar to that in the single square cylinder case (Fig. 2d) for $L/d = 6.0$.

To understand why the sharp spectral peak was observed for the closely-arranged cylinder pair ($L/d = 3.6$), Fig. 3 shows the correlation coefficient (R) which was measured using two hot-wires separated in the spanwise direction, located at the same x/d and y/d coordinates; one hot-wire was fixed at (x/d, y/d, z/d) = (2, 3.3, 13), (2, 3.75, 13) and (2, 4.5, 13) for $L/d = 3.6$, 4.5 and 6.0, respectively, and the other was traversed in the spanwise direction (i.e., $z/d = 13 + \Delta z$). High spanwise coherency ($R > 0.5$) was observed even at $\Delta z \sim 11d$ for the square-cylinder-pair with $L/d = 3.6$. For $L/d = 4.5$, the coherence length was only slightly reduced to $\sim 10d$, while it was considerably reduced to $\sim 5d$ for $L/d = 6.0$ (though still larger than the single-cylinder-case). Thus, the sharp spectrum in the case of two side-by-side square cylinders with $L/d = 3.6$ and 4.5 was no doubt resulted from the high spanwise coherency of vortex shedding. Figure 4 displays a waveform of sound pressure measured by two microphones placed at $y = \pm 1$ m for $L/d = 3.6$. Sound waves were in-phase, which is similar to the numerical result at a low Reynolds number

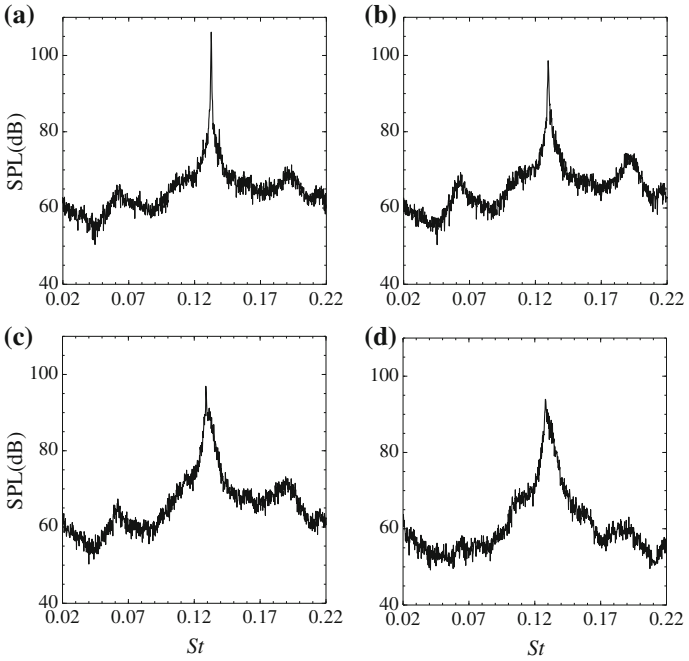


Fig. 2 Spectra of sound pressure for a pair of square cylinders at $U_\infty = 50$ m/s. **a** $T/d = 3.6$, **b** $T/d = 4.5$, **c** $T/d = 6.0$, **d** single cylinder

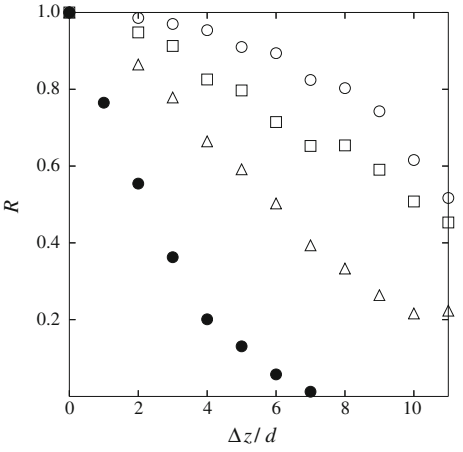


Fig. 3 Correlation coefficient (R) for a pair of square cylinders at $U_\infty = 50$ m/s. ○, $L/d = 3.6$; □, $L/d = 4.5$; △, $L/d = 6.0$; ●, single cylinder ($U_\infty = 52.5$ m/s)

($Re = 150$) by Inoue et al. [3]. The corresponding vortex shedding pattern is shown in Fig. 5 which illustrates an instantaneous vorticity field measured by PIV. The vortex shedding from two cylinders is planar-symmetric, causing in-phase sound radiation.

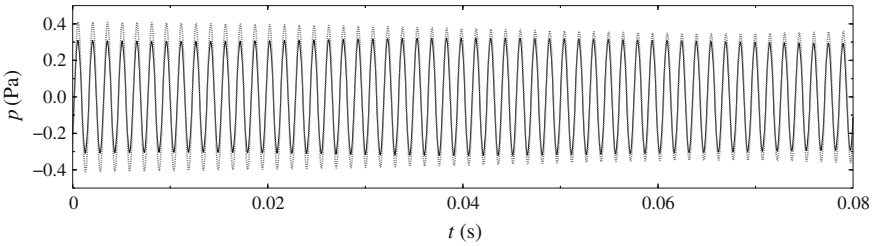


Fig. 4 Waveforms of sound pressure (p) for a pair of square cylinders with $L/d = 3.6$. ——, Microphone 1 ($y = +1$ m); – –, Microphone 2 ($y = -1$ m)

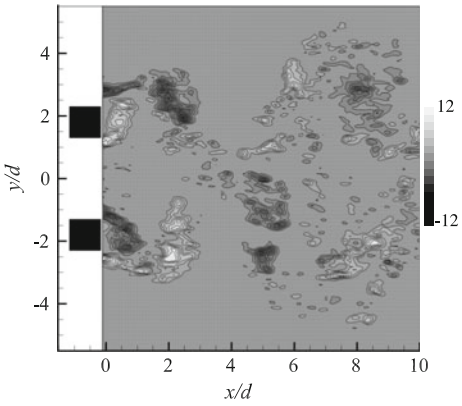


Fig. 5 Instantaneous vorticity ($\omega d/U_\infty$) of square cylinders pair with $L/d = 3.6$ at $U_\infty = 50$ m/s

Next, we examined effects of small-length splitter-plate on sound radiation from a pair of square cylinders with $L/d = 3.6$. Figure 6a displays the waveforms of sound pressure at $y = \pm 1$ m when a small splitter plate of 2 mm long ($c/d = 0.2$) was glued on the back side of each square cylinders. Comparing with the case without splitter plates (Fig. 4), we see that in-phase sound waves were generated, similar to the case in the absent of splitter plates, but the amplitude of sound was significantly reduced; the SPL was reduced by about $6 - 7$ dB. This was also the case for a staggered configuration of 100 mm long splitter plates with $c/d = 0.2$. Another interesting result was obtained when a small splitter plate ($c/d = 0.2$) was installed on one cylinder alone. Figure 6b displays the waveforms of sound pressure in such a case. A very short splitter plate could alter the nature of sound radiation, from in-phase sound to anti-phase sound, though synchronization still occurred with a single frequency. In addition, the SPL measured at $y = +1$ m (the splitter-plate side) was reduced by about 6–7 dB, while SPL measured in the opposite side ($y = -1$ m) was almost the same as that in the absence of splitter plate; compare the amplitudes of sound pressure. Thus, only a tiny splitter plate (like a protuberance) could affect sound generation. Note that the similar effects were observed for splitter plate(s) of $c/d = 0.5$.

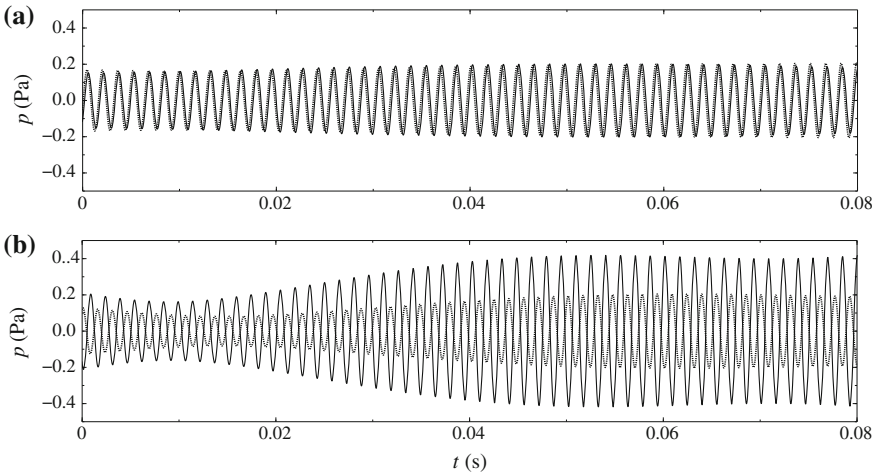


Fig. 6 Waveforms of sound pressure (p). **a** a pair of square cylinders with splitter plates of $c/d = 0.2$; **b** one square cylinder and one square cylinder with splitter plate ($c/d = 0.2$). ——, Microphone 1 ($y = +1$ m); – – –, Microphone 2 ($y = -1$ m)

4 Conclusion

The sound radiation from two side-by-side square cylinders was examined experimentally with $L/d = 3.6,\ 4.5$ and 6.0 mainly at $Re = 3.3 \times 10^4$. It was found that for $L/d = 3.6$ and 4.5, the vortex shedding exhibited a high spanwise coherency compared to that for a single square cylinder, and correspondingly the spectrum of sound pressure became very sharp like a line spectrum. For such cases, in-phase sound radiation corresponding to the planar-symmetric vortex shedding was dominant. It was also found that the sound pressure level was reduced by ∼6 dB when a small splitter plate ($c/d \leq 0.5$) were glued on the rear side of each cylinder. Furthermore, when a splitter plate with $c/d = 0.2$ was applied only to one of the pair of each cylinder, the sound field changed from in-phase to anti-phase.

Acknowledgments This work was, in part, supported by Grant for Scientific Research from Tokyo Metropolitan Government.

References

1. D. Sumner, J. Fluid Struct. **26**, 849 (2010)
2. M.M. Alam, Y. Zhou, X.W. Wang, J. Fluid Mech. **669**, 432 (2011)
3. O. Inoue, W. Iwakami, N. Hatakeyama, Phys. Fluids **18**(4) (2006)
4. H. Fujita, H. Suzuki, A. Sagawa, T. Takaishi, AIAA Paper 99-1849, 305–309 (1999)
5. H. Fujita, Fluid Dyn. Res. **42**(1), 015002 (2010)
6. M.S.M. Ali, C.J. Doolan, V. Wheatley, J. Sound Vib. **330**, 3620 (2011)

Turbulent Jet Noise Simulation and Propagation Using a 3rd Order MUSCL/CD Scheme on Unstructured Grid and Ffowcs-Williams Hawkings

Mirela Caraeni, Alastair West and Doru Caraeni

Abstract The noise generation by a turbulent high speed jet is simulated using Large Eddy Simulation (LES) and a newly implemented MUSCL/CD 3rd order numerical scheme. The acoustic wave propagation in the far-field is performed using a permeable formulation Ffowcs Williams-Hawkings (FW-H) approach, available in the STAR-CCM+ code. The flow-field results and the predicted sound pressure levels are both in good agreement with experiments. The predicted sound pressure levels using LES are within a 1–2 dB deviation for all measured observer locations.

1 Introduction

Demanding noise level regulations at national and international airports have determined aerospace engine manufacturers to increase their efforts to reduce jet noise. These efforts have resulted into numerous experimental and computational studies. For computational studies, turbulence modeling using Large Eddy Simulation (LES) is the method of choice for jet noise research. Although most computational studies have used block-structured high-order finite difference methods [1], Spalart, Shur and Strelets [2] have pointed out the need to develop unstructured-grid methods for such simulations in complex geometries. Today there is a growing interest in unstructured methods for high fidelity turbulence and aeroacoustic simulations, including in jet noise research.

For jet noise simulations, a typical approach to reduce total computational effort is to couple the numerical simulation of turbulence and noise generation, with integral methods, like Ffowcs-Williams Hawkings, to perform the propagation of sound in the far-field.

M. Caraeni (✉) · D. Caraeni
CD-adapco, Lebanon, USA
e-mail: mirela.caraeni@cd-adapco.com

A. West
CD-adapco, London, UK

© Springer International Publishing Switzerland 2016

A. Segalini (ed.), *Proceedings of the 5th International Conference on Jets, Wakes and Separated Flows (ICJWSF2015)*,
Springer Proceedings in Physics 185, DOI 10.1007/978-3-319-30602-5_49

The goal of this study is to demonstrate the capability of the fully-unstructured code, STAR-CCM+, to correctly predict jet noise using Large Eddy Simulation. Compressible LES is conducted for a high subsonic jet with the round nozzle geometry included within the computational domain. The experimental conditions of Jordan et al. [3, 4] were matched, such that the time-averaged flow-field and far-field sound pressure levels could be compared with experimental data.

2 Computational Set-Up

Results from simulations of a Mach 0.75 jet exiting a round nozzle configuration will be presented. The flow properties are summarized in (1) and (2). The Reynolds number was artificially reduced in the same vein as Andersson et al. [5], with the assumption that the flow is only weakly Reynolds number dependent. Thus, the Reynolds number based on nozzle exit diameter and jet velocity at the nozzle exit plane, Re_D is 50,000 (that of the experiment is Re_D 10^6).

Mach	T_j/T_∞	P_∞ (Pa)	ρ (kg/m^3)	c_∞(m/s)
0.75	1.0	99,670	1.225	337.75

(1)

U_∞ (m/s)	T_∞ (K)	P_j (Pa)	Re_D
0.0	283.15	144,400	50,000

(2)

The nozzle dimensions are those of the JEAN (Jet Exhaust aerodynamics and Noise) project nozzle [3, 4] which has a nozzle length of 0.38 m and an exit diameter of 0.05 m. The axial length of the domain is 80 D_j and the radial distance extends from 80 D_j to 120 D_j at the far-field inlet and outlet boundaries respectively. An unstructured grid topology using trimmed hexahedra and boundary prismatic cells was constructed using 6 successive 8:1 volumetric refinements towards the jet nozzle exit and initial shear-layer area (see Fig. 1). The total number of cells is 23 million.

The flow conditions at the nozzle inlet: $\mathrm{Mach}_\infty = 0.16$, Pressure = 44800 Pa, Temperature = 315 K, have been specified as constant profiles, to match the experimental condition at nozzle jet exit, e.g. Mach = 0.75.

All external fluid boundaries use non-reflecting free-stream boundary conditions (based on characteristics theory) and are positioned far enough from the nozzle jet exit such as to minimize the acoustic reflections produced by turbulence vortical structures traveling through the exit boundary. To completely eliminate this spurious acoustic reflections the Acoustic Suppression Zone model in STAR-CCM+ has been used to complement the free-stream characteristics based boundary conditions. This model adds an appropriate damping source term to the solved equation system:

$$\frac{\sigma_{\max}}{2}(1+\cos(\pi\frac{d}{w}))(Q-\overline{Q}) \tag{3}$$

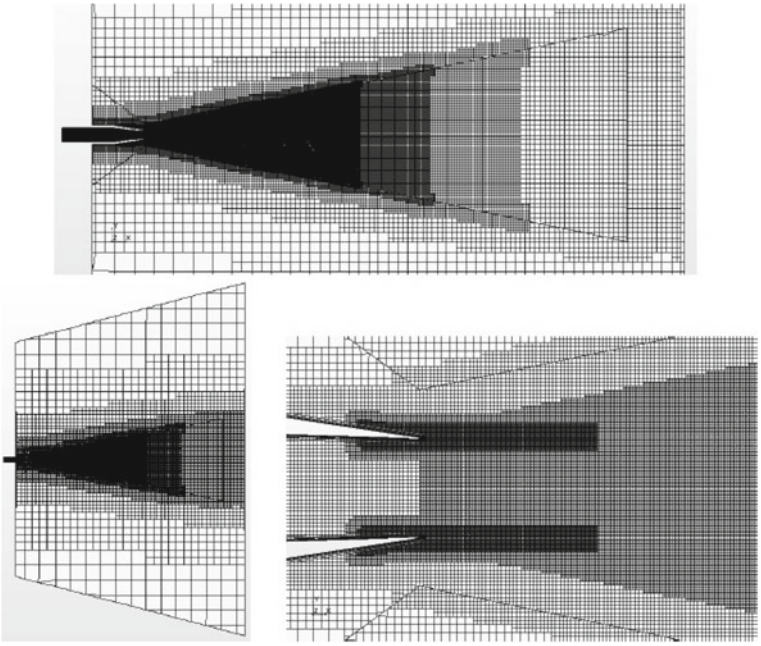


Fig. 1 Unstructured grid topology using trimmed hexahedra and boundary prismatic cells

where Q is the vector of conserved variables (ρ, ρU_i, ρE) and $\overline{Q}$ is their time-average, $\sigma_{\max} = 1000\,\mathrm{s}^{-1}$ is the inverse of the relaxation time-scale, w is the suppression zone thickness, $w = 5\ D_j$, and d is the distance from the external boundary to the cell-centroid. The effect of the introduced source term is to exponentially damp the unsteady flow-field towards a (time-mean) steady field given by $\overline{Q}$, as it approaches the external fluid boundaries, to completely eliminate any acoustic reflection.

3 Numerical Method

A cell-centered finite-volume algorithm on unstructured-mesh with arbitrary polyhedral cells has been employed. An implicit unsteady Pressure-based algorithm is applied, with Rhie-Chow dissipation to avoid spurious pressure oscillations [6]. The temporal integration scheme is 2nd order with 5 inner iterations per time step (Under-relaxations factors of 0.9 and 0.8 were used for the velocity and pressure solvers, respectively). The Least-Squares gradient reconstruction method, with the Min-Mod gradient reconstruction limiter is used, with Total Variation Bounded (*TVB*) gradient limiting, with the acceptable field variation set to 0.1 (10 %). The 3rd order MUSCL/CD scheme was used for convection, with Upwind Bounding Factor of 0.15, and 2nd order for diffusion. The ideal gas law, $\rho = p/RT$ is used for the constitutive equation.

For Large-Eddy Simulation modeling the Dynamic Smagorinsky SGS model proposed by Germano et al. [7] was used, with the least-squares minimization procedure proposed by Lilly [8].

3.1 Hybrid MUSCL 3rd-Order/CD

For convection scheme, the hybrid MUSCL 3rd order /CD is recommended for high-fidelity turbulence (LES/DES), aeroacoustic and aerodynamic simulations. The MUSCL 3rd order/CD can be used for both steady and unsteady simulations, where one model parameter σ is used to control the numerical dissipation in the scheme. Similar as the Bounded Central-Differencing scheme, this hybrid MUSCL 3rd order /CD uses a Normalized-Variable Diagram (NVD) value ς to ensure the boundedness of the scheme by switching to the first-order scheme in regions of non-smooth flows. When smooth local flow conditions are detected, the hybrid MUSCL 3rd order /CD is constructed as a blend between a MUSCL 3rd order upwind and the 3rd order central-differencing reconstruction schemes.

The convective flux is computed as following:

$$(\dot{m}\phi)_f = \begin{cases} \dot{m}\phi_{\text{fou}} & \text{for} \quad \varsigma < 0 \quad \text{or } 1 < \varsigma \\ \dot{m}(\sigma\phi_{\text{muscl3}} + (1-\sigma)\phi_{\text{cd3}}) & \text{for} \quad 0 \le \varsigma \le 1 \end{cases} \tag{4}$$

The upwind blending factor σ is user-controlled and must be decided based on the physical problem or model (and mesh quality considerations). For the same jet noise application, the authors published a study [9], where the sensitivity of the aerodynamic computation and aerodynamic noise prediction for far-field to the different upwind blending factor of $\sigma = 0.02$, 0.15 and 0.5 was assessed.

The MUSCL 3rd order upwind reconstructed value ϕ_{muscl3} is limited at high speeds so as to not affect the formal order of accuracy while preventing spurious oscillations. The high speed limiting is based on WENO (Weighted Essentially Non-Oscillatory) principles and is only applied to the quadratic part of the face-value reconstruction. WENO-based averaging is computed based on three different stencils. In the regions next to the strong shocks, the ϕ_{muscl3} accuracy is reduced to second order. The switch between the unlimited and the WENO-limited ϕ_{muscl3} is done based on a Mach-number-based flux-limiter. For incompressible simulations, ϕ_{muscl3} is unlimited (the flux limiter is 1), thus only relying on the use of the NVD (Normalized-Variable Diagram) value ς to ensure the boundedness of the scheme.

The hybrid MUSCL 3rd order /CD scheme provides improved (reduced) dissipation when compared with both second-order and Bounded Central Differencing (BCD) schemes. It is robust (due to its boundedness) and capable of simulating steady and unsteady flows from incompressible to high-speed compressible regimes.

3.2 Ffowcs-Williams Hawkings algorithm

Due to the high computational cost of direct simulations, a hybrid method is proposed to evaluate the far-field sound propagation. Firstly, all near-field sources of sound are simulated using LES modeling. Then the Ffowcs-Williams Hawkings (FW-H) acoustic analogy gives the propagation of sound into far field using the near-field sound sources as the input.

This aeroacoustic model is based on the Farassat's Formulation 1*A* of the FW-H analogy [10] which uses an advanced-time formulation (or source time dominant algorithm) proposed by Casalino [11]. This yields the far-field acoustic pressure fluctuations computed using the FW-H surface integral formula:

$$\begin{aligned} 4\pi p(\underline{x},t) = & \int_S \left[\frac{\rho_0(\dot{U}_n + U_{\dot{n}})}{r(1-M_r)^2} + \frac{\rho_0 U_n(r\dot{M}_r + c_0 M_r - c_0 M^2)}{r^2(1-M_r)^3} \right]_{ret} \mathrm{d}S \\ & + \frac{1}{c_0} \int_S \left[\frac{\dot{L}_r}{r(1-M_r)^2} + \frac{L_r(r\dot{M}_r + c_0 M_r - c_0 M^2)}{r^2(1-M_r)^3} \right]_{ret} \mathrm{d}S \\ & + \int_S \left[\frac{L_r - L_M}{r^2(1-M_r)^2} \right]_{ret} \mathrm{d}S \end{aligned} \tag{5}$$

where the first term is the thickness noise, where $U_i = \rho u_i/\rho_0 + v_i(1-\rho/\rho_0)$ and the second and third terms are the loading noise, where $L_i = P_{ij}n_j + u_i(u_n - v_n)$. On the loading noise term, one defines $P_{ij} = (p-p0)\delta_{ij} - \sigma_{ij}$ as the compressive stress tensor and σ_{ij} as the viscous stress tensor. Here, ρ_0 is the far-field reference density, v_i is the velocity at the surface and $M_i = v_i/c_0$ is the surface Mach number vector based on the far-field speed of sound c_0. Dots on quantities denote time derivative with respect to the source time. Subscripts denote a scalar product with either the surface outer normal, unit vector n_i, the unit radiation direction vector $\hat{r}_i$ or the Mach number vector M_i as $\dot{M}_r = \dot{M}_i r_i$.

This formulation explicitly omits the quadrupole volume integral, which reduces the computational time. The quadrupole volume integral omission does not mean that the quadrupole generated noise is not captured. By using permeable FW-H surface integrals proposed by di'Francescantonio [12], non-negligible volumetric sources can be taken into account. The FW-H permeable formulation describes the noise source terms distributed on the surface, as monopole and dipole terms, and the contribution to the total noise of volumetric sources enclosed by the integration surface. This formulation assumes that the contribution to the total noise of volumetric sources outside a chosen integration surface is negligible. For more details about the implementation the reader is referred to Caraeni et al. [13].

The permeable FW-H surface used is an open cone shape of length 62 D_j, shown in Fig. 2. The open shape results in some contamination at the very high frequency range which has been reported by Shur et al. [14] and Mendez et al. [15] (among others). For this reason a band-pass filter is used to cut off the lower frequencies when calculating overall sound directivity ($0.05 < S_t < 2.0$).

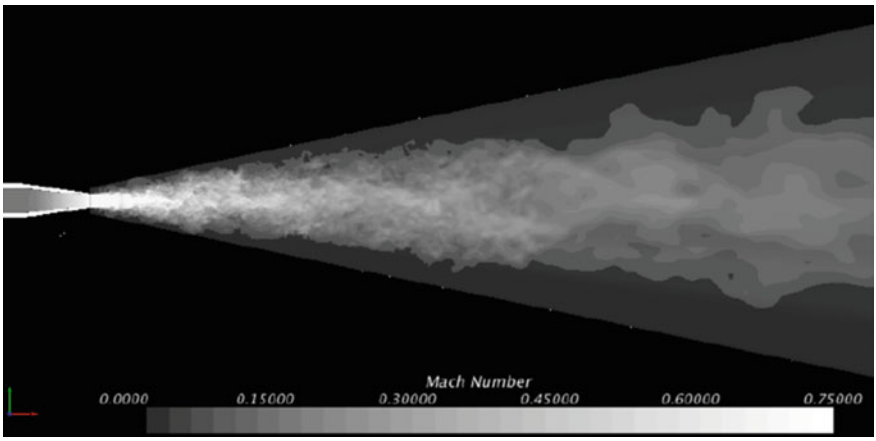


Fig. 2 View of permeable FW-H surface with Mach number field

4 Results

The unsteady simulation was started from a steady RANS simulation. Averaging and sampling began once a statistically steady flow was obtained, roughly 0.03 s of simulated time, using a time step of $\Delta t = 0.05D/Uj$ [10^{-5} s], computing the far-field noise at the same time-step as unsteady LES simulation. Sampling of statistical data was then gathered for a sampling interval of $T_{sampling} = 10,000\ D/Uj$ [0.1 s]. Therefore, the resolved frequencies are theoretically bounded by the time step of sampling (here every time step) and the length of the sampling time interval, giving $St_{max} = 1/(2\Delta t) = 10$[50 kHz] and $St_{min} = 1/T_{sampling} = 0.002$[10 Hz]. However in reality this range is narrower as the functions are not perfectly periodic in time so resolved frequencies corresponding to periods will be typically 5–10 times less than the sampling time (so $St_{min} \simeq 0.01 - 0.02$) [16]. Similarly mesh resolution means that only sound waves longer than say 6 cells can be accurately resolved, i.e. $St_{max} = c_\infty/(6\Delta)$. Therefore the maximum frequency resolution decreases from $\mathrm{St}_{max} = 5.5$ where FW-H surface is closest to the nozzle exit, to $\mathrm{St}_{max} = 0.52$ downstream approaching the outlet where the cell size Δ is coarse. Some authors argue that this is the reason for using a band-pass filter to cut-off low frequencies at 255 Hz, respective cut-off high frequencies at 5100 Hz. However, if the mesh is unable to resolve these frequencies they should not contribute much to the overall sound intensity.

For the time-averaged statistics averaging was performed both in time and over the azimuthal direction. Figures 3 and 4 show the mean streamwise velocity, U and mean streamwise turbulence intensity $\sqrt{\overline{u'^2}}$ along the jet centerline axis, compared to the experiment. The length of the potential core is underpredicted by the LES, with predictions coming rather close to the experiment. Our LES result is very similar to

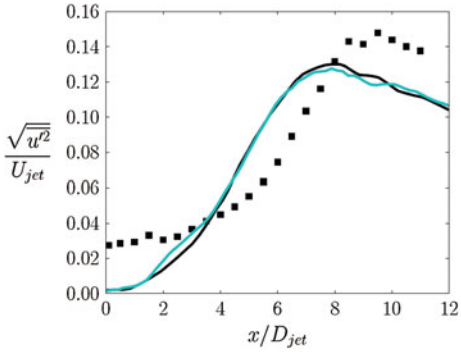


Fig. 3 Time-averaged centerline velocity along axis centerline

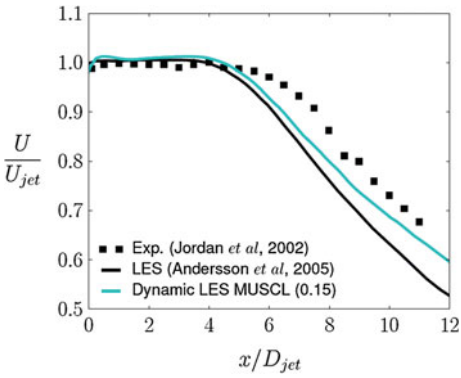


Fig. 4 Time-averaged axial profile of streamwise rms of velocity

the LES results of Andersson et al. [5] matching the center-line velocity and rms velocity closely.

This is hardly surprising because this LES simulation and Andersson LES simulation use the same laminar inflow conditions, which are clearly different from those used in the experiment. From Fig. 4 the streamwise turbulence intensity is approaching 3 % at the nozzle exit. This result conflicts with Jordan et al's subsequent measurement of the same streamwise turbulent intensity and they noticed the difficulty in maintaining a controlled environment and the lack of flow conditions within the settling chamber causing a low frequency flutter of the potential core.

Figure 5 shows the predicted far-field sound pressure levels (SPL) compared to the levels measured by Jordan et al. [4] ±5 dB of the experimental data at the far-field observer locations. Overall sound pressure levels (OASPL) are normally obtained using all the spectral information available. However previous authors (Shur et al. [14] and Andersson et al. [5]) use the frequency range $0.05 < St < 1.0$ so these results are displayed. The predicted sound pressure levels using LES are within a 1–2 dB deviation for all measured observer locations, with most observer locations within 1 dB. On the same authors published study [9], there were investigated two convective schemes: BCD scheme with upwind blending factor 0.02 and MUSCL-3rd order/CD scheme for different upwind blending factor of $\sigma = 0.02$, 0.15 and 0.5.

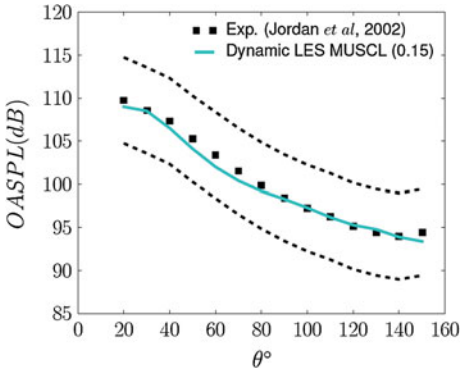


Fig. 5 OASPL at microphone locations from nozzle exit at 30 Dj

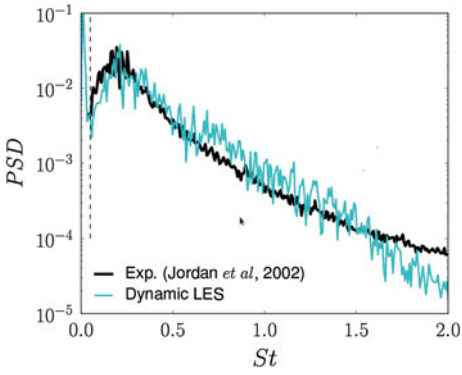


Fig. 6 PSD of far-field pressure fluctuations at 20°, at 30D compared with measurements by Jordan et al.

It was observed the well-known behaviour that even small contributions of upwind blending can introduce enough numerical dissipation to delay the onset of turbulence by dampening the turbulent structures that LES wants to capture. Selected simulation with MUSCL-3rd order/CD convective scheme using $\sigma = 0.15$ appears to be the correct balance between the sub-grid scale viscosity and numerical dissipation introduced by the convective scheme because the break-up of the shear layer occurs smoothly without vigorous roll-up and vortex pairing. This leads to lower degree of mixing and consequently a longer potential core length.

Far-field sound pressure levels have the highest deviation corresponding to lower angles ($50° < \theta < 80°$). Figure 6 shows the power spectral density of far-field pressure fluctuations compared to those measured by Jordan et al. [4] for 20 observer angles at $30D$. The predictions of the lowest and highest angles are in good agreement with the experimental data. The experimental results do not show any tonal peak, and no clear tonal frequency was observed in the above simulation, on any of the observer angles.

Acknowledgments The authors would like to thank Mr. Richard Clayton and Dr. Paul Dawson for fruitful discussions on this topic.

References

1. S. Mendez, M. Shoeybi, A. Sharma, F. Ham, S. Lele, P. Moin, Large-eddy simulations of perfectly-expanded supersonic jets: Quality assessment and validation, in *48th AIAA Aerospace Sciences Meeting Including the New Horizons Forum and Aerospace Exposition, AIAA 2010–271*, vol. 271, Orlando, Florida (2010)
2. M. Spalart, M. Shur, M. Strelets, Identification of sound sources in large-eddy simulations of jets, in *13th AIAA/CEAS Aeroacoustics Conference (28th AIAA Aeroacoustics Conference), AIAA 2007–3616*, Rome, Italy (2007)
3. P. Jordan, Y. Gervais, J.-C. Valiere, H. Foulon, Final results from single point measurements, in *Project deliverable D3.6, JEAN-EU 5th Framework Programme, G4RD-CT2000-00313* (2002)
4. P. Jordan, Y. Gervais, J.-C. Valiere, H. Foulon, Results from acoustic field measurements, in *Project deliverable D3.6, JEAN-EU 5th Framework Programme, G4RD-CT2000-00313* (2002)
5. N. Andersson, L.E. Eriksson, L. Davidson, Investigation of an isothermal Mach 0.75 jet and its radiated sound using large-eddy Simulation and Kirchhoff surface integration. Int. J. Heat Fluid Flow **26**(3), 393–410 (2005)
6. I. Demirdzic, S. Muzaferija, Numerical method for coupled fluid flow, heat transfer and stress analysis using unstructured moving meshes with cells of arbitrary topology. Comput. Methods Appl. Mech. Eng. **125**(1), 235–255 (1995)
7. M. Germano, U. Piomelli, P. Moin, W. H. Cabot, A dynamic subgrid–scale eddy viscosity model. Phys. Fluids A Fluid Dyn. (1989–1993) **3**(7), 1760–1765 (1991)
8. D.K. Lilly, A proposed modification of the Germano subgrid–scale closure method. Phys. Fluids A: Fluid Dyn. (1989–1993) **4**(3), 633–635 (1992)
9. M. Caraeni, A. West, Jet noise prediction using a permeable FW-H solver, in *21st AIAA/CEAS Aeroacoustics Conference, AIAA 2015–2371*, Dallas, TX (2015)
10. F. Farassat, G.P. Succi, A review of propeller discrete frequency noise prediction technology with emphasis on two current methods fortime domain calculations. J. Sound Vibr. **71**(3), 399–419 (1980)
11. D. Casalino, An advanced time approach for acoustic analogy predictions. J. Sound Vibr. **261**(4), 583–612 (2003)
12. P. di Francescantonio, A new boundary intergral formulation for the prediction of sound radiation. J. Sound Vibr. **202**(4), 491–509 (1997)
13. M. Caraeni, O. Aybay, S. Holst, Tandem cylinder and idealized side mirror far-field noise predictions using des and an efficient implementation of FW-H equation, in *17th AIAA/CEAS Aeroacoustics Conference, AIAA 2011–2843*, Portland, Oregon (2011)
14. M. Shur, P. Spalart, M. Strelets, Noise prediction for increasingly complex jets. Part I: methods and tests. Int. J. Aeroacoust. **4**(3), 243–285 (2005)
15. S. Mendez, A. Sharma, M. Shoeybiand, S. Lele, *Post-processing of large-eddy simulations for jet noise predictions* (Center for Turbulence Research, Stanford University, Annual Research Briefs, 2009)
16. M.L. Shur, P.R. Spalart, M.K. Strelets, A.K. Travin, Towards the prediction of noise from jet engines. Int. J. Heat Fluid Flow **24**(4), 551–561 (2003)

Investigation of the Effect of a Realistic Nozzle Geometry on the Jet Development

Mehmet Onur Cetin, Matthias Meinke and Wolfgang Schröder

Abstract Highly resolved large-eddy simulations (LES) of a helicopter engine jet including the nozzle geometry are performed. A flow solver for compressible flow based on hierarchically refined Cartesian meshes and a conservative cut-cell method is used for the computations. The impact of the nozzle geometry on the jet development is analyzed for two variants of the nozzle geometry, a simplified geometry with only a center body and the full geometry of the engine nozzle including four struts which support the center body. A synthetic turbulence formulation is used to prescribe inlet boundary conditions for the nozzle, which mimic the exit conditions after the last turbine stage. To verify the numerical method, a single cold round jet is computed and the results are compared to reference data. Results for the helicopter engine jet are presented for the time-averaged velocity field and turbulence intensities.

1 Introduction

Most studies for the prediction of jet flows have been conducted for simplified inlet conditions for the jet without taking into account the details of the nozzle geometry to keep the required computational resources within reasonable limits, e.g. [1–3]. However, the jet development in the near field of the jet with the potential core region, where significant noise sources are generated, is strongly influenced by the turbulence level and length scales at the nozzle exit. Therefore, it can be assumed that geometric details upstream of the nozzle exit generating a specific turbulence field should not be neglected and the engine nozzle should be included in the flow

M.O. Cetin (✉) · M. Meinke · W. Schröder
Institute of Aerodynamics, RWTH Aachen University,
Wüllnerstr. 5a, 52062 Aachen, Germany
e-mail: office@aia.rwth-aachen.de

M. Meinke · W. Schröder
Forschungszentrum Jülich, JARA – High-Performance Computing,
52425 Jülich, Germany

© Springer International Publishing Switzerland 2016

A. Segalini (ed.), *Proceedings of the 5th International Conference on Jets, Wakes and Separated Flows (ICJWSF2015)*,
Springer Proceedings in Physics 185, DOI 10.1007/978-3-319-30602-5_50

domain to obtain a more realistic jet flow field. In this study, the impact of a realistic helicopter engine nozzle on the jet development is studied by simulating the jet for two variants of the engine nozzle geometry, i.e., a baseline nozzle geometry including only a centerbody, referred to as "Model 1", and a nozzle including the center body and four support struts, referred to as "Model 2". The simulations that include the engine nozzle involve a high mesh resolution, since the boundary layers on the nozzle wall have to be adequately resolved to avoid, e.g., unphysical boundary layer separation in the divergent section of the nozzle, and also the larger scales of turbulent structures generated downstream of the centerbody have to be captured accurately. To verify that the mesh resolution is adequate for the prediction, a grid convergence study for Model 1 is performed, where a fine mesh with 330 million cells and a very fine mesh with 1097 million mesh cells are used. The numerical method, the computational domain, and the boundary conditions are briefly outlined in Sect. 2. First, the results for a validation test and subsequently, for a jet including the nozzle are discussed in Sect. 3. Finally, conclusions are drawn in Sect. 4.

2 Numerical Method

A computational method based on a finite volume scheme is used to solve the spatially filtered Navier-Stokes equations for compressible, unsteady, and turbulent flow. An implicit grid filter is assumed and the LES model corresponds to the monotone integrated large-eddy simulation (MILES) approach [4], i.e., the dissipative truncation error of the numerical scheme is responsible to mimic the dissipation of the unresolved subgrid scale stresses. The convective fluxes of the governing equations are formulated by a low dissipation version of the advection upstream splitting method (AUSM) [5]. The cell center gradients are computed using a second-order accurate least-squares reconstruction scheme [6], i.e., the overall spatial approximation is second-order accurate. For stability reasons, small cut-cells are treated using an interpolation and flux-redistribution method developed by Schneiders et al. [7]. A second order 5-stage Runge-Kutta method is used for the temporal integration. This solution method has been validated and used successfully with several test cases, see e.g. [1, 8, 9]. A Cartesian unstructured fully parallel mesh generator with hierarchical mesh refinement is used for the grid generation [10]. Further details of the numerical methods, i.e., the discretization and computation of the viscid and inviscid fluxes, are given in [5].

2.1 Computational Setup

The inlet of the domain is located downstream of the last turbine stage. Corresponding flow conditions are set at the inlet boundary which are taken from the measurements of a full scale turbo-shaft engine [11]. Isotropic synthetic turbulence is

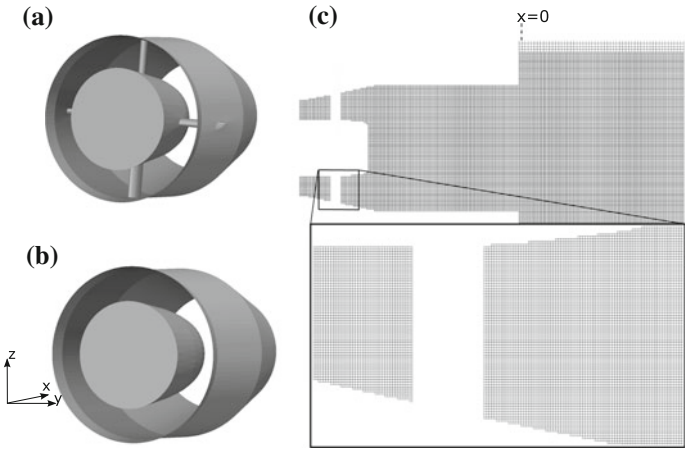


Fig. 1 **a** Geometry of the Model 2, **b** geometry of the Model 1, **c** 2D view of a coarse Cartesian mesh with 41 million cells for the Model 2, where the zoomed view shows the resolution of the fine mesh

generated at the inlet plane with a turbulence intensity of approx. 10 % [12]. For the outflow and lateral boundaries of the jet domain, the static pressure is set to be constant and other variables are extrapolated from the internal domain along linearized characteristics. To damp numerical reflections at the boundaries, sponge layers are used [13]. At the nozzle wall, the no-slip condition with a zero wall-normal pressure gradient and adiabatic wall conditions are applied. Figure 1a and b show the interior of the two nozzle variants. The ratio of the radii of the center body and the exit cross section is $R_{cb}/R = 0.42$ and the ratio of the chord length and the maximum radial extent of the struts is $C_s/R_s = 0.57$. Two meshes, i.e., a fine and a very fine grid, are generated for Model 1 by a Cartesian unstructured grid generator [10] to analyze the impact of the grid resolution on the jet development. Computational details are given in Table 1. The computation and sampling time are chosen large enough to ensure

Table 1 Simulation parameters

	Model 1 very fine	Model 1 fine	Model 2 fine	Validation Test
Mach number	0.341	0.341	0.341	0.9
Re number	7.5×10^5	7.5×10^5	7.5×10^5	4×10^5
Mesh points	1097×10^6	329×10^6	328×10^6	58×10^6
Min. cell length	$\Delta_{x,y,z} = 0.00148D$	$\Delta_{x,y,z} = 0.00297D$	$\Delta_{x,y,z} = 0.00297D$	$\Delta_{x,y,z} = 0.019D$
Simulation time	$440D/u$	$480D/u$	$480D/u$	$720D/u$
Mean flow sampling	$210D/u$	$260D/u$	$260D/u$	$140D/u$
Number of samples	3000	2250	2250	3125

convergence of the statistical data. The domain possesses a streamwise and radial extent of 36 and 16 diameters for the validation study and 42 and 32 diameters for the jet with nozzle. There are 336 grid points in the radial direction at the nozzle-exit for the fine meshes. Figure 1c illustrates the structure of the Cartesian mesh.

3 Results

3.1 Validation Test

To validate the numerical method, a round jet exhausting into a quiescent air at standard room conditions with $\mathrm{M} = \frac{U_j}{a} = 0.9$ and $\mathrm{Re}_D = \frac{\rho U_j D}{\eta} = 4 \times 10^5$ is simulated, where U_j is the inflow velocity at the centerline, a the speed of sound, D the jet diameter, ρ the density and η the dynamic viscosity. The results are compared to data from previous studies [1, 2, 14, 15]. To promote the transition to turbulence, the jet is forced via vortex rings [2] plus random perturbations, that are only introduced in the shear layer of the jets, defined by a hyperbolic-tangent velocity profile [2]. The streamwise velocity profiles are compared in Fig. 2. In agreement with the reference results, the velocity decays downstream of the potential core at about $x \approx 10R$ in Fig. 2a, where R is the radius of the jet defined at the inlet of the computational domain $R = D/2$. The streamwise profile of the RMS value of the axial velocity fluctuations is illustrated in Fig. 2b. The comparison shows a slight discrepancy of the axial location and the magnitude of the peaks, due to the different numerical method and the mesh resolution used for the present simulation. In general, however, it can be stated that there is a reasonable agreement between the reference data and the results of the present method.

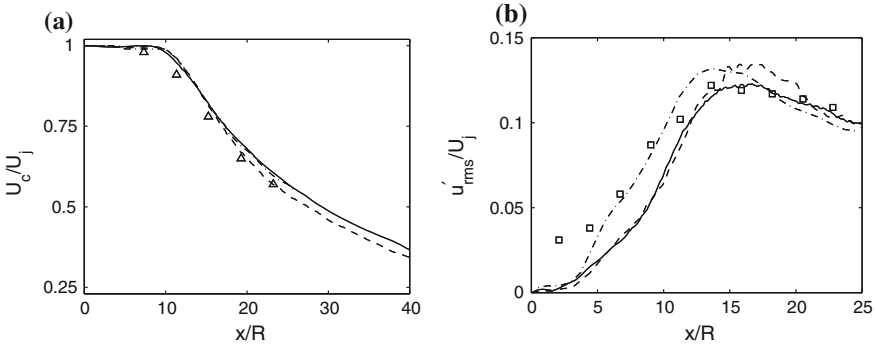


Fig. 2 Streamwise distributions of the **a** axial velocity and **b** axial turbulence intensity for: (—) current simulation ($M = 0.9, Re_D = 4 \times 10^5$), (-·-) Bogey et al. [2] ($M = 0.9, Re_D = 4 \times 10^5$), (−−) Koh et al. [1] ($M = 0.9, Re_D = 4 \times 10^5$), (△) Lau et al. [15] ($M = 0.9, Re_D = 10^6$) and (□) Arakeri et al. [14] ($M = 0.9, Re_D = 5 \times 10^5$)

3.2 *Influence of the Engine Nozzle*

LES of the helicopter engine jet including the engine nozzle are performed. The decay of the centerline velocity and the turbulence intensity profile of the streamwise velocity component are illustrated in Fig. 3 for Model 1 for the fine and very fine mesh, and for Model 2 for the fine mesh. The comparison of the results for the fine and very fine mesh for Model 1 indicates the results to be grid converged, since there are only slight differences in the results for the two meshes.

Comparing the results for Model 1 and 2 shows that the jet develops substantially different until the end of the unperturbed core is reached, while downstream of the core the centerline velocity profile for the two nozzle geometries are quite similar. The presence of the 4 struts in Model 2 is obviously responsible for a higher turbulence intensity and consequently, an enhanced mixing, which leads to a smaller centerline velocity and a shorter core length of the jet. This result is confirmed by the results in Fig. 3b, where the profile of the streamwise velocity fluctuations along the streamwise direction is shown. Two maxima in the turbulence intensity profile are visible, where the first peak occurs downstream of the centerbody in the nozzle due to the flow separation at approx. x $\approx -1.2R$ where R is the nozzle exit radius, where also a negative axial velocity occurs. The second peak occurs at the end of the core region at about x $\approx 10.5R$. Comparing the values for the turbulence intensity for Model 1 and 2, a 20 % higher turbulence intensity due to the struts can be observed in the region $x/R < 0$, i.e., inside the nozzle. The turbulence intensity at the end of the potential core at $x/R \approx 10$ is 15 % lower. This comparison shows that the wake of the struts interacts with the wake of the bluff-body, which amplifies the turbulent intensity upstream of the nozzle exit. The existence of the struts diminishes, however, the turbulence intensity at the end of the core. This is important, since the most dominant noise sources occur in this region.

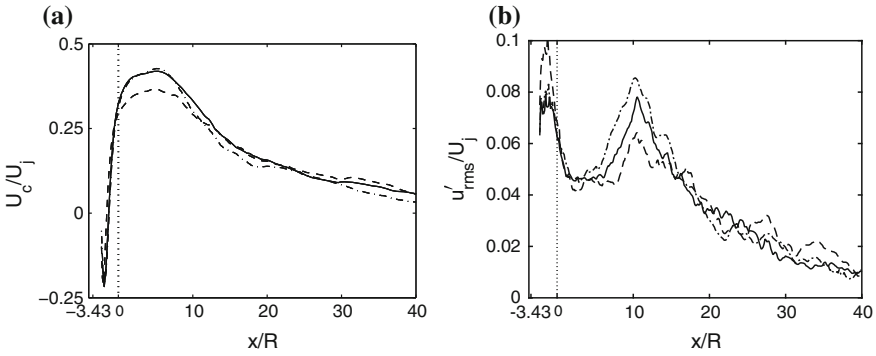


Fig. 3 Streamwise distributions of the **a** axial velocity and **b** axial turbulence intensity for: (—) Model 1 fine, (-·-) Model 1 very fine, (−−) Model 2 fine

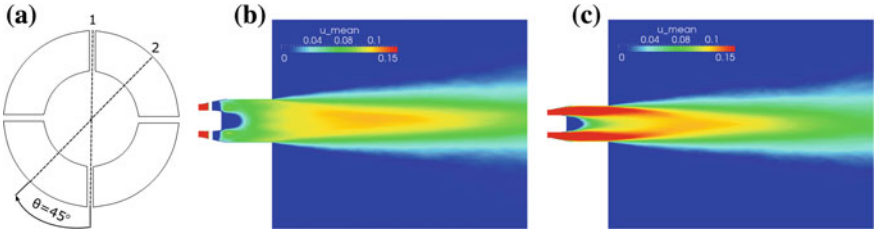


Fig. 4 **a** Cross section of the nozzle geometry for Model 2 at x $\approx -2.8R$. Time-averaged countours of the axial velocity component for Model 2 (**b**) at plane 1, (**c**) at plane 2

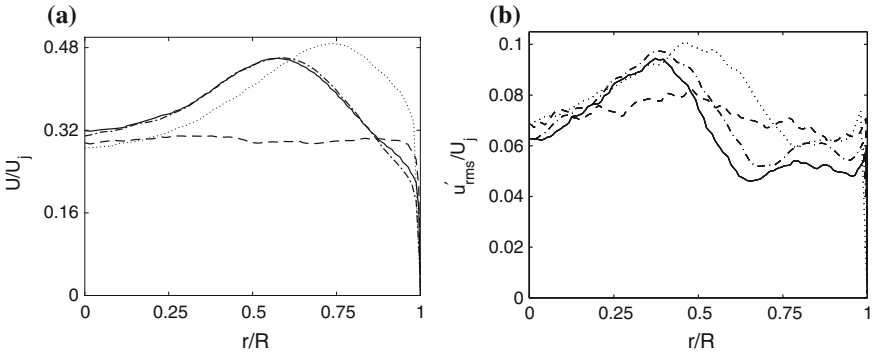


Fig. 5 Radial distributions at the nozzle exit $x/D = 0$ for **a** axial velocity and **b** axial turbulence intensity for: (—) Model 1 fine, (-·-) Model 1 very fine, (−−) Model 2 fine at plane 1, and (···) Model 2 fine at plane 2

To analyze the mean flow field for Model 2 in more detail, contours of the axial velocity component are illustrated in two planes in Fig. 4. It can be seen that the effect of the non-axisymetry of the nozzle geometry on the flow field is still visible downstream of the nozzle-exit and only vanishes after the core region.

Finally, Fig. 5 presents the radial profiles of the axial velocity and RMS axial-velocity fluctuations at the nozzle-exit for Model 1 and 2. It is obvious that the profiles for Model 1 and 2 differ substantially due to the four struts. Furthermore, Model 2 shows a strongly non-axisymmetric flow field. The wake of the struts reduces the magnitude of the velocity distribution such that an almost flat distribution is obtained at the nozzle exit. Between the struts in plane 2, the axial velocity shows a higher maximum value which is also located at a larger radius such that a stronger shear occurs in this region. The comparison of the axial turbulence intensity profiles in Fig. 5b shows the pronounced impact of the struts on the turbulence intensity. Due to the higher shear in plane 2 of Model 2 a higher turbulence intensity can be observed which peaks at a larger radius compared to Model 1.

4 Conclusion and Outlook

LES results for a helicopter engine jet including details of the nozzle geometry were presented. A grid convergence study for a simplified nozzle showed a resolution with approx. 329 million cells to be sufficient for the simulation. Two geometries of the helicopter engine nozzle were used to analyze their impact to the jet development. The presence of four struts noticeably changes the results for the velocity distribution and the turbulence intensity in the core region of the jet. The struts enhance the turbulence mixing inside the nozzle and reduce the centerline velocity as well as the turbulence intensity of the axial velocity component in the core region of the jet. Next, the impact of the nozzle geometry on the aeroacoustic noise will be studied based on a hybrid LES-CAA method.

Acknowledgments The research was funded by the European Community's Seventh Framework Programme (FP7, 2007–2013) PEOPLE programme under the grant agreement No. FP7-290042 (COPAGT project). The authors gratefully acknowledge access to the computing hardware of the High Performance Computing Center Stuttgart (HLRS) and FZ Jülich (JSC).

References

1. S.R. Koh, W. Schröder, M. Meinke, Comput. Fluids **78**, 24 (2013)
2. C. Bogey, C. Bailly, AIAA J. **43**(5), 1000 (2005)
3. J.B. Freund, J. Fluid Mech. **438**, 277 (2001)
4. J.P. Boris, F.F. Grinstein, E.S. Oran, R.L. Kolbe, Fluid Dyn. Res. **10**(4–6), 199 (1992)
5. M. Meinke, W. Schröder, E. Krause, T. Rister, Comput. Fluids **31**(4), 695 (2002)
6. D. Hartmann, M. Meinke, W. Schröder, Comput. Fluids **37**(9), 1103 (2008)
7. L. Schneiders, D. Hartmann, M. Meinke, W. Schröder, J. Comput. Phys. **235**, 786 (2013)
8. M. Konopka, M. Meinke, W. Schröder, AIAA J. **50**(10), 2102–2114 (2012)
9. N. Alkishriwi, M. Meinke, W. Schröder, Comput. Fluids **37**(7), 786–792 (2008)
10. A. Lintermann, S. Schlimpert, J.H. Grimmen, C. Günther, M. Meinke, W. Schröder, Comput. Methods Appl. Mech. Eng. **277**, 131 (2014)
11. B. Pardowitz, U. Tapken, K. Knobloch, F. Bake, E. Bouty, I. Davis, G. Bennett, in *20th AIAA/CEAS Aeroacoustics Conference* (2014)
12. R.P. Kunnen, C. Siewert, M. Meinke, W. Schröder, K.D. Beheng, Atmosph. Res. **127**, 8–21 (2013)
13. J.B. Freund, AIAA J. **35**(4), 740–742 (1997)
14. V. Arakeri, A. Krothapalli, V. Siddavaram, M. Alkislar, L. Lourenco, J. Fluid Mech. **490**, 75 (2003)
15. J.C. Lau, P.J. Morris, M.J. Fisher, J. Fluid Mech. **93**(1), 1 (1979)

Linear Stability Analyses and Large Eddy Simulations for Acoustic Wave Generation Mechanism of a Transitional Supersonic Jet

Taku Nonomura and Kozo Fujii

Abstract The flow fluctuation and acoustic waves generated in a transitional supersonic jet are investigated by a linear stability analysis (LSA) and a large-eddy simulation (LES). Using the LSA code developed here and the LES results reported previously, the development of an instability wave and the transition behavior are discussed. As predicted by the LSA code, helical modes are more unstable than axisymmetric modes in LES results. The LES results show that the fluctuation of the helical mode leads to the transition, but sound generation from the transition is much weaker than that from a subsonic transitional jet investigated in the previous studies.

1 Introduction

A supersonic jet is observed in the exhausts of jet engines for supersonic airplanes or the rocket engines, and it radiates significantly strong acoustic waves which cause the engineering problems. A group of the present authors conducted series of analyses of acoustic waves from a supersonic jet and tried to establish a highly accurate prediction method of acoustic waves from rocket plumes. The acoustic waves generated from a supersonic jet can be categorized into following four kinds of acoustic waves: (1) acoustic waves from the large scale structure of turbulence (so-called Mach waves), (2) acoustic waves from the fine scale structure of turbulence, (3) broadband shock associated acoustic waves and (4) screech. The acoustic waves (3) and (4) are generated from the interaction of the shock and the shear layer, and they

T. Nonomura (✉) · K. Fujii
Japan Aerospace Exploration Agency, Institute of Space and Astronautical Science, Sagamihara, Japan
e-mail: nonomura@flab.isas.jaxa.jp

K. Fujii
e-mail: fujii@flab.isas.jaxa.jp

© Springer International Publishing Switzerland 2016

A. Segalini (ed.), *Proceedings of the 5th International Conference on Jets, Wakes and Separated Flows (ICJWSF2015)*,
Springer Proceedings in Physics 185, DOI 10.1007/978-3-319-30602-5_51

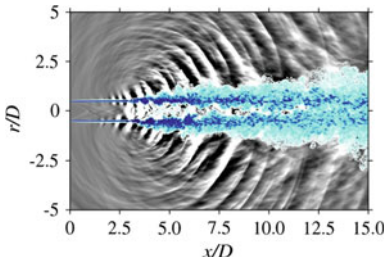


Fig. 1 A large-eddy simulation of a transitional supersonic jet

are weaker in the ideally expanded jet in which the shock waves are not generated. On the other hand, the acoustic waves (1) and (2) are generated only from the shear layer and difficult to control or eliminate them.

Thus far, generation mechanism of the Mach waves are explained to be supersonically convective instability waves and the theoretical prediction are in qualitative agreement. The sound pressure level is reported to be changed by 5 dB, depending on the jet Reynolds number or the jet inlet condition in the experimental study, which is much insensitive than that of a subsonic jet (which has 10dB difference in thin and thick initial shear layer thickness in the previous report [2]). It is important to understand the sensitivity of the supersonic jet on the jet Reynolds number and the jet inlet condition for the highly accurate prediction (less than 2dB error) and to clarify the difference between the supersonic [1] and subsonic jets [2].

Nonomura and Fujii [1] conducted series of the large-eddy simulations (LES) (shown in Fig. 1) with changing the initial shear layer thickness and adding the random disturbance, and analyzed the sensitivity of the Reynolds number and the inlet condition on the acoustic waves generation. In their result, the case with the thick inlet shear layer has the delayed transition and the steep increase in the shear layer thickness after the transition, while the case with the thin inlet shear layer has early transition and smooth increase in the shear layer thickness after the transition. In addition, they showed that the strength of the velocity fluctuation at the transition position relates with the acoustic wave strength: the case with thicker inlet shear layer has stronger velocity fluctuation at the transition and resulting stronger acoustic waves from it, similar to the subsonic jet cases [2]. However, the difference between SPLs of thicker and thinner shear layer cases is less than that of subsonic cases [1]. The mechanism of insensitivity of acoustic waves from a supersonic jet has not been clarified.

The above effects of the inlet shear layer can be comprehended with considering the instability and transition process of a supersonic jet. Thus, in this study a linear stability analysis (LSA) tool for the compressible axisymmetric parallel flows are developed and the LSA and LES results are compared and discussed in order to clarify the mechanism of aeroacoustic wave generation.

2 Numerical Methods

The LES data obtained in the previous study are analyzed. The LES data are obtained using 100–200 million grid points [1] with the sixth order compact scheme [3]. The computational data agree well with the corresponding experimental data [4]. The cases used here are summarized in Table 1. These computations do not include the nozzle inside. Using the relatively thick shear layer case, the sufficient grid resolution per the shear layer thickness is obtained, and this sufficient grid resolution for the shear layer is maintained for all the case in the computation.

The nondimensional parameters employed in this study are the jet Mach number M_j, the Reynolds number Re, and the initial shear layer thickness δ/D. Here, δ and D are the boundary layer thickness and the nozzle diameter, respectively.

The LSA tool developed here is almost the same as that by Luo and Sandham [5]. In this tool, the linearized perturbation equation is solved by the shooting method. Here, disturbance is assumed to be

$$\phi = \tilde{\phi} \exp(\alpha x + \omega t + m\theta), \tag{1}$$

where ϕ, α, ω, m are fluctuation of quantities and spatial, temporal and azimuthal wave numbers, respectively. Here, x, t, and θ are axial, temporal, and azimuthal coordinates.

The validation is conducted with the Mach 3 isothermal jet case and Fig. 2 illustrates that results of the tool developed in this study agree well with those obtained in the previous study [5]. This results shows that the LSA tool developed here is reliable for the quantitative discussion. The LSA is conducted with the hyperbolic-tangent-function-approximated profile of the averaged data of LES at which the linear growth is observed later shown in Fig. 3. Here, the position where $\sqrt{<(u'/u_j)^2>} = 0.03$ is obtained has linear growth for all the cases (as in the intersect points with the horizontal line shown in Fig. 3) and the profile of this position is used for the LSA analysis. Here, u' and u_j is the axial direction velocity fluctuation and the average, respectively. The bracket is an averaging operator.

Table 1 Computational conditions

Case name	M	Re	TR_c	δ_{inflow}/D	Disturbances
th02	2.1	70,000	1	0.2	Not imposed
th01	2.1	70,000	1	0.1	Not imposed
th005	2.1	70,000	1	0.05	Not imposed
th0025	2.1	70,000	1	0.025	Not imposed
th00125	2.1	70,000	1	0.0125	Not imposed

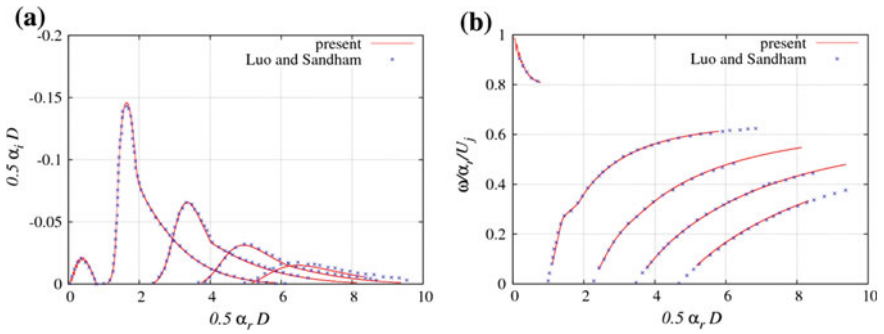


Fig. 2 Comparison of test problem (Mach 3 jet) with the previous study. **a** imaginary part, **b** real part

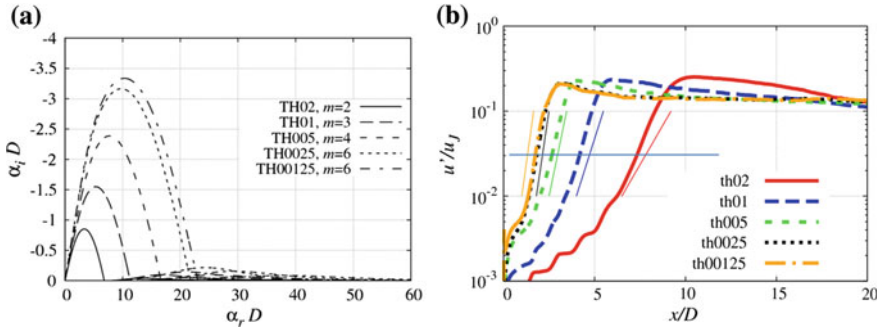


Fig. 3 Most unstable mode for jets with various shear layer thickness and comparison of their growth rate with the LES data. **a** LSA results, **b** comparison with LES data, where the *thin line* indicates the most unstable growth rate predicted by LSA

3 Results

The LSA analyses are conducted for the jet computed in LES of the previous study. The jet cases are summarized in Table 1. The most unstable mode obtained by LSA for jets with various inlet shear layers are shown in Fig. 3(left). Here, the m indicates the number of the azimuthal mode. The number of the most unstable azimuthal mode becomes higher in the cases with smaller shear layer thickness. The obtained linear growth rate is shown by the thin line with the actual growth rate in LES. The growth rate of the fluctuation in jet shear are well captured by LSA as shown in Fig. 3(right).

Then, the LES results of azimuthal and frequency spectra of velocity fluctuation of the th02 and th00125 jets are shown in Figs. 4 and 5, respectively, with the arrows of the azimuthal mode and frequency of the most unstable mode which is predicted by the LSA tool. The results show that the helical mode is grown as predicted by the LSA tool as shown in left figures of Figs. 4 and 5. The most unstable mode in th02 case is corresponding to $m = 2$, which has the most largest amplitude at the

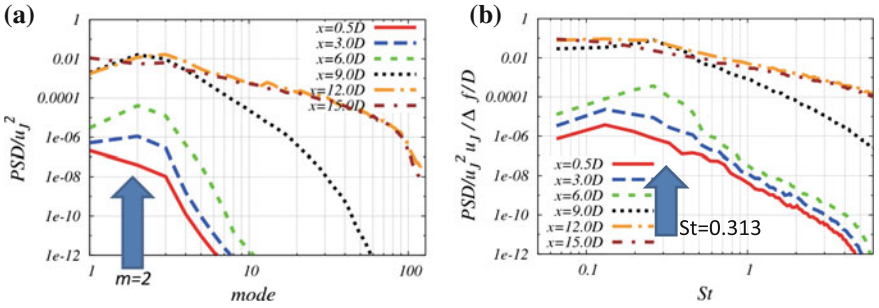


Fig. 4 Development spectra of **a** azimuthal wave number and **b** frequency of LES data of th02, together with the indication of the most unstable mode computed by LSA

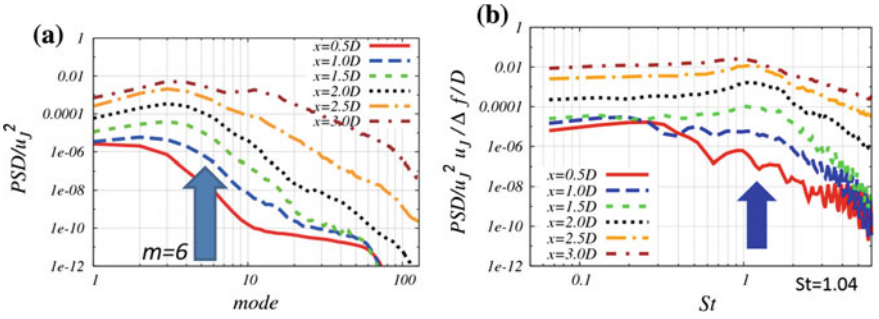


Fig. 5 Development spectra of **a** azimuthal wave number and **b** frequency of LES data of th00125, together with the indication of the most unstable mode computed by LSA

transition position (approximately $x = 12D$). Interestingly, the most amplified mode is $m = 6$ for the th00125 case which is corresponding to the LSA prediction, but the mode with the most largest amplitude is $m = 3$. This is because the azimuthal mode $m = 3$ has larger fluctuation even just after the nozzle exit. This might be explained as follows: the acoustic wave radiation is well observed in the azimuthal mode of the lower number (i.e. 0, 1, 2, and 3) in the supersonic jet as reported in the reference [6], and the generated acoustic waves of the azimuthal mode of the lower number feed the small disturbance into the shear layer just after the nozzle exit. This might lead to the fact that the azimuthal mode m = 3 has larger fluctuation even though it has lower amplification than the mode m = 6.

Anyway, the helical mode is very strong in the supersonic jet because of its characteristics of the linear instability and receptivity, and pairing of helical vortices seems to be less dramatic than that of axisymmetric ones which are observed in the transitional subsonic jet. This explains the why the supersonic jet is more insensitive than the subsonic jet. For more detailed discussion, the Mach number effects of strength of disturbance given by the upstream going acoustic waves discussed above should be carefully investigated.

4 Conclusions

In this paper, the large-eddy simulation (LES) and linear stability analysis (LSA) data of a transitional supersonic jet are analyzed. The LES data obtained in the previous study are analyzed with the validated LSA tool for axisymmetric parallel flow. The results illustrate that the most unstable mode developed in the LES data corresponds to that predicted by the LSA tool. As discussed in the previous study, the most unstable mode is not found to be an axisymmetric mode as in the subsonic case, but to be a helical mode. The results shows that the thiner shear layer case, the number of the azimuthal mode with the largest amplitude is lower than that of the most unstable mode. This is because the lower azimuthal mode has larger amplitude even at the near jet nozzle region, which seems to be caused by the excitation of shear layer by the acoustic waves going upstream side. Anyway, the helical mode is stronger in the supersonic jet than the axisymmetric mode unlike the subsonic jet, which appears to lead to less dramatic transition and acoustic wave generation process of the supersonic jet than those of the subsonic jet.

Acknowledgments This work was supported by KAKENHI (25709009).

References

1. T. Nonomura, K. Fujii, in *AIAA Paper 2013-2237* (2013)
2. C. Bogey, C. Bailly, J. Fluid Mech. **663**, 507 (2010)
3. S.K. Lele, J. Comput. Phys. **103**(1), 16 (1992). doi:10.1016/0021-9991(92)90324-R
4. T.R. Troutt, D.K. McLaughlin, J. Fluid Mech. **116**, 123 (1982)
5. K.H. Luo, N.D. Sandham, Phys. Fluids **9**(4), 1003 (1997)
6. T. Suzuki, D. Bodony, J. Ryu, S.K. Lele, Noise sources of high-mach-number jets at low frequencies studied with a phased-array approach based on les database, in *Annual Research Briefs 2007* (Center for Turbulence Research, 2007)

Can Jet Noise Be Predicted Using Linear Instability Wavepackets?

Onofrio Semeraro, Lutz Lesshafft and Richard D. Sandberg

Abstract According to a recent hypothesis corroborated by experimental investigations, large-scale coherent structures in turbulent jet flows can be modelled as wavepackets. This conjecture suggests that these structures can be responsible for low-frequency acoustic radiation. In this contribution, we compute optimally forced stability wavepackets, based on meanflow data of a turbulent jet. The dataset is obtained from fully compressible DNS. The final aim is to assess the validity of the hypothesis by verifying to what extent the jet noise can be predicted by means of these linear structures.

1 Flow Case and Formalism

During the last decade, experimental results have corroborated the hypothesis that low-frequency noise in turbulent jets can be related to the presence of large-scale coherent structures developing in the near-field (see the review by [4]). We refer to these spatio-temporal structures as *wavepackets*. A large bulk of the recent literature on the subject has been devoted to the statistical description of these wavepackets as linear or non-linear modal solutions. An example is given by the use of parabolized stability equations (PSE) [2]. We compute instability wavepackets as the frequency response of the flow to harmonic excitations [5]. The formalism relies on Reynolds-averaged Navier-Stokes modelling, obtained by introducing a triple-decomposition of the flow field,

$$\mathbf{u} = \mathbf{U} + \tilde{\mathbf{u}} + \mathbf{u}', \tag{1}$$

O. Semeraro (✉)
LIMSI–CNRS, Orsay, France
e-mail: semeraro@ladhyx.polytechnique.fr

L. Lesshafft
LadHyX, Ecole polytechnique, Palaiseau, France

R.D. Sandberg
University of Southampton, Southampton, UK

© Springer International Publishing Switzerland 2016

A. Segalini (ed.), *Proceedings of the 5th International Conference on Jets, Wakes and Separated Flows (ICJWSF2015)*,
Springer Proceedings in Physics 185, DOI 10.1007/978-3-319-30602-5_52

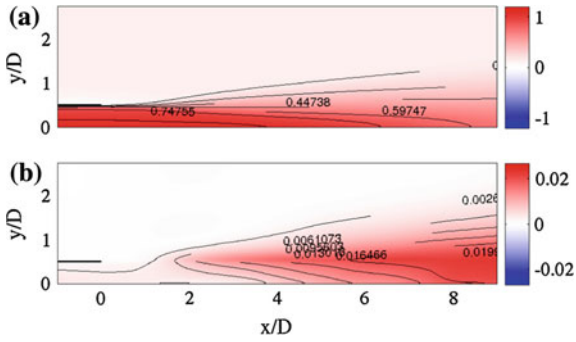


Fig. 1 The streamwise meanflow velocity of the turbulent jet under investigation is shown in (**a**). The meanflow is obtained from full DNS, at $Ma_j = 0.84$ and $Re_D \approx 7500$; the coflow Mach number is $Ma_{cf} = 0.1$. In **b**, the turbulent viscosity is shown, see (2)

into the full compressible, axysimmetric Navier-Stokes equations in cylindrical coordinates. The meanflow quantities are indicated by $\mathbf{U}$, the instantaneous harmonic fluctuations (i.e. the wavepackets) by $\tilde{\mathbf{u}}$, while $\mathbf{u}'$ represents the incoherent part of turbulence. In our analysis, we focus on the quantity $\tilde{\mathbf{u}}$, by neglecting the quadratic nonlinear terms and incoherent fluctuations $\mathbf{u}'$. Within this approximation, the effects of turbulence are taken into account by introducing a turbulent viscosity ν_t [6].

The nozzle of the pipe is placed at $x/D = 0$; all quantities are scaled with the diameter of the pipe, D. The meanflow data are computed using full DNS, at Mach number $Ma_j = 0.84$, co-flow $Ma_{cf} = 0.1$ [7]. The Reynolds number, based on the diameter, is $Re_D \approx 7500$ at the nozzle. The streamwise component is shown in Fig. 1a. The potential core extends down to $x/D \approx 4 - 5$. Downstream of the potential core, the velocity profile is self-similar. In Fig. 1b, the turbulent viscosity ν_t is shown, computed using the quantities extracted from the DNS as

$$\nu_t = -\frac{< \overline{uv} >}{(dU/dr + \epsilon)}, \tag{2}$$

where u and v are the streamwise and radial *total* fluctuations (i.e. coherent and stochastic). Care is required when processing the original data; indeed, the appearence of the derivative in the denominator of (2) in combination with local non-smoothness of the velocity profiles can lead to nearly singular results. Yet, a non-null, small value ϵ was deemed sufficient to regularize the incorrect results.

Following our initial hypothesis, the harmonic component is obtained as solution of an optimally forced problem. In particular, the governing equations can be expressed in compact form as

$$\frac{d\mathbf{q}}{dt} - \mathbf{L}\mathbf{q} = \mathbf{B}\hat{\mathbf{f}}e^{-i\omega t}. \tag{3}$$

On the left-hand side $\mathbf{q} \in \mathscr{C}^n$ is the complex state vector, including density, streamwise velocity, radial velocity and internal energy and n, the number of degrees of freedom; $\mathbf{L}$ is the discretized, compressible Navier-Stokes operator, linearized around the meanflow, including boundary conditions and turbulent viscosity. On the

right-hand side the system is driven by harmonic forcing $\hat{\mathbf{f}}$ at a given frequency ω. Introducing the *ansatz*, $\mathbf{q} = \hat{\mathbf{q}}e^{-i\omega t}$, (3) can be rewritten as the following input-output system

$$\hat{\mathbf{q}} = -\left(\mathbf{L} + i\omega\right)^{-1}\mathbf{B}\hat{\mathbf{f}} = \mathbf{C}\left(\omega\right)\mathbf{B}\hat{\mathbf{f}}, \tag{4}$$

where the Resolvent operator $\mathbf{C}\left(\omega\right)$ plays the role of a transfer function at a given frequency ω. The forcing $\hat{\mathbf{f}}$ is the unknown of our system: it is defined such that the ratio between the energy of the frequency response and the energy of the forcing input is maximed, i.e.

$$\sigma_{max} = max\frac{\|\hat{\mathbf{q}}\|_{\mathbf{Q}}^2}{\|\hat{\mathbf{f}}\|_{\mathbf{Q}}^2} = max\left(\frac{\hat{\mathbf{f}}^{\dagger}\mathbf{B}^{\dagger}\mathbf{C}^{\dagger}\mathbf{Q}\mathbf{C}\mathbf{B}\hat{\mathbf{f}}}{\hat{\mathbf{f}}^{\dagger}\mathbf{Q}\hat{\mathbf{f}}}\right), \tag{5}$$

where the superscript † indicates the transpose. We indicate with $\mathbf{B}$ a weight-function used for the localization of the forcing. In this contribution, the solution is restricted to the pipe (i.e., the weight function is null elsewhere). The real positive-definite matrix $\mathbf{Q}$ is the weight for the energy norm. We choose the total kinetic perturbation energy (integrated in space) of the wavepackets for both forcing and frequency response: their ratio provides the energy gain, σ, at a given frequency. Finally, the resulting frequency response is obtained by *optimally* forcing the linear simulations, see (3). This formalism corresponds to a singular values analysis of the linear global Resolvent operator; recent works have highlighted the robustness of this strategy, in particular when convective flows are analysed [3]. Due to the dimensions of the dynamical system, the underlying optimization problem is solved using a direct-adjoint iteration, based on time-stepping of the linearized Navier-Stokes equations.

2 Results

The discretization of (3) employs sixth-order centered finite-difference schemes [1]. Characteristic boundary conditions are applied at the inflow and outflow of the domain in combination with a sponge region. Symmetry boundary conditions are applied at $y/D = 0$. More details on the implementation can be found in [3]. The physical domain has the dimensions $x/D \in [-20, 30]$ and $y/D \in [0, 20]$ and a resolution of 700×300 grid points; the mesh is Cartesian, with denser resolution in the proximity of the nozzle, where the shear of the baseflow is strongest. The maximum resolution is $\Delta x/D = 7.5 \times 10^{-3}$ and $\Delta y/D = 6.0 \times 10^{-3}$, along the streamwise and radial directions, respectively. A coarser resolution is used for the far-field, where the sponge region is applied. The resolution was deemed sufficient for getting converged results.

Optimal forcing and near-field wavepackets. In Fig. 2, we observe two distinct mechanisms characterizing the optimal forcing $\hat{\mathbf{f}}$: (i) a downstream-propagating acoustic wave that occupies the full width of the pipe; (ii) a vortical structure of

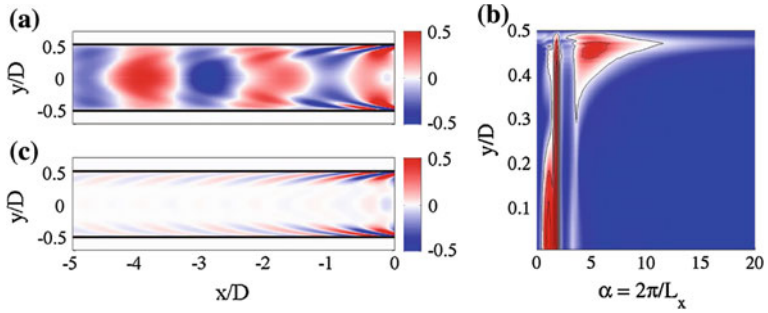


Fig. 2 Optimal forcing at $St = 1.0$. The result of the optimization is shown (streamwise component) in physical domain (**a**) and Fourier space (**b**). After the convolution filter is applied, the resulting forcing is obtained in (**c**)

shorter wavelength, localized in the wall-near region and close to the nozzle exit. The figure shows the forcing at $St = \omega D/2\pi U = 1.0$, where St is the Strouhal number. The tilted structure aligned against the gradient of the shear closely resembles the typical shape of optimal initial perturbations in shear flows. The aim of this study is to describe the noise that is generated aerodynamically by instability wavepackets; the direct external forcing of acoustic waves is an unwanted effect. We therefore attempt to remove this component of the forcing and only retain the part that creates an instability wavepacket. This is achieved through a filtering procedure [8]:

1. The Fourier transform in x is computed for each radial position inside the pipe, $0 < y/D < 0.5$. The spectrum is shown in Fig. 2b. The acoustic (low-wavenumber) and the hydrodynamic (higher wavenumber) components can be clearly distinguished.
2. The convolution filter is applied: a narrow Butterworth band-reject filter is used, such that only the acoustic wavelengths are removed from the spectrum.
3. An inverse transform of the filtered spectrum yields the purely hydrodynamic forcing component.

Only this filtered forcing, stripped of direct acoustic sources, is applied in the generation of results discussed in the following. The cases $St = 0.3$ and 0.6 are shown in Fig. 3a, c. The response structures, generated inside the pipe at a tilted angle against the flow direction, rotate to align themselves with the shear gradient. This is the known Orr mechanism, which provides a first non-normal perturbation energy growth inside the pipe. The resulting instability wavepackets in the free jet are shown in Fig. 3b, d. The energy gain variation as a function of Strouhal number is displayed in Fig. 4a. Two curves are shown, the black one for calculations with only the molecular viscosity, the red one for calculations where the turbulent viscosity is taken into account. In both cases, the maximum energy gain is observed in a band of Strouhal numbers between 0.5 and 1. The turbulent viscosity leads to much stronger damping of perturbations, visible in the comparison between the two wavepackets in Fig. 4b, c, and therefore yields lower values of the gain. However, the band of maximally amplified frequencies is very similar in both cases.

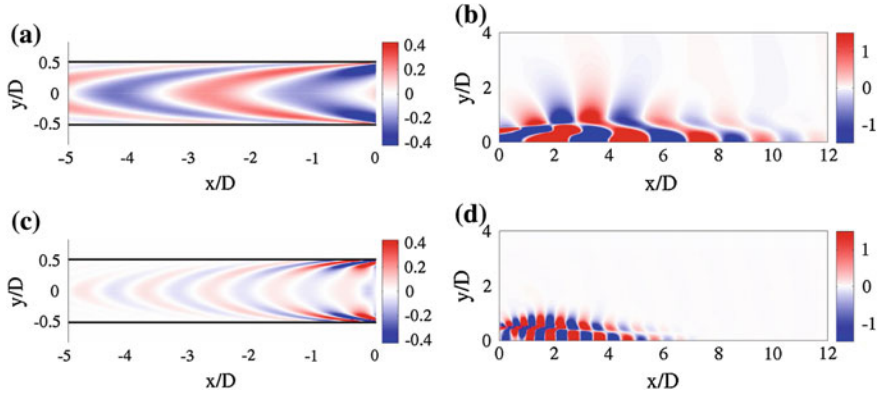


Fig. 3 Optimal forcings at $St = 0.3$ and $St = 0.6$ are shown in (**a**) and (**c**), respectively; the corresponding wavepackets are shown in (**b**) and (**d**). For all the cases, the streamwise component is shown

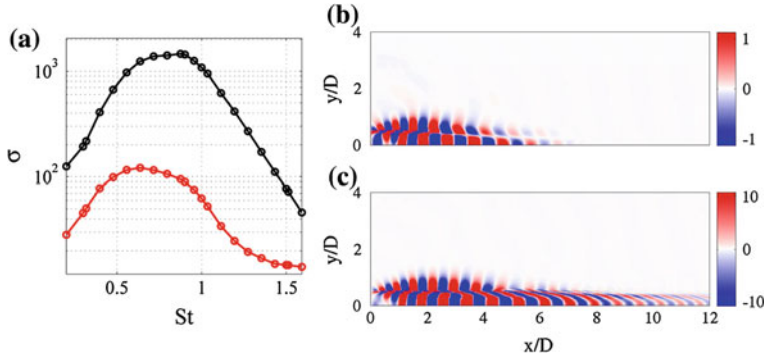


Fig. 4 Turbulent viscosity (ν_t) effects. The energy gain σ is shown as a function of St, with and without ν_t (*red* and *black solid line*, respectively). The near field at $St = 0.6$ is shown for the two cases (**b** and **c**); in **b** the presence of the turbulent viscosity shortens the distribution of the wavepacket along the streamwise direction (when compared with **c**)

DNS comparison and acoustic field. A qualitative comparison between the frequency response wavepacket at $St = 0.6$ and the corresponding axisymmetric Fourier mode obtained from full DNS simulations is shown in Fig. 5. A close resemblance is observed in the vicinity of the nozzle (i.e. $0 < x/D < 3 - 4$). Indeed, this is the region where the behaviour of the wavepacket is described by linear equations. In the same figures, the low amplitudes in the acoustic field are resolved. This is an advantage of the frequency response analysis as it provides a direct prediction of the acoustic field. Comparing Fig. 5a, b, we observe that the patterns of the main beam and the directivity are in reasonable agreement; moreover, the acoustic beam originates approximately from the same position along x/D, roughly corresponding to the *linear* region. However, it is possible to observe a second beam propagating

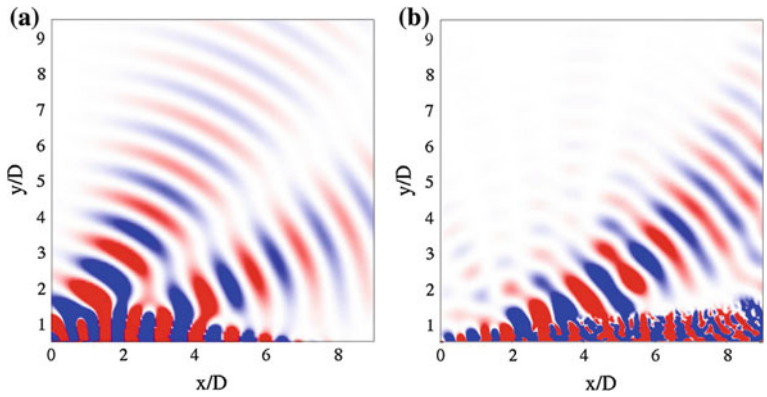


Fig. 5 Acoustic fields at $St = 0.6$: in **a** the linear wavepacket is shown and compared to the corresponding Fourier axisymmetric mode educed from full DNS (**b**). The streamwise component is shown for both cases

upward in the linear prediction which is not present in the DNS results. A preliminary quantitative analysis (not shown here) clearly reveals that the intensity of the acoustic noise is underpredicted in the linear case. We are currently investigating a number of improvements for such an analysis, including the nonlinear evolution of the optimally forced wavepackets.

Acknowledgments This work is being supported by the Agence Nationale de la Recherche (ANR) under the "Cool Jazz" project, grant number ANR-12-BS09-0024.

References

1. J. Berland, C. Bogey, O. Marsden, C. Bailly, High-order, low dispersive and low dissipative explicit schemes for multiple-scale and boundary problems. J. Comput. Phys. **224**, 637–662 (2007)
2. A.V.G. Cavalieri, D. Rodríguez, P. Jordan, T. Colonius, Y. Gervais, Wavepackets in the velocity field of turbulent jets. J. Fluid Mech. **730**, 559–592 (2013)
3. X. Garnaud, L. Lesshafft, P.J. Schmid, P. Huerre, Modal and transient dynamics of jet flows. Phys. Fluids **25**, 044103 (2013)
4. P. Jordan, T. Colonius, Wave packets and turbulent jet noise. Ann. Rev. Fluid Mech. **45**, 173–195 (2013)
5. A. Monokrousos, E. Åkervik, L. Brandt, D.S. Henningson, Global three-dimensional optimal disturbances in the Blasius boundary-layer flow using time-steppers. J. Fluid Mech. **650**, 181–214 (2010)
6. S.B. Pope, *Turbulent Flows* (Cambridge University Press, 2000)
7. R.D. Sandberg, DNS of turbulent round jets using acoustically lined canonical nozzles, in *19th Australasian Fluid Mechanics Conference*, Melbourne, AU (2014)
8. S. Sinayoko, A. Agarwal, Z. Hu, Flow decomposition and aerodynamic sound generation. J. Fluid Mech. **668**, 335–350 (2011)

Part VII
Turbomachinery Flows

A Numerical Model of Fluid Structure Interaction of a Fluttering Valve

Umut Can Coskun, Hasan Gunes and Kemal Sarioglu

Abstract Fluttering suction valves are important components of hermetic reciprocating compressors used in refrigerators. The design parameters of the valve reed strongly determine the mass flow rate and consequently the compressor efficiency. Therefore, it is necessary to carefully design the reed valves to maximize compressor performance. In this study, a numerical flow model to mimic a fluttering suction valve in hermetic reciprocating compressors is developed. To simulate the unsteady flow dynamics and the motion of the fluttering valve in the cylinder, a simplified test geometry is used, where a fully coupled fluid structure interaction (FSI) problem is solved. The main goal of the study is to reveal the effects of some important design parameters of the valve reed such as the thickness, diameter of the circular part of the valve and the distance between valve reed and valve plate. These design parameters are vital for improving the aerodynamic and aero-acoustic behavior of the flow in the compressor. It is shown that increasing thickness of the valve reed decreases the mass flow rate significantly where the head diameter of the reed and distance between the reed and the plate have minor effects on both mass flow rate and displacement of the reed.

1 Introduction

In recent studies engineering problems concerning fluid structure interaction gain popularity with the developments in computational and computer sciences. Therefore numerical modeling of fluid structure interaction is today applicable in a

U.C. Coskun (✉) · H. Gunes
Department of Mechanical Engineering, Istanbul Technical University,
Gumussuyu, 34437 Istanbul, Turkey
e-mail: ucoskun@itu.edu.tr

H. Gunes
e-mail: guneshasa@itu.edu.tr

K. Sarioglu
Arcelik Research and Development Center, 34950 Tuzla, Istanbul, Turkey
e-mail: kemal.sarioglu@arcelik.com

© Springer International Publishing Switzerland 2016

A. Segalini (ed.), *Proceedings of the 5th International Conference on Jets, Wakes and Separated Flows (ICJWSF2015)*,
Springer Proceedings in Physics 185, DOI 10.1007/978-3-319-30602-5_53

wide range engineering problems from biological systems to many industrial applications. One of the challenging problem in industrial applications is the occurrence of the fluttering valve (reed valve) in reciprocating compressors and modeling of the phenomenon by means of computational fluid dynamics (CFD) involving valve and piston dynamics. The understanding and modeling of the flow behavior through the valve reed is important to improve the valve design.

In previous studies, the flow inside a suction muffler [1] and effects of geometric parameters of the suction muffler [2] were investigated numerically. In those studies, in lieu of solving the current FSI problem, experimentally obtained transient pressure data at the outlet section was used as outlet boundary condition. However, this pressure data depends on the muffler geometry as well as the valve characteristics and further experiments are needed for a proposed modification to obtain the actual pressure data for the simulations for different muffler prototypes. For an optimization process, the valve and piston dynamics has to be included into the model. Thus, in this paper a numerical flow model is proposed. The interaction between valve reed, piston and the refrigerant fluid is investigated thoroughly and the valve dynamics are taken into account to optimize the unsteady flow in the cylinder.

In the analytical study conducted by (1) the design parameters of a fluttering valve reed are investigated with a simplified model consisting of 3-beam elements. In their study, the force acted as point loads and their analytical results show satisfactory agreement with numerical models. Their analytical model serves as the starting point in valve design. Additionally, the mathematical tool provides an initial estimate on stresses in order to achieve required valve deflection.

In this study, the effects of geometric design parameters of suction valve reed on mass flow rate and the reed displacement investigated numerically. The strong interaction between the valve reed, valve plate, piston and the working fluid is modelled using a segregated solver in ANSYS-Fluent. Control volume of the problem is started from inlet of the suction channel to outlet of the cylinder in order to focus on flow around suction valve reed. Once the numerical setup of the problem is constructed and validated, a parametric study is conducted by varying the thickness and head diameter of the reed and the distance between the reed and the valve plate, which has to be provided due to the numerical model. The transient reed displacement/dynamics and the mass flow rate through suction channel is compared between cases.

2 Numerical Procedure

Computational Domain and Boundary Conditions

In a reciprocating compressor, the motion of the piston along with the opening of the valves changes the pressure inside the cylinder. Pressure difference between the muffler and cylinder causes valve reed to deflect and deform which eventually controls the mass flow rate. Since the focus of this study is to reveal the effects of

the geometric design parameters of the suction port and the valve reed, some simplification steps have been conducted. In order to exclude the effects of the complex suction muffler design, a circular cylinder body is used which represents a simplified suction muffler.

Even though a more realistic way to model this problem is to change the cylinder volume by moving the piston surface according to experimental piston motion data, it is also numerically expensive as it requires moving mesh due to the piston motion. In our model, instead of moving the piston surface as wall boundary condition, a transient pressure profile is used as outlet boundary condition at a stationary surface which is sufficiently away from the valve reed. The computational domain, the pressure profile used as outlet boundary condition is shown at Fig. 1.

Operating pressure is chosen 0.624 bar as is appropriate for hermetic piston compressors according to ASHRAE test conditions where "0 Pa" constant effective pressure is used as inlet boundary condition. As for the boundary conditions, the pressure inlet boundary condition is used with zero gauge pressure and 5 % turbulence intensity at inlet surface, while pressure outlet boundary condition is used with a transient pressure data at the outlet section (see Fig. 1), which mimics the variation of the cylinder pressure in a reciprocating compressor due to piston motion. Since the effect of the temperature variation is not in the scope of this study, the inlet and initial temperatures of the fluid is kept as 300 K and walls are treated as adiabatic.

Tetrahedral cells are used for fluid domain where hexahedral elements are used for transient structural analyses. A non-conformal fluid-solid interface separates fluid and solid meshes. Dependence of the results to the grid resolution is investigated for reference configuration. Mass flow rate through inlet section of the cylinder is used for mesh independency criteria. Computational grid for fluid and solid domains and grid resolution test results can be seen in Fig. 2 respectively.

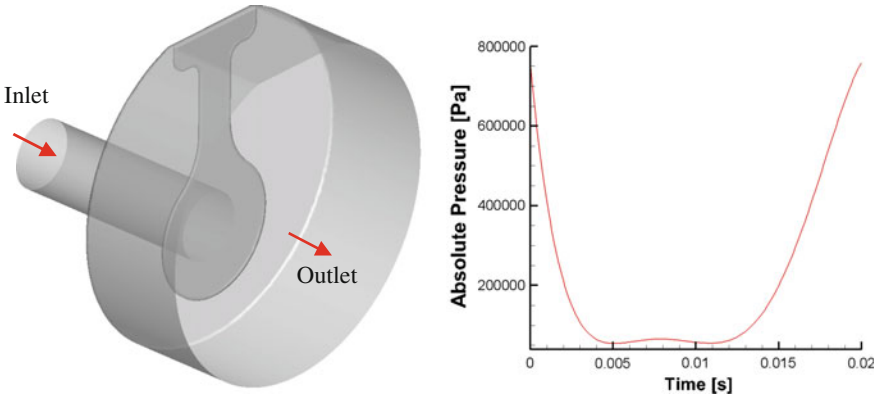


Fig. 1 Computational domain and transient pressure profile at outlet boundary

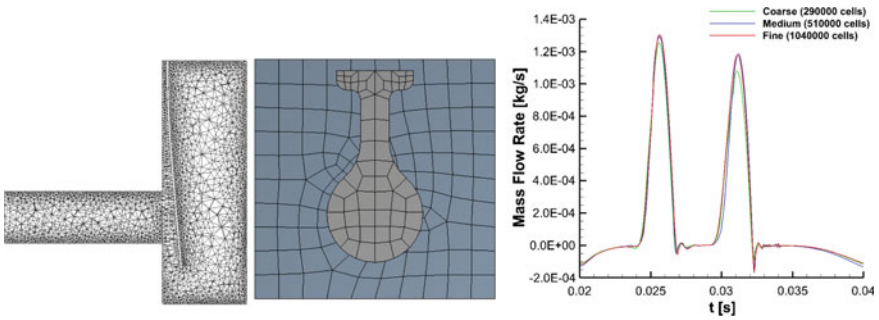


Fig. 2 Fluid mesh at the *mid-section* (instantaneous view), solid mesh and mesh independecy results

Solution Process

Fluid flow into the cylinder is greatly influenced from the deflection/displacement of the valve reed while the valve reed displacement entirely depends on the flow induced forces. This phenomena creates a two-way, physically strong coupled FSI problem. The solution of this FSI problem is solved with a segregated approach by using ANSYS commercial software. A finite volume based flow solver "Ansys-Fluent" is used to calculate the transient flow field and a finite element based structural solver "Ansys-Mechanical" is used for structural analyses where "System Coupling" module is used for exchange information between two solvers on fluid-solid interface. At the start of a time step, the flow solver passes previously calculated surface pressure acting on valve reed (fluid-solid interface) and the structural solver uses transferred data as input to calculate the valve displacement. Once structural solver converges, it passes the displacement information of the valve reed which, in turn, flow solver uses it as input to calculate the "new" flow field. In order to create a strong coupled FSI algorithm, this cycle repeats itself until a converged solution. This sequential solution converges faster with fewer coupling iterations than as simultaneous solution since the subsequent solver uses the most recently calculated inputs [4].

The flow in a reciprocating compressor is periodic since the flow is governed by the periodic motion of the piston as specified in Fig. 1b. A cycle of the compressor is 0.02 s and since the flow becomes periodic soon after first period, all cases are simulated for 2 periods and all shown results are belong to the second period.

In its periodic movement, large deformations occur on valve reed. It hits to the valve plate with a fluttering motion and for most of the period, valve reed stays in contact with valve plate. For this reason, a frictionless contact model is used between the valve reed and the valve plate. Since the actual contact of two boundaries are not allowed in the flow solver, a proper contact offset distance is employed. A direct solver (Gaussian elimination approach) is used for structural analyses where Newmark [5] algorithm is used for time integration. A constant time step size of "0.00005 s" (i.e., 400 time steps per cycle) is chosen for both structural and flow solvers.

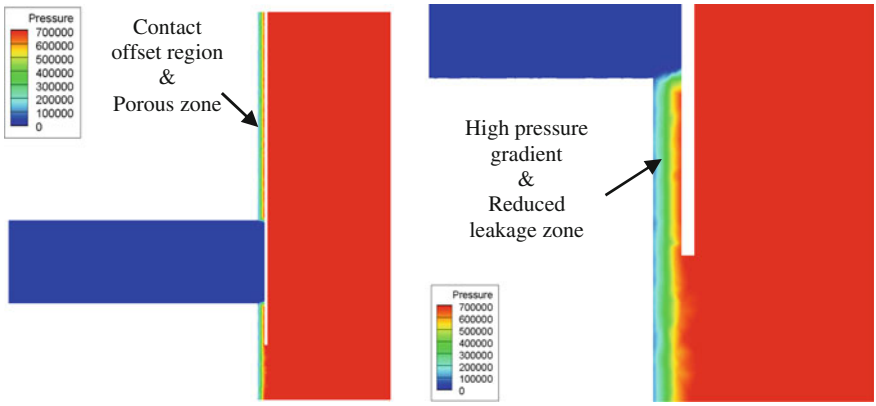


Fig. 3 Initial flow field and the contact region modeled as a porous zone

The flow is modeled as transient, compressible and turbulent. Realizable k-ε turbulence model with non-equilibrium wall function is used for turbulence modeling. "Simple Algorithm" is used for velocity-pressure coupling. Both spatial and temporal discretizations are first order and the convergence criteria (residuals) is chosen as 1e-4 for all flow variables.

The volume inside the cylinder between valve reed and outlet boundary is initialized with 7.6 bar effective pressure while cylindrically represented muffler part is initialized with zero pressure. Inside the contact offset distance, pressure between the reed and plate initially changes from 7.6 bar to 0 linearly. Since a contact offset distance had to be used for requirement of the flow solver, this strong pressure gradient around valve reed causes massive fluid leakage from cylinder to muffler. In order to prevent or reduce the unrealistic refrigerant leakage from the cylinder chamber to the suction chamber (inlet channel), a position dependent source term according to Darcy-Forchheimer porosity model is added to the momentum equation to make the contact offset flow region "porous medium" by employing user defined functions which eventually act as a gasket or seal. Figure 3. shows porous zone and initial flow field.

3 Results

In order to investigate the effects of the design parameters of the valve reed, seven different prototypes are created with varying reed thickness, reed head diameter and contact offset distance. Table 1 shows the values of the design parameters investigated.

In reference case, the value of reed thickness, reed head diameter and the contact offset distance are chosen as $w_{ref} = 0.18$, $d_{ref} = 10$ and $x_{ref} = 0.3$ mm respectively. In the parametric study, three different values for each parameter including the

Table 1 Values of the design parameters for each case

Case	Reed Thickness "w" (mm)	Reed Head Diameter "d" (mm)	Contact Offset Distance "x" (mm)
1	0.15	10	0.3
2	0.18		
3	0.21		
4	0.18	8	0.3
5		12	
6	0.18	10	0.2
7			0.4

reference value is employed while keeping the other two parameters at reference values. The effect of the valve thickness on reed displacement and the mass flow rate in cylindrical "muffler" inlet section are shown in Fig. 4.

It can be seen from Fig. 4 that as the thickness of the valve reed decreases, the reed stays open slightly longer with much wider gap hence the mass flow rate increases. The effect of the read head diameter on the reed displacement and the mass flow rate in cylinder inlet section are shown in Fig. 5.

According to Fig. 5, even though the reed displacement increases with the reed head diameter, the difference is very minor. This effect is even smaller on the mass flow rate. The effect of contact offset distance on the reed displacement and the mass flow rate in cylinder inlet section are shown in Fig. 6.

Even though the contact offset distance is not a physical design parameter of a reed valve, it is important for numerical modeling the interaction between the fluid flow and fluttering valve. It can be seen from Fig. 6 that, the mass flow rate of the leakage decreases as the contact offset distance gets smaller. As the contact offset distance goes to zero, the necessity to contact offset vanishes. However, as the contact distance decreases, in order to keep the mesh skewness in an acceptable

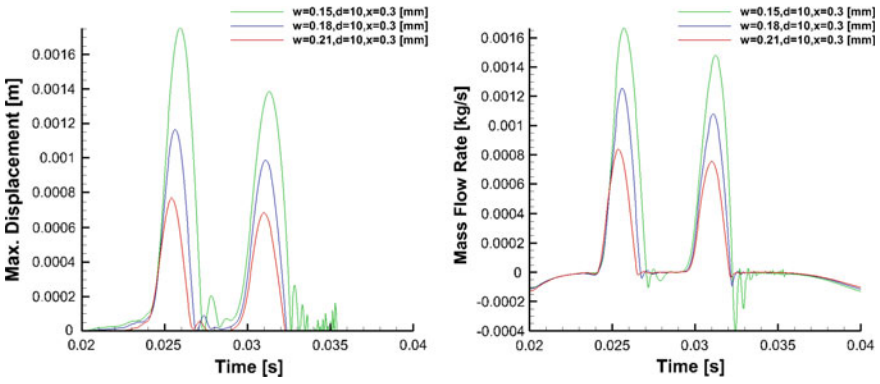


Fig. 4 Effect of valve thickness on reed displacement and mass flow rate respectively

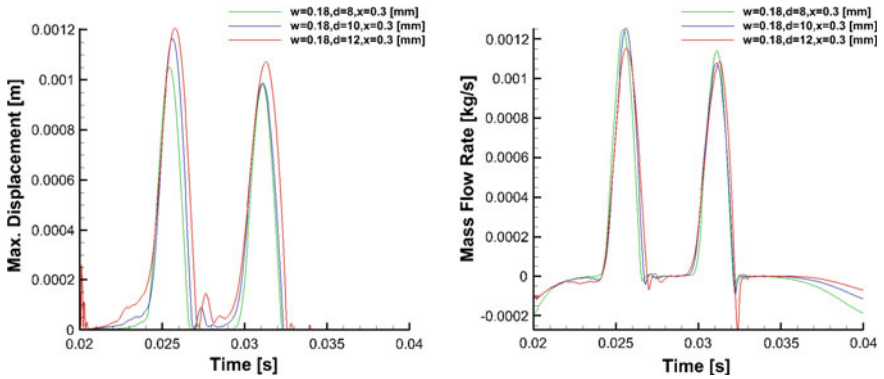


Fig. 5 Effect of reed head diameter on reed displacement and mass flow rate respectively

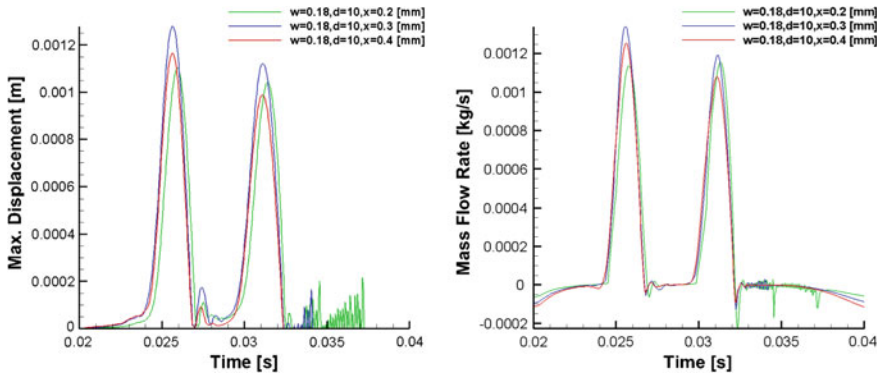


Fig. 6 Effect of contact offset distance on reed displacement and mass flow rate respectively

level, size of the minimum cell decreases in other two directions as well. This results in difficulties on remeshing process and increase the number of cells in the dynamic region considerably and the possibility of actual contact of two boundaries due to structural penetration. Fortunately, it can be seen that increasing the contact offset distance does not have a major effect on either reed displacement or the mass flow rate. The average effects of each parameter is shown in Fig. 7 to compare with each other.

According to the average mass flow rates shown in Fig. 7, the reed thickness has a major effect in the mass flow rate. A slight change in the thickness can greatly affect the coupled system. Even though a thin reed is aerodynamically more favorable, it also cause durability issues. Increasing the diameter of the reed head also increases the mass flow rate and has no negative effect on durability of the reed however it is also less effective on increasing the mass flow rate.

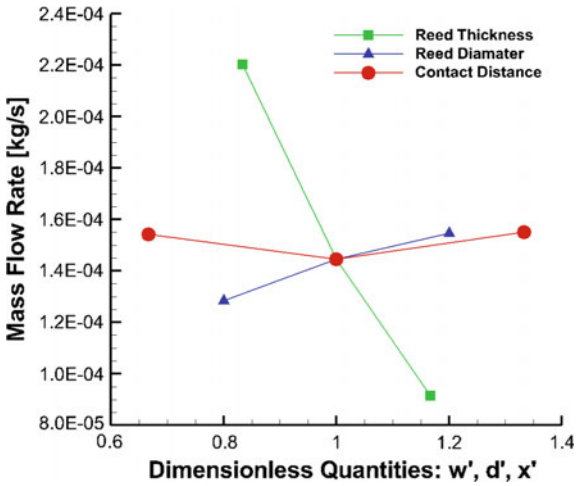


Fig. 7 Effect of various design parameters in comparison. Dimensionless quantities are width of reed, diameter of reed head and contact offset distance divided by their reference values $w' = \frac{w}{w_{ref}}$, $d' = \frac{d}{d_{ref}}$, $x' = \frac{x}{x_{ref}}$

4 Conclusion

We present a numerical study to investigate the geometric design parameters of suction valve reed in a reciprocating piston compressor used in household refrigerators. The effect of reed thickness, the reed head diameter and the contact offset distance resulting from a modeling concept are investigated numerically in terms of on both reed displacement and mass flow rate through the valve. In order to reveal the interaction between structural dynamics of the valve and the fluid flow, we established a two-way coupled FSI model. We found that the mass flow rate through a suction valve mostly affected by the thickness of the reed among other investigated parameters. Even though it is less effective, increasing the valve head diameter also increases the mass flow rate without durability issues. We also show that the flow through a fluttering valve can be modeled with a relatively large contact offset distance in order to decrease the computational time considerably without much effecting the results. This study also constitutes to be an important step forward to model a full compressor refrigerant simulation with FSI modeling.

Acknowledgments We gratefully acknowledge the financial support of Arçelik A.S. and Scientific Research Office (BAP) of Istanbul Technical University.

References

1. U.C. Coskun, H. Gunes, K. Sarioglu, Numerical investigation of suction muffler in household refrigerator compressor, in *Proceedings of International Conference of Mechanics, Fluids, Heat, Elasticity and Electromagnetic Fields* (2013), pp. 85–89
2. U.C. Coskun, H. Gunes, K. Sarioglu, H. Kerpicci, Unsteady flow simulation in suction muffler of a hermetic reciprocating compressor, in *ASME 2014 12th Biennial Conference on Engineering Systems Design and Analysis*, Copenhagen, 25.06.2014–27.06.2014
3. S. Dhar, B. Tanna, A. Bhakta, M. Krishna, A simplified CFD model for simulation of the suction process of reciprocating compressors, in *International Compressor Engineering Conference*, Purdue, 14–17.07.2014
4. ANSYS System Coupling Guide, Release 15.0
5. ANSYS Theory Reference for the Mechanical APDL and Mechanical Applications, Release 12.0

Capacity Testing and Local Flow Analysis of Geometrically Complex Trims Installed Within a Commercial Control Valve

Taimoor Asim, Rakesh Mishra, Matthew Charlton and Antonio Carlos Oliveira

Abstract Industrial control valves often handle flows with very high pressure drops (conditions often referred to as severe service). In order to cope with these pressure drops, geometrically complex valve trims with many stages of pressure loss, are designed to prevent undesirable side effects such as cavitation, excessive noise or erosion. These effects are maintained under control by gradually decreasing the pressure in each stage of pressure letdown of the trim. There are many different product designs for control valve trims produced by different manufacturers. One such design uses cylindrical obstructions in the flow field to control the pressure drop. The design of these trims is based on their capacity (Cv) values. With the advent of advanced computational tools, such as Computational Fluid Dynamics, it has become possible to test these trims in flow conditions which are difficult to achieve in laboratories, but do exist in real time functioning of the trims. Hence, this study presents capacity testing and local flow analysis of a complex geometry trim, installed within a commercial control valve for severe service. The results show that the capacity of this particular design of trim decreases as the valve opening position decreases.

Nomenclature

Q	Volumetric flow rate (m^3/h)
Cv	Capacity of the valve $\left(\sqrt{m^7/kg}\right)$
P	Static pressure (Pa)
v	Flow velocity (m/s)
A	Cross-sectional area of the control valve (m^2)
k	Loss coefficient of control valve (–)
ρ	Density of the fluid (kg/m^3)

T. Asim (✉) · R. Mishra
University of Huddersfield, Huddersfield, UK
e-mail: t.asim@hud.ac.uk

M. Charlton · A.C. Oliveira
Weir Valves & Controls UK Ltd, Britannia House, Elland, UK

© Springer International Publishing Switzerland 2016

A. Segalini (ed.), *Proceedings of the 5th International Conference on Jets, Wakes and Separated Flows (ICJWSF2015)*,
Springer Proceedings in Physics 185, DOI 10.1007/978-3-319-30602-5_54

g	Gravitational acceleration (m/s^2)
ΔP	Pressure drop across the valve (kPa)
SG	Specific gravity of the working fluid (–)
VOP	Valve Opening Position (%)
Cv_{Trim}	Capacity of the Trim $\left(\sqrt{m^7/kg}\right)$

1 Introduction

The control valve and trim considered in the present study have been designed specifically to minimize the negative aspects of control valves, such as excessive noise and cavitation. These effects commonly occur during severe service environments such as in boiler feed-water, and also in highly erosive conditions such as oil and gas sector. The patented trim design studied in this work uses a staggered cylindrical arrangement on discs which are stacked on top of each other to better control the flow.

Generally these valves are designed using a combination of analytical, experimental and numerical tools to meet process requirements of the valve capacity. From the design point of view the valve capacity Cv is the most important parameter and it can be derived from the energy equation, which can be represented as:

$$\frac{P_1}{\rho g} + \frac{v^2}{2g} = \frac{P_2}{\rho g} + \frac{v^2}{2g} + k\frac{v^2}{2g} \tag{1}$$

where P_1 and P_2 are the static pressures at the inlet and outlet sections of the control valve. Assuming that the flow within the control valve is incompressible and the size and ground elevation of the inlet and outlet sections of the control valve remains the same, (1) becomes:

$$\frac{\Delta P}{\rho g} = k\frac{v^2}{2g} \tag{2}$$

where the flow velocity can be replaced as:

$$\frac{\Delta P}{\rho g} = \frac{k}{2g}\frac{Q^2}{A^2} \tag{3}$$

Rearranging (3) gives:

$$Q = \sqrt{\frac{2A^2\Delta P}{k\rho}} \tag{4}$$

or

$$Q = constant \sqrt{\frac{\Delta P}{SG}} \tag{5}$$

In the present study, the working fluid is water and hence SG = 1. Advanced CFD tools have proven to be extremely powerful design tools and increasingly being incorporated into the design stage for many different products [1–4]. CFD allows for the testing of various designs without the need to manufacture and flow test each and every single trim design. In the present study, CFD and experimental results have been used to test a continuous resistance trim with a cylindrical arrangement of stacked discs.

2 Numerical Modelling

According to the industrial standard [5], the test setup for control valves should be such that the inlet and the outlet of the valve should be attached with straight pipes of lengths 2*D and 6*D, where D is the nominal diameter of the pipeline. Furthermore, Fig. 1a depicts the fluid domain of the valve body and the inlet and outlet pipes used in the present study. Figure 1b shows the trim installed in the valve body. The studied trim comprises of 11 discs and each disc has 5 rows of cylinders. A section view of a single disc can be seen in Fig. 1c.

Hybrid meshing has been used for the meshing of the flow domain. The inlet and outlet pipes have been meshed using hexahedral mesh elements of a constant size of

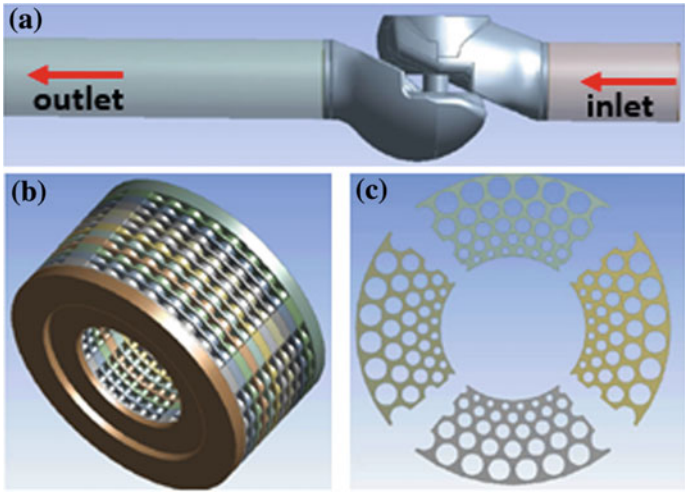


Fig. 1 Numerical model of the valve body and inlet/outlet pipes **a** and trim **b**, **c**

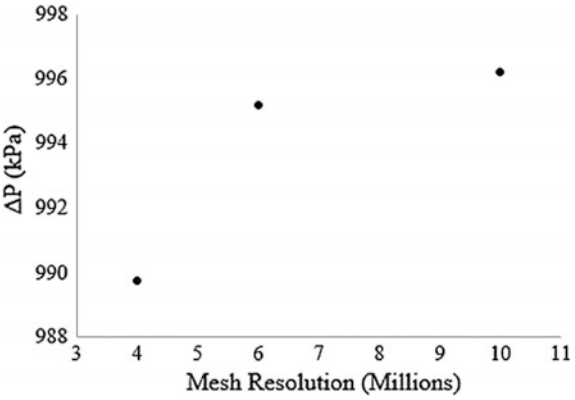


Fig. 2 Grid independence study

3 mm. The control valve with the trim installed has been meshed using tetrahedral mesh elements with a minimum and maximum size of 0.3 and 3 mm, the total number of elements is 6 million. It has been noticed that these mesh settings result in accurate results, with maximum deviation of 2.1 % at any valve opening position. Furthermore, spatial discretization of the flow domain has been carried out using three different mesh settings, one being already discussed, and the others resulting in 4 million and 10 million grid elements respectively. It can be clearly seen in Fig. 2 that from 6 million elements onwards, there are marginal variations in pressure drop across the valve.

Three dimensional Navier-Stokes equations, together with the continuity equation, have been numerically solved in an iterative manner for the steady flow of water through the valve and the trim. The scope of the present study is limited to the isothermal and incompressible flow within the aforementioned control valve, and hence pressure based solver has been used, keeping the density of water constant at 998 kg/m^3. As mentioned in [6, 7], extreme pressure and velocity gradients exist in these types of trims. Hence, Shear Stress Transport—kω model has been used to model turbulence within the control valve and the trim. SST-kω model depicts superior flow predictive properties at the near wall region i.e. within the boundary layer where extreme flow gradients are expected. Furthermore, it behaves as a standard k-ε model in the regions away from the walls.

The boundary conditions specified to the numerical model were defined as pressure inlet for the inlet, pressure outlet for the outlet and stationary walls for the trim and valve walls.

3 Results and Analysis

The aforementioned control valve has been tested numerically to evaluate the capacity of the trim. The results of this study have been presented in the following sub-sections.

Table 1 Verification of CFD results

Valve opening position (%)	ΔP (kPa)	Difference between experimental and CFD based Cv_{Trim} (%)
100	341	5.06
60	370	0.88
10	375	0.33

3.1 Verification of the Numerical Model

In order to justify that the aforementioned mesh size settings are able enough to predict the capacity of the valve/trim with reasonable accuracy, CFD results for the same have been compared against the experimental/flow-loop test results, so that the CFD results can be validated. The flow-loop test results of the same valve and trim were obtained from the technical report regarding the valve and the various trims [8]. Because the flow-loop tests were carried out at much lower pressure differentials, the boundary conditions were changed accordingly. The results are shown in Table 1 which clearly show that there is good agreement between experimentally found capacity of the trim (Cv_{Trim}) and CFD based Cv_{Trim}.

The different numerical simulations presented in Table 1 were repeated using standard k-ε turbulence model and it was found out that k-ε is, on average, roughly 7 % more inaccurate in the prediction of the capacity of the valve/trim as compared to SST-kω turbulence model, and hence is more advisable than k-ε model in case of severe service control valves. It is noteworthy that convergence was judged based on the variations in the mass flow rate within the control valve. The solution was considered converged once the variations dropped below 1 %.

3.2 Performance Analysis of Trim

Figure 3 depicts the variations in the static pressure (in kPa) and the flow velocity (in m/sec) within a single disc of the trim for a pressure drop of 1,000 kPa across the valve and at 10 % valve opening position. The flow direction is from the outermost row towards the innermost row of the trim. It can be seen that the inlet section has higher pressure as compared to outlet section of the trim. It can be further seen that pressure drops within the trim from one row to another. As water passes between two cylinders, due to area reduction, pressure drops. As water exits a row and enters another one, due to increase in area available for the flow, pressure increases again. Hence, the pressure drops in successive steps within a trim, rather than a single continuous drop within the valve alone.

It can be seen in Fig. 3b that the flow velocity increases between the cylinders of a row, where the area available for the flow to take place is less; hence forming jet effects. As water exits a row and enters another one, due to area increase, velocity

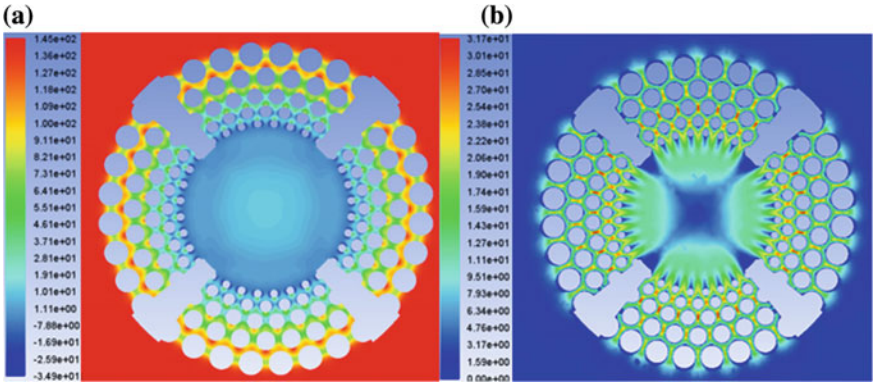


Fig. 3 Variations of flow variables in the trim at 1,000 kPa inlet pressure and 10 % valve opening position **a** Static pressure (psi) **b** Flow velocity (m/s)

reduces to satisfy continuity [9]. The minor asymmetries observed in Fig. 3 may be due to convergence issues, were a convergence criteria of 1×10^{-5} has been specified in the present study.

After carrying out detailed qualitative analysis on the flow structure within a trim, the static pressure variations within the rows need to be analysed to predict the onset of cavitation in the trim. Figure 4 depicts these variations along with the vapor pressure line (in red). It can be noticed that the static pressure reduces in steps due to the resistance offered by the different rows of the trim. In this way, flow within the valve can be controlled, and hence the primary reason to use this type of trims in severe service control valves. Furthermore, it can be observed that the local static pressure drops slightly below the vapour pressure line in the last row of the trim only, and hence cavitation is expected here.

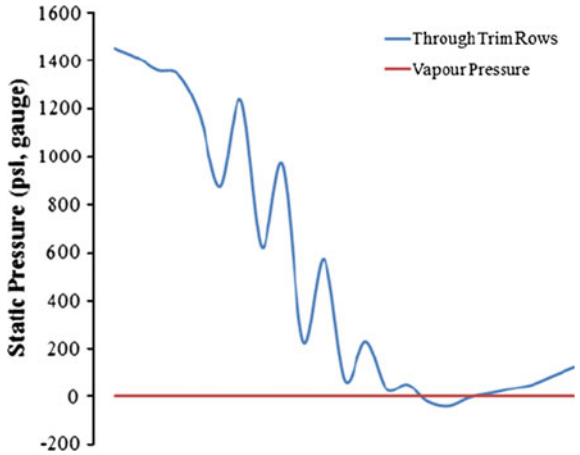


Fig. 4 Variations in the static pressure in the trim's lower most disc at 10 % valve opening position and for 1,000 kPa inlet pressure

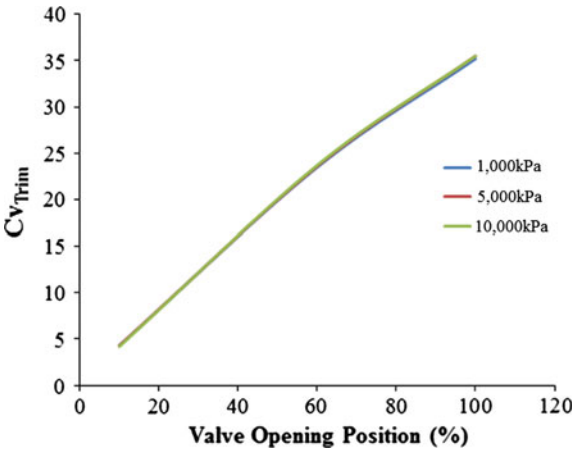


Fig. 5 Variations in Cv_{Trim} of full cylinder trim at various valve opening positions and flow conditions

Figure 5 summarizes the capacity results for the trim for various severe service pressure differentials across the control valve.

The results presented in Fig. 5 can be summarised as follows:

1. As the valve opening position (VOP) decreases, Cv_{Trim} decreases
2. Cv_{Trim} remains almost constant for various flow conditions (pressure drops) for the same valve opening position

This suggests that Cv_{Trim} is a function of the valve opening position only, and not of the flow conditions. Figure 3 depicts the variations in Cv_{Trim} w.r.t. valve opening position at different flow conditions considered in the present study. It can be seen That as the valve opens more, Cv_{Trim} increases. This is because there is more area available for the flow to take place, and hence the capacity of the valve increases.

In order to express Cv_{Trim} as a function of valve opening position, multiple variable regression analysis has been carried out on the results presented in Fig. 3. The following predictor expression has been developed:

$$Cv_{Trim} = \frac{VOP}{\sqrt{7}} \tag{6}$$

Equation (6) shows that as the valve opening position increases, Cv_{Trim} increases linearly, which indicates that the pressure drop and the flow rate relationship is linearly dependent on the valve opening position. In order to check the validity of (6), Cv_{Trim} values have been calculated using (6) and compared against the results presented in Fig. 5. It has been observed that (6) gives an average percentage error of 7.4 % compared to the results presented in Table 1, and hence this equation can be used to predict the capacity of full cylinder trims with 93.6 % accuracy.

4 Conclusions

Computational Fluid Dynamics based investigations have been carried out on a severe service control valve with a geometrically complex trim installed. Capacity results have been evaluated and compared with experimental data. It has been shown that the pressure reduces, and hence the flow velocity increases, within a row of a trim due to area reduction. The capacity results suggest that that Cv_{Trim} values are dependent on the valve opening position only, and independent of the flow conditions. Furthermore, Cv_{Trim} decreases as the valve opening position decreases, due to reduced area for the flow to take place.

A novel predictor expression for the capacity of the trim considered have been developed that can be useful in the design process of these trims.

References

1. A. Marquis, CFD in fluid machinery design, in *Proceedings of the Institution of Mechanical Engineers*. ISSN: 0957-6509. 06/2000 J. Power Energy **214**(6), 699 (2000)
2. P. Dvorak, CFD speeds fan design. Mach. Des. **75**(19), 60 (2003)
3. M. Kacik, P. Dvorak, How CFD streamlines fluid designs. Mach. Des. **74**(20), 64 (2002)
4. J. Wu, K. Shimmei, K. Tani, J. Sato, CFD-based design optimization for hydro turbines. J Fluids Eng. **129**(2), 159 (2007)
5. IEC60534-2-1 Industrial-process control valves part 2-1: flow capacity—sizing equations for fluid flow under installed conditions Edition 2.0 2011-03
6. J. Green, R. Mishra, M. Charlton, R. Owen, Validation of CFD predictions using process data obtained from flow through an industrial control valve. J Phys. Conf. Ser. **164** (2012)
7. J. Green, R. Mishra, M. Charlton, R. Owen, Local analysis of flow conditions within a geometrically complex control valve trim using CFD. J Phys. Conf. Ser. **164** (2012)
8. T. Asim, Capacity testing of X-Stream valves for single-component single-phase flows. Technical Report (2013)
9. R. Mishra, S.N. Singh, V. Seshedri, Study of Wear Characteristics and Solid Distribution in Constant Area and Erosion-Resistant Long-Radius Pipe Bends for the flow of Multisized Particulate Slurries. J. Wear **217**, 297 (1998)

Wall Treatment Effects on the Heat Transfer in a Radial Turbine Turbocharger

Shyang Maw Lim, Anders Dahlkild and Mihai Mihăescu

Abstract Contradicting results about heat transfer effects on the performance of turbine turbocharger motivated this study. It was aimed to assess the effects that the wall treatment in a numerical sense has on the performance of a radial turbine of automotive turbocharger operating under a continuous flow condition. Adiabatic and non-adiabatic conditions were analyzed by using Unsteady Reynolds Averaged Navier-Stokes (URANS), Large Eddy Simulations (LES) and Detached Eddy Simulations (DES) approaches. When considering heat transfer, heat transfer loss at various locations is highly dependent on the near-wall modelling approach employed. Development of thermal boundary layer in the upstream region of turbine affects how the gas is convected in the downstream components, such as the scroll and the rotor. As long as the deviation in predicting thermal boundary layer does not affect the prediction of gas temperature at the inlet and outlet of the rotor, the difference in turbine power prediction by different near-wall modelling approaches was found to be small.

1 Introduction

Turbochargers are usually not thermally insulated and heat transfer is known to have an effect on their performance. Most of the literature focuses on the heat transfer effects on the performance of the compressor, with little focus on heat transfer affecting the performance of the turbine. As for the effect of heat transfer on the turbine performance, most studies concluded that this effect is small. Under gas stand similar operative conditions, maximum turbine efficiency improvement in hot test conditions compared with cold test conditions is about 4 %, which is within measurement uncertainty range [8]. Improved mechanical efficiency due to lower oil viscosity in hot test conditions is one of the given reasons [8]. In a numerical

S.M. Lim (✉) · A. Dahlkild · M. Mihăescu
Competence Center for Gas Exchange (CCGEx), KTH Royal Institute of Technology, Stockholm, Sweden
e-mail: smlim@kth.se

© Springer International Publishing Switzerland 2016

A. Segalini (ed.), *Proceedings of the 5th International Conference on Jets, Wakes and Separated Flows (ICJWSF2015)*,
Springer Proceedings in Physics 185, DOI 10.1007/978-3-319-30602-5_55

study by Hellström and Fuchs [6], the difference in shaft power of a turbine between adiabatic and non-adiabatic scenarios was found to be as small as 1 % based on LES data with near wall treatment. However, recent experimental measurements performed on a combustion chamber test rig at University of Hannover shows 55 % reduction in actual turbine power due to heat losses associated with the turbine [9]. Contradicting results in the literature suggest that more work is needed to understand the effects of heat transfer on turbine performance.

The objective of this numerical study was to analyze the performance of a turbine of an automotive turbocharger under adiabatic and non-adiabatic situations and for different numerical treatments of the near-wall region. It was shown in this study that heat transfer loss at various locations is highly dependent on near wall modelling approaches.

2 Set-up and Methodology

The computational domain represents the steady gas stand experimental set-up. It consists of an inlet pipe, a scroll, a rotor and an outlet pipe. Exhaust manifolds, waste gate and its by-pass channel were not modelled in this study because they were not included in the steady gas stand experiment. The gap between the rotor and the backplate, and the tip clearance between the rotor blade and the shroud wall, were modelled to account for windage loss and tip leakage flow respectively.

The CFD finite volume based solver Star-CCM + by CD-Adapco was used to perform the numerical simulations. Previously, it was employed for a similar turbine configuration without considering the heat transfer problem [3]. The fluid domain was discretized by using a polyhedral mesh with prism layers. Table 1 summarizes the set-ups investigated under adiabatic and non-adiabatic assumptions by using URANS, LES with standard Smagorinsky Subgrid Scale (SGS) model and DES, respectively. The LES part of DES is modelled by using standard Smagorinsky SGS model in the solver and therefore LES with standard Smagorinsky SGS model was used so that meaningful comparison of results can be made in this study. Figure 1 shows the computational domain and a mesh detail. Note that the mesh size in the core region of the flow is the same for all cases. A very fine near-wall resolution was used for DES for accurately solving the walls. Prism layers and standard wall functions are used with URANS and LES calculations.

Table 1 Test cases setup

Cases	Near-wall modelling	Mesh size	Prism layers	y^+ max
URANS/LES	Standard wall functions	3.2 million	3	30
DES	SST-kω	7 million	12	1

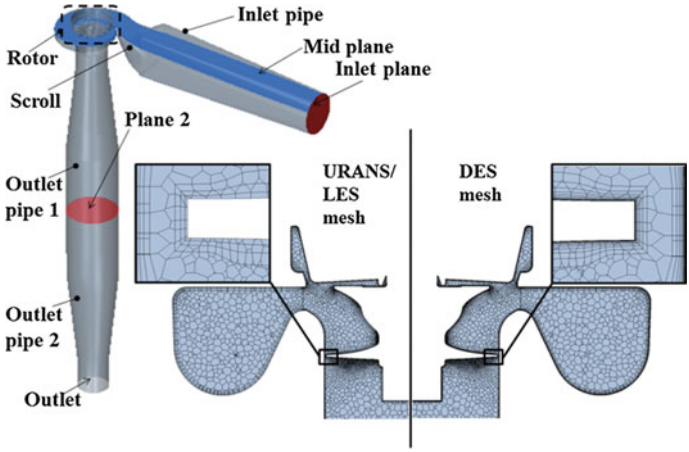


Fig. 1 Computational domain and mesh. Computational domain consists of the fluid region only. Inlet and outlet pipes geometry is modelled according to the gas stand setup

The boundary conditions imposed correspond to a maximum efficiency operating point on a low speed line for the turbine under investigation. Choosing this particular operating condition was motivated based on the reports in literature that heat transfer has impact on turbine performance at low speed lines [1, 9]. At the inlet plane of the computational domain, mass flow rate of 0.058 kg/s and a total inlet temperature of 1173.15 K were employed. Furthermore, 10 % of turbulent intensity was employed at the inlet boundary, as according to literature [3]. A constant atmospheric pressure was considered at the outlet. Smooth and no slip conditions were employed to all the walls in the computational domain.

The rotation of the turbine rotor was handled with constant rotational speed of 84533 rpm by using the sliding mesh technique, i.e. the rotor is displaced to a new position per time step. Sliding mesh technique was chosen because it takes into account the transient blade passing effects and it was found to be better as compared with Multi Reference Frame (MRF) approach [4, 5]. The time-step used corresponds to one degree rotation of the rotor and it was chosen to give convective courant number of less than unity in most of the computational domain.

Heat transfer can be modelled by assigning the heat flux across the fluid wall boundary or the wall temperature. In this study, heat transfer was considered by assigning a constant wall temperature of 1002 K, because wall temperature could be estimated from literature [7] for the given total inlet temperature.

Then, mass, momentum and energy conservation equations were solved simultaneously in time marching manner by using a density-based coupled solver. The non-linear system of equations of mass, momentum and energy were closed by using ideal gas law. The convective and diffusive terms in the governing equations were discretized by using the finite volume method. For the spatial discretization, an implicit second order bounded-central differential (BCD) scheme was employed

in URANS and LES, and an implicit hybrid BCD scheme was used in DES, as recommended in the Star-CCM + documentation [2]. Implicit second order temporal discretization was used in all cases.

Prior to transient simulations, steady-state RANS simulations based on SST k-ω turbulence model was carried out using mixing plane interface, a method that conserves quantities across the stationary-rotating domains interface by using circumferential averaging technique. Transient simulations of URANS, LES and DES were then performed with steady- state RANS data as flow field initialization. All transient simulations were run until statistically convergence of global performance parameters (e.g. pressure ratio, turbine power and heat transfer across the wall boundary) has reached.

3 Results and Discussions

Figure 2 shows the mean absolute static pressure contours at the mid plane (see also Fig. 1 for orientation purposes) cutting through the scroll of the turbine and the rotor, as calculated with the three approaches. Both adiabatic and non-adiabatic cases show radially outward pressure gradients in the scroll, with only slightly lower static pressure in the scroll for non-adiabatic cases. This is because at the investigated operating condition (maximum efficiency), the flow is attached to the wall and no severe secondary flow motion is observed for the scroll and rotor regions, as can be seen from the mean velocity magnitude contour plot in Fig. 3. Despite of this fact, there are significant differences in the temperature distributions

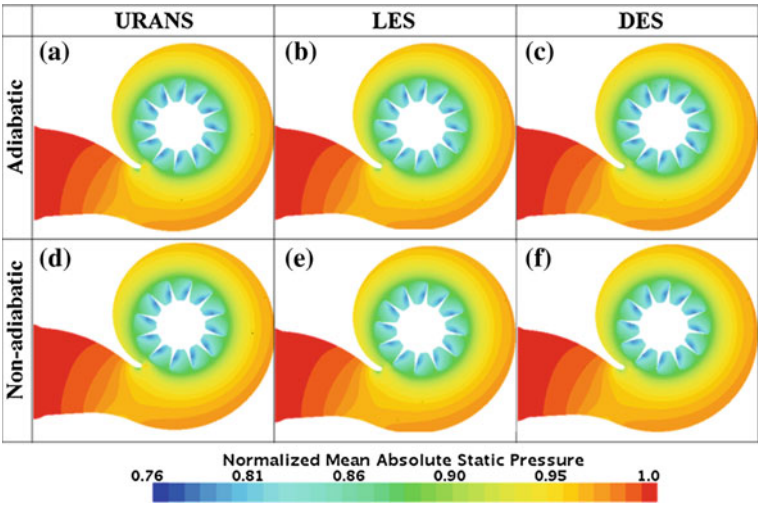


Fig. 2 Comparisons of normalized mean absolute static pressure field. The mean absolute static pressure is normalized by inlet gas static pressure

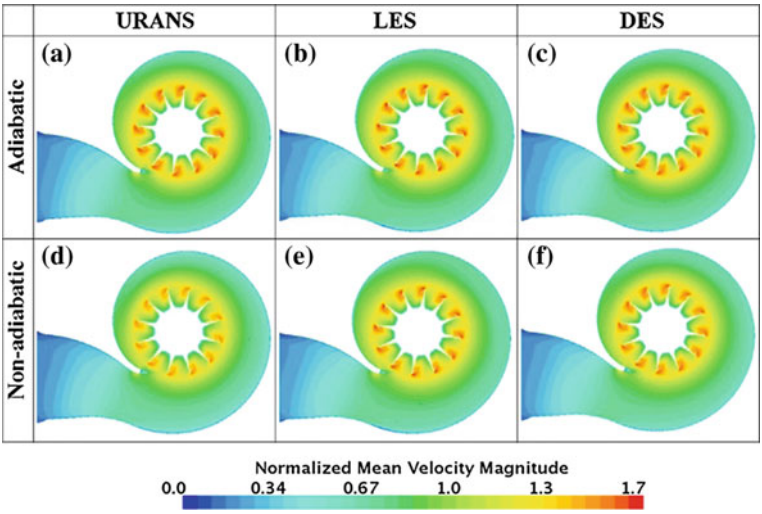


Fig. 3 Comparisons of normalized mean velocity field. The mean velocity is normalized by the rotor blade speed at the inlet

around the scroll as calculated under adiabatic and non-adiabatic conditions, as depicted in Fig. 4. By assuming adiabatic walls, no thermal boundary layer is developed. As the pressure increases radially outward (hence velocity decreases radially outward, as shown in Fig. 3) in the scroll, higher gas temperature is

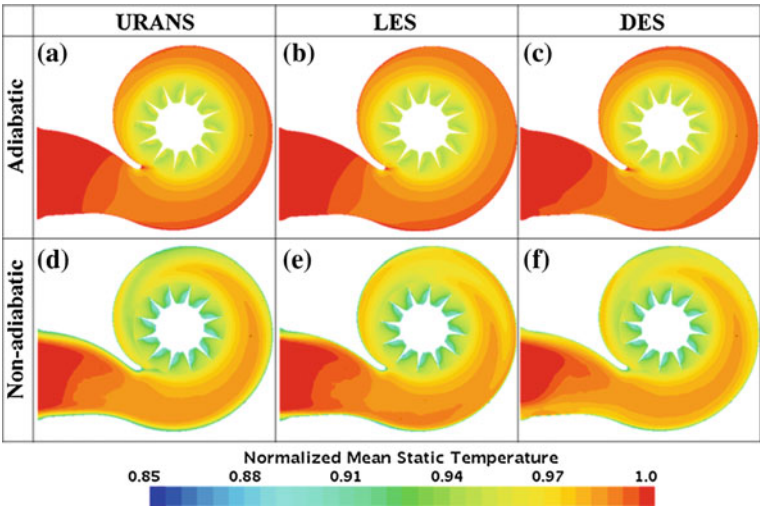


Fig. 4 Comparisons of normalized mean static temperature. The mean static temperature is normalized by inlet gas total temperature

observed near the scroll wall because of constant total temperature in adiabatic condition. On the other hand, for non-adiabatic cases, the thermal boundary layer starts to develop in the inlet pipe and the gas enters the scroll with a prominent temperature profile. The gas is separated into two distinct regions at the scroll's inlet, i.e. lower gas temperature near the wall and higher temperature in bulk flow. Temperature profile at the scroll's inlet plays an important role in creating circumferential temperature variation in the scroll. Also, as compared with adiabatic cases, lower gas temperature is observed at the inlet of the rotor.

Among the different near-wall modelling approaches of the methods employed, difference in the temperature field (Fig. 4) is observed. For example, under adiabatic assumption, DES (with highly refined near-wall region) predicts higher gas temperature near the wall. No large differences in gas temperature at the rotor inlet are observed among URANS, LES, and DES, under adiabatic assumption.

Figure 5a shows the comparisons of global turbine performance between non-adiabatic and adiabatic conditions. Pressure ratio is defined as the ratio of total pressure at the inlet plane to the static pressure at plane 2 (see Fig. 1 for the locations of the planes), and turbine power is calculated by multiplying the rotational speed with the integrant of torque over the rotor's surface area. It can be seen that pressure ratio is about 0.2 % lower in non-adiabatic cases, compared with adiabatic cases. Small reduction in pressure ratio due to heat transfer is also reported in the literature [6, 8]. On the other hand, according to Fig. 5a, the turbine power is predicted to be about 3 % lower due to heat transfer loss.

Turbine power is proportional to the rate of change of the angular momentum of the fluid at the inlet and outlet of the rotor, as described by Euler turbomachine equation (1).

$$\dot{W}_t = \dot{m}\omega(r_{in}C_{\theta in} - r_{out}C_{\theta out}) \tag{1}$$

Here $\dot{m}$ is the mass flow rate, ω is the rotational speed of the rotor, r is the radius of the rotor and C_θ is the absolute velocity component in the tangential direction. Subscripts *in* and *out* denotes the inlet and outlet of the rotor respectively.

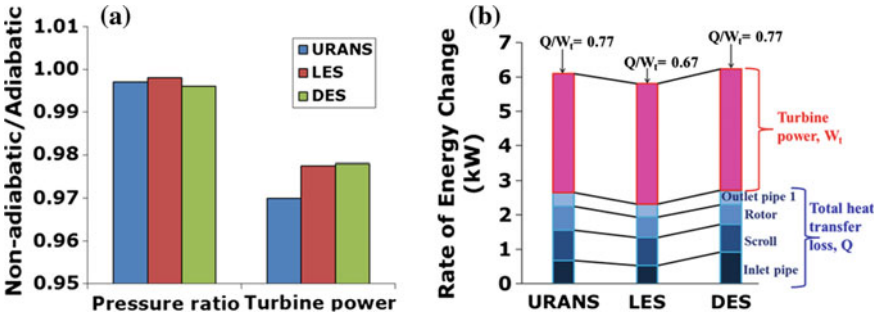


Fig. 5 Comparisons of turbine global performance. **a** Adiabatic versus non-adiabatic. **b** URANS versus LES versus DES for non-adiabatic conditions

In the investigated operating condition (maximum efficiency), the ratio between the absolute velocity component in the tangential direction at the inlet ($C_{\theta in}$) and outlet ($C_{\theta out}$) of the rotor, $\frac{C_{\theta in}}{C_{\theta out}}$ is predicted to be about 14. Since the radius of the rotor at the inlet is greater than the outlet in radial turbine, this means that the second term in the bracket of 1 can be neglected in the investigated operating point because $r_{in}C_{\theta in} \gg r_{out}C_{\theta out}$. By using ideal gas law and velocity triangle relationship, the turbine power can be related to the thermodynamics properties as shown in 2.

$$\dot{W}_t = \frac{\dot{m}^2 \omega r_{in} tan(\alpha_{in}) R}{A_{in}} \times \frac{T_{in}}{P_{in}} \tag{2}$$

Here α is the absolute flow angle, R is the specific gas constant, A is the cross sectional area, T is the temperature and P is the pressure, while $\dot{m}$, ω and r were already defined. Again, subscript *in* denotes the inlet of the rotor.

From Figs. 2, 4 and 5, it can be seen that the heat transfer has a small influence on the pressure field but reduces the temperature at the rotor inlet when compared the adiabatic and non-adiabatic cases. Since 2 states that turbine power is directly proportional to the gas temperature at the rotor's inlet, the reduction in turbine power might be caused by the lower gas temperature at the rotor inlet due to heat transfer. It can also be seen from Fig. 5a that the effects of heat transfer on turbine power predicted by URANS, LES and DES are almost the same (<1 % difference). This is because the gas temperature predicted by the three modelling approaches at the rotor inlet is almost the same despite the observed variation of temperature contours in the scroll.

Figure 5b compares the predicted total heat transfer to the turbine power for URANS, LES and DES. Heat transfer loss in Fig. 5b is calculated by integrating the heat flux over the wall boundary area. From Fig. 5b, it can be seen that heat transfer loss at various locations is highly dependent on the near-wall modelling approaches. For example, DES (with fine mesh at near-wall region) predicts higher heat transfer loss at inlet pipe and scroll, as compared with URANS and LES. Furthermore, the ratio of total heat transfer loss to turbine power is predicted to be more than 0.6 for all near-wall modelling approaches. This is consistent with experimental measurements by Burke et al. [1], which predicted a value of about 0.88 for the turbine power obtained in this study. High total heat loss as compared with turbine power indicates that the amount of energy wasted to the environment is large and one might expect that some portion of heat loss energy to be converted to useful turbine work if there is no heat transfer, e.g. adiabatic condition. However, as discussed earlier, the turbine power is predicted to be about 3 % lower due to heat transfer loss (see Fig. 5a). This shows that although the turbine is operating under adiabatic condition, not all available energy in the system can be harvested by the turbine for useful work, as also reported by Hellström and Fuchs [6]. In adiabatic condition, all the unextracted fluid energy is convected downstream. On the other

hand, in non-adiabatic case, besides convection of unextracted fluid energy to the downstream, a portion of the un-extracted fluid energy is discharged to the environment through heat transfer mechanisms.

4 Conclusions

This work represents an effort towards understanding how the numerical treatment at the wall region in a radial turbine operating under continuous flow conditions affects turbine performance. Within URANS and LES frameworks, the near-wall region was modelled using prism layers and standard wall functions, while within DES calculations, the resolved near-wall region was treated using the SST-kω model. It can be concluded that heat transfer loss at various locations is highly dependent on near-wall modelling approaches. Development of thermal boundary layer in the upstream region of turbine affects how the gas is convected in the downstream components, such as the scroll and rotor. As long as the deviation in predicting thermal boundary layer does not affect the prediction of gas temperature at the inlet and outlet of the rotor, the difference in turbine power prediction is small. At low pressure ratio operating condition, in order to reduce computational effort, the adiabatic wall assumption can be used if pressure ratio is the performance parameter of interest.

Note that turbine power reduction due to heat transfer predicted in this study is significantly lower than 55 % reduction as reported from experiment [9]. Also, a reduction of turbine power was observed in this study whereas an increment of turbine efficiency due to heat transfer was measured in another experimental study [8]. Differences in turbine geometry, e.g. Variable Geometry Turbine (VGT) in literatures but Fixed Geometry Turbine (FGT) in this study, might be the reason. Nevertheless, no measured flow field data is available for comparisons to perform further investigation.

Acknowledgments This work was carried out within the framework of the Competence Center for Gas Exchange (CCGEx) at KTH. The support and contributions from the Swedish Energy Agency, Scania, Volvo Cars, Volvo GTT, and Borg Warner are greatly acknowledged. The Swedish National Infrastructure for Computing via Parallel Computing Center (PDC) at KTH is acknowledged for providing the computational resources.

References

1. R.D. Burke, C.R.M. Vagg, D. Chalet, P. Chesse, Heat transfer in turbocharger turbines under steady, pulsating and transient conditions. Int. J. Heat Fluid Flow **52**, 185–197 (2015)
2. CD-adapco STAR-CCM + User Guide 9.06 (2014)
3. J. Fjällman, M. Mihăescu, L. Fuchs, Analysis of 3-Dimensional Turbine flow by Using Mode Decomposition Techniques. ASME Paper, GT2014-26963 (2014)

4. F. Hellström, L. Fuchs, Effects of inlet conditions on the turbine performance of a radial turbine. ASME paper, GT2008-51008, 1985–2001 (2008)
5. F. Hellström, L. Fuchs, Numerical computation of the pulsatile flow in a turbocharger with realistic inflow conditions from an exhaust manifold. ASME paper, GT2009-59619, 1317–1329 (2009)
6. F. Hellström, L. Fuchs, Assessment of heat transfer effects on the performance of a radial turbine using large eddy simulation, in *IMechE, 9th Conference on Turbochargers and Turbocharging* (2010)
7. A. Romagnoli, R. Martinez-Botas, Heat transfer analysis in a turbocharger turbine: an experimental and computational evaluation. Appl. Therm. Eng. **38**, 58–77 (2012)
8. J.R. Serrano, C. Guardiola, V. Dolz et al., Experimental study of the turbine inlet gas temperature influence on turbocharger performance. SAE Technical Paper, 2007-01-1559 (2007)
9. S. Shaaban, J. Seume, Impact of turbocharger non-adiabatic operation on engine volumetric efficiency and turbo lag. Int. J. Rotating Mach. (2012)

On the Characteristics of the Jet in Film Cooling Applications

Hossein Nadali Najafabadi, Arman Farhanieh, Roland Gårdhagen and Matts Karlsson

Abstract Numerical and experimental investigations are conducted to study the jet characteristics on the pressure side of a film-cooled turbine guide vane. CFD simulations, including both the steady RANS turbulence model, $k-\omega$ shear stress transport (SST), as well as the hybrid approach, Scale-Adaptive Simulation (SAS), are utilized to comprehend the turbulent flow structures and the vortex dynamics associated to the film cooling jet. For this purpose the commercial CFD code FLUENT has been utilized to study flow with injection of coolant through fan-shaped holes for two blowing ratios (0.6 and 1.2). Although, both turbulence models predict the vortical structures and jet dynamics similarly, the findings suggest that by resolving large energy containing vortices, the SAS model can improve the modeling of mixing properties and thereby approximation of the surface temperature.

1 Introduction

The problem of jet in crossflow have been studied extensively by a broad spectrum of researchers due to its importance for many technical applications. One of the occurrences of this flow problem is within film cooling applications. In film cooling, a thin layer of cold air is injected through discrete or slot holes to provide a protective layer between the hot gas stream and external surfaces of gas turbines. Because of the complexity of this flow problem stemming from a number of flow and geometrical parameters, finding an optimum film cooling design has become an engineering challenge. Therefore both experimental and numerical approaches are used quite extensively not only to investigate different aspects of film cooling but also to understand the physical phenomena involved.

H. Nadali Najafabadi (✉) · A. Farhanieh · R. Gårdhagen · M. Karlsson
Department of Management and Engineering,
Linköping University, 581 83 Linköping, Sweden
e-mail: hossein.nadali.najafabadi@liu.se

© Springer International Publishing Switzerland 2016

A. Segalini (ed.), *Proceedings of the 5th International Conference on Jets, Wakes and Separated Flows (ICJWSF2015)*,
Springer Proceedings in Physics 185, DOI 10.1007/978-3-319-30602-5_56

Numerous studies have conducted computational film cooling investigations to address both numerical aspects as well as parametric investigations, e.g. Ferguson et al. [1], Harrison and Bogard [2] and Colban et al. [3]. Since RANS simulations often fail in acceptable predictions of the time averaged quantities and physical phenomena involved such as the turbulent flow structures and the vortex dynamics of the film cooling jet, some studies have used Large Eddy Simulations (LES) to address this problem, e.g. see Guo et al. [4] and Renze et al. [5], Peet and Lele [6]. These studies however consider low Reynolds number flow and simplified computational domains. Thus due to high spatial and temporal resolution for high Reynolds number wall bounded flows for real turbine configurations, the applicability of LES is limited in practice. Also most available studies have considered the flow dynamics of cylindrical holes and there exist limited references on jet dynamics of fan-shaped holes, which are being replaced by cylindrical holes during recent years.

This study investigates the vortical structures and the vortex dynamics of the jet due to injection of coolant through discrete fan-shaped holes on the pressure side of a turbine guide vane. The RANS turbulence model, $k-\omega$ SST and the hybrid model, Scale-Adaptive Simulation (SAS) have been used to enhance the understanding about this flow problem, the mixing properties and their effect on surface temperature and at the same time to address the practical applicability of the SAS model. Also comparison between the CFD results and experiments in terms of adiabatic film effectiveness highlights the strength and weaknesses of the models.

2 Method

The measurement technique and geometrical dimensions related to the experimental set-up are described in detail by Nadali et al. [7]. The comparisons between the computational and experimental results are performed in terms of adiabatic film effectiveness (AFE), denoted as η. This parameter is essentially the normalized adiabatic wall temperature, and is defined as:

$$\eta = \frac{T_\infty - T_{aw}}{T_\infty - T_c} \tag{1}$$

where T_∞, T_{aw} and T_c, are the corresponding temperatures associated with the freestream, the adiabatic wall and the coolant, respectively. In the followings a short review of the turbulence models and estimation of the spatial and temporal resolution are addressed.

Turbulence Models: The steady RANS model selected is the $k-\omega$ SST model developed by Menter [8]. This model uses two transport equations for the turbulence kinetic energy and the specific dissipation rate and blends effectively the $k-\omega$ formulation for the near wall region with the $k-\epsilon$ in the far field.

The hybrid model is the Scale-Adaptive Simulation (SAS) model, developed by Menter and Egorov [9], stems from the transport equation for kL, which is used first by Rotta [10]. Here k refers to the turbulence kinetic energy (TKE) and L is the turbulence integral length scale. In this model sufficient numerical mesh resolution along with enough inherent flow instabilities will activate an additional source term, which in turn leads to local reduction in the eddy viscosity and hence resolving turbulent fluctuations.

Spatial and Temporal Resolution: Since the SAS model is acquired to resolve turbulent scales, special considerations should be given with respect to spatial and temporal resolution requirements especially in the jet interaction region. The definition of the inertial subrange has been used to estimate the geometry dependent vortices with high energy content and accordingly to approximate the time step Δt, see Pope [11]. The calculated time step, estimated to be $\Delta t = 3.0 \times 10^{-6}$ s, is then used to approximate the grid spacing based on the relation given in (2).

$$\Delta x = l_0 \left(\frac{u_0 \Delta t}{l_0} \right)^{3/2} \tag{2}$$

For a jet in cross flow the size of large eddies, l_0 is in the order of magnitude as the jet diameter, D. This jet has also the characteristic velocity, u_0 in the order of U_∞. Although, yet the statistical turbulence modeling will be used for universal turbulent fluctuations within the inertial sub-range, the above-mentioned estimations for temporal and spatial resolutions can ensure resolving the larger energy containing and geometry dependent vortices. According to the given discussion the ultimate mesh consists of about 28×10^6 hexahedral elements. Figure 1 shows the computational grid resolution in the vicinity of the cooling hole exit. It should be noted that the steady RANS model, SST uses the same mesh. The CFD simulations were carried out using the finite-volume based solver FLUENT 15.0 (ANSYS. Inc., Pittsburgh, PA, USA) on the Linux Cluster Triolith at National Supercomputer Centre (NSC, Linkping University, Sweden).

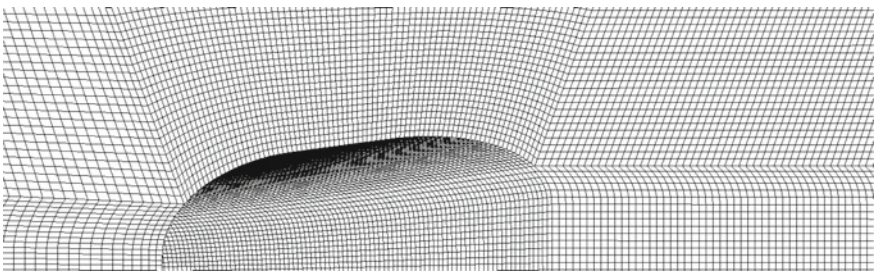


Fig. 1 The computational mesh resolution in the vicinity of the cooling hole exit

3 Results and Discussions

The flow separation in the film hole that creates a slow moving zone next to the hole downstream along the wall, causes flow acceleration upstream of this zone. The intermediate zone between these two regions is a shear layer region which carries high levels of turbulence into the crossflow region. This region corresponds to the maximum TKE area shown in Fig. 2a–d. Figure 2 also indicates that the turbulence models in general predict similar jet dynamic properties. The jetting effect inside the hole, due to the flow separation from the downstream wall of the film hole, causes a recirculating flow at the transverse planes of the film hole, which is indicated by rotating vortices in Fig. 2.

This recirculating flow, consistent with findings of Leylek et al. [12], is extended until the end of cylindrical part of the hole where the surface streamlines are plotted and its strength for the higher M is evident, Fig. 2b, d. As M increases, the intermediate zone will increase as the gap between highly accelerated flow and low flow region will become larger and the shear layer will become wider, see Fig. 2b, d. The

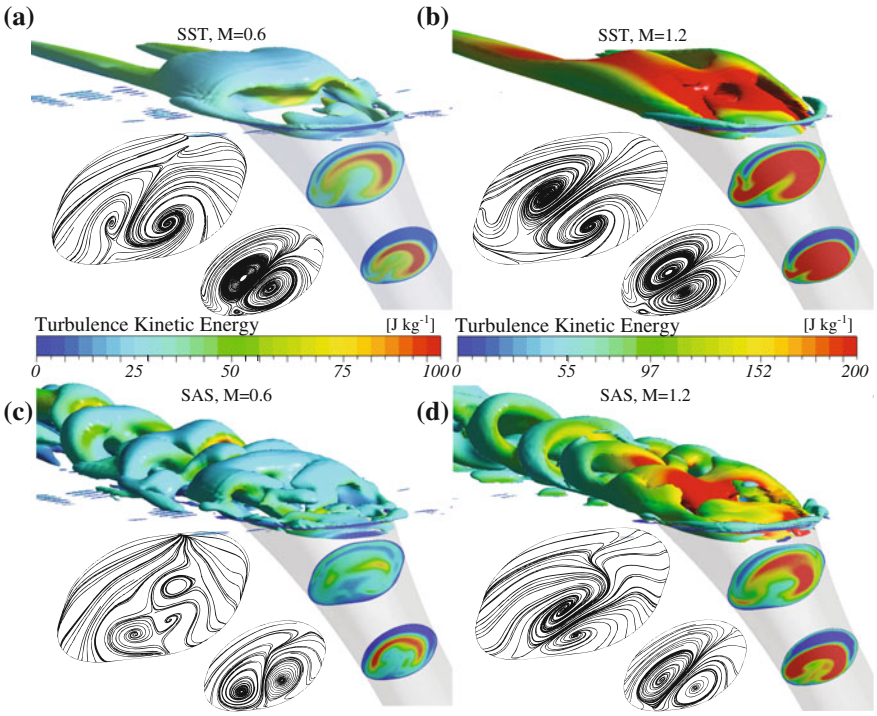


Fig. 2 Flow development through the cooling hole shown by 2D streamlines (in *black* and *white*) and TKE contour continued with the jet interaction represented by Q-criterion colored by TKE, **a** SST, $M = 0.6$, **b** SST, $M = 1.2$, **c** SAS, $M = 0.6$, **d** SAS, $M = 1.2$

SAS model exhibits different capability in predicting the shear layer zone as it shows lower level of TKE. Figure 2 also shows that by resolving the vortical structures with high energy content at the hole exit, the associated TKE is decreased for the far filed flow. This can in turn effect the jet entrainment and consequently the mixing properties.

A dominant vortical structure associated with jet-crossflow interaction, due to roll-up of the shear layer vorticity on the lateral sides of the jet, is the counter-rotating vortex pair (CRVP), which can be seen clearly in Fig. 3. From this figure it is seen that the SST model predicts one additional vortex between CRVP for the lower M. As indicated by this figure, the two mushroom-like lobes, which correspond to the legs of CRVP, are lifted from the surface when the blowing ratio is increased, which gives indication of slight jet separation from the surface.

From the film effectiveness contours, it can be seen that CRVP has a detrimental effect on film performance as it helps the hot flow to lie in between the surfaces and jet, indicated by low film effectiveness in the contours. For the higher M this also will increase the jet core temperature as the mixing properties of the jet is enhanced. These results are consistent with findings of Peet and Lele [6]. For blowing ratio 1.2 comparison between Fig. 3c, d indicate that the center of CRVP is shifted more towards $Z/D = 0$ for SAS model. Also from the contours the mixing is seen to be unsymmetrical for the higher M. Furthermore, for this blowing ratio SAS shows slight improvement in mixing properties. It is worth mentioning that the abovementioned jet characteristics are to a large extent similar to cylindrical holes in this study. The reason for such a similarity is that the fan-shaped holes have an area ratio, $A_{exit}/A_{in} \approx 1.8$, implying low level of jet diffusion at the hole exit. This low area ratio also explains the moderate jet lift-off for the investigated cooling hole at $M = 1.2$. For larger fan-shaped hole area ratio, for example $AR = 3.9$, Colban et al. [13] have reported that no jet separation may occur for blowing ratios even higher than 2.

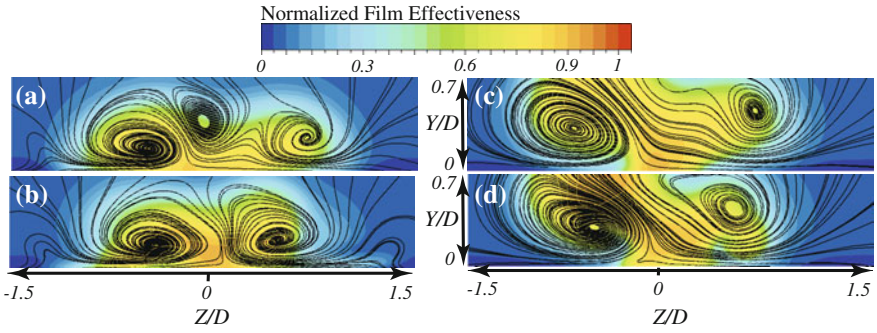


Fig. 3 Surface streamline and contour of normalized temperature represented by film effectiveness at the position of 3D downstream of the hole exit. **a** SST $M = 0.6$, **b** SAS $M = 0.6$, **c** SST $M = 1.2$, **d** SAS $M = 1.2$

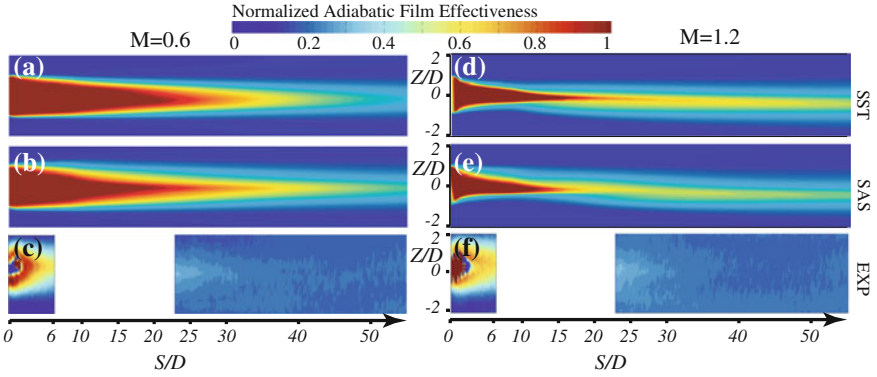


Fig. 4 Lateral and streamwise distribution of adiabatic film effectiveness. **a** SST $M = 0.6$, **b** SAS $M = 0.6$, **c** EXP $M = 0.6$, **d** SST $M = 1.2$, **e** SAS $M = 1.2$, **f** EXP $M = 1.2$. Note that EXP refers experiments and the discontinuity in data is due to limited accessibility to the test object through IR camera

Figure 4 demonstrates that compared to the experiments, CFD simulations, in general, maintain higher level of AFE in the jet center and can sustain this for a much longer distance, *S*/*D*. Where, *S*/*D* represents the surface length of the vane normalized by the hole diameter indicating the downstream distance from the cooling hole center. The results also suggest better lateral spreading for the experiments compared to the CFD. Thus, it can be stated that CFD results suffer from over prediction of the AFE in the streamwise direction and under prediction in the lateral direction. Comparison between different turbulence models illustrate that for the lower *M* both models maintain the same jet dispersion, although SAS model shows better lateral spread for far-field region.

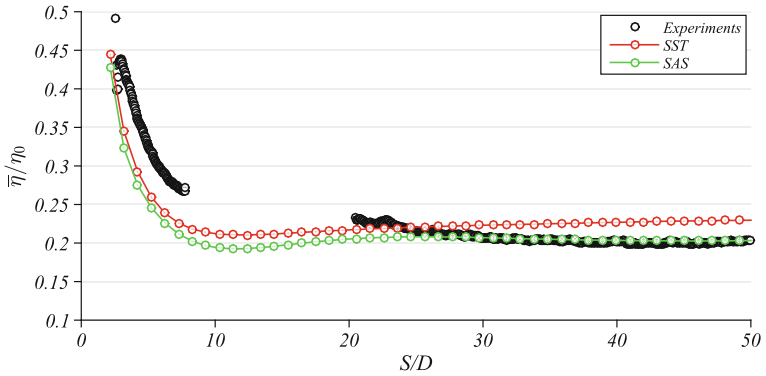


Fig. 5 Normalized laterally averaged adiabatic film effectiveness comparison between the experiments and CFD simulations for $M = 1.2$

For the higher M the jet dispersion happens first for the SAS (max AFE till $S/D \approx 20$ in Fig. 4e. The SST model sustains the jet momentum the longest (max AFE till $S/D \approx 35$ in Fig. 4d. The improved mixing properties of the SAS model are correlated with the prediction of the CRVP and shear layer roll-up predictions. Thus the results suggest that by resolving the turbulence spectrum associated with large vortical structures in the jet crossflow, more accurate predictions will be achieved. This can be clearly seen in Fig. 5. The quantitative comparison between the results in terms of laterally averaged AFE, indicate improved agreement for SAS model compared to the SST in particular when $S/D > 25$.

It can be concluded that despite of general similarities between the turbulence models, the SAS model may improve the mixing predictions and thereby surface temperature predictions due to the injection of coolant through fan-shaped hole on the pressure side of a turbine guide vane, where the results are compared in terms of AFE versus experiments. The SAS capability in capturing the jet dynamics and also resolving high energy content and geometrical dependent vortical structures indicates its potential for further investigations as well as future industrial usage.

Acknowledgments This research has been funded by the Swedish Energy Agency, Siemens Industrial Turbomachinery AB, Volvo Aero Corporation, and the Royal Institute of Technology through the Swedish research program TURBOPOWER, the support of which is gratefully acknowledged.

References

1. J.D. Ferguson, J.H. Leylek, F.A. Buck, Film cooling on a modern HP turbine blade: part III: axial shaped holes, ASME paper GT2002-30522 (2002)
2. K.L. Harrison, D.G. Bogard, Comparision of RANS turbulence models for prediction of film cooling performance, ASME paper GT2008-51423 (2008)
3. W. Colban, K.A. Thole, M. Haendler, Experimental and computational comparison of fan-shaped film cooling on a turbine surface. ASME J. Turbomach. **129**, 2331 (2007)
4. X. Guo, W. Schröder, M. Meinke, Large-eddy simulations of film cooling flows. Comput. Fluids **35**, 587606 (2006)
5. P. Renze, W. Schröder, M. Meinke, Large-eddy simulation of film cooling flows at density gradients. Int. J. Heat Fluid Flow **29**(1), 18–34 (2008)
6. Y.V. Peet, S.K. Lele, Near field of film cooling jet issued into a flat plate boundary layer: LES study, ASME Turbo Expo (GT2008-50420) (2008)
7. H.N. Nadali, M. Karlsson, M. Kinell, E. Utriainen, Film-cooling performance of a turbine vane suction side: the showerhead effect on film-cooling hole placement for cylindrical and fan-shaped holes. J. Turbomach. **137**(9), 091005 (2015)
8. F.R. Menter, Two-equation eddy-viscosity turbulence models for engineering applications. AIAA J. **32**(8), 15981605 (1994)
9. F.R. Menter, Y. Egorov, The scale-adaptive simulation method for unsteady turbulent flow predictions. Part 1: theory and model description. Flow Turbul. Combust. **85**(1), 113–138 (2010)
10. J.C. Rotta, *Turbulente Strmungen* (Teubner, Stuttgart, 1972)
11. S. Pope, *Turbulent Flows* (Cambridge University Press, 2000)
12. J.H. Leylek, R.D. Zerkle, Discrete-jet film cooling: a comparison of computational results with experiments. J. Turbomach. **116**(3), 358–368 (1994)
13. W.F. Colban, K.A. Thole, D.G. Bogard, A film-cooling correlation for shaped holes on a flat-plate surface. J. Turbomach. **133**(1), 011002 (2011)

Similarities and Differences Concerning Flow Characteristics in Centrifugal Compressors of Different Size

Elias Sundström, Bernhard Semlitsch and Mihai Mihăescu

Abstract The aim of the present investigation is to explain the differences in the compressor map by analyzing the compressible flow in two compressor designs, i.e. a small passenger car design and a sportive car design. The two different compressor designs are assessed with steady state Reynolds Averaged Navier-Stokes simulations for several operating conditions. Similar flow features are observed near optimal efficiency operating conditions when the flow field parameters are scaled properly. The present investigation elucidates the reason for the different limiting shapes of the surge line for the two compressor maps at high speed lines.

1 Introduction

Downsizing of an automotive internal combustion engine is playing an important role for improving the energetic efficiency and reducing pollutant emissions [1]. Turbocharging is a key and matured technology, used for achieving these aims. However, its application range is bound to certain limits by appearance of unwanted fluid flow phenomena leading to conditions like *surge* at low mass flow rates and *choke* at high mass flow rates [2]. The lack of detailed knowledge concerning the compressible flow behavior associated with turbomachinery at off-design operating conditions, demands restrictive security margins on turbocharger's operating range. This is done in order to avoid the occurrence of the violent flow phenomena, as e.g. surge, which can damage the compressor. Nevertheless, the surge line (indicating

E. Sundström (✉) · B. Semlitsch · M. Mihăescu
Department of Mechanics, Linné FLOW Centre and Competence Center for Gas Exchange (CCGEx), KTH Royal Institute of Technology, Osquars Backe 18, 10044 Stockholm, Sweden
e-mail: elias@mech.kth.se

B. Semlitsch
e-mail: bernhard@mech.kth.se

M. Mihăescu
e-mail: mihai@mech.kth.se

© Springer International Publishing Switzerland 2016

A. Segalini (ed.), *Proceedings of the 5th International Conference on Jets, Wakes and Separated Flows (ICJWSF2015)*,
Springer Proceedings in Physics 185, DOI 10.1007/978-3-319-30602-5_57

when surge occurs) is experienced to be individual for each compressor design and a generalization of surge limit to other designs is a desired but challenging task. Commonly, the surge phenomenon limits the application range more at the high rotational speed lines than at low rotational speed lines.

Gas stand measurements are carried out for experimental assessment of turbochargers, to quantify their performance parameters [3]. Such tests cannot give an indication about the three-dimensional flow and pressure fields associated with different operating conditions. Nevertheless, the examination of the flow field is relevant to understand the behavior of the centrifugal compressor under various operating conditions.

In the present analysis, steady state, three-dimensional Reynolds Averaged Navier-Stokes (RANS) simulations are used to explain the differences in the compressor performance maps for two automotive centrifugal compressors of different sizes. Special emphasis is put on the conditions closer to the surge line, over different speed lines.

2 Geometry and Numerical Method

The two investigated compressor geometries and the corresponding specifications are shown in Fig. 1. One is named small compressor (diffuser area ratio = 0.56) and the other is named large compressor (diffuser area ratio = 0.62). The surge by-pass channel with a lock valve, the ball bearing features, and the impeller nut have been

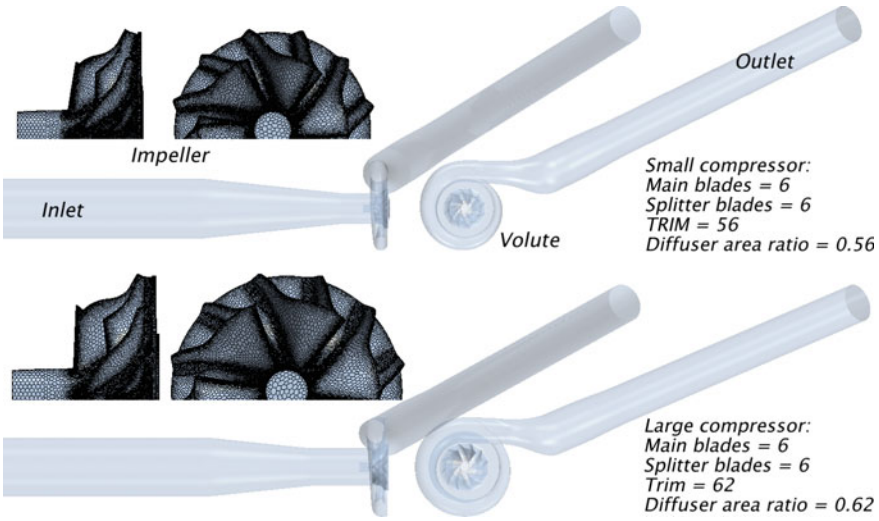


Fig. 1 Side and front views of the compressor geometry, small compressor at the *top* and the large compressor at the *bottom*. The mesh resolution is indicated in the enlarged impeller surface insets

removed to simplify the simulation setup. The inlet and volute exit pipes are extruded several diameters in the boundary normal directions, where the piping systems are equal for both compressors. Hence, an idealized installation of the compressor is considered (replicating the gas stand experiment) under cold operating conditions with adiabatic wall boundary conditions.

In order to characterize the flow behavior occurring in the two compressors, a large number of operating conditions need to be simulated (different rotational speeds and mass flow rates). Computational techniques based on the steady state RANS formulation are relatively fast, robust, and affordable as compared with unsteady approaches [4], which can capture the mean flow features and trends corresponding to the measured global performance parameters. Despite their limitations, steady state RANS modeling can be utilized for covering an impressive number of cases within the stable compressor operating conditions, in a relatively short computational time [5].

Industry-standard modeling is employed to provide fast (3 h) turn-around at each compressor operating point on a 6 core CPU workstation. The flow governing equations are solved by a compressible implicit coupled solver [6] based on the finite volume approach. The two-equation $k - \omega$ SST turbulence model [7] is employed. About one million polyhedral computational cells are used to discretize the computational volume of the two compressors. Two prism-layers are considered towards the no-slip walls. The Moving Reference Frame (MRF) approach is considered to take the effects of impeller's rotation into account. Moreover, mixing-plane interfaces are used, which give a circumferential averaged flow at the interfaces between the impeller region and the stationary domain. This treatment allows for mean radial variation of the flow field quantities.

3 Results

The global performance prediction in terms of the total-to-total pressure ratio (PR) and total-to-total efficiency are shown in Fig. 2. A perfect match of the predicted values with the experimental measurements is not expected, due to the simplifications in the geometry considered in the simulations as well as in the setup. Nevertheless, the comparison of the overall trend is satisfactory apart from a more pronounced humpback feature at peak PR at the higher speed lines. It was also observed that the steady state RANS convergence characteristics deteriorate as compressor operation approaches stall at low mass flow rates, which is due the onset of large-scale flow instabilities.

The predicted total-to-total efficiency is in an overall good agreement with the experimental data although the levels are overpredicted in the simulation for both the small and the larger compressor. In the simulation setup, adiabatic walls are assumed. This is not the case in the experimental setup where the turbocharger is running under hot operating conditions. Therefore the omission of wall heat transfer is seen to lead to efficiency overprediction at low mass flow rates, when the fluid has a long

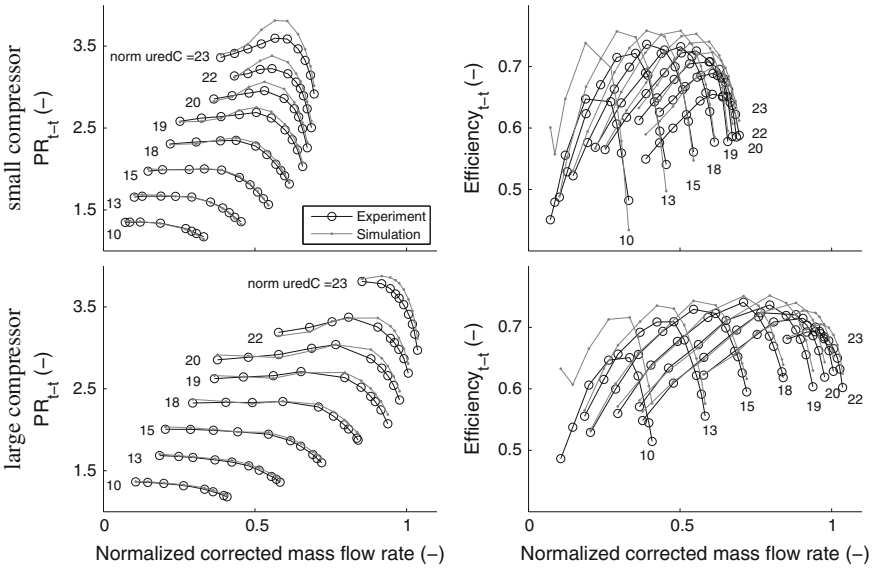


Fig. 2 Compressor pressure ratio and efficiency versus corrected mass flow (small compressor at the *top row* and the large compressor at the *bottom row*)

residence time in the heated section. At higher mass flow rates the assumption of an adiabatic wall improves. This is in agreement with Serrano et al. [8].

The flow field characteristics of the two investigated centrifugal compressors are presented in Fig. 3 for the same impeller speed line (normalized $u_{redC} = 19$), which are designed to operate in different mass flow rate regimes. The smaller compressor is aimed for the usage at lower mass flow rates, while the larger compressor can cope with larger mass flow rates for e.g. a higher performance engine. The flow enters from the left into the domain and is accelerated towards the impeller. The compressor wheel is turning into the clockwise direction. At the tips of the wheel, the highest flow velocities are provoked. The imposed kinetic energy by the wheel blades is converted into pressure energy in the diffuser (the flow velocities decrease). From the diffuser, the stream exits tangentially into the volute. Since the volute increases its cross-sectional volume in clockwise direction (consistent with the wheel rotation), the pressure increases towards the outlet, see Fig. 3. The observed flow features for the two compressor designs are similar at the near optimum efficiency operating condition.

Towards the surge line, lower mass flow rates push against a high outlet pressure. The generated kinetic flow energy is not high enough to overcome the high static pressure built at the outlet and local flow reversal occurs. Thus, the flow is pushed from the diffuser region through the tip leakage (at the periphery of the impeller) against the main flow direction. This is obvious for both compressors in Fig. 3 (left column), where the annular high velocity flow can be seen at the outer periphery.

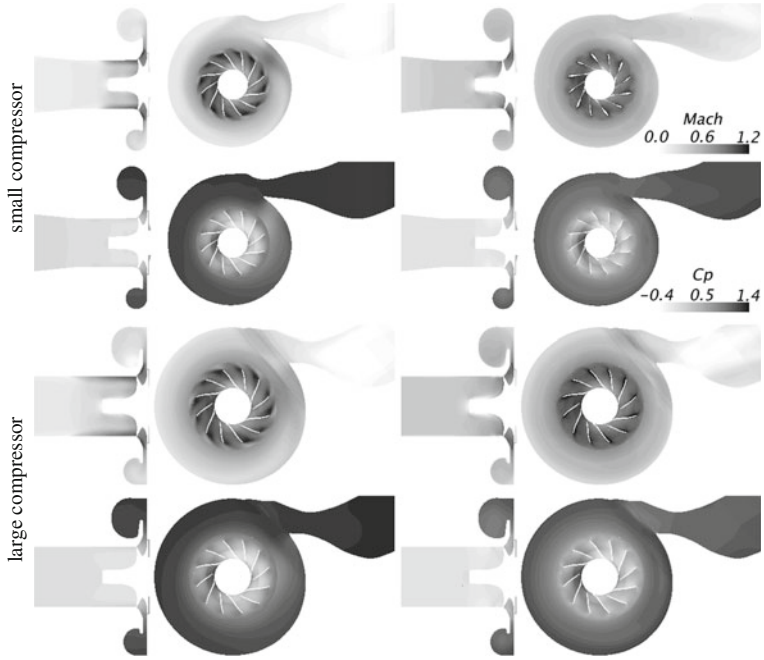


Fig. 3 Mach number and pressure coefficient contours on side and front view planes (small compressor at the *top rows* and large compressor at the *bottom rows* for speed line $u_{redC} = 19$)

This flow feature is characteristic towards the surge margin and lowers the compressor performance. The reversed flow emerging from the tip leakage reaches far further upstream for the larger compressor. This is an effect of the larger compressor operating at higher mass flow rates towards its surge line. The interaction between the reversed flow near the periphery of the impeller and the incoming flow triggers the surge occurrence at different locations in the compressor map.

Figure 4 shows the velocity vector field together with normalized Turbulent Kinetic Energy (TKE) contours around the blades near the shroud. As approaching the surge line, i.e. reduced mass flow rate, separated flow can be observed on the suction side of both the main and splitter blades. It commences on the mid-blade towards the rear of the blades. This relates with the increased incidence flow angle upstream of the blade passages. For the lowest mass flow rate considered for each compressor the upstream steady state velocity field exhibits a wave-like characteristics which relates with partially blocked flow. Generally, the normalized TKE levels amplify with reduced mass flow rate and significant elevated levels are localized near the splitter blade leading edge. This relates to a growing velocity gradient and flow separation towards surge condition. Under such conditions this may lead to a Kelvin-Helmholtz instability with periodic vortex formation [9]. The overall flow

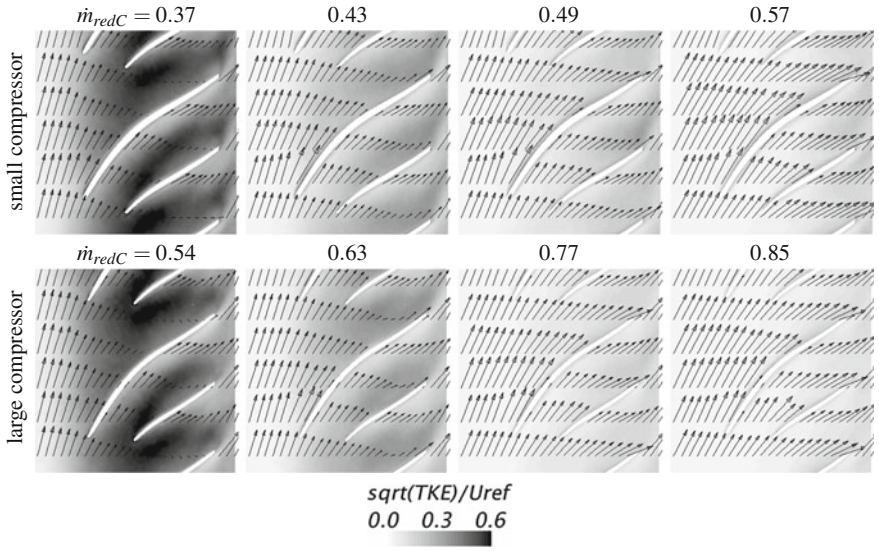


Fig. 4 Velocity vectors and turbulent kinetic energy contour on a flattened surface at 85 % blade span for speed line $u_{uredC} = 19$ (increasing normalized $\dot{m}_{redC}$ from *left* to *right*). The TKE scalar is normalized with the upstream axial velocity

field evolves generally similar for the two different compressors. Towards the diffuser inlet the flow accelerates before it expands in the volute.

Figure 5 compares the axial velocity profiles upstream of the impeller face for all points on the speed line $u_{redC} = 19$. Near the shroud surface towards the surge line the flow separates with flow reversal going in the upstream direction. For more stable operating conditions and towards the choke line the profiles approach a self-similar solution with no separation at the shroud. Closer to the compressor axis at $r/R = 0$ the solution deviates from self-similarity since the flow is decelerating in front of the impeller nut. It can be seen that the large compressor has a narrower surge margin compared to the smaller compressor where flow reversal is seen for both the last stable and the second from last stable operating point respectively.

Figure 6 compares velocity profiles for all speed lines for the last stable operating point. Similarly the flow is seen to separate near the shroud surface, but gradually approach a fully attached flow profile for the two highest speed lines. This trend is similar for both compressors, which highlights that an approximate similarity solution might exist, which is independent of the compressor size provided that the profiles are scaled appropriately. However, the larger compressor is seen to operate with more flow reversal near the shroud surface which again suggest that the this compressor has a narrower surge margin.

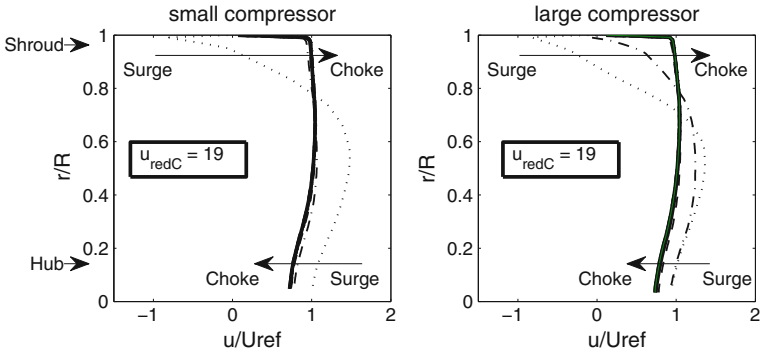


Fig. 5 Axial velocity profiles upstream at impeller face for all operating points on the constant speed line $u_{redC} = 19$. Small compressor to the *left* and the large compressor to the *right*

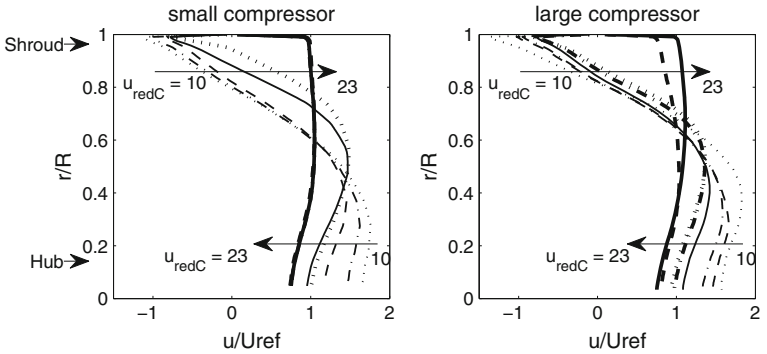


Fig. 6 Axial velocity profiles upstream at impeller face for the last stable operating point for different speed lines. Small compressor to the *left* and large compressor to the *right*

4 Conclusions

The global compressor performance in terms of the pressure ratio efficiency are predicted numerically using a computationally fast steady state RANS approach for two different compressors. Trends in an acceptable agreement with measurements in an idealized installation are achieved for a range of operating conditions and different speed lines between the last stable operating point to choke conditions. The use of adiabatic wall conditions results in an efficiency overprediction if comparison is made with measurements conducted under hot conditions with heat transfer. However, the adiabatic assumption is seen to improve with the larger compressor since it operates at higher mass flow rates than the smaller compressor. Towards higher speed lines a so-called camel-back feature manifests in the PR map, which is more pronounced in the adopted steady state RANS approach as compared to the

measurements. This might be due to onset of flow instabilities, which motivate a transition towards unsteady calculations. These will be the focus of future work.

The observed flow features for the two compressor designs are similar at the near optimum efficiency operating condition when the velocity and the pressure fields are appropriately scaled. As conditions approach the surge line (last stable operating point) the mass flow rate is lower and separated flow is observed on the suction side of both the main and the splitter blade. It commences on the mid-blade towards the rear end of the blade edges. Despite of the separation, large parts of the flow still remain attached, which could explain the relatively small positive slop of the PR. Towards surge operating conditions the normalized TKE level amplifies with elevated intensity localized near the splitter blade leading edge. This relates with a growing velocity gradient and possible onset for a Kelvin-Helmholtz instability.

Near the shroud surface at a station just upstream of the impeller face, the flow is seen to separate with flow reversal going in the upstream direction as conditions approach the last stable operating point. The flow in this area is gradually reattaching with increasing speed lines along the last stable operating point and the scaled axial velocity profile approach a self-similar flow solution.

Acknowledgments The Competence Center for Gas Exchange (CCGEx), the Swedish Energy Agency (STEM), Volvo Group and SCANIA are acknowledged for supporting this project. The computations were performed on resources provided by the Swedish National Infrastructure for Computing (SNIC) at PDC Centre for High Performance Computing (PDC-HPC) and High Performance Computing Center North (HPC2N). Special thanks to BorgWarner for sharing the CAD geometries.

References

1. W. Knecht, Diesel engine development in view of reduced emission standards. Energy **33**(2), 264–271 (2008)
2. B. Semlitsch, V. JyothishKumar, M. Mihăescu, L. Fuchs, E. Gutmark, M. Gancedo, Numerical flow analysis of a centrifugal compressor with ported and without ported shroud. SAE Paper, 2014-01-1655 (2014)
3. J. Galindo, F. Arnau, A. Tiseira, R. Lang, H. Lahjaily, T. Gimenes, Measurement and Modeling of Compressor Surge on Engine Test Bench for Different Intake Line Configurations. SAE Paper, 2011-01-0370 (2013)
4. O. Baris, F. Mendonca, Automotive Turbocharger Compressor CFD and extension towards incorporating installation effects. ASME Turbo Expo, GT2011-46796 (2011)
5. E. Sundström, B. Semlitsch, M. Mihăescu, Assessment of the 3D flow in a centrifugal compressor using steady-state and unsteady flow solvers. SAE Paper, 2014-01-2856 (2014)
6. STAR-CCM+, release version 10.02, CD-adapco, http://www.cd-adapco.com, Feb 2015
7. F. Menter, Two-equation eddy viscosity models for engineering applications. AIAA J. **32**(8), 1598–1605 (1994)
8. J. Serrano, P. Olmeda, F. Arnau, M. Reyes-Belmonte, A. Lefebvre, Importance of heat transfer phenomena in small turbochargers for passenger car applications. SAE Int. J. Eng. **6**(2), 716–728 (2013), http://dx.doi.org/10.4271/2013-01-0576
9. Y. Bousquet, X. Carbonneau, I. Trebinjac, N. Binder, G. Dufour, Numerical investigation of Kelvin-Helmholtz instability in a centrifugal compressor operating near stall. ASME Paper, GT2015-42495 (2015)

Part VIII
Multiphase and Reacting Flows

Study of Liquid Breakup Mechanism Through a High-Speed Gas Flow

Ryoichi S. Amano and Yi-Hsin Yen

Abstract Investigation of liquid breakup mechanism is an important role to improve performance of solid rocket motor (SRM) to reduce the erosion damage near nozzle a throat section. Protection of the nozzle wall could be achieved by enhancing liquid breakup mechanism of the liquid alumina inside combustion chamber before bulk alumina slug erodes the nozzle section. This paper presents a study of air and water two-phase straight channel experiment that simulates the breakup mechanism of alumina. The study of liquid breakup mechanism is carried out by analyzing high-speed camera image through image processing technic during this straight channel two-phase experiment. This image processing extract the particle size and counts data from each frame of high-speed pictures, therefore, we have mass accumulation distribution from different particle size and his information could be useful information for combustion channel design.

1 Introduction

Aluminum-based propellants are widely used in a solid rocket motor (SRM) due to its high energy density, easiness to prepare, and store and maintain [1]. When aluminum based propellant combusts, it release about 30 MJ/kg of energy during aluminum oxidized into alumina (Al_2O_3). The alumina is in liquid status in the combustion chamber under the working temperature over 3,200 K and pressure over 2.0×10^7 Pa. That liquid status alumina formed in the combustion chamber that easily agglomerates into chunks of droplets. Those droplets solidify through the flow path and impinge on the chamber walls and then flow along the nozzle wall. This behavior results in erosive damage to the inner walls of the nozzle geometry. The chemical and mechanical erosion resulting must be avoided in an SRM to

R.S. Amano (✉) · Y.-H. Yen
Mechanical Engineering, University of Wisconsin Milwaukee, Milwaukee, WI, USA
e-mail: amano@uwm.edu

Y.-H. Yen
e-mail: yeny@uwm.edu

© Springer International Publishing Switzerland 2016

A. Segalini (ed.), *Proceedings of the 5th International Conference on Jets, Wakes and Separated Flows (ICJWSF2015)*,
Springer Proceedings in Physics 185, DOI 10.1007/978-3-319-30602-5_58

prevent a decrease in ballistic performance [2]. The solid rocket working fluid velocity contour is affected by the multiphase particle motion inside the combustion chamber; resulting in the non-equilibrium effect of exhaust gas limits the performance, as reported by Nayfeh and Saric [3]. Moreover, because of the geometry of the motor, molten alumina agglomerates can form resulting in two-phase flow losses [4–6]. These agglomerates lower the propulsive efficiency of the exhaust flow because the agglomerates do not expand in the nozzle and also create a drag force with the flow [7, 8]. Depending on the alumina particle size and the alumina particle-gas mixture percentage, two-phase flow losses can reduce the propellant specific impulse by as much as 6 % [9, 10]. The breakup mechanism of the liquid phase of liquid alumina is one of the factors of performance improvement. Therefore, the liquid breakup study is critical of SRM. In this paper, a liquid breakup is considered by analyzing images from a high-speed camera. The characterization method is carried out by an imaging process code which quantifies the total number of droplet and droplet size in the observation field of the images captured by a high-speed camera operated on 1,000 fps.

2 Experimental Setup

Two-phase flow experiment was conducted in a rectangular channel in this study, as shown in Fig. 1a. The dimension of the channel has a 0.2 m inlet, where a 30 mm thick layer of liquid flows through the lower inlet section and air flows through the

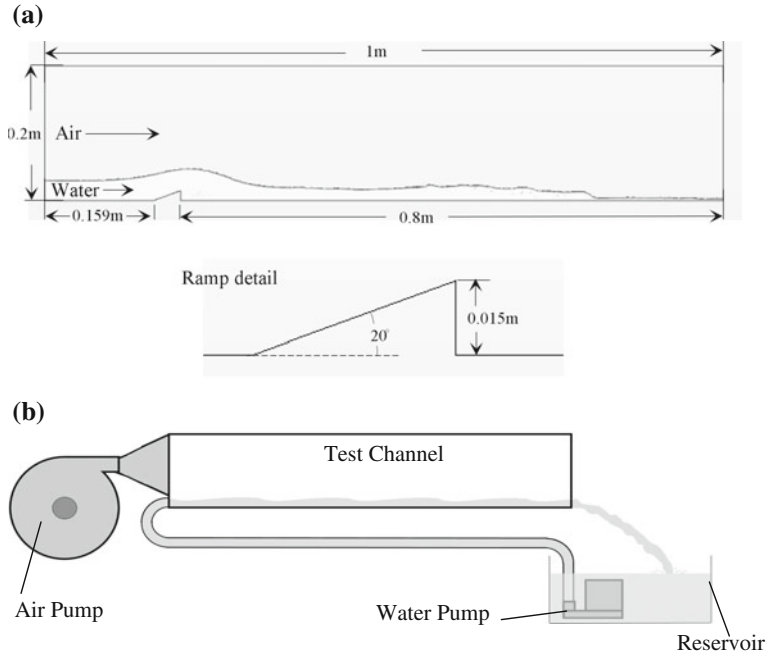


Fig. 1 Flow geometry of experiment two-phase flow channel

remaining upper inlet section. A ramp with a height of 15 mm and an angle of 20° is placed at a location 0.159 m from the inlet that is used to create a flow separation of liquid. The total length of the channel is 1 m. The inlet velocity of the liquid is maintained at Fr = 1.24 (0.67 m/s) with air inlet Reynolds number Re_{air} = 5.3e+4, 8.0e+4, and 1.1e+5 (velocity setting of 20 m/s, 30 m/s, and 40 m/s) respectively. The system schematic is shown in Fig. 1b; four major component compose the system are air pump, water pump, test channel, and reservoir. The performance capability of pumps is Re_{air} = 1.1e+5 and Re_{water} = 1.8e+3 (40 and 3.5 m/s) for air and water respectively.

3 Liquid Breakup Analysis

The liquid breakup has period and cycle that related to the liquid wave frequency. Liquid breakup cycle starts at time = 20 ms at the point of liquid wave crest as shown in Fig. 2a with an arrow pointing its location, at this moment, little breakup activity could be observed. At time = 30 ms (shown in Fig. 2b), as the wave crest propagates toward the area of the ramp, the liquid breakup is about to begin. At time = 60 ms as shown in Fig. 2e, the breakup activity reaches a peak point, and

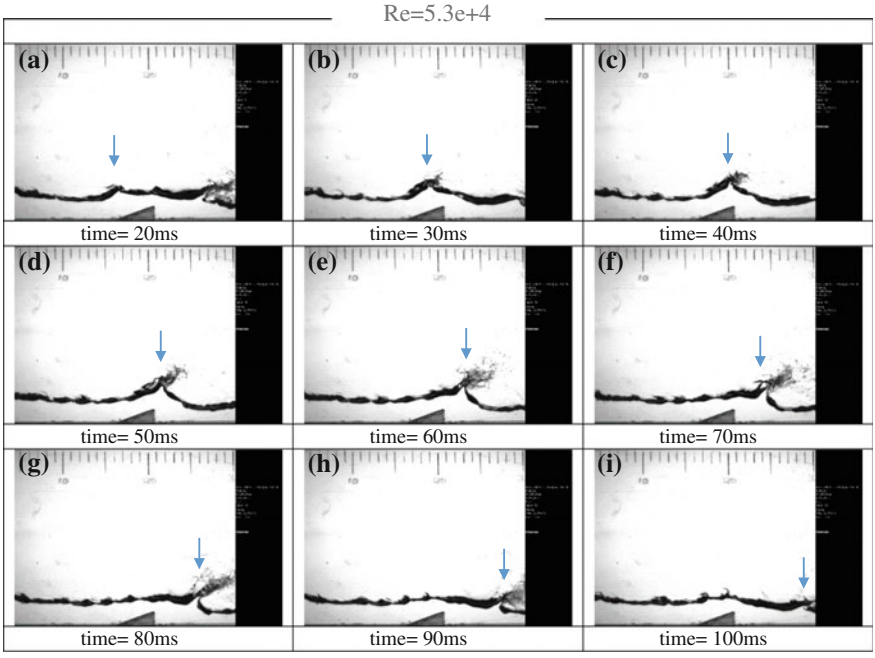


Fig. 2 The liquid breakup cycle of Re_{air} = 5.3e+4 with Fr = 1.24 with display time step of 10 ms. (Length scale: cm)

numerous smaller liquid droplets separate from major liquid body. Beyond this point, the breakup phenomenon becomes less active as times goes by, and finally as shown in Fig. 2 (i) at time = 100 ms, it comes to the end of this breakup cycle. Similar features are also shown in Figs. 3 and 4 for the liquid breakup cycle for Re_{air} of 8.0e+4 and 1.1e+5, respectively.

From Fig. 2 through Fig. 4 we could find that, despite the difference of V_{air}, all three cases share a similar liquid wave period around 80 ms or frequency of 12.5 Hz. From the observation, on the other hand, we could tell large difference appearing from case to case. Figure 5 shows the breakup stage of all three cases, and we could find the breakup mechanism is least active for Re_{air} = 5.3e+4 and gradually becomes more active for Re_{air} = 1.1e+5.

Although all three cases share a similar major wave frequency, it is obvious that, for the case with higher air velocity, there occurs more breakup phenomenon and more fluctuation on the liquid free surface. The liquid breakup droplet size and their count could be extracted by image processing tool from each frame of the different case. In this study, the high-speed camera operates at 1,000 fps and capable capturing 2,180 frames for each filming trigger. Each V_{air} setting is filming twice. Therefore, there are 4,360 frames for each V_{air} setting. Each frame has its particle size and counts distribution curve. By averaging all information from 4,360 frames in each case, we could have database information with particle counts from different

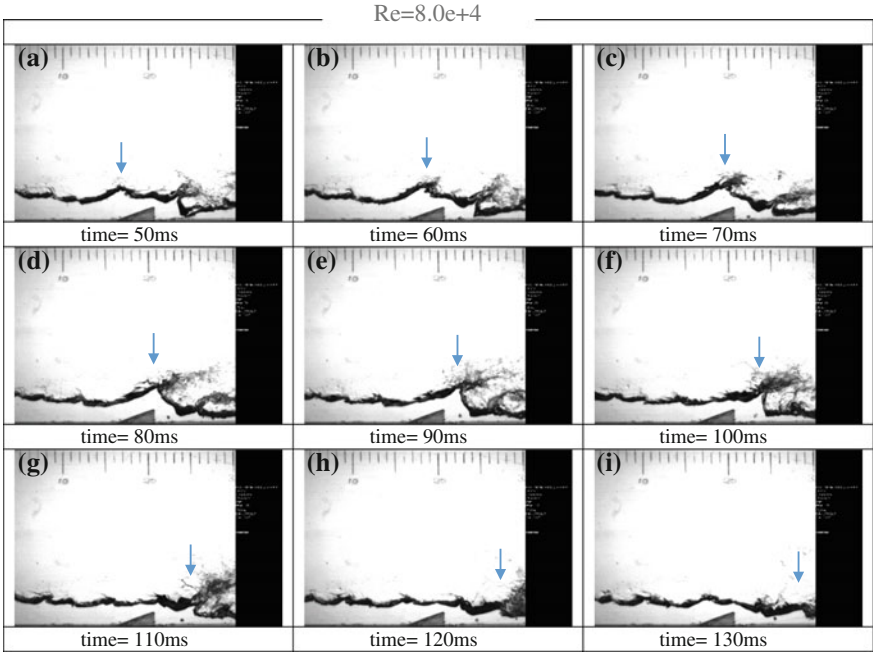


Fig. 3 The liquid breakup cycle of Re_{air} = 8.0e+4 with Fr = 1.24 with display time step of 10 ms. (Length scale: cm)

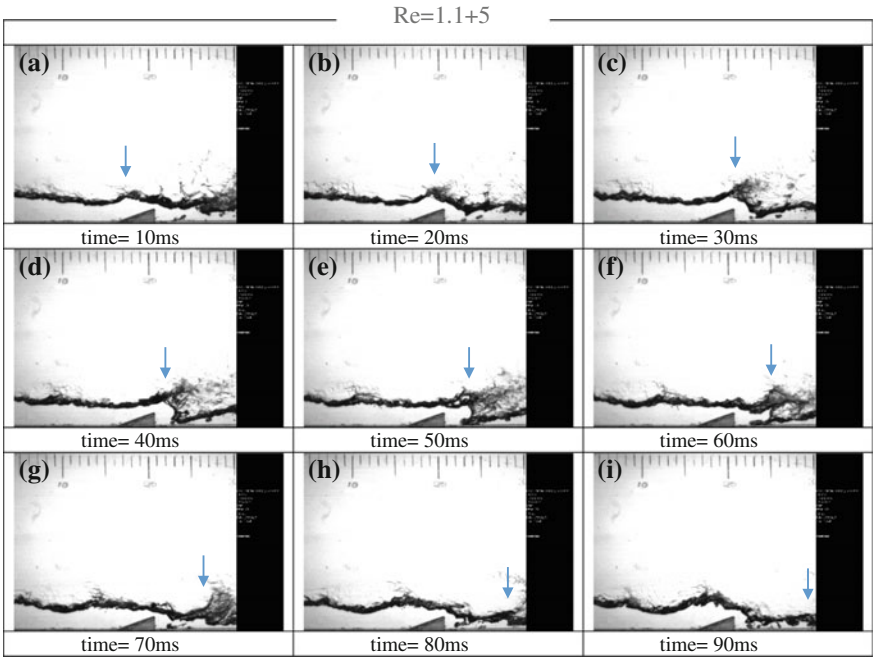


Fig. 4 The liquid breakup cycle of Re_{air} = 1.1e+5 with Fr = 1.24 with display time step of 10 ms. (Length scale: cm)

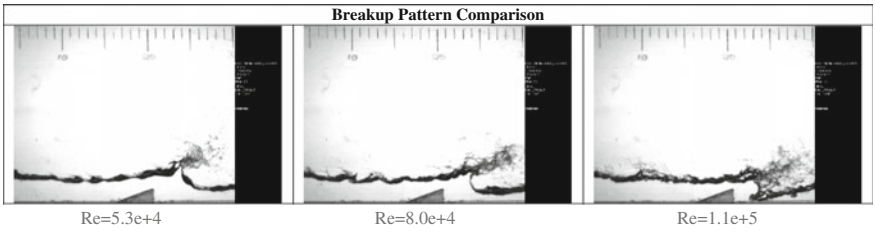


Fig. 5 Breakup pattern comparison

particle size and base on this information. We could also calculate the total liquid mass carried by specific droplet size. In Fig. 6, the average particle counts contribute as a function of the droplet size distribution is presented. We can observe that the trend that the particle counts drops with the particle size. The particle counts curve also increases with the air velocity since higher air velocity carries more energy that enhances breakup mechanism and brings more and smaller particle counts separated from the main water body.

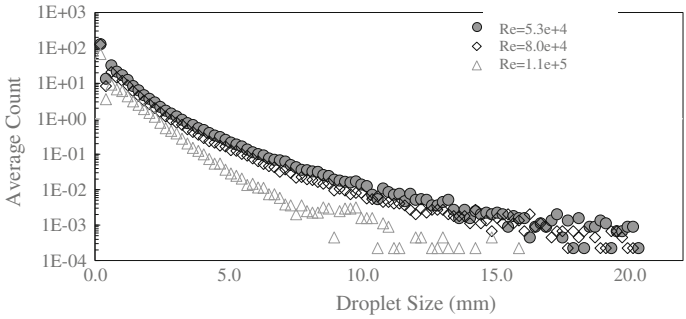


Fig. 6 Average count per frame to droplet size distribution

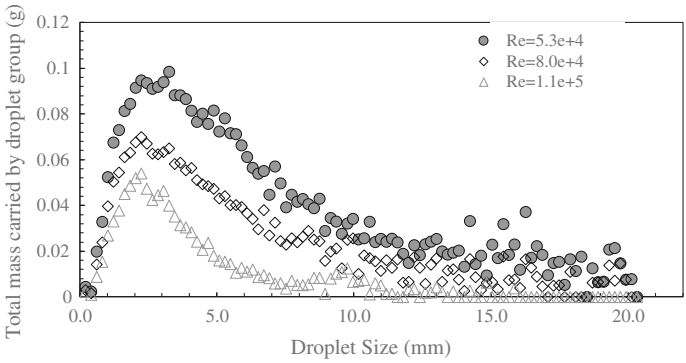


Fig. 7 Mass accumulation to droplet size distribution

The total mass carried by different droplet size group is shown in Fig. 7, where the mass data is obtained by a calculation of multiplication of density of water, volume of each droplet, and droplet counts in each particular size. This calculation also assumes the droplet is spherical in shape when calculating the volume of droplets. The peak mass carrying a value of droplet sizes are 2.2 mm, 2.2 mm and 3.3 mm for the case of Reynolds number 5.3e+4, 8.0e+4, 1.1e+5, respectively. The mass percentage carried by all droplet group compare to main water body mass as shown in Fig. 8. In this figure it is clearly shown that the trend of the total mass percentage carried by droplet in all size group increases with the air speed, $V_{air,}$ due to more kinetic energy of air that could trigger breakup and bring more mass separate from main water body.

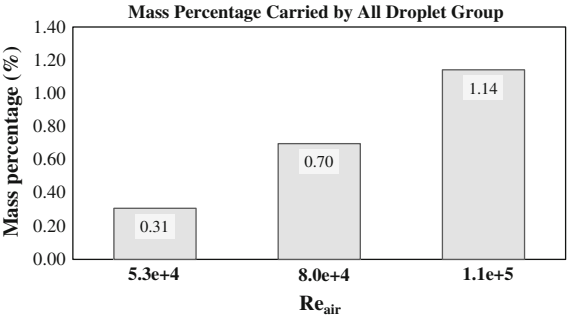


Fig. 8 Mass percentage carried by all droplet with size under 20 mm

4 Conclusions

- The liquid wave frequency of all three different V_{air} cases is similar around 12.5 Hz due to the same water depth in all three cases. However, the breakup level increases with the increasing air speed, V_{air}.
- For the average droplet count for all different size groups, higher air velocity increases the number of droplets separating from the main water body. By comparing the droplet number of the cases with the Reynolds number 5.3e+4, 8.0e+4, 1.1e+5, respectively, the counts difference ranges between 1 and 2 orders magnitude of difference.
- The mass carried by the droplet distribution also shows a similar trend of higher air velocity increase the mass carried by droplet due to more kinetic energy of air that could trigger breakup mechanism and bring more mass separating from the main water body.

References

1. D.C. Rapp, *High Energy-Density Liquid Rocket Fuel Performance* (Sverdrup Technology, Inc, NASA Lewis Research Center, Brook Park, Ohio, 1968)
2. P. Thakre, V. Yang, Chemical erosion of refractory-metal nozzle inserts in solid-propellant rocket motors. J. Propul. Power **25**(1) (2009)
3. A.H. Nayfeh, W.S. Saric, Nonlinear stability of a liquid film adjacent to a supersonic stream. J. Fluid Mech. **58**, 39–51 (1973)
4. S. Borass, Modeling slag deposition in the space shuttle solid rocket motor. J. Spacecraft Rockets **21**, 47–54 (1984)
5. M. Salita, Deficiencies and requirements in modeling of slag generation in solid rocket motors. J. Propul. Power **11**, 10–23 (1995)
6. E. Hess, K. Chen, P. Acosta, D. Brent, F. Fendell, Effect of aluminized-grain design on slag accumulation. J. Spacecraft Rockets **29**, 697–703 (1992)

7. Y. Xiao, R.S. Amano, T. Cai, J. Li, A new method to determine the velocities of particles on a solid-propellant surface. ASME J. Heat Transfer **127**, 1057–1061 (2005)
8. Y. Xiao, R.S. Amano, T. Cai, J. Li, Particle velocity on solid-propellant surface using X-Ray real time radiography. AIAA J. **41**(9), 1763–1770 (2003)
9. A. Bandera, F. Maggi, L.T. Deluca, Agglomeration of aluminized solid rocket propellants in *45th AIAA/ASME/SAE/ASEE Joint Propulsion Conference & Exhibit*, Denver, Colorado
10. R. Holtzmann, Introduction-The Nature of an Advanced Propellant. Aerojet-General Corporation Von Karman Center http://www.web.anl.gov/PCS/acsfuel/preprint%20archive/Files/Volumes/Vol09-1.pdf

Clustering and Settling of Inertial Particles in Turbulence

Sholpan Sumbekova, Alberto Aliseda, Alain Cartellier and Mickael Bourgoin

Abstract Particle laden flows are of a great interest in many industrial and natural systems. When the carrier flow is turbulent, a striking feature named preferential concentration takes place: particles denser than the carrier fluid tend to inhomogeneously distribute in space, forming clusters and depleted regions. The present study aims at giving new insight into the possible connection between preferential concentration and particles settling in homogeneous isotropic turbulence. Preferential concentration is quantified using Voronoï diagrams, while 2D Lagrangian Particle Tracking is used to access particles dynamics and in particular statistics of settling velocity. Independent and joint statistics of local concentration and settling velocity are discussed. More paticularly, the possible dependence of particle settling rates on clustering properties are investigated.

1 Introduction

A striking feature of turbulent flows laden with inertial particles is the so-called preferential concentration (or clustering) that leads to strong inhomogeneities in the particles concentration field at any scale. This has now been widely observed in

S. Sumbekova (✉) · A. Cartellier
Université Grenoble Alpes, LEGI, F-38000 Grenoble, France
e-mail: sholpan.sumbekova@legi.grenoble-inp.fr; sholpan.sumbekova@ujf-grenoble.fr

S. Sumbekova · A. Cartellier
CNRS, LEGI, F-38000 Grenoble, France
e-mail: alain.cartellier@legi.grenoble-inp.fr

A. Aliseda
Department of Mechanical Engineering, University of Washington,
Stevens Way, Box 352600, Seattle, WA 98195, USA
e-mail: alberto.aliseda@u.washington.edu

M. Bourgoin
Laboratoire de Physique, Univ Lyon, ENS de Lyon, Univ Claude Bernard, CNRS,
F-69342 Lyon, France
e-mail: mickael.bourgoin@ens-lyon.fr

© Springer International Publishing Switzerland 2016

A. Segalini (ed.), *Proceedings of the 5th International Conference on Jets, Wakes and Separated Flows (ICJWSF2015)*,
Springer Proceedings in Physics 185, DOI 10.1007/978-3-319-30602-5_59

many experimental and numerical realizations including homogeneous and isotropic turbulence [3, 10, 11]. Several properties of preferential concentration seems now to be robustly established with consensual results in the litterateture [8, 9]. We can mention among others: (i) the fractal geometry of clusters, (ii) the fact that the typical clusters scale is of the order of ten times the Kolmogorov scales of the carrier turbulence and (iii) the fact the maximal clustering effects are observed for particles whose Stokes number (defined as the ratio of the particle relaxation time to the Kolmogorov viscous time of the carrier turbulence) is close to unity. However, a clear theoretical description of preferential concentration remains a challenge, in particular regarding the specific mechanism(s) leading to clustering [5, 6] and the further impact clustering may have on the collective dynamics (and particularly on the settling rate) of particles [1]. An important question addressed in the present study concerns the possible enhancement of settling velocity within clusters, as reported by Aliseda et al. [1], and more generally the connection between local particle concentration and settling properties.

Recently, our group has introduced Voronoï tesselations analysis, obtained from snapshots of the particles in a given area in a flow field, to quantify clustering [7, 8]. Here we propose to take benefit of the capacity of such analysis to be coupled to Lagrangian tracking of particles, in order to investigate the interplay between clustering and settling. Our experimental study gives access to unprecedented statistics of settling velocity conditioned to particles local concentration field, whose first results are presented in this article.

2 Experimental Setup

Experiments are conducted in a large wind tunnel with a square cross-section of 0.75 m × 0.75 m (see Fig. 1a). Turbulence is generated with an active grid [9], capable to produce moderate to high turbulence with still relatively good homogeneity

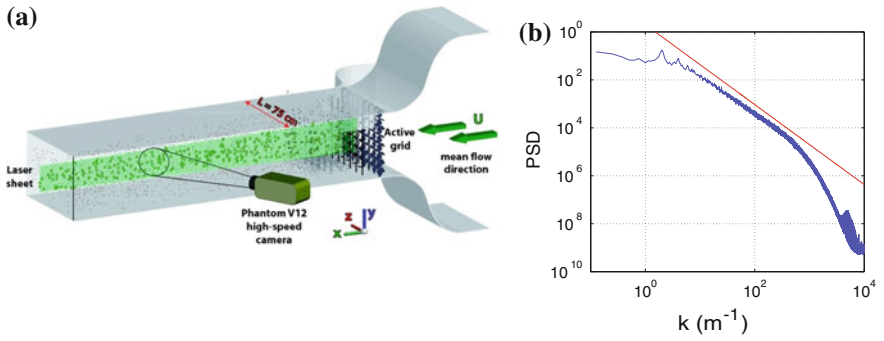


Fig. 1 **a** Sketch of the experimental setup. **b** Typical velocity spectrum of turbulence produced by the active grid (*red solid line* represents a $k^{-5/3}$ trend)

and isotropy levels. The mean stream velocity U of the wind was varied from 2.5 to 10 m/s. The active generates velocity fluctuations with a turbulence intensity (defined as the ratio between the standard deviation of velocity σ_U to the mean stream velocity U) of the order of 20 %. The corresponding of Reynolds number based on Taylor microscale, $Re_\lambda = \sigma_U \lambda / \nu$ ranges between 200 and 500 ($\lambda = \sqrt{\frac{15/\nu}{\epsilon}} \sigma_U$ is the Taylor microscale, with $\nu = 1.5e-5$ m^{2}s^{-1} the kinematic viscosity of air at working temperature and ϵ the turbulent energy dissipation rate per unit mass). Figure 1b represents a typical velocity spectrum of the turbulence produced by the active grid. Inertial particles are water droplets generated by 18 injectors located in a transverse plane 15 cm downstream the grid. The average diameter of the particles is constant for all velocities, with a typical mean sauter diameter $D_p \simeq 60\,\mu$m (although size distribution has a significant polydispersity of the order of 50 %). We define the typical Stokes number of the particles as $St = \frac{1}{36}\left(\frac{D_p}{\eta}\right)^2 (1 + 2\rho_p/\rho_f)$, with η the Kolmogorov dissipative scale of the carrier turbulence and ρ_p/ρ_f the particle to fluid density ratio (which in our case, water particles in air, is of the order 815). In our experiments, the size of the particles is kept constant, and variations of Stokes numbers are explored by varying the dissipation scale η of the flow, which decreases as the wind velocity increases. Stokes and Reynolds number are therefore linked parameters, which do not vary independently. Further experiments will be carried in near future to disentangle more precisely Stokes and Reynolds number effects. Note also that in our experiments the flow rate of water through the atomizing injectors producing the droplets is kept constant. This means that the particle volume fraction given by $\frac{Q_L}{Q_L+Q_G}$, where Q_L is an injected flow rate and Q_G is a main air flow rate within the flow decreases linearly as the wind speed increases. Finally, a longitudinal laser sheet (with millimetric width) is used to illuminate the particles (as shown in Fig. 1). Images were recorded with one high speed camera Phantom V12 from Vision Research Inc., with a field of view of the order of the integral scale of the carrier flow of 12 cm.

3 Results

3.1 Voronoï Tesselations

Voronoï analysis is used for quantifying the phenomenon of preferential concentration [7, 8]. Voronoï diagrams give a tesselation of 2D space (though the analysis can be extended to any spatial dimension) where each cell of the tesselation is assigned to a particle, with all points of one cell closer to its associated particle than to any other particle. Figure 2 shows the tesselation of one instantaneous recorded image. Each visible cell (we shall refer to cells as *Voronoï cells*) contains one unique particle. Consequently, the inverse area of each Voronoï cell represents the local concentration

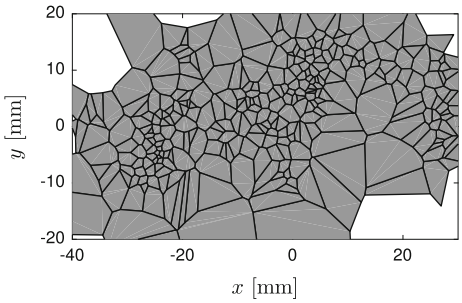


Fig. 2 Example of Voronoï tesselation. Each Voronoï cell contains a unique particle

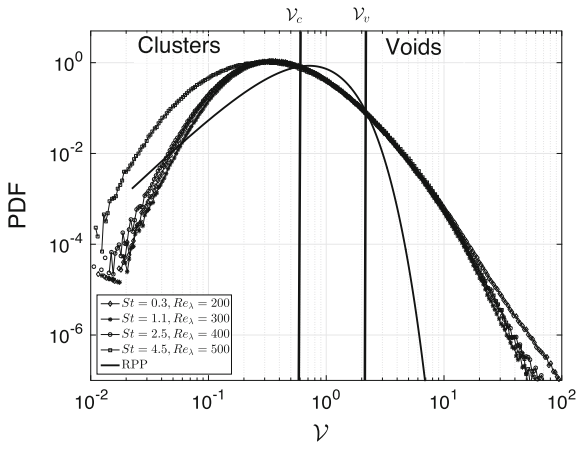


Fig. 3 PDF of normalised Voronoï areas $\mathscr{V}$. The *solid line* represents the Voronoï area PDF expected for a Random Poisson Process, which is well approximated by a Gamma function [2]

of particles. The higher the local concentration of the particle, the smaller its corresponding Voronoï area $\mathscr{A}$. Figure 3 shows the probability density function (PDF) of normalized Voronoï cell areas $\mathscr{V} = \mathscr{A}/\overline{\mathscr{A}}$ (where $\bar{\cdot}$ represents the ensemble average over the full set of images for each experiment) for the several experiments we carried at different wind velocities (hence different Stokes and Reynolds numbers). The deviation of the experimental PDF compared to the PDF expected for a pure random Poisson process (RPP), represented by the solid line in the figure, is representative of the existence of preferential concentration, as small areas (dense regions) and large areas (depleted regions) are over-represented in the experiments with respect to the RPP case. A detailed description of trends of clustering with Stokes and Reynolds number in our experiment goes beyond the scope of the present article, but can be found in [9]. We can just emphasize here that, in the range of parameters explored here, the level of clustering is significant (this can be quantified by the standard deviation of the PDFs shown in Fig. 3, which is of the order $\sigma_{\mathscr{V}} \simeq 1.2$, while the corresponding value for a RPP is $\sigma_{\mathscr{V}}^{RPP} \simeq 0.53$) with a weak dependency on the explored parameters, although small areas (over-concentrated regions) are slightly over-represented for the largest Stokes numbers explored and large areas (under-concentrated regions) are for the lowest Stokes numbers explored (note however that this effect appears amplified

by the log-log representation of the figure, but contributes marginally to the change of $\sigma_{\mathcal{V}}$, which remains in the range $\sigma_{\mathcal{V}} \in [1.1, 1.25]$ for the full set of experiments).

We use now the comparison between the measured PDFs and the RPP PDF to determine clusters and voids, following the definition proposed by Monchaux et al. [7]: *clusters* and *voids* are composed, respectively, by Voronoï cells feeding the small and large area tails of the PDF, corresponding to over-represented events with respect to the RPP case. Intersections of the measured PDFs and the RPP PDF near the maximum therefore define two thresholds $\mathcal{V}_c$ and $\mathcal{V}_v$ (with $\mathcal{V}_c < \mathcal{V}_v$) such that cells with normalized area below $\mathcal{V}_c$ belong to clusters and cells with normalized area above $\mathcal{V}_v$ belong to voids. In our experiments, we found that these thresholds do not depend significantly on the experimental parameters (Stokes number or Reynolds number) and we have $\mathcal{V}_c \simeq 0.6$ and $\mathcal{V}_v \simeq 2.1$ (see Fig. 3).

3.2 Joint Analysis of Concentration and Settling Velocity

Particle Tracking Velocimetry was used to reconstruct particle trajectories and measure the instantaneous velocity of each individual particle. In the present case, the use of one single camera and a laser sheet illumination allows to access 2 components of particles velocity in the illumination plane. The key point of the present study is that besides this information on particles velocity, the above mentioned Voronoï analysis allows to attribute to each individual particle an instantaneous Voronoï area (representing the instantaneous local particle concentration in the vicinity of each particle). We can therefore consider accessing joint statistics of particles local concentration and velocity.

Figure 4 shows the dependence of the average settling velocity V_z on Stokes number (or equivalently on Reynolds number) for three types of particles in each experiment: (i) $V_{z,all}$ refers to the average settling velocity of the full set of particles, regardless of the value of their associated Voronoï area (ii) $V_{z,cluster}$ refers to the average settling velocity of particles belonging to clusters only (*i.e.* we condition

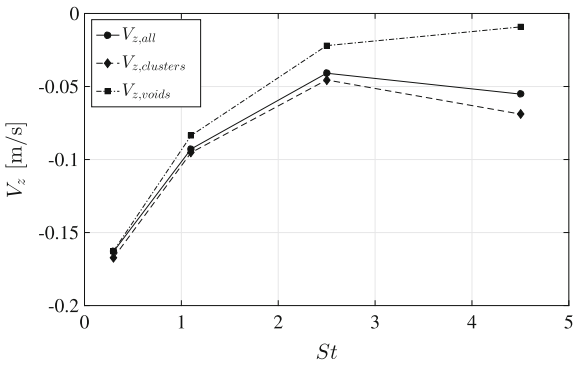


Fig. 4 Mean settling velocity calculated (i) for the full set of particles for each experiment ($V_{z,all}$), (ii) for particles belonging to clusters only ($V_{z,clusters}$) and (iii) for particles belonging to voids only ($V_{z,voids}$)

the average of settling velocity by keeping only particles with Voronoï area $\mathscr{V} < \mathscr{V}_c$) and (iii) $V_{z,voids}$ refers to the settling velocity of particles belonging to voids only (*i.e.* we condition the average of settling velocity by keeping only particles with Voronoï area $\mathscr{V} < \mathscr{V}_c$). Several points are worth being highlighted and discussed from this plot:

1. All curves follow a similar trend, with globally a reduction of settling velocity with increasing Stokes number (or equivalently in our case with increasing Reynolds number). For the largest Stokes numbers explored we may observe a saturation, or even a decrease (except for particles in voids). Since the particle diameter is kept constant, this effect is purely due to the interaction between the particles and the carrier turbulence. Further studies are required to draw robust conclusions on these trends. In particular, when turbulence and inertia contribute to enhance or reduce settling is a subtle matter, as shown by a recent study focusing on the case of individual particles (in very dilute conditions) in turbulence [4]. A systematic study, where seeding concentration, Stokes number and Reynolds number are varied independently is a requisite to identify robust generic trends. This goes beyond the scope of the present article, but will be addressed in coming studies.
2. The most striking feature on the curves in Fig. 4 is the systematic difference between the settling rate of particles in clusters compared to particles in voids. Clustered particles settle systematically faster than particles in voids. Besides, this difference increases with increasing Stokes number (or increasing Reynolds number). This observation is consistent with measurements reported by Aliseda et al. [1]. A natural question now concerns the possible origin of this effect. Two main mechanisms can be considered: (i) a signature of preferential sampling of the turbulent flow by the particles, in the spirit of the preferential sweeping mechanism, where clusterized particles would for instance explore preferentially high strain downward regions [6] or (ii) a role of collective effects, where the collective settling of clusters would enhance the individual settling of particles [1]. In our experiment, we observe that the level of clustering (which can be quantified for instance by the standard deviation of the normalized Voronoï areas) does not vary by more than 10 % over the range of Stokes number (or Reynolds number) explored here. We therefore do not expect a significant difference in the way particles preferentially sample the turbulence and believe that the observed trends are mostly attributable to collective effects. A possible dominant role of collective effects is further supported by the fact that the particle volume fraction is reduced by almost a factor 4 between the experiments at lowest wind-speed (*i.e.* lowest Stokes number) and those at higher wind-speed (*i.e.* higher Stokes number)), that impacts the overall concentration, but also the concentration within clusters and voids, and hence is expected to modify the collective settling behavior [1].
3. Even if this may seem obvious, it is still worth pointing that the fact that the global mean settling velocity follows more closely the settling velocity of clustered particles (rather than particles in voids) is expected as, by essence, particles in voids are less numerous and therefore contribute less to the global mean.

4 Conclusion

By combining Voronoï analysis of the concentration field of inertial particles in turbulence and Lagrangian particle tracking, we have shown that in presence of preferential concentration, particles within clusters settle systematically faster than particles in voids, what we tend to attribute to the additional influence of collective settling of clusters. Further studies are now required to support this interpretation and to understand other observed trends (as the diminution of settling rate with increasing Stokes number). In particular, carrying experiments where Stokes number, Reynolds number and seeding concentration are varied independently is of primary importance. Such experiments are in progress at the moment.

Acknowledgments This work has been supported by the LabEx Tec 21 (Investissements dAvenir - grant agreement ANR-11-LABX-0030), the French *Agence Nationale pour la Recherche* (project ANR-12-BS09-011-03) and the COST action on "Flowing Matter" MP1305.

References

1. A. Aliseda, A. Cartellier, F. Hainaux, J.C. Lasheras, Effect of preferential concentration on the settling velocity of heavy particles in homogeneous isotropic turbulence. J. Fluid Mech. **468**, 77–105 (2002). doi:10.1017/S0022112002001593. http://journals.cambridge.org/article_S0022112002001593
2. J.S. Ferenc, Z. Neda, On the size distribution of Poisson Voronoi cells. Phys. A-Stat. Mech. Appl. **385**(2), 518–526 (2007). doi:10.1016/j.physa.2007.07.063. http://www.sciencedirect.com/science/article/pii/S0378437107007546
3. J. Fessler, J. Kulick, J. Eaton, Preferential concentration of heavy-particles in a turbulent channel flow. Phys. Fluids **6**(11), 3742–3749 (1994). doi:10.1063/1.868445. http://scitation.aip.org/content/aip/journal/pof2/6/11/10.1063/1.868445
4. G.H. Good, P.J. Ireland, G.P. Bewley, E. Bodenschatz, L.R. Collins, Z. Warhaft, Settling regimes of inertial particles in isotropic turbulence. J. Fluid Mech. **759**, R3 (2014). doi:10.1017/jfm.2014.602. http://journals.cambridge.org/abstract_S0022112014006028
5. S. Goto, J. Vassilicos, Sweep-stick mechanism of heavy particle clustering in fluid turbulence. Phys. Rev.Lett. **100**(5), 54,503 (2008). doi:10.1103/PhysRevLett.100.054503. http://link.aps.org/doi/10.1103/PhysRevLett.100.054503
6. M. Maxey, The gravitational settling of aerosol-particles in homogeneous turbulence and random flow-fields. J. Fluid Mech. **174**, 441–465 (1987). doi:10.1017/S0022112087000193. http://journals.cambridge.org/article_S0022112087000193
7. R. Monchaux, M. Bourgoin, A. Cartellier, Preferential concentration of heavy particles: a Voronoi analysis. Phys. Fluids **22**(10), 103,304 (2010). doi:10.1063/1.3489987. http://scitation.aip.org/content/aip/journal/pof2/22/10/10.1063/1.3489987
8. R. Monchaux, M. Bourgoin, A. Cartellier, Analyzing preferential concentration and clustering of inertial particles in turbulence. Int. J. Multiph. Flow **40**, 1–18 (2012). doi:10.1016/j.ijmultiphaseflow.2011.12.001. http://www.sciencedirect.com/science/article/pii/S030193221100245X
9. M. Obligado, T. Teitelbaum, A. Cartellier, P.D. Mininni, M. Bourgoin, Preferential concentration of heavy particles in turbulence. J. Turbul. **15**(5), 293–310 (2014). doi:10.1080/14685248.2014.897710. http://www.tandfonline.com/doi/abs/10.1080/14685248.2014.897710

10. J.P.L.C. Salazar, J. de Jong, L. Cao, S.H. Woodward, H. Meng, L.R. Collins, Experimental and numerical investigation of inertial particle clustering in isotropic turbulence. J. Fluid Mech. **600**(1), 245–256 (2008). doi:10.1017/S0022112008000372. http://journals.cambridge.org/production/action/cjoGetFulltext?fulltextid=1818596
11. K.D. Squires, J.K. Eaton, Preferential concentration of particles by turbulence. Phys. Fluids A **3**(5), 1169–1178 (1991). doi:10.1063/1.858045. http://scitation.aip.org/content/aip/journal/pofa/3/5/10.1063/1.858045

On Mechanics of Turbulent Gas-Liquid Flows

Alexander V. Gorin

Abstract A sequential spatial-temporal averaging procedure taking into account fluctuations of concentration and their correlation with the kinematic characteristics of the gas-liquid mixture is employed to derive governing and constitutive equations for description of two-phase systems. The momentum balance provides the basis for the turbulent viscosity and bubble diffusion models, and an additional impulse due to virtual mass force as a result of bubble pulsations is considered. Closed-form theoretical expressions have been obtained for mixtures of bubble sizes predicting the bubble concentration profiles for each size fraction as well as the total concentration profile in the pipe cross-section exhibiting experimentally found non-uniform multi-peaked bubble concentration profiles. The local homogeneous approximation enables the concept of turbulent boundary layer with vanishing viscosity to be employed. In the limiting case of high Reynolds number, analytical solutions for the wall shear stress, velocity and void fraction distributions, and the basic average parameters of the gas-liquid flow are obtained from a relative friction law with a single additional empirical constant only.

1 Introduction

Study of transport phenomena in gas-liquid flows is a challenging task that still requires advanced general models which are able to predict the main transport properties, the phase velocities and distributions, and wall shear stress.

A great number of both theoretical and experimental investigations of gas-liquid flows of basic configurations have been carried out over the last decades. Turbulent bubbly flow is one of the most difficult for theoretical analysis flow pattern due to a wide spectrum of bubble sizes forming the gaseous phase, complicated kinematics of individual bubbles, their deformation, interaction with each other and a liquid

A.V. Gorin (✉)
Swinburne University of Technology, Sarawak Campus, Jalan Simpang Tiga,
93350 Sarawak, Kuching, Malaysia
e-mail: agorin@swinburne.edu.my

© Springer International Publishing Switzerland 2016

A. Segalini (ed.), *Proceedings of the 5th International Conference on Jets, Wakes and Separated Flows (ICJWSF2015)*,
Springer Proceedings in Physics 185, DOI 10.1007/978-3-319-30602-5_60

resulting in substantial discrepancies between the experimental data in steady-state, fully-developed upward flows in vertical ducts, even at similar experimental conditions. The glowing examples of such the discrepancies are the abnormal behavior of the wall shear stress at moderate Reynolds number and low volumetric gas fraction, and different void fraction profiles that can be classified as coring void profiles with bubbles mostly concentrating along the pipe centerline, wall-peaking profiles exhibiting the peak of bubble concentration near the wall, and saddle-type profiles with local peaks in void fraction profiles at the centerline and near the wall. Even additional local peaks at the intervening space between the centerline and wall were observed. Although the authors do not provide detailed information about the bubble size distribution, from the information available in their studies it follows that the bubble size and the bubble kinematics are of primary importance in the bubbly flow structure formation thus determining the transfer processes scenario [1–5].

Theoretical investigations of two-phase system are based on governing equations derived employing one or other averaging technique to the first principles [see for example, 6–9]. Since the technique itself and closure methodology introducing for example effective transport coefficients and gradient hypotheses, are in fact a phenomenological approach, leaning upon intuition, dimensional and scale analysis, and experimental data, the development of the governing equations remains the topical problem of mechanics of multiphase systems.

The lecture provides a general theoretical framework containing most of the relevant physical mechanisms of transfer processes involved to describe turbulent bubbly flows. Given the complexity of the phenomena, the simplified versions of the theory capturing the main physics were used to describe analytically mechanical effects in turbulent bubbly flows in pipes and boundary layers. Therefore, a strong emphasis has been put on the rational approach to the derivation of the averaged equations for conservation of mass and momentum for each phase, on the assumption that no phase change occurs and constitutive modelling for transfer mechanisms in bulk fluids. It is shown that the theory is able to predict the fields of average kinematic properties of both gas and liquid phases, the wall shear stress, a drag reduction mechanism, and explain the bubble migration phenomenon in a bubbly flow with a wide spectrum of bubble sizes.

2 Average Governing Equations

The averaged equations for conservation of mass and momentum for each phase taking into account the fluctuations of concentration and their correlation with the kinematic characteristics of the gas-liquid mixture are derived using the sequential spatial-temporal averaging procedure [10, 11]:

$$\hat{\Phi}_n = \frac{1}{\varphi}\int \Phi_n d; \quad \bar{\Phi}_n = \frac{1}{\Delta t}\int_t \hat{\Phi}_n dt = \overline{\left(\frac{n}{\varphi_n}\right)}$$

The averaging of Φ_n, the functions characterising the nth component of the concentration φ_n in the region Ω, yields the following relation (a prime denotes fluctuations)

$$\overline{\Phi_n \varphi_n} = \bar{\Phi}_n \bar{\varphi}_n + \overline{\Phi_n' \varphi_n'} \tag{1}$$

The momentum balance provides the basis for the turbulent viscosity and bubble diffusion models taking into account the additional impulse due to virtual mass force as a result of bubble fluctuations. The continuity equations represented for the flux $\vec{p}_n$ of bubbles of a given size and the corresponding flux vector $\vec{q}_n$ for the liquid flow are transformed into a set of diffusion equations [12] taking into account the liquid volume displaced by an equal volume of the rising bubbles this being particularly important near the wall:

$$\vec{p}_n = \vec{u}_n \varphi_n - \varsigma_n \nabla \varphi_n \tag{2}$$

$$\vec{q}_n = \vec{u}_l \left(1 - \sum \varphi_n\right) - \varsigma_l \nabla \left(1 - \sum \varphi_n\right) \tag{3}$$

where ς_n, ς_l are the diffusivity for this particular bubble size and a liquid, and $\vec{u}_n$, $\vec{u}_l$ are the bubble and liquid convection; the summation is over all the bubble size fractions.

3 Bubbly Flow with Different Bubble Sizes

The derived governing equations were employed to bubbly flow of a wide bubble size distribution. The acceleration of the sphere of radius a induces a resistance force on the sphere equal to one-half the mass of the displaced fluid times the acceleration of the sphere, $(2/3)\pi a^3 \rho_p \left(\mathrm{v}_p - \mathrm{v}_g\right)/T$ (suffixes l and g denote liquid and gas phases respectively). T is the bubble relaxation time.

Disregarding triple correlations and in view of $\rho_g << \rho_l$ the Reynolds shear stress, as it follows from the definition (3), now becomes

$$\tau = (1-\varphi)\rho_l \overline{u_l' \mathrm{v}'_l} + (1/2)\varphi \rho_l \overline{u_g' \mathrm{v}'_g} \tag{4}$$

Using the hypothesis of Boussinesq and estimating single-point temporal correlations in terms of characteristic frequency of pulsation motion ω and time T as [13]

$$\overline{u_g^2}/\overline{u_l^2} = \frac{1}{2}\frac{1+9\omega T}{1+\omega T} \tag{5}$$

for the diffusivity for bubbles of particular size one can get,

$$D_n = (1/2)\varsigma_n\varphi_n(1+9\omega_n T_n)/(1+\omega_n T_n). \tag{6}$$

The diffusion equations are applied for a gas-liquid flow with two bubble sizes considering the bubble transverse migration speed is conjectured to be due to the "shear" lift.

From (4–6) it follows

$$\varsigma_n\frac{d\varphi_n}{dy} + \varphi_n\left\{\mathrm{v}_{rn} - \frac{\varsigma_l\sum \mathrm{v}_{rn}\varphi_n/\varsigma_n}{1-\sum\varphi_n+\varsigma_l\sum(\varphi_n/\varsigma_n)}\right\} \tag{7}$$

and

$$U_l = \frac{\varsigma_l\sum \mathrm{v}_{rn}\varphi_n/\varsigma_n}{1-\sum\varphi_n+\varsigma_l\sum(\varphi_n/\varsigma_n)} \tag{8}$$

where $\mathrm{v}_r = u_g - u_l$ is the relative phase velocity.

By way of example let us consider dispersed phase consisting of two bubble sizes fractions (identified in the text by suffixes 1 and 2). Equation (7) are reduced to

$$\varsigma_l\frac{d\varphi_1}{dy} + \frac{11\mathrm{v}_{r1}-2\mathrm{v}_{r2}}{13} = 0$$
$$\varsigma_l\frac{d\varphi_2}{dy} + \frac{11\mathrm{v}_{r2}-2\mathrm{v}_{r1}}{13} = 0$$

This set of equations shows that the type of a particular bubble-size-fraction distribution depends on the ratio of fractional transverse velocities.

The bubble transverse migration speed is conjectured to be due to the "shear" lift. For the bubbles obeying linear resistance law this can be estimated from the following force balances:

$$12\pi\mu a u_B = \frac{4}{3}\pi a^3\rho_l g,$$
$$12\pi\mu a\mathrm{v}_r = -\frac{4}{3}\pi a^3\rho_l u_B\frac{dU_l}{dy}$$

where u_B is the bubble rise velocity in the axial direction (the terminal rise velocity of a single bubble in stagnant liquid); U_l is the mean liquid phase velocity profile in a pipe.

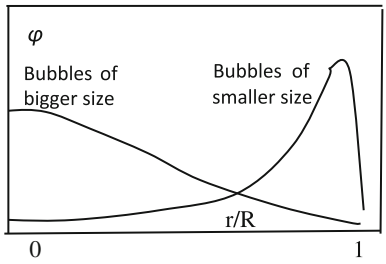


Fig. 1 Void fraction profiles as shown by our analysis

This set of equations, with the liquid turbulent viscosity $\varsigma_l = const$, gives the following bubble concentration profiles for each size fraction

$$\varphi_{1(2)}(y) = -\left(\frac{B_{1(2)}}{\varsigma_0}\right) U_l(y) + \text{const} \tag{9}$$

where $B_{1(2)} = \frac{2}{1053}\frac{a_{2(1)}^4 g}{\nu_l^2}\left[\frac{11}{2} - \left(\frac{a_{1(2)}}{a_{2(1)}}\right)^4\right]$; the integration constant is determined from the gas quality for each bubble size fraction.

Multi-peaked type of bubble fractions distribution over the pipe cross-section is exhibited for the mixture of a wide range of bubble sizes (Fig. 1).

4 Gas–Liquid Turbulent Boundary Layers

Consider the turbulent shear stress tensor for two-dimensional flow. It is suggested that $u_l' \approx u_g' = u'$, $v_l' \approx v_g' = v'$, $u_g = u_l + u_B$. Since $\rho_g u_B \overline{v'\varphi'} \ll \rho_l u_l \overline{v'(1-\varphi)'}$ and disregarding triple correlations such as $\overline{u'v'\varphi_n'}$, for the gas-liquid mixture of the velocity u and the density of $\rho = \rho_l(1-\varphi) + \rho_g\varphi$ the turbulent shear stress tensor then takes the form

$$\tau = u_l \overline{v'\rho'} + \rho \overline{u'v'} + v \overline{u'\rho'} \tag{10}$$

Equation (10) can be used as a basis for the calculation of friction loses in gas-liquid mixtures. The turbulent momentum and mass transfer are assumed to be of the same nature, we define the fluctuation components according to the mixing length theory with l as the mixing length (the overscribed bar denoting the sequential spatial-temporal averaging is omitted):

$$\tau = l^2 \frac{du}{dy}\frac{d(\rho u)}{dy} \tag{11}$$

The relation between ρ and u can be found using the assumption of similarity for the fields of the velocity and mass concentrations that is well justified for gas-liquid flows at high Reynolds numbers and relatively high gas content, and representing the mass fraction in terms of volumetric fraction

$$\rho = \frac{\rho_l}{1 - Au/u_s} \quad \text{where } A = 1 - \rho_l/\rho_s$$

Herein after index s refers to the parameters on the outer edge of the boundary layer (channel axis).

From (11) it follows that

$$\tau = \rho_l \left(\frac{l}{1 - A(u/u_s)} \frac{du}{dy} \right)^2 \tag{12}$$

To avoid difficulties related to the necessity of specifying the turbulent shear stresses in gas-liquid flows and the use of empirical constant from the single-phase theory of turbulence we will employ the theory of turbulent boundary layers with vanishing viscosity, which was developed in [14] for the calculation of single-phase turbulent boundary layers and used in two-phase flows for the first time in [15].

Introduce the dimensionless variables: $\tilde{u} = \frac{u}{u_s}; \tilde{\tau} = \frac{\tau}{\tau_w}; \tilde{l} = \frac{l}{\delta}; \tilde{y} = \frac{y}{\delta}; \zeta = \frac{2\tau_w}{\rho_{su_s^2}}$, where τ_w is the wall shear stress, δ is the boundary layer thickness (for the case of a tube, instead of δ one should use the tube radius R and the friction factor is then defined by the mixture velocity averaged over the tube cross section, $\zeta = \frac{2\tau_w}{(\rho_s u^2)}$). The flow of an incompressible liquid with parameters at the outer edge of the boundary layer (tube axis) corresponding to the parameters of the introduced homogeneous mixture with variable density is taken as a "standard" flow. These parameters are marked by the index "0".

Equation (12) takes the form:

$$\left(\frac{\zeta_0}{2} \tilde{\tau}_0 \right)^{1/2} \frac{d\tilde{y}}{\tilde{l}_0} = \left(\frac{\rho_L}{\rho_s} \frac{\tilde{\tau}_0}{\tilde{\tau}} \frac{1}{\Psi} \right)^{1/2} \frac{\tilde{l}}{\tilde{l}_0} \frac{d\tilde{u}}{1 - A\tilde{u}} \tag{13}$$

where $\Psi = (\zeta/\zeta_0)_{\mathrm{Re}}$ is the relative resistance at Re = idem. The Reynolds number is defined by the mixture velocity and the liquid viscosity.

For the limiting $(\mathrm{Re} \to \infty)$ relative friction law for a pipe flow under the assumption that $\tilde{\tau}/\tilde{\tau}_0 = 1, \quad \tilde{l}/\tilde{l}_0 = k = const$ it follows that

$$\frac{\zeta}{\zeta_0} = \frac{\rho_l}{\rho_S} \left[\frac{kln(\rho_S/\rho_l)}{1 - \rho_l/\rho_s} \right]$$

Velocity and void fraction distributions, and the basic average parameters of the gas-liquid flow are obtained from a relative friction law with only a single additional empirical constant (Figs. 2 and 3).

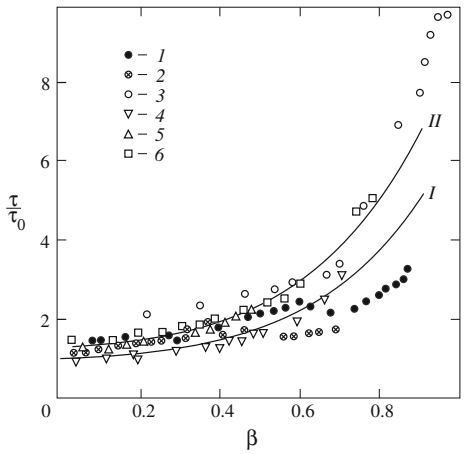


Fig. 2 Wall shear stress: *1*, *2*, *3*—G = 10.9; 27.2; 78.4 cm^3/s and D = 10 mm, respectively; *4*—Re = 82,600; *5*, *6*—Re = $1.8 \cdot 10^5$ and Re = 10^5. *I*, *II*—our calculations at k = 1, k = 1.17

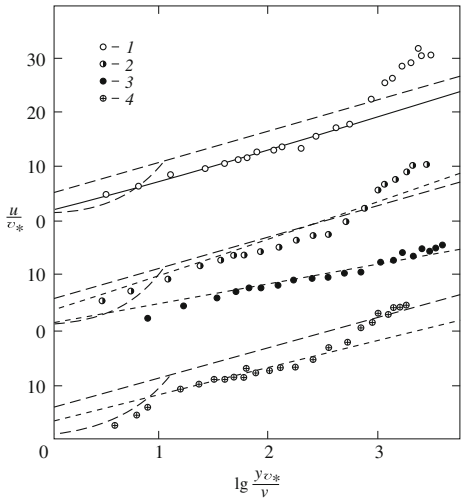


Fig. 3 Velocity profiles in upward flows in tubes—Re = $7 \cdot 10^4$, β : *1*—0.46; *2*—0.315; Re = $7 \cdot 10^4$, β : *3*—0.172; *4*—0.254. *1*, *2*, *4*—slug regime; *3*—inter-mediate regime; *solid lines*—our calculations; *dashed lines*—single-phase profile

5 Reduction of the Wall Shear Stress by the Bubble Diffusion

The concept of the turbulent boundary layer with vanishing viscosity can be applied to the problem of friction change during gas injection into the liquid boundary layer. One can get an explicit relation between the relative skin friction C_f/C_{f0} and the permeability parameter b_1 (Fig. 4):

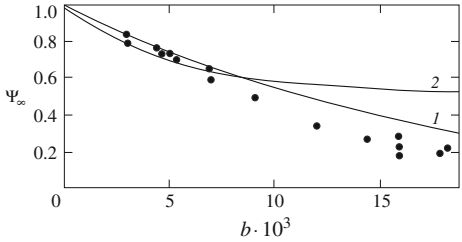


Fig. 4 Relative skin friction of gas-liquid mixture flow along a permeable flat plate. *1*—our calculations *2*-calculations [16]

$$\frac{C_f}{C_{f0}} = \frac{\rho_w}{\rho_l}\frac{k^2}{(A+b_1)}ln^2\left\{\frac{\rho_w}{\rho_l}\frac{\sqrt{A+b_1}+\sqrt{A(1+b_1)}}{\sqrt{A+b_1}+\sqrt{A}}\right\}$$

where $A = 1-\rho_w/\rho_l$; $b_1 = \frac{2}{c_f}\frac{\rho_w v_w}{\rho_l v_s}$; ρ_w is the density of a mixture at the wall;

The relative limiting skin friction law used here enables also the velocity and void fraction distribution, and the critical values of the permeability parameter corresponding to $C_f/C_{f0} = 0$ to be determined:

$$b_{cr} = 4k^2\frac{\rho_g}{\rho_l-\rho_g}ln^2\left[\sqrt{\frac{\rho_l}{\rho_g}}\left(1+\sqrt{1-\frac{\rho_g}{\rho_l}}\right)\right]$$

References

1. A. Serizawa, I. Kataoka, in *Phase Distribution in Two–Phase Flow*, ed. by N.H. Afgan. Transient Phenomena in Multiphase Flow (Hemisphere, Washington, 1988)
2. V.E. Nakoryakov, O.N. Kashinsky, A.P. Burdukov et al., Local characteristics of upward gas-liquid flows. Int. J. Multiph. Flow **7**(1), 63–81 (1981)
3. T. Hibiki, M. Ishii, Z. Xiao, Axial interfacial area transport of vertical bubbly flows. Int. J. Heat Mass. Transf. **44**, 1869–1888 (2001)
4. K. Felton, E. Loth, Diffusion of sphrerical bubbles in a turbulent boundary layer. Int. J. Multiph. Flow **28**, 69–92 (2002)
5. T. Hibiki, M. Ishii, Experimental study of interfacial area transported in bubbly two-phase flows. Int. J. Heat Mass Transf. **42**, 3019–3035 (1999)
6. L.D. Landau, E.M. Lifshitz, *Fluid Mechanics*, 2nd edn. (Pergamon Press, London, 1987)
7. G.K. Batchelor, Statistical hydrodynamics of dispersed systems. J. Fluid Mech. **49**, 489–507 (1970)
8. M. Ishii, *Thermo-Fluid Dynamic Theory of Two-Phase Flow* (Eyrolles, Paris, 1975)
9. D.A. Drew, Mathematical Modeling of Two-Phase Flow. Ann. Rev. Fluid Mech. **15**:261–291 (1983)
10. A.K. Dujnin, *Fundamentals of Mechanics of Multicomponent Flows* (SB AS USSR, Novosibirsk, 1965)

11. V.E. Nakorykov, A.V. Gorin, Heat and Mass Transfer in Two-Phase Systems, (SB RAS, Novosibirsk, 1994)
12. J.N. Hunt, On the turbulent transport of heterogeneous sediment. Q. J. Mech. Appl. Math. **22** (2), 235–246 (1969)
13. A.V. Gorin, in *On Analysis of Turbulent Bubbly Flow*, ed. by S.S. Kutateladze. Hydrodynamics and Heat Transfer of Single- and Two-Phase Media, (ITF SO AN SSSR, Novosibirsk, 1979), pp. 115–121
14. S.S. Kutateladze, A. Leont'ev, *Heat and Mass Transfer And Friction In Turbulent Boundary Layer*, (Energoatomizdat, Moscow, 1985)
15. A.V. Gorin, Friction and the velocity and gas-content profiles of a turbulent gas-liquuid flow. J. Eng. Physics **35**, 1029–1036 (1978)
16. A.M. Basin, A.I. Korotkin, L.F. Kozlov, *Control of Ship Boundary Layer*, (Sudostroenie, Leningrad, 1968)

Film Behavior of Two-Phase Flow in a Horizontal Pipe with a Sudden Contraction

Takahiro Fujimatsu, Mizuki Kito and Kunikazu Kondo

Abstract The flow regime transitions in a horizontal pipe with a sudden contraction were investigated in detail using a high-speed video camera and the developing process of the two-phase flow was clarified. In the present study, five flow regimes were observed, then the flow regime of the liquid film was classified into seven categories of regimes. Moreover, at high gas and liquid velocities, DW_3 which was transitional wave to "Misty wave" from DW_2 (three-dimensional disturbance wave) was newly observed. The two-phase distribution patterns were analyzed through the concept of the standard deviation, skewness and kurtosis. DW_3 occurs erratically, while other disturbance waves occur regularly.

1 Introduction

Gas-liquid two-phase flows exist in piping systems of various power plants, such as thermal energy plants, nuclear power plants and solar plants as well as chemical plants, cooling and heating equipment. It is essential to understand characteristics of two-phase flows for improving the energy efficiency of the power plants or the energy equipment.

In order to elucidate the film mechanism of annular mist flow in a pipe, the authors have thus further studied the flow characteristics, such as flow regime, wave frequency, entrainment and deposition of droplets and so on [1]. Understanding of the exiting flow patterns in different piping components can also contribute a better design of two-phase flow systems. Therefore, extensive investigations have been made in regard to the classification of flow patterns in 90° [2] or 180° [3] U-bends, a coiled tube [4], a T junction [5], a rod bundle [6], micro-channels [7] and so on.

T. Fujimatsu (✉) · M. Kito · K. Kondo
Department of Mechanical Engineering, National Institute of Technology, Suzuka College Shirokocho, Suzuka, Mie 510-0294, Japan
e-mail: fujimatu@mech.suzuka-ct.ac.jp

© Springer International Publishing Switzerland 2016

A. Segalini (ed.), *Proceedings of the 5th International Conference on Jets, Wakes and Separated Flows (ICJWSF2015)*,
Springer Proceedings in Physics 185, DOI 10.1007/978-3-319-30602-5_61

Chang et al. [2] investigated the effects of channel height-to-width ratio on the behavior of air-water flows through horizontal and vertical U-bend rectangular channels. They analyzed the two-phase flow patterns by visualizing the interfacial flow transitions through the U-bend using a CCD camera and demonstrated the pressure drop and the heat transfer process. They presented that slug and slug-annular flows in flow pattern maps shifted towards the higher superficial gas velocities as the height-to-width ratio decreased. Air-water flows through horizontal to the vertical through a 90° bend were analyzed by Saidj et al. [3] using ring-shaped conductance probes. They identified the flow patterns both in the horizontal pipe upstream and the vertical pipe downstream, using the Probability Density Function (PDF) of the time series of the cross sectional averaged void fraction. Whalley [4] studied air-water flows in a helically coiled tube. They showed the difference in the liquid film thickness and liquid film flowrate around the tube periphery between presented flows and vertical annular flows. Azzopardi and Whalley [5] investigated the effects of flow patterns in a T junction. They found that the entering flow direction of air-water flows were strongly dependent on the flow patterns upstream the junction. Air-water flows through a vertical rod bundle were investigated by Venkateswararao et al. [6] in order to understand the flow pattern transitions. They concluded by comparing the flow pattern transitions with those of others that further research on the subject was still needed. Saisorn and Wongwises [7] compared air-water flows through a horizontal circular micro-channel with two-phase flows through ordinarily size channels. They investigated the flow patterns using a high speed camera and a stereozoom microscope. They classified the observed flow patterns into three flow regimes and showed comparisons of the observed flow patterns with the flow regime maps proposed by some previous researchers. As mentioned above, a number of studies regarding two-phase flows through pipes in a variety of shapes have been conducted. Nevertheless, relatively few reports have focused on the film mechanism of annular mist flow in a horizontal pipe with a sudden contraction. The flow pattern transitions were not considered, although an attempt was made to demonstrate the pressure drop across a sudden contraction by Schmidt and Friedel [8]. It is, however, still necessary to predict flow-pattern transition.

In this study, the flow regime transitions in a horizontal pipe with a sudden contraction were investigated in detail using a high-speed video camera and the developing process of the two-phase flow was clarified. The flow regime transitions were examined to elucidate the developing process of the two-phase flow. Two other statistical characteristics were also calculated to analyze the phase distribution patterns quantitatively: skewness and kurtosis. Then, disturbance wave occurrence frequencies were analyzed with the mean, standard deviation, skewness and kurtosis.

2 Experimental Apparatus and Procedure

Figure 1 shows the schematic experimental apparatus. The contraction area ratio $(d_2/d_1)^2$ was obtained 0.36 from the inlet diameter with $d_1 = 50$ mm and the outlet pipe diameter with $d_2 = 30$ mm. Compressed air was applied from a compressor to the mixing device where it combines with water drawn from a storage tank. The mixing device consisted of an annular section surrounding a porous sinter wall. The two-phase flow travels for 4320 mm down to the contraction along a 50 mm diameter horizontal pipe, then enters a 30 mm diameter transparent acrylic horizontal pipe. The experiments were carried out for various values of superficial gas and liquid velocities. The superficial gas velocity after mixing (j_{G1}) ranged from 5.15 to 18.1 m/s (velocity measured just downstream of the sudden contraction $j_{G2} = 14.3$–50.3 m/s) and the superficial liquid velocity (j_{L1}) ranged from 10.5 to 72.3 mm/s ($j_{L2} = 29.2$–201 mm/s). The liquid film behavior in the horizontal pipe after the sudden contraction were obtained in detail using a high-speed video camera at three locations $z_2/d_2 = 10$, 40 and 80 denoting the normalized streamwise distance from the sudden contraction. Passing frequencies of disturbance waves were measured for 10 min by visual observations at every measurement point under each condition. The average values of the measured frequencies which were taken for 3 min; 1 min at the beginning, at the middle and at the end of the measurements, were used as disturbance wave occurrence frequencies.

3 Experimental Results and Discussion

Figure 2 shows actual selected images and schematic illustrations of typical flow regimes observed at $z_2/d_2 = 10$, 40, 80. In the present study, five flow regimes were observed, namely, quasi-ripple (QR), huge-wave (HW), two-dimensional disturbance wave (DW_1), three-dimensional disturbance wave (DW_2) and bow wave

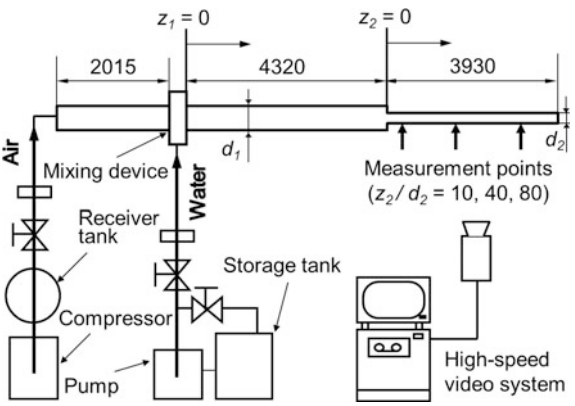


Fig. 1 Schematic experimental apparatus

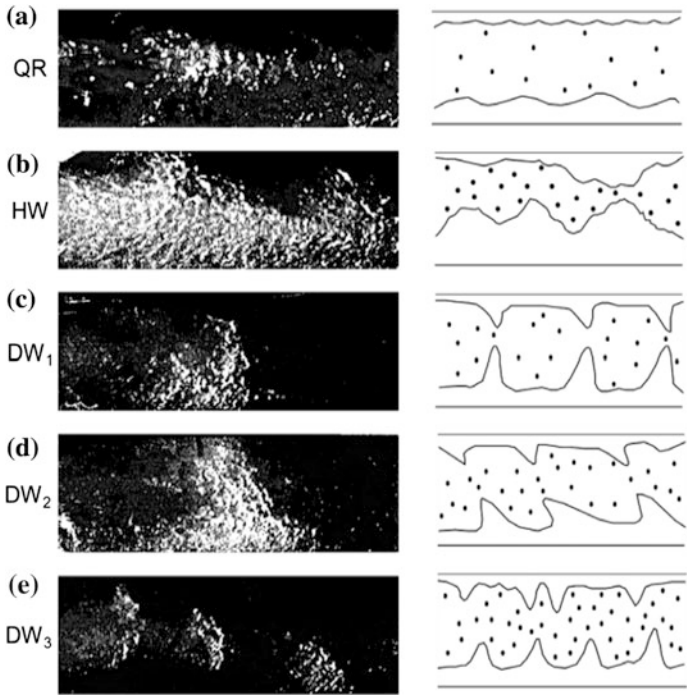


Fig. 2 Actual selected images and schematic illustrations of typical flow regimes observed at $z_2/d_2 = 10, 40, 80$

(DW_3) regions. In this study, conventional disturbance waves are subdivided into two types of disturbance waves, DW_1 and DW_2, in order to clarify the developing process of the waves on the liquid film in detail. In particular, as shown in Fig. 2c, DW_1 is formed perpendicularly to the pipe axis and coherent around the pipe circumference, while DW_2 is distorted in the streamwise direction, then a part of the ringwise waves begins to be broken (see, Fig. 2d). These waves with no coherence around the pipe circumference three-dimensional disturbance waves were termed DW_2, as distinguished from DW_1. At high gas and liquid velocities, as depicted in Fig. 2e, DW_3 which was transitional wave to "Misty wave (MW)" from DW_2 was newly observed. DW_3 is a comparable wave to "Bow wave (BW)", which Azzopardi and Gibbons [9] have been mentioned in their study of two-phase flow through a large diameter vertical pipe. DW_3 is not formed perpendicularly to the pipe axis but curved like a bow.

Under the same condition, several flow regimes were observed at the measurement point in the present study. The observed flow patterns were compared with the flow maps proposed by Mandhane et al. [10] based on experimental observations by several researchers for horizontal flows and found to be classified as annular and annular/mist flow. The visual observation, however, allowed a more detailed classification of the two- phase flows. Thus, the flow regime of the liquid

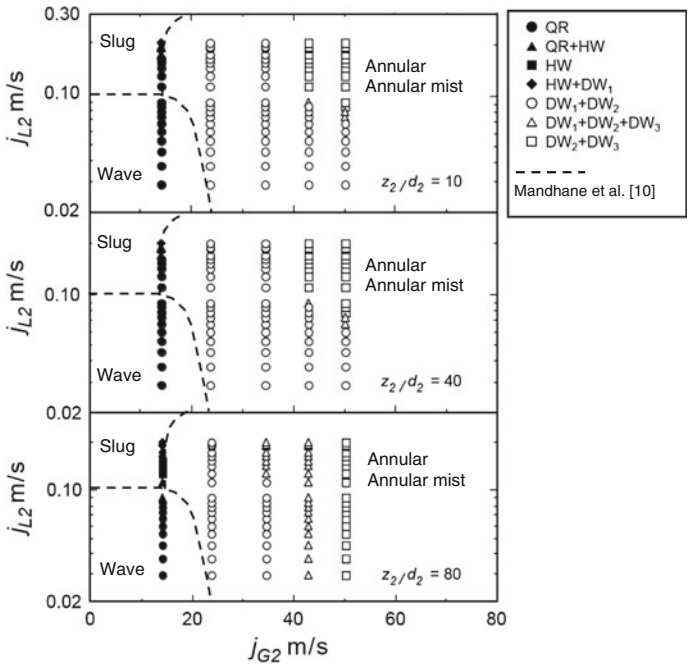


Fig. 3 Flow regime maps. QR: quasi-ripples, HW: huge-waves, DW_1: two-dimensional disturbance waves, DW_2: three-dimensional disturbance waves, DW_3: bowwaves

film is classified into seven categories of regime: QR, QR + HW, HW, HW + DW_1, $DW_1 + DW_2$, $DW_1 + DW_2 + DW_3$ and $DW_2 + DW_3$. Figure 3 shows observed flow regime maps at $z_2/d_2 = 10$, 40, 80 downstream of the sudden contraction. The flow pattern transition curves of Mandhane et al. are illustrated by broken lines in Fig. 3. As the superficial gas and liquid velocities increase, DW_1 is distorted and subsequently DW_2 is formed and then formed DW_3. The flow regime of $DW_1 + DW_2$ is limited at lower j_{G2} and DW_3 occurs at lower j_{G2} as z_2/d_2 increases. The flow regime $DW_1 + DW_2 + DW_3$ is observed at relatively wide range at $z_2/d_2 = 80$.

Figure 4 shows the change in the mean frequency of disturbance wave with the superficial gas velocity j_{G2} at $j_{L2} = 0.201$ m/s, $z_2/d_2 = 80$ in order to analyze the developing process of the two-phase flow. The authors define wave occurrence frequency as the mean number of waves per second passing an arbitrary point in the pipe. The frequencies of DW_1, DW_2, DW_3 and DW: the sum of these frequencies, are denoted by f_{D1}, f_{D2}, f_{D3} and f_D, respectively.

The DW_2 occurs over wide range of the superficial gas and liquid velocities. The frequency of DW_2: f_{D2} increases with j_{G2}, whereas f_{D1} decreases gradually as j_{G2} increases. Moreover, f_{D3} increases significantly as j_{G2} increases. As j_{G2} increases, transition occurs from DW_1 to DW_2, subsequently DW_3 occurs. Frequencies of the whole disturbance waves f_D increase significantly with f_{D3}. In addition, when the

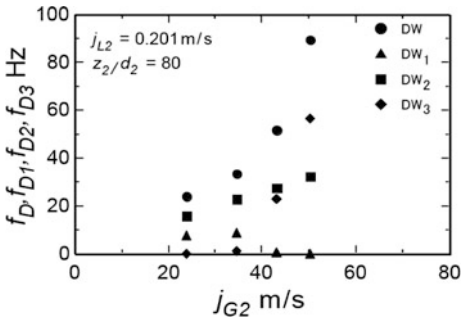


Fig. 4 Mean frequencies for disturbance waves at $z_2/d_2 = 80$

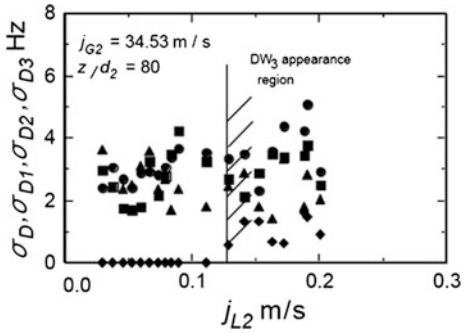


Fig. 5 Standard deviations for disturbance wave occurrence frequency at $z_2/d_2 = 80$

superficial liquid velocity j_{L2} increased, the frequencies f_{D2} and f_D also increased significantly, however the frequency of DW_1, f_{D1} decreased gradually. When the superficial gas velocity j_{G2} increased up to 50.25 m/s, DW_1 hardly appeared, in contrast, DW_3 occurs at higher j_{G2}. Although the figure is omitted, it was found that as z_2/d_2 increased, f_{D1} decreased and f_{D3} increased rapidly, on the other hand, f_{D2} decreased very slightly.

The two-phase distribution patterns were analyzed through the concept of the standard deviation of disturbance wave occurrence frequency. The standard deviations at $z_2/d_2 = 80$ are plotted against the superficial liquid velocity at $j_{G2} =$ 34.53 m/s in Fig. 5, in which the DW_3 occurrence is highlighted by hatching. The standard deviations for DW_1 (σ_{D1}) and DW_2 (σ_{D2}) remain low between 1 and 5 independently of increasing j_{L2} and j_{G2}. This implies that the disturbance waves occur regularly. In contrast, the values of σ_{D3} are scattered as j_{L2} and j_{G2} increase. Thus the DW_3 occurs erratically in the experimental conditions. Two other statistical characteristics were also calculated to analyze the phase distribution patterns quantitatively: skewness and kurtosis. Values of skewness and kurtosis are presented in Fig. 6a and b, respectively. The values of skewness S_{D1} and S_{D2} are close to zero; and the values of kurtosis K_{D1} and K_{D2} are $1 < K_{D1}, K_{D2} < 5$, indicating that the frequency distributions are nearly symmetrical about the mean value and the waves occur regularly. The skewness S_{D3} is positive at $j_{L2} \geq 0.128\,\mathrm{m/s}$; and K_{D1} are scattered at large values, suggesting that the distribution has a longer tail greater than the maximum and the waves occur erratically.

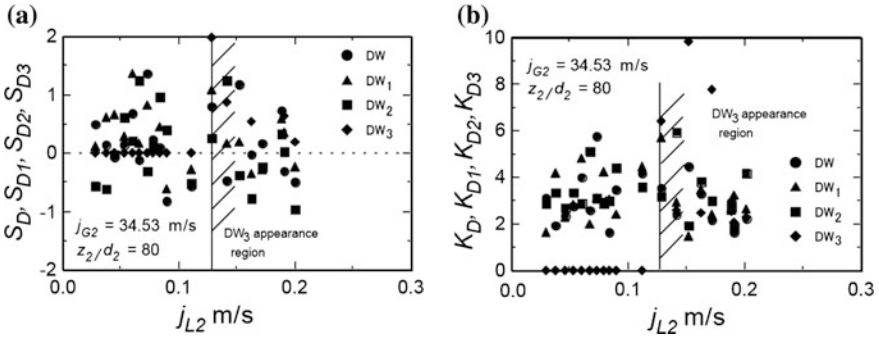


Fig. 6 Skewness and kurtosis for disturbance wave occurrence frequency at $z_2/d_2 = 80$. **a** Skewness. **b** Kurtosis

4 Conclusions

The flow regime transitions in a horizontal pipe with a sudden contraction were investigated in detail using a high-speed video camera and the developing process of the two-phase flow was clarified. The following main results were obtained in the experimental conditions.

(1) DW3 which was transitional wave to "Misty wave" from DW_2 was newly observed at high gas and liquid velocities.
(2) The flow regime of the liquid film is classified into seven categories of regimes.
(3) DW_3 occurrence shifts to higher j_{G2} and j_{L2} with z_2/d_2 increasing.
(4) The frequency of DW_2: f_{D2} increases with j_{G2} and j_{L2}, whereas the frequency of DW_1: f_{D1} decreases gradually as j_{G2} and j_{L2} increase.
(5) DW_3 occurs erratically, while DW_1 and DW_2 occur regularly.

References

1. O. Okada, T. Fujimatsu, H. Fujita, Y. Nakajima, Measurement of droplet size distribution in an annular mist flow in a vertical pipe by immersion liquid method, *Proceeding of the 2nd International Conference on Multiphase Flow*, vol. **1**, (1995), pp. IP2-11–IP2-18
2. S.W. Chang, K.F. Chiang, C.Y. Lin, Channel aspect ratio effect on thermal performance of air-water slug flow through U-bend channels. Int. J. Therm. Sci. **76**, 11–29 (2014)
3. F. Saidj, R. Kibboua, A. Azzi, N. Ababou, B.J. Azzopardi, Experimental investigation of air-water two-phase flow through vertical 90° bend. Exp. Therm. Fluid Sci. **57**, 226–234 (2014)
4. P.B. Whalley, Air-water two-phase flow in a helically coiled tube. Int. J. Multiph. Flow **6–4**, 345–356 (1980)
5. B.J. Azzopardi, P.B. Whalley, The effect of flow patterns on two-phase flow in a T junction. Int. J. Multiph. Flow **8–5**, 491–507 (1982)

6. P. Venkateswararao, R. Semiat, A.E. Dukler, Flow pattern transition for gas-liquid flow in a vertical rod bundle. Int. J. Multiph. Flow **8–5**, 509–524 (1982)
7. S. Saisorn, S. Wongwises, An experimental investigation of two-phase air-water flow through a horizontal circular micro-channel. Exp. Therm. Fluid Sci. **33**, 306–315 (2009)
8. J. Schmidt, L. Friedel, Two-phase pressure drop across sudden contractions in duct area. Int. J. Multiph. Flow **23–2**, 283–284 (1997)
9. B.J. Azzopardi, D.B. Gibbons, Annular two-phase flow in a large diameter tube. Chem. Eng. **398**, 19–31 (1983)
10. J.M. Mandhane, G.A. Gregory, K. Aziz, A flow pattern map for gas-liquid flow in horizontal pipes. Int. J. Multiph. Flow **1–4**, 537–553 (1974)

Some Aspects of Design and Modelling of Multi-phase Separation Process in Complex Channels Under Magnetic Fields

Maxim Kireitseu

Abstract Multiphase fluids within separated flows in complex channels were described by Navier-Stokes and Reynolds full equations for the case of complex wall configuration. Heat transfer, turbulence, presence of mass inertial forces were taken into account from multi-physics approach perspective. Modelling of separation flows was carried out using the algorithms of SIMPLE and L.M. Simuni's approach with generalization for the case with variable radius of a longitudinal gradient of pressure. Experimental validation of the modelling approach has proven to be effective for the optimisation of separators design and fluids engineering.

1 Introduction

Industrial metalworking technology requires clean and efficient processing of cutting fluids that can be contaminated by various particles both metallic and non-metallic. Separation process of working industrial fluids, often complex mixture of water-, oil-based solutions, can be described using the principles of fluids dynamics and multi-physics modelling with non-linear multi-parametric algorithms.

Separation technology for complex industrial fluids, often consisting of water-, oil-based mixture with particles produced by a working process, such as metals-cutting, can be challenging due to the several factors. First, from its physical nature a range of solid and fluid materials in separation flows can influence fluid dynamics through change of particles size and concentration, which influence fluid viscosity and flow rate. Second, size and concentration of particles in fluids affect the efficiency of separation technology in terms of both number and size of particles removed from working fluid. Third, the processing parameters of working fluids such as temperature, flow velocity, viscosity, and others can influence non-linear behaviour of fluids and result in turbulences, vortex rings and other phenomena

M. Kireitseu (✉)
Aerospace Faculty, Department of Structural Integrity and Composites,
Delft University of Technology, Kluwer weg 1, 2628HS Delft, The Netherlands
e-mail: M.Kireitseu@tudelft.nl

© Springer International Publishing Switzerland 2016

A. Segalini (ed.), *Proceedings of the 5th International Conference on Jets, Wakes and Separated Flows (ICJWSF2015)*,
Springer Proceedings in Physics 185, DOI 10.1007/978-3-319-30602-5_62

reducing the operational performance of separation technology. As a result predictive modelling of separation non-linear dynamics in multi-phase fluids are commonly unknown due to multi-parametric and multi-physics aspects of this process.

Multi-phase flows and configurations of convective heat transfer in channels were consistently studied [1] by mathematical and numerical modelling of complex shear internal flows. Computational models [2, 3] were improved with the development of complex multi-parametric turbulent model of the second order for a component of full tensor of Reynolds stresses and specific scalar fluxes with original basic bases from the transport equations for scales of dissipative dynamic and thermal stress. However, these models have certain limitations. First, calculated time of these models is for simple one-parametrical models. Secondly, there is no satisfactory consent in the description of essentially anisotropic movement. In order to combine the theory and experiment the modelling was not updated with experiments.

On another side RSAM-turbulent models have been developed in order to reduce calculations of the differential equations in RANS-models. In some cases RANS-models are expressed as algebraic relationships for stresses through introduction of simplifying assumptions for convective and diffusive terms in the transport equations for Reynolds stresses. RSAM-models are used together with $k\varepsilon$—kL—or kω-equations in the form expanding two-parametrical model. Additional effects (curvature of streamlines, rotation, buoyancy etc.) can be added to governing equations through additional terms.

In the past two decades a progress in turbulence modelling was primarily focused on the possibility of complex flows analysis using RANS-models. However RANS-models do not describe effects of molecular viscosity that present significant limitations concerning modelling in terms of redistribution, diffusion, dissipation. High-Reynolds models, the study of low-Reynolds closing was not completed enough to account for the complex flows. And it is a subject of intensive research on turbulent modelling conducted by Launder, Hanjalic, Gibson, Najot [6–8]. These RANS-ε-models have provided a comprehensive modelling of flow parameters such as velocity fields, shear components of Reynolds stresses full tensor. However, these versions of RANS-models with base in the form of ε-equation cannot predict autocorrelations of pulsations of axial velocity component $\overline{u'^2}$ and a positive value of normal pressure at a wall.

The analysis of RANS-models in [6] B.E. Launder underlines, that preservation of terms to the third order in a fast part of a redistributing term appears sufficient for modelling of near-wall behaviour of turbulence. In addition research on diffusive modelling for $\overline{u_i' u_j'}$-equations has demonstrated the use of simpler form of gradient type for D_{ij}. Therefore this research and testing of these models will provide both accurate yet multi-physics approach accounting for the complexity of engineering physical and mathematical models of flow and heat transfer.

In this part developed turbulent fluids flow and heat transfer in cylindrical pipes and channels with constant and weak-changeable cross-section section is considered. It is supposed that a flow is one-component chemically inert media but consisting of multi-phase fluids such as water or oil-based solutions. Movement is

axisymmetrical and carried out in the absence of external forces, gravity and volumetric sources of heat. Temperature drops can be considerable so that it is necessary to account for variability of thermos-physics characteristics of a working fluid from temperature.

The system of the equations defining a flow and heat transfer includes the equation of continuity, movement (Reynolds full equations), energy and a condition and looks like, which is presented in tensor form:

$$\frac{\partial(\rho U_j)}{\partial x_j} = 0; \tag{1}$$

$$\frac{\partial(\rho U_i U_j)}{\partial x_j} = -\frac{\partial p_1}{\partial x_i} + \frac{\partial}{\partial x_j}\left(\mu \frac{\partial U_i}{\partial x_j} - \rho\overline{u_i' u_j'}\right) + \frac{\partial}{\partial x_j}\left[\mu\left(\frac{\partial U_j}{\partial x_i} - \frac{2}{3}\frac{\partial U_i}{\partial x_i}\delta_{ij}\right)\right]; \tag{2}$$

$$c_p \frac{\partial(\rho U_i T)}{\partial x_i} = \frac{\partial}{\partial x_i}\left(\lambda \frac{\partial T}{\partial x_i} - \rho c_p \overline{u_i' t'}\right); \tag{3}$$

$$p_0 = \rho R_0 T; \tag{4}$$

The used designations in these (1)–(4) are standard, all values are averaged ones (Reynolds averaging). For closing of the defining equations the model of turbulence with the equations of balance of the one-point correlation moments of the second order of pulsations of velocity field ($\overline{u_i' u_j'}$) and temperatures ($\overline{u_i' t'}$) is involved.

The (4)–(6) are integrated at the input (X = 0)—homogeneous profiles of averaged and fluctuated values, at the exit (X = XK)—so-called "soft" boundary conditions. At the wall (r = R)—absence of flow for hydrodynamic values and thermal stability for averaged temperatures (T = Tw or qw = const), the turbulent heat flux is neglected due to small value. At the axis (r = 0)—a condition of symmetry for all values, except shear stresses and a radial heat flux.

$$\frac{D}{Dt} = U\frac{\partial}{\partial x} + V\frac{\partial}{\partial r}; \quad a = \frac{\nu}{\mathrm{Pr}}; \quad P_{ij} = -\overline{u_i' u_\alpha'}\frac{\partial U_j}{\partial x_\alpha} - \frac{\partial U_i}{\partial x_\alpha}; \tag{4}$$

$$\begin{aligned} &f_\mu = (1 + 3.45/\sqrt{\mathrm{Re}_t})[1 - \exp(-y^+/85)]; \quad f_{\mu\theta} = f_\mu f(\mathrm{Pr}); \\ &f(\mathrm{Pr}) = 0.5 \cdot \left(1 + 0.871/\sqrt{\mathrm{Pr}}\right); \end{aligned} \tag{5}$$

$$f_2 = \left[1 - \exp\left(\frac{-y^+}{4.9}\right)\right]^2; \quad \mathrm{Re}_t = k\tau/\nu \; l_{\overline{u_i' t'}} = f(\mathrm{Pr})\tau\sqrt{k}; \tag{6}$$

$c_{k1} = 0.9$; $c_{d1} = 1.853$; $c_{d2} = 0.83$; $c_{d3} = 1.7$; $c_{d4} = 1.44$; $d_2 = 1.4$; $d_3 = 140$; $d_4 = 0.7$; $c_{\mu\theta} = 0.15$; $c_\mu = 0.09$; $c_{\mu 1} = 0.225$; $c_{\mu 2} = 0.066$; $c_{\varepsilon 1} = 1.44$; $c_{\varepsilon 2} = 1.7$.

2 Results

The modelling and experiments are validated for the cases of turbulent convective swirled and direct-flows. Computational modelling and experimental validation of mechanical design for separation equipment resulted in the following findings.

The multiphase flows in complex channels were described by Navier-Stokes and Reynolds full equations for the cases of complex wall configuration (sudden expansion, narrowing, condenser-diffuser sections) and accounted for heat transfer, turbulence, presence of mass inertial forces (i.e. swirling was carried out by a method of local swirling in the field of an input and method of a rotating wall of a pipe round the longitudinal axis). Modelling of stationary laminar and turbulent subsonic, chemically inert, not isothermal axisymmetric flows was carried out finite elements technique using the joined algorithms of SIMPLE and L.M. Simuni's approach with generalization for a case variable radius of a longitudinal gradient of pressure.

The modelling approach with the SIMPLE algorithm can be applied to strong swirled laminar and turbulent flows observed in the studies system with magnetic fields (Ro > 4, h/d = 0.5—flows in pipes with local swirling in the field of an input; Ro > 2, h/d = 0.5—a rotating wall) and with L.M. Simuni's generalised algorithm for other cases of isothermal and not isothermal, laminar and turbulent axisymmetric flows in cylindrical pipes with complex surface (condenser-diffuser sections, sections of expansion—narrowing). Calculations were well supported and correlated with experimental results. For swirled isothermal and not isothermal turbulent flows the modelling approach included the transport equations for a component of full tensor of Reynolds stresses, specific turbulent thermal fluxes and basic bases from two-parametrical kL, k_ dynamic and thermal models with the equations for dissipative times of scalar and dynamic fields, integrated scale of turbulence presented in Figs. 1, 2, and 3. In Fig. 1 calculation is solid line, symbols lines are experimental data [4, 5]: Ro = 0 (1, ■), 0.5—(2, ▲), 1—(3, ●).

Hydrodynamics and heat transfer modelling was completed for the case of a flow laminarisation. Results of modelling have good correlation of calculations of local

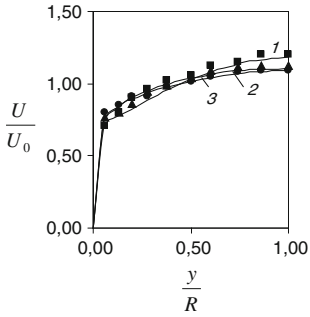


Fig. 1 Radial distribution of U/U_0 axial velocity in section $x/D = 4$ at various swirling parameter Ro

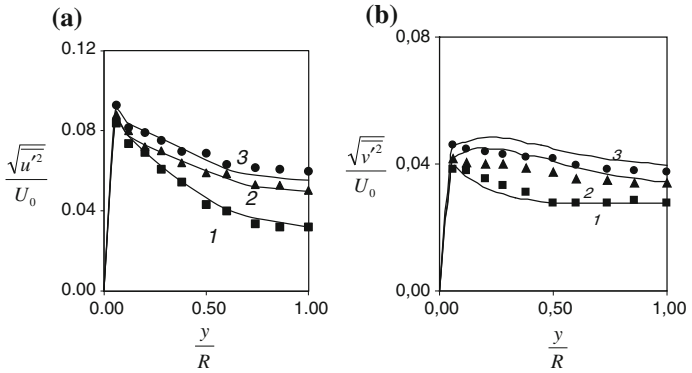


Fig. 2 Radial distributions of correlations of velocity pulsations $\overline{u_i' u_j'}$ in channel section x/D = 4 at various parameters Ro

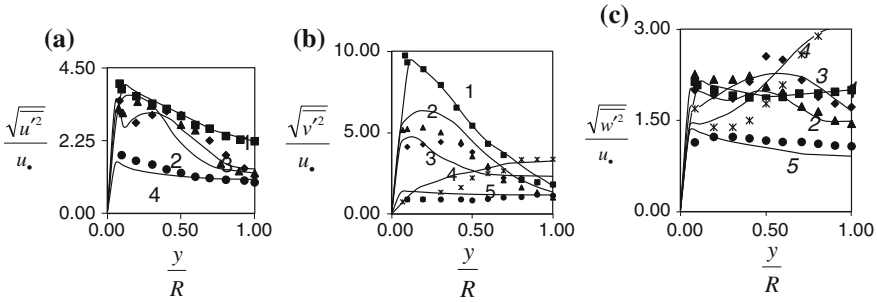


Fig. 3 Radial distributions of pulsated intensity of normal velocity components (axial—**a**, radial—**b**, tangential—**c**) at Ro = 3 in an entrance site. Line is calculation, symbols are experimental data [6]: ■—x/D = 0.35, ▲—5.1, ♦—10, *—50, ●—100

anisotropic turbulence on RANS-, RSAM-models. Modelling results could be used for the general theory of rotating turbulent flows and universal statistical models for turbulent momentum and heat transfer in internal systems, in Figs. 4, 5 and 6.

3 Discussion

This research presented the preliminary results of MAGFIS project that aims to provide the technology advancements and innovation in separation magnetic equipment design. This research contributed to the development of Navier-Stokes and Reynolds equations for the cases of complex wall configuration and includes the algorithms of SIMPLE and L.M. Simuni's approach with generalization for a variable gradient of pressure. The experiments with fluids and modeling approach

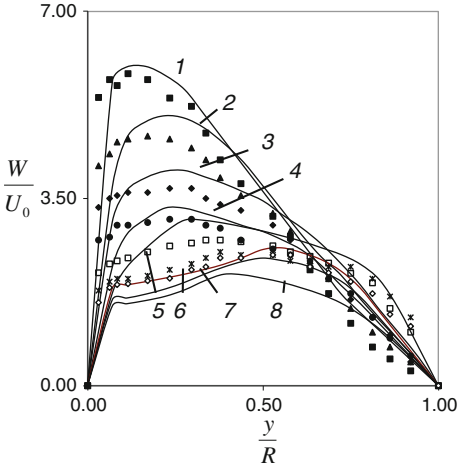


Fig. 4 Radial profiles of tangential velocity at K = 6. *Solid line* is calculation, symbols are experiments—x/D = 0 (■), 2–2 (▲), 3–4.5 (♦), 4–7.05 (●), 5–10.6 (○), 6–14.1 (*), 7–16

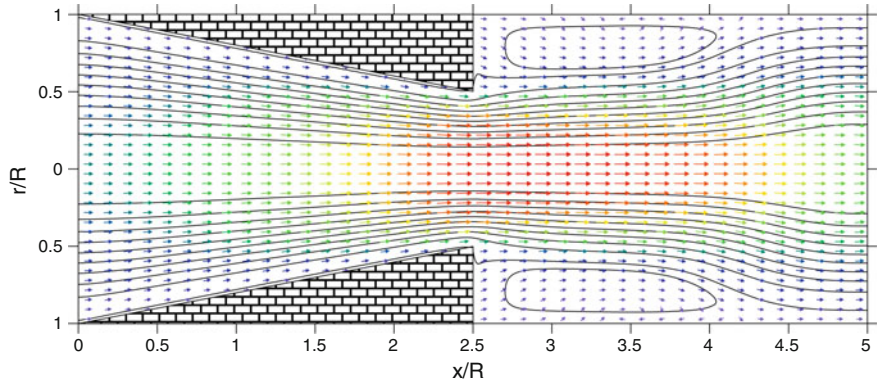


Fig. 5 Streamlines and a vector field in the channel flow with gradual narrowing to the channel middle (Re = 20, hR/R = 0.5, hx/L = 0.5)

was effective in optimising operational regimes and design approach to complex channels with magnetic fields, affecting transport of industrial fluids. A range of benefits also include (a) the ability to optimize performance and efficiency of equipment, (b) understanding of multi-phase flow allowing savings of processing materials and (c) the ability to reduce the environmental impact of fluids by materials recycling and removal.

The novelty of the works lies in the systematic approach to design, modelling and experimental validation of industrial magnetic separator with innovative design

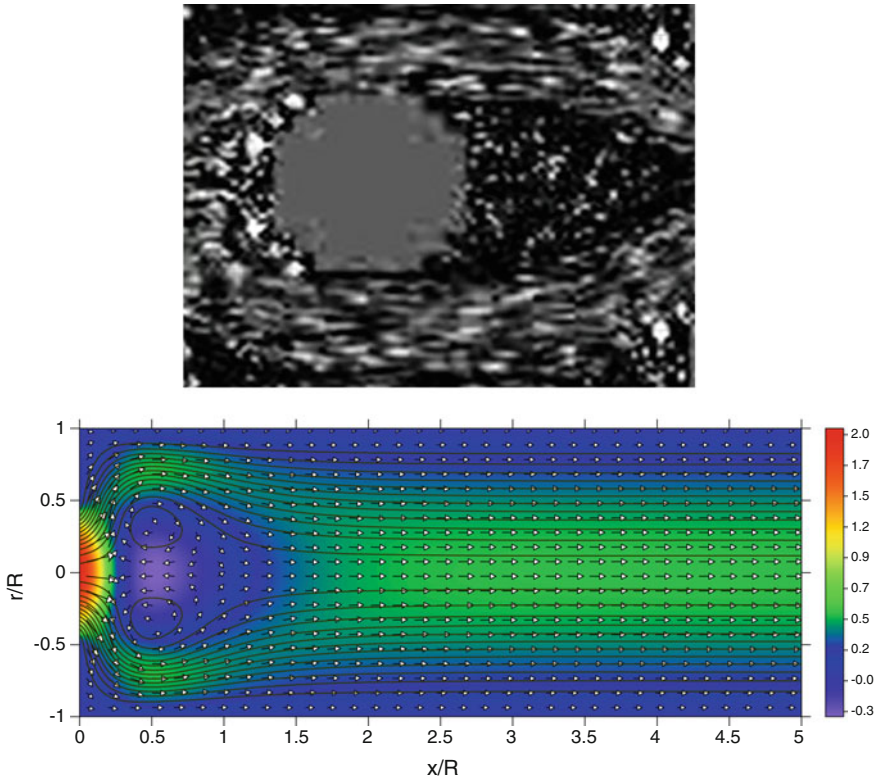


Fig. 6 Experimental streamlines and modelled vector fields of swirled flow at the input in conditions of suddenly extended chamber of separation channel (Re = 20, h/R = 0.5, Ro = 6)

and engineering concepts. Ideas presented here also enabled wider application of magnetic separators in the metals-working industry.

In conclusion it might worth mentioning the application and benefits of this research. Application of these modelling results include the following: (a) the ability to optimize performance and efficiency of separation technology, (b) the fundamental understanding of multi-phase flow of industrial fluids with particles affecting dynamic behaviour of process flows and stability of equipment and (c) the ability to improve both the economy of industrial process and environmental efficiency arising from recycling of extracted materials from contaminated fluids. The main scientific contributions of this research lies in the combination of the following: (I) the development of computational methods and tools to predict performance of the separation systems, (II) the development of some aspects for design of next generation separators with magnetic elements and (III) multi-physics modelling tools for experimental validation and practical assessment of separators performance. Modelling in its way can provide the foundation for design and development of separation technology and innovative equipment, which uses for

example magnetic columns and pipes in order to separate magnetic materials from industrial fluids, thereby assisting to achieve longer fluids life, environmental and economic benefits yet the quality of surface engineering.

Acknowledgments Project is partially supported by FP7-PEOPLE-2013-IIF—Marie Curie Action Reference: 913974 and Professor S.N. Kharlamov at the Laboratory of Hydrodynamics, Tomsk University.

References

1. M. Rai, P. Moin, AIAA J. **91**, 1607–1612 (1991)
2. W. Rodi, N.N. Mansour, V. Michelassi, J. Fluids Eng. **115**, 195–205 (1993)
3. U. Piomelli, P. Moin, H. Ferziger, Phys. Fluids **31**, 1884–1891 (1998)
4. M. Anwer et al., AIAA Pap. **88**, 3581–3588 (1988)
5. M. Anwer et al., Exp. Fluids. **8**, 33–40 (1989)
6. B.E. Launder, S.P. Li, Phys. Fluids **6**, 999–1006 (1994)
7. M.M. Gibson, B.E. Launder, J. Fluid Mech. **86**, 491–509 (1978)
8. K. Hanjalic, B.E. Launder, J. Fluid Mech. **74**, 593–610 (1976)

Tire Water Splash Modeling

Dragos Moroianu and Alper Cesur

Abstract This paper presents the numerically modeled multiphase flow of a splash phenomenon generated by a wheel traveling at relatively low speeds through shallow water depths. The flow of interest is complex and involves effects of free surface dynamics and formation of large-scale droplets. The framework used to model the process is Eulerian, Large Eddy Simulation (LES) and incompressible fluid flow. Topological changes of the interface between the gaseous and liquid phase are predicted by using Volume of Fluid (VOF) method. OpenFOAM, the open source based library-kit, has been used for the flow simulations. The main responsible mechanism for the splash is considered to be the hydraulic jump generated by the tire pressing onto the free surface of the water. In association to this hypothesis the performance of 2 models, linear and parabolic, for the velocity distribution has been conveyed and compared with experimental data of splash-related contamination on a fixed plate. It is found that the parabolic velocity distribution agrees closer to experimental data.

1 Introduction

The multiphysical phenomenon describing the collision of the free surface of a liquid with a solid object or liquid surface, referred to as *splash*, is both fascinating and of significant importance in a number of different industrial applications. Examples of areas with ongoing research may be the study of drop splashing during steel-making processes such as Electric Arc Furnace (EAF) and the Basic Oxygen Furnace (BOF) where a gas jet impinges on a liquid surface, with the aim of improving productivity by reducing splashing, [1, 2]; the investigation of the level of quality in coating processes by controlling the film thickness applied on a substrate by means of delaying the occurrence of splashing, [3, 4]; the utilization of water spray cooling of high-temperature surfaces, where the understanding of impingement physics and the identification of the threshold for splashing represents a key role within indus-

D. Moroianu · A. Cesur (✉)
Volvo Cars, Gothenburg, Sweden
e-mail: alper.cesur@volvocars.com

© Springer International Publishing Switzerland 2016

A. Segalini (ed.), *Proceedings of the 5th International Conference on Jets, Wakes and Separated Flows (ICJWSF2015)*,
Springer Proceedings in Physics 185, DOI 10.1007/978-3-319-30602-5_63

trial situations representative for thermal and steel processing, [5, 6]; the research area of inkjet-printing where detrimental secondary droplets caused by splashing is an unwanted effect that needs to be inhibited during the manufacturing process, [7]; and, the implementation of spray-drying during powder processing where splashing has a favorable impact in the dispersion of the liquid into gaseous phase, [8].

The occurrence of the phenomenon of splashing is further revealed within the automotive industry. High-efficiency devices, such as gearboxes, are strongly dependent on the control of lubrication-related splash losses otherwise considered as one of the driving mechanisms in the overall power loss in a transmission system, [9, 10]. Further, splash and spray, two correlated processes within multiphase flows, is considered as one of the most frequent safety complaints on the roads, [11]. In particular, truck splash can cause large visibility reduction for aft-driving vehicles. Therefore, an understanding of how to mitigate this safety hazard of splash and spray around heavy vehicles, a field associated to the interaction of fluid flow and rotating-object dynamics, makes it deserve a dedicated research in itself. Nevertheless, support for preventive techniques against contamination of vehicle surfaces has, for instance, been reported in [12], where particular splash and spray reduction devices together with a cost-effectiveness analysis is documented. Moreover, a detailed study of the aerodynamics and spray dispersion due to wheel rotation has been reported in [13, 14], yielding valuable technical information for splash/spray modeling purposes. Similarly, various mechanisms contributing to splash and spray generation was suggested in [15], where the level of nuisance to road users could be highlighted with the implemented model.

High complexity of the physics encountered in turbulent free-surface flows and the associated nonlinear interface regime poses conditions in the available computational resources. Refined turbulence models and accurate numerical methods with higher order discretization schemes becomes inevitable in order to allow for handling stability issues and the topological evolution of the moving interface between existing phases. For this purpose, a number of surface tracking methods have been developed for computing the interface movement and predicting its time dependent topological changes, [16, 17]. In general, these methods can be categorized as interface *tracking* and interface *capturing* methods with respect to the type of grids used. The interface tracking techniques identifies an interface; (1) by explicitly tracking the location of the interface by advection of Lagrangian markers, [18], or (2) by defining the interface as a boundary between two subdomains of a moving grid, [19]. Interface tracking approaches are known to provide great accuracy, however, they are limited to moderate interface motion. In addition, the technique requires the mesh to be updated as the flow evolves making these methods computationally expensive. Interface capturing methods, on the other hand, rely on implicit description of the interface given through a separate phase function discretized on a fixed grid. Among the most common representatives are the Level Set (LS) and the Volume of Fluid (VOF) method, relying on the principle of volume fraction and distance function, respectively. The LS methods, [20], offer highly accurate numerical technique for capturing complex topological changes of the moving interface in which the interface moving speed is sensitive to the front curvature and normal direction.

An important disadvantage of the method, however, is its need of accurate transport schemes in order to suppress volume leakage which results in numerical diffusion and hence causing a smoothing of the edges of the interface. In comparison to LS methods, [17], it is documented that the VOF technique is able to capture the mean effects of instabilities while providing mass conservation. Difficulties arise though when one is about to capture interfaces with strong deformation.

Referring to the previous discussions, high demands are put on the interface capturing method and the associated flow model used in order to predict splash-related dynamics. Time-averaged methods, for instance Reynolds Averaged Navier-Stokes (RANS), [21], will not be suitable due to the transient nature of the problem. Most turbulent flows consist of vortex filaments and sheets with characteristic scales on the order of the Taylor and Kolmogorov scales, l_T and l_K, respectively, typically being many orders of magnitude smaller than the integral scales, l_I. In Direct Numerical Simulation (DNS) all flow scales, down to l_K, are resolved which makes such simulations too expensive for engineering applications. Instead Large Eddy Simulation (LES), [22, 23], in which all the flow scales smaller than approximately l_T are modeled, thus having weaker resolution requirements, have emerged as a viable alternative for engineering predictions. Large Eddy Simulation (LES), when used in a proper way, will provide the details of the predicted flow necessary for the above-mentioned studies.

2 Mechanism

There are two numerical models advocated herein: a linear and a parabolic one. They are designed for the multiphase flow splash phenomenon generated by a wheel rolling at relatively low speeds through shallow water depths, as seen in Fig. 1. Both models are related to a physical phenomenon called *hydraulic jump*, [24].

The automotive industry considers the splash phenomenon rather important mainly due to the water contamination and injection in the engine bay cavity. A second reason for the current study is overloading of the wheel arch liner and underbody panels due to water splash generated forces. Most of the focus of water splash phe-

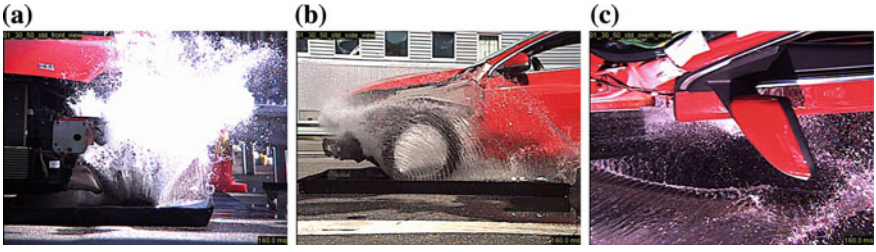


Fig. 1 Tire water splash—experiments. **a** Front view, **b** side view, **c** top view

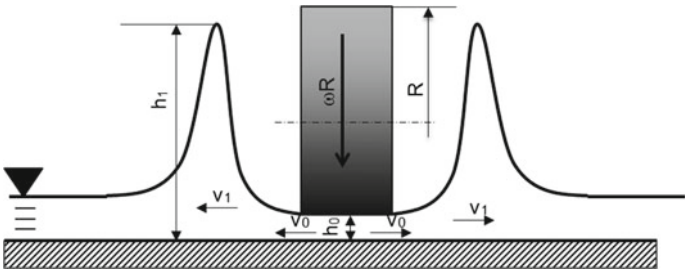
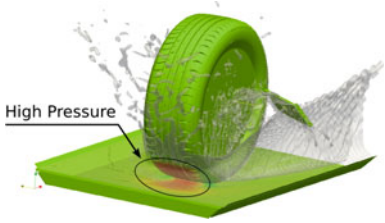


Fig. 2 Hydraulic jump

Fig. 3 Pressure distribution



nomenon has been directed toward hydroplaning, [25, 26], a phenomenon appearing in similar conditions though at relatively high speeds. The main responsible mechanism for the splash is considered to be the hydraulic jump generated by the tire pressing onto the free surface of the water, as suggested in Fig. 2. A wheel rolling in shallow waters of height h_0 with velocity v_0 will generate a high pressure region in front of it, which in turn will drive the fluid upstream and aside of the wheel, as can be seen in Fig. 3. A one dimensional approximation of the hydraulic jump phenomenon, known as Belanger's equation, [24], has the following expression (1):

$$\frac{h_1}{h_0} = \frac{\sqrt{1 + 8Fr^2} - 1}{2}, \tag{1}$$

where $Fr^2 = \frac{v_0^2}{gh_0}$ is the Froude number.

However, the velocity distribution v_0, is far from constant in real cases, and it has to be either resolved or modeled. This paper will present 2 models for the velocity distribution v_0, and their associated experimental validation.

3 Numerical Method

The problem is regarded as an incompressible three-dimensional multiphase flow, in which one phase is gaseous (air) and the second phase is liquid (water). Both phases are integrated in an Eulerian framework. The Volume of Fluid (VOF) model is used

in this particular approach. It is a surface tracking technique applied to distinguish between the two immiscible fluids by tracking the volume fraction of each of the fluids in each cell of the computational domain. Further, the model considers the flow as one mixture and solves one set of equilibrium equations which is shared by the two phases. In tensorial format the mass, momentum and energy conservation laws have the following expression (2):

$$\begin{cases} \frac{\partial \rho}{\partial t} + \frac{\partial \rho u_i}{\partial x_i} = 0, \\ \frac{\partial (\rho u_i)}{\partial t} + \frac{\partial (\rho u_i u_j)}{\partial x_j} = -\frac{\partial p}{\partial x_i} + \frac{\partial \sigma_{ij}}{\partial x_j}, \\ \frac{\partial (\rho e)}{\partial t} + \frac{\partial (\rho u_j h)}{\partial x_j} = \frac{\partial (\sigma_{ij} u_i)}{\partial x_j} + \frac{\partial}{\partial x_j}\left(\lambda \frac{\partial T}{\partial xJ}\right), \\ \sigma_{ij} = \mu \left[\left(\frac{\partial u_i}{\partial x_j} + \frac{\partial u_j}{\partial x_i}\right) - \frac{2}{3}\delta_{ij} \cdot \frac{\partial u_k}{\partial x_k}\right], \\ h = \frac{k \cdot R \cdot T}{k-1} + \frac{u_i \cdot u_i}{2}, \\ p = \rho \cdot R \cdot T. \end{cases} \tag{2}$$

For the current application the Mach number is small enough ($M < 0.3$), which makes the compressibility effects to be negligible, therefore constant density is assumed for both phases (liquid and gaseous). This assumption will simplify (2), by decoupling the energy equation from the system, which consequently becomes (3):

$$\begin{cases} \frac{\partial u_i}{\partial x_i} = 0, \\ \frac{\partial u_i}{\partial t} + u_j \cdot \frac{\partial u_i}{\partial x_j} = -\frac{1}{\rho}\frac{\partial p}{\partial x_i} + \nu \cdot \frac{\partial^2 u_i}{\partial x_j x_j}. \end{cases} \tag{3}$$

As mentioned before, the system presented in (3), was used to simulate a mixture of the two immiscible phases (water and air). Considering the interface between them, a transport equation for the fluid volume fraction, $\frac{\partial \alpha}{\partial t} + \nabla \cdot (\alpha \cdot \vec{V}) = 0$, has been used for tracking purposes. Here, α is the volume fraction associated to the liquid phase.

4 Results

4.1 Computational Set-Up

The computations were performed for the case of a cross-flow past a tire in a rectangular channel with quadratic cross section at a Reynolds number, $Re = V_{\infty}^{air} D/\nu$, of 363724, where $V_{\infty}^{air} = 8.333$ m/s is the air free-stream velocity, $\nu_{air} = 1.48e\text{-}05$ m^2/s^2 the air kinematic viscosity and $D = 0.646$ m the tire diameter. The dimensions of the computational fluid domain are $7.95D$, $5.96D$ and $3.48D$, in the x-, y- and z-direction, respectively, see Fig. 4a.

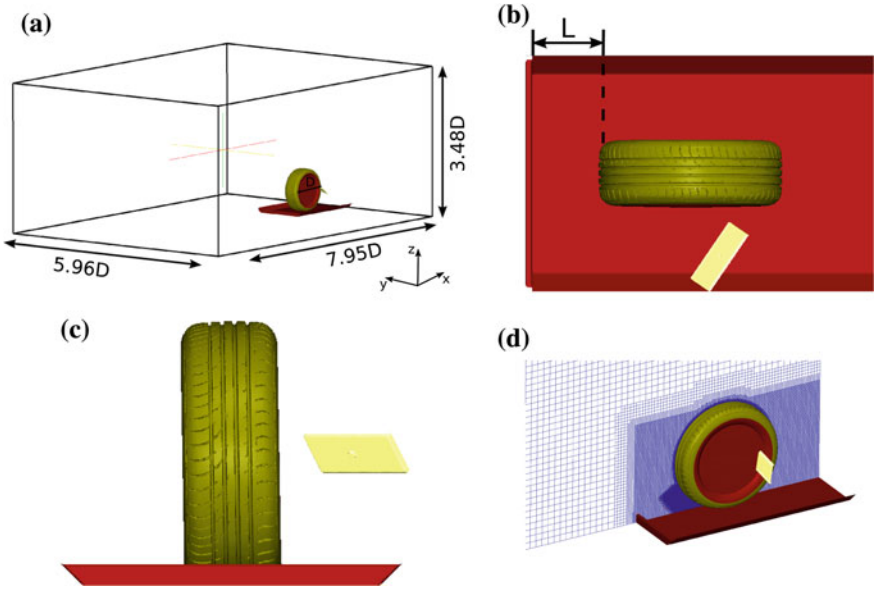


Fig. 4 Computational domain and geometry of the tire tread; pressure-plate; splash-channel. **a** Computational domain, **b** top view of tire-assembly, **c** front view of tire-assembly, **d** mesh topology for 25 M cells

The splash phenomenon is initiated by releasing water flow from a rectangular shaped channel with dimensions $1.084D$, $1.966D$ and $0.077D$, where the water release velocity and its kinematic viscosity is $V_{\infty}^{water} = V_{\infty}^{air}$, $\nu_{water} = 1e\text{-}06$ m^2/s^2, respectively. The channel is horizontally centered about the tire in order to assure for symmetrical flow conditions on both sides of the tire. Its leading edge is placed at $L = 0.364D$ in front of the tire edge in the x-direction, see Fig. 4b. Further, a pressure-plate (marked with yellow color) is positioned to the left of the tire for measurement of fluid forces, see Fig. 4b, c. It is positioned at a distance of [| $0.147D$ |, | $0.437D$ |, | $0.008D$ |] from the center of the tire to the center of the pressure-plate.

A slice of the fluid domain in the z plane is shown in Fig. 4d for a simulation on a grid with 25 M cells. The mesh is hexahedra dominated with refinements applied to the tire tread surface (marked with brown color) together with a cylindrical zone, which starts slightly in front of the tire tread and extends to just aft of the pressure-plate.

At the inlet of the domain, a Dirichlet condition is applied for the velocity and a Neumann type condition for the pressure. At the outlet, Neumann condition is used for the velocity and a Dirichlet condition for the pressure. The top and sides are modeled using slip type. Moreover, the vehicle dynamics is taken into account by applying Dirichlet conditions for the velocity at the ground and the tire tread. Boundary conditions for the splash-channel is applied with the same type as for the domain inlet for both the velocity and pressure, whereas a mixed Dirichlet-Neumann

Table 1 Case summary

Mesh size [M cells]	$\bar{F}_N$ [1]	y^+ [1]
6	0.346	974
8	0.644	588
25	0.948	153

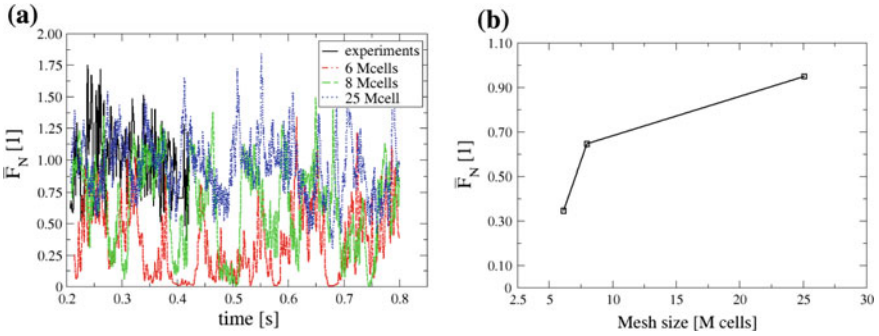


Fig. 5 Computational domain and geometry of the tire tread; pressure-plate; splash-channel. **a** Computational domain, **b** top view of tire-assembly

type is used for the phase fraction at the inlet surface of the splash-channel. The corresponding initial conditions are specified to 1 at the inlet surface and 0 in the rest of the domain. Surface tension has been ignored throughout the computations.

4.2 Convergence Analysis

In this section the convergence analysis summarized in Table 1 will be discussed. The computations contain the impact of splash-related fluid forces on the pressure-plate shown in Fig. 4. As post-processing, the results have been normalized with experimental data (denoted with suffix N). Three different meshes of size 6, 8 and 25 M cells have been considered for this purpose.

The objective with the mesh study was to entitle the need of effective refinement zones in order to resolve proper fluid flow behavior. Figure 5a shows the transient behavior of the Euclidean norm of total pressure forces, $F_N = \|(f_x, f_y, f_z)\|$ on the pressure-plate for the three mesh resolutions. The associated averaged quantities, $\bar{F}_N$, resulted in 0.346, 0.644 and 0.948 units for 6 M, 8 M and 25 M cells, respectively, see Fig. 5b. The observations from Fig. 5 and Table 1 indicate that the coarsest mesh, 6 M cells, deviates from the rest and experimental data in both integrated force at the pressure-plate and y^+ values at the tire tread. The finest mesh, 25 M cells, on the other hand demonstrates a converging behavior in the correct order of magnitude. This gives confidence for resolving enough scales and therefore generating optimal conditions in the modeling approach of the velocity profile.

Table 2 Velocity profile modeling

Method	$\bar{F}_N$ [1]	$\sigma(F_N)$ [1]
Default LES	0.735	0.117
Linear profile	0.948	0.243
Parabolic profile	0.952	0.236

4.3 Modeling the Velocity Profile

The nature of LES makes modeling unavoidable in order to replicate actual flow behavior. The convergence analysis presented above was therefore conducted for a case where an explicit enforcement of the flow velocity profile was applied to the first cell layer of the tire, shown in Fig. 4. The type of enforcement was *linear* and obeys the following relation with respect to tire properties:

$$\mathbf{V}(y) = \frac{C_y}{y_{max} - y_{med}} \left(y - y_{med}\right), \tag{4}$$

where y is the parameter of variation, C_y is a model constant and, y_{med} and y_{max} are the center and outer coordinates of the tire width, respectively. In addition, a second order parabolic profile was applied in order to remedy for the discontinuous behavior of the linear profile at $y = 0$:

$$\mathbf{V}(y) = \frac{C_y}{y_{max}^2 - y_{med}^2} \left(y^2 - y_{med}^2\right). \tag{5}$$

Table 2 compares the default LES (no model) simulations and the applied models with experiments. The intrinsic discrepancy of 0.265 units between default LES simulations and experiments clearly exhibits the need of modeling. In the first instance, one can discuss the marginally larger magnitude in predicted $\bar{F}_N$ of the parabolic velocity profile compared to the linear model. Nevertheless, its associated standard deviation, $\sigma(F_N)$, indicates a higher degree of reliability in its expected value. Based on these characteristics, the parabolic velocity profile is deemed to be the better representative of the flow evolution in time and space during splashing.

5 Conclusions

A two-phase flow model dedicated to the simulation of splashing within the automotive industry, based on LES-equations coupled with the Volume of Fluid method for unsteady free surface flows, has been presented. The hydraulic jump is considered to be the main responsible mechanism for the occurrence of large-scale splashing. A

linear and a parabolic velocity profile has been conveyed to model the under-resolved flow features near the tire-ground region and it was shown that the parabolic profile agrees better with experiments.

In future work, next step would be to investigate in detail the splashing rate based on the formation and detachment of developed flow structures as surface tension, tire surface pattern and surrounding aerodynamics are altered.

References

1. M. Alam, G. Irons, G. Brooks, A. Fontana, J. Naser, Inclined jetting and splashing in electric arc furnace steelmaking, in *ISIJ International*, vol. 51 (2011) pp. 1439–1447
2. J. Solórzano-López, R. Zenit, M.A. Ramírez-Argáez, Mathematical and physical simulation of the interaction between a gas jet and a liquid free surface. Appl. Math. Model. **35**, 4991–5005 (2011)
3. K. Myrillas, A. Gosset, P. Rambaud, M. Anderhuber, J.-M. Mataigne, J.-M. Buchlin, Technique for delaying splashing in jet wiping process. Chem. Eng. Process. **50**, 466–470 (2011)
4. K. Myrillas, A. Gosset, P. Rambaud, M. Anderhuber, J.-M. Mataigne, J.-M. Buchlin, Cfd simulation of gas-jet wiping process. Eur. Phys. J. Spec. Top. **166**, 93–97 (2009)
5. A. Labergue, M. Gradeck, F. Lemoine, Comparative study of the cooling of a hot temperature surface using sprays and liquid jets. Int. J. Heat Mass Transf. **81**, 889–900 (2014)
6. P.J. Kreitzer, J.M. Kuhlman, Monte-carlo spray cooling model, in *AIP Conference Proceedings*, vol. 1208 (2010) pp. 84–98
7. A. Mähönen, M. Kuusisto, U. Lindqvist, R. Nyrhilä, The splashing of ink drops in cij printing, in *Proceedings of IS & T* 13*th International Conference on Digital Printing Techniques* (1997) pp. 600–603
8. N. Persson, *Spray drying in cyclone separators* (Chalmers University of Technology, 2014)
9. C. Gorla, F. Concli, K. Stahl, B.-R. Höhn, M. Klaus, H. Schultheiß, J.-P. Stemplinger, Cfd simulations of splash losses of a gearbox. Adv. Tribol. (2012)
10. C. Gorla, F. Concli, K. Stahl, B.-R. Höhn, K. Michaelis, H. Schultheiß, J.-P. Stemplinger, Hydraulic losses of a gearbox. Tribol. Int. **66**, 337–344 (2013)
11. M.P. Manser, R. Koppa, P. Mousley, Evaluation of splash and spray suppression devices on large trucks during wet weather. *Technical Report, AAA Foundation for Traffic Safety* (2003). http://www.aafoundation.org/
12. G.B. Pilkington, Splash and spray: surface characteristics of roadways. Int. Res. Technol. ASTM STP **528–541**, 1990 (1031)
13. J.S. Paschkewitz, Simulation of spray dispersion in a simplified heavy vehicle wake *Technical Report, Energy and Environment Directorate, LLNL Heavy Vehicle Aerodynamics Project* (2006)
14. J.S. Paschkewitz, A computational study of tandem dual wheel aerodynamics and the effect of fenders and fairings on spray dispersion. *Technical Report, Energy and Environment Directorate, LLNL Heavy Vehicle Aerodynamics Project* (2006)
15. H. Viner, A. Dunford, F. Coyle, K. Nesnas, Development of a prediction model for splash and spray, in *7th Symposium on Pavement Surface Characteristics: SURF 2012* (2012) pp. 1–16
16. S. Popinet, S. Zaleski, A front tracking algorithm for the accurate representation of surface tension. Int. J. Numer. Methods Fluids **30**, 775–793 (1999)
17. P. Trontin, S. Vincent, J.L. Estivalezes, J.P. Caltagirone, Detailed comparisons of front-capturing methods for turbulent two-phase flow simulations. Int. J. Numer. Methods Fluids **56**, 1543–1549 (2008)
18. S. Unverdi, G. Tryggvason, A front-tracking method for viscous, incompressible, multi-fluid flows. J. Comput. Phys. **100**, 25–37 (1992)

19. B. Maury, O. Pironneau, Characteristics ALE method for the unsteady 3D navier-stokes equations with a free surface. Int. J. Comput. Fluid Dyn. **6**, 175–188 (1996)
20. F. Pochet, K. Hillewaert, P. Geuzaine, J.-F. Remacle, E. Marchandise, A 3D strongly coupled implicit discontinuous Galerkin level set-based method for modeling two-phase flows. Comput. Fluids **87**, 144–155 (2013)
21. D. Wilcox, *Turbulence Modeling for CFD* (DWC Industries, La Cãnada, California, 2006)
22. P. Sagaut, *Large eddy simulation for incompressible flows: An introduction*, 3rd edn. (Springer, Berlin, 2006)
23. C. Fureby, Towards the use of large eddy simulation in engineering. Prog. Aerosp. Sci. (2008)
24. H. Chanson, Development of the belanger equation and backwater equation by J.-B. Belanger (1828). J. Hydraul. Eng. ASCE, 159–163 (2009)
25. S. Vincent, A. Sarthou, J.-P. Caltagirone, F. Sonilhac, P. Février, C. Mignot, G. Pianet, Augmented lagrangian and penalty methods for the simulation of two-phase flows interacting with moving solids. application to hydroplaning flows interacting with real tire tread patterns. J. Comput. Phys. **230**, 956–983 (2011)
26. J.R. Cho, H.W. Lee, J.S. Sohn, G.J. Kim, J.S. Woo, Numerical investigation of hydroplaning characteristics of three-dimensional patterned tire. Eur. J. Mech. A Solids **25**, 914–926 (2006)

Algorithm for Automatic Quantification of Flashback and Flash Forward Events from High-Speed Chemiluminescence Recordings

Robert-Zoltán Szász, Arman Ahmed Subash, Andreas Lantz, Robert Collin, Laszlo Fuchs and Ephraim J. Gutmark

Abstract Three methods are employed to identify and quantify flashback and flash forward events based on chemiluminescence recordings of swirling flames. The approaches differ in the procedure to determine the instantaneous flame position. The results revealed that the most robust method is to determine a threshold relative to the instantaneous maximum intensity. Analysis of the complete dataset indicated that flashback events are significantly slower than flash forward events.

1 Introduction

The current trend in gas turbine development is to improve fuel flexibility. The use of a wider variety of fuels, however, has impact on the reliability of the gas turbine. The increased span of fuel properties may lead to the appearance of flame instability issues. Such issues are flashback and blow-out, intensively studied in the literature (see e.g. [1–5]). In order to avoid the occurrence of flashback and blow-out, beside determining the safe working intervals for different fuels, one has to understand the dynamics of such events.

High speed recording of the chemiluminescence signal during flashback or blow-out is a relatively easy method to collect data which can help understanding the flame dynamics. Due to the large number of parameters one commonly needs to consider, such measurement campaigns often result in a large number of recordings leading to a need for automatic processing of the collected datasets. Such automatization is

R.-Z. Szász (✉)
Department of Energy Sciences, Lund University, PO.Box 118, 22100 Lund, Sweden
e-mail: robert-zoltan.szasz@energy.lth.se

A.A. Subash · A. Lantz · R. Collin
Department of Physics, Lund University, Lund, Sweden

L. Fuchs
Department of Mechanics, Royal Institute of Technology, Stockholm, Sweden

E.J. Gutmark
Department of Aerospace Engineering, University of Cincinnati, Cincinnati, USA

© Springer International Publishing Switzerland 2016

A. Segalini (ed.), *Proceedings of the 5th International Conference on Jets, Wakes and Separated Flows (ICJWSF2015)*,
Springer Proceedings in Physics 185, DOI 10.1007/978-3-319-30602-5_64

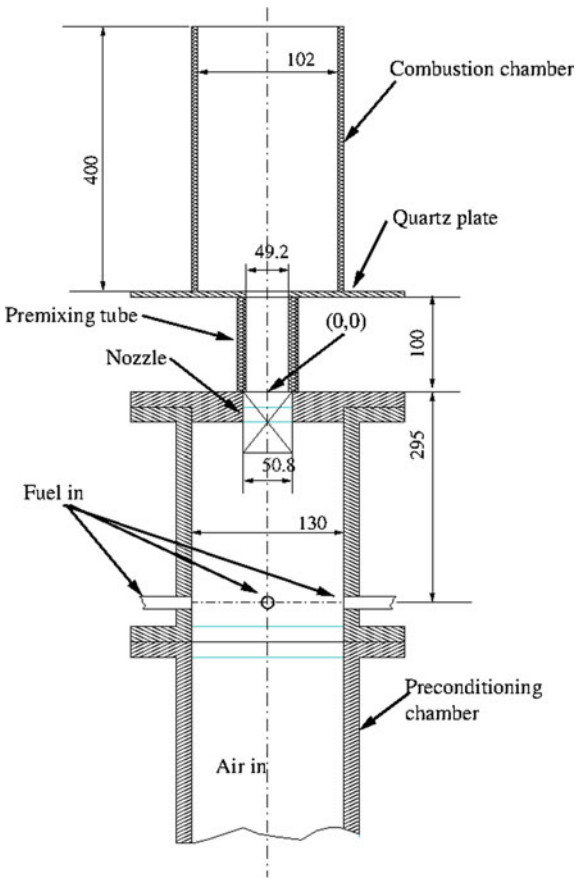


Fig. 1 Experimental rig

preferred also in order to obtain consistent postprocessing across datasets and avoid the often subjective human decisions. Here we propose such a method to postprocess high-speed chemiluminescence recordings.

2 Experimental Procedure

Figure 1 shows the experimental rig. Methane is premixed with air in a preconditioning chamber. The mixture passes through three co-annular swirlers into a quartz premixing tube having a length of two tube diameters. Above the premixing tube a quartz plate and a quartz combustion chamber are mounted. In the present paper, flash-forward denotes the propagation of the flame from the premixing tube into the combustion chamber.

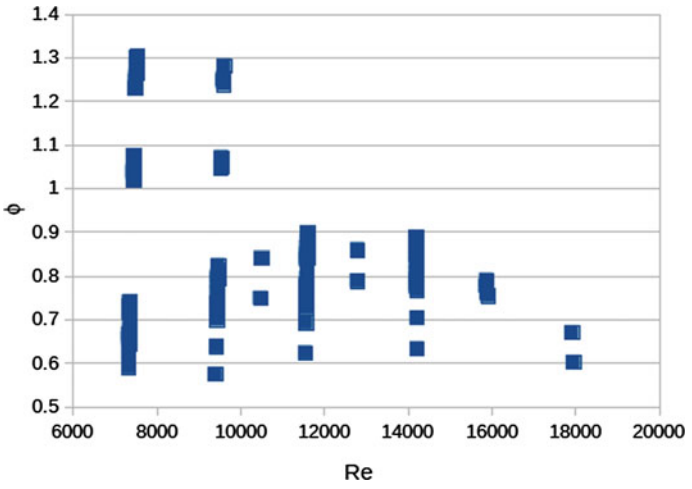


Fig. 2 Reynolds number and equivalence ratio ranges studied in the experiments

For combustion applications one of the important parameters controlling the flame is the fuel-air ratio, *FAR*, defined as the ratio of the fuel and air mass flow rates (see (1)).

$$FAR = \frac{\dot{m}_F}{\dot{m}_A} \tag{1}$$

The equivalence ratio, ϕ, is the actual fuel-air ratio normalized with the fuel-air ratio in stoichiometric conditions (2). Thus, equivalence ratio values smaller then unity indicate lean conditions (i.e. there is more oxidizer available than needed by the fuel), whereas values larger than one correspond to rich conditions, when fuel is in excess.

$$\phi = \frac{FAR}{FAR_{st}} \tag{2}$$

During the measurements the Reynolds number was fixed to prescribed values and the equivalence ratio interval was scanned, by altering the fuel flow rate, from very lean to very rich conditions to trigger flashback or flash forward events. Figure 2 shows a scatter plot of the Reynolds number and equivalence ratio ranges covered in the experiments.

A high speed video camera (Phantom V7.1, Vision Research) was used to record the chemiluminescence signal from the flame. The camera features an 800 × 600 pixel SR-CMOS monochromatic sensor and has a repetition rate of 4.8 kHz at full resolution. The camera was equipped with a gated image-intensifier (Hamamatsu) in order to enhance its sensitivity and a UV sensitive camera lens (UV-Nikkor, f/2.5, f = 105 mm). To capture the flashback and flash forward events a recording rate of 1 kHz was used, pre-triggering 1000 samples, the total number of samples being 1200. Both the premixing tube and part of the combustion chamber have been recorded to be able to follow the flame front during flashback or flash forward.

3 Post Processing Method

The method was tested on the database consisting of 260 videos obtained by varying several flow parameters. The algorithm consists of three stages, schematically visualized on the block diagram in Fig. 3. In the block diagram ellipses mark input/output data and rectangles denote processing stages of the algorithm.

First, the intensity of the chemiluminescence frames is integrated along radial lines resulting in an intensity vector for each time instance. Let $I(x, y, t)$ denote the intensity of an image recorded at time instance t and horizontal and vertical positions x and y, respectively. Furthermore, N_x and N_y are the number of pixels in horizontal and vertical directions, whereas N_t is the number of recorded frames. The integrated intensity vector is then computed using (3).

$$II(y, t) = \sum_{x=1}^{N_x} I(x, y, t) \tag{3}$$

Figure 4 shows the time evolution of these intensity vectors for a flash forward event (top) and a flashback event (bottom). The dark horizontal line in the middle of the image is due to the quartz plate separating the premixing tube from the combustion chamber.

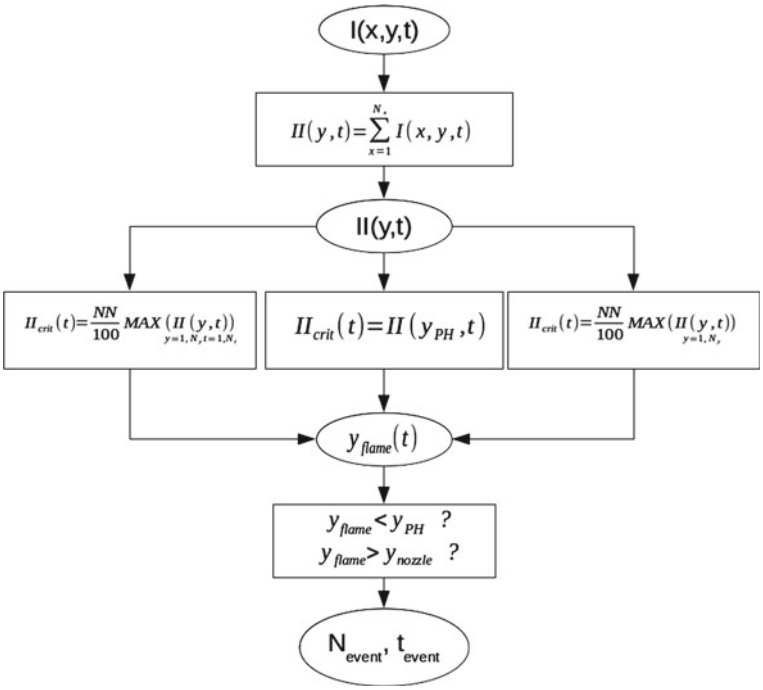


Fig. 3 Block diagram of the post-processing method

In the second stage the flame position is determined. For each time instance, beginning at the lowest position (close to the nozzle) and moving towards the combustion chamber, the integrated intensity values are compared to a critical value. It is assumed that the flame is located where this critical value is first exceeded, $II(y,t) > II_{crit}$. Since the intensity at the flame position depends on the equivalence ratio, the idea of using a fixed threshold for the whole database was discarded. Three types of thresholds were tested:

1. The first method is based on the idea to set the critical pixel intensity as a certain percentage of the maximum pixel intensity during an entire recording, $II_{crit} = NN/100 \cdot MAX(II(y,t))_{\forall y,\forall t}$. These cases are denoted as TI*NN* in the followings, *NN* being the critical threshold (in %). A larger value of *NN* results thus in a larger value of the critical intensity and the predicted flame position is expected to be located at higher vertical positions, closer to the lighter areas of the intensity-integrated images.
2. Since the quartz plate separating the premixing tube from the combustion chamber generates a shadow in the images, regions with larger intensities than in this region can be regarded as flame locations. When the flame flashes back (or forward), the areas in the vicinity of the plate shadow must have a sudden change in intensity. Thus, in the second approach, the critical intensity value is set to the values located in the shadowed areas, $II_{crit}(t) = II(y_{PH}, t)$, y_{PH} being the vertical position of the quartz plate in the image. This method is denoted next as PH.
3. It was observed, that the intensity of the flame was varying in time even for constant air and fuel flow rate settings, thus different frames of a certain recorded sequence had different maximum intensity values. The third method to detect flame position is setting the threshold relative to the maximum intensity at a certain time instance, $II_{crit}(t) = NN/100 \cdot MAX(II(y,t))_{\forall y}$. These methods are denoted as L*NN*, where *NN* again denotes the percentage of the maximum intensity.

Eight tests have been carried out, three based on method 1, one based on method 2 and four based on method 3, these cases being summarized in Table 1. As one can conclude from the table, the optimal thresholds are 15 % total intensity and 30 % instantaneous snapshot intensity, leading to only 2 (in case TI15) and 1 (case L30) missed event out of the total of 260 flashback and flash-forward events. Both the lower and larger tested limits result in worse performance.

Figure 5 shows the time evolution of the flame tip position for the same cases as the ones shown in Fig. 4. For clarity, only the best performing test from each approach is shown. One can observe that the flame position in the TI15 and L30 cases are almost identical, especially in the flashback case, whereas the PH method detection is poor, the flashback event is detected for example as being much shorter and being followed by an unsuccessful flash forward event.

As a last step, based on the time evolution of the flame position relative to the quartz plate (incomplete and complete) flashback and flash forward events are identified and their parameters are quantified. Incomplete events are the ones that begin before a certain recording started or finish after the recording was stopped. By iden-

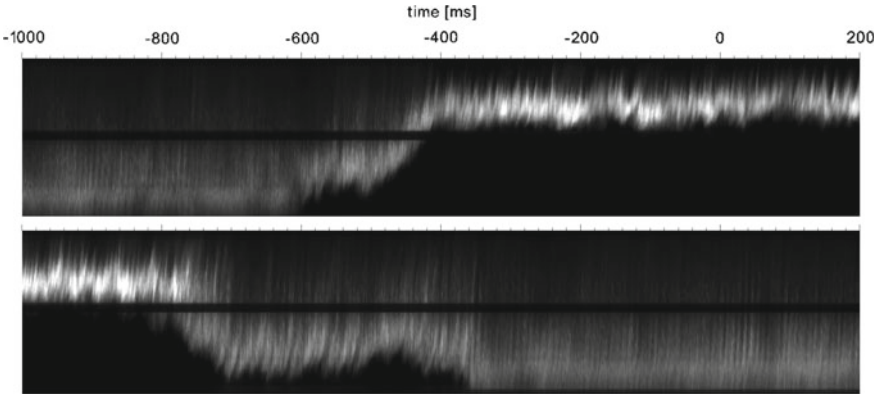


Fig. 4 Time evolution of the chemiluminescence intensity signal integrated along radial *lines*. Case with flash-forward (*top*) and flashback (*bottom*)

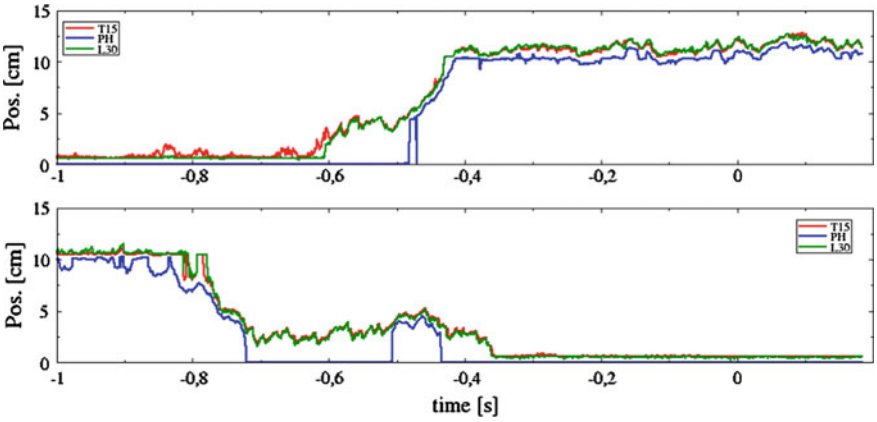


Fig. 5 Time evolution of the detected flame tip position. Case with flash-forward (*top*) and flashback (*bottom*)

tifying the time instances when the flame tip enters/leaves the premixing tube and when it attaches/detaches from the nozzle one can compute the duration of the phenomena and their average speed.

To check the accuracy of the detected durations, eight cases have been chosen out of the 260 recordings. The chosen cases were recorded for four flashback (denoted with FB1...FB4) and four flash forward events (denoted FF1...FF4). The duration of the events for the eight cases has been determined by visual analysis of the recordings and the predictions from the suggested methods have been compared to these values. Figure 6 shows the error (relative to the visually determined values) in the predicted event durations using the suggested approaches. Columns 3 and 4 of Table 1 shows the average and rms of the errors. Although the number of samples is small (eight)

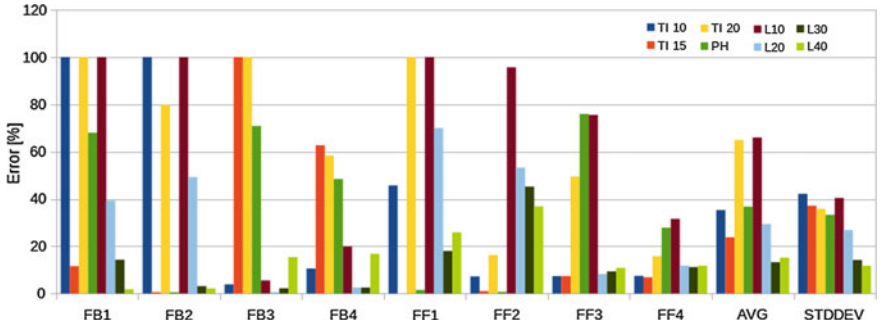


Fig. 6 The error in the event duration for four flashback (FB*X*) and flash forward (FF*X*) events. Average and RMS of the errors for the selected eight cases

Table 1 Summary of the methods

Method	Nr. missed	Avg. err. [%]	RMS err. [%]	Avg. flash-forward duration [s]	Avg. flashback duration [s]
TI10	12	35	42	0.145	0.291
TI15	2	24	37	0.201	0.291
TI20	14	65	36	0.124	0.381
PH	22	37	33	0.085	0.193
L10	19	66	40	0.107	0.225
L20	3	29	27	0.113	0.246
L30	1	13	14	0.114	0.247
L40	3	15	12	0.130	0.241

the results still provide information regarding the prediction quality of the suggested methods. One can observe that the L30 method results in the lowest error. Although L40 had one more missed event compared to TI15, it has smaller error in the prediction of the events' duration. It is also important to notice, that the methods based on the maximum intensity in an individual snapshot have generally lower fluctuations in the errors, thus they are expected to be more robust.

The average duration of all flashback events and all flash forward events were computed with the proposed approaches and are reported in the last two columns of Table 1. Since the 260 events accounted in the averaging cover a wide range of flow parameters (Reynolds number, equivalence ratio, combustor geometry, etc.) the averaged duration should not be interpreted physically. Nevertheless, important conclusions can be drawn from the results. As it regards the detection methods, one can conclude that the method based on the maximum intensity in a snapshot is the most robust. Changing the threshold from 10 to 40 % results in relatively small change in the predicted average duration of the events. The method based on the maximum intensity for a complete recording is much more sensitive, for 5 % change in the threshold the predicted average durations can change more than 25 %.

Another important conclusion is that flash-forward events are significantly faster than flashback events. Looking at Fig. 5 one can see that the slope of the flame position evolution in time is similar for flashback and flash forward when the flame is in the upper part of the premixing tube. Thus, one reason for the longer flashback duration might be stagnation of the flame front in the lower half of the premixing tube before a complete flashback occurs. However, experiments repeated for the same flow conditions revealed that the time evolution of the flame tip position can differ even for the same set-up, thus no conclusions should be drawn from individual events and more thorough analysis of the recorded data is necessary.

4 Conclusions

Methods have been suggested to automatically detect and quantify flashback and flash forward events from high-speed chemiluminescence videos of swirling flames. All suggested methods are divided in three stages. First, the intensity along radial lines has been integrated for each frame. Second, the flame tip position is determined by checking where this radially integrated intensity exceeds critical threshold. In the final stage the occurrence and duration of flashback or flash forward events is determined by identifying the time instances when the flame enters or leaves the premixing tube and attaches or detaches from the nozzle. The suggested methods differ in the second stage, three different ways of setting a critical threshold has been evaluated. The results show that the most robust method is to set the critical limit as a percentage of the maximum intensity of an individual frame. The statistics over the whole recorded dataset revealed that generally flashback events are significantly slower than flash forward events.

Acknowledgments The authors would like to acknowledge the support provided through the Center for Combustion Science and Technology, CECOST.

References

1. Y. Sommerer, D. Galley, T. Poinsot, S. Ducruix, F. Lacas, D. Veynante, J. Turbul. **5**(037) (2004)
2. J. Fritz, M. Kröner, T. Satt elmayer, J. Eng. Gas Turbines Power **126**(2), 276 (2004). doi:10.1115/1.1473155, http://link.aip.org/link/JETPEZ/v126/i2/p276/s1&Agg=doi
3. S.M. Hosseini, R.Z. Szasz, P. Iudiciani, L. Fuchs, A. Lantz, R. Collin, M. Aldén, E. Gutmark, in *46th AIAA/ASME/SAE/ASEE Joint Propulsion Conference & Exhibit* (2010), pp. 1–12
4. R. Lückerath, O. Lammel, M. Stöhr, I. Boxx, U. Stopper, W. Meier, B. Janus, B. Wegner, in *Proceedings Of The ASME Turbo Expo* (2011), GT2011–45790
5. C. Mayer, J. Sangl, T. Sattelmayer, T. Lachaux, S. Bernero, in *Proceedings Of The ASME Turbo Expo* (2011), GT2011–45125

Effect of Grouping of Fuel Droplets on a Flame Formed by an Oscillating Spray Jet

David Katoshevski and J.B. Greenberg

Abstract The sensitivity to the vaporization Damkohler number of the behavior of a co-flow laminar spray diffusion flame in an oscillating flow field is investigated. Droplet grouping induced by the host gas flow oscillations is accounted for. The effect of droplet grouping is described through a specially constructed model for the vaporization Damkohler number that responds to the proximity of the droplets as they cluster due to the spray-flow oscillations. A formal analytical solution is developed for Schwab-Zeldovitch parameters through which the dynamics of the spray flame front shapes and thermal fields are deduced. Computed results based on the solutions demonstrate how strongly the vaporization Damkohler number including droplet grouping effects impacts on the type of primary homogeneous flame formed and on the possible existence of multiple flame sheets as a result of dynamic changes from under- to over-ventilated flames as the flow field oscillates.

1 Introduction

In some previous publications [1–5] different aspects of the impact of the phenomenon of droplet clustering or grouping on laminar spray diffusion flame dynamics were investigated. Earlier research on this topic is well documented there and will be omitted here for brevity. Suffice to say that it had been had discovered that grouping of droplets in a spray can occur under a variety of conditions. However, apart from three dimensional direct numerical simulations [6] which found that droplet segregation occurs in isotropic homogeneous turbulence in combusting situations, all other research had dealt with the non-combusting case. In [6] it was found that what is called droplet segregation leads to local clusters of

D. Katoshevski (✉)
Department of Environmental Engineering, Ben-Gurion University of the Negev, Beer-sheva, Israel
e-mail: davidk@bgu.ac.il

J.B. Greenberg
Faculty of Aerospace Engineering, Technion-I.I.T, Haifa, Israel

© Springer International Publishing Switzerland 2016

A. Segalini (ed.), *Proceedings of the 5th International Conference on Jets, Wakes and Separated Flows (ICJWSF2015)*,
Springer Proceedings in Physics 185, DOI 10.1007/978-3-319-30602-5_65

droplets surrounded by high levels of fuel vapor thereby reducing the evaporation rate and exerting a strong influence on whether premixed or partially premixed combustion takes place.

In the current work we consider the way in which droplet grouping in a realistic oscillating polydisperse spray jet influences the laminar diffusion flame it fuels. The work is of relevance for understanding the importance of droplet grouping in determining the quality of combustion in diesel and jet engines in which the liquid spray is polydisperse.

2 Governing Equations—General Formulation

The Burke-Schumann spray flame configuration (see Fig. 1) is considered, in which fuel vapor and droplets flow in an inner duct (of half width L) and air flows in outer ducts (each of width R). Under appropriate operating conditions, after diffusive mixing of the streams, a laminar, spray diffusion flame is established. The velocities of the streams in the inner and outer ducts are taken to be identical but, unlike in Burke-Schumann's original gas flame analysis, they are *not* constant and, under the assumption of infinite Peclet number, are specified by

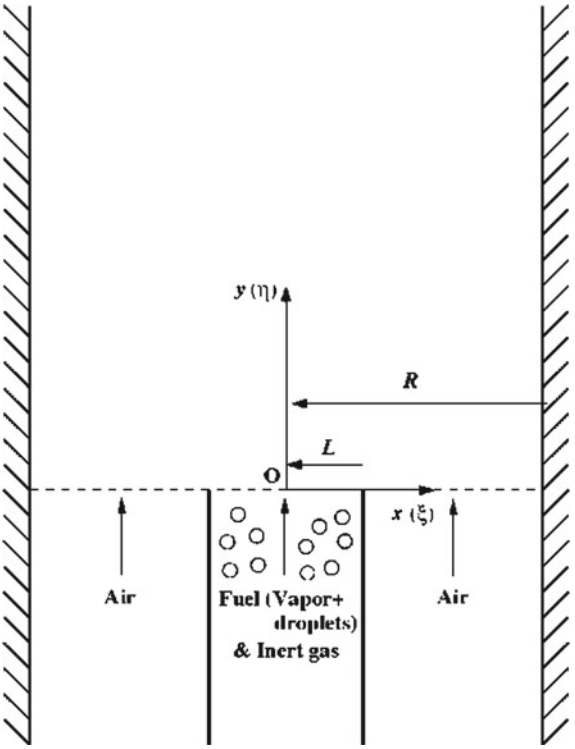


Fig. 1 Configuration for formation of Burke-Schumann spray diffusion-flame

$$\vec{v}(\xi,\eta,t) = (0, (V_a - V_b sin(\kappa\eta - \Omega t))) \tag{1}$$

$\vec{v}(x,y,t)$ is the velocity vector normalized by a characteristic velocity, $v_{ch.}$, V_a is the mean flow velocity, V_b is the amplitude of oscillation in the axial direction, $\kappa = kv_{ch.}R^2/D_g$ is the normalized wave number (with k being the actual wave number and D_g the diffusion coefficient, taken to be identical for the fuel vapor and the oxygen), $\Omega = \omega R^2/D_g$ is the normalized angular velocity (with ω the actual angular velocity) and the normalized coordinates are $(\xi,\eta) = \left(x/R, yD_g/v_{ch.}R^2\right)$ with time, t, normalized using R^2/D_g. Without sacrificing generality, V_a and V_b are taken to be positive. The description of the spray is based on the sectional approach [7]. A polydisperse fuel spray is considered thereby linking the model to what actually happens in practice. In addition, the Lewis number is supposed to be unity. The governing equations then assume the following compact non-dimensional form. For the spray:

$$\frac{\partial u_j}{\partial t} + v_j\frac{\partial u_j}{\partial \eta} = -\frac{1}{\tilde{\tau}_j}u_j + \Psi_j\frac{\gamma_{j+1}}{\gamma_j}\left(u_{j+1} - u_j\right), \quad j = 1,2\ldots N_S \tag{2}$$

$$\frac{\partial v_j}{\partial t} + v_j\frac{\partial v_j}{\partial \eta} = \frac{1}{\tilde{\tau}}\left(v - v_j\right) + \Psi_j\frac{\gamma_{j+1}}{\gamma_j}\left(v_{j+1} - v_j\right), \quad j = 1,2\ldots N_S \tag{3}$$

$$\frac{\partial \gamma_j}{\partial t} + v_j\frac{\partial \gamma_j}{\partial \eta} = -\Delta_j\gamma_j + \Psi_j\gamma_{j+1} - \left(\frac{\partial v_j}{\partial \eta}\right)\gamma_j, \quad j = 1,2\ldots N_S \tag{4}$$

The droplet size distribution is subdivided into N_S size sections. The first $2N_S$ equations contained in (2) and (3) are the sectional conservation of momentum equations for the droplets in the spray with u_j, v_j being the transverse and axial average jth-sectional droplet velocity components, respectively, $\tilde{\tau}_j = \tau_j D_g/R^2$ are the normalized sectional Stokes numbers (with τ_j the sectional Stokes number). The right hand sides of these equations are the drag terms relating to the movement of the droplets in their gaseous surroundings, the momentum transfer terms as droplets leave a given section and move to the next section down as they evaporate and the momentum transfer as droplets collide with one another and coalesce. Droplet collisions of this nature are expected to occur in those regions in which droplet clustering is to be found. The last N_S components of (4) are for γ_j which is the jth-sectional mass fraction of liquid fuel in the spray normalized by the total mass fraction of fuel (i.e. vapor + liquid), $m_{totfuel}$, at the outlet of the inner duct. The right hand sides of these equations contain the vaporization terms describing (a) the rate of removal of liquid fuel from a given section to the next section down as droplets become ineligible for membership in the section due to evaporation and reduction in size, (b) the rate at which liquid fuel joins the given section from the neighboring higher section as droplets in that section evaporate, and (c) the rate at which droplets enter section j due to droplet coalescence. In this context

$(\Delta_j, \Psi_j) = (\tilde{C}_j, \tilde{B}_j)R^2/D_g$ are the sectional vaporization Damkohler numbers with $\tilde{C}_j$ and $\tilde{B}_j$ the sectional vaporization coefficients relating to the rate of departure/arrival of droplets from/to section j as a result of evaporation. Note that $\tilde{B}_{N_S} = 0$. The second term on the right hand side of the sectional conservation of liquid fuel equations is an extra source-like term which essentially describes a liquid phase compressibility type of effect (see [8] where this effect is discussed at length for non-evaporating particles).

Coupled to these equations are the conservation equations for the Schwab-Zeldovitch parameters γ, γ_T which are derived from the conservation equations for fuel vapor, oxygen and energy

$$\frac{\partial \gamma}{\partial t} + v\frac{\partial \gamma}{\partial \eta} = \frac{\partial^2 \gamma}{\partial \xi^2} + S_d \tag{5}$$

$$\frac{\partial \gamma_T}{\partial t} + v\frac{\partial \gamma_T}{\partial \eta} = \frac{\partial^2 \gamma_T}{\partial \xi^2} + (1-\beta)S_d \tag{6}$$

where

$$(\gamma, \gamma_T) = (\gamma_F - \gamma_O/\nu,\ \gamma_F + T) \tag{7}$$

and

$$S_d = \sum_{j=1}^{N_S} \left(\Delta_j \gamma_j - \Psi_j \gamma_{j+1}\right) \tag{8}$$

is the total rate of production of fuel vapor through evaporation of all droplets in the spray. In these equations the subscripts F, O refer to fuel vapor and oxygen, respectively, and ν is the stoichiometric coefficient associated with the single step global chemical reaction that is assumed to describe the chemistry of the diffusion flame, $F + \nu O \rightarrow$ *Products*. It is further assumed that the chemical Damkohler number Da is infinitely large so that the flame is limited to a thin surface into which fuel vapor and oxidant flow from opposite sides of the front.

In order to arrive at these equations we have taken typical data of relevance in order to cast the equations in the right setting for which Katoshevski et al. [9] showed that droplet grouping occurs. In this way solution of the equations under the appropriate conditions should shed light on the way droplet grouping effects the combustion characteristics. We use the following orders of magnitude for the data: $D_g \approx 10^{-6} - 10^{-7}\mathrm{m}^2/\mathrm{s}$, $R \approx 10^{-2}\mathrm{m}$, $v_{ch.} \approx 10^{-2}\mathrm{m/s}$. This leads to $Pe \approx 10^2 - 10^3$ from which we deduce that the large Peclet number limit can be adopted. Katoshevski et al. [9] also demonstrated that for a stable or persistent grouping phenomenon to occur the following condition must apply:

$$\left|\frac{V_a - V_w}{V_b}\right| < 1 \quad \left(V_w = \frac{\omega}{k}\right) \tag{9}$$

The data they quote from non-combusting experiments with axisymmetric jets indicate that $V_w \approx 0.8V_a$. Thus, if V_a and V_b are both of the order of $v_{ch.}$ it is not hard to show that with $\omega \approx 10$ a value of $k \approx 10^3$ is implied.

The boundary conditions for the governing equations are:

$$0 \le \xi \le c,\ \eta \ge 0,\ t > 0:\ \left(u_j, v_j\right) = \left(u_{j0}, v_{j0}\right),\ \gamma_j = \delta_j \tag{10a}$$

$$\gamma = 1 - \sum_{j=1}^{N_S} \frac{v_{jo}}{v}\delta_j,\ \gamma_T = 1 - \sum_{j=1}^{N_S} \frac{v_{jo}}{v}\delta_j + T_0 \tag{10b}$$

$$c \le \xi \le 1,\ \eta \ge 0,\ t > 0:\ \ \gamma = -V,\ \gamma_T = T_0 \tag{10c}$$

$$\xi = 0, 1,\ \eta \ge 0,\ t > 0:\ \frac{\partial \gamma}{\partial \xi} = \frac{\partial \gamma_T}{\partial \xi} = 0 \tag{10d}$$

with $c = L/R$, the non-dimensional inner ducts half width, and δ_j the initial fraction of liquid fuel in section j in the total fuel supply. Conditions (10a) specify the liquid phase's sectional entrance velocity components and normalized mass fractions, (10b) the inlet fuel vapor mass fraction and temperature, (10c) the inlet oxygen mass fraction (V) and temperature, and (10d) symmetry and impermeability of the outer wall of the chamber, respectively.

3 Solution of Governing Equations

Because of the sparse evidence in the literature droplet grouping was incorporated, in previous work [1–5], via appropriate modification of the vaporization Damkohler numbers using increasing/decreasing of this parameter according to the relative proximity of liquid phase droplet characteristic lines. For simplicity at the current stage explicit droplet coalescence will be omitted but will be taken to express itself in a general way via the vaporization Damkohler numbers.

The details of the solution of the governing equations of the spray appear in [5] and will not be repeated here. The solution for the Schwab-Zeldovitch parameters can be shown to be

$$\left(\gamma(\xi,\eta,t), \gamma_T(\xi,\eta,t)\right) = \left(\gamma_0(\eta,t), \gamma_{T,0}(\eta,t)\right) + 2\sum_{n=1}^{\infty}\left(\gamma_n(\eta,t), \gamma_{T,n}(\eta,t)\right) cos\, n\pi\xi \tag{11}$$

where

$$\begin{aligned}\left(\gamma_n(\eta,t),\gamma_{T,n}(\eta,t)\right) &= \left(\gamma_n(0,t_0),\gamma_{T,n}(0,t_0)\right)exp\Big(-(n\pi)^2(t-t_0)\Big)\\ &+exp\Big(-(n\pi)^2(t-t_0)\Big)\int_{t_0}^{t}(1,1-\beta)exp\Big((n\pi)^2(t-t_0)\Big)S_{d,n}dt\end{aligned} \tag{12}$$

$$\left(\gamma_n(0,t_0),\gamma_{T,n}(0,t_0)\right) = \left(\left[1+V\right]-\sum_{j=1}^{N_S}\delta_j\frac{v_j(0,t_0)}{v(0,t_0)},\left[1-\sum_{j=1}^{N_S}\delta_j\frac{v_j(0,t_0)}{v(0,t_0)}\right]\right)\frac{sin\,n\pi c}{n\pi},\quad n\neq 0 \tag{13a}$$

$$\left(\gamma_0(0,t_0),\gamma_{T,0}(0,t_0)\right) = \left(c\left(1-\sum_{j=1}^{N_S}\delta_j\frac{v_j(0,t_0)}{v(0,t_0)}\right)-V(1-c),c\left(1-\sum_{j=1}^{N_S}\delta_j\frac{v_j(0,t_0)}{v(0,t_0)}\right)+T_0\right),\quad n=0 \tag{13b}$$

and

$$S_{d,n}=\int_0^c S_d\,cos(n\pi\xi)d\xi \tag{14}$$

The location of the flame front is given at any instant of time, $\tilde{t}$ say, by those points (ξ,η) satisfying $\gamma(\xi,\eta,\tilde{t})=0$.

4 Results and Discussion

In Fig. 2 a series of stills of flame shape development are shown; the black lines are for the case when droplet grouping is modeled and gray lines for the case when grouping is not accounted for. Consider first the evaluation of the flame when grouping is not accounted for. From time $t = 2$ throughout the entire time range considered an under-ventilated flame is seen to be growing with a branch extending towards the outer wall of the chamber. Eventually (see $t = 3.75$), the flame develops an inverted "S" shape and will split into a lower under-ventilated flame front (as seen at $t = 2$) and an upper front that straddles the entire width of the channel and is convected downstream.

In contrast, when droplet grouping is accounted for, three initial flame fronts are observed: a small over-ventilated flame front at the chamber's entrance, a second flame "bubble" further downstream at the axis and a complete flame front even further downstream which is the remnant of earlier flame pinching. Later in time the

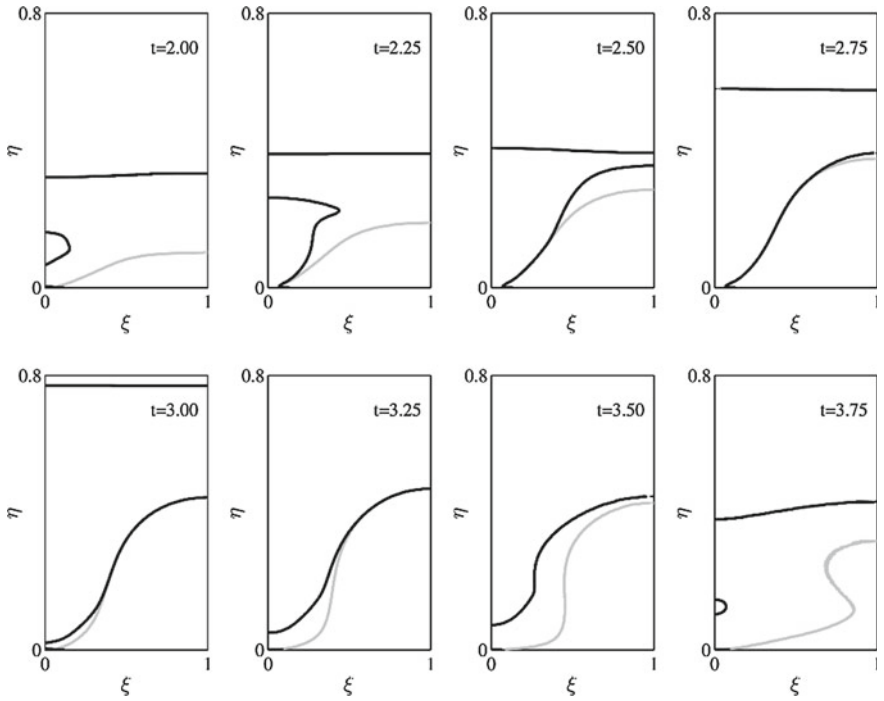


Fig. 2 Stages in the evolution of a spray diffusion flame; Notation: *black lines* are flame fronts when droplet grouping is modeled, *gray lines* are flame fronts when droplet grouping is not accounted for

two lower flames merge into a shape that leans towards the outer wall, whilst the upper flame is convected downstream. The merged flame grows and becomes under-ventilated eventually becoming identical to the flame obtained when grouping was not accounted for ($t = 2.75$). Subsequently, it begins to collapse and is pinched off leading to almost the same multiple-flame situation seen at the first time instant shown.

In Fig. 3 two time instances in the evolution of a spray flame's thermal field are drawn when grouping is modelled (red is "hot" blue is "cold", black are the flame fronts). This shows how the temperature field distorts as the lower flame becomes under-ventilated and a second upper flame front is pinched off. Both the upper flames will eventually move downstream and be replaced by further pinched-off flames as the entire process repeats itself.

Finally, we point out the role of the enhancement effect (see [4, 8]) in these polydisperse flames. We consider an initial monosectional distribution with all droplets in the 40–50 μm range. The enhancement effect is quite evident, as can be observed in Fig. 4 which shows the total liquid fuel mass fraction as a function of the axial coordinate at time $t = 2.5$. The solid line is what is obtained when no grouping is taken into account whereas the broken line shows the profile when

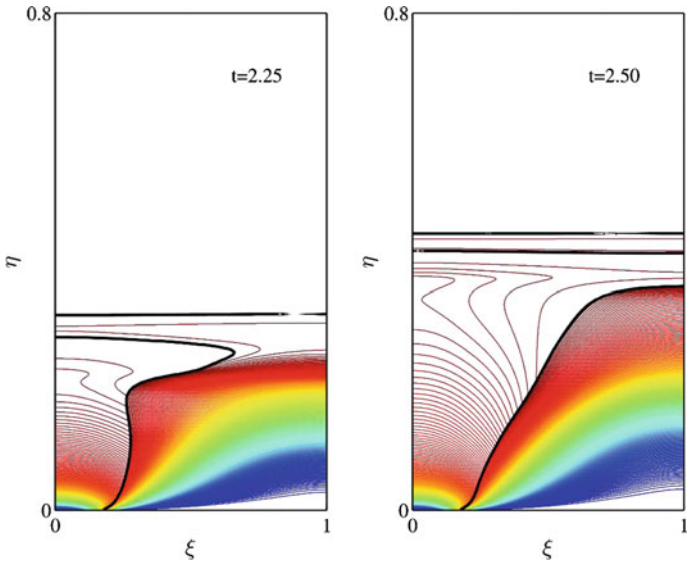


Fig. 3 Evolution of thermal field in spray diffusion flames—with droplet grouping included, and the formation of multi-flame situation presented at t = 2.75 (non-dimensional time)

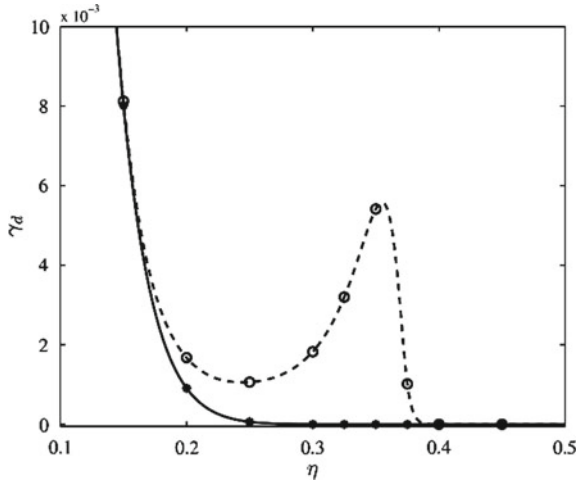


Fig. 4 Enhancement effect in polydisperse spray diffusion flame in an oscillating flow field; γ_d is the total liquid fuel (normalized) mass fraction; the *solid line* is when grouping is not accounted for, the *broken line* when it is accounted for

grouping is accounted for. The enhancement in the latter case involves a factor of about five. Similar factors were obtained for other different initial size distributions. Such enhancement has a profound impact of the distribution of fuel vapor to fuel the main homogeneous diffusion flame as has been discussed in the context of monosectional sprays [4].

References

1. J.B. Greenberg, D. Katoshevski, The influence of droplet grouping on a Burke-Schumann spray diffusion flame in an oscillating flow field. Proc. Combust. Inst. **33**, 2055–2062 (2011)
2. J.B. Greenberg, D. Katoshevski, Spray flame dynamics with oscillating flow and droplet grouping. Combust. Theory Model. **16**(2), 321–340 (2012)
3. J.B. Greenberg, D. Katoshevski, Parametric study of droplet grouping in spray diffusion flames, in *AIAA Paper 2012-0343, 50th AIAA Aerospace Sciences Meeting*, Nashville, Tn., Jan 2012
4. J.B. Greenberg, D. Katoshevski, Vaporization Damkohler number and enrichment effects in spray diffusion flames in an oscillating flow field. Combust. Sci. Technol. **185**, 898–919 (2013)
5. J.B. Greenberg, D. Katoshevski, Aspects of Droplet Grouping in Polydisperse Spray Diffusion Flames, in *AIAA Paper 2015-0421, AIAA SCITECH 2015 Meeting*, Florida, USA, Jan 2015
6. J. Reveillon, F.–X. Demoulin, Evaporating droplets in turbulent reacting flow, in *Proceedings of the Combustion Institute,* vol. 31 (2007) pp. 2319–2326
7. J.B. Greenberg, I. Silverman, Y. Tambour, On the origins of spray sectional conservation equations. Combust. Flame **93**, 90–96 (1993)
8. J.F. de la Mora, D.E. Rosner, Inertial deposition of particles revisited and extended: eulerian approach to a traditionally Lagrangian problem. PhysicoChem. Hydrodyn. **2**(1), 1–21 (1981)
9. D. Katoshevski, Z. Dodin, G. Ziskind, Aerosol clustering in oscillating flows: mathematical analysis. At. Sprays **15**, 401–412 (2005)

Influence of Coaxial Dielectric Barrier Discharge Plasma Actuator on Jet Flame

Jun Asakura and Motoaki Kimura

Abstract A dielectric barrier discharge plasma actuator was used to control a jet flame produced using a gas mixture of 16−55 % propane volume concentration in air from a round convergent nozzle with a diameter of 6 mm. The electrode structure consisted of a dielectric body and a pair of coaxial copper electrodes. The applied voltage was 5−8 kV at a frequency of 6 and 8 kHz. The stability limit and flame shape were investigated with and without plasma generation using a high-speed camera. The results indicated that a longer flame could be maintained in the presence of plasma, and that the stability of the flame increased with applied voltage. This is thought to be due to the generation of an induced flow and active species by the plasma.

1 Introduction

Diffusion combustion, which occurs in a combustor, is enhanced by the mixing of fuel and air. There has been considerable interest in the stabilization of diffusion flames, because of the desire to suppress the formation of NOx [1]. In addition, small scale distributed generation systems such as gas micro turbines are expected to play a major role in establishing energy reliability and resolving environmental issues. However, when such small combustors are subjected to large load fluctuations, mixing between the fuel and discharged air is likely to deteriorate due to the low Reynolds number. There has been a great deal of effort to improve the degree of mixing in such situations. In one approach, miniature flap actuators were used to confine a coaxial jet [2]. More recently, a dielectric barrier discharge plasma actuator [3] has been applied to a wing surface to control flow separation at a high angle of attack [4]. In the present study, the effectiveness of a dielectric barrier discharge plasma actuator (DBDPA) in controlling a jet flame is investigated for different propane/air mixtures.

J. Asakura · M. Kimura (✉)
Nihon University, Tokyo, Japan
e-mail: kimura@mech.cst.niohn-u.ac.jp

© Springer International Publishing Switzerland 2016

A. Segalini (ed.), *Proceedings of the 5th International Conference on Jets, Wakes and Separated Flows (ICJWSF2015)*,
Springer Proceedings in Physics 185, DOI 10.1007/978-3-319-30602-5_66

2 Experimental Apparatus and Method

Figure 1 shows the electrode assembly used in the actuator. The DBD electrode structure consists of a dielectric body and two coaxial electrodes. The dielectric material is a heat-resistant machinable ceramic (MACOR) and the electrodes are made of copper. The inner diameter of both the electrode assembly and the nozzle outlet is $d = 6$ mm. Figure 2 shows a photograph and a cross-sectional schematic of the nozzle and coaxial DBDPA used in the jet flame experiments. The jet was produced using a gas mixture of 16−55 % propane volume concentration in air. The air was supplied by a compressor and the propane by a gas cylinder. The flow rates for both gases were maintained constant using a digital mass flow controller. The gases were premixed in the chamber, and then ejected from the nozzle. After ignition, an applied voltage of 5−8 kV at 6 and 8 kHz was applied to the DBDPA from the high voltage amplifire (PSI-PG1040F) in order to generate a plasma induced

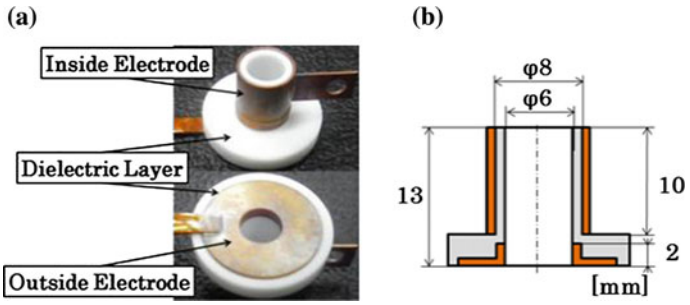


Fig. 1 Structure and dimensions of electrode assembly

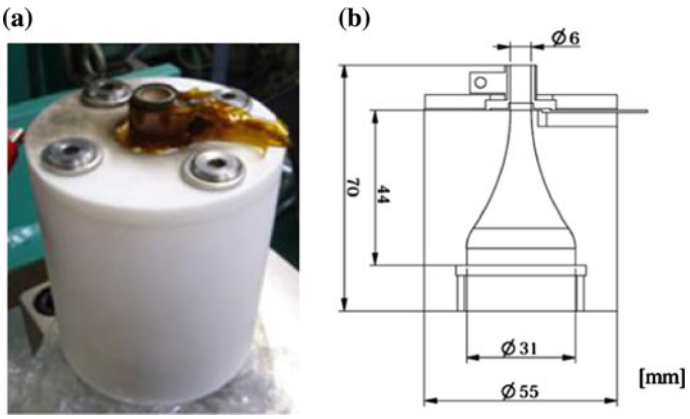


Fig. 2 Photograph and dimensions of nozzle and plasma actuator

flow. The stability limit and flame shape were investigated with and without plasma generation using a high speed camera. In addition, an analysis of the air flow pattern after the nozzle was performed using particle image velocimetry (PIV : DIPP-FLOW Ver.2.00e).

3 Experimental Results and Discussion

Figure 3 shows a set of images of a pure propane diffusion flame for different voltages applied to the DBDPA. For reference, the case for zero applied voltage is also shown in order to compare the flame characteristics in the absence of plasma. The vertical scale is x/d, which is the ratio of the distance from the nozzle outlet to the nozzle diameter. In all cases, the gas flow rate is $Q = 2.0$ L/min, and the propane content is $\Phi = 100$ %. It can be seen that for an applied voltage of 6 kV and above, the presence of plasma significantly affects the flame brightness and shape, giving it a wrinkled appearance.

Figure 4 shows the effect of the applied voltage on a mixed propane/air flame for $Q = 1.2$ L/min and $\Phi = 16.7$ %. In the absence of plasma, the inner flame has a stable conical shape and extends to a distance $x/d \geq 3$. In contrast, in the presence of plasma, the inner flame is shorter and has a distorted shape. In addition, a large change in shape occurs between 6 and 7 kV. This change in the inner flame shape is thought to be due to the flow induced by the plasma, which causes an imbalance between the jet velocity and the burning rate. Increasing the applied voltage leads to

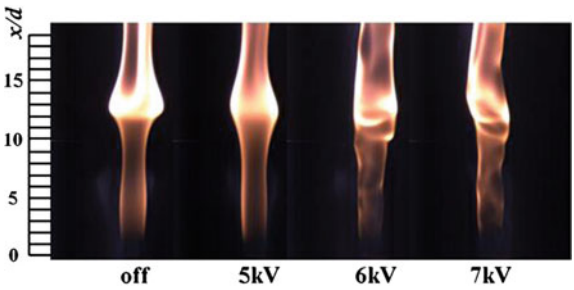


Fig. 3 Effect of voltage applied to DBDPA on propane diffusion flame ($Q = 2.0$ L/min, $\Phi = 100$ %, 8 kHz)

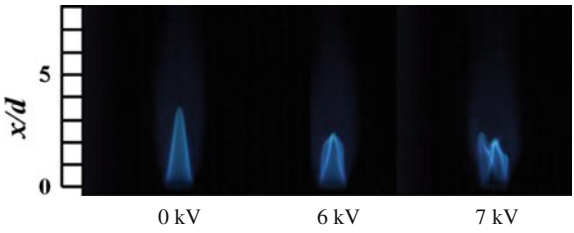


Fig. 4 Dependence of inner flame shape on applied voltage for propane/air mixture ($Q = 1.2$ L/min, $\Phi = 16.7$ %, 8 kHz)

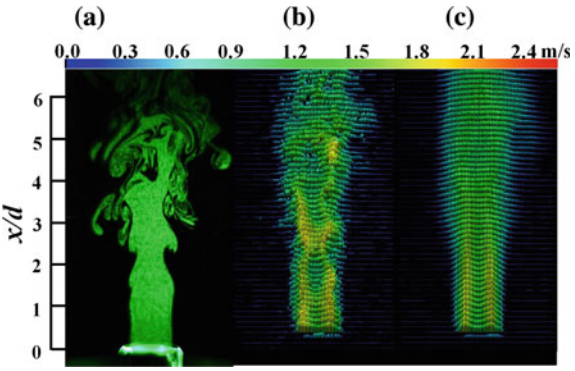


Fig. 5 Flow visualization and PIV analysis results for air (Re = 1000, 6 kHz, 6.3 kV). **a** Flow visualization **b** Flow visualization by PIV **c** Average vector chart by PIV

an increase in the velocity of the induced flow, thus causing a more dramatic effect on the flame shape.

In order to determine the cause of the deformation of the flame front, the velocity distribution in pure air jets was investigated by flow visualization and PIV. The results are shown in Fig. 5 for an applied voltage of 6 kHz, 6.3 kV. Figure 5a show the visualization image, and Fig. 5b, c show instantaneous and average velocity vector diagrams, respectively, determined by PIV analysis. For $x/d \leq 3$, the average velocity is seen to be highest at a radial distance from the jet axis of close to the nozzle radius. Figure 6 shows cross-sectional profiles of the average velocity at different distances from the nozzle.

For $x/d = 0.5-3$, the maximum velocity is at about $y/d = 0.4$, where y is the radial distance from the central axis of the nozzle. However, for $x/d \geq 5$, the profile resembles a normal distribution with the maximum at the center. Figure 7 shows a schematic diagram of the flow induced by the plasma in the DBDPA. This is believed to increase the jet flow velocity near the nozzle wall. Since the mass of the air passing through the nozzle is fixed, the increase in velocity near the nozzle wall leads to a decrease in velocity near the central axis, as seen in Fig. 6.

The change in the velocity distribution after the nozzle is thought to give rise to the deformation of the flame seen in Fig. 4. In places where the burning rate and the

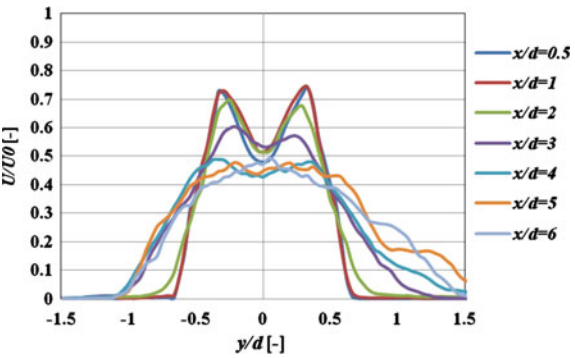


Fig. 6 Cross-sectional velocity profiles for air jet at different distances from nozzle (Re = 1000, 6 kHz, 6.3 kV)

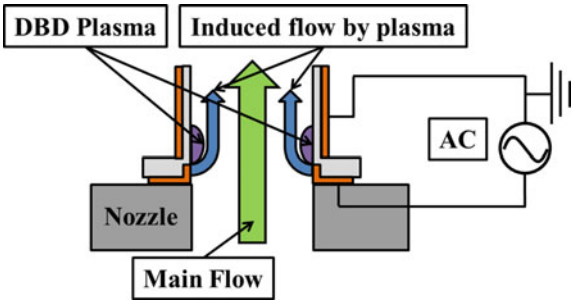


Fig. 7 Schematic diagram showing interaction between induced flow and main flow in DBDPA

premixed gas velocity are balanced, the flame surface appears. In the absence of plasma, the flame front is conical. However, in the presence of plasma, since the velocity near the central axis is reduced, it is believed that the flame front becomes recessed.

Figure 8 shows the dependence of the jet flow rate Q for a mixed gas flame on the propane content Φ. The blue and green symbols are for the case without plasma, and when the flame remains attached to the nozzle exit. The purple symbols are also for the case without plasma, but when the flame has lifted. Finally, the red and yellow symbols are for the case with plasma, and when the flame remains attached to the nozzle exit. In the absence of a plasma, for $\Phi = 17-35$ %, there is a jet flow limit to hold the burner flame; the flame is blown away in the further flow. For $\Phi > 35$ %, until the ejection flow limit above the burner flame is maintained. As the flow rate increases, the burner flame becomes lifted, and is eventually blown away.

In contrast, in the presence of a plasma, the flow rate is limited so that the flame remains attached to the nozzle in the range $\Phi = 16-51$ %, without the flame being lifted or being blown away. Thus, the presence of plasma allows a higher flow rate

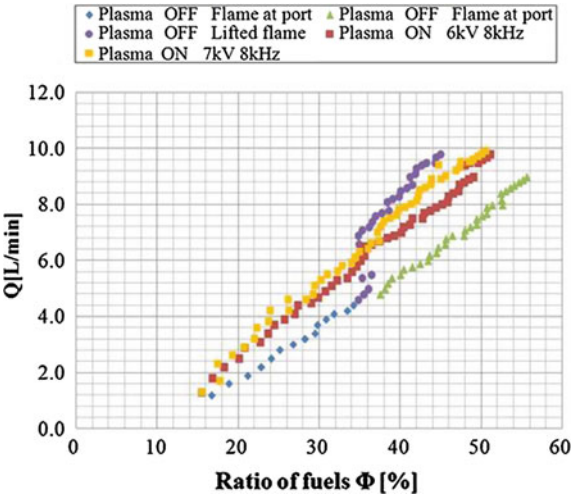


Fig. 8 Relation between jet flow rate and propane content

without causing the flame to be lifted. As stated previously, the increased velocity at the boundary layer due to the plasma-induced flow leads to a decrease in velocity near the center of the jet, which results in a balance with the reduced burning rate. It can also be seen in Fig. 8 that the stability limit is higher for an applied voltage of 7 kV than for 6 kV. Jetting flow rate $Q = 6.0$ L/min is larger when the stability limit during plasma ON than min becomes lower than the stability limit of the lifted flame. Nevertheless, it is possible to maintain the burner flame for a longer distance than in the case without plasma. However, for $\Phi > 35$ %, since the flame becomes lifted in the absence of a plasma, the flame is held by the ejection flow velocity higher than the plasma ON.

Figure 9 shows example images illustrating the stability limit for $Q = 2.2$ L/min without a plasma ($\Phi = 22.7$ %) and with a plasma ($\Phi = 22.7$ and 18.2 %). It can be seen that in the presence of a plasma, the flame was not blown away even for $\Phi = 18.2$ %.

Figure 10 shows images of flames produced at $Q = 8.1$ L/min, $\Phi = 45.7$ %, and without and with a plasma (applied voltage of 6 and 7 kV). In the absence of plasma, the flame is seen to be lifted, in contrast to the cases with plasma. For an applied voltage of 6 kV, the flame is seen to be slightly detached from the nozzle. In contrast, at 7 kV, the flame is fully attached and has a stable shape.

Thus, it is possible to maintain a longer flame in the presence of plasma by increasing the applied voltage. This is thought to be due to the generation of an

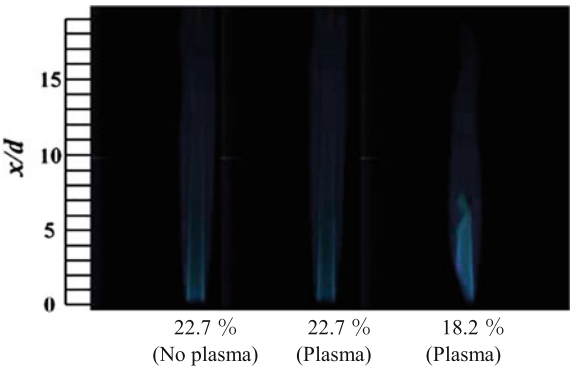


Fig. 9 Flames produced without and with plasma ($Q = 2.2$ L/min, 6 kV, 8 kHz)

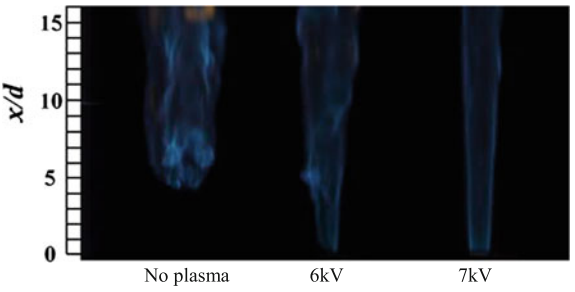


Fig. 10 Flames produced without and with plasma ($Q = 8.1$ L/min, $\Phi = 45.7$ %, 8 kHz)

induced flow and active species by the plasma. The induced flow alters the jet velocity gradient, whereas active species such as OH are expected to affect the burning rate.

To investigate the reason why flame blow-off is suppressed in the presence of plasma, the flame temperature was measured using a thermocouple. Regardless of whether or not plasma was produced, the temperature of the flame front was found to be around 1950 K, indicating that a normal flame was formed in both cases. To identify the presence of active species, the flames were then subjected to a spectroscopic analysis. In the emission spectrum, a peak at a wavelength of 310 nm, which is associated with OH, and peaks at 390 and 430 nm, which are associated with CH, was detected. However, these peaks were more intense in the presence of plasma. Therefore, the plasma increases the concentration of active species, and thus the burning rate. Together with the increased flow velocity, this leads to suppression of blow-off.

4 Conclusion

The effects of a dielectric barrier discharge plasma actuator (DBDPA) on an air jet and a mixed propane/air jet flame were investigated. At a frequency fixed, the diffusion effect on the main jet increased with applied voltage. The effect also increased with the frequency of the applied voltage. If the presence of plasma, the flow velocity near the boundary layer was found to increase, with a corresponding decrease in the velocity in the central region of the jet. The shape of the flame was also found to change due to the flow induced by the plasma. For a propane content of 35 % in the mixture, the flame blow-off limit was increased in the presence of plasma. In the absence of plasma, a lifted flame was formed for a propane content of 35 % or higher. In the range of the flame and lift, stability limit in the case of plasma ON becomes wider than the plasma OFF. By increasing the applied voltage, the range of propane concentration and gas flow rate for maintaining a stable flame can be extended.

Acknowledgement This work was supported by JSPS KAKENHI Grants-in-Aid for Scientific Research (C) Number 22560176 and 25420132.

References

1. M. Hirota, K. Hashimoto, H. Oso, G. Masuya, Improvement of laminar lifted flame stability excited by high frequency acoustic oscillation. Trans. J. Soc. Mech. Eng. Ser. B **74**(748), 2697–2703 (2008) (in Japanese)
2. N. Kasagi, Toward smart control of turbulent jet mixing and combustion, JSME Int. J. Ser. B **49** (4), 941−950 (2006)

3. T.C. Corke, C.L. Enloe, S.P. Wilkinson, Dielectric barrier discharge plasma actuators for flow control. Annu. Rev. Fluid Mech. **42**, 505–529 (2010)
4. M.L. Post, T.C. Corke, Separation control on high angle of attack airfoil using plasma actuators. AIAA J. **42–11**, 2177–2184 (2004)

Part IX
Vortex Dynamics

Vortex Rings Formed Behind a Free-Flight Butterfly and Their Dynamic Behaviors

Masaki Fuchiwaki and Kazuhiro Tanaka

Abstract A number of studies on not only the mechanism of insect flight but also the flow field around insect wings have been performed using experimental and numerical approaches. However, these results are for the flow field under a tethered condition. It is considered that the flow field around a butterfly wing in free-flight assumes a more complicated vortex flow structure. In the present study, we attempt to clarify the dynamic behavior of the vortex rings from the viewpoint of the velocity fields in the wake of a free-flight butterfly. We conducted a stereo PIV measurement in the wake of a free-flight butterfly (*Cynthia cardui*) and measured the three-component velocity fields in the wake. Jets are induced by the vortex rings in the wake, and they grow strong even after two or three wing chord lengths. That is, the vortex rings grow over time and spread gradually in the transverse direction. The maximum velocity of the jets was almost the same as the flight velocity even after two or three wing chord lengths. Therefore, it is expected that the butterfly is given a reactive force (lift) by the jets of the vortex ring, and the jets strongly influence the butterfly's flight.

1 Introduction

The flow field around a moving elastic body is treated as a fluid–structure interaction (FSI) problem, and the motion and deformation of elastic bodies (and the associated vortex flow phenomena) are complicated [1–3]. A typical example of the flow field around a moving elastic body is that around butterfly wings, which contain many veins and can undergo elastic deformation. Butterflies fly by skillfully

M. Fuchiwaki (✉) · K. Tanaka
Kyushu Institute of Technology, Iizuka, Japan
e-mail: futiwaki@mse.kyutech.ac.jp

K. Tanaka
e-mail: kazuhiro@mse.kyutech.ac.jp

© Springer International Publishing Switzerland 2016

A. Segalini (ed.), *Proceedings of the 5th International Conference on Jets, Wakes and Separated Flows (ICJWSF2015)*,
Springer Proceedings in Physics 185, DOI 10.1007/978-3-319-30602-5_67

controlling this deformation, and vortices are generated around their bodies. The motion of their elastic wings produces a fluid force by manipulating the flow field, which allows butterflies to rapidly accelerate, turn and hover. For this reason, there has been increased academic interest in the flow field and dynamic fluid force produced by butterfly wings.

A number of studies on the mechanism of insect flight have been performed [4, 5]. Moreover, a number of recent studies have examined the flow field around insect wings. Dickinson et al. used flow visualization and instantaneous force measurements of tethered fruit flies (*Drosophila melanogaster*) to study the dynamics of the force generation during flight and presented an animated reconstruction of the vortex loop formed during the downstroke and ventral flap [6]. Willmott et al. clarified the leading edge vortices (LEVs) generated on wings based on the visualization of the flow field around a hawk moth wing using the smoke-wire method [7]. Based on these works, the flow field generated by the flapping motion of a flying organism was clarified, and it was suggested that the flow field around its wing contributes to the generation of fluid force. Bomphrey et al. carried out the first digital particle image velocimetry (DPIV) around the wings of an insect (*Manduca sexta*) and reported the relationship between the LEV structure and force production [8, 9]. Subsequently, Bomphrey et al. used classical smoke visualization techniques to analyze the aerodynamic mechanisms of free-flying bumblebees and reported the independent LEVs on each wing [10]. Furthermore, some studies have examined the flow field around wing models that mimics the wing motion of an insect wing. Berg et al. visualized a vortex ring generated on the wing of a flapping robot that mimics the wing motion of a hawk moth in hover and estimated the resulting dynamic lift [11]. Birch et al. examined two-dimensional digital particle image velocimetry (DPIV) to visualize the flow patterns around the flapping wing of a dynamically scaled robot for a series of reciprocating strokes starting from rest [12].

The present authors conducted a particle image velocimetry (PIV) measurement around the flapping wings of *Cynthia cardui* and *Idea leuconoe* and investigated the vortex structure and dynamic behavior produced [13] A vortex ring is formed over the butterfly's wings when the wings flap downward to the bottom dead position. The vortex ring then passes over the butterfly completely and grows until it reaches the wake at the bottom dead position. Vortex rings are formed over the wings of all butterflies; however, the scale of the vortex ring varies with the species. These vortex rings that form over the butterflies are similar to those described for other insects [6]. However, these results are for the flow field under a tethered condition. We expect that the flow field around a butterfly wing in free-flight assumes a more complicated vortex flow structure. The vortex flow structure and the dynamic behavior generated by the wings of a butterfly in free-flight are expected to be important for generating the aerodynamic forces required for flight.

In the present study, we attempt to clarify the dynamic behavior of the vortex rings from the viewpoint of the velocity fields in the wake of a free-flight butterfly. We conducted a stereo PIV measurement in the wake of a free-flight butterfly (*Cynthia cardui*) and measured the three-component velocity fields in the wake. We also investigated the three-component absolute velocity vector fields in the wake of

the free-flight butterfly, inspected the dynamic behavior of the vortex rings that were formed in the downward and upward flapping of the wings, and discussed the relationship between the wake structure and the butterfly's flight.

2 Experimental Setup

The butterfly considered in the present study is *Cynthia cardui*. The wing span length l, wing chord length c, wing aspect ratio AR, flapping frequency f, and average flight velocity V of the butterfly are 65 mm, 25 mm, 2.6, 25 Hz, and 1.5 m/s, respectively [13].

Figure 1 shows the scanning PIV system, which consists of a polypropylene container (of dimensions 900 × 900 × 1200 mm^3), two high-speed cameras (Photoron: SA-X2, 1000 fps), and a high-speed YLF laser (Litron Laser, DLYF-L15T). In order to control the flight of the butterfly, a phototaxis is applied to the butterfly. As indicated in Fig. 1, we placed a chemical light that emits light at a wavelength to which insects react in the container. Tracer particles (Di-Ethyl-Hexyl-Sebacat (DEHS); mean particle diameter $d = 0.4$ μm, specific gravity $\gamma = 0.912$) are filled in the polypropylene container using an oil mist generator. In the experiments, the butterfly is released from the inlet of the test section, and images were captured by two high-speed cameras located at the sides of the container. The angle of the light axis relative to the laser sheet of the two high-speed cameras was 45°. The resolution and measurement domain for the two cameras were 1024 × 1024 pixels and 180 × 180 mm^2, respectively. The PIV images were processed using the Davis 8.2 software from LaVision GmbH, which incorporates recursive cross-correlation to realize high accuracy and high resolution of the derived velocity and vorticity fields. A primary correlation window of 64 × 64 pixels was selected with a sub-correlation window of 32 × 32 pixels with 50 % overlap.

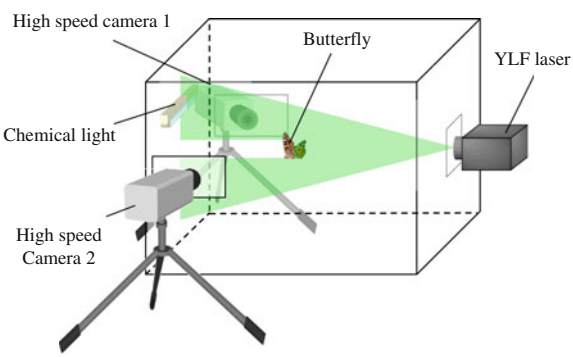


Fig. 1 Experimental system for our stereo PIV measurement

3 Results and Discussion

Figure 2 shows a raw image of the stereo PIV measurement captured by one camera. The butterfly flew from left to right in the image, and the laser sheet was irradiated on the center of the left wing. A white dashed line and a yellow dashed line show the trajectories of the left wing tip and the center of gravity of the butterfly, respectively, and the red and blue circles show the bottom and top dead positions of the flapping motion (BDP and TDP), respectively. The butterfly flies to the upper side slightly, and it moves forward two wing chord lengths during one flapping cycle.

Figure 3 shows the three-component velocity vectors around a free-flight butterfly from the stereo PIV measurement. The black dashed lines represent the flight trajectory of the butterfly. Figure 3a, b, c, d, and e show the results at $t/T = 0$, 1, 2, 3, and 4, respectively. Strong downward jets (A and B) were formed behind the butterfly, as shown in Fig. 3a. It is expected that they are induced by the vortex rings. These jets grow strong as the butterfly flies to the right side, as shown in Fig. 3b, c. In particular, at $t/T = 2$ as shown in Fig. 3c, jet B grew stronger while jet A began to decrease, and jet B was formed at a right angle with the flight trajectory. At $t/T = 3$ and 4, as shown in Fig. 3d, e, the jets progressively weakened; however, it is seen that the jet areas were widespread.

The authors focused on the time variation of jet B in Figs. 3, and 4 shows the maximum velocity profiles of the red area in Fig. 3. The horizontal and vertical axes indicate the x-direction spatial coordinate and the absolute velocity V, respectively. The results represented by the circles, triangles, squares, diamonds, and crosses correspond to the results in Fig. 3a, b, c, d, and e, respectively. In all cases, the jets were formed in the wake of the butterfly, and it was expected that the butterfly is given the reactive force of the jets. However, these profiles varied with the time variation. Here, $t/T = 2$ corresponded to Fig. 3c, and a strong peak was clearly seen in the jet profile. The maximum velocity was 1.3 m/s and was 0.9 times larger than the flight speed of the butterfly. After that, $t/T = 3$ corresponded to

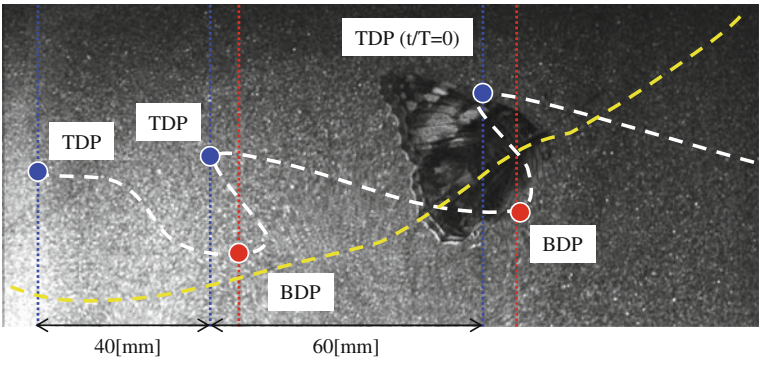


Fig. 2 Flight and left side wing tip trajectories of a free flight butterfly

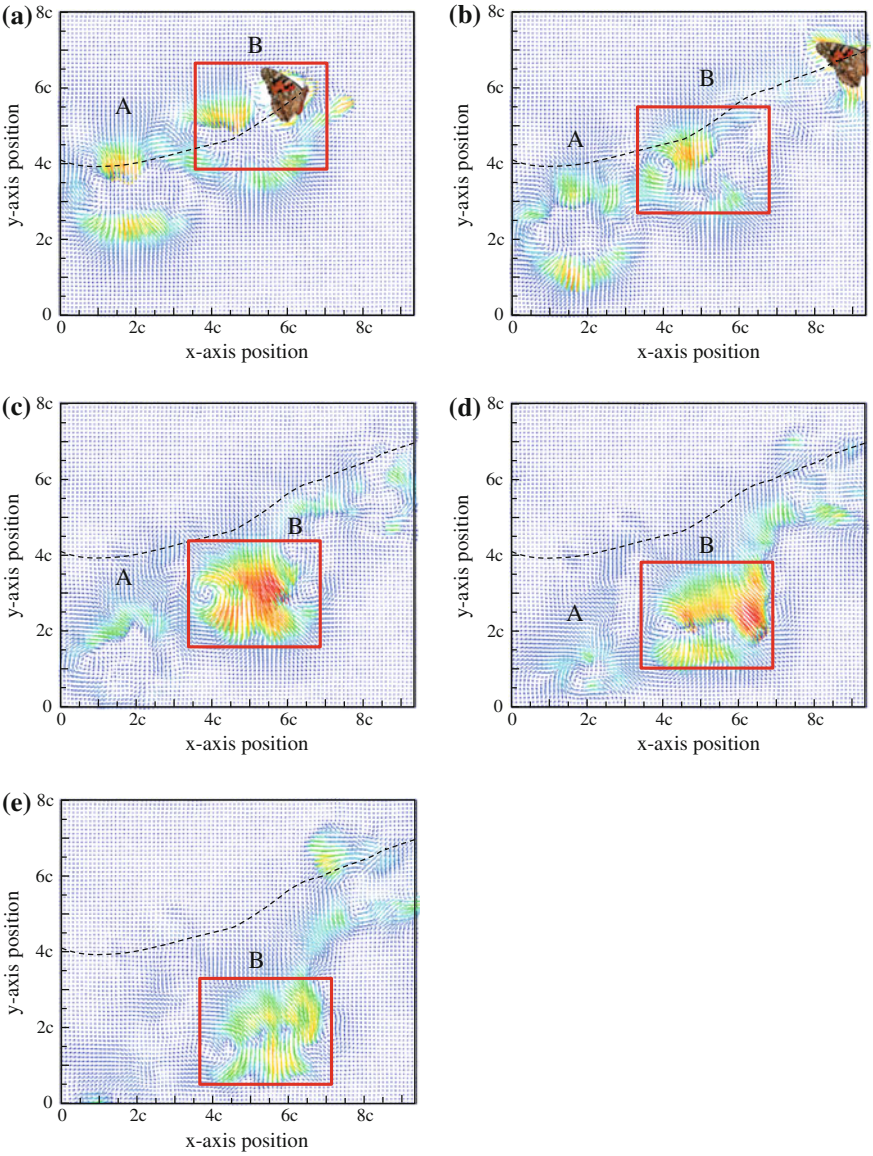


Fig. 3 Velocity vectors in the wake of a free flight butterfly. **a** $t/T = 0$, **b** $t/T = 1$, **c** $t/T = 2$, **d** $t/T = 3$, **e** $t/T = 4$

Fig. 3d, and the peak in the jet profile at $t/T = 2$ divided into two peaks, which means that the vortex rings formed in the wake of the free-flight butterfly grow over time and spread in the transverse direction. The authors have reported that vortex rings form on a tethered butterfly wing in upward and down ward flapping and

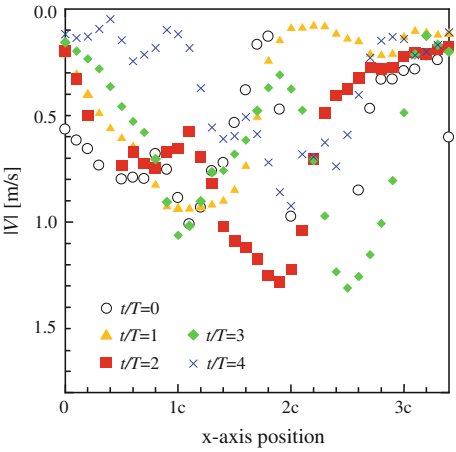


Fig. 4 Maximum velocity profiles in the wake of a free flight butterfly in the red area in Fig. 3

grow in the wake [13]. Moreover, in the case of the free-flight butterfly, the vortex rings formed during upward and downward flapping cause interference and became an L-shaped vortex structure in the wake [14]. Furthermore, Brodsky et al. have also reported that the vortex rings formed in the upward and downward flapping cause interference in the wake [15]. From these results, it is considered that the jets shown in Figs. 3 and 4 are induced velocities in the vortex rings that are formed in downward flapping. In this work, the flight trajectory of the butterfly begins to move upward. Therefore, it is expected that the butterfly is given a reactive force (lift) by the jets of the vortex ring. These jets grow stronger even after two or three wing chord lengths and their maximum velocity was almost the same as the flight velocity. The authors have not yet clarified how long the butterfly is given the energy from the jets induced by the vortex ring. However, it is considered that the jets induced by the vortex ring formed in the wake strongly influence the butterfly's flight.

4 Conclusions

The three-component velocity vectors formed in the wake of a free-flight butterfly were obtained by stereo PIV measurements, and the growth of the vortex ring was discussed. Jets are induced by the vortex rings in the wake, and they grow stronger even after two or three wing chord lengths. That is, the vortex rings grow over time and spread gradually in the transverse direction. The maximum velocity of the jets was almost the same as the flight velocity even after two or three wing chord lengths. Therefore, it is expected that the butterfly is given a reactive force (lift) by the jets of the vortex ring, and the jets strongly influence the butterfly's flight.

Referrences

1. Y.L. Young, Fluid–structure interaction analysis of flexible composite marine propellers. J. Fluid Struct. **24**, 799–818 (2008)
2. M. Fuchiwaki, T. Kurinami, K. Tanaka, Detailed wake structure behind an elastic airfoil. J. Fluid Sci. Technol. **4**(2), 391–400 (2009)
3. T. Kurinami, M. Fuchiwaki, K. Tanaka, Vortex flow developed in the vicinity of a wall of an elastic heaving airfoils and its wake structure. J. Fluid Sci. Technol. **6**(4), 562–574 (2011)
4. T. Maxworthy, Experiments on the weis-fogh mechanism of lift generation by insects in hovering flight. part. 1 dynamics of the 'fling'. J. Fluid Mech. **93**(1), 47–63 (1979)
5. M.H. Dickinson, F.O. Lehmann, S.P. Sane, Wing rotational and aerodynamic basis of insect flight. Science **284**, 1954–1960 (1999)
6. M.H. Dickinson, K.G. Gotz, The wake dynamics and flght forces of the fruit fly Drosophila melanogaster. J. Exp. Biol. **199**, 2085–2104 (1996)
7. A.P. Willmott, C.P. Ellington, A.L.R. Thomas, Flow visualization and unsteady aerodynamics in the flight of the hawkmoth, Manduca sexta. Phil. Trans. R. Soc. Lond. B **352**, 303–316 (1997)
8. R.J. Bomphrey, N.J. Lawson, N.J. Harding, G.K. Taylor, A.L.R. Thomas, The aerodynamics of Manduca sexta: digital particle image velocimetry analysis of the leading-edge vortex. J. Exp. Biol. **208**, 1079–1094 (2005)
9. R.J. Bomphrey, N.J. Lawson, G.K. Taylor, A.L.R. Thomas, Application of digital particle image velocimetry to insect aerodynamics: measurement of the leading-edge vortex and near wake of a hawkmoth. Exp. Fluids **40**, 546–554 (2006)
10. R.J. Bomphrey, G.K. Taylor, A.L.R. Thomas, Smoke visualization of free-flying bumblebees indicates independent leading-edge vortices on each wing pair. Exp. Fluids **46**, 811–821 (2009)
11. C.V.D. Berg, C.P. Ellington, The vortex wake of a 'hovering' model hawkmoth. Phil. Trans. R. Lond. B **352**, 317–328 (1997)
12. J.M. Birch, M.H. Dickinson, The influence of wing–wake interactions on the production of aerodynamic forces in flapping flight. J. Exp. Biol. **206**, 2257–2272 (2003)
13. M. Fuchiwaki, T. Kuroki, K. Tanaka, T. Tabata, Dynamic behavior of the vortex ring formed on a butterfly wing. Exp. Fluids **54**, 1450 (2013)
14. M. Fuchiwaki, T. Kuroki, K. Tanaka, T. Tabata, Wake structure behind a free flight butterfly and its growth process, in *Proc. 16th Int. Symp. Flow Vis.* (2014)
15. A.K. Brodsky, Vortex formation in the tethered flight of the peacock butterfly inachis io l. (lepidoptera, nymphalidae) and some aspects of insect flight evolution. J. Exp. Biol. **161**, 77–95 (1991)

Experimental and Computational Observation of Air Bubble Ring Due to Plughole Vortex

Rayhan Ahmed and HeeChang Lim

Abstract Plughole vortex generation and its consequences were observed both experimentally and computationally for draining water from a stationary rectangular tank. Critical heights were measured in each case and compared with previous experimental and numerical results. We observed air bubble transportation in the drain pipe due to plughole vortex. Bubble formation, its transformation to ring shaped bubble and generation of sound during bubble formation were observed and possible reasons are explained. The shape and sizes of air bubbles were studied, and a comparative study is presented. In addition, vortex shape and sizes were visualized using vortex core method from the computation analysis result and are presented here.

1 Introduction

Plughole vortex or bathtub vortex, an ineluctable process in draining water from a steady or rotating tank, induces a dip on the free surface of water with or without apparently visible whirling motion in the water. The vortex has close similarity with some other vortices like pump intake vortex, tornado vortices and gas core vortices in the primary cooling systems of conventional thermal nuclear reactors and some others. The formation of dip on the free surface causes air to enter into the drain pipe which, in many cases, is totally undesirable.

Lubin and Springer [1] tried to find out the conditions for which the dip on the liquid surface reaches close to the bottom of the container and drain. Experimenting with stationary cylindrical tanks they observed that during the liquid draining dip develops on the free surface when the fluid level reaches at a certain height from the

R. Ahmed · H. Lim (✉)
School of Mechanical Engineering, Pusan National University,
Busan, South Korea
e-mail: hclim@pusan.ac.kr

R. Ahmed
e-mail: rayhan@pusan.ac.kr

© Springer International Publishing Switzerland 2016

A. Segalini (ed.), *Proceedings of the 5th International Conference on Jets, Wakes and Separated Flows (ICJWSF2015)*,
Springer Proceedings in Physics 185, DOI 10.1007/978-3-319-30602-5_68

bottom of the surface and they termed it as 'Critical height'. Analyzing theoretically with Bernoulli equation they suggested an empirical correlation to find out the critical height for fluid layers with density variation. Anderson et al. [2] worked on both experimental and theoretical model of bathtub vortex generated during draining of a rotating cylindrical container through a small drain hole. They obtained similar flow structure as of Lundgren but their works included surface tension and Ekman upwelling. In addition, they observed a bubble-forming instability at high rotation rates at the tip of the needlelike surface depression. Computational analysis on plughole vortex during draining stationary vessels were investigated by Robinson et al. [3]. They modeled several combination of tanks, drain pipes and fluids to assess the potential capability of computational fluid dynamics in solving the vortex. They used ANSYS FLUENT as a solver and compared their result with the experimental result of Lubin, and observed some deviation. Moreover, they clearly described the computational methodology and the reasons of choosing different models and parameters. Although some significant progress have been achieved in identifying the vortex and some of its critical parameters, however, the consequences of plughole vortex in the drain pipe has never been observed or analyzed.

In this study we aimed to observe the generation and aftermaths of plughole vortex, and the effect of vortex on the drain flow rate. The study involved both experimental and computational work of draining water form a stationary rectangular tank. Computational analysis were done using commercial software ANSYS Fluent to calculate the parameters that were difficult to measure and observe experimentally.

2 Experimental Setup

A rectangular tank of 0.6 × 0.5 × 0.4 m and made of 15 mm thick transparent acrylic sheets was used as a stationary tank. Eight different transparent acrylic drain pipes having internal diameter 6, 12, 19.5, 26.2, 31.9, 39.3, 44.0 and 49.8 mm, and each of 400 mm length were used to have different flow rates. In order to take clear picture of the plughole vortex, the drain pipe inlet was raised by 66 mm inside the tank from the bottom of the tank. The pipe outlet was blocked with rubber pipe cap before draining. Steady state condition of water was achieved by settling water for at least 45 min before each experiment and was confirmed by putting color dye in the water. A capacitive level transmitter, equipped with LabVIEW software from National Instrument, was placed inside the tank close to the distant wall of the tank to measure depth of water during draining and the measurement was taken at 50 Hz frequency. A scale was leveled on the inside wall of the tank to observe the water level visually. A high speed camera was used @ 7500 fps to capture fluid flow pattern into the drain pipe. Vortex sound intensity level was measure by a portable sound analyzer within 200 mm distance from the source. A stopwatch was used to measure the event timings (Fig. 1).

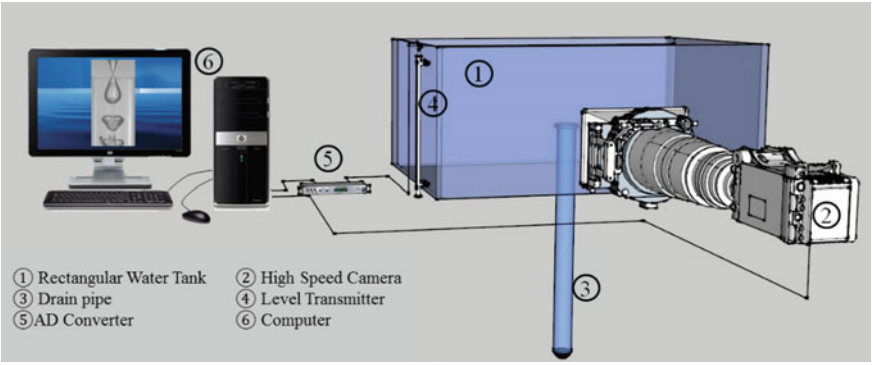


Fig. 1 Schematic diagram of experimental setup

3 Computational Methodology

In parallel to the experiment, several models were also analyzed computationally using commercial software ANSYS FLUENT. One model was selected with the true scale of experimental setup and others were selected on a random basis. Drain pipe inlet was set at the bottom of the tank in order to avoid mesh and computational difficulties, whereas, in experiment it was raised. The computational parameters were selected with reference to the computational investigation work of Robinson et al. [3].

4 Experimental Results

4.1 Critical Height and Drain Flow Rate

Starting with the impulsive start of draining until the formation of plughole vortex the experimentally obtained drain flow rate found to be matched with theoretically calculated drain flow rate using transient Bernoulli's equation. In theoretical calculation the applied discharge coefficient C_d, obtained from curve fitting, seemed to be varied with the pipe radius i.e. discharge coefficient found to be increased with the increase of pipe radius which seemed to be usual. The discharge coefficient varied from 0.725 to 0.78 depending on the pipe diameter.

Figure 2 clearly shows that up to critical height, the experimentally obtained drain flow rate closely matched with the theoretically drain flow and the critical height seemed to be independent of the initial height of water above the drain pipe inlet which supported Lubin's findings. The height at which plughole started to develop was difficult to measure as it occurred within milli-second. However, when the air plug entered into the drain pipe the drain flow rate reduces sharply.

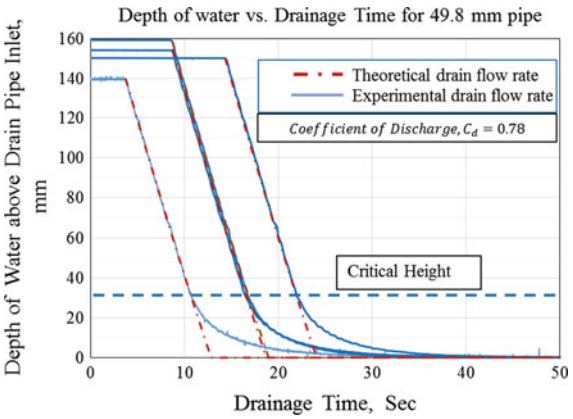


Fig. 2 Comparison of theoretical and experimental drain flow rate

Table 1 Critical height for different size drain pipe

Drain pipe radius, mm	Avg. drain flow rate, $\times 10^{-3}$ m^3/s	Critical height (Exp.), mm	Critical height (Lubin's), mm
6	0.18920	9	14.17
9.75	0.63097	14	22.95
13.1	1.19231	18	29.60
15.95	1.84601	21	35.26
19.65	2.77030	25	41.47
22	3.61031	28	46.11
24.9	4.70949	31	51.28

The experimentally obtained critical heights were compared with the critical heights obtained from Lubin's proposed correlation equation for water–air combination and presented in Table 1. Although the drain flow rate varied with time but to calculate critical height from Lubin's proposal the averaged drain flow rate was used from the experimental data obtained before the formation of plughole vortex.

4.2 Droplet Shaped Bubble from Plughole Vortex

Plughole vortex generated when water level reached at a certain depth above the drainpipe inlet. The vortex caused multiple concentric surface dip development over the free surface. Each dip formed and spread over the free surface. The final dip extended to the drain pipe inlet within milli-seconds, as shown in Fig. 3.

As the dip entered into the drain pipe, it turned to a droplet shaped air bubble Fig. 4. The size of the droplet varied with the pipe diameter and the depth of water above the drainpipe inlet. Droplet size increased with the decrease of water depth. Figure 4 shows the change of bubble size with the decrease of water depth above

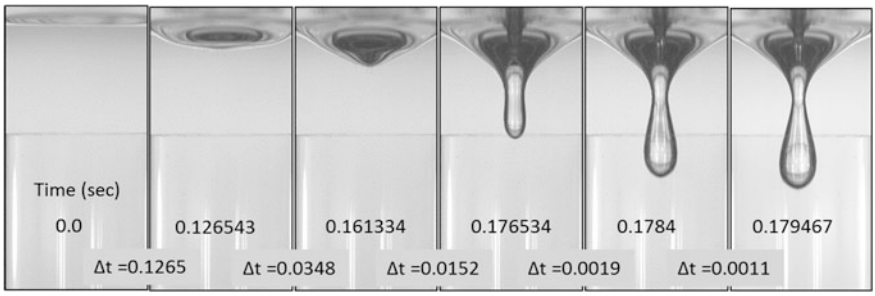


Fig. 3 Surface dip development due to plughole vortex

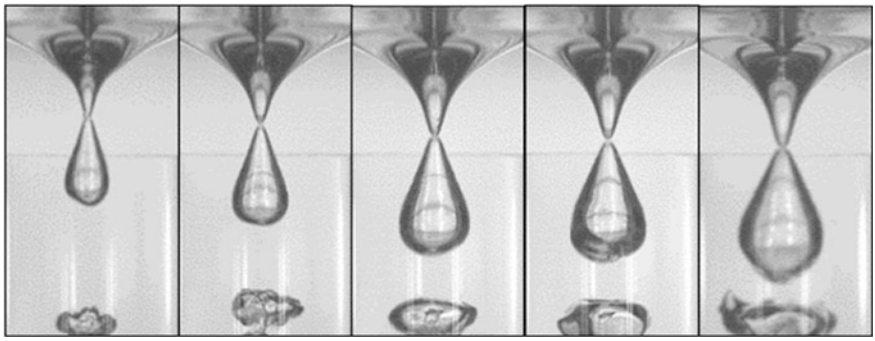


Fig. 4 Bubble size increased as the depth of water decreased above the drain pipe inlet

the drain pipe inlet. During the bubble formation intense noise generation was observed and measured around 105 dB at a distance of approximately 200 mm from the plughole center.

4.3 Droplet Shape to Donut Shape Bubble Ring

The droplet shaped air bubble had a downward forces due to the flowing water which separated the droplet shaped air bubble from the surface dip. Just after the separation, the droplet shaped bubble made a transformation from droplet to donut shape air bubble ring releasing another cone shaped air bubble which had higher downward velocity than the donut shaped bubble ring, as shown in Fig. 5.

An analysis using PIV showed that the vertex of droplet penetrated itself with a velocity at around 5 times higher than the velocity of the droplet shaped bubble. The air bubbles flowing with the drain water initially caused bubbly flow in the drainpipe. As the droplet size increased with the decrease of water depth, it caused slug flow, plug flow and finally ended up with annular flow in the drain pipe.

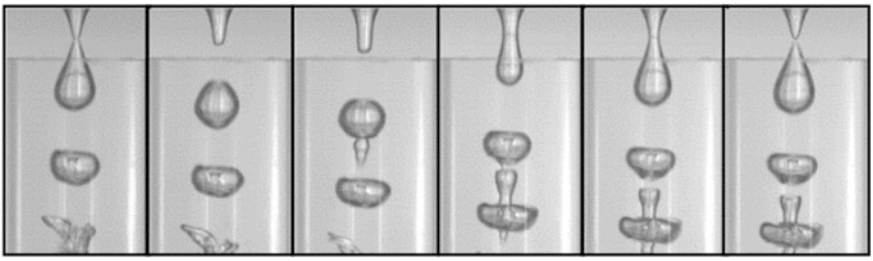


Fig. 5 Transformation of droplet to donut shape air bubble ring

5 Results from Computational Analysis

Computational analysis were performed using k-ε model for a tank of 600 mm × 500 × 140 mm with a concentric drain pipe of 44 mm internal diameter and 300 mm length. The drain pipe was connected to the bottom of the pipe. The computational analysis well predicted the formation of plughole vortex and its bubbly flow as shown in Fig. 6.

5.1 Cause of Droplet Formation and Its Transformation

The computational analysis revealed that close to the drain pipe inlet there was negative pressure region due to vena contracta. The tip of the cylindrical surface dip started to expand, like the shape of a droplet as shown Fig. 7, when it entered in the low pressure region, whereas, the base of the cylindrical dip remained constant for a moment and formed a neck in between the converging and diverging section. The increasing size of droplet tried to suck more air from atmosphere through the neck. Negative pressure generated by the high velocity inside the neck caused strangling

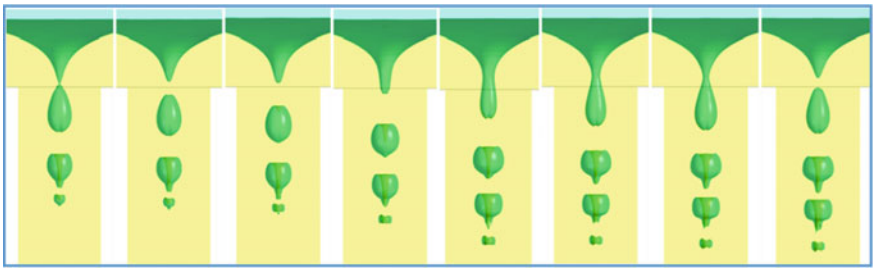


Fig. 6 Formation of droplet shaped bubble and bubble transformation in computational analysis

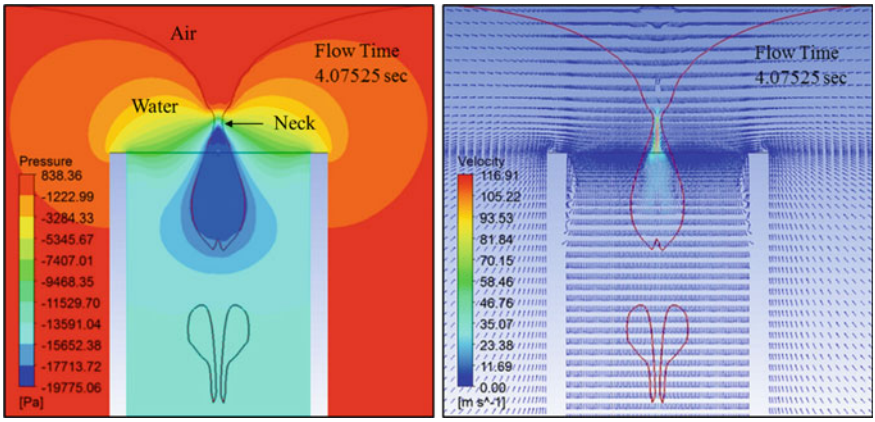


Fig. 7 Pressure contour and velocity vector during bubble formation

the neck and reduced its diameter which finally separated the droplet shaped bubble. When the droplet shaped bubble separated from the surface dip, a high pressure zone was generated in place of the merging neck. The high pressure and velocity inertia at the vertex of the droplet shape bubble, and negative pressure inside the droplet pulled the vertex inside the droplet at almost 5 times the velocity of the droplet shaped bubble. When vertex went inside the droplet it looked like a slender water column was penetrating the bubble and made bubble ring.

5.2 Identification of Vortex Core Region in Drainpipe

In the computational analysis the vortex generated due to draining was irrotational vortex as the Coriolis force was not taken into account during the simulation. In the experiment the vortex was rotational; however, it was very weak and the weak rotation didn't have much impact on bubble formation and its transformation. The vortex core analysis was done using velocity swirling strength method. Velocity swirling strength is the imaginary part of complex eigenvalues of velocity gradient tensor. Velocity swirling strength is positive if and only if the discriminant is positive and its value represents the strength of swirling motion around local centers. The computational analysis revealed two distinct source of vortex, one is due to the suction of air in the bubble and the other source is the vena contracta due to the flowing water in the pipe inlet region. In Fig. 8 the left most image at drainage time 6.55 s shows that during the normal draining, without any surface dent, a steady vortex ring exists in the vena contracta region. The dent on the free surface of water causes vortex rings to appear in air. Multiple concentric vortex ring in air can be observed at drainage time 9.84 s when the surface dip starts to enter in the drain pipe. Images at drainage time 9.851 and 9.856 s shows that when a bubble



Fig. 8 Vortex ring observed using velocity swirling strength method

separates from the surface dip it also separates a vortex ring from the vena contracta region and the air bubble also contains a vortex ring inside it. Vortex ring generated in water from the vena contracta is larger compared to the vortex ring in air bubble, and it flows with the drain water and finally diminishes in the drainpipe wall. The right most image in Fig. 8 shows the vortex ring distribution during the bubble generation.

6 Conclusion

The experimental and computational observation revealed the flow pattern inside the drain pipe. Some notable observations are-

- Surface dip generates droplet shape bubbles when it enters into the drain pipe.
- The droplet shape bubble takes a transformation from droplet to donut shape bubble ring just after the separation from the surface dip.
- The Initial bubble rings create bubbly flow in the drain pipe which later on transforms to slug flow and finally ended up as an annular in the drainpipe.

The formation of air bubble and the transformation of droplet shaped to ring shaped bubble revealed an interesting flow phenomenon which would lead us to find something new.

Acknowledgments This work was supported by the Human Resources Development of the Korea Institute of Energy Technology Evaluation and Planning (KETEP) grant funded by the Korea government Ministry of Knowledge Economy (No. 20113020020010, 20124010203230). This research was supported by Basic Science Research Program through the National Research Foundation of Korea (NRF) funded by the Ministry of Education (NRF2013R1A1A2005347).

References

1. B.T. Lubin, G.S. Springer, The formation of a dip on the surface of a liquid draining from a tank. J. Fluid Mech. **29**, 385–390 (1967)
2. A. Andersen, T. Bohr, B. Stenum, J.J. Rasmussen, B. Lautrup, Anatomy of a bathtub vortex. Phys. Rev. Lett. **91**, 104502 (2003)
3. A. Robinson, H. Morvan, C. Eastwick, Computational investigations into draining in an axisymmetric vessel. J. Fluid Engineering **132**, 121104 (2010)

Penetration by a Negatively Buoyant Vortex Ring

Takashi Naitoh, Nobuyuki Okura, Tomomi Tanaka and Fumihito Goto

Abstract In order to investigate the vortex motion affected by buoyancy force, we experimentally formed a negatively buoyant vortex ring by pushing less dense fluid vertically downward out of a nozzle and measured the penetration depth of it in the wide Reynolds number range, $3{,}000 < \mathrm{Re} < 30{,}000$. We confirmed that the penetration depth of negatively buoyant vortex rings generally depends only on the Froude number and it is larger than that of the jet for the same Froude number in the range of $\mathrm{Fr} > 2$. The formation conditions of buoyant vortex rings to be turbulent or laminar are also examined, since the characteristic features of buoyant turbulent vortex rings are markedly different from those of buoyant laminar rings.

1 Introduction

The dynamic behavior of vortex rings affected by buoyancy force is of inherent interest not only with respect to atmospheric phenomena but also in engineering applications such as environmental problems. Since the motion of a vortex ring is relatively stable and it can be translated over a long distance due to the self-induced velocity, it has been employed to study the characteristic features of vortex motion, such as interaction of a vortex with another vortex (e.g., merging, pairing, mutual slip-through) and interaction of a vortex with a solid body [1–3]. In this paper, by the use of vortex rings formed by pushing lighter fluid vertically downward out of a nozzle, we investigate the vortex motion affected by negative buoyancy force.

T. Naitoh (✉) · T. Tanaka · F. Goto
Nagoya Institute of Technology, Gokiso-cho, Showa-ku,
Nagoya 466-8555, Japan
e-mail: naitoh.takashi@nitech.ac.jp

N. Okura
Meijo University, 1-501 Shiogamaguchi, Tempaku-ku,
Nagoya 468-8502, Japan
e-mail: ohkura@meijo-u.ac.jp

© Springer International Publishing Switzerland 2016

A. Segalini (ed.), *Proceedings of the 5th International Conference on Jets, Wakes and Separated Flows (ICJWSF2015)*,
Springer Proceedings in Physics 185, DOI 10.1007/978-3-319-30602-5_69

A buoyant vortex ring can be classified as positively and negatively buoyant, depending on the direction of the buoyancy force and momentum flux of ejected fluid. In the case of positively buoyant vortex rings, Turner (1957) [4] analyzed the motion of buoyant vortex rings by assuming that the circulation remains constant and the impulse increases owing to the buoyant force in the far field. Bond and Johari (2010) [5] examined the development of a positively buoyant vortex ring in the near field experimentally with LIF and PIV measurements. Flow visualization and some quantitative experiments for this kind of vortex rings were also conducted on small-scale simulated microbursts [6, 7].

In the case of negatively buoyant vortex rings, several papers have examined the motion of vortex rings generated in a starting jet [8–12]. Myrtroeen et al. [12] studied the combined effect of buoyancy and dimensionless piston stroke on the maximum rise height of heavy fluid injected upward from inside a cylinder. Since the buoyancy force decelerates the velocity of the vortex ring, special interest has been paid to the penetration depth (or the rise height) of these non-homogeneous jets and rings, and these lengths are found to be dependent only on the Froude number, $\mathrm{Fr} = U_j/\sqrt{g(\rho_{amb} - \rho_j)D_O/\rho_{amb}}$, where U_j is the fluid ejection velocity, g is gravitational acceleration, $(\rho_\mathrm{amb} - \rho_\mathrm{j})$ is the difference in density between the ambient and the ejected fluid, and D_O is the diameter of the nozzle.

However, these studies are carried out within a small range of Reynolds numbers, $\mathrm{Re} = U_\mathrm{j}\, D_\mathrm{O}/\nu$, Re = 1000 to 3000. In several industrial applications and in nature, however, vortex rings for Reynolds numbers several times larger than this range should be examined. Therefore, in the present study, we investigate primarily the maximum penetration depth of a negatively buoyant vortex ring over a wide range of Reynolds numbers, $3{,}000 < \mathrm{Re} < 30{,}000$.

2 Experimental Apparatus

We used two size of the water tanks with dimensions of 300 mm L × 300 mm W × 700 mm H and 300 mm L × 600 mm W × 1200 mm H. A vortex ring generator which consists of a piston-cylinder mechanism and a nozzle is fixed at the center of the open surface of the tank. The vortex rings are generated by pushing the fluid inside the cylinder via a piston. A linear motor (LAS 4B 500 AW, Oriental Motor) configured by a stepping motor and rack-and-pinion mechanism drives the piston. The movement of the piston is controlled by pulse signals generated by an embedded microcomputer.

In order to produce enough momentum of a vortex ring, small nozzles ranging from 20.0 to 40.0 mm diameter and two size of piston diameters (D_p = 70 mm, 120 mm) were used for all the experiments. The outer contour of the cylindrical nozzle was shaped to form a wedge with a tip angle of 45 degrees so as not to prevent the rolling up.

3 Transition Map

The characteristic features of buoyant turbulent vortex rings are markedly different from those of buoyant laminar rings. Then it is important to investigate the formation conditions of buoyant vortex rings to be turbulent or laminar. Note that most of the negatively buoyant vortex ring generated by the present formation conditions becomes turbulent, whereas that in the literature [8–12] might be laminar. According to Glezer (1988) [13], vortex rings at $Re_\Gamma < 2.0 \times 10^4$ with a small jet length-to-diameter ratio, $L_O/D_O = 2$ generated in a homogeneous fluid remain laminar until the azimuthal wavy deformation appears, where Re_Γ is defined by the ratio of the circulation of a vortex ring to the kinematic viscosity ν. However, for the case of a non-homogeneous fluid, the vortex ring at $Re_\Gamma < 2.0 \times 10^4$ becomes turbulent because of fluid ejection from the vortex ring and Rayleigh-Taylor instability. Figure 1 shows the successive cross sections of the vortex ring at $L_O/D_O = 2$ for $Re_{\Gamma slug} = 9000$ and Fr = 7.2 by using planar laser induced fluorescence. Here, $Re_{\Gamma slug}$ is defined by the ratio of the circulation of a vortex ring estimated based on the slug model [1] to the kinematic viscosity ν. When the shear layer separated from the nozzle tip is rolling up, the spiral streak lines are distorted due to Rayleigh-Taylor instability, because ambient dense fluid is entrained into a vortex ring which is consisted of lighter fluid with spirals in the process of vortex formation as shown in Fig. 1a. Subsequently the state of the ring becomes laminar once from $t = 1.0$ to 3.0 s judging from the orderly streak lines. However, after that the spiral streak lines are blurred and distorted at about $t = 4.0$ s, then the ring becomes turbulent.

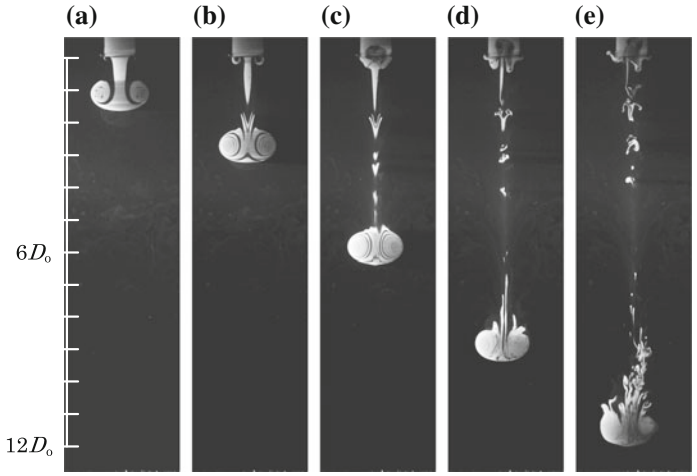


Fig. 1 Successive visualization of negatively buoyant vortex ring ($Re_{\Gamma slug} = 9000$, Fr = 7.2): **a** $t = 0.67$ s, **b** $t = 1.33$ s, **c** $t = 2.67$ s, **d** $t = 4.00$ s, **e** $t = 5.33$ s

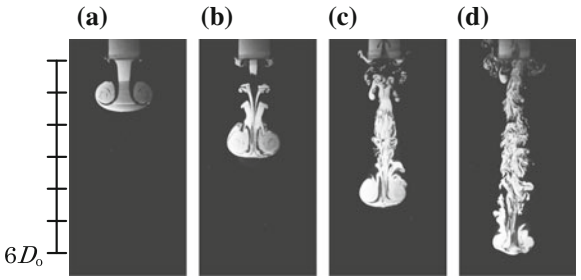


Fig. 2 Successive visualization of negatively buoyant vortex ring ($Re_{\Gamma slug}$ = 9000, Fr = 3.6): **a** t = 0.67 s, **b** t = 1.33 s, **c** t = 2.00 s, **d** t = 2.67 s

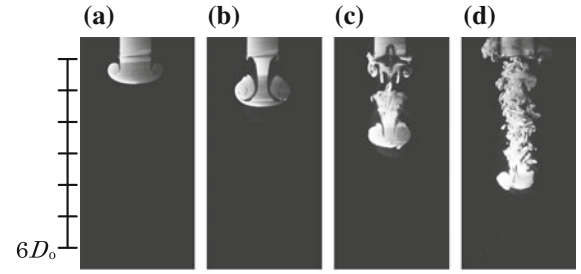


Fig. 3 Successive visualization of negatively buoyant vortex ring ($Re_{\Gamma slug}$ = 9000, Fr = 2.6): **a** t = 0.33 s, **b** t = 0.67 s, **c** t = 1.33 s, **d** t = 2.00 s

The vortex rings generated by the same formation condition except for the Froude number are presented in Figs. 2 and 3. The effect of Rayleigh-Taylor instability grows and the period being laminar is shorten as Fr decreases. The transition to turbulence is seen at about t = 1.5 s in Fig. 2. For the case of Fr = 2.6 observed in Fig. 3, the turbulent vortex ring appears just after the ring formation and the laminar state can't be observed.

Figure 4 shows the transition map of the negatively buoyant vortex ring at $L_O/D_O = 2$. These data are classified by the states of vortex ring. Here, x_t is defined as the position where the transition to turbulence occurs. It is worth noting that the transition of vortex rings depends on both Froude number and Reynolds number.

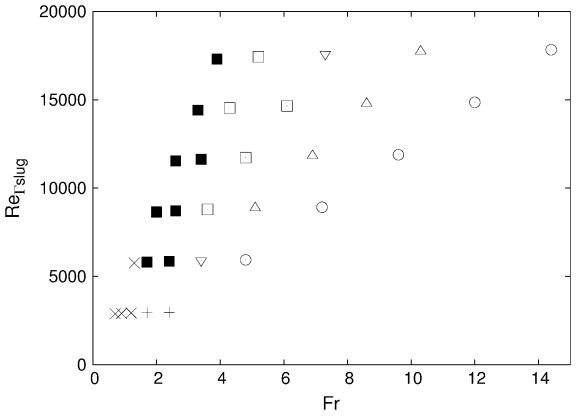


Fig. 4 Transition map of the negatively buoyant vortex ring at Lo/Do = 2.0.: *filled squares*, x_t/Do < 2; *open squares*, 2 < x_t/Do < 4; *down-pointing triangles*, 4 < x_t/Do < 6; *triangles*, 6 < x_t/Do < 8; *open circles*, 8 < x_t/Do < 10; *crosses*, no vortex ring is formed at all; *plus signs*, a vortex ring that keeps laminar until it stops moving

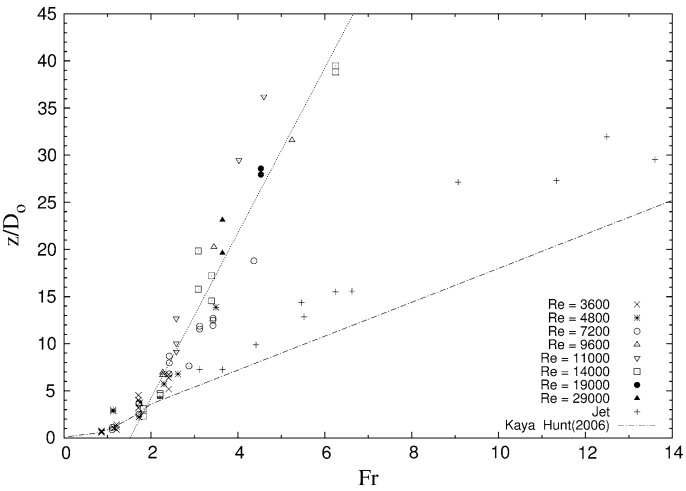


Fig. 5 Maximum penetration depth of the negatively buoyant vortex ring and jet

4 Penetration Depth

Figure 5 shows the maximum penetration depth of negatively buoyant vortex rings and jets. Although the scatter of the data is not small, the trend of the penetration depth of the vortex rings with respect to the Froude number can be determined. Fitting a line to the penetration depth yields the equation $z/D_O = 8.8\ \mathrm{Fr} - 13.3$ ($\mathrm{Fr} > 2$). The plotted symbols are changed according to the Reynolds number and the trend of the penetration depth with respect to the Reynolds number is examined. However, the dependency of these data on the Reynolds number cannot be identified.

The "+" symbol represents the initial penetration depth of jets generated in the same apparatus, and the dot-dashed line shows the fitting equation of the penetration depth of jets in a steady state reported by Kaye and Hunt [14]. Turner [15] presented experimental results that showed the initial rise height is larger than the steady-state rise height. Therefore, it is reasonable that the data denoted by "+" exceed the dot-dashed line.

Based on these results, the Reynolds number is confirmed to have an insignificant effect on the penetration depth of negatively buoyant vortex rings, regardless of the wide Re range, $3{,}000 < \mathrm{Re} < 30{,}000$, and the penetration depth of the negatively buoyant vortex ring is larger than that of the jet for the same Froude number in the range of $\mathrm{Fr} > 2$.

References

1. T.T. Lim, T.B. Nickels, *Fluid Vortices* (Kluwer Academic Publishers, Dordrecht, 1995), pp. 95–149
2. K. Shariff, A. Leonard, Vortex rings. Annu. Rev. Fluid Mech. **24**, 235 (1992)
3. P.G. Saffman, *Vortex Dynamics* (Cambridge University Press, Cambridge, 1992)
4. J.S. Turner, Buoyant vortex rings. Proc. Roy. Soc. Lond. A **239**, 61–75 (1957)
5. D. Bond, H. Johari, Impact of buoyancy on vortex ring development in the near field. Exp. Fluids **48**, 737–745 (2010)
6. A. Alahyari, E.K. Longmire, Particle image velocimetry in a variable density flow: application to a dynamically evolving microburst. Exp. Fluids **17**, 434–4340 (1994)
7. T.S. Lundgren, J. Yao, N.N. Mansour, Microburst modelling and scaling. J. Fluid Mech. **239**, 461–488 (1992)
8. R.-Q. Wang, A.W.-K. Law, E.E. Adams, O.B. Fringer, Buoyant formation number of a starting buoyant jet. Phys. Fluids **21**, 125104 (2009)
9. R.-Q. Wang, A.W.-K. Law, E.E. Adams, Pinch-off and formation number of negatively buoyant jets. Phys. Fluids **23**, 052101 (2011)
10. C. Marugán-Cruz, J. Rodríguez-Rodríguez, C. Martínez-Bazán, Negatively buoyant starting jets. Phys. Fluids **21**, 117101 (2009)
11. C. Marugán-Cruz, J. Rodríguez-Rodríguez, C. Martínez-Bazán, Formation regimes of vortex rings in negatively buoyant starting jets. J. Fluid Mech. **716**, 470–486 (2013)
12. O.J. Myrtroeen, G.R. Hunt, Negatively buoyant projectiles—from weak fountains to heavy vortices. J. Fluid Mech. **657**, 227–237 (2010)
13. A. Glezer, The formation of vortex rings. Phys. Fluids **31**, 3532–3542 (1988)
14. N.B. Kaye, G.R. Hunt, Weak fountains. J. Fluid Mech. **558**, 319–328 (2006)
15. J.S. Turner, Jets and plumes with negative or reversing buoyancy. J. Fluid Mech. **26**, 779–792 (1966)

Part X
Energy-Related Flows

Development of Near Wake of a HAWT Depending on Hub Height

Ivan Dobrev and Fawaz Massouh

Abstract This paper studies the wake of horizontal axis wind turbine. Flow exploration is conducted in wind tunnel, where the turbine is placed in vicinity of the tunnel wall. The objective is to investigate the wake and its interaction with the wall. The influence of the wall on the wake characteristics is studied for ratios "hub height/rotor diameter" h/D of 0.7, 1.0 and 2.25. The boundary layer on the wind tunnel wall permits to study the rotor blades operating inside and outside this boundary layer. The measurements of velocity field behind the rotor are obtained by means of particle image velocimetry. The analysis of results shows that the vortex tubes close to the wall, i.e. in the lower part of the wake, have lower intensity in comparison with the same vortex tubes in the upper part. The averaged velocity profiles of the wake, expressed in a coordinate system with the origin located at the rotor axis, show the influence of hub height on velocity distribution in the wake.

1 Introduction

The wind turbine wake and its interaction with the atmospheric boundary layer (ABL) is an important problem for the design of both the wind turbine and the wind park. The wind turbine rotor converts kinetic energy of wind into mechanical energy and as result the wind velocity behind the rotor becomes lower than the upstream velocity. So, the accurate prediction of the wake is of great importance for the study of optimal placement of wind turbines in the wind farm. As rule of thumb, the distance between the wind turbines is nearly seven diameters, if the wind farms have multiple rows of turbines [1]. However, depending on local land use requirements, ground surface relief or conditions of the atmospheric boundary layer, this rule cannot be always applied. Thus, it is necessary to have a good

I. Dobrev (✉) · F. Massouh
DynFluid, ENSAM, 151 bvd L'Hopital, 75013 Paris, France
e-mail: ivan.dobrev@ensam.eu

F. Massouh
e-mail: fawaz.massouh@ensam.eu

© Springer International Publishing Switzerland 2016

A. Segalini (ed.), *Proceedings of the 5th International Conference on Jets, Wakes and Separated Flows (ICJWSF2015)*,
Springer Proceedings in Physics 185, DOI 10.1007/978-3-319-30602-5_70

understanding of the development of the wake behind the rotor. The wake can be divided in two regions, near wake and far wake. In near wake, the flow is organized and blade presence can be observed. The near wake is characterized by the presence of tip and root vortices. In the far wake, the turbulence is more important and its diffusion depends largely on environmental conditions.

Unfortunately, it is difficult to obtain useful information about the wake by means of in situ experiments. The most significant difficulties are due to the large spatial dimension and the irregularity of the wind. Therefore, it still important to conduct experiments under controlled conditions as a complement to in situ studies. The particle image velocimetry (PIV) is a non-intrusive and efficient method for studying flow field and it is widely used for investigations in case of wind turbine. The first explorations of wind turbine wake applying PIV method are presented in [2, 3]. Lately, the studies in [4–7] present many aspects of wake development such as tip vortex path, vortex intensity, stability etc. Recently, very interesting explorations of the flow behind the wind turbine are presented in [8–11] which permit to understand better the different aspects of the wake. While the above cited papers deal with non-obstructed wake, there are several researchers who study the wake behind the wind turbine placed in the wind tunnel boundary layer [12–17]. In these papers, neutral, stable and unstable atmospheric boundary layers are studied as well as the effects of turbulence and surface roughness.

The experiments presented in this paper are undertaken to acquire more information about the structure of wind turbine wake, the influence of the hub height on the wake and also the vortex breakdown. PIV exploration is carried out in wind tunnel boundary layer and the velocity fields are taken synchronously with angular position of the rotor, up to seven rotor diameters downstream.

2 Experimental Setup

Experiments are conducted in the wind tunnel of ENSAM-Paris. The horizontal axis wind turbine used in tests has a two-blade rotor with a diameter $D = 100$ mm. The rotor has a hub diameter of 14 mm and tapered blades with a root chord of 9 mm and a tip chord of 6 mm. The blade is non-twisted, straight with pitch of 8°. The blade section is a flat plate airfoil with thickness of 0.5 mm. The nacelle support is a horizontal tube with a diameter of 2.5 mm. The wind turbine rotor is mounted on the shaft of DC generator, whose speed of rotation is controlled by a rheostat. The PIV system is controlled by Dynamics Studio 2.30 of Dantec. The images are taken using NdYag laser with pulse energy of 200 mJ and two cameras Dantec FlowSense 4 M with resolution of 4Mpx.

The study is conducted for tip speed ratio $\lambda = 4.57$, which corresponds to 11,900 rpm and upstream velocity of 13.75 m/s. For the near wake, each series of measurements is composed of 500 snapshots for 12 angular positions from 0° to 165°, for each 15° degree. For the far wake, each series is composed of 2×500 snap shots for 6 angular positions from 0° to 150°, for each 30° degree. For all

measurements, image capture is synchronized with rotor and the PIV system is triggered when the blade is positioned at the desired angular position. For this study, the reference angle is taken, as the blade is horizontal. For the far wake, the interrogation window has 16 × 16 px with 50 % overlap, resulting in a spatial resolution of 1.227 mm. For the near wake, the interrogation window also has 16 × 16 px with 50 % overlap, resulting in a spatial resolution of 0.372 mm.

3 Results and Discussion

The wake behind the wind turbine is characterized by velocity deficit due to energy extraction and aerodynamic drag of rotor. The variation of circulation along the blade and the blade boundary layers create vortex sheets which roll-up rapidly into tip vortices which concentrate large amount of the rotor vorticity. These tip vortices and eventually root vortices establish a helical-like vortex structure, which dominates the near wake. The flow in near wake is periodic and it is easy to detect the blade passages. Usually after a distance of one diameter, the flow becomes more and more disordered and turbulent. Consequently, the tip vortices breakdown appears depending on vortex intensity, pitch and also other factors which influence the helical vortex instability [18]. After several diameters behind the rotor the flow turbulence increases rapidly, the individual presence of the blades disappears and the far wake begins its development.

The image on the left side of Fig. 1 shows the axial velocity for hub height/diameter ratio $h/D = 2.25$. Regardless of the blade twist, the optimum point of operation of the rotor is determined mostly by sections in the outermost part of the blade, because the peripheral velocities in the inner part of the blade are much smaller. Therefore, for the blades, which have low twist, the angle of attack for innermost blade sections is always high, the flow detaches, and aerodynamic drag increases. As result of this high drag the axial velocity near the blade root decreases

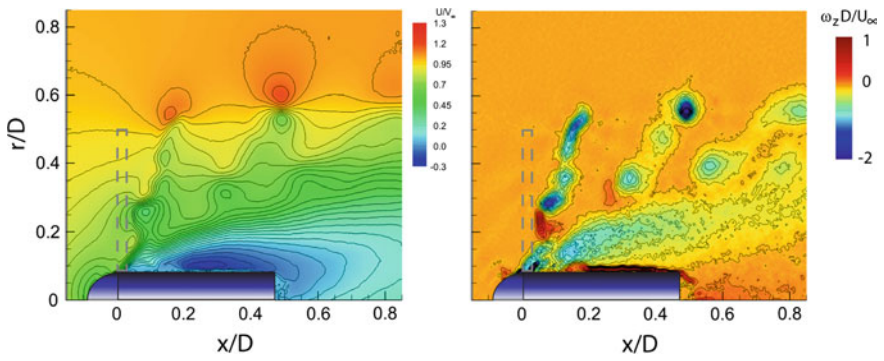


Fig. 1 Axial velocity (*left*) and out-of-plane-vorticity (*right*) for $h/D = 2.25$ and horizontal blade

significantly, left side of Fig. 1. The consequence of variation of axial velocity along the rotor radius can be observed on the right side of Fig. 1. As the blade vortex sheets move with the fluid, so they advance farther near the blade tip than near the blade root. This fact leads to the observed stretching of vortex sheets, of Fig. 1 (right).

Similar results are presented in [19] for PIV exploration of helicopter blades in hover. The experiments show that the axial velocity through rotor varies significantly for non-twisted blades, while for twisted blades the variation is much lower.

It is interesting to note on Fig. 1 the lack of root vortices, which "must" appear near the root. In this study, the root chord of the blade is connected directly to the hub, without any transition sections. Thus, the helical root vortices do not exist and the circulation around the hub is equal to the sum of root circulation of the blades. The breakdown of the hub vortex depends on the value of swirl ratio S, defined as the ratio between angular and axial momentum fluxes. For the wind turbines with non-twisted blades, where the flow decelerates significantly, the swirl ratio has high values and the flow detaches immediately behind the rotor. The vortex breakdown creates a large recirculation bubble despite of the streamlined hub. This recirculation zone is visible on the left side of Fig. 1. On the right side of Fig. 1, the negative vorticity represents the limits of the recirculation bubble. The phenomenon of hub vortex breakdown is already observed by [3] who presents PIV exploration of wake behind a wind turbine with non-twisted blades. Similar results are presented by [20] for a turbine with twisted blades and streamlined nacelle.

The image on the right side of Fig. 1 shows another phenomenon represented by two contra-rotating vortices, which appear at $0.3R$. The appearance of these vortices is due to the circulation discontinuity along the blade. In [21] the author analyzes the experimental data and suggests that the inboard delayed stall creates two adjacent contra-rotating vortices, when the effect of high angle of attack appears at root blade sections. The assumption of circulation discontinuity is confirmed also by the study [22]. The authors present the LDV investigation of circulation along the blade and show important increasing circulation for inner blade section at relative radial position of $0.4R$. This increasing has the same order and sign as circulation variation at the blade tip, therefore the vortex shed from this radial position has the same strength and direction of rotation as the tip vortex.

To separate the effect of the rotor, flow is investigated behind the nacelle alone, Fig. 2 (left). In this case the length of nacelle wake is in order of $3.5D$ while the wake diameter remains comparable to nacelle diameter. This fact supports hypothesis that the big recirculation zone behind rotor is due to its operating, Fig. 1 (left). The right image of Fig. 2 shows wind tunnel boundary layer which is similar to turbulent boundary layer on flat plate. Its thickness is in order of $0.45D$ and the turbulence level at height of $1D$ is 4 %.

In this study, the wind turbine is tested for three different hub height/diameter ratios. For the ratio $h/D = 0.7$, the lower half of the rotor operates in the tunnel boundary layer. For the ratio of $h/D = 1.0$, the rotor operates in vicinity of the boundary layer. For these cases, the wall has a significant influence on the wake. For the ratio $h/D = 2.25$, the wake development is practically free.

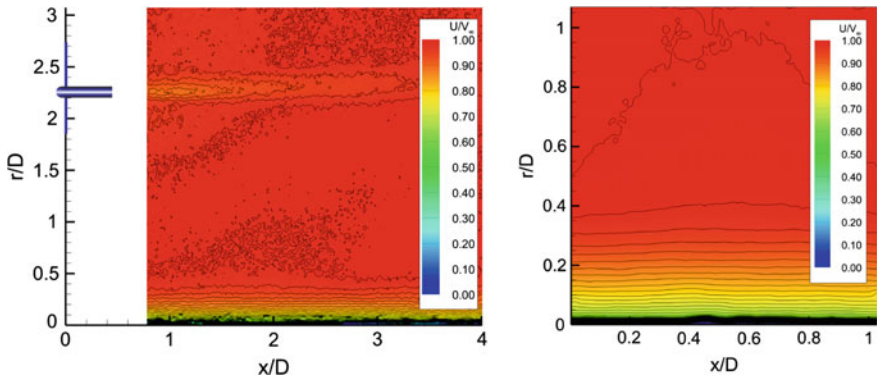


Fig. 2 Nacelle wake (left) for $h/D = 2.25$ and close view of wind tunnel boundary layer (right)

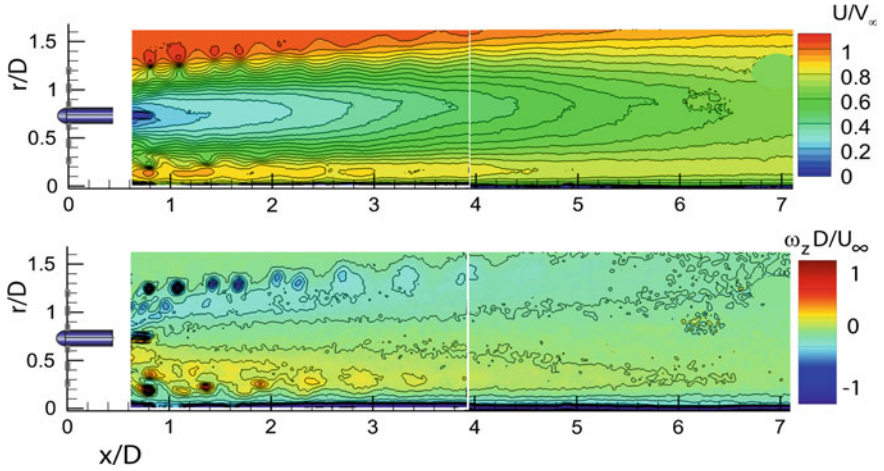


Fig. 3 Axial velocity and out-of-plane vorticity for $h/D = 0.75$ for horizontal blade

The Fig. 3 presents the wake for the smaller ratio of $h/D = 0.7$ and shows how the rotor accelerates slightly the flow in the boundary layer, in vicinity of the wall. Near the wall, the wake is confined, the isolines of axial velocity become almost horizontal and the wake centerline rises. When the vortex is located near the wall, it has lower intensity velocity gradient in comparison with its upper position. Partially, this lower intensity presented on average velocity field comes from the larger amplitudes of wandering.

The Fig. 3 also presents the out-of-plane vorticity. The counter-clockwise rotation is assumed positive, so the lower tip vortices appears as positive and the upper vortices appears as negative. These tip vortices induce velocities, which decrease the flow velocity in the wake and accelerate external flow. The vorticity

shows that the distance between the vortex cores in lower part of the wake differs from this distance in upper part. The difference comes because the vortex moves with the local flow and the velocities in these parts are different. Additionally the vortex wandering near the wind tunnel is almost in horizontal direction and vortex core seems to be deformed. The out-of-plane vorticity shows that after a vortex pairing, which take place 2.0D downstream the rotor, the tip vortices disappear after 4.0D. This fact can be observed also from the curvature of the velocity isolines.

The Fig. 4 presents the wake for $h/D = 1.0$. In this case, the rotor operates outside of the boundary layer, but still the wake is confined by the tunnel wall. As the previous case, the centerline of wake deviates and rises, but the vortices wandering is not constrained by the tunnel wall. The out-of-plane vorticity shows again clearly the vortex pairing, firstly the two cores approaches and then appears as one large vortex cores with much lower intensity. Mostly, this lower intensity is due to the increased vortex wandering and the averaging. The conditional averaging avoids the smearing of the results and permits to obtain the real average value. The results for $h/D = 2.25$ are not presented, in this case the wind tunnel wall should not perturb the wake, but even here, the centerline of wake deviates and the tip vortices seems to be perturbed.

The Fig. 5 presents the averaged velocity profiles of the wake for $h/D = 0.7$ at left and for $h/D = 1.0$ at right. These velocity profiles are obtained by averaging all phase locked measurements. The velocity profiles show how the velocity in the wake varies with length, from 1D behind the rotor up to 7D. Initially the velocity in the wake centerline represents only $0.2U_\infty$ but progressively increase up to $0.7U_\infty$ despite of low turbulence. It is evident that the wake interacts significantly with the

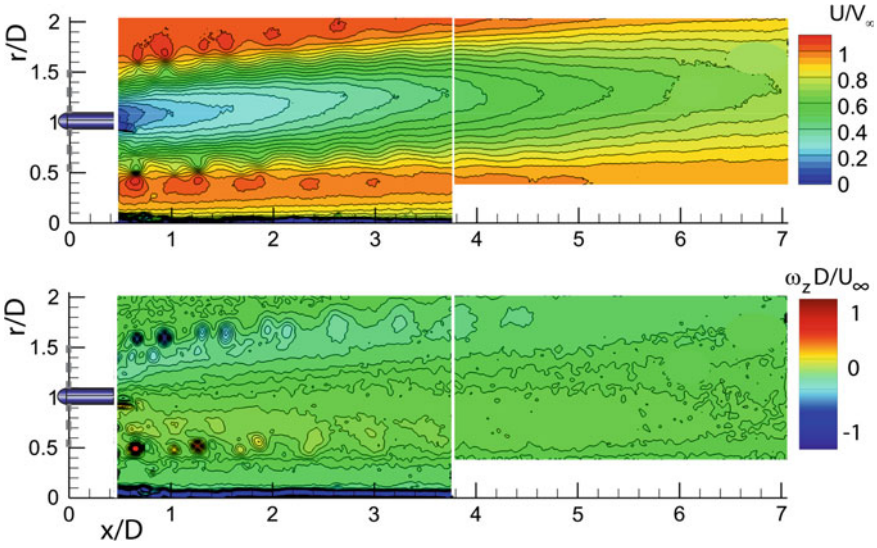


Fig. 4 Axial velocity and out-of-plane vorticity for h/D = 1.0 for horizontal blade

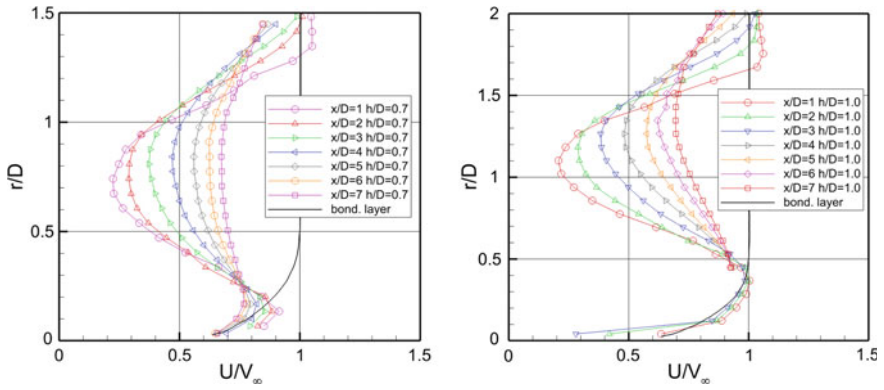


Fig. 5 Axial velocity profile of wake for h/D = 0.7 at *left* and for h/D = 1.0 at *right*

boundary layer for $h/D = 0.7$. This interaction is almost insignificant for $h/D = 1.0$, but the wake is limited by the tunnel wall and deviates exactly as the previous case and wake centerlines rises nearly $0.3D$. The risings of wake center line increases in the case of $1D$ in comparison with $0.7D$ which is a bit unexpected. It is difficult to explain this phenomenon without further studies of interaction between vortex wake and wall.

It is interesting to observe, how at distance of $1D$ behind the rotor, the tip vortices accelerate the flow outside the wake. This acceleration is clearly visible for the upper part of the wake.

4 Conclusion

This paper describes a wind tunnel experimental study of the effect of hub height on the wake of a horizontal wind turbine with non-twisted blades. In this study, the velocity is measured by particle image velocimetry. Initially, the wake is governed by the helical vortex system, which shed from the blades. The vortex breakdown of the swirling flow creates a large recirculation bubble near the hub. After a distance of $2.5D$ downstream of rotor, the vortex pairing occurs and at a distance of $4.0D$ the vortices diffuse. For the hub height to diameter ratio (h/D) of 0.7, half part of the rotor operates in the boundary layer. The wandering of lower tip vortices is mostly in horizontal direction and its intensity is lower compared to when they are at the top positions. This effect does not exist for the case of $h/D = 1.0$ when the rotor operates completely outside of boundary layer. However, for both cases, the wake is limited by the presence of wind tunnel wall and the wake centerline rises vertically nearly $0.3D$. Thus, the study permits to separates the effect of boundary layer from the effect of the wall as mirror-type boundary condition.

References

1. T. Wizelius, *Developing Wind Power Projects: Theory and Practice* (Earthscan, 2007)
2. I. Grant, P. Parkin, X. Wang, Optical vortex tracking studies of a horizontal axis wind turbine in yaw using laser-sheet, flow visualisation. Exp. Fluids **23**(6), 513–519 (1997)
3. J. Whale, C. Anderson, R. Bareiss, S. Wagner, An experimental and numerical study of the vortex structure in the wake of a wind turbine. J. Wind Eng. Ind. Aero. **84**(1), 1–21 (2000)
4. F. Massouh, I. Dobrev, Exploration of the vortex wake behind of wind turbine rotor. J. Phys. Conf. Ser. **75**(1) (2007)
5. I. Dobrev, B. Maalouf, N. Troldborg, F. Massouh, Investigation of the wind turbine vortex structure, in *14th International Symposium on Applications of Laser Techniques to Fluid Mechanics,* Lisbon, Portugal (2008), pp. 1–7
6. J. Xiao, J. Wu, L. Chen, Z.Y. Shi, Particle image velocimetry (PIV) measurements of tip vortex wake structure of wind turbine. Appl. Math. Mech. **32**, 729–738 (2011)
7. M. Sherry, J. Sheridan, D. Jacono, Characterisation of a horizontal axis wind turbine's tip and root vortices. Exp. Fluids **54**(3), 1–19 (2013)
8. Z. Jin, Q. Dong, Z. Yang, A stereoscopic PIV study of the effect of rime ice on the vortex structures in the wake of a wind turbine. J. Wind Eng. Ind. Aero. **134**, 139–148 (2014)
9. L. Lignarolo, D. Ragni, C. Krishnaswami, Q. Chen, C. Ferreira, G. Van Bussel, Experimental analysis of the wake of a horizontal-axis wind-turbine model. Renew. Eng. **70**, 31–46 (2014)
10. B. Akay, D. Ragni, C.J. Simão Ferreira, G. Bussel, Experimental investigation of the root flow in a horizontal axis wind turbine. Wind Energy **17**(7), 1093–1109 (2014)
11. I. Naumov, R. Mikkelsen, V. Okulov, PIV and LDA measurements of the wake behind a wind turbine model. J. Phys. Conf. Ser. **524**(1), 012168 (2014)
12. L. Chamorro, F. Porté-Agel, A wind-tunnel investigation of wind-turbine wakes: boundary-layer turbulence effects. Bound.-Layer Meteorol. **132**(1), 129–149 (2009)
13. L. Chamorro, F. Porté-Agel, Effects of thermal stability and incoming boundary-layer flow characteristics on wind-turbine wakes: a wind-tunnel study. Bound.-Layer Meteorol. **136**(3), 515–533 (2010)
14. H. Hu, Z. Yang, P. Sarkar, Dynamic wind loads and wake characteristics of a wind turbine model in an atmospheric boundary layer wind. Exp. Fluids **52**(5), 1277–1294 (2012)
15. W. Zhang, C. Markfort, F. Porté-Agel, Wind-turbine wakes in a convective boundary layer: a wind-tunnel study. Bound.-Layer Meteorol. **146**(2), 161–179 (2013)
16. P. Hancock, F. Pascheke, S. Zhang, Wind tunnel simulation of wind turbine wakes in neutral, stable and unstable offshore atmospheric boundary layers, *Wind Energy-Impact of Turbulence* (Springer, Berlin, 2014), pp. 109–114
17. P. Hancock, S. Zhang, F. Pascheke, P. Hayden, Wind tunnel simulation of a wind turbine wake in neutral, stable and unstable wind flow. J. Phys. Conf. Ser. **555** (1), 012047 (2014)
18. J.N. Sørensen, Instability of helical tip vortices in rotor wakes. J. Fluid Mech. **682**, 1–4 (2011)
19. M. Ramasamy, N. Gold, M. Bhagwat, Rotor hover performance and flowfield measurements with untwisted and highly-twisted blades. *36th Eur Rotor Forum*, Paris, France (2010)
20. I. Dobrev, F. Massouh, A. Memon, Experimental and numerical study of flow around a wind turbine rotor. Int. J. Eng. Syst. Model. Simul. **5**(1), 137–146 (2013)
21. J.L. Tangler, Insight into wind turbine stall and post-stall aerodynamics. Wind Energy **7**(3), 247–260 (2004)
22. Y. Kamada, T. Maeda, Experimental studies on velocity field around wind turbine rotor, in *International Conference and Utility Exhibition on Power and Energy Systems (ICUE)* (IEEE, 2011), pp. 1–7

Leading Edge Vortex Development on Pitching and Surging Airfoils: A Study of Vertical Axis Wind Turbines

Reeve Dunne, Hsieh-Chen Tsai, Tim Colonius and Beverley J. McKeon

Abstract Vertical axis wind turbine blades undergo dynamic stall due to the large angle of attack variation they experience during a turbine rotation. Particle image velocimetry on a pitching and surging airfoil was used to perform time resolved measurements at blade Reynolds numbers near turbine operating conditions of 10^5. These experiments were compared to simulations performed in the rotating turbine frame as well as the linear, experimental, frame at a Reynolds number of 10^3 to investigate rotational and Reynolds number effects. The flow was shown to develop similarly prior to separation, but the kinematics of vortices shed post separation were reference frame dependent.

1 Introduction

Due to their relatively smaller footprint, vertical axis wind turbines (VAWTs) can be placed in tightly spaced arrays, resulting in an increase of energy density (defined as energy per acre of land) as compared to horizontal axis wind turbines (HAWTs) which suffer from destructive interference unless well spaced [4, 6]. The vertical axis of rotation however makes the aerodynamics of VAWTs much more complicated, and as a result the efficiency of individual VAWTs is over 10 % lower than HAWTs.

R. Dunne (✉) · H.-C. Tsai · T. Colonius · B.J. McKeon
California Institute of Technology, 1200 E California Blvd,
Pasadena, CA 91125, USA
e-mail: rdunne@caltech.edu

H.-C. Tsai
e-mail: htsai@caltech.edu

T. Colonius
e-mail: colonius@caltech.edu

B.J. McKeon
e-mail: mckeon@caltech.edu

© Springer International Publishing Switzerland 2016

A. Segalini (ed.), *Proceedings of the 5th International Conference on Jets, Wakes and Separated Flows (ICJWSF2015)*,
Springer Proceedings in Physics 185, DOI 10.1007/978-3-319-30602-5_71

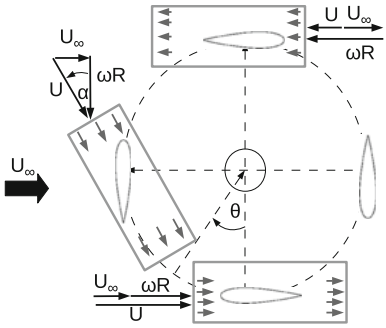


Fig. 1 *Top* view of a VAWT, showing the conditions encountered by a single blade at four angles during VAWT rotation. Wind speed U_∞, effective velocity U, blade velocity ωR. Experimental field of view shown by *grey boxes* (not to scale)

The turbines considered in this study are similar to the commercial 1.2 kW Windspire turbines used by Kinzel et al. [6] and rotate at a tip speed ratio $\eta = \frac{\omega R}{U_\infty} = 2$ where R is the radius of the turbine, U_∞ is the wind velocity and ω is the turbine rotation rate. A schematic of a VAWT is shown in Fig. 1 demonstrating angle of attack α and effective velocity U. Only blades in the upstream half of the turbine cycle ($0° < \theta < 180°$) will be considered here as it has been shown that blades in the downstream half of the turbine rotation produce negligible power when compared to the upstream blades [5].

Dynamic stall on a representative one-bladed VAWT has been studied experimentally in the rotating frame at a limited number of angular positions at Reynolds numbers near operating conditions and tip speed ratios of 2, 3 and 4 by Ferreira et al. [7]. The growth of leading edge and trailing edge vorticity was analysed at several positions around the turbine cycle and the total vortex circulation was shown to grow until the vortex is shed at the point of dynamic stall. In order to capture the evolution of vortical structure, time resolved velocity measurements of a pitching and surging airfoil as a surrogate for a VAWT blade were performed by Dunne and McKeon [3]. They developed a simple 5 mode model using the dynamic mode decomposition that captures LEV development and the dynamic stall process. Computations by Tsai and Colonius at similar conditions but a much lower Reynolds number investigated the effect of the Coriolis force by comparing the pitch/surge motion of Dunne and McKeon to the rotating frame of the turbine [8].

This paper combines experiment and simulation to investigate the effect of Reynolds number and the rotating reference frame on the dynamic stall process. Experimental data in the equivalent planar pitch/surge reference frame, hereafter $\mathbf{EPM}^E$, provides measurements at Reynolds numbers characteristic of full scale VAWTs at the expense of neglecting the Coriolis effect. Direct numerical simulations provide comparisons at low Reynolds number of the equivalent planar motion ($\mathbf{EPM}^C$) and VAWT frame including Coriolis forces ($\mathbf{VAWT}^C$). The rationale for looking at the two-dimensional, low Reynolds number regime in computation is that a much larger parameter space can be considered, and effects of blade rotation, pitch, surge, and so on can be isolated independently from uncertainties associated with turbulence models. Of course, the disadvantage of this approach is computations and

experiments can only be compared qualitatively. In this paper, the different techniques are used to model a region of the parameter space corresponding to VAWT operation. The **EPM**^{C} and **VAWT**^{C} results offer a self-consistent investigation of the influence of rotation within an immersed boundary condition simulation, while a comparison of **EPM**^{C} and **EPM**^{E} cases isolate Reynolds number effects and the differences between experiment and simulation, including all considerations of relevant boundary conditions, which are assumed to be small.

2 Experimental and Computational Methods

Conditions for experiment were chosen to closely match those of a representative $\eta = 2$ vertical axis wind turbine using a NACA 0018 airfoil. Sinusoidal pitch between $\alpha_\pm = -30$ and 30° about the leading edge (where the subscript $\pm$ indicates pitch up $+$ and down $-$) and surge of $\frac{U_{max}-U_{min}}{\bar{U}} = 0.9$ at reduced frequency $k = \frac{\omega c}{2\eta U_\infty} = 0.12$ were selected to mimic the frequency, angle of attack and velocity variation of the turbine consisting of slightly skewed sinusoids at with similar magnitude ($-30° \leq \alpha \leq 30°$ and $\frac{U_{max}-U_{min}}{\bar{U}} = 1$). Experimental Reynolds numbers of 10^5 match the physical turbine in the American Wind Energy Association (AWEA) national average wind velocity of 5 m s^{-1} [1].

This field of view shown by grey boxes in Fig. 1 is fixed in the lab frame, and the airfoil pitches/surges inside it to achieve the desired angle of attack and velocity. Multiple experiments were performed using particle image velocimetry in overlapping forward and aft fields of view to measure the velocity field over the entire airfoil motion, then ensamble averaged and knit together to form a composite field of view shown in the airfoil reference frame by white lines in Fig. 2. Further detail of the experimental setup including hardware, PIV setup, and processing details can be found in Dunne and McKeon 2015 [3].

In the computation, the chord Reynolds numbers were limited to $Re \leq 1500$, but both the experimental, pitch/surge frame (**EPM**^{C}), and the full turbine frame (**VAWT**^{C}) including Coriolis forces were investigated. Computations were performed on a single NACA 0018 airfoil using the immersed boundary projection method developed by Colonius and Taira [2] to compute two-dimensional incompressible flows in an airfoil-fixed reference frame. To account for the non-inertial reference frame appropriate forces were added to the momentum equation. Further details, including a discussion of the verification and validation of the algorithm, can be found in Tsai and Colonius 2015 [8].

3 Results

An isocontour of the spanwise vorticity colored by the velocity magnitude (scaled by the maximum velocity) of the phase averaged velocity fields from experiment (**EPM**^{C}) is shown in Fig. 2 where time is extruded along the Z axis for two periods of the airfoil motion. The period begins at point A, $\theta = 0°$, with maximum freestream velocity (maximum surge) and zero angle of attack. At this point the flow is attached to the airfoil. As the airfoil pitches up and decelerates it separates at point B ($\alpha_+ \sim 25°$), well beyond the static stall point of $\alpha_{ss} \sim 11°$, forming a separated shear layer indicated by the vorticity isocontour lifting away from the airfoil. Finally the airfoil pitches down to point C near $\alpha_- = 0$ when the flow reattaches to the airfoil. From C to A', at the start of the second cycle, the airfoil is at negative angle of attack and the vorticity indicates the shear due to the no-slip condition on the pressure side of airfoil surface. The dynamic stall process including leading edge vortex (LEV) growth is described in Dunne and McKeon 2015 [3].

The vorticity is plotted in the lab frame at various phases of the airfoil motion in Fig. 3 for all three cases. The lower Reynolds numbers in the simulation result in much more coherent vortices appearing at all angles of attack. Furthermore the experimental data is an ensemble average of multiple experiments, and as such the coherent vortex shedding apparent at $\alpha_+ = 0°$ that is not exactly coupled to the airfoil phase is smeared out in experimental results. This phase averaging also significantly weakens the positive (counter-clockwise) vorticity at the airfoil surface due to the interaction of the recirculation region and the airfoil surface after separation, and as such is only apparent in the computations.

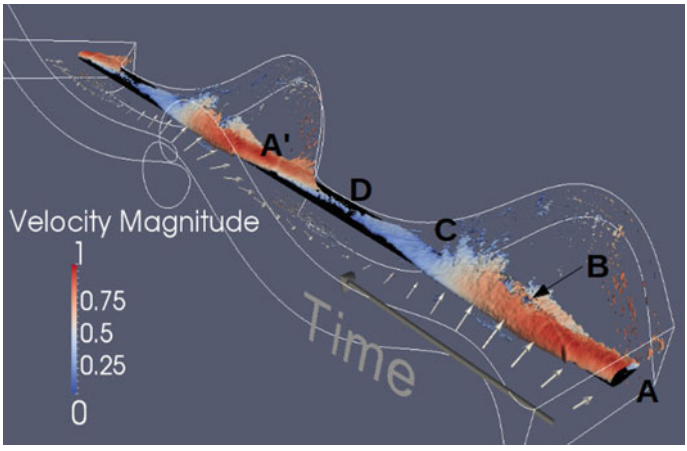


Fig. 2 Vorticity isocontour *colored* by scaled velocity magnitude ($\frac{\sqrt{u^2+v^2}}{max(\sqrt{u^2+v^2})}$). Two periods shown. *Arrows* indicate incoming angle of attack variation. Points A, A' correspond to $\alpha = 0$, B to separation location, and C to reattachment D to minimum angle of attack. *White lines* show field of view in airfoil fixed frame

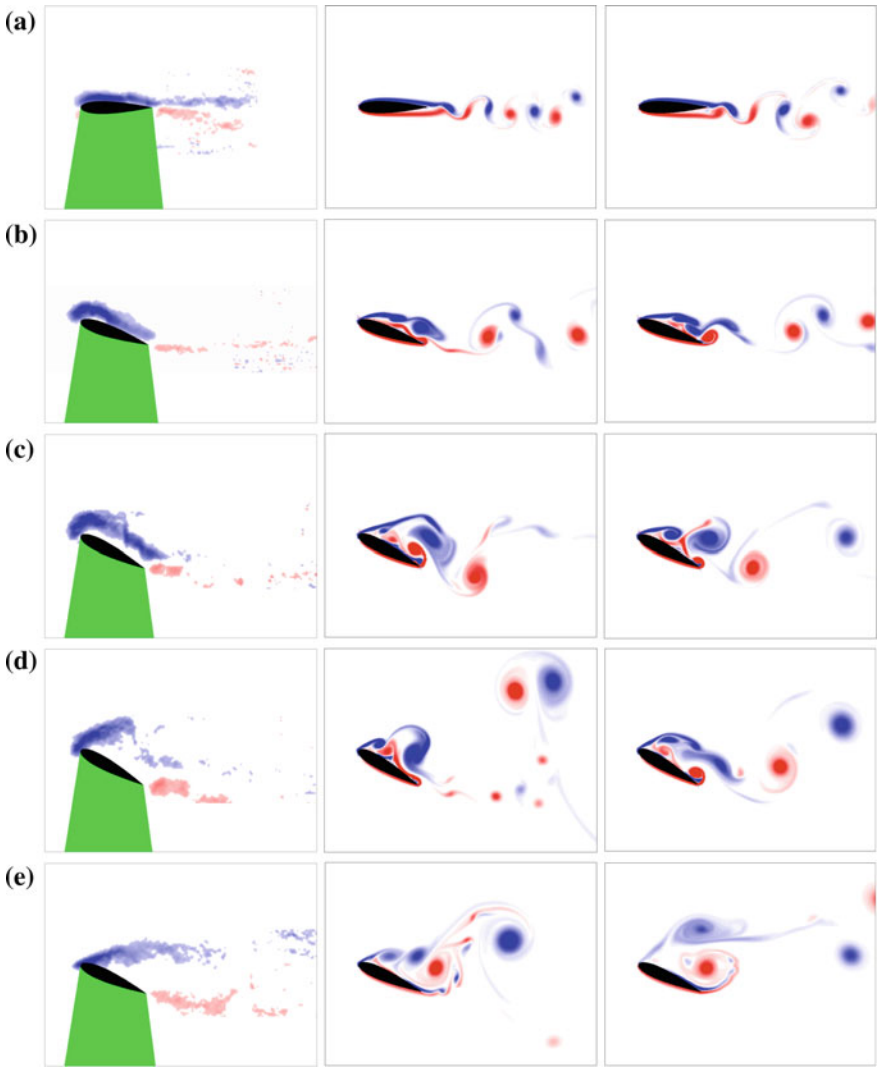


Fig. 3 Vorticity contours from experiment $\mathbf{EPM}^E$ (*left*) and computation of the pitch/surge motion $\mathbf{EPM}^C$, (*middle*) and the computation of the $\mathbf{VAWT}^C$, (*right*). *Red* and *blue* contours indicate positive and negative vorticity respectively and *green* area indicates the PIV laser *shadow*. **a** $\theta = 0°, \alpha_+ = 0°$, **b** $\theta = 60°, \alpha_+ = 19.1°$, **c** $\theta = 90°, \alpha_+ = 26.6°$, **d** $\theta = 120°, \alpha = 30°$, **e** $\theta = 150°, \alpha_- = 23.8°$

Apart from these Reynolds number and experimental differences the flow evolution is similar between the three cases and qualitatively similar to the experiments of Ferreira et al. [7]. Initially at $\alpha_+ = 0°$ the flow is attached and a symmetrical wake can be seen behind the airfoil. At $\alpha_+ = 19°$ a leading edge vortex begins to form,

visible as a distinct structure in computation and indicated by increased intensity in experiment. At this point the flow remains primarily attached without a large reversed region behind the airfoil. At $\alpha_+ = 27°$ the LEV appears even stronger in experiment, and the flow has just begun to separate, in both computations however the LEV has moved downstream, indicating flow separation occurring slightly earlier at low Reynolds number. At maximum $\alpha = 30°$ the flow is fully separated in both experiment and computation with a shear layer between stagnant and freestream flow visible in experiment, and large scale vortex shedding from leading and trailing edge continuing in the computation, while the initial leading and trailing edge vortices, apparent further downstream in computation corresponding to the slightly earlier separation point. Slight differences can be seen in the trajectories of the shed vortices between the EPM and VAWT frames, with a vortex pair moving up away from the airfoil in the linear frame and, two distinct but opposite vortices moving downstream in the rotating one. Finally on pitch down at $\alpha_- = 24°$ the VAWT shows two vortices captured by the airfoil, while in the linear frame vortices can be seen to shed from the leading and trailing edges. More detail of this wake capture phenomenon can be found in Tsai and Colonius 2015 [8].

Vorticity contours are plotted in the turbine reference frame for both the experiment and the VAWT simulation at various points in the airfoil cycle in Fig. 4. Similar to Fig. 3 the VAWT computation shows more coherent vortices as to be expected due to the lower Reynolds number. The effect of the experimental and turbine reference frame can be seen clearly, as the vortices in the airfoil reference frame convect from

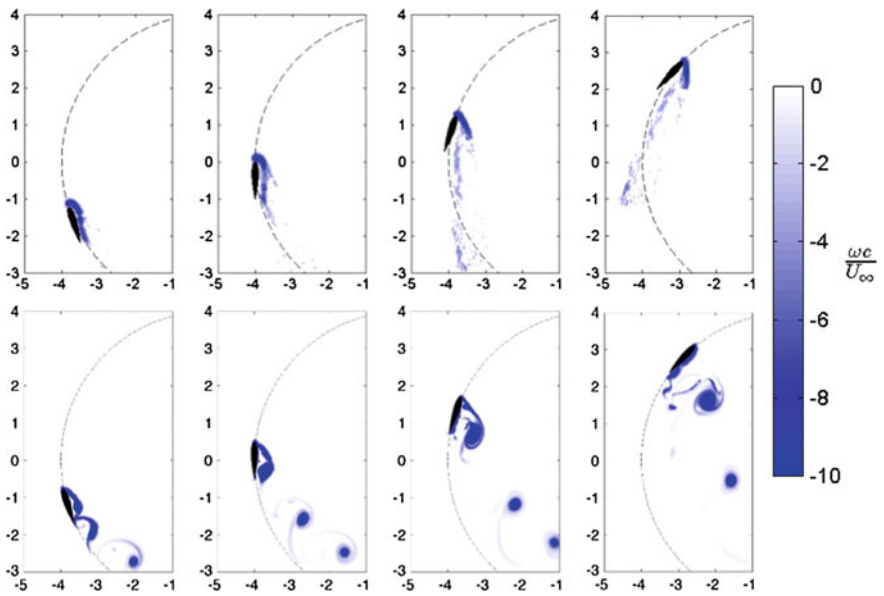


Fig. 4 *Clockwise* vorticity contours from experiment $\mathbf{EPM}^E$ (*top*) and VAWT computation $\mathbf{VAWT}^C$ (*bottom*) at $\theta = 70°, 90°, 108°$ and 133° respectively from *left* to *right*

left to right with the turbine relative freestream, while the vortices in the experiment convect behind the airfoil with the blade relative free stream. However, at the blade level and immediately behind it, agreement is good.

4 Conclusion

Dynamic stall, flow separation and leading edge vortex development were studied to analyse the flow experienced by vertical axis wind turbine blades. The VAWT flow was modeled in two different ways: using experiments on a blade undergoing linear motion and by simulation of both rotating and linearly traversing blades using an immersed boundary condition code. A 'pitch/surge' model of the flow was used experimentally to perform time resolved measurements at full scale turbine blade Reynolds numbers, at the expense of a change of reference frame, which excluded the rotational, Coriolis force. The high Reynolds numbers of physical turbines were not simulated in computation, however both experimental (pitch/surge) and turbine reference frames were calculated such that self-consistent comparisons across all three conditions can be made. As such this dual approach provides insight into the evolution of vortical structure and separation on VAWT blades as well as understanding of the effect of Reynolds number and Coriolis forces.

Acknowledgments This work was supported by the Gordon and Betty Moore Foundation through grant GBMF#2645 to the California Institute of Technology.

References

1. S. Brent, AWEA standard update, in *2009 Small Wind Turbine Testing Workshop. National Wind Technology Center (NWTC)* (2009)
2. T. Colonius, K. Taira, A fast immersed boundary method using a nullspace approach and multi-domain far-field boundary conditions. Comput. Methods Appl. Mech. Eng. **197**(25–28), 2131–2146 (2008)
3. R. Dunne, B. McKeon, Dynamic stall on a pitching and surging airfoil. Exp. Fluids **56**:157 (2015). (see also AIAA Paper 2015-3142)
4. E. Hau, *Wind Turbines: Fundamentals, Technologies, Application, Economics* (Springer, Berlin, 2013)
5. M. Islam, D.S.K. Ting, A. Fartaj, Desirable airfoil features for smaller-capacity straight-bladed VAWT. Wind Eng. **31**(3), 165–196 (2007)
6. M. Kinzel, Q. Mulligan, J.O. Dabiri, Energy exchange in an array of vertical-axis wind turbines. J. Turb. **13**(38), 1–13 (2012)
7. C. Simão Ferreira, G. van Kuik, G. van Bussel, F. Scarano, Visualization by PIV of dynamic stall on a vertical axis wind turbine. Exp. Fluids **46**(1), 97–108 (2009)
8. H.C. Tsai, T. Colonius, Coriolis effect on dynamic stall in a vertical axis wind turbine. AIAA J. **54**(1), 216–226 (2016)

Performance Comparison of a Vertical Axis Wind Turbine Using Commercial and Open Source Computational Fluid Dynamics Based Codes

Taimoor Asim, Rakesh Mishra, Sree Nirjhor Kaysthagir and Ghada Aboufares

Abstract Computational Fluid Dynamics (CFD) is a very effective tool to analyse the flow characteristics within and around different mechanical artifacts such as automotive vehicles, turbomachines etc. CFD based analysis provides beneficial information about the flow behavior within a component, hence reducing the costs involved in the design process of that component. This has led the researchers to develop an Open Source CFD code, commonly known as Open Field Operation and Manipulation, or OpenFOAM. The development of OpenFOAM has made scientific research in the field of fluid dynamics available for almost no cost. Designers who rely on commercial CFD packages are hesitant on using Open Source CFD codes because of accuracy. They need to be convinced by proving its simulation capability as compared to any commercial CFD package. Hence, this study investigate the flow phenomenon in the vicinity of a Vertical Axis Wind Turbine (VAWT), using such open source code combinations that yields reasonably accurate results, which can be compared against any commercial CFD code.

1 Introduction

Computational Fluid Dynamics based commercial codes are in practice all over the world, and are helping the designers of turbomachines in accurate performance prediction of such machines. With special regards to Vertical Axis Wind Turbines (VAWT), [1] shows that the commercial CFD based code ANSYS-FLUENT is capable of predicting the performance output of a VAWT with very high level of accuracy. Similar trends have been reported in [2] where the experimental results match closely with the predicted numerical results from commercial CFD based codes. Further studies [3–5] all have reported that the use of commercial CFD based codes are capable of predicting the variations in the flow phenomena in the vicinity of a VAWT with reasonable accuracy.

T. Asim (✉) · R. Mishra · S.N. Kaysthagir · G. Aboufares
University of Huddersfield, Huddersfield, UK
e-mail: t.asim@hud.ac.uk

© Springer International Publishing Switzerland 2016

A. Segalini (ed.), *Proceedings of the 5th International Conference on Jets, Wakes and Separated Flows (ICJWSF2015)*,
Springer Proceedings in Physics 185, DOI 10.1007/978-3-319-30602-5_72

More recently, various studies have been conducted on the performance evaluation and flow field prediction around a VAWT using open source CFD codes. Reference [6] has reported that the flow field prediction capability of the open source code (OpenFOAM) matches very closely with that of ANSYS-FLUENT. The study also reports that the libraries of OpenFOAM can be modified in order to suit specific applications. Hence, OpenFOAM provides the flexibility of altering the source code to suit various applications, which is not easily possible in case of commercial CFD based codes, like ANSYS-FLUENT, because the source code is not provided with the software.

Reference [7] compares the flow field prediction capability of OpenFOAM with commercial CFD package for flow around an aeroplane. It has been reported that OpenFOAM predicts the flow field that matches closely with that obtained through the use of commercial CFD package. However, it has been concluded that it is necessary to prepare templates for standard cases because of different requirements for different applications. Hence, this study has been carried out to develop a standardised code combination for simulating and analysing a Vertical Axis Wind Turbine. Although this work could have been carried out for a simpler case, the authors need to establish the accuracy of these software for commercial applications, and hence, this particular case has been analysed in the present study.

2 Numerical Modeling

A three dimensional Vertical Axis Wind Turbine model, similar to [8] comprising of 12 inner rotor blades and 12 outer stator blades has been numerically modeled in both ANSYS-FLUENT and OpenFOAM. The VAWT model is shown in Fig. 1. The height of the VAWT is 1 m, and its flow domain's dimensions are 11 m, 9 m and 3 m for length, width and height respectively.

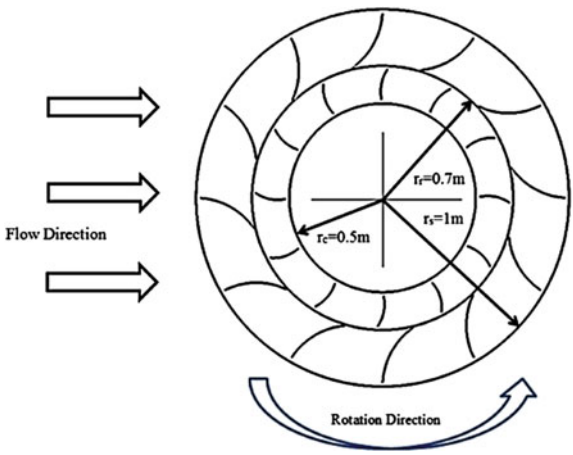


Fig. 1 Geometrical characteristics of the VAWT

The meshing techniques used by commercial CFD packages and OpenFOAM are very different to each other. Default ANSYS Meshing is controlled by the geometrical characteristics of the model and dominated by tetrahedral mesh elements. Hence, the geometrical integrity of the model is not violated even if the mesh quality is not good. However, in OpenFOAM, meshing is a two-step process, where a dominant hexahedral base mesh is initially generated for the flow domain. A special meshing tool, called Snappy Hex Mesh, is used afterwards to connect the geometrical model to the base mesh. Therefore, if the mesh quality is not good, the structural integrity of the model is violated. Hence, it is necessary to have an appropriate base mesh sizing for accurate geometrical interaction with the flow field.

For effective comparison between the flow field predictions from ANSYS-FLUENT and OpenFOAM, the total numbers of mesh elements are maintained between 1.2 and 1.3 million. Table 1 summarises the type and number of mesh elements generated in both ANSYS and OpenFOAM. ANSYS mesh contains approximately 87 % of tetrahedral elements from a total number of 1.3 million mesh elements. On the hand, the percentage of mesh dominated by the hexahedral elements is about 83 % in case of OpenFOAM.

The hexahedral elements are preferred over tetrahedral mesh elements due to their lesser numerical diffusion. The maximum aspect ratio for OpenFOAM mesh is 10.74 % less than ANSYS mesh, which shows that the overall mesh quality in OpenFOAM is better. Due to superiority in accurately modeling the wake regions and extreme pressure gradients, SST k-ω model with Multiple Reference Frame (MRF) for rotating the rotor zone has been chosen for both solvers. Default gradient and interpolation schemes have been used in the present study. Most recent studies [9–12] also show that k-ω turbulence model predicts the changes in the flow parameters in the vicinity of a VAWT with reasonable accuracy.

In the present study, the density of air is assumed to be constant. Since the flow of air in the present study is at low speeds (4 m/s), pressure based solver has been incorporated in the numerical modeling. It should be noted that OpenFOAM uses kinematic pressure as its primary pressure parameter and ANSYS-FLUENT uses static pressure as its primary pressure parameter. Hence, for comparison purposes, static pressure in ANSYS-FLUENT has been customised to represent kinematic pressure by dividing it with the density of air. For boundary condition, inlet velocity of 4 m/s (representing average wind speed in Huddersfield), Tip Speed Ratio of 0.2 (representing maximum torque production point), and an outlet boundary condition of atmospheric pressure (referring to zero gauge static pressure) has been used throughout this study [1]. No-slip condition is applied for all the walls.

Table 1 Mesh quality comparison between ANSYS Fluent and OpenFOAM

Type of cells	ANSYS	OpenFOAM
Mixed cells	67,762	216,661
Hexahedral cells	103,752	1,046,568
Tetrahedral cells	1,182,046	7
Total	1,353,560	1,263,236

3 Result and Discussion

Figures 2 and 3 depict the variations in the kinematic pressure and axial velocity respectively from both ANSYS-FLUENT and OpenFOAM. These contours have been drawn on the same scale for effective comparison.

The results regarding the axial flow velocity have been obtained using careful ANSYS-FLUENT and OpenFOAM simulations, as shown in Fig. 3. It can be seen that the wake is different in both the cases, which may happen due to the difference in both the meshes used, and needs further investigation which is beyond the scope of the present work. Nevertheless, the focus of this study is obtaining design parameters and hence a detailed qualitative analysis is required in order to make these differences prominent. For this purpose, local flow features along predominant

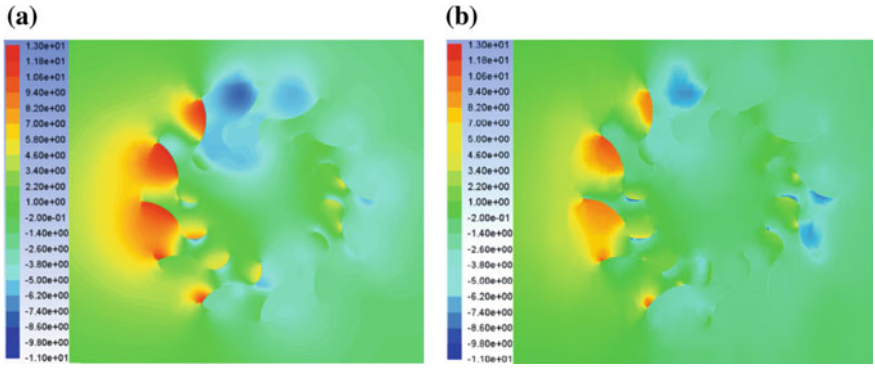


Fig. 2 Variations in kinematic pressure **a** ANSYS-FLUENT, **b** OpenFOAM

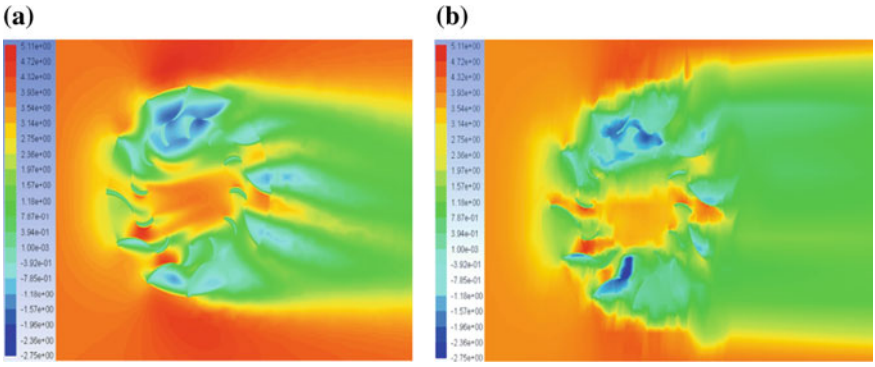


Fig. 3 Variations in axial velocity **a** ANSYS-FLUENT, **b** OpenFOAM

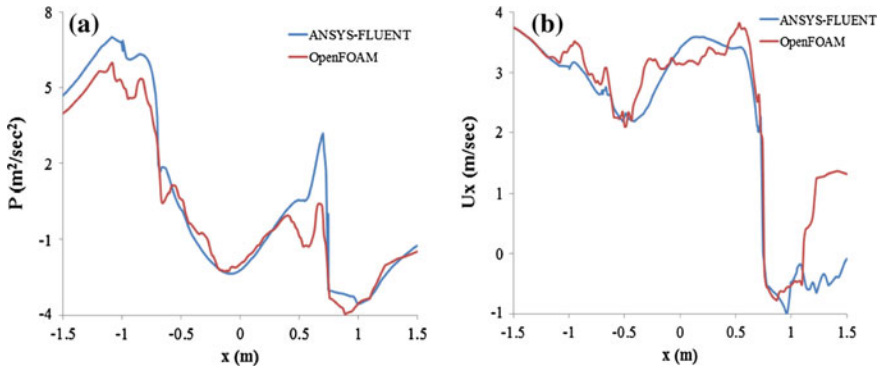


Fig. 4 Comparison between **a** Kinematic pressure and **b** Axial velocity on the analysis line from ANSYS-FLUENT and OpenFOAM

directions have been compared, as shown in Fig. 4. Nevertheless, the magnitudes of the parameters vary to some extent in both these figures.

A straight horizontal line, termed as analysis line, has been generated in both the solvers that pass through the center of the VAWT. Flow field analysis has been carried out on this line for kinematic pressure and axial velocity variations in the vicinity of the VAWT.

Figure 4a, b depict the variations in the kinematic pressure and the axial velocity on the analysis line obtained from both the solvers. It can be seen in both the figures that both the CFD solvers under consideration predict the flow features in the vicinity of the VAWT with reasonable accuracy. The trends in kinematic pressure and the axial velocity profiles remains the same in both these solvers within the VAWT; however the axial velocities are different downstream the VAWT. These values seem not to affect the torque and power outputs of the VAWT. A careful examination of this aspect will be included in future studies. It is concluded here that OpenFOAM has the ability to predict the flow behaviour in turbomachines with reasonable accuracy, and that it has the potential to replace commercial CFD packages for the numerical analysis of such machines.

From Fig. 4b, it can be seen that apart from the wake region ($x > 1$ m), the axial velocities predicted by OpenFOAM matches closely with that obtained from ANSYS-FLUENT.

VAWTs are used to harness energy from the wind, hence the torque output of the VAWT is considered to be the primary performance parameter. The computed torque outputs from ANSYS-FLUENT and OpenFOAM are 7.74 and 7.68 Nm respectively, having less than 1 % difference between them. Hence, OpenFOAM not only predicts the local flow features with reasonable accuracy, but has the tendency to predict the global performance parameters of turbomachines as well.

4 Conclusion

A study has been presented here on the effectiveness of OpenFOAM in predicting the local flow features and global performance parameters of a Vertical Axis Wind Turbine. The results have been compared against a well-known and globally used commercial CFD package called ANSYS-FLUENT. The mesh size and the modeling techniques used in both these solvers has been kept the same for a realistic comparison.

The comparative study shows close matching between the two solvers. It has been shown that OpenFOAM not only predicts the local flow features, but also the global performance parameters of a VAWT with reasonable accuracy. For this purpose, kinematic pressure and axial velocity have been chosen for analysis between the two solvers. Hence, it can be concluded that OpenFOAM can be used as an effective tool for the analysis of turbomachines.

References

1. K. Park, Optimal design of a micro vertical axis wind turbine for sustainable urban environment. Ph.D. thesis, University of Huddersfield, Huddersfield, U.K. (2013)
2. A. Shahzad, T. Asim, R. Mishra, A. Paris, Performance of a vertical axis wind turbine under accelerating and decelerating flows. Procedia CIRP **11**, 311–316 (2013)
3. K. Park, T. Asim, R. Mishra, Computational fluid dynamics based fault simulations of a vertical axis wind turbine, J. Phys.: Conf. Ser. **364**(012138)
4. G. Colley, Design, operation and diagnostics of a vertical axis wind turbine. Ph.D. thesis, University of Huddersfield, Huddersfield, U.K. (2013)
5. F. Mohammed, K. Park, S. Pradhan, R. Mishra, K. Zala, T. Asim, A. Al-Obaidi, The effect of blade angles of the vertical axis wind turbine on the output performance, in *27th International Congress of Condition Monitoring and Diagnostic Engineering*, Brisbane, Australia (2014)
6. F. Ambrosino, A. Funel, OpenFOAM and fluent features in CFD simulations on CRESCO high power computing system, *Final Workshop of Grid Projects*, PON RICERCA (2006)
7. A. Kosik, The CFD simulation of the flow around the aircraft using OpenFOAM and ANSA, *5th ANSA and μETA International Conference* (2006)
8. K. Park, T. Asim, R. Mishra, Effect of blade faults on the performance characteristics of a vertical axis wind turbine, in *26th International Congress on Condition Monitoring and Diagnostic Engineering Management*, Helsinki, Finland (2013)
9. K. Park, T. Asim, R. Mishra, Simulation based approach to predict vertical axis wind turbine faults using computational fluid dynamics, in *International Conference on Through–Life Engineering Services*, Cranfield, U.K. (2012)
10. K. Park, T. Asim, R. Mishra, Condition based monitoring of vertical axis wind turbines using computational fluid dynamics, in *39th National Conference on Fluid Mechanics and Fluid Power*, Surat, India (2012)
11. A. Shahzad, T. Asim, K. Park, S. Pradhan, R. Mishra, Numerical simulations of effects of faults in a vertical axis wind turbine's performance, in *2nd International Workshop and Congress on eMaintenance*, Lulea, Sweden (2012)
12. J. Luo, R. Issa, A. Gosman, Prediction of impeller-induced flows in mixing vessels using multiple frames of reference, in *IChemE Symposium Series*, No. 136 (1994), pp. 549–556

Measurement and Control of Forces Acting on a Solar Panel

Yuta Ikeya, Koji Fukagata, Noriaki Ichijo, Masakazu Hasegawa and Shinsuke Matsuno

Abstract The aerodynamic forces acting on a solar panel was measured in a wind tunnel and their dependency on the angle of attack and the aspect ratio of the panel was investigated using scaled models. The experiment was carried out at the Reynolds number on the order of 10^4 and 10^5. It was found that the forces have a Reynolds number dependency, which suggests that the current standard defined by Japanese Industrial Standards might not be sufficient to capture such a characteristics. Furthermore, a simple passive control method was proposed to reduce the lift force by enlarging a separation bubble over the panel. It was demonstrated that the lift force acting on the panel was successfully reduced by this control method.

1 Introduction

The utility of photovoltaic power system is one of the solutions for the lack of energy resources. It has been introduced into company buildings, apartments, and even detached houses. As solar panels are usually fixed with a tilted angle, the aerodynamic forces acting on it becomes a problem to design the equipment. It was actually reported that it was damaged because of strong wind. There is also a risk that the panels can be blown away if their fix is not strong enough.

Japanese Industrial Standards (JIS) Committee defines in JIS C8955 [1] the wind force as the force acting normal to a solar panel. Following this standard, the wind force W is calculated by

$$W = C_W \cdot \frac{1}{2}\rho U_\infty^2 A \cdot EI \tag{1}$$

Y. Ikeya (✉) · K. Fukagata
Keio University, Hiyoshi 3-14-1, Kohoku-ku, Yokohama 223-8522, Japan
e-mail: yuta.ikeya@kflab.jp

N. Ichijo · M. Hasegawa · S. Matsuno
IHI Corporation, Shin-nakahara-cho 1, Isogo-ku, Yokohama 235-8501, Japan

© Springer International Publishing Switzerland 2016

A. Segalini (ed.), *Proceedings of the 5th International Conference on Jets, Wakes and Separated Flows (ICJWSF2015)*,
Springer Proceedings in Physics 185, DOI 10.1007/978-3-319-30602-5_73

where U_∞ is wind velocity, A is the area of a panel, E is a constant dependent on the roughness of the surface where the panel is installed, and I is a constant dependent on the usage of the system. The coefficient C_W is called the wind force coefficient, which depends on the angle of attack of a solar panel. In this paper, $E = 1$ and $I = 1$ are assumed similarly to the previous studies [2, 3].

JIS proposes a formula for calculating the wind force coefficient C_W, for example,

$$C_W = 0.71 + 0.016\theta \quad (15° \leq \theta \leq 45°), \tag{2}$$

where θ is the angle of attack. Although this equation is proposed according to the wind tunnel experiment in a NEDO project [4], some experimental conditions are not clarified. Moreover, it is not applied to angles smaller than 15°, at which recent panels are sometimes installed. Because of these issues, many experimental studies have been conducted to reassess the wind force coefficient. While most of the previous experiments have been carried out at Reynolds number based on the short side length of the panel on the order of 10^4 or less, the actual Reynolds number can be on the order of 10^6 or more in the case of strong wind like a typhoon, which has the wind velocity over 30 m/s. Therefore, the first objective of the present study is to investigate the Reynolds number dependency of the wind force coefficient. Moreover, we propose a simple control method to reduce the wind force and discusses its usefulness.

2 Experiment

The experiment was performed using The Thermally Stratified Wind Tunnel of IHI Corporation, Yokohama Plant, under an isothermal condition. As shown in Fig. 1, the ground surface was set 0.2 m above the floor in the test section, on which the scale models of a solar panel are placed. The flow toward a panel was made nearly uniform by cutting out the boundary layer developed of on the ground surface on the wind tunnel.

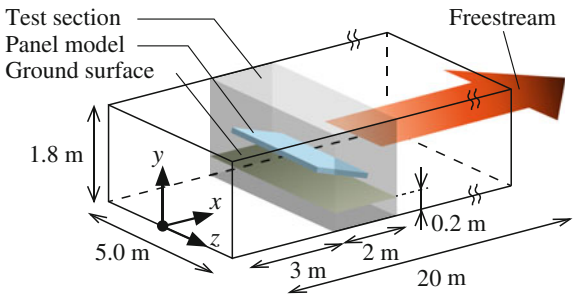


Fig. 1 Test section in the wind tunnel

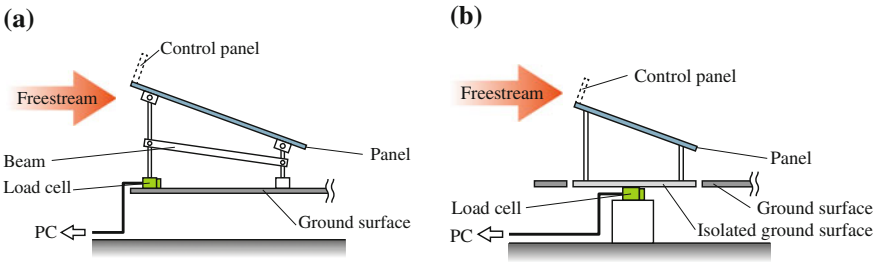
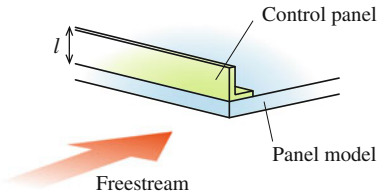


Fig. 2 Experimental setup: **a** 1/4 model; **b** 1/20 model

Fig. 3 A close-up sketch of the control panel installed on the panel models



Two scales of model were prepared for this experiment: 1/4 and 1/20 scale model, which are shown in Fig. 2. The 1/20 scale model was used for comparison with the previous study [3], of which Reynolds number is similar, i.e., $Re = 7.2 \times 10^4$, while the 1/4 scale model was used to study the case of higher Reynolds number, $Re = 2.7 \times 10^5$. Their sizes are 1.5 m × 0.90 m and 0.30 m × 0.18 m, respectively. The length of the longer side of the panel and the angle of attack were set as parameters.

The aerodynamic forces acting on the panel was measured by a load cell installed on the strut: the lift and drag forces were measured at the same time and the wind force was calculated from them. The streamwise and the wall-normal velocity components around the scale models were measured simultaneously with a hot-wire anemometer.

A simple passive control method called *a control panel* was also introduced, in which an additional short panel is fixed normally to the original panel surface at the leading edge as shown in Fig. 3. The aim of the control panel is to promote separation on the upper surface of the model, which is considered to decrease the lift. The height of the control panel was set as a parameter to see its effects on the aerodynamic forces. The experimental conditions without and with the control are listed in Tables 1 and 2. Here, b, c and l denote the longer side and the shorter side of the panel, and the length of the control panel, respectively.

Table 1 Experimental conditions without the control

Case	Scale	c [m]	b [m]	θ [°]	U_∞ [m/s]	Re
LN20	1/4	0.90	1.5	20	4.5	2.7×10^5
LM20	1/4	0.90	2.0	20	4.5	2.7×10^5
LN12	1/4	0.90	1.5	12	4.5	2.7×10^5
LM12	1/4	0.90	2.0	12	4.5	2.7×10^5
SN20	1/20	0.18	0.30	20	6.0	7.2×10^4
SM20	1/20	0.18	0.40	20	6.0	7.2×10^4
SW20	1/20	0.18	0.90	20	6.0	7.2×10^4
SN12	1/20	0.18	0.30	12	6.0	7.2×10^4
SM12	1/20	0.18	0.40	12	6.0	7.2×10^4
SW12	1/20	0.18	0.90	12	6.0	7.2×10^4

Table 2 Experimental conditions without the control

Case	Scale	c [m]	b [m]	l [m]	θ [°]	U_∞ [m/s]	Re
LN20-C10	1/4	0.90	1.5	0.090	20	4.5	2.7×10^5
LN20-C33	1/4	0.90	1.5	0.15	20	4.5	2.7×10^5
LN12-C10	1/4	0.90	1.5	0.090	12	4.5	2.7×10^5
LN12-C33	1/4	0.90	1.5	0.15	12	4.5	2.7×10^5
SN20-C10	1/20	0.18	0.30	0.018	20	6.0	7.2×10^4
SN20-C33	1/20	0.18	0.30	0.030	20	6.0	7.2×10^4
SN12-C10	1/20	0.18	0.30	0.018	12	6.0	7.2×10^4
SN12-C33	1/20	0.18	0.30	0.030	12	6.0	7.2×10^4

3 Results and Discussion

Figure 4 shows the wind force coefficient measured in the present experiment plotted together with error bars calculated from the uncertainties of the measured forces. The results of the experiment by Kimura et al. [3] are also plotted on the same figure. The broken line on the graph denotes the estimate (2) defined by JIS, where the applicable range of θ is extended just for the comparison with the experimental results. The value obtained in Case SW20 shows an excellent agreement with the result of Kimura et al. [3], which suggests that the present experiment was properly conducted. The cases at $Re = 2.7 \times 10^5$ exhibit larger values of the wind force compared to the cases at $Re = 7.2 \times 10^4$, which indicates that the wind force coefficient depends on the Reynolds number and it can exceed the estimates by JIS. Also, it is noticed that the wind force increases when the aspect ratio of the panel is increased, which is the tendency similar to the previous study [3]. This is due to the effect of finite span on the lift coefficient which applies to a wing in general [5]. Note that the error in 1/20 cases is relatively large due to the minimum resolution of the load cell used, i.e., ± 0.15 N in the normal direction.

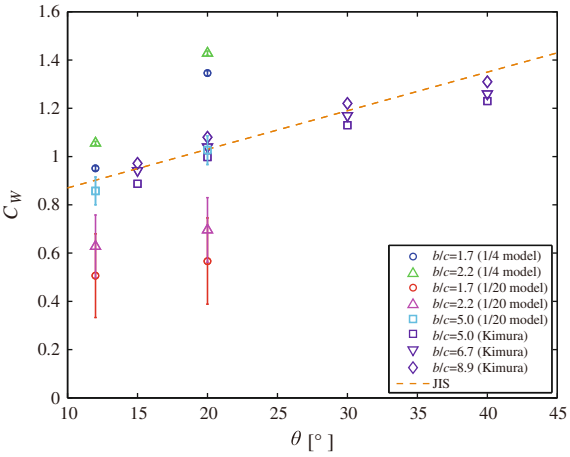


Fig. 4 The wind force coefficient, C_W, as a function of the angle of attack, θ, where b and c denote the longer and shorter sides of the panel, respectively. The results from the present experiment and the previous study by Kimura et al. [3] are plotted. The broken line is the estimate by JIS [1]

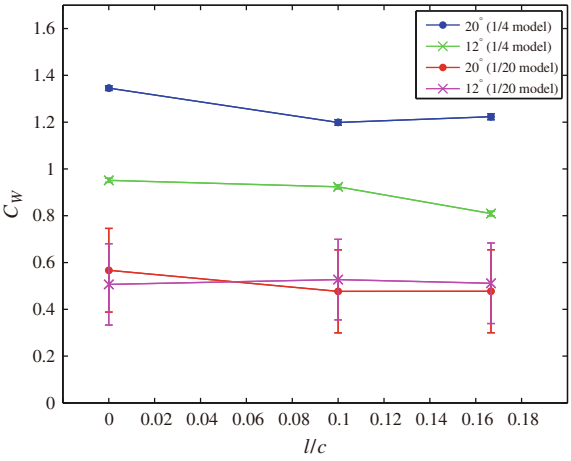


Fig. 5 The wind force coefficient, C_W, as a function of the height of the control panel, l, where l denotes the length of the control panel

Figure 5 shows the wind force coefficient when the control panel is applied, where $l/c = 0$ means the cases without control. For the $1/4$ scale model, the wind force was decreased when the control panel was attached, which means that this control worked well: C_W was decreased by 11 % at $\theta = 20°$, 14 % at $\theta = 12°$ at most. For the $1/20$ scale model, however, the uncertainty noted above was too large to confirm the effect of the control panel. From the velocity profiles (not shown), it was found that the velocity downstream of the panels was decreased when control panel was attached, which implies that the separation bubble became larger as expected: it also coincides with the result of decreased lift force.

4 Conclusions

We measured the aerodynamic forces acting on a solar panel in a wind tunnel and investigated their dependency on the angle of attack and the aspect ratio of the panel using scaled models. It can be concluded from the present study that the aerodynamic forces acting on a solar panel significantly depends on a Reynolds number and the aspect ratio, which is not accounted for the estimate of the wind force coefficient by JIS. In addition, we demonstrated that the wind force can be reduced by introducing a simple control panel which enlarges the separation bubble.

Acknowledgments The authors are grateful to Drs. Shinnosuke Obi and Keita Ando (Keio University) and Mr. Hiroaki Kuroda (Altenergy Inc.) for fruitful discussion. This work was supported through a collaborative research agreement between IHI Corporation and Keio University.

References

1. Japanese Industrial Standards Committee: Design guide on structures for photovoltaic array, JIS C 8955 (2011)
2. H. Ikeda, K. Kimura, T. Kobayashi, K. Kato, Y. Kubo, K. Ikeda, A study on the effects of wind direction on the wind force coefficient of solar panels arranged in rows for a solar panel power plant. J. Struct. Eng. **58A**, 559–566 (2012)
3. K. Kimura, T. Kobayashi, S. Kajiwara, K. Kato, Y. Kubo, E. Hidaka, H. Ikeda, Basic characteristics of wind force coefficient on a solar panel caused by their arrangements used at a solar panel power plant. J. Struct. Eng. **57A**, 592–598 (2011)
4. Kandenko Company, Ltd.: Research and development of solar cells stand. NEDO Achievement Report, No. 20090000000097 (1993) (in Japanese)
5. F.M. White, *Fluid Mechanics, Seventh Edition in SI Units* (McGraw-Hill, New York, 2013), p. 516

Part XI
Numerical Analyses

Two- and Three-Dimensional Numerical Analysis for Flow Field Characteristics at Various Low Reynolds Numbers

Donghwi Lee, Taku Nonomura, Akira Oyama and Kozo Fujii

Abstract Two- (2D) and three-dimensional (3D) simulation of flow over a flat plate at various low Reynolds numbers (*Re*) are conducted. The predictability of instantaneous flow fields in the 2D simulation and variation of the flow field characteristics with *Re* are discussed in this study. The results show that 2D simulations can predict qualitative characteristics of averaged features such as surface pressure and skin friction coefficients. Moreover, two types of critical *Re* are specified; separation *Re* (Re_s) and bubble-length *Re* (Re_{bl}). Detailed analysis for the averaged pressure distribution predictability are performed by deriving a Reynolds averaged pressure gradient equation and budgeting each term.

1 Introduction

Characteristics of low Reynolds number (*Re*) flow are drastically changed with a little variation of the *Re*. Thus, it is important to understand the flow field characteristics in a wide range of low *Re*. Especially when the laminar separation bubble (LSB) is formed, there is a possibility of accompanying unsteady three-dimensional (3D) turbulent structures, so the 3D simulation (e.g., large-eddy simulation) is necessary for accurate flow field analyses. From an engineering point of view, however, a 3D simulation still needs huge computational resources despite improvement of computer performances, and a two-dimensional (2D) simulation is more desirable.

D. Lee (✉)
Department of Aeronautics and Astronautics, University of Tokyo, Tokyo, Japan
e-mail: lee@flab.isas.jaxa.jp

T. Nonomura · A. Oyama · K. Fujii
Institute of Space and Astronautical Science, JAXA, Tokyo, Japan
e-mail: nonomura@flab.isas.jaxa.jp

A. Oyama
e-mail: oyama@flab.isas.jaxa.jp

K. Fujii
e-mail: fujii@flab.isas.jaxa.jp

© Springer International Publishing Switzerland 2016

A. Segalini (ed.), *Proceedings of the 5th International Conference on Jets, Wakes and Separated Flows (ICJWSF2015)*,
Springer Proceedings in Physics 185, DOI 10.1007/978-3-319-30602-5_74

Many studies have been performed to compare the 2D and 3D simulation in respect to the LSB. The results show that the flow near the LSB is 2D-like structures [9] and fine scale 3D turbulence provides a weaker influence to the LSB characteristics [12]. Moreover, vortex shedding frequency [15] and length of the LSB [17] are well predicted in the 2D simulation. Detailed discussion, however, is still necessary in terms of the verification of the 2D simulation reliability and variation of the flow field characteristics at various *Re*. Thus, the 2D and 3D simulations are conducted using 5 % blunt leading edge flat plate, and predictability of the 2D simulation and flow field characteristics in a wide range of low *Re* region are discussed.

2 Numerical Setup

In the 2D simulation, the 3*rd* order MUSCL [16] with SHUS [13] is employed for evaluating the convective terms. The viscous terms are computed by the 2*nd* order central differencing without any turbulence model. It has been shown that the present 2D method which does not adopt turbulence models shows good reliability for evaluating qualitative aerodynamic and flow field characteristics around the LSB [7, 9]. In the 3D simulation, the 6*th* order compact difference scheme [11] with the 10*th* order filtering [5, 11] is used for evaluating the convective and viscous terms. The 2*nd* order backward differencing converged by the ADI-SGS method [4] is adopted for time integration in both 2D and 3D simulations. The time step Δt is set to be 2.0×10^{-4}. The freestream Mach number is 0.2 and zero turbulence intensity is imposed. The chord length based *Re* (Re_c) in the 2D simulation are set to be $1, 2, 5, 1.0 \times 10^1, 2.0 \times 10^1, 5.0 \times 10^1, 1.0 \times 10^2, 2.0 \times 10^2, 5.0 \times 10^2, 1.0 \times 10^5$, and intervals of every 1,000 in the range of $1.0 \times 10^3 \sim 4.0 \times 10^4$ (50 cases). Re_c of the 3D simulation are 5.0×10^3, 6.1×10^3, 8.0×10^3, 1.1×10^4, and 2.0×10^4 (5 cases).

3 Accuracy Assessments

Three types of grid refinement are conducted at $Re_c = 2.0 \times 10^4$ to evaluate the grid convergence of the 3D simulations. The number of grid points in streamwise (N_x), wall-normal (N_y), and spanwise direction (N_z) are shown in Table 1. The outer boundary is extended to 25 times of the chord length and non-slip, adiabatic conditions are adopted on the surface. The minimum size of the grid in y direction is set to be 2.0×10^{-4}. Furthermore, 20 % of the chord length is applied to the spanwise direction with the periodic boundary condition. The maximum grid spacing and time step size based on the wall unit are shown in Table 1. It has been reported that the grid resolution of $\Delta x^+ \simeq 36$, $\Delta y^+ \simeq 1$, and $\Delta z^+ \simeq 15$ and $\Delta t^+ < 0.4$ are required to resolve coherent turbulent structures at the transitional region [6] and to obtain proper temporal resolution using an implicit time integration method [2]. The maximum grid spacing and time step size of three grids satisfy the criterion above. Figure 1 shows

Table 1 The number of grid points, maximum grid spacing and time step size values for grid convergence of the 3D simulation

Grid types	N_x	N_y	N_z	Δx^+	Δy^+	Δz^+	Δt^+
Coarse	373	285	81	10.3	0.503	6.29	0.0129
Middle	471	359	101	8.49	0.466	4.65	0.0110
Fine	571	433	125	6.45	0.455	3.67	0.0105

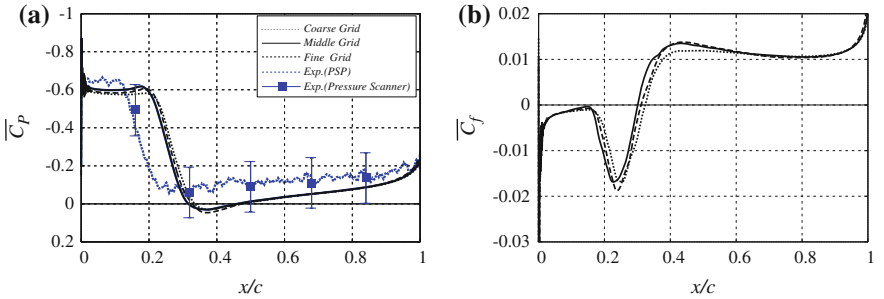


Fig. 1 **a** Pressure distribution and **b** skin friction coefficient obtained by three types of grid refinement and experimental results [1]

the averaged pressure ($\overline{C}_P$) and skin friction coefficients ($\overline{C}_f$) of three grid types and experimental data [1]. From the results, the computational results are quantitatively good agreement with the experimental result and there is no significant difference among the three grids. Therefore, the middle grid is chosen for the 3D simulation, and one cross section of the spanwise direction of the 3D grid is used in the 2D simulation.

4 Instantaneous and Averaged Features

Figure 2 shows instantaneous spanwise vorticity fields of the 2D and 3D simulations. At lower Re ($Re_c = 5.0 \times 10^3$, 6.1×10^3, and 8.0×10^3), the flow structures remains 2D in the entire flow fields in the 3D simulation, and similar fields are observed in the 2D simulation. On the other hand, at relatively higher Re ($Re_c = 1.1 \times 10^4$ and 2.0×10^4), 3D turbulent structures appear in the 3D simulation while convection of the 2D vortices without vortex breakdown are observed in the 2D simulation. In spite of the instantaneous flow fields discrepancy at higher Re, qualitatively similar features are obtained between the 2D and 3D simulations in terms of averaged flow characteristics. Figure 3 shows the averaged streamwise velocity flow fields of the 2D and 3D simulations. The averaged data is obtained by temporal and temporal-and-spanwise-averaging in the quasi-steady state for the 2D and 3D simulations, respectively. From the figure, formation and length of the LSB in the 2D simulations

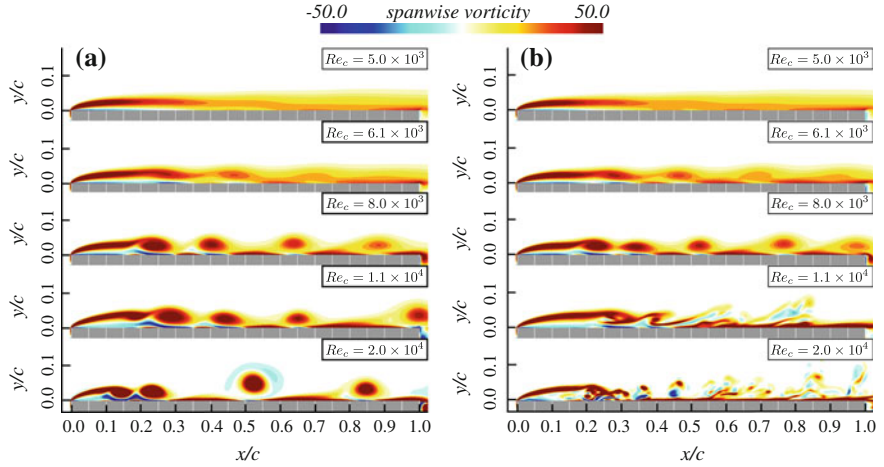


Fig. 2 Instantaneous spanwise vorticity fields of **a** 2D and **b** 3D simulation

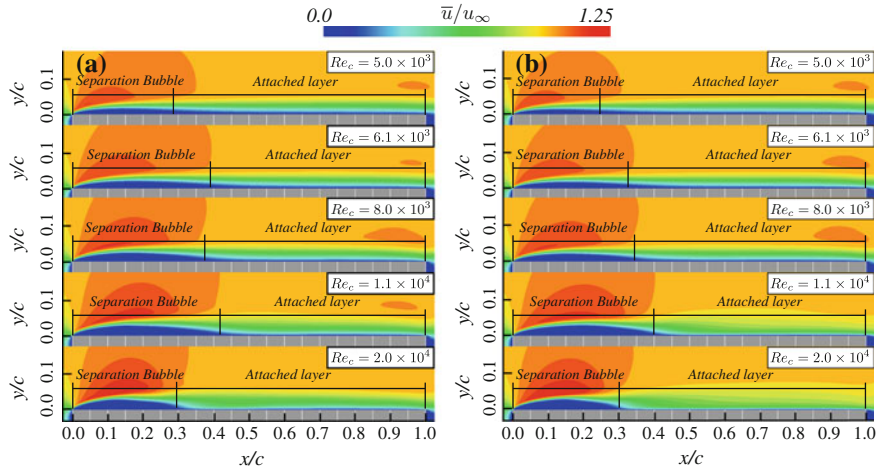


Fig. 3 Averaged streamwise velocity fields of **a** 2D and **b** 3D simulation

are similar to those in the 3D simulations. The averaged $\overline{C}_P$ and $\overline{C}_f$ are shown in Fig. 4. At lower *Re*, good agreement between the 2D and 3D results are shown in both $\overline{C}_P$ and $\overline{C}_f$ distributions. At higher *Re* where 3D structures appear, qualitatively good agreement between the 2D and 3D results are also observed in the reattachment point and shapes of each distribution except for the overshoot distribution in $\overline{C}_P$ (e.g., $x/c \simeq 0.2$ at $Re_c = 1.1 \times 10^4$) and $\overline{C}_f$ (e.g., $x/c \simeq 0.1$ at $Re_c = 2.0 \times 10^4$).

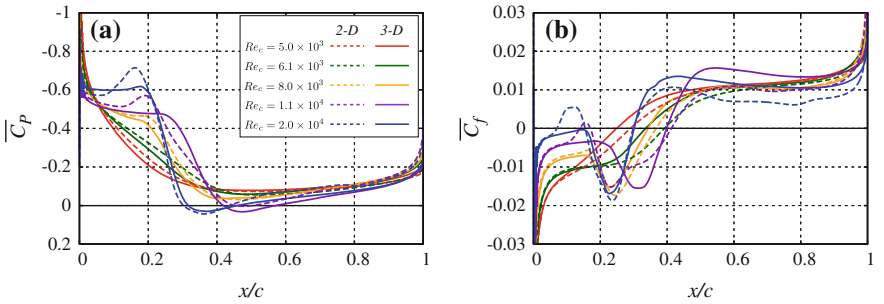


Fig. 4 **a** Pressure distribution and **b** skin friction coefficient for 2D (*dashed lines*) and 3D (*solid lines*) simulations

5 Critical Reynolds Numbers

In the previous section, it is shown that the averaged results of the 2D simulation can predict qualitative flow field features. From the observation of the 2D simulation results, the flow characteristics are changed based on the two types of critical *Re*: the separation *Re* (Re_s) and bubble length *Re* (Re_{bl}). First of all, Re_s is observed in $1.0 \times 10^3 < Re_c < 2.0 \times 10^3$. Figure 5a shows the averaged reattachment points at various *Re*. At $Re < Re_s$, the flow is fully attached as the laminar state on the entire upper surface. The averaged drag coefficient ($\overline{C}_D$) of the upper surface are in a good agreement with the Kuo's assumption [8] as shown in Fig. 5b. At $Re > Re_s$, on the other hand, the flow begins to separate from the leading edge and $\overline{C}_D$ is deviated from the Kuo's assumption. Secondly, Re_{bl} is observed in $9.0 \times 10^3 < Re_c < 1.1 \times 10^4$. After appearing the reattachment point, as shown in Fig. 6a, the bubble length becomes longer with increasing *Re*. Around Re_{bl}, however, the reattachment point moves to upstream as *Re* increases. At $Re > Re_{bl}$, as shown in Fig. 6b, $\overline{C}_D$

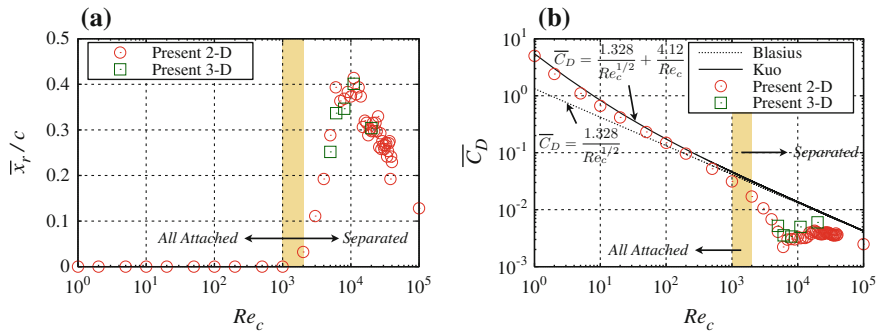


Fig. 5 Averaged **a** Reattachment points and **b** drag coefficient on the upper surface of the flat plate of the 2D and 3D simulation results with Blasius and Kuo's assumption [8]

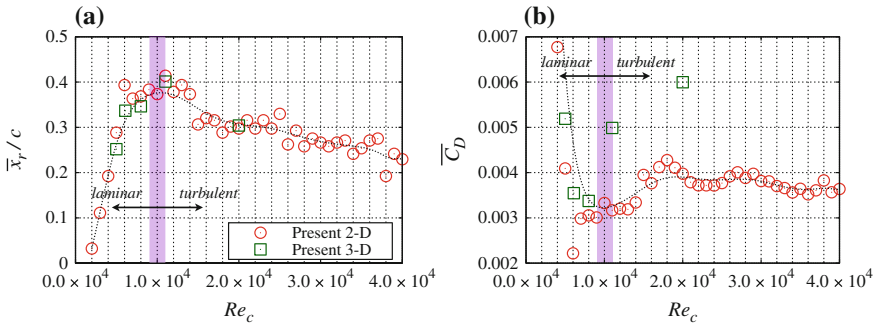


Fig. 6 Averaged **a** laminar separation bubble length and **b** drag coefficient on the upper surface of the flat plate of the 2D and 3D simulation results

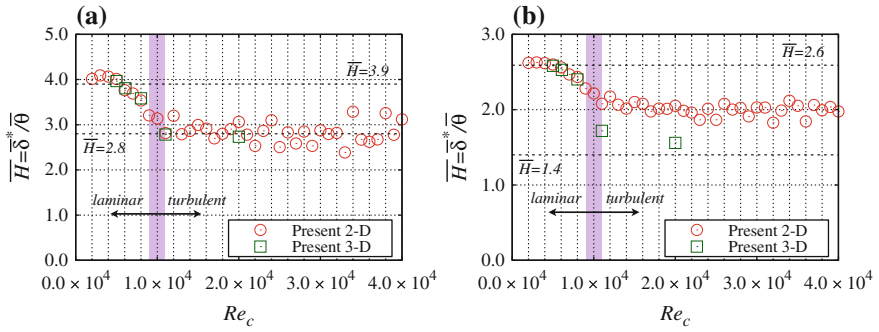


Fig. 7 Averaged shape factors at **a** reattachment points and **b** $0.7x/c$ of the 2D and 3D simulation results.

increases in the 2D simulation by decreasing the separation region. Similar trend appears in the 3D simulation but larger increment than those of the 2D simulation is observed. It is caused by formation of the turbulent boundary layer. In terms of the reattachment state, change of the reattachment state in the 2D simulation are captured as similar to those in the 3D simulation. Figure 7 shows the averaged shape factor ($\overline{H}$) at two specific points. At the reattachment points shown in Fig. 7a, $\overline{H}$ is approximately 3.9 at $Re < Re_{bl}$. At $Re > Re_{bl}$, on the other hand, $\overline{H}$ is dropped to 2.8 in both of the 2D and 3D simulation, which is similar value reported in the previous studies [3]. Figure 7b shows $\overline{H}$ at $0.7x/c$. In attached boundary layers, the conventional values of $\overline{H}$ for laminar and turbulent boundary layers are referred as $\overline{H} = 2.6$ and $\overline{H} \simeq 1.4$ [14], respectively. $\overline{H}$ of the 2D simulation is close to the value of the laminar boundary layer at $Re < Re_{bl}$. On the other hand, at $Re > Re_{bl}$, $\overline{H}$ of the 2D simulation is slightly higher but close to those of the turbulent boundary layer. Therefore, it can be considered that the turbulent reattachment occurs at $Re > Re_{bl}$, and the 2D simulation can capture change of the reattachment state despite defect of the 3D fluctuation predictability.

6 Pressure Distribution Predictability of 2D Simulation

Qualitative shape of $\overline{C}_P$ in the 2D simulation is similar to those of the 3D simulation except for the overshoot phenomena already shown in Fig. 4, Sect. 4. It can be explained by Reynolds averaged pressure gradient equation written as below [10],

$$\frac{\partial \overline{p}}{\partial x} = -\frac{\partial}{\partial x_j}(\overline{\rho}\,\overline{u}\,\overline{u}_j) + \frac{1}{Re_c}\frac{\partial}{\partial x_j}\left(\mu\frac{\partial \overline{u}}{\partial x_j}\right) + \frac{1}{3}\frac{1}{Re_c}\frac{\partial}{\partial x}\left(\mu\frac{\partial \overline{u}_j}{\partial x_j}\right) + \frac{\partial}{\partial x_j}(-\overline{\rho u' u'_j}) - \frac{\partial}{\partial x_j}\left(\overline{u}\overline{\rho' u'_j} + \overline{u}_j\overline{\rho' u'} + \overline{\rho' u' u'_j}\right), \quad (j = 1, 2). \tag{1}$$

The flow considered in the present study can be assumed as incompressible because of the low freestream Mach number. Therefore, the density fluctuation ρ' can be ignored and the last term of (1) is negligible. It is confirmed that ρ' is smaller than 0.7 % in respect to the freestream density. Thus, the averaged streamwise pressure gradient equals to sum of the convective, viscous diffusion, and Reynolds stress. Figure 8 shows the momentum budget in (1) at $Re_c = 2.0 \times 10^4$. In the 3D simulation shown in Fig. 8b, all terms of R.H.S. in (1) are negligible and the plateau pressure distribution ($\partial \overline{p}/\partial x \simeq 0$) is formed. In the 2D simulation shown in Fig. 8a, similar trends with the 3D results are observed at $0.05x/c$ and $0.075x/c$. On the other hand,

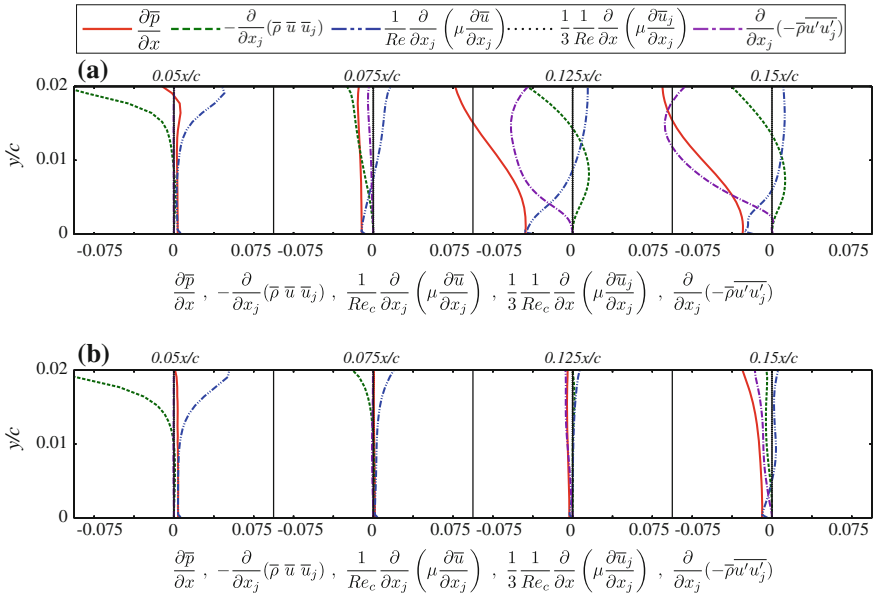


Fig. 8 Momentum budgets in (1) in the wall-normal direction for all the Reynolds numbers at $0.05x/c$, $0.075x/c$, $0.125x/c$, and $0.15x/c$ at $Re_c = 2.0 \times 10^4$

at $0.125x/c$ and $0.15x/c$ where the overshoot phenomena is observed, the Reynolds stress is generated away from the surface and they contribute to create $\partial\overline{p}/\partial x < 0$. Therefore, the negative friction coefficient near the surface is generated to balance with the Reynolds stress away from the surface, and thus the overshoot phenomena in $\overline{C}_P$ occur.

7 Conclusion

Two- (2D) and three-dimensional (3D) simulations are conducted at various low Reynolds numbers (*Re*). At lower *Re* where the flow structures are maintained as 2D ($Re_c \leq 8.0 \times 10^3$), instantaneous fields of the 2D simulation have a good consistency with those of the 3D simulation. At relatively higher *Re* ($Re_c \geq 1.1 \times 10^4$), 3D turbulent structures are observed in the 3D simulation while convection of the 2D vortices appears in the 2D simulation. Despite these discrepancy of the instantaneous fields, 2D simulations can predict qualitative characteristics of averaged properties in terms of the pressure distribution and skin friction. From the 2D simulation results, two types of critical *Re* are specified such as separation *Re* (Re_s at $1.0 \times 10^3 < Re_c < 2.0 \times 10^3$) and bubble length *Re* (Re_{bl} at $9.0 \times 10^3 < Re_c < 1.1 \times 10^4$). Especially, changing trend of the reattachment state can be predicted by the 2D simulation using the averaged shape factor at several specific positions. The reason for the overshoot that appears in $\overline{C}_P$ of the 2D simulation is explained by deriving the Reynolds averaged pressure gradient equation. From the budgeting of each term, the Reynolds stress created away from the surface contributes to generated the pressure gradient. Thus the negative friction coefficient near the surface is generated and the overshoot in $\overline{C}_P$ is created.

Acknowledgments This work was supported by the Asahi Glass Scholarship foundation and the graduate school of engineering, the university of Tokyo doctoral student special incentives program. Computer resources were provided by Japan Aerospace Exploration Agency (JAXA) Supercomputer system. This work was also partially supported by the Mars Exploration Airplane Working Group of Institute of Space and Astronautical Science, Scientific Research (A), No. 24245136.

References

1. M. Anyoji, K. Nose, S. Ida et al., Aerodynamic measurements in the Mars wind tunnel at Tohoku university. AIAA 2011–0852 (2011)
2. H. Choi, P. Moin, Effects of the computational time step on numerical solutions of turbulent flow. J. Comput. Phys. **113**, 1–4 (1994)
3. P. Dengel, H.H. Fernholz, An experimental investigation of an incompressible turbulent boudary layer in the vicinity of separation. J. Fulid Mech. **212**, 615–636 (1990)
4. K. Fujii, Simple ideas for the accuracy and efficiency improvement of the compressible flow simulation methods, in *Proceedings of International CFD Work Supersonic Transport Des:20–23* (1998)

5. D.V. Gaitonde, M.R. Visbal, Pade-type higher-order boundary filters for the Navier-Stokes equations. AIAA J. **38**, 2103–2112 (2000)
6. S. Kawai, K. Fujii, Compact scheme with filtering for large-eddy simulation of transitional boundary layer. AIAA J. **46**, 690–700 (2008)
7. R. Kojima, T. Nonomura, A. Oyama et al., Large-eddy simulation of low-Reynolds-number flow over thick and thin NACA airfoils. J. Aircr. **50**, 204–216 (2013)
8. Y.H. Kuo, On the flow of an imcompressible viscous fluid past a flat plate at moderate Reynolds numbers. J. Math. Phys. **32**, 83–101 (1954)
9. D. Lee, T. Nonomura, A. Oyama et al., Comparison of numerical methods evaluating airfoil aerodynamic characteristics at low Reynolds number. J. Aircr. **52**, 296–306 (2015)
10. D. Lee, S. Kawai, T. Nonomura et al., Mechanisms of surface pressure distribution within a laminar separation bubble at different Reynolds numbers. Phys. Fluids **27**, 023602 (2015)
11. S.K. Lele, Compact finite difference schemes with spectral-like resolution. J. Comput. Phys. **103**, 16–42 (1992)
12. M. Ripley, L. Pauley, The unsteady structure of two-dimensional steady laminar separation. Phys. Fluds A **5**, 3099–3106 (1993)
13. Shima E, Jounouchi T (1997) Role of CFD in aeronautical (No.14)-AUSM type upwind schemes, in *Proceedings of the 14th NAL Symposium on Aircra Computational Aerodynamics*, pp. 7–12
14. K. Suluksan, E. Juntasaro, Assessment of intermittency transport equations for modeling transition in boundary layers subjected to freestream turbulence. Int. J. Heat Fluid Flow **29**, 48–61 (2008)
15. D. Tafti, S. Vanka, A numerical study of flow separtion and reattachment on a blunt plate. Phys. Fluds A **7**, 1749–1759 (1991)
16. B. van Leer, Towards the ultimate conservation difference scheme. J. Comput. Phys. **23**, 101–136 (1979)
17. P. Wilson, L. Pauley, Two- and three-dimensional large-eddy simulations of a transitional separation bubble. Phys. Fluds **10**, 2932–2940 (1998)

Increasing the Critical Reynolds Number by Maximizing Energy Dissipation Problem

Takashi Nakazawa

Abstract This paper presents a numerical result for generalized eigenvalue problems in the optimum shape obtained by conducting the maximizing and minimizing problems of the energy dissipation. The shape optimization problem addressed in this paper is defined as a two-dimensional lid-driven cavity flow. As an objective cost function, the energy dissipation is used, and the domain volume is used as a constraint cost function, where the shape of the boundaries aside the top boundary is optimized. By solving a generalized eigenvalue problem, linear neutral curves between the initial domain Ω_0 and the optimum shape domains Ω_1 and Ω_2 for maximizing and minimizing problems respectively are compared. Numerical results reveal that the shape is optimized by satisfying the volume constraint. Based on generalized eigenvalue problems, the critical Reynolds numbers of the optimum shapes Ω_1 and Ω_2 are larger and smaller than that of the initial shape Ω_0.

1 Introduction

A shape optimization problem is generalized as a problem of optimizing the boundary design of a domain in which a boundary value problem of partial differential equations is defined, where the domain topology is fixed as that of the initial domain. In this problem, cost functions are defined as functionals of the domain and the solution of the boundary value problem.

Along with computer development, numerical examinations of shape-optimization problems have been conducted. Based on results of these trials, it was noted that the direct application of the gradient method often results in oscillating shapes. Subsequently, the oscillation was suppressed by reduction of the degrees of freedom on the boundary. Oscillation is caused by a lack of smoothness of the first variation. To avoid oscillation without reducing the degrees of freedom, a method using the Laplace operator as smoother was proposed by Azegami et al. [1]. This

T. Nakazawa (✉)
Tohoku University, Aoba-ku Aramaki Aza Aoba 6-3, Sendai, Japan
e-mail: nakazawa@math.is.tohoku.ac.jp

© Springer International Publishing Switzerland 2016

A. Segalini (ed.), *Proceedings of the 5th International Conference on Jets, Wakes and Separated Flows (ICJWSF2015)*,
Springer Proceedings in Physics 185, DOI 10.1007/978-3-319-30602-5_75

method was called the H^1 gradient method. In the H^1 gradient method, domain variation that minimizes the objective functional is obtained as a solution to a boundary value problem of a linear elastic continuum defined in the design domain. In fluid dynamics, Katamine et al. [2] demonstrated the applicability of the H^1 method to a shape optimization problem of an isolated body in a domain defined stationary Navier-Stokes equations as the governing equations, where the energy dissipation is used as the cost function. However, in [2], the stability of solutions of stationary Navier-Stokes equations on the optimum shape is not discussed.

By the way, the energy dissipation depending on the strain tensor $\mathbf{E(u)}$ is expressed as $\frac{2}{\mathrm{Re}} \int_\Omega \mathbf{E(u)} \cdot \mathbf{E(u)} dx$, where $\mathbf{u}$ and Ω respectively denote a velocity and the domain of interest. With increasing Re, a linear disturbance becomes unstable in case of $Re > Re_c$. As a result, the stability of the solution of the stationary Navier–Stokes equations can break down.

To define the cost function, the stationary Navier–Stokes problem is used as the main problem which is the two-dimensional lid-driven cavity flow. Using the solution of the stationary Navier–Stokes problem, the energy dissipation is used as the cost function. The shape derivative of the cost function is evaluated by using the Lagrange multiplier method. For a reshaping scheme, the H^1 gradient method is employed. In this study, the maximizing and minimizing problems of the cost function are demonstrated to obtain optimum shapes Ω_1 and Ω_2, under the volume constraint. After the shape optimization problems, flows in Ω_1 and Ω_2 are taken as base flows for the linear stability analyses. Based on the linear stability analyses, the neutral curves is determined to compare with the initial domain Ω_0.

2 Formulation of Problem

A Cartesian coordinate system is used and a position vector is generally denoted by $\mathbf{x} = (x, y)$. An initial domain $\Omega_0 = \{(x, y) \mid ([0, 1] \times [0, 1])\} \subset \mathbb{R}^2$ is considered, and the top boundary and the wall boundary are set as $\Gamma_{\mathrm{top}} = \{(x, y) \mid 0 \leq x \leq 1,\ y = 1\}$ and $\Gamma_{\mathrm{wall}} = \partial\Omega \backslash \Gamma_{top}$.

Using the initial domain, the domain variation is defined in the following way. Let $\boldsymbol{i} + \boldsymbol{\phi} : \mathbb{R}^2 \to \mathbb{R}^2$ be a bi-Lipschitz transform and D be the set of $\boldsymbol{\phi}$, where $\boldsymbol{i}$ denotes identity mapping. For a $\boldsymbol{\phi} \in D$, let a varied domain $\Omega(\boldsymbol{\phi})$ and boundary $\Gamma_{\mathrm{wall}}(\boldsymbol{\phi})$ be defined respectively as $(\boldsymbol{i} + \boldsymbol{\phi})(\Omega_0)$ and $(\boldsymbol{i} + \boldsymbol{\phi})(\Gamma_{\mathrm{wall}})$. The function space of the Fréchet derivative with respect to arbitrary domain variation $\boldsymbol{\phi}$ is defined as

$$X = \left\{ \boldsymbol{\phi} \in H^1(\mathbb{R}^2; \mathbb{R}^2) \mid \boldsymbol{\phi} = \mathbf{0} \text{ on } \Gamma_{\mathrm{top}} \right\}. \tag{1}$$

The shape derivatives of functionals are obtained as follows. For such $\varphi(\boldsymbol{x}) \in X$, the following functional is introduced:

$$L(\boldsymbol{\phi}, \boldsymbol{x}, \Omega(\boldsymbol{\phi})) = \int_{\Omega(\boldsymbol{\phi})} \zeta(\boldsymbol{\phi}, \boldsymbol{x}, \varphi(\boldsymbol{x}), \nabla\varphi(\boldsymbol{x})) dx,$$

where $\zeta(\boldsymbol{\phi}, \boldsymbol{x}, \varphi(\boldsymbol{x}), \nabla\varphi(\boldsymbol{x})) \in \mathbb{R}$ for $\nabla\varphi(\boldsymbol{x}) \in \mathbb{R}^2$. Using the shape derivative ζ' of ζ, the shape derivative JL of L is given as

$$JL(\boldsymbol{\phi}, \boldsymbol{x}, \Omega) = \int_{\Omega(\boldsymbol{\phi})} \zeta' dx + \int_{\Gamma_{\text{wall}}(\boldsymbol{\phi})} \zeta \boldsymbol{\nu} \cdot \boldsymbol{\varphi} d\gamma, \tag{2}$$

where the deformed boundary is denote by $\Gamma_{\text{wall}}(\boldsymbol{\phi})$ and where $\boldsymbol{\nu}$ denotes an outward unit normal vector on the boundary ([1] Eq. (18), p. 274).

2.1 Governing Equations and Linear Stability Analysis

Next a steady-state viscous flow of an incompressible Newtonian fluid in domain Ω_0 with boundary $\Gamma_{\text{top}} \cup \Gamma_{\text{wall}}$ is considered. A set of velocity fields $U = \{\mathbf{u} = (u, v) \in H^1(\Omega(\boldsymbol{\phi}); \mathbb{R}^2) \mid \mathbf{u} = \mathbf{u}_{\text{D}} \text{ on } \Gamma_{\text{top}},\ \mathbf{u} = \mathbf{0} \text{ on } \Gamma_{\text{wall}}\}$ is introduced, where $\mathbf{u}_{\text{D}} = \left(u_{\text{D}}, v_{\text{D}}\right)$ denotes a prescribed fluid velocity field on an inhomogeneous Dirichlet boundary. Below it is always $u_{\text{D}} = 16x^2(1-x)^2$ and $v_{\text{D}} = 0$ on Γ_{top}. As a set of a pressure fields, $Q = \left\{ q \in L^2(\Omega(\boldsymbol{\phi}); \mathbb{R}) \mid \int_{\Omega(\boldsymbol{\phi})} q dx = 0 \right\}$ is introduced.

Taking R_1 which is the length of meas$(\Gamma_{\text{top}}) = 1$, and $u_{\max}$ which is the maximum value of u_{D}, as the characteristic length and velocity, the Reynolds number is defined as $\text{Re} = \frac{u_{\max} R_1}{d}$, where d represents the kinematic viscosity. The stationary Navier–Stokes equation and the equation of continuity in non-dimensional form are considered, where $\mathbf{u}, p$ denote non dimensional velocity and pressure. The weak forms are written as

$$\int_{\Omega(\boldsymbol{\phi})} \left\{ ((\boldsymbol{u} \cdot \boldsymbol{\nabla})\boldsymbol{u}) \cdot \boldsymbol{w} - p\boldsymbol{\nabla} \cdot \boldsymbol{w} + \frac{1}{\text{Re}} (\boldsymbol{\nabla}\boldsymbol{u}^{\text{T}}) \cdot (\boldsymbol{\nabla}\boldsymbol{w}^{\text{T}}) - q\boldsymbol{\nabla} \cdot \boldsymbol{u} \right\} dx = 0, \tag{3}$$

for all $(\boldsymbol{w}, q) \in W \times Q$, where $(\boldsymbol{w}, q)$ represents trial functions for velocity $\boldsymbol{u}$ and pressure p, and $W = \left\{ \boldsymbol{w} \in H^1(\Omega(\boldsymbol{\phi}); \mathbb{R}^2) \mid \boldsymbol{w} = \mathbf{0} \text{ on } \partial\Omega(\boldsymbol{\phi}) \right\}$.

A set of velocity fields and pressure for the disturbance

$$\bar{U} = \left\{ \bar{\boldsymbol{u}} \in H^1(\Omega(\boldsymbol{\phi}); \mathbb{C}^2) \mid \bar{\boldsymbol{u}} = \mathbf{0} \text{ on } \partial\Omega(\phi) \right\},$$
$$\bar{Q} = \left\{ \bar{q} \in L^2(\Omega(\boldsymbol{\phi}); \mathbb{C}) \mid \int_{\Omega(\boldsymbol{\phi})} q dx = 0 \right\},$$

are introduced. Eigenvalue equations in weak form are written as

$$\int_{\Omega(\boldsymbol{\phi})} \{ \lambda \bar{\boldsymbol{u}} \cdot \bar{\boldsymbol{w}} + ((\boldsymbol{u} \cdot \boldsymbol{\nabla})\bar{\boldsymbol{u}}) \cdot \bar{\boldsymbol{w}} + ((\bar{\boldsymbol{u}} \cdot \boldsymbol{\nabla})\boldsymbol{u}) \cdot \bar{\boldsymbol{w}}$$
$$-\bar{p}\boldsymbol{\nabla} \cdot \bar{\boldsymbol{w}} + \frac{1}{\text{Re}} (\boldsymbol{\nabla}\bar{\boldsymbol{u}}^{\text{T}}) \cdot (\boldsymbol{\nabla}\bar{\boldsymbol{w}}^{\text{T}}) - \bar{q}\boldsymbol{\nabla} \cdot \bar{\boldsymbol{u}} \Big\} dx = 0, \tag{4}$$

for all $(\bar{\boldsymbol{w}}, \bar{q}) \in \bar{W} \times \bar{Q}$, where $(\bar{\boldsymbol{w}}, \bar{q})$ represents trial functions for $\bar{\boldsymbol{u}}$ and $\bar{p}$, and $\bar{W} = \left\{\bar{\boldsymbol{w}} \in H^1(\Omega(\boldsymbol{\phi}); \mathbb{C}^2) \mid \bar{\boldsymbol{w}} = \boldsymbol{0} \text{ on } \partial\Omega(\boldsymbol{\phi})\right\}$.

3 Shape Optimization Problem

The minimization problem of the energy dissipation under volume constraint M, which is the volume of the initial domain, is formulated as

$$\begin{aligned}
&\text{Find } \Omega_p \\
&\text{that minimizes } \pm \int_{\Omega(\boldsymbol{\phi})} \frac{2}{\mathrm{Re}} \boldsymbol{E}(\boldsymbol{u}) \cdot \boldsymbol{E}(\boldsymbol{u}) dx \\
&\text{subject to } (\boldsymbol{u}, p) \in U \times Q \text{ such that (3) and } \int_{\Omega(\boldsymbol{\phi})} dx = M.
\end{aligned}$$

As described in this paper, the shape derivative of the Lagrange function L is evaluated by application of the Lagrange multiplier method, where the Lagrange function L is written as

$$\begin{aligned}
L(\boldsymbol{\phi}, \boldsymbol{u}, p, \boldsymbol{w}, q, \Lambda) = &\pm \int_{\Omega(\boldsymbol{\phi})} \frac{2}{\mathrm{Re}} \boldsymbol{E}(\boldsymbol{u}) \cdot \boldsymbol{E}(\boldsymbol{u}) dx + \Lambda \left(\int_{\Omega(\boldsymbol{\phi})} dx - M \right) \\
&- \int_{\Omega(\boldsymbol{\phi})} \left\{ ((\boldsymbol{u} \cdot \boldsymbol{\nabla}) \boldsymbol{u}) \cdot \boldsymbol{w} - p \boldsymbol{\nabla} \cdot \boldsymbol{w} + \frac{1}{\mathrm{Re}} (\boldsymbol{\nabla} \boldsymbol{u}^{\mathrm{T}}) \cdot (\boldsymbol{\nabla} \boldsymbol{w}^{\mathrm{T}}) - q \boldsymbol{\nabla} \cdot \boldsymbol{u} \right\} dx \quad (5)
\end{aligned}$$

and $\boldsymbol{w}, q, \Lambda$ respectively denote the Lagrange multiplier for velocity $\boldsymbol{u}$ and pressure q, the volume constraint. The shape derivative JL of L with respect to arbitrary variation of $(\boldsymbol{\varphi}, \boldsymbol{u}', p', \boldsymbol{w}', q', \Lambda') \in X \times W \times Q \times W \times Q \times \mathbb{R}$ is obtainable as

$$JL(\boldsymbol{\phi}, \boldsymbol{u}, p, \boldsymbol{w}, q, \Lambda) = L_{\boldsymbol{\phi}}[\boldsymbol{\varphi}] + L_{\boldsymbol{u},p}[\boldsymbol{u}', p'] + L_{\boldsymbol{w},q}[\boldsymbol{w}', q'] + L_{\Lambda}[\Lambda'], \quad (6)$$

where

$$\begin{aligned}
&L_{\boldsymbol{\phi}}[\boldsymbol{\varphi}] = \pm \int_{\Gamma_{\mathrm{wall}}(\boldsymbol{\phi})} \frac{2}{\mathrm{Re}} \{\boldsymbol{E}(\boldsymbol{u}) \cdot \boldsymbol{E}(\boldsymbol{u})\} \boldsymbol{\nu} \cdot \boldsymbol{\varphi} d\gamma + \int_{\Gamma_{\mathrm{wall}}(\boldsymbol{\phi})} \Lambda \boldsymbol{\nu} \cdot \boldsymbol{\psi} d\gamma \\
&- \int_{\Gamma_{\mathrm{wall}}(\boldsymbol{\phi})} \left\{ ((\boldsymbol{u} \cdot \boldsymbol{\nabla}) \boldsymbol{u}) \cdot \boldsymbol{w} - p \boldsymbol{\nabla} \cdot \boldsymbol{w} + \frac{1}{\mathrm{Re}} (\boldsymbol{\nabla} \boldsymbol{u}^{\mathrm{T}}) \cdot (\boldsymbol{\nabla} \boldsymbol{w}^{\mathrm{T}}) - q \boldsymbol{\nabla} \cdot \boldsymbol{u} \right\} \boldsymbol{\nu} \cdot \boldsymbol{\varphi} d\gamma, \\
&L_{\hat{\boldsymbol{u}}, \hat{p}}[\hat{\boldsymbol{u}}', \hat{p}'] = \pm 4 \int_{\Omega(\boldsymbol{\phi})} \frac{1}{\mathrm{Re}} \boldsymbol{E}(\boldsymbol{u}') \cdot \boldsymbol{E}(\boldsymbol{u}) dx \\
&- \int_{\Omega(\boldsymbol{\phi})} \left\{ \left((\boldsymbol{u}' \cdot \boldsymbol{\nabla}) \boldsymbol{u} \right) \cdot \boldsymbol{w} + \left((\boldsymbol{u} \cdot \boldsymbol{\nabla}) \boldsymbol{u}' \right) \cdot \boldsymbol{w} - p' \boldsymbol{\nabla} \cdot \boldsymbol{w} + \frac{1}{\mathrm{Re}} (\boldsymbol{\nabla} \boldsymbol{u}'^{\mathrm{T}}) \cdot (\boldsymbol{\nabla} \boldsymbol{w}^{\mathrm{T}}) - q \boldsymbol{\nabla} \cdot \boldsymbol{u}' \right\} dx, \\
&L_{\boldsymbol{w},q}[\boldsymbol{w}', q'] = - \int_{\Omega(\boldsymbol{\phi})} \left\{ ((\boldsymbol{u} \cdot \boldsymbol{\nabla}) \boldsymbol{u}) \cdot \boldsymbol{w}' - p \boldsymbol{\nabla} \cdot \boldsymbol{w}' + \frac{1}{\mathrm{Re}} (\boldsymbol{\nabla} \boldsymbol{u}^{\mathrm{T}}) \cdot (\boldsymbol{\nabla} \boldsymbol{w}'^{\mathrm{T}}) - \hat{q}' \boldsymbol{\nabla} \cdot \boldsymbol{u} \right\} dx \\
&L_{\Lambda}[\Lambda'] = \Lambda' \left(\int_{\Omega(\boldsymbol{\phi})} dx - M \right).
\end{aligned}$$

Stationary conditions for the variables $\boldsymbol{u}', \boldsymbol{w}'$ and p', q', which are known as the Kuhn–Tucker conditions in the optimization theory ([1], Sect. 4.2 Optimality criteria, p. 275), are the following.

$$L_{\boldsymbol{u},p}[\boldsymbol{u}', p'] = 0 \quad \forall (\boldsymbol{u}', p') \in W \times Q, \tag{7}$$

$$L_{\boldsymbol{w},q}[\boldsymbol{w}', q'] = 0 \quad \forall (\boldsymbol{w}', q') \in W \times Q, \tag{8}$$

$$L_{\Lambda}[\Lambda'] = 0. \tag{9}$$

Equations (8), (9) agrees with the weak form of the stationary Navier-Stokes equations (3) and the volume constraint. Equation (7) is obtained as the weak form of the adjoint equations of (3) for $(\boldsymbol{w}, q) \in W \times Q$.

By substituting $(\boldsymbol{u}, p)$ and its adjoint variables $(\boldsymbol{w}, q)$ satisfying (8) and (7) into (6), the shape derivative JL of the Lagrange function L is obtained as

$$JL(\boldsymbol{\phi}, \boldsymbol{u}, p, \boldsymbol{w}, q) = \int_{\Gamma_{\text{wall}}(\boldsymbol{\phi})} G\boldsymbol{v} \cdot \boldsymbol{\varphi} d\gamma, \tag{10}$$

where $(\boldsymbol{u}, p)$ and its adjoint variables $(\boldsymbol{w}, q)$ meet (7) and (8) of the Kuhn–Tucker conditions, and the remainder of the Kuhn–Tucker conditions (9) are clear because of $\int_{\Omega(\boldsymbol{\phi})} dx = M$. Regarding to $L_{\boldsymbol{\phi}}[\boldsymbol{\varphi}]$, $\boldsymbol{\nabla} \cdot \boldsymbol{u} = \boldsymbol{\nabla} \cdot \boldsymbol{w} = 0$ in $\Omega(\phi)$ and $\hat{\boldsymbol{w}} = \boldsymbol{0}$ on $\Gamma_{\text{wall}}(\boldsymbol{\varphi})$ are substituted into $L_{\boldsymbol{\phi}}[\boldsymbol{\varphi}]$. As described in this paper, $G = G_0 + G_1$ denotes the sensitivity as

$$G_0 = \frac{1}{\text{Re}} \left\{ \pm 2\boldsymbol{E}(\boldsymbol{u}) \cdot \boldsymbol{E}(\boldsymbol{u}) - (\boldsymbol{\nabla}\boldsymbol{u}^{\text{T}}) \cdot (\boldsymbol{\nabla}\boldsymbol{w}^{\text{T}}) \right\}, \quad G_1 = \Lambda.$$

4 Reshaping Scheme

The H^1 method is applicable to optimize the geometrical domain shape if the shape gradient is obtained. The H^1 method has been proposed as a procedure for solving the domain variation $\boldsymbol{\varphi} \in X$ by

$$c_a \int_{\Omega(\boldsymbol{\phi})} \boldsymbol{E}(\boldsymbol{\varphi}) \cdot \boldsymbol{E}(\boldsymbol{y}) dx = - \int_{\Gamma_{\text{wall}}(\boldsymbol{\phi})} G\boldsymbol{v} \cdot \boldsymbol{y} d\gamma, \tag{11}$$

for all $\boldsymbol{y} \in W$, where c_a is a positive constant to control the step size. The reshaping of the boundary can be operated with the degree of freedom discretized with the finite element method for numerical calculations, without reductions of the degree of freedom on the boundary and in the domain. Taking account of a bilinear equation (11) and $G = G_0 + G_1$, the domain variation is expressed as $\boldsymbol{\varphi} = \boldsymbol{\varphi}_0 + \Lambda\boldsymbol{\varphi}_1$.

By calculating (11), $\boldsymbol{\varphi}_0, \boldsymbol{\varphi}_1 \in X$ are obtained after substituting $\boldsymbol{\varphi} = \boldsymbol{\varphi}_0 + \Lambda\boldsymbol{\varphi}_1$ into (11). Based on a previous study ([3], Problem 7, p. 7, (30)), the Lagrange multi-

plier Λ for the volume constraint is determined by calculating the following expression $\int_{\Gamma_{\text{wall}}(\boldsymbol{\phi})} \boldsymbol{\nu} \cdot \boldsymbol{\varphi}_0 d\gamma + \Lambda \int_{\Gamma_{\text{wall}}(\boldsymbol{\phi})} \boldsymbol{\nu} \cdot \boldsymbol{\varphi}_1 d\gamma = 0$. Finally, because $\boldsymbol{\varphi}_0, \boldsymbol{\varphi}_1, \Lambda$ are given, the domain $\boldsymbol{x} \in \Omega(\boldsymbol{\phi})$ is moved into $\boldsymbol{x} + \boldsymbol{\varphi} \in \Omega(\boldsymbol{\phi})$.

5 Numerical Calculations and Discussions

In this study, firstly, the maximization and minimization problems of the energy dissipation under volume constraint are demonstrated to obtain optimal domain Ω_1, Ω_2, respectively, based on the numerical procedures of [2]. And secondly, generalized eigenvalue problem (4) is solved in Ω_1, Ω_2, using velocity fields in Ω_1, Ω_2 as base flows. FreeFEM++ is used for the numerical calculations. In this study, we use a finite-element model with the number of nodes and elements (8281, 16200), where the P2/P1 finite element for the velocity and the pressure is used to spatially discretize all the equations.

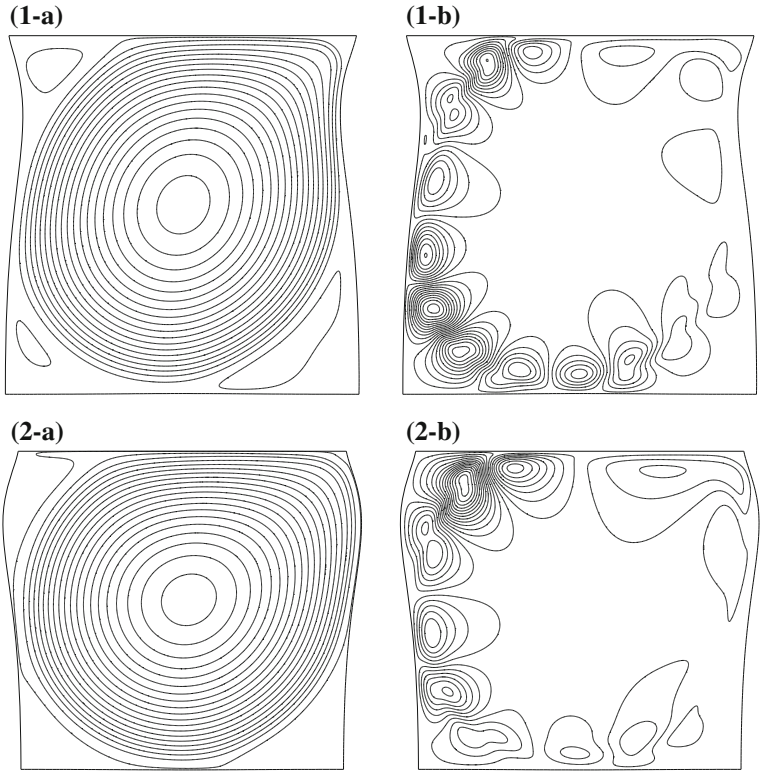


Fig. 1 **a** and **b** depict the stream function of stationary velocity fields and an absolute value real parts of eigenfunctions in the optimum domains Ω_1, and **c** and **d** for Ω_2

Figure 1 shows the stream function of stationary velocity fields and an absolute value of real parts of eigenfunctions in the optimum domains Ω_1, Ω_2 at Re = 11500. As a result of the shape optimization problem, the side walls are moved in the inward and outward directions, respectively. Furthermore, at Re = 11500, generalized eigenvalue problems are solved to depict eigenvalues for the initial shape Ω_0 and the optimum shapes Ω_1, Ω_2, as presented in Fig. 2. In case of Fig. 2a, the maximum value of real parts of eigenvalues on Ω_1 is smaller than that on Ω_0. On the other hand, for Fig. 2b, the maximum value of real parts of eigenvalues on Ω_2 is larger than that on Ω_0. Next, generalized eigenvalue problems from Re = 9500 to 12500 are solved to depict linear neutral curves for the initial shape Ω_0 and the optimum shapes Ω_1, Ω_2, as presented in Fig. 3. As figure shows, the critical Reynolds numbers of the optimum shapes Ω_1, Ω_2 are larger and smaller than that of the initial shape Ω_0.

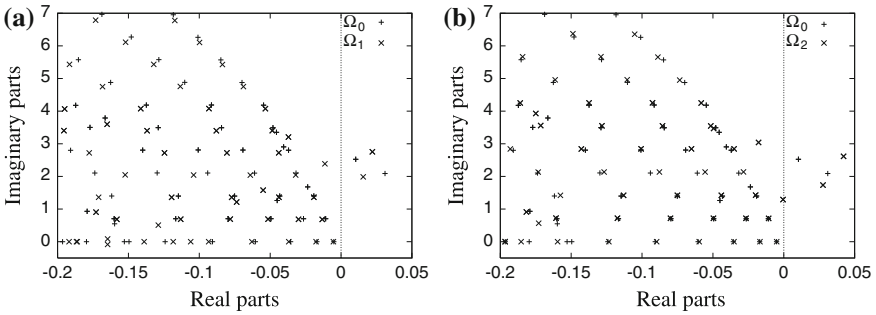


Fig. 2 Distributions of real and imaginary parts of eigenvalues for the initial shape Ω_0 and the optimum shapes Ω_1, Ω_2 at Re = 11500

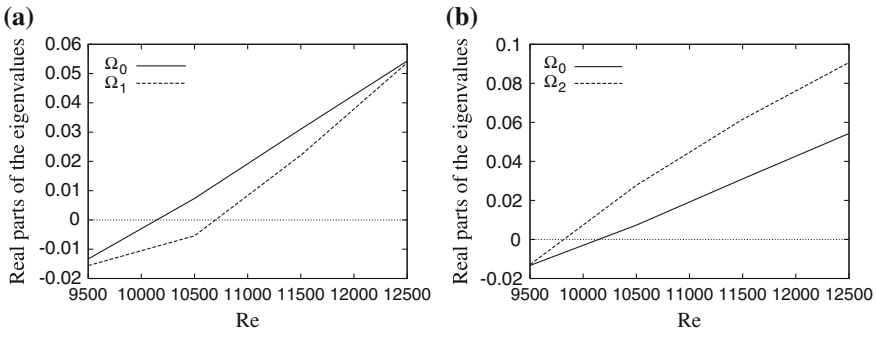


Fig. 3 Linear neutral curves for the initial shape Ω_0 and the optimum shapes Ω_1, Ω_2

6 Conclusions

In this study, on the lid-driven cavity flow, the shape optimizations for the maximizing and minimizing problems for the energy dissipation are demonstrated. And generalized eigenvalue problems in Ω_0, Ω_1 and Ω_2 are also solved to compare eigenvalues with each other. As result of numerical calculations, it is confirmed that the maximizing problem can make the critical Reynolds number Re_c increase, and Re_c is decreased for the minimizing problem. However, the physical cause of changes of Re_c by the shape optimization problem considered is not investigated here.

References

1. H. Azegami, Z. Wu, Domain optimization analysis in linear elastic problems: approach using traction method. JSME Int. J. Ser. A **39**, 272–278 (1996)
2. E. Katamine, Y. Nagatomo, H. Azegami, Shape optimization of 3D viscous flow fields. Inverse Probl. Sci. Eng. **17**, 105–114 (2009)
3. K. Shintani, H. Azegami, Shape optimization for suppressing brake squeal. Struct. Multi. Optim. doi:10.1007/s00158-014-1102-2